



BRNO UNIVERSITY OF TECHNOLOGY

VYSOKÉ UČENÍ TECHNICKÉ V BRNĚ

FACULTY OF ELECTRICAL ENGINEERING AND COMMUNICATION

FAKULTA ELEKTROTECHNIKY A KOMUNIKAČNÍCH TECHNOLOGIÍ

DEPARTMENT OF MICROELECTRONICS

ÚSTAV MIKROELEKTRONIKY

ADVANCED THIN FILMS AND MICROFABRICATION TECHNIQUES FOR SENSORS AND MICROFLUIDIC SYSTEMS

POKROČILÉ TENKÉ VRSTVY A TECHNIKY MIKROOBRÁBĚNÍ PRO SENZORY
A MIKROFLUIDNÍ SYSTÉMY

HABILITATION THESIS

HABILITAČNÍ PRÁCE

AUTHOR

Autor

Ing. Imrich Gablech, Ph.D.

BRNO 2024

Abstract

My habilitation thesis explores the advanced techniques and applications of thin films and microfabrication and demonstrates their essential roles in modern planar technologies. Thin films, known for their unique physical and chemical properties, are crucial when combined with microfabrication techniques, allowing for precise pattern creation down to the nanometer scale. I covered fundamental aspects of thin films, their characterization methods, and various deposition techniques, highlighting their applications in sensors, microfluidics, and other devices and structures. Furthermore, I examined how thin films are used in sensor technology and contribute to fabricating complex microfluidic devices for biological and chemical analysis. Additionally, I discussed the use of thin films in optical and electronic devices and their role in protective coatings. Microfabrication techniques such as lithography, etching, and doping are essential for producing these advanced devices. The work I contributed to supports all the mentioned chapters.

Keywords

Thin films, characterization methods, deposition techniques, microfabrication, sensors, microfluidics.

Abstrakt

V mé habilitační práci zkoumám pokročilé techniky a aplikace tenkých vrstev a mikroobrábění a ukazuji jejich důležitou roli v moderních planárních technologiích. Tenké vrstvy, které jsou známé pro své jedinečné fyzikální a chemické vlastnosti, jsou nezbytné pro kombinaci s technikami mikroobrábění, což umožňuje přesné vytváření motivů až do velikosti v řádu nanometrů. V práci se zabývám základními aspekty tenkých vrstev, metodami jejich charakterizace, různými depozičními technikami a zdůrazňuje jejich aplikace v senzorech, mikrofluidice a dalších zařízeních a strukturách. Dále popisuji využití tenkých vrstev v technologii senzorů a jak přispívají k výrobě komplexních mikrofluidních zařízení pro biologickou a chemickou analýzu. V habilitační práci také diskutuji využití tenkých vrstev v optických a elektronických zařízeních a jejich roli v ochranných povlacích. S tím spojené techniky mikroobrábění, jako je litografie, leptání a dopování, jsou nezbytné pro výrobu těchto pokročilých zařízení. Všechny zmíněné kapitoly jsou podpořeny články, na kterých jsem se podílel.

Klíčová slova

Tenké vrstvy, charakterizační metody, depoziční metody, mikroobrábění, senzory, mikrofluidika.

In Brno / V Brně dne: 1. 8. 2024

Ing. Imrich Gablech, Ph.D.

Content

1	INTRODUCTION	4
2	THEORETICAL PART	6
2.1	FUNDAMENTALS OF THIN FILMS	6
2.1.1	<i>Physical and chemical properties</i>	6
2.1.2	<i>Deposition techniques</i>	9
2.1.3	<i>Material characterization techniques</i>	19
2.2	MICROFABRICATION TECHNIQUES	26
2.2.1	<i>Lithography techniques</i>	26
2.2.2	<i>Etching techniques</i>	29
2.2.3	<i>Doping and Surface Modification</i>	31
2.3	THIN FILMS AND MICROFABRICATION IN SENSOR APPLICATIONS	32
2.3.1	<i>Residual stress control in Ti thin films prepared by Kaufman ion-beam source deposition for MEMS devices (Manuscript 1)</i>	33
2.3.2	<i>Preparation of AlN piezoelectric thin films using a dual Kaufman ion-beam source setup (Manuscript 2)</i>	34
2.3.3	<i>Utilization of MEMS-based micro-bolometers for energy monitoring of surface plasmon resonance of silver nanoparticles (Manuscript 3)</i>	34
2.3.4	<i>MEMS-based cantilevers for investigation of graphene electrical properties changes due to induced mechanical strain (Manuscript 4)</i>	35
2.3.5	<i>Technology for fabrication of piezoelectric harvesters without need of silicon-on-insulator wafers (Manuscript 5)</i>	36
2.3.6	<i>Selective wet etching of SiO₂ sacrificial layer for MEMS devices (Manuscript 6)</i>	36
2.3.7	<i>Nanostructures-based gas sensor for H₂ and NO₂ (Manuscript 7)</i>	37
2.4	APPLICATIONS IN MICROFLUIDICS	38
2.4.1	<i>Design and fabrication of complex microfluidic geometries (Manuscript 8)</i>	38
2.4.2	<i>Microfluidics heat transfer (Manuscript 9)</i>	39
2.4.3	<i>Microfluidics with embedded heater for cryogenic experiments (Manuscript 10)</i>	40
2.5	PROTECTIVE COATINGS AND BIOMEDICAL APPLICATIONS	40
2.5.1	<i>Development of high-performance microelectrode arrays (Manuscript 11)</i>	41
2.5.2	<i>Development of sub-micrometer PEDOT transistors for signal recording (Manuscript 12)</i>	42
2.6	MICRO- AND NANOSTRUCTURED SURFACES	43
2.6.1	<i>Micropillars for cellular traction force evaluation (Manuscript 13)</i>	43
2.6.2	<i>Development of hydrophilic and superhydrophobic surfaces (Manuscript 14)</i>	44
3	CONCLUSION	45
4	REFERENCES	47
5	MANUSCRIPTS	60

1 INTRODUCTION

Thin films are fundamental elements of modern technologies, significantly contributing to various applications, from electronics to sensors. In today's fast-paced technological advancements, thin films are crucial for developing high-performance materials and devices that power smartphones, medical devices, and environmental sensors. As new applications and efforts demand smaller, more efficient, and more powerful devices, the importance of thin film technology increases rapidly. [1-3]

High-performance sensing devices require specific electrical, mechanical, optical, and chemical properties, which can be achieved through several microtechnology processes. Incorporating graphene and other two-dimensional materials into thin films has created highly responsive sensors capable of detecting subtle changes in environmental conditions. These sensors have applications in various fields, including environmental monitoring, healthcare diagnostics, and industrial process control. [4,5]

Thin films also play an essential role in fabricating complex microfluidic devices, providing precise control over their structural and functional properties. Techniques such as photolithography, microfabrication or femtosecond laser photoablation, and various coating and milling methods enable the creation of desired microfluidic channels and structures suitable for biological and chemical analysis. These advancements are fundamental for developing lab-on-a-chip (LOC) devices used in point-of-care (POC) and point-of-need (PON) diagnostics focused on environmental testing and biochemical assays. [3,6,7]

The advancement of optical and electronic devices heavily depends on thin films. Materials such as indium tin oxide (ITO), zinc oxide (ZnO), and various semiconducting polymers create thin films with specific electronic and optical properties. These materials are crucial for producing displays, solar cells, light-emitting diodes (LEDs), and other optoelectronic devices. The ability to deposit ultra-thin, uniform layers with high precision is essential for achieving the desired performance characteristics in these devices. [8-10]

Protective coatings are another essential area of interest for thin films, shielding devices, or materials against corrosion, wear, and other forms of degradation. Hard coatings like titanium nitride (TiN), aluminum nitride (AlN), including their composites such as TiAlN, and diamond-like carbon (DLC) are applied on cutting tools, medical implants, and other components to extend their lifespan and enhance performance. The versatility of thin film deposition techniques enables the creation of coatings with optimized properties, fulfilling the specific requirements of various applications. [11-13]

Integration of thin films with micro- and nanostructured materials is widely used to improve the properties and reliability of advanced applications. Combining thin films with nanoparticles or nanowires allows for the preparation of composite materials with enhanced properties, such as increased mechanical strength or improved thermal conductivity. These composites can be tailored for specific uses, ranging from aerospace components to thermal management systems in electronics. [14-17]

Microfabrication techniques are crucial in producing thin films and the devices that utilize them. Standard deposition techniques are divided into two main categories: physical vapor deposition (PVD) and chemical vapor deposition (CVD). These methods are commonly employed to create thin films with precise control over their properties. Each method offers unique advantages but has drawbacks, enabling the fabrication of films with the desired electrical and mechanical properties, which can be verified by several characterization techniques ranging from simple electrical measurements to sophisticated material analyses. For example, CVD allows for the deposition of highly uniform films over large areas, making it suitable for semiconductor manufacturing. PVD methods are widely used for depositing metal and dielectric films, which are essential for creating multilayer structures in electronic devices. Microfabrication involves techniques such as lithography, etching, and doping combined with thin films to create complex microstructures and devices. Lithography, including photolithography and electron-beam lithography, patterns high-resolution thin films. Etching techniques, such as reactive ion etching (RIE), deep reactive ion etching (DRIE), and wet chemical etching, selectively remove material, creating desired patterns and structures. Conversely, doping processes modify the electrical properties of semiconductor materials, enabling the creation of p-n junctions and other electronic components. [18-20]

Therefore, microfabrication techniques became vital in developing microelectromechanical systems (MEMS) and nanoelectromechanical systems (NEMS), which integrate mechanical and electrical components at the microscale and nanoscale. MEMS, primarily, are commonly utilized in a wide range of applications, including sensors, actuators, and communication devices, where the high precision and versatility of microfabrication techniques are required to reach exact mechanical and electrical parameters. [21]

Overall, thin films and microfabrication are rapidly evolving, with ongoing research focused on developing new materials and improving existing technologies. The unique properties of thin films, combined with the precision and versatility of microfabrication techniques, offer significant potential for various applications, from electronics and energy storage to catalysis and biomedical devices. In conclusion, thin films represent an important area of research and development in modern science and engineering. Their ability to be precisely engineered and integrated into various devices makes them central in numerous technological advancements. [13,22]

2 THEORETICAL PART

In this habilitation thesis, I explored the advanced techniques and applications of thin films, materials characterization, and microfabrication, emphasizing their critical roles in developing sensors and microfluidic devices based on thin films. Thin films' unique physical and chemical properties, such as optical transparency with electrical conductivity and chemical resistance as well as piezoelectric properties, make them essential in modern technology when combined with microfabrication techniques, which allow us to create patterns at the limiting scale from units of nanometers to tens of nanometers.

The following sections of this thesis explore the fundamental aspects of thin films, their characterization and deposition techniques and microfabrication methods, and their applications in various fields. Additionally, the thesis demonstrates the role of microfabrication techniques in creating devices and structures based on the material properties of thin films.

2.1 Fundamentals of thin films

Thin films are defined as material layers with thicknesses ranging from a few nanometers to several micrometers. They can be classified based on their composition (metallic, ceramic, and organic or polymeric), electrical conductivity (conductors, semi-conductors, or insulators), or structure (amorphous, polycrystalline, or crystalline). Thin films are used extensively in electronics, optics, and materials science due to their customizable properties. [1]

2.1.1 Physical and chemical properties

Thin films exhibit different physical and chemical properties than their bulk counterparts, including electrical conductivity, optical transparency, mechanical strength, and chemical stability. The control of these properties depends on the chosen deposition method and its conditions, making them essential for applications in semiconductor devices, photovoltaic cells, sensors, actuators, protective coatings, and flexible electronics. [1]

The electrical conductivity of thin films can significantly differ from bulk materials due to film thickness, grain size, and defects or impurities. Depending on the specific application and the material's properties, these variations can lead to enhanced or diminished conductivity. For instance, due to scattering at grain boundaries and surfaces, thin films of metals like Au, Ti, Cu, and Al can exhibit lower conductivity than their bulk counterparts. [23-25]

The modern and straightforward use of thin films is for fabricating thin film transistors (TFTs). TFTs are critical in modern display technologies, including liquid crystal displays (LCDs) and organic light-emitting diode (OLED) displays. TFTs enable the control of individual pixels in these displays, allowing for high resolution and low power consumption. Additionally, thin films of transparent conductive oxides (TCOs) like ITO and aluminum-doped zinc oxide (AZO) are widely used in applications requiring transparency and conductivity. These materials are essential for touchscreens, solar cells, and flat-panel displays. The ability

to deposit these films with uniform thickness and precise control over their electrical properties is crucial for achieving high operation performance. [26-32]

MEMS and other sensor technologies often rely on metal thin films. Au thin films are frequently used due to their excellent conductivity and resistance to oxidation, making them ideal for electrical contacts and interconnections in MEMS devices. Pt is often used in sensors due to its stability and resistance to high temperatures, which is beneficial for applications such as temperature sensors and catalytic sensors. Ti and NiCr thin films are utilized for their mechanical properties and ability to form strong adhesion layers between different materials. [33-40]

Moreover, conductive polymers such as polyaniline and poly(3,4-ethylenedioxythiophene) polystyrene sulfonate (PEDOT:PSS) are increasingly used in thin film applications for their flexibility, processability, and tunable electrical properties. These materials are found in flexible electronics, wearable devices, and organic solar cells. [41-43]

The control of electrical conductivity in thin films is also critical for developing sensors and actuators. For instance, aluminum nitride (AlN) and lead zirconate titanate (PZT) are two widely used piezoelectric thin films with distinct advantages. AlN is favored for its high thermal conductivity, chemical stability, and compatibility with silicon-based technologies, making it suitable for integration into MEMS devices. AlN thin films are commonly used in high-frequency surface acoustic wave devices, bulk acoustic wave resonators, and as substrates in microelectronics due to their excellent piezoelectric properties and compatibility with standard semiconductor processes. [44-48]

On the other hand, PZT offers higher piezoelectric coefficients, which makes it more effective in converting electrical signals into mechanical movement and vice versa. This characteristic makes PZT ideal for applications requiring high sensitivity, such as precision actuators and sensors in NEMS. However, PZT's integration with silicon technology is more complex due to potential lead contamination and processing difficulties. [49-51]

Thermoelectric thin films, such as bismuth telluride (Bi_2Te_3) and silicon-germanium (SiGe) alloys, can generate electricity from temperature gradients, offering potential applications in energy harvesting and thermal management systems. These films are integral to developing devices that convert waste heat into usable electrical energy, enhancing the efficiency of various electronic systems. [52-54]

Mechanical properties of thin films, such as hardness, elasticity (Young's modulus), and adhesion, are critical for their performance in various applications. Flexible materials like parylene, polyimide, and metallic thin films such as Al, Au, or Ti exhibit suitable values of Young's modulus, making them ideal for use in MEMS and flexible electronics. These materials are designed to ensure reliability and durability in applications where flexibility and robustness are essential. Parylene, known for its flexibility and chemical resistance, is widely used as an insulating layer and protective coating in flexible electronic devices. Polyimide, valued for its thermal stability, flexibility, and excellent mechanical properties, is commonly employed in flexible circuits and as an insulating layer. [55-63]

In addition to these materials, silicon nitride (Si_3N_4) is frequently used in MEMS applications for its high mechanical strength, low internal stress, and excellent thermal and chemical stability. Silicon carbide (SiC) also applies in environments requiring high hardness and resistance to wear and thermal degradation. TiN, well-known for its hardness and corrosion resistance, is also used in protective coatings for tools and components exposed to harsh conditions. It is often employed in bioelectronics as a neural interface electrode. The mechanical strength of these films, combined with their flexibility, ensures that they can withstand mechanical stresses encountered in various technological applications. This combination of properties makes thin films crucial in the ongoing development of MEMS, flexible electronics, and other technologies. [64-66]

The optical properties of thin films cover a range of characteristics, including transparency, reflectivity, absorption, and refractive index, which are crucial for applications in optoelectronics and photonics. These properties can be precisely engineered by controlling film composition, thickness, and structure, including surface roughness. Thin films can be tailored to be optically transparent, making them ideal for applications where light transmission is essential. [67-69]

Materials such as ITO and ZnO are commonly used as TCOs in photovoltaic cells, touchscreens, and display technologies. The optical bandgap and carrier concentration can be tailored to optimize transparency and conductivity by varying the deposition parameters and doping levels. [70-73]

In addition to transparency, thin films exhibit important reflective properties. Reflectivity can be controlled through the choice of materials and the design of multilayer structures used to create mirrors and anti-reflective coatings. For example, dielectric materials, such as silicon dioxide (SiO_2) and titanium dioxide TiO_2 , are often combined to produce Bragg reflectors and anti-reflective coatings for optical lenses and solar panels. [74-76]

Absorption is another fundamental optical property of thin films that is important for photodetectors and solar cells. Materials such as cadmium telluride (CdTe) and copper indium gallium selenide (CIGS) are used in thin film solar cells due to their strong absorption of sunlight. The absorption coefficient of these materials can be tuned by adjusting the film thickness and composition, ensuring efficient light harvesting and energy conversion. [68,77-79]

Additionally, thin metal films like Au and Ag are utilized for their plasmonic properties, which enhance light absorption and scattering at specific wavelengths, improving the performance of sensors and photonic devices. [79-81]

On the other hand, materials for simple infrared radiation (IR) absorption are used in bolometers. Bolometers measure the power of incoming electromagnetic radiation by heating an absorbing element with an embedded temperature sensor. Transition vanadium oxide (VO_x) and amorphous silicon ($\alpha\text{-Si}$) are common materials for bolometers' temperature sensors. These materials are chosen for their high-temperature coefficient of resistance and high absorption

coefficients, thus having the ability to convert absorbed radiation into a measurable change in resistance. [82-84]

The refractive index of thin films is a fundamental optical property influencing light propagation through the material. Thin films can be designed to manipulate light in various ways, such as bending, focusing, or filtering, by engineering their refractive index. This is particularly important in applications like waveguides, optical filters, and lenses. Materials such as aluminum oxide (Al_2O_3) and tantalum pentoxide (Ta_2O_5) create high-refractive-index layers in these optical devices, enabling precise control over light propagation and enhancing device performance. [85-89]

Chemical stability is another important property of thin films that significantly impacts reliability and stability. Thin films can be designed to resist oxidation, corrosion, and chemical attack, making them suitable for use in protective coatings and environmental sensors. For instance, thin films of Si_3N_4 , or SiC , are widely used as protective layers in microelectronics to prevent contamination and degradation of underlying materials. Additionally, in chemical sensors, thin films of metal oxides like TiO_2 and tin dioxide (SnO_2) are used for their stability and sensitivity to various gases, enabling the detection of pollutants and hazardous substances. [90-94]

2.1.2 Deposition techniques

The fabrication of thin films relies on various deposition techniques, each with specific advantages and applications. These techniques can be divided into physical and chemical methods.

Physical vapor deposition

PVD is a method for creating thin films and coatings by physically transferring material from a source to a substrate in a vacuum. Techniques like evaporation and sputtering involve the physical ejection of atoms or their clusters, condensing on the substrate. PVD is widely used in electronics, optics, and materials science. [95]

Evaporation is a widely used thin film deposition technique involving a material phase transition from solid to vapor in a high-vacuum environment. This vapor then condenses on a substrate, forming a thin film. The evaporation process begins with placing the source material in a crucible or a boat inside a vacuum chamber. The chamber is usually evacuated to a high vacuum (pressure is lower than 10^{-5} Pa) to reduce contamination. The source material is typically heated to its vaporization point using resistive (*Figure 1A*) or electron beam heating (*Figure 1B*). As the material evaporates, its atoms or molecules travel through the vacuum due to the large mean free path and condense on the more relaxed substrate, forming a thin film. Resistive heating involves an electrical current passing through a resistive element, such as a tungsten filament, which heats the source material. This method is suitable for materials with relatively low melting points. Electron beam heating directs a high-energy electron beam onto the source material, causing localized heating and evaporation. This highly efficient method can evaporate refractory materials with high melting points, such as Pt or W. [95-100]

The advantages of evaporation include its simplicity, which makes it easy to implement and operate, and its ability to provide acceptable control over film thickness by adjusting the evaporation rate and deposition time using quartz crystal microbalance (QCM). Its measurement precision is required in applications where uniformity and thickness control are essential, such as optical coatings and semiconductor devices. Additionally, evaporation can deposit many materials, including metals like Au, Ag, and Al, alloys such as NiFe and NiCr, dielectrics like SiO₂, and some organic compounds. [99,101-109]

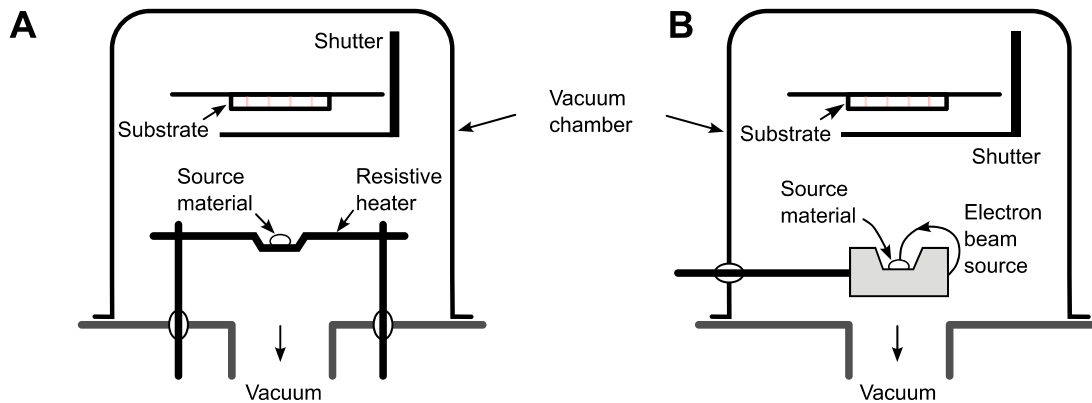


Figure 1: Schematic diagrams of two standard thin film deposition techniques: (A) thermal evaporation method and (B) electron beam evaporation method.

Evaporation is extensively used to produce optical materials, such as anti-reflective coatings, mirrors, and beam splitters. Magnesium fluoride (MgF₂) and TiO₂ are commonly evaporated to create multi-layer coatings with precise optical properties. In the semiconductor industry, evaporation is typically used to deposit metal layers for electrical contacts and interconnections. Al and Au are frequently evaporated to form conductive interconnections in integrated circuits and TFTs. The technique is also employed in fabricating high-performance thin film solar cells, where materials like CdTe and CIGS are deposited to form the active layers. The jewelry and watch industries use the evaporation method to deposit thin films of precious metals, such as Au, Pd, Rh, Pt, or Si, creating aesthetically pleasing and durable finishes. Moreover, evaporation is used to apply protective coatings to various components, enhancing their resistance to wear, corrosion, and environmental degradation. While evaporation offers many advantages, it also has some limitations and challenges. The process is inherently directional, meaning it deposits material in a line-of-sight manner. This can lead to non-uniform coatings on complex geometries or substrates with high aspect ratios. Additionally, some materials, particularly those with very high melting points or decomposed when heated, are challenging to evaporate, limiting the range of materials that can be deposited using this technique. Furthermore, the kinetic energy of deposited materials is typically low, which can negatively influence adhesion by leading to less dense and less adherent films. However, this lower energy can be advantageous in specific applications, as it minimizes damage to delicate or temperature-sensitive underlayers. [99,103,109-122]

Magnetron sputtering is a widely utilized thin film deposition technique that involves the ejection of atoms or molecules and their clusters from a target material due to the bombardment of ions generated in a plasma. These ejected atoms travel through the vacuum chamber and deposit onto a substrate. The magnetron sputtering process begins with introducing an inert gas, typically Ar, into the vacuum chamber. A high voltage is applied between the target material (cathode) and the source plate/shield (anode), creating an electric field that ionizes the argon gas and forms a plasma (*Figure 2*). This plasma primarily forms near the target surface, which is in the strongest electric field. Magnets behind the target generate a magnetic field, confining the electrons close to the target surface. This confinement increases the probability of collisions between electrons and argon atoms, enhancing the ionization efficiency and maintaining a stable plasma. The positively charged argon ions in the plasma are then accelerated toward the negatively charged target material. When these high-energy ions collide with the target, they sputter atoms from the target surface. [95,123]

A simple method called direct current (DC) magnetron sputtering is commonly used for depositing conductive materials. It involves applying a constant direct current to the target, which is effective for metals and other conductive targets. Radiofrequency (RF) magnetron sputtering is used for depositing insulating and dielectric materials by applying a high-frequency alternating current, typically at 13.56 MHz, which maintains the plasma even with non-conductive targets. Pulsed DC magnetron sputtering combines the benefits of DC and RF sputtering, allowing for the deposition of both conductive and non-conductive materials by pulsing the DC power, which prevents charge buildup on the target surface and is effective for dielectric materials. [124-126]

Magnetron sputtering offers numerous advantages, making it a preferred method for thin film deposition. It provides excellent film uniformity and better adhesion to the substrate than evaporation, which is essential for high-performance coatings and devices. This technique can deposit various materials, including metals, oxides, and nitrides, making it suitable for diverse applications. Process parameters such as gas pressure, power, and substrate temperature can be controlled to alter and achieve desired thin film properties, including thickness, density, microstructure surface roughness, and crystallography. [127-129]

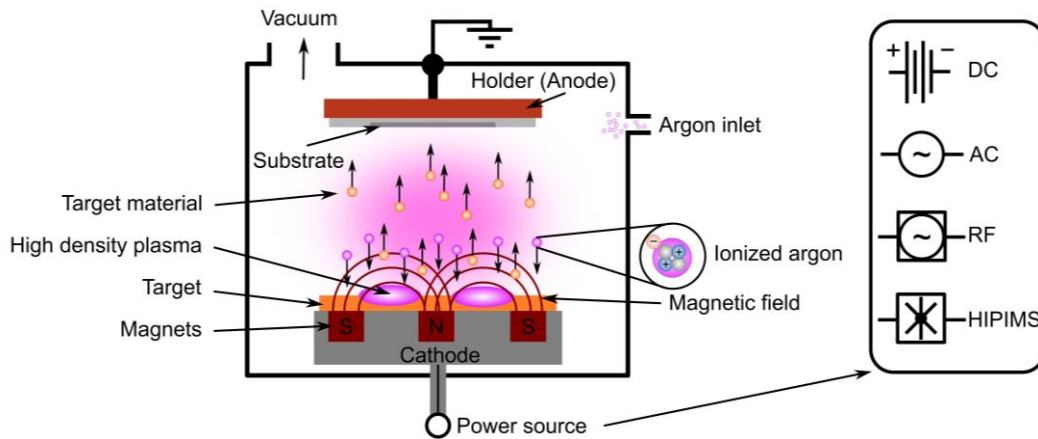


Figure 2: Schematic diagram of a magnetron sputtering system showing various power sources such as direct-current (DC), alternating-current (AC), radio-frequency (RF), or high-power impulse magnetron sputtering (HIPIMS).

Moreover, magnetron sputtering is scalable from small research setups to large industrial systems and can coat large areas and complex geometries. Magnetron sputtering is employed across various industries and research fields due to its versatility and reliability. It is extensively used to deposit metal contacts, interconnects, and barrier layers in integrated circuits and other semiconductor devices. Materials like Al, Cu, other metals, and electrically conductive nitrides like TiN, hafnium nitride (HfN), or zirconium nitride (ZrN) are commonly sputtered for these applications. The technique also produces optical coatings similar to the ones made by evaporation. Sputtering of materials like ITO and MgF₂ provides precise control over the optical properties of the coatings. In addition, reactive magnetron sputtering can be used to apply hard coatings on tools, and components such as TiN and DLC-based coatings are typical examples. [130-141]

The method is also employed in fabricating thin film solar cells, where materials like CdTe and CIGS are deposited to form the active layers that absorb sunlight and generate electricity. Furthermore, magnetron sputtering produces magnetic thin films such as cobalt alloys. While magnetron sputtering offers many benefits, it also presents limitations and challenges. In reactive sputtering, for instance, in the case of oxide or nitride deposition, reactive gases can “poison” the target material, affecting the deposition rate and film properties. The role of impurities is significantly higher. Notably, the kinetic energy of the deposited materials by magnetron sputtering is typically higher than by evaporation. Therefore, the magnetron sputtered layers have better adhesion than the evaporated ones. [142-147]

Ion-beam sputtering is a thin film deposition technique that, like magnetron sputtering, involves material sputtering from a target. The plasma is generated in an ion-beam source, either a gridded Kaufman ion-beam source or a gridless end-hall source. Generated ions are accelerated toward the target material. The ion beam's energy and direction can be finely tuned, allowing precise control over sputtering. [148]

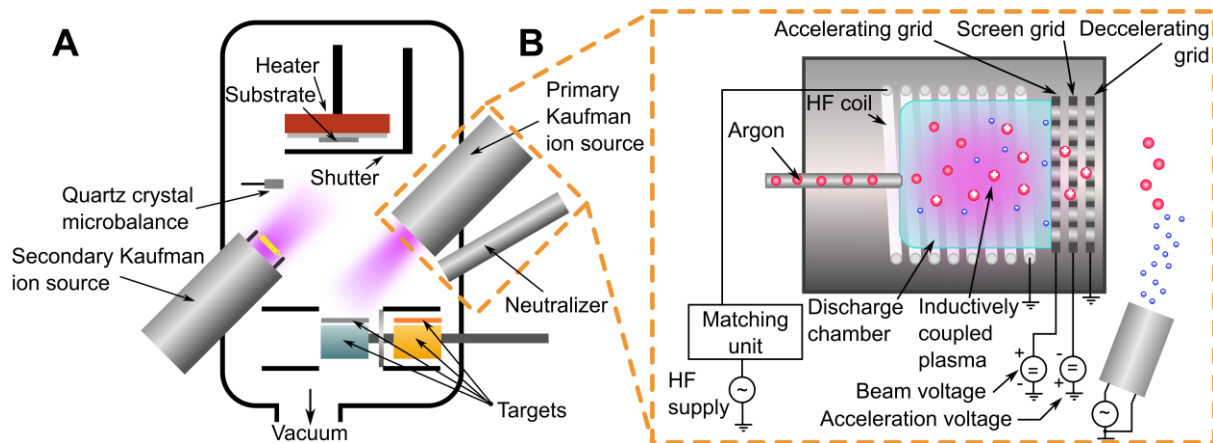


Figure 3: Schematic illustration of a dual ion-beam deposition system: (A) overview of the vacuum chamber, showing positions of primary and secondary Kaufman ion-beam sources and neutralizer; (B) detailed view of the 3-grid Kaufman ion-beam source.

One of the critical advantages of ion-beam sputtering is that ions are not generated directly in front of the target, unlike magnetron sputtering (Figure 3A). This separation reduces the chances of collisions and contamination, leading to higher-purity films. The directional nature of the ion beam allows for controlled and consistent erosion of the target material, resulting in films with superior surface quality and homogeneity. This leads to enhanced control of the process compared to magnetron sputtering, making this method ideal for producing high-quality thin films with enhanced purity and uniformity. [148]

Ion-beam sputtering also offers the flexibility to modify the properties of the deposited film through ion-beam assisted deposition (IBAD). In this process, a secondary ion beam (Figure 3B) is used to bombard the growing film, enhancing its density, adhesion, and overall quality. This additional control is beneficial for tailoring the film properties to specific application requirements. The mentioned dual ion-beam source setup allows for precise control over the composition and properties of the deposited films, enabling the formation of complex compounds and alloys such as TiN or AlN. This method is especially useful for creating thin films of oxides, nitrides, and other compound materials. These are critical in various advanced technological applications and can provide high-quality layers at low temperatures $< 350\text{ }^{\circ}\text{C}$. Applications of ion-beam sputtering are diverse and cover several high-tech industries. In optics, ion-beam sputtering creates anti-reflective coatings, mirrors, waveguides, and filters with precise optical properties. [148-151]

Moreover, the kinetic energy of the materials deposited in ion-beam sputtering is usually higher than in the magnetron sputtering process, contributing to better adhesion and denser films. Still, it can also induce residual compressive stress in the deposited layers. This residual stress can lead to issues such as film cracking, delamination, and substrate deformation, particularly in thicker films or when the substrate material has a lower tolerance for stress. [152,153]

Pulsed laser deposition (PLD) utilizes high-power pulsed lasers to ablate material from a target, which is then deposited as a thin film on a substrate. The PLD process typically uses an excimer or Nd laser directed onto the surface of a target material inside a high-vacuum chamber

(Figure 4). This intense energy rapidly heats, melts, and vaporizes the target material in a process known as laser ablation. This creates a plasma plume of ions, atoms, and clusters that expand away from the target. One of the critical advantages of PLD over methods like evaporation and magnetron sputtering is its ability to reproduce the stoichiometry of complex oxides and multi-component materials accurately. This precision is crucial for applications in superconductors, ferroelectrics, and magnetic materials, where exact composition control is essential. PLD also produces high-purity films due to the absence of working gas and negligible contamination from the laser ablation process, which is beneficial for the deposition of high-purity materials for electronic and optoelectronic applications. [154-157]

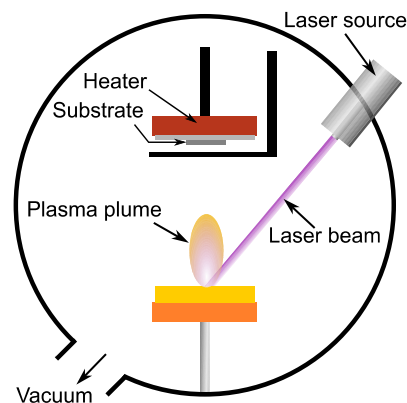


Figure 4: Schematic diagram of a pulsed laser deposition (PLD) system.

PLD is highly versatile and can deposit various materials, including metals, semiconductors, insulators, and polymers. Its rapid deposition rates and the ability to perform in-situ monitoring and control, for example, with reflection high-energy electron diffraction, make it an efficient method for thin film growth. However, the technique also has some drawbacks, including the formation of particulates or droplets due to the high-energy laser pulses, which can affect the smoothness and uniformity of the films. [157-161]

Additionally, the small deposition area of the plasma plume makes scaling up for large-area coatings challenging. PLD is extensively used in various advanced applications, such as the deposition of high-temperature superconducting films like $\text{YBa}_2\text{Cu}_3\text{O}_7$ (YBCO), ferroelectric materials like PZT for memory devices and sensors, and magnetic thin films for spintronics and data storage. It is also used to fabricate optoelectronic devices, including LEDs and photodetectors. [162-166]

Chemical vapor deposition

CVD is a group of methods for creating thin films and coatings by chemically reacting gaseous precursors on a substrate at a typically elevated temperature. The fundamental CVD process involves the decomposition of these precursors, resulting in the deposition of material in a controlled manner (Figure 5). Compared to PVD, CVD often provides better step coverage and conformity of deposited material. CVD is used to produce uniform films and is important for fabricating semiconductive and insulation layers in semiconductor devices, protective coatings, and advanced materials research. It is used to prepare materials such as semiconductors like Si

and GaAs and dielectrics like SiO_2 and Si_3N_4 . It can deposit metals such as W and T, metal nitrides such as TiN, and carbides such as TiC. Additionally, CVD is employed to prepare oxides like ZnO, composites such as carbon nanotubes (CNTs) or graphene, and superconductors such as YBCO. [167-169]

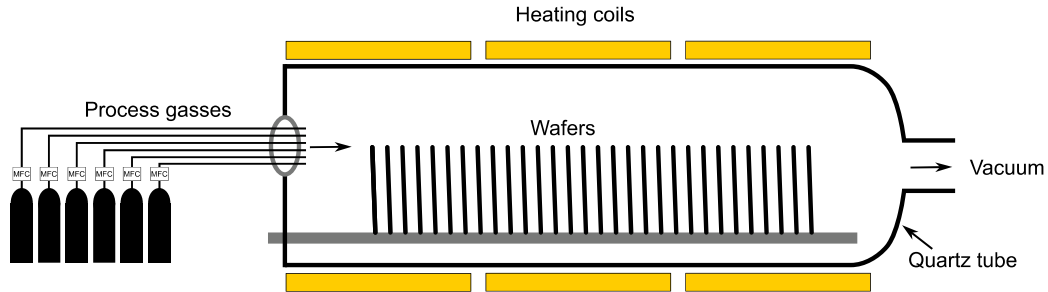


Figure 5: Schematic diagram of a chemical vapor deposition (CVD) system.

Plasma-enhanced chemical vapor deposition (PECVD) is a thin film deposition technique that uses plasma to enhance chemical reactions, enabling the deposition of thin films from gaseous precursors. Gaseous precursors are delivered into a vacuum chamber where plasma is generated using an external power source, typically radio frequency (RF) or microwave power (Figure 6). The plasma is formed by ionizing the gas molecules, creating a mixture of ions, electrons, and reactive species. These reactive species then interact with the substrate surface, resulting in chemical reactions that form a thin film. PECVD is particularly advantageous because it operates at lower temperatures (typically below $400\text{ }^\circ\text{C}$) than conventional CVD. The lower temperature operation also reduces thermal stress and potential damage to the substrate and thin films, enabling the deposition in a broader range of materials, including polymers and other temperature-sensitive substrates. [167,170-173]

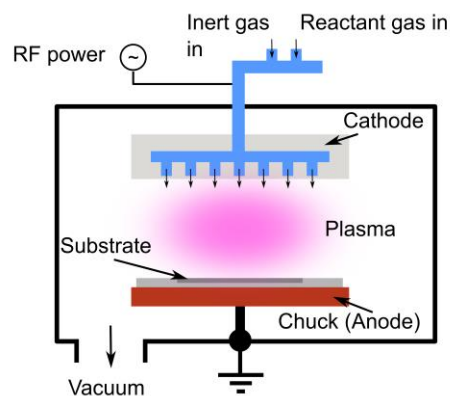


Figure 6: Schematic diagram of a plasma-enhanced chemical vapor deposition (PECVD) system.

PECVD can deposit a wide variety of Si-based materials, such as oxides (SiO_2), nitrides (Si_3N_4), carbides (SiC), and diamond-like carbon layers (DLC), and polymers. Furthermore, properties of layers, including thickness, composition, and residual stress, prepared by PECVD techniques can be tailored by setting the process parameters, such as gas flow rates, plasma power, and substrate temperature. PECVD-based thin films are usually well-suited for the fabrication of MEMS or optical coatings and solar cells. PECVD is also widely used in the

semiconductor industry to produce high-quality dielectric layers, such as Si_3N_4 and SiO_2 , which are essential for various applications in semiconductor devices. [167,170,171,174-179]

However, there can be specific cases where the electrical properties of PECVD-grown layers are not optimal compared to other methods, such as thermal oxidation for SiO_2 , which is caused by higher defect densities or different impurity levels in PECVD films, resulting in worse electrical properties. Furthermore, the energetic species in the plasma can potentially cause damage to the substrate and thin films on top. [180-182]

Low-pressure chemical vapor deposition (LPCVD) is a thin film deposition technique that operates under reduced pressure to enhance film uniformity and quality. Gaseous precursors are introduced into a vacuum chamber where a chemical reaction occurs at the substrate surface, resulting in thin film deposition. The process operates at a reduced pressure, typically from 10^{-2} Pa to 10^{-1} Pa, which helps to minimize gas-phase reactions and ensures that the chemical reactions occur primarily at the substrate surface. The substrate is heated to a high temperature, usually between ≈ 300 °C and ≈ 800 °C, to facilitate the decomposition of the precursor gases and the subsequent thin film formation. It produces highly conformal films with excellent step coverage, which is ideal for coating complex device structures and high aspect ratio features. This method can deposit various materials, including insulating and semiconducting films such as SiO_2 , Si_3N_4 , and polysilicon (p-Si). LPCVD offers precise control over the process parameters, such as gas flow rates, chamber pressure, and substrate temperature, which is necessary for optimal thin film properties. [183-187]

LPCVD is widely used in the semiconductor industry for depositing high-quality dielectric layers, such as SiO_2 and Si_3N_4 , essential for dielectric isolation, passivation, and gate dielectrics in transistors. It is also used to deposit poly-Si layers for gate electrodes of transistors and interconnects. In addition, LPCVD is employed in the fabrication of MEMS, which is used to deposit structural and sacrificial layers with precise control over film thickness and properties critical for MEMS performance. Furthermore, LPCVD is applied in the solar cell industry to deposit thin films of Si_3N_4 and other materials on solar cell wafers to improve surface passivation and light trapping, leading to higher efficiency of photovoltaic cells. The most significant disadvantage of the LPCVD method, contrary to PECVD, is the high temperature required for the processes, which can limit its use with temperature-sensitive materials and potentially cause thermal stress. [184,186,188-193]

Atomic layer deposition (ALD) is a thin film deposition technique that enables the formation of extremely thin and uniform films with precise control over thickness at the atomic scale. This technique relies on the sequential exposure of the substrate to different precursors in a self-limiting reaction, ensuring that only one atomic layer is deposited during each reaction cycle. The heated substrate (typically 100 °C – 300 °C) is exposed to the first precursor, which reacts with the surface to form a monolayer (*Figure 7AB*). The chamber is then purged to remove any excess precursor and reaction by-products. Next, the substrate is exposed to the second precursor, which reacts with the previously adsorbed layer to form the desired material.

Another purge follows this second exposure. These steps are repeated in cycles until the wanted film thickness is achieved (*Figure 7B*). [167,194-196]

ALD offers several advantages such as high uniformity and conformal coverage on complex and high aspect ratio structures. This makes it ideal for applications requiring precise and high-quality thin films, such as microelectronics, nanotechnology, and biomedical devices. ALD can deposit many materials, including oxides such as Al_2O_3 and HfO_2 or nitrides such as TiN and AlN . The addition of plasma into the ALD process (*Figure 7A*) is called plasma-enhanced ALD (PEALD). It enhances the reactivity of the precursors, allowing lower deposition temperatures (in some cases ambient temperature) and improved film properties. [194,197-201]

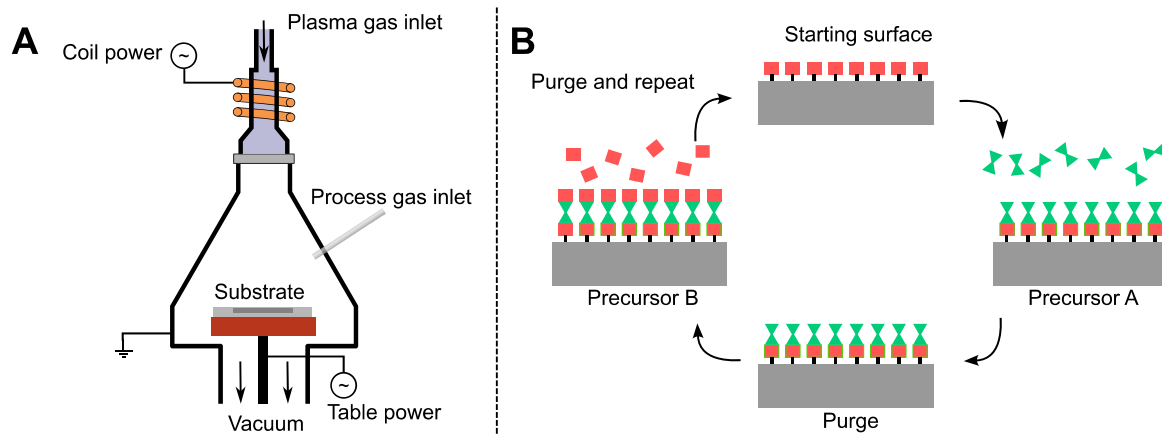


Figure 7: (A) Schematic diagram of an (plasma-enhanced) atomic layer deposition (PE)-ALD system. (B) Detailed illustration of the ALD process cycle.

PEALD is beneficial for depositing materials on temperature-sensitive substrates, such as polymers or organic materials, where elevated temperatures could cause damage. Additionally, PEALD can improve film density, reduce impurities, and enhance the electrical and mechanical properties of the deposited films. ALD and PEALD are widely used in various industries. Semiconductors use ALD for high-k dielectrics, gate oxides, and diffusion barriers. ALD coats nanoparticles and nanowires in nanotechnology, providing precise control over material properties. In biomedical applications, ALD creates biocompatible coatings for implants and medical devices. The most critical limitation is the process deposition rate given by the sequential nature of the deposition cycles. However, the ability to produce films with atomic-scale precision and high conformality makes ALD and PEALD essential for advanced thin film applications. [201-209]

Metal-organic chemical vapor deposition (MOCVD) is a thin film deposition technique that utilizes metal-organic compounds as precursors to form high-quality thin films. Gaseous precursors containing the desired metal and organic ligands are introduced into a reaction chamber, decomposing or reacting on a heated substrate to form a thin film (*Figure 8*). The substrate is typically heated to temperatures ranging from 300 °C to 1,000 °C, depending on the deposited material. Metal-organic precursors are chosen for their volatility and ability to decompose at relatively low temperatures, which allows the deposition of films with high purity and uniformity. [167,210-212]

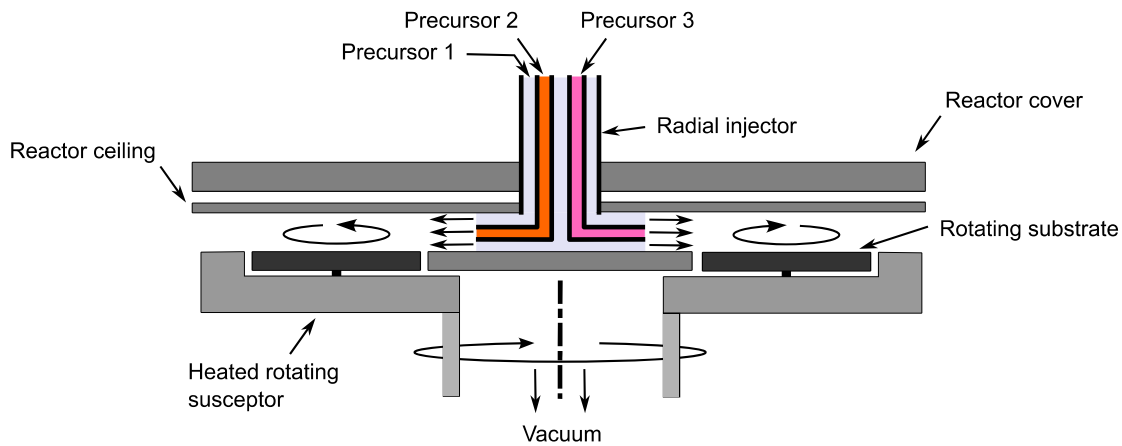


Figure 8: Schematic diagram of a metal-organic chemical vapor deposition (MOCVD) system.

One of the significant advantages of MOCVD is its ability to deposit a wide range of materials, including compound semiconductors (GaAs, InP), oxides (Al_2O_3 , ZnO), and nitrides (GaN, InN, AlN) or piezoelectric materials (PZT, AlN). This versatility makes MOCVD a crucial technique in the semiconductor industry for fabricating devices such as LEDs, laser diodes, and high-electron-mobility transistors (HEMTs). MOCVD is also used to produce thin film for solar cells, where materials like CIGS are deposited to create efficient photovoltaic devices. The MOCVD process allows excellent control over film composition, thickness, and doping levels. The ability to precisely control deposition parameters is important for fabricating heterostructures and superlattices, where layers of different materials are deposited and controlled to achieve desired electronic and optical properties. MOCVD systems are designed to operate under low-pressure conditions, which helps to improve the uniformity of the deposited films and reduces the likelihood of unwanted gas-phase reactions. The process parameters, such as precursor flow rates, substrate temperature, and reactor pressure, can be controlled to optimize the growth conditions for specific materials. Additionally, MOCVD can achieve high deposition rates, making it suitable for large-scale production. Despite its many advantages, MOCVD also has some limitations. The high temperatures required for the deposition process can restrict its use with temperature-sensitive substrates. [213-225]

Thermal Oxidation is a process used to grow an oxide layer on the surface of silicon wafers, usually from units of nm to units of μm , which is an important step in semiconductor device fabrication. This technique involves exposing Si substrates to an oxidizing environment at elevated temperatures, typically $\approx 700\text{ }^\circ\text{C}$ to $\approx 1,200\text{ }^\circ\text{C}$, in a furnace. The oxidizing environment can be composed of dry oxygen (O_2) or water vapors (H_2O), leading to two oxidation processes: dry and wet oxidation. [226]

Dry oxidation produces high-quality SiO_2 layers with excellent electrical properties. It is ideal for gate oxides in metal oxide semiconductor field effect transistor (MOSFET) technology and other applications requiring thin, high-integrity oxide films. Wet oxidation typically results in a faster growth rate than dry oxidation. It is often used to grow thicker oxide layers, which is helpful for applications such as field oxide in isolation structures and as a masking layer during

ion implantation. One of the primary advantages of thermal oxidation is the excellent interface quality formed between the Si and the SiO₂ layer. This high-quality interface is crucial for the performance of semiconductor devices, as it reduces interface states that can trap charge carriers and degrade device performance. [227-230]

Contrary to other CVD methods, a certain thickness of the Si surface is consumed during the process. Additionally, thermal oxidation also offers excellent control over the thickness and uniformity of the SiO₂ layer. The growth rate of the oxide can be precisely controlled by adjusting the temperature, oxidizing environment, and process time. However, thermal oxidation has some limitations. The high temperatures required for the process can introduce thermal stress and potential damage to the Si wafers. Thus, this process is typically incompatible with other thin films. Hence, the process is practically limited to Si as the other materials (Ta, Ti, Al) forming stable oxides at high temperatures are not commonly employed. [231]

2.1.3 Material characterization techniques

Material characterization techniques are essential for understanding the properties of thin films and fabricated patterns. These techniques range from simple electrical and electrochemical methods to advanced surface topography and microstructure and composition analyses. This section provides an overview of several common methods used for material characterization.

Electrical characterization of thin films involves measuring their electrical properties, such as resistance, conductivity, and capacitance. Simple methods like current-voltage (I - V) measurements provide information about the electrical behavior of materials, including information about their conductivity. Techniques such as four-point probe and Hall effect measurements are commonly used to evaluate the resistivity and carrier concentration in thin films, respectively. The four-point probe method involves placing four equally spaced probes (*Figure 9A*) on the surface of the film and passing I through the outer probes while measuring the V between the inner probes. This method eliminates the contact resistance influence and provides accurate measurements of sheet resistance. The Hall effect measurement on the van der Pauw pattern involves placing the thin film in a magnetic field and measuring the V developed perpendicular to the I flow determining the magnetic field amplitude (*Figure 9B*). The same structure is also used to get information about the type (n-type or p-type), concentration, and mobility of charge carriers in the semiconductors. [232-235]

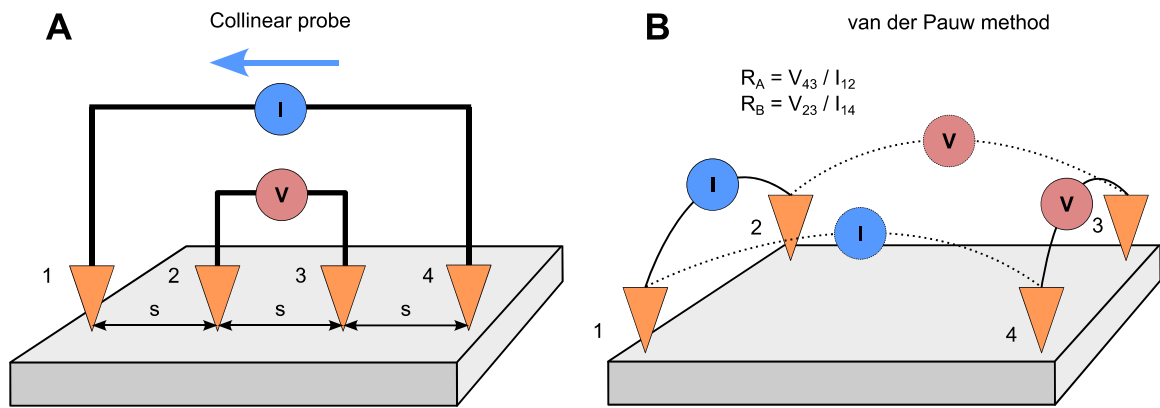


Figure 9: Schematic of (A) simple four-probe method and (B) van der Pauw method used for Hall effect measurements.

Additionally, advanced techniques such as impedance spectroscopy are used to study the frequency-dependent electrical properties of thin films. This method involves applying an AC voltage to the film and measuring the resulting current to obtain the impedance spectrum. The impedance data can be analyzed to extract information about the film's dielectric properties, charge transport mechanisms, and interfacial phenomena. [236-238]

Electrochemical characterization techniques are important for evaluating the electrochemical properties of thin films and are often used in sensors and energy storage devices. Methods like cyclic voltammetry (CV) and electrochemical impedance spectroscopy (EIS) are used to study the material redox behavior, charge transfer resistance, and capacitive properties of thin films. These techniques, commonly based on a three-electrode setup (Figure 10), help to understand the material suitability for applications in batteries, supercapacitors, electrochemical sensors, and bioelectronics. [239-243]

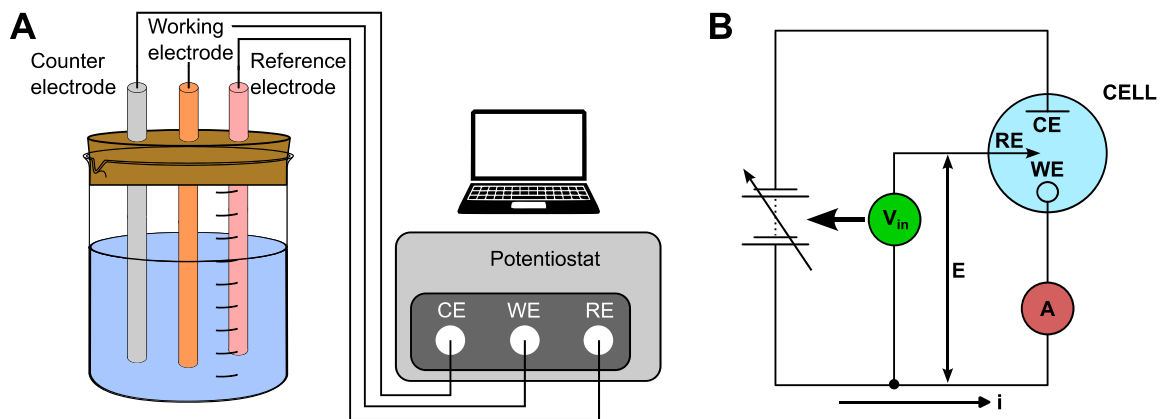


Figure 10: Schematic view of common three-electrode setup showing Counter (CE), Working (WE), and Reference (RE) electrodes connected to potentiostat and their simplified electrical circuit.

CV involves sweeping the potential of the working electrode (thin film) at a fixed rate and measuring the resulting current. The resulting CV curve provides information about the oxidation and reduction processes occurring in the layer, as well as the stability and reversibility of these processes. Peaks in the CV curve correspond to specific redox reactions, and the peak

currents and potentials provide insights into the kinetics and thermodynamics of these reactions. [239,240]

EIS measures the impedance of the thin film over a range of frequencies. The resulting impedance spectrum is typically plotted as a Nyquist plot, which provides information about the charge transfer resistance, double-layer capacitance, and diffusion processes in the film. By fitting the impedance data to an equivalent circuit model, one can extract detailed information about the electrochemical processes occurring in the film. [243,244]

Surface topography analysis provides detailed information about the surface morphology and roughness of thin films. Techniques such as atomic force microscopy (AFM), profilometry, and scanning electron microscopy (SEM) are widely used for this purpose. AFM offers imaging of surface features at the nanoscale, allowing for the measurement of surface roughness and texture. SEM provides detailed images of the film surface, enabling the observation of surface defects, grain structure, and overall morphology. [245-247]

AFM operates by scanning a sharp tip with a radius of a few nm or smaller over the surface of the thin film while measuring the interaction forces between the tip and the surface (*Figure 11A*). The resulting topographical map provides information about the surface roughness, texture, and features such as grains, pits, and cracks. AFM can also be used in different modes, such as contact mode, tapping mode, and non-contact mode, to study various surface properties including work function determination, piezoelectric properties, electrostatic forces, etc. The simplified method is a stylus profilometer (*Figure 11B*), which is well suitable for the determination of fabricated pattern thickness. It provides worse resolution than AFM, but the measurements are simpler and more intuitive. [246,248-253]

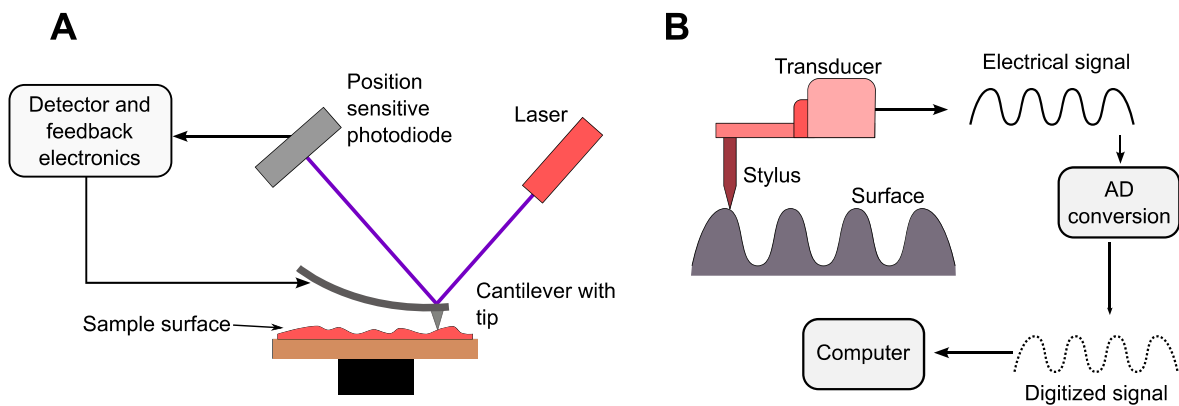


Figure 11: Schematics showing the principle of (A) AFM and (B) stylus profilometer methods.

SEM uses a focused beam of electrons to scan the surface of the thin film. The electrons interact with the atoms in the material, producing secondary electrons, backscattered electrons, and characteristic X-rays. These signals can be detected and used to create high-resolution images of the surface (*Figure 12*). SEM provides detailed information about the surface morphology, sometimes including the size, shape, and distribution of grains, as well as surface defects and contaminants. [254-256]

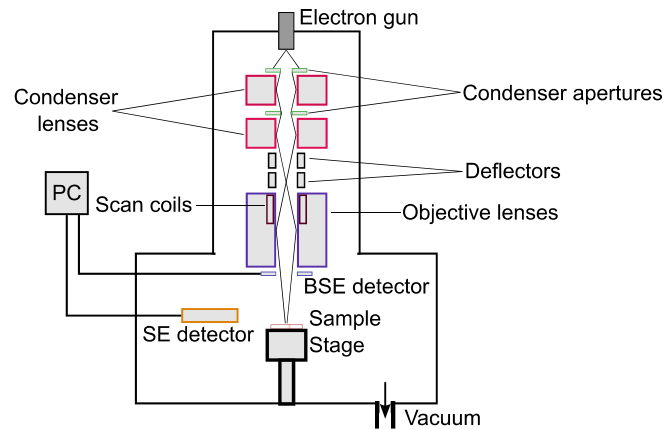


Figure 12: Schematic of SEM instrument showing the vacuum chamber, electron gun, and detectors for secondary electrons (SE) and back scattered electrons (BSE).

Mechanical properties are important for the evaluation of the material's performance and its suitability for various technological applications. One of the most widely used methods for measuring mechanical properties such as hardness and Young's modulus is nanoindentation. This technique involves pressing a hard, sharp indenter into the surface of a material under controlled conditions and measuring the resulting indentation depth and load (Figure 13). Nanoindentation provides precise and localized measurements of mechanical properties, making it ideal for thin films and small-scale structures. It allows for the determination of properties at the nanometer scale, providing detailed insights into the material's behavior under mechanical stress. This method possesses high accuracy, repeatability, and ability to perform tests on a wide range of materials, from polymers to metals and ceramics. [257-259]

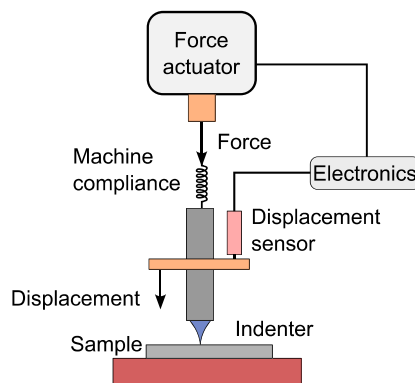


Figure 13: Schematic of nanoindentation technique.

Additionally, Guckel rings are another important tool in the determination of mechanical properties, particularly in MEMS applications. Guckel rings, or stress rings, are used to measure residual stress in thin films. They consist of a patterned ring structure that deforms under residual stress, and the deformation is measured to determine the stress within the film. This technique is beneficial for understanding how thin films will behave under operational conditions, ensuring reliability and performance in practical applications. Combining nanoindentation and Guckel rings provides important data about the mechanical properties of

thin films, showing both intrinsic material properties and residual stress induced during fabrication processes. [260,261]

The microstructure of the thin films can be determined by the X-ray diffraction (XRD) technique, which is used for analyzing the crystal structure of thin films. It provides information about the phase composition, crystallographic orientation, and lattice parameters of the material. Obtained diffraction patterns are used to determine the degree of crystallinity and identify any present crystalline phases. This technique is crucial for understanding the structural properties of thin films used in various applications, from semiconductors to protective coatings. The basic principle of XRD involves directing X-rays at the thin film and measuring the intensity of the diffracted X-rays as a function of the diffraction angle. The resulting diffraction pattern consists of peaks corresponding to the various crystallographic planes in the material. By analyzing the position, intensity, and width of these peaks, one can obtain information about the crystal structure, phase composition, residual stress, and crystallite size of the thin film. The most common X-ray optical setups are parallel beam (PB, *Figure 14A*) and Bragg-Brentano (BB, *Figure 14B*) parafocusing geometry. The BB is often sufficient for thin films since it is typically faster than PB, but it possesses lower precision of data. Therefore, PB is more suitable for the examination of monocrystalline structures to obtain highly accurate data. [262-264]

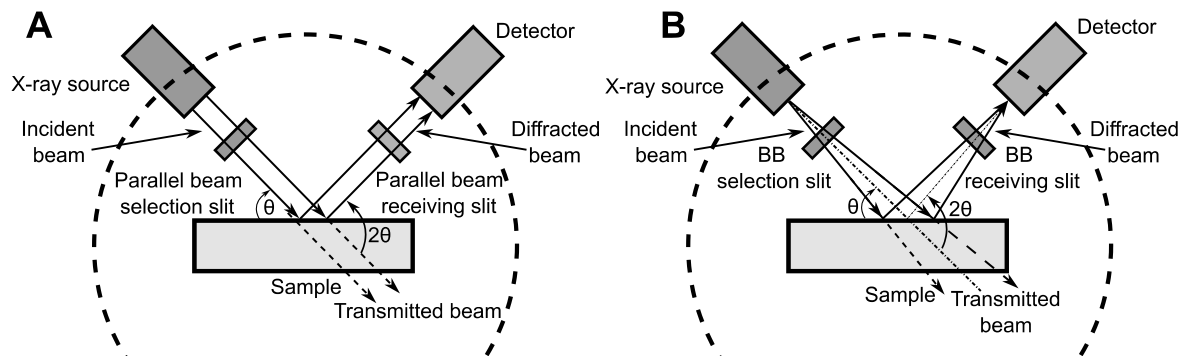


Figure 14: Simplified schematic of fundamental parallel beam and Bragg-Brentano XRD optics.

XRD can be performed in different modes, such as θ - 2θ scans, grazing incidence XRD (GIXRD), and in-plane XRD, to study various aspects of the film structure. θ - 2θ scans provide information about the out-of-plane crystallographic orientation, while GIXRD is used to study thin films with very low thicknesses. In-plane XRD provides information about the in-plane crystallographic orientation and strain in the film. Furthermore, the X-ray reflection (XRR) method can be used to determine the density and thickness of thin films. [262]

The material composition can be determined by X-ray photoelectron Spectroscopy (XPS) which provides detailed information about the elemental composition and chemical states of the elements present in thin films. By analyzing the binding energies of core electrons, XPS can identify the oxidation states and chemical environments of the atoms in the material. This technique is useful for studying the surface chemistry and electronic structure of thin films and is extremely important for the development of materials for catalysis, sensors, and electronic devices. The thin film is irradiated with X-rays, causing the ejection of core electrons from the

atoms in the material (*Figure 15*). The kinetic energy of these ejected electrons is measured, and the binding energy is calculated using the known energy of the incident X-rays. The resulting XPS spectrum consists of peaks corresponding to the different core levels of the elements present in the thin film. By analyzing the position and shape of these peaks, we can obtain information about the elemental composition, chemical states, and electronic structure of the thin film. XPS can also provide information about the composition of the thin films through depth profiling. This involves sputtering away successive layers of the film while performing XPS measurements, allowing for the determination of the composition and chemical states as a function of depth. This is particularly useful for studying layered structures and interfaces in thin films. [265-269]

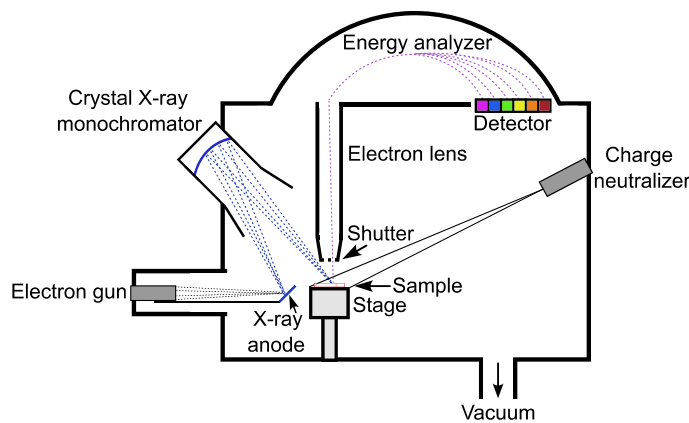


Figure 15: Schematic of XPS instrument showing the X-ray source and detector for ejected electrons.

Another method usually employed during SEM analysis is energy-dispersive X-ray spectroscopy (EDX). It provides qualitative and quantitative information about the elements present in the thin film. EDX is particularly useful for identifying and mapping the distribution of elements across the sample but is suitable for relatively thick materials due to the penetration depth of incident electrons. As it was mentioned, electron bombardment of the sample causes the emission of X-rays which is characteristic of the material. These X-rays are detected and analyzed to determine the elemental composition. Each element produces X-rays with a unique set of energy levels, allowing for the identification of the elements present in the sample. The intensity of the X-rays can be used to estimate the relative concentrations of the elements. [270-272]

The optical properties of thin films are critical for understanding their structural and compositional characteristics. These properties, including refractive index, absorption, scattering, and vibrational modes, provide insights into the material's molecular structure, chemical composition, and also thickness. Techniques such as Raman spectroscopy, Fourier transform IR spectroscopy (FTIR), and ellipsometry are used for characterizing a wide range of materials, including polymers, semiconductors, and nanomaterials. [273-275]

Raman spectroscopy is an optical technique used to study vibrational modes in materials. It provides information about the molecular structure, chemical composition, and phase transitions in thin films. Raman spectra can reveal details about the bonding and molecular

interactions within the material, making it a valuable tool for characterizing a wide range of materials, including polymers, ferroelectrics, semiconductors, and nanomaterials. [276,277]

The thin film is irradiated with monochromatic light, typically from a laser. The light interacts with the molecular vibrations in the material, resulting in the scattering of light at different frequencies. The Raman spectrum is obtained by measuring the intensity of the scattered light as a function of frequency shift (*Figure 16A*). The positions and intensities of the Raman peaks provide information about the vibrational modes, chemical composition, and molecular structure of the thin film. Raman spectroscopy is particularly useful for studying carbon-based materials, such as graphene and carbon nanotubes, as well as semiconductors and oxides. The technique can provide information about the crystalline quality, defects, and strain in the material. Additionally, Raman spectroscopy can be used to study phase transitions and chemical reactions in thin films, making it a versatile tool for material characterization. [274,277-279]

Furthermore, the FTIR is another optical technique (*Figure 16B*) used to study the vibrational properties of thin films. It provides complementary information to Raman spectroscopy by measuring the absorption of infrared light, which corresponds to the vibrational frequencies of the chemical bonds in the material. FTIR is particularly useful for identifying functional groups, studying molecular interactions, and analyzing the chemical composition of organic and inorganic thin films. Material is irradiated with a wide spectrum of infrared light. The light is absorbed by the material at specific frequencies corresponding to the vibrational modes of the chemical bonds. The resulting absorption spectrum provides information about the functional groups and chemical bonds present in the material. Positions and intensities of the absorption peaks are used to identify the chemical composition and molecular structure of the thin film. [280]

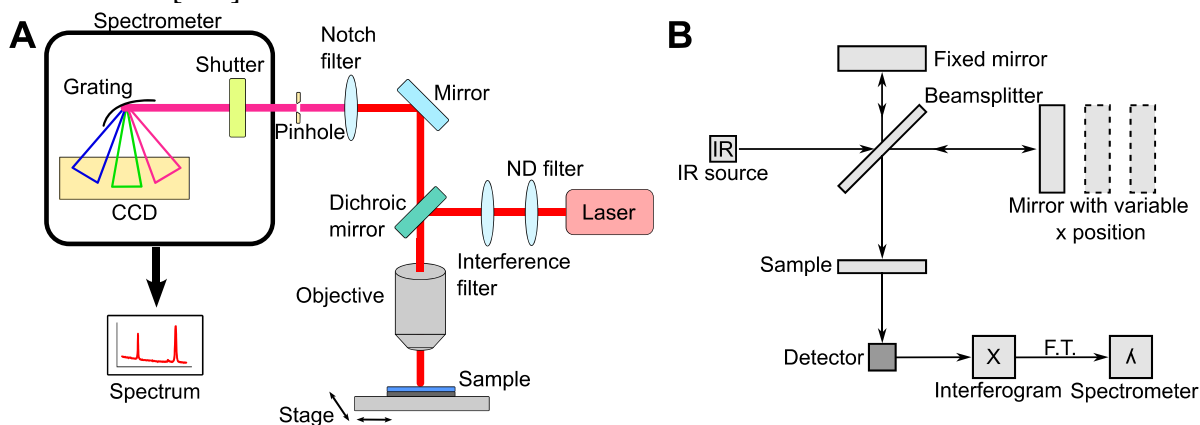


Figure 16: Schematic principle of (A) Raman and (B) FTIR methods showing optics configuration.

FTIR can be performed in different modes, such as transmission, reflection, and attenuated total reflectance (ATR), to study various aspects of the film. Transmission FTIR involves passing the infrared light through the film, while reflection FTIR measures the light reflected from the film surface. ATR-FTIR is particularly useful for studying thin films and surface

layers, as it involves measuring the light that is internally reflected within the film, providing information about the surface composition and chemical interactions. [280-282]

The next method is ellipsometry (*Figure 17*), which is usually employed to determine the thickness and optical constants (refractive index and extinction coefficient) of thin films. It is based on the measurement of the changes in the polarization state of light reflected from the surface of a thin film. This technique is highly sensitive to changes in film thickness and optical properties, making it an essential tool for thin film characterization. Polarized light is directed at the thin film surface at an oblique angle. Upon reflection, the light changes its polarization state, which is detected and analyzed. The change in polarization is described by the parameters Ψ and Δ , which represent the amplitude ratio and phase difference between the p- and s-polarized light components, respectively. Fitting of measured Ψ and Δ values to an optical model can be used for precise determination of the film thickness and its optical constants. Furthermore, ellipsometry can be used to determine the optical bandgap of thin films by analyzing the absorption edge in the optical spectrum. [275,283,284]

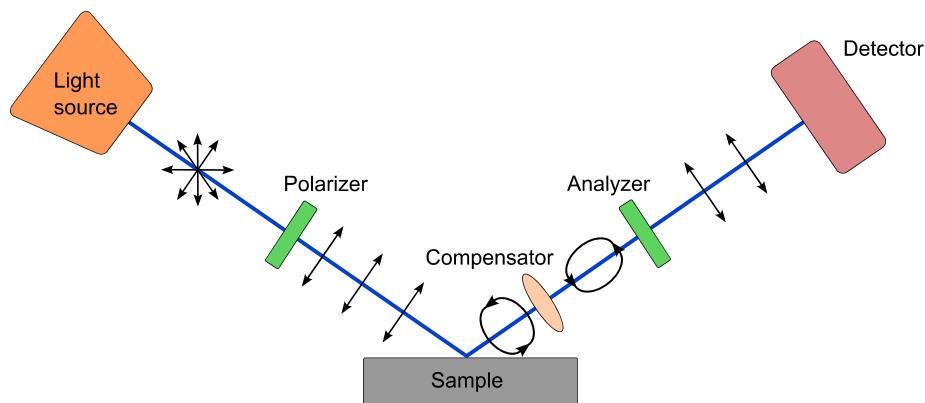


Figure 17: Schematic of ellipsometry optical setup.

2.2 Microfabrication techniques

Microfabrication techniques are the critical element of modern microelectronics and MEMS, enabling the fabrication of complex structures and devices at the micro- and nanoscale. These techniques include a variety of processes, including photolithography, etching, deposition, doping, and bonding, each playing an essential role in shaping and defining microstructures on Si wafers and other substrates. The precision and sophistication of these methods enable the fabrication of complex, high-performance microdevices to be used in a wide range of applications, from integrated circuits and sensors to biomedical devices and microfluidic systems. Understanding microfabrication techniques is essential for advancing technology and innovation in numerous scientific and industrial fields. [285-287]

2.2.1 Lithography techniques

Photolithography is a crucial microfabrication technique to pattern parts of a thin film or the bulk of a substrate. It involves the transfer of geometric patterns from a photomask or direct

laser irradiation (*Figure 18A*) to a light-sensitive photoresist (PR) on the substrate (*Figure 18B*). The PR layer is typically deposited on the substrate by spin-coating methods. Another options are either spray coating, which is suitable for uneven surfaces and theoretically uses smaller amounts of photoresist, or dip coating, which coats both sides of the substrate at once. Photolithography has evolved from simple ultraviolet (UV) lithography to more precise techniques such as deep UV (DUV) and extreme UV (EUV) lithography, pushing the boundaries of resolution down to 1 nm. [286,288,289]

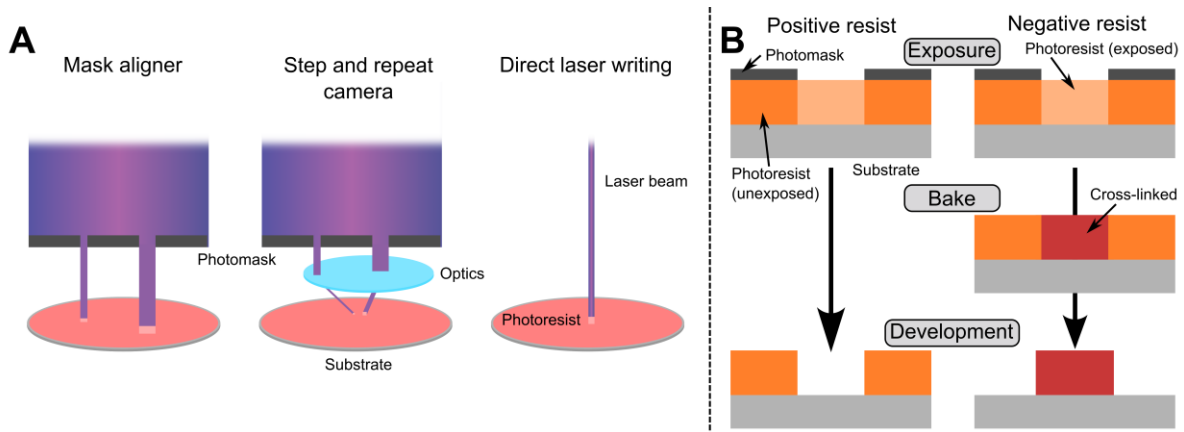


Figure 18: (A) Schematic diagram of photolithography techniques: the mask aligner method (left), the step and repeat camera technique and direct laser writing (right). (B) Photolithography process for positive and negative resists.

- **UV lithography** is one of the earliest and most widely used forms of photolithography. It employs ultraviolet light with wavelengths typically ranging from 365 nm (Hg i-line) to 436 nm (Hg g-line). This technique is well-suited for creating micro-scale features and is commonly used to fabricate printed circuit boards (PCBs), MEMS, and other μm scale devices and structures. UV lithography is valued for the instrument's simplicity compared to other methods. [290]
- **DUV lithography** uses light sources with either 248 nm or 193 nm wavelengths, allowing for smaller feature sizes than traditional UV lithography. DUV lithography is widely used in semiconductors to produce integrated circuits with feature sizes of up to ≈ 20 nm. The shorter wavelength enables better control over photochemical reactions in the PR, resulting in more precise patterning. [291,292]
- **EUV lithography** represents the next milestone in photolithographic technology. It utilizes even shorter wavelengths of ≈ 13.5 nm or less, which belong to the soft X-ray region. This allows for feature sizes below 10 nm, which is crucial for semiconductor device scaling. EUV lithography (*Figure 19*) employs complex reflective mask-based optics to manage the shorter wavelength light, as there is no transparent material for the wavelength below 157 nm. The EUV wavelength is generated by focusing high-energy laser pulses at an Sn droplet, creating a plasma that emits EUV radiation. The plasma is then collected and focused using specialized optics to produce the required radiation for precise

photolithographic processes. EUV lithography is essential for producing the latest generation of high-performance integrated circuits. [293,294]

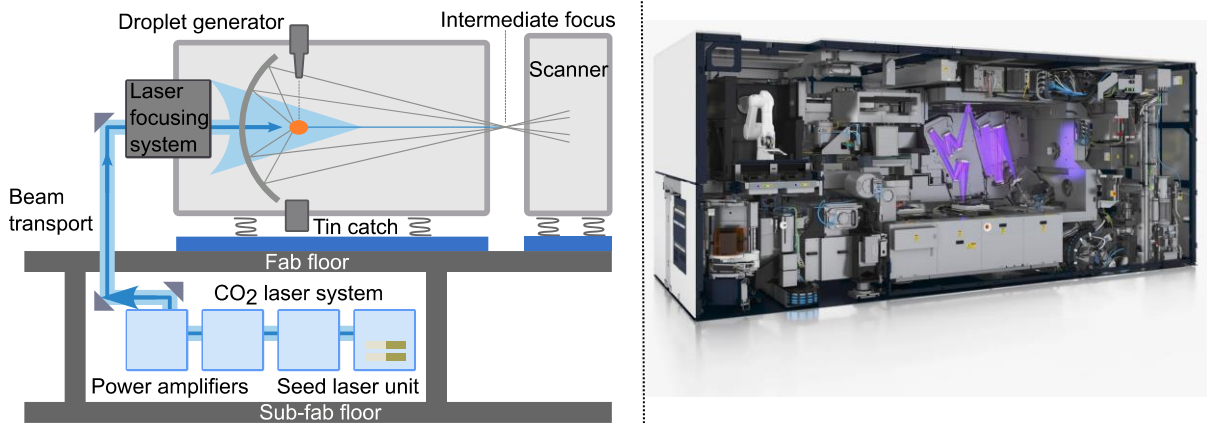


Figure 19: Schematic diagram and model of an extreme ultraviolet (EUV) lithography system (source: www.asml.com).

Electron-beam lithography (EBL) is another advanced technique used to create fine patterns, often at the nanoscale. Unlike photolithography, which uses light, EBL utilizes a focused beam of electrons to write patterns directly onto an e-beam resist-coated substrate. This allows much higher resolution and precision, making it suitable for applications requiring smaller features than photolithography. Nevertheless, EUV lithography is rapidly advancing and now competes with EBL in terms of feature size. EBL tools are considered rather expensive; however, compared with EUV or DUV steppers, they are far more cheaper. Also, EBL allows quick changes to the patterned layout without additional cost. EBL is particularly advantageous for researching, developing, and fabricating specialized components such as quantum devices, nanophotonic structures, and advanced sensors. Then, the exposed areas are developed, similarly to photolithography, to reveal the underlying substrate for further processing. Modern layout tools also allow for the correction of the proximity effect. [295-297]

Comparison and applications of lithography techniques. Each lithography technique has its strengths and limitations. Photolithography, particularly with DUV and EUV advancements, is the main method used by the semiconductor industry due to its high throughput and suitability for mass production. However, it requires expensive equipment and masks, making it less flexible for prototyping or low-volume production. Only one company (ASML) can make the high-end lithography instruments used in the most advanced processes. In contrast, EBL allows the direct writing of patterns without masks, which offers design flexibility. However, it is a much slower process, suitable for applications requiring precision rather than high-volume manufacturing. While photolithography drives large-scale production of semiconductor devices, EBL enables nanoscale research of a wide spectrum of structures and devices. In summary, lithography techniques have undergone significant evolution over the last few decades, especially when we discuss the transformation of photolithography from μm to nm (Figure 20). [290]

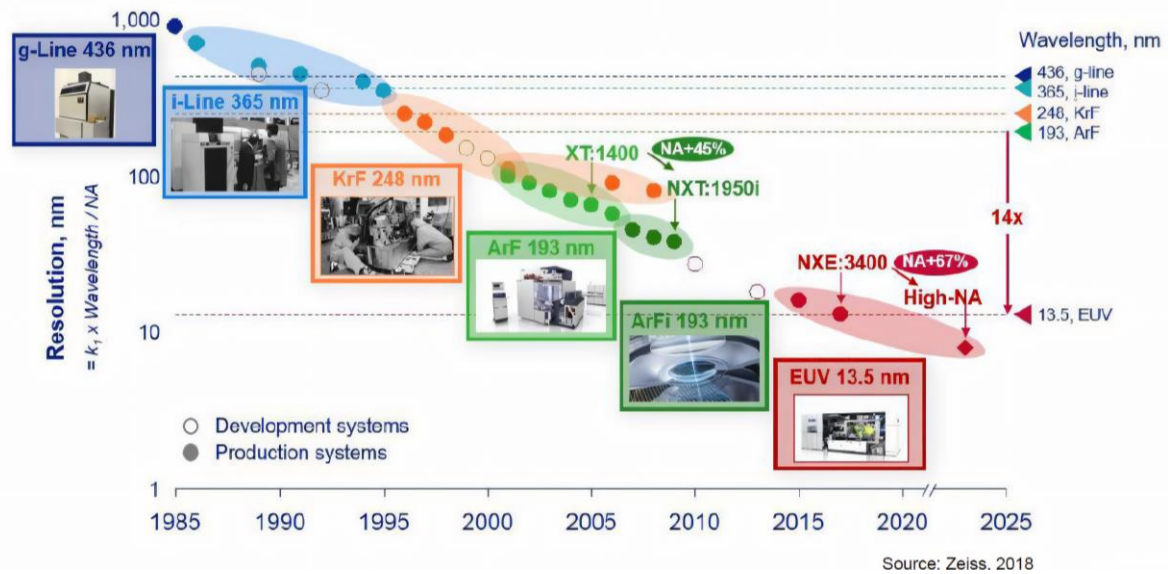


Figure 20: Evolution timeline of lithography wavelength and resolution advancements from 1985 to 2025. The graph shows the transition from g-line (436 nm) and i-line (365 nm) lithography systems through KrF (248 nm) and ArF (193 nm) systems, leading to the high-end EUV (13.5 nm) lithography systems. (source: www.zeiss.com)

2.2.2 Etching techniques

Etching is a fundamental process in microfabrication, essential for patterning and structuring materials at the microscopic scale. It is based on removing material from a substrate to create the desired pattern. Etching techniques can be broadly classified into isotropic (Figure 21A) and anisotropic etching (Figure 21B), with further subdivisions into wet and dry etching methods (Figure 21C). Each technique has specific advantages, limitations, and applications in fabricating microelectronic devices, MEMS, and other micro- and nanoscale structures. [287]

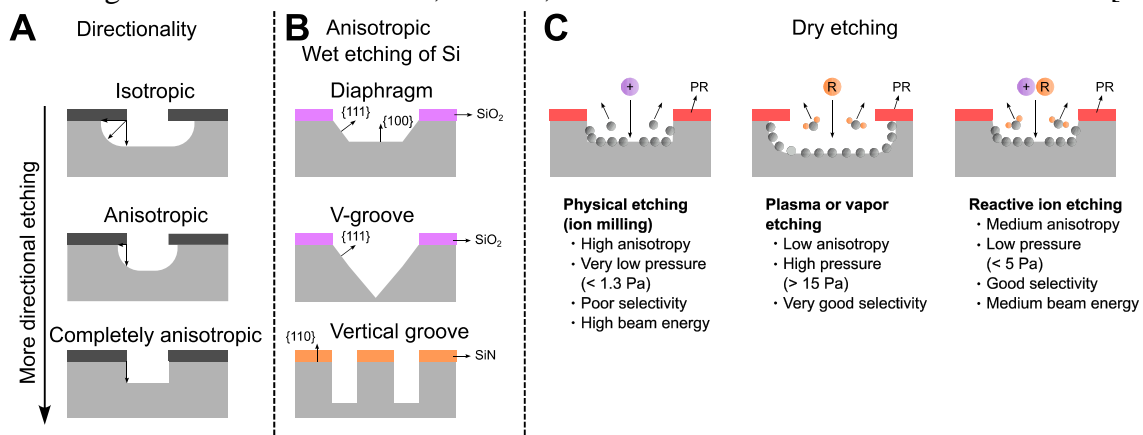


Figure 21: Different etching techniques and their characteristics. (A) Directionality of etching showing isotropic, anisotropic, and completely anisotropic etching profiles. (B) Anisotropic wet etching of Si shows the formation of diaphragms, V-grooves, and vertical grooves based on different crystallographic orientations. (C) Dry etching methods include physical etching (ion milling), plasma or vapor etching, and reactive ion etching.

Isotropic vs. anisotropic etching

Isotropic etching removes material uniformly in all directions (*Figure 21A*), creating rounded profiles. It is often used when precise etch profile control is not critical. Isotropic etching can be performed using wet chemical etchants or gaseous etchants and is typically faster than anisotropic etching. However, its uniform nature can undercut the masking material, causing undesired etching of material underneath the fabricated pattern. This method is well-suited for Si etching using XeF₂ vapors for MEMS fabrication. Furthermore, this all-directional phenomenon is employed in wet etching to remove sacrificial layers under thin films. [298,299]

Anisotropic etching removes material at different rates in different directions (*Figure 21A*) allowing for more precise control over the etch profile. This type of etching is essential for creating structures with well-defined vertical walls. It is widely used to fabricate MEMS and integrated circuits and can be further employed in various non-conventional applications. Anisotropic etching can be achieved using both wet and dry etching techniques. Wet etching is usually based on the crystallographic orientation of the etched material (*Figure 21B*). In contrast, dry etching is mainly related to the selected technique and process parameters. [300,301]

Wet etching

Wet etching involves immersing the substrate in a liquid etchant solution that reacts with the material, which should be removed. This technique can be isotropic or anisotropic, depending on the choice of etchant and the material being etched. Wet chemical etching is relatively simple and cost-effective, making it suitable for many applications in microfabrication. Common etchants include acids, bases, and solvents, each suitable for different materials. For example, a hydrofluoric acid (HF) in combination with ammonium fluoride (NH₄F) solution known as buffer oxide etchant (BOE) is used for etching of SiO₂, while potassium hydroxide (KOH) solution is used for Si etching. Wet etching is ideal for applications requiring smooth surfaces and is usually used with masking PR to protect areas that should not be etched. However, isotropic wet etching can lead to undercutting of the mask layer, limiting the precision of the etch profile. Selectivity for wet etching techniques is generally higher than for dry techniques. [298,302-305]

Dry Etching

Reactive ion etching (RIE) is a type of dry etching that combines physical sputtering and chemical reactions to remove material from the substrate (*Figure 21C*). The substrate is placed in a vacuum chamber, and a gas mixture is introduced. The plasma is generated using an RF power source, creating reactive species that chemically react with the substrate. Simultaneously, ions from the plasma bombard the substrate, providing additional energy to enhance the etching process and partially causing sputtering of the material. RIE offers high precision and the ability to etch complex patterns with excellent control over the etch profile, making it suitable for applications requiring anisotropic etching. The process parameters, such as gas composition and flow rate pressure, substrate temperature, and RF power, can be controlled to achieve the desired etch rate and selectivity. In the case of material stacks, the

process control can be moderate due to the lower selectivity of the etching process in comparison to wet etching. Therefore, monitoring the process using an optical method called endpoint detection is necessary. It determines when the desired material has been precisely etched through. This is typically achieved using techniques such as optical emission spectroscopy, which analyzes the light emitted by the plasma, or laser interferometry, which measures changes in the surface reflectivity of the substrate. [300,306,307]

Deep reactive ion etching (DRIE) is an advanced form of RIE designed explicitly for creating deep, high aspect-ratio structures and trenches with vertical sidewalls. DRIE is commonly used for MEMS fabrication, modern transistors, and other applications that require deep trenches or pillars. The process involves alternating cycles of etching and passivation. During the etching cycle, reactive ions remove material from the substrate. In contrast, the passivation cycle deposits a protective polymer layer on the sidewalls, which prevents lateral etching and creates anisotropic profiles. DRIE is known for its high etch rates and excellent control over etch profiles, making it ideal for fabricating complex structures, including membranes and cantilevers. Two DRIE methods are applicable, either the faster Bosch process or the finer cryogenic etch. [306,308,309]

Ion milling is a physical etching technique that uses a focused beam of ions to sputter material from the substrate (*Figure 21C*). It generally uses ion-beam sources, as mentioned before. In some cases, it can be referred to as reactive ion-beam etching (RIBE) if a reactive gas provides chemical etching. Unlike RIE and DRIE, ion milling does not rely on chemical reactions and is purely a physical process. This makes it suitable for etching materials that are resistant to chemical etching. Compared to RIE and DRIE, ion milling is a highly directional technique that precisely controls the etch profile. It is sometimes used for pattern etching over PR masks for III-V semiconductors and MEMS fabrication and can be employed for etching materials such as metals, dielectrics, and composites. It is usually combined with time-of-flight secondary ion mass spectrometry (TOF-SIMS) to monitor the etching process, allowing for precise etch-stop to avoid over-etching and damage to the underlying layers. However, this process is relatively slow compared to RIE and DRIE. [310-312]

2.2.3 Doping and Surface Modification

Doping and surface modification are fundamental in materials science and semiconductor technology. These techniques are essential for tuning materials' electrical, chemical, and physical properties for specific applications.

Doping involves the introduction of impurities into a semiconductor to modify its electrical properties, creating p-type or n-type semiconductors. N-type doping adds elements with more valence electrons than the host material, like P or As in Si, increasing electron conductivity. P-type doping, using elements with fewer valence electrons, such as B, increases hole conductivity (*Figure 22*). Techniques like ion implantation and diffusion are commonly used. Ion implantation offers precise control over dopant concentration and depth, while diffusion is more straightforward but less controlled. Another possible method is in-situ doping

during epitaxy, CVD, or molecular beam epitaxy (MBE) processes, which ensures uniform doping throughout the deposited layer. Doping is crucial in semiconductor devices and is necessary for the optimization of electrical parameters of transistors, diodes, and solar cells. A significant drawback of in situ doping is the requirement to handle highly toxic gases, such as phosphine, diborane, and arsine, using a facility equipped accordingly. [226,313,314]

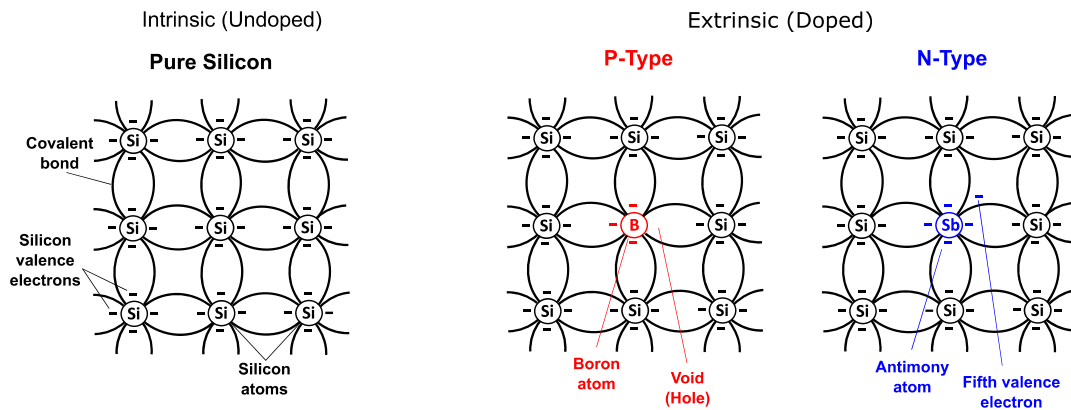


Figure 22: Comparison of intrinsic (undoped) Si on the left and extrinsic (doped; p-type and n-type) Si on the right.

Surface modification alters the surface properties of materials to achieve desired characteristics such as increased adhesion, reduced friction, enhanced biocompatibility, or improved corrosion resistance. Techniques include plasma treatment, which enhances surface energy and adhesion; chemical functionalization, attaching specific groups to the surface for further reactions; ion-beam modification, altering surface chemistry and roughness; thermal treatments, changing crystallinity and hardness; and coating, applying protective or functional layers via PVD, CVD, or ALD. These modifications are essential in various industries, from improving the biocompatibility of medical implants to enhancing corrosion resistance in electronics and durability in aerospace components. [60,315,316]

2.3 Thin films and microfabrication in sensor applications

Thin films are essential in developing various sensor physical and chemical sensors. Physical sensing mechanisms often involve changes in the thin film's electrical resistance, capacitance, or optical properties in response to external stimuli such as pressure, temperature, or light. For example, piezoelectric thin films can convert mechanical stress into an electrical signal, making them useful for pressure sensors, microphones, or cochlear implants. Chemical sensing mechanisms rely on the interaction between the thin film and specific analytes, leading to measurable changes in properties like conductivity or mass. This is commonly seen in gas sensors where the adsorption of gas molecules on a metal oxide thin film alters its electrical resistance. Electrochemical sensing mechanisms involve redox reactions at the surface of the thin film, which can be detected by measuring changes in current or voltage. These mechanisms are fundamental in biosensors, where thin films of materials such as Au, Pt, TiN, etc., are used to detect biological molecules through electrochemical signals. [317-319]

Furthermore, integrating thin films into functional sensor devices requires advanced microfabrication techniques. Lithography is essential for patterning thin films into precise micro and nanostructures required for sensor applications. Etching techniques are employed to define the geometries of thin film sensors, allowing the creation of patterns and structures. Furthermore, deposition techniques are crucial for the deposition or growth of thin films or microstructures with the desired parameters. In general, combining the mentioned techniques enables the development of highly sensitive, reliable, and miniaturized sensors capable of operating in various environments and applications, from industrial monitoring to healthcare diagnostics. [320-322]

2.3.1 Residual stress control in Ti thin films prepared by Kaufman ion-beam source deposition for MEMS devices (Manuscript 1)

Manuscript title: Stress-free deposition of [001] preferentially oriented titanium thin film by Kaufman ion-beam source. [323]

Authors: GABLECH, I.; CAHA, O.; SVATOŠ, V.; PEKÁREK, J.; NEUŽIL, P.; ŠIKOLA, T.

Contribution: Inventor of the idea, preparation of thin films, and material analyses.

Motivation

Managing and reducing residual stress in thin films is crucial for MEMS fabrication, as high-stress levels can cause cracking and buckling, compromising device integrity. This manuscript focuses on residual stress in Ti thin films, which are favored for their mechanical strength, corrosion resistance, and biocompatibility. However, Ti thin films often suffer from compressive residual stress. Conventional methods like magnetron sputtering and evaporation usually do not induce compressive stress due to the sputtered materials with lower kinetic energy than ion-beam sputtering. On the other hand, they cannot provide a high level of crystallinity with preferential orientation, which can be essential for the growth or deposition of other materials with desired crystallographic orientation. This study explores RFICP Kaufman ion-beam source deposition, focusing on temperature control to achieve stress-free (001) preferentially oriented Ti thin films. We aimed to reduce residual stress by varying deposition temperature, which can eliminate compressive residual stress while keeping the process temperature in the compatible range (typically below ≈ 475 °C) of standard CMOS technology.

Conclusion

Our research demonstrated that precise temperature control during RFICP Kaufman ion-beam deposition is critical for achieving stress-free, (001) preferentially oriented Ti thin films. This method mitigates the compressive stress associated with high kinetic energy deposition techniques. Maintaining a lower deposition temperature compatible with CMOS processes significantly reduces thermal expansion-induced stress and enhances the reliability and durability of Ti thin films in MEMS fabrication. Results demonstrate that Kaufman ion-beam source deposition can prepare high-quality, stress-free thin films with preferential crystallographic orientation. Such optimized Ti layers were further used to fabricate MEMS

micro-bolometers and AlN-based piezoelectric resonators and harvesters, where the crystallography of the underlayer is critical.

2.3.2 Preparation of AlN piezoelectric thin films using a dual Kaufman ion-beam source setup (Manuscript 2)

Manuscript title: Preparation of high-quality stress-free (001) aluminum nitride thin film using a dual Kaufman ion-beam source setup. [47]

Authors: GABLECH, I.; SVATOŠ, V.; CAHA, O.; DUBROKA, A.; PEKÁREK, J.; KLEMPA, J.; NEUŽIL, P.; SCHNEIDER, M.; ŠIKOLA, T.

Contribution: Inventor of the idea, preparation of thin films, fabrication of structures, material analyses, and manuscript writing.

The motivation

Achieving high-quality, stress-free aluminum nitride (AlN) thin films is essential for various electronic and optoelectronic applications, mainly in MEMS-based piezoelectric devices. AlN is known for its excellent thermal conductivity, high acoustic velocity, and electrical insulation properties. However, conventional PVD-based deposition techniques often result in residual stress and poor stoichiometry, which results in worse electrical and mechanical properties and often leads to low performance of the thin films. This study explores the preparation of high-quality, stress-free (001) oriented AlN thin films using a dual Kaufman ion-beam source setup. Such a setup allows complex control of deposition parameters, which is critical for deposition process optimization. This approach aimed to minimize residual stress and enhance film quality and electrical properties. The deposition process was done under standard processing compatibility, including CMOS technology, which is important for developing high-performance devices.

Conclusion

Our findings demonstrated that the dual Kaufman ion-beam source setup effectively prepares high-quality, stress-free (001) oriented AlN thin films. This method significantly reduces residual stress compared to traditional deposition techniques, ensuring the structural integrity and reliability of the films in demanding applications. The complex control of ion-beam parameters during deposition leads to uniform film growth, superior crystalline quality, and a high piezoelectric coefficient value. The crystallinity level was incomparably better compared to other published results where AlN was prepared using other PVD methods. The optimized stress-free AlN reached a high value of the piezoelectric coefficient (d_{33}) = (7.33 ± 0.08) pC·N⁻¹.

2.3.3 Utilization of MEMS-based micro-bolometers for energy monitoring of surface plasmon resonance of silver nanoparticles (Manuscript 3)

Manuscript title: The collective photothermal effect of silver nanoparticles probed by a microbolometer. [324]

Authors: ZHU, H.; GABLECH, E.; GABLECH, I.; NEUŽIL, P.

Contribution: Co-inventor of the idea, bolometer characterization, image capturing, data evaluation, and manuscript writing.

The motivation

Understanding the photothermal effects of nanoparticles is essential for advancing applications in nanotechnology, biomedical diagnostics, and environmental sensing. The interaction of light with silver nanoparticles (AgNPs) leads to localized surface plasmon resonance (LSPR), resulting in significant heat generation. This heat can be measured precisely in situ using sensitive devices like microbolometers, enabling us to monitor nanoparticles' thermal properties and behavior under various conditions. Our work aimed to explore these photothermal effects and provide insight into the fundamental heat generation mechanisms.

The conclusion

This study demonstrated the capability of microbolometers to measure the collective photothermal effect of AgNPs accurately. We observed significant thermal responses correlated with the LSPR of AgNPs, which verifies the sensitivity and precision of MEMS microbolometers. These findings allowed us to calculate the heat generated by one AgNP and show the possible ways in which innovations in applications require precise thermal management and monitoring at the nanoscale could be made. The outcomes gained from this research are promising for advanced development in nanotechnology, medical diagnostics, and environmental monitoring.

2.3.4 MEMS-based cantilevers for investigation of graphene electrical properties changes due to induced mechanical strain (Manuscript 4)

Manuscript title: Mechanical strain and electric-field modulation of graphene transistors integrated on MEMS cantilevers. [325]

Authors: GABLECH, I.; BRODSKÝ, J.; VYROUBAL, P.; PIASTEK, J.; BARTOŠÍK, M.; PEKÁREK, J.

Contribution: Inventor of the idea, fabrication of devices and their characterization, data evaluation, and manuscript writing.

The motivation

Integrating graphene field effect transistors (FETs) with MEMS offers exciting possibilities for advanced sensing applications. With its exceptional electrical, mechanical, and thermal properties, graphene has significant potential for developing high-performance transistors that can be modulated by mechanical strain and electric fields. It has already been demonstrated that mechanical strain can effectively modulate the electronic properties of graphene, which makes it a promising candidate for strain-sensitive devices or gas sensors that can alter sensitivity and selectivity. Therefore, integrating graphene with MEMS cantilevers presents an innovative approach to creating highly sensitive and tunable sensors. This study explored the synergistic effects of mechanical strain and electric-field modulation on graphene transistors integrated into MEMS cantilevers.

The conclusion

We demonstrated that mechanical strain and electric-field modulation can effectively alter the electrical properties of graphene transistors integrated with the MEMS cantilevers. The graphene transistors exhibited significant conductivity and carrier mobility changes when subjected to mechanical strain. This integration resulted in a platform capable of detecting mechanical deformations and electric field variations. These devices can be suitable for applications in flexible electronics, wearable sensors, biomedical devices, and environmental monitoring.

2.3.5 Technology for fabrication of piezoelectric harvesters without the need of silicon-on-insulator wafers (Manuscript 5)

Manuscript title: Simple and efficient AlN-based piezoelectric energy harvesters. [46]

Authors: GABLECH, I.; KLEMPA, J.; PEKÁREK, J.; VYROUBAL, P.; HRABINA, J.; HOLÁ, M.; KUNZ, J.; BRODSKÝ, J.; NEUŽIL, P.

Contribution: Inventor of the idea, fabrication of devices, material characterization, physical simulations, data evaluation, and manuscript writing.

Motivation

Interest in energy harvesting systems has significantly increased, primarily due to the rising demand for sustainable and renewable energy sources. Among the various methods, piezoelectric energy harvesting stands out because it converts mechanical energy into electrical energy efficiently. Traditional devices often rely on silicon-on-insulator (SOI) wafers, which are high-cost and usually require more complex fabrication processes. This study introduces a simple and efficient approach to developing piezoelectric energy harvesters using AlN thin films with standard microfabrication techniques. The primary technological idea employs the precise control of DRIE etching, thus removing the necessity of expensive SOI wafers.

Conclusion

Development of our AlN-based piezoelectric energy harvesters showed a new, more straightforward approach to fabricating Si-based energy harvesters. The experimental results demonstrated that the AlN thin films achieved higher normalized power density than the published results of harvesters with AlN layers. Finite element model physical simulations verified all results with negligible deviation from the determined normalized power density. Notably, using an optimized DRIE protocol allowed us to precisely control the harvester beam's thickness, achieving high performance without the high costs associated with SOI wafers.

2.3.6 Selective wet etching of SiO₂ sacrificial layer for MEMS devices (Manuscript 6)

Manuscript title: Infinite selectivity of wet SiO₂ etching in respect to Al. [305]

Authors: GABLECH, I.; BRODSKÝ, J.; PEKÁREK, J.; NEUŽIL, P.

Contribution: Fabrication of chips, profile measurements, image capturing, data evaluation, and manuscript writing.

The motivation

Wet etching processes are still very important due to the demand for selective material removal in microfabrication. Among various etching techniques, achieving high selectivity between different materials is critical for ensuring the integrity and performance of microfabricated devices. Traditional etching processes often face challenges in selectively etching SiO₂ without affecting other materials like Al, commonly used in semiconductor devices. This study introduces a wet etching process that offers practically infinite selectivity of SiO₂ etching concerning Al.

Conclusion

The infinitely selective wet etching process for SiO₂ concerning Al presents a new approach suitable for microfabrication technology. The experimental results demonstrated that the optimized etching solution, consisting of a mixture of 48 % HF and 20 % oleum in a ratio of 1:1, is ideal for SiO₂ while leaving the Al layers unaffected. This was verified through various analytical techniques, confirming the integrity of the Al layers. We performed optical imaging and electrical measurements to verify that the Al layer was not etched. This approach is suitable for the fabrication of complex microelectronic and MEMS devices.

2.3.7 Nanostructures-based gas sensor for H₂ and NO₂ (Manuscript 7)

Manuscript title: ChemFET gas nanosensor arrays with alignment windows for assembly of single nanowires. [326]

Authors: CHMELA, O.; GABLECH, I.; SADÍLEK, J.; BRODSKÝ, J.; VALLEJOS VARGAS, S.

Contribution: Electrical characterization of devices, data evaluation, and manuscript writing.

The motivation

The increased demand for highly sensitive and selective gas sensors capable of detecting low concentrations of hazardous gases in various environments is still real. Gas sensors often struggle with sensitivity, selectivity, and the integration of nanoscale components. Chemically sensitive field-effect transistors (ChemFETs) have shown promise in addressing these challenges due to their ability to provide real-time, highly sensitive detection of gas molecules. This study aimed to further enhance ChemFET performance by integrating gas nanosensor arrays with alignment windows designed to assemble single nanowires precisely. The research focuses on reliable and efficient nanostructures-based gas sensor development by improving the alignment and positioning of nanowires.

The conclusion

We demonstrated the effectiveness of ChemFET-based gas nanosensor arrays equipped with alignment windows to assemble single nanowires precisely. The developed sensor arrays exhibited high sensitivity and detected H₂ and NO₂, confirming their potential for advanced gas sensing applications. The alignment windows significantly improved the accurate positioning of nanowires, which resulted in the reliability of the technology and sensor fabrication. Such structures can be suitable for environmental monitoring, industrial safety, and healthcare

diagnostics. The study shows the possibilities of nanostructure utilization in thin film technology and sensors.

2.4 Applications in Microfluidics

Microfluidic devices are essential in various scientific and industrial fields because they can precisely manipulate small fluid volumes within microscale or nanoscale channels. Additionally, thin films can be an essential part of these microfluidic systems since they enable the development and fabrication of sophisticated structures with complex functionality of devices used in chemical analysis, biological assays, and environmental monitoring. Fabricating microfluidic devices involves combining lithography, etching, and deposition techniques to define and fabricate a network of channels and reservoirs. Sealing of the channels can be done using various methods, including the fabrication of buried channels or anodic bonding (glass to Si), which perfectly fits requirements for biochemical systems and allows optical in-situ monitoring. Common materials such as Si, SiO₂, polymers (parylene, PMMA, polyimide, etc.), and metals form substrates and channels, while films are often employed as coatings or functional layers to improve performance. [327-330]

For instance, thin films of hydrophobic or hydrophilic materials can be deposited to control fluid flow within the channels. Hydrophobic coatings, often made of Teflon-like materials or parylene, prevent fluid adhesion to the channel walls, ensuring smooth flow and reducing the risk of clogging. Conversely, hydrophilic coatings enhance fluid wettability. Another important application of thin films in microfluidics is the development of LOC devices. These devices integrate multiple laboratory functions onto a single chip, allowing for high-throughput screening, POC or PON diagnostics, and environmental monitoring. Thin films of materials such as silicon dioxide, silicon nitride, and various metals create sensors and actuators within these chips, providing the necessary sensitivity and selectivity for detecting biological and chemical analytes. [330-333]

Moreover, thin films are employed in microfluidic devices designed for thermal management. In applications requiring precise temperature control, such as polymerase chain reaction (PCR) or other biochemical reactions, thin films of metals like Pt are used as heating elements or temperature sensors. These films offer excellent thermal conductivity and stability, ensuring accurate temperature regulation and uniform heat distribution across the microfluidic device. [60,334,335]

2.4.1 Design and fabrication of complex microfluidic geometries (Manuscript 8)

Manuscript title: Nanolithography Toolbox - Simplifying the design complexity of microfluidic chips.[336]

Authors: ZHANG, H.; PEKÁREK, J.; FENG, J.; LIU, X.; Li, H.; ZHU, H.; SVATOŠ, V.; GABLECH, I.; PODEŠVA, P.; NI, S.; YOBAS, L.; NEUŽIL, P.

Contribution: Design and fabrication of devices, as well as manuscript writing.

Motivation

This work focused on simplifying the design and fabrication processes of microfluidic chip layout. Various geometries are necessary for applications ranging from simple mixing channels to more complex biological assays. The complexity and costs associated with the design and fabrication of complex devices are often extremely time-consuming and expensive; therefore, our research aimed to address these challenges by developing methods to streamline the design process and reduce risk factors of microfluidic chip design and fabrication. This processing simplification allows us to make microfluidic technology more accessible and cost-effective.

Conclusion

We showed a practical approach for designing complex microfluidic channels and structures on chips with a positive influence on fabrication difficulty, functionality, and time consumption, covering the period from design to fabrication. We demonstrated that producing high-quality microfluidic devices with reduced time and costs is possible. Experimental results confirm that this simplified attitude does not compromise the performance and reliability of microfluidic systems. It offers a simple framework for developing versatile microfluidic platforms. Such methodology can be well-suited for various physical, chemical, and biochemical applications, including solutions, particles, living organisms, or cells.

2.4.2 Microfluidics heat transfer (Manuscript 9)

Manuscript title: Heat transfer time determination based on DNA melting curve analysis. [337]

Authors: ZHU, H.; LI, H.; ZHANG, H.; FOHLEROVÁ, Z.; NI, S.; YOBAS, L.; KLEMPA, J.; GABLECH, I.; HUBÁLEK, J.; CHANG, H.; NEUŽIL, P.

Contribution: Device design and fabrication, as well as manuscript writing.

Motivation

The motivation of this study is to analyze the importance of precise heat transfer measurements in biological systems, such as deoxyribonucleic acid (DNA) analysis. Understanding DNA's thermal properties, such as melting temperature, is fundamental for various applications in genomics, molecular biology, and medical diagnostics. The DNA melting curve describes the denaturation process of double-stranded DNA into single strands as temperature increases and provides information about the system stability and composition of DNA sequences. Accurate determination of heat transfer time is essential for optimizing thermal cycling protocols in techniques such as polymerase chain reaction (PCR) and developing advanced thermal management systems in DNA analysis equipment. This study aimed to enhance the accuracy of heat transfer time measurements using known DNA melting temperature of the dsDNA and contribute to developing a more efficient and precise microfluidics system.

Conclusion

This study demonstrated the capability of precise determination of heat transfer times based on DNA melting curve analysis. The results highlight the importance of precise thermal profiling in DNA analysis, which is critical for the effectiveness of PCR and other genomic applications. This research provides precise data about DNA thermal properties and offers practical insights

for developing more advanced diagnostic tools. The improved measurement techniques can lead to better thermal management in DNA analysis instruments.

2.4.3 Microfluidics with embedded heater for cryogenic experiments ([Manuscript 10](#))

Manuscript title: Parylene-bonded micro-fluidic channels for cryogenic experiments at superfluid He-4 temperatures. [338]

Authors: MIDLIK, S.; GABLECH, I.; GOLEŇA, M.; BRODSKÝ, J.; SCHMORANZER, D.

Contribution: Co-inventor of device technology, device fabrication, and manuscript writing.

Motivation

Superfluid He-4 has significant potential to investigate quantum fluid dynamics and low-temperature physics. Superfluid He-4 possesses intriguing properties for research, such as null viscosity, high thermal conductivity, and the ability to flow without dissipating energy. However, conducting precise experiments at these temperatures requires advanced microfluidic systems that can withstand extreme conditions. Traditional materials and designs must often maintain integrity and performance at cryogenic temperatures. Parylene, Si, and Pt are promising candidates for creating robust microfluidic channels that can withstand low-temperature environments. This study aimed to develop perylene-bonded microfluidic channels capable of operating reliably in superfluid He-4 environments to provide controlled cryogenic experiments.

The conclusion

We demonstrated the feasibility of using a parylene-bonded Si/SiO₂/Pt microfluidic system for cryogenic experiments at superfluid He-4 temperatures. Experimental results showed that parylene can provide excellent structural integrity and functionality of the microfluidic channels under extreme cryogenic conditions. The developed system exhibited reliable performance while maintaining stable behavior during the experiments without noticeable He-4 leaks. This technological advancement enabled more precise and controlled studies of superfluid He-4 and can also serve as a guide for low-temperature physics experiments at the microscale level.

2.5 Protective coatings and biomedical applications

Protective coatings and biomedical applications represent critical areas where thin films enhance performance, durability, and functionality. These applications exploit the unique properties of thin films to provide protective mechanical and chemical barriers, improve biocompatibility, and enable the fabrication of advanced biomedical devices for acute and chronic utilization. Protective coatings are essential in extending the lifespan and performance of various components exposed to harsh environments. [339]

Thin films are widely used as protective layers due to their excellent resistance to wear, corrosion, and high temperatures. Common materials for protective coatings include TiN, DLC, and Al₂O₃. These coatings are applied using techniques such as PVD and CVD. For instance, in the automotive and aerospace industries, thin film coatings protect engine components, turbine blades, and other critical parts from extreme conditions. TiN coatings often enhance

the wear resistance of cutting tools and mechanical components. In contrast, DLC coatings provide low friction and elevated surface hardness, which is ideal for reducing wear in high-stress applications. [339-341]

In the biomedical field, thin films are utilized to improve the biocompatibility and functionality of medical devices. Materials such as parylene, Ti, Pt, AlN, TiN, ITO, or PEDOT are commonly used for coating implants, sensors, and other medical devices. Parylene, for instance, is known for its excellent biocompatibility, chemical resistance, and barrier properties, which makes it a popular choice for coating stents, catheters, and pacemakers. Polyimide can also give similar properties, where its biocompatibility depends on the preparation formula. [342-345]

Thin film coatings in biomedical applications serve multiple purposes. They can provide a biocompatible interface between the device and the biological environment, reducing the risk of undesired reactions and promoting tissue integration. Additionally, coatings can enhance the mechanical properties of implants, such as increasing their wear resistance and reducing the risk of failure. Functional coatings, such as those incorporating antimicrobial agents, can also help prevent infections and improve the overall performance of medical devices. One of the critical advancements in biomedical thin films is the development of drug-eluting coatings. These coatings are designed to release therapeutic agents over time, leading to targeted drug delivery directly at the implantation site. This approach is particularly beneficial for preventing restenosis in stents or delivering localized chemotherapy in cancer treatments. [342]

2.5.1 Development of high-performance microelectrode arrays (Manuscript 11)

Manuscript title: High-Conductivity Stoichiometric Titanium Nitride for Bioelectronics. [346]

Authors: GABLECH, I.; MIGLIACCIO, L.; BRODSKÝ, J.; HAVLÍČEK, M.; PODEŠVA, P.; HRDÝ, R.; EHLICH, J.; GRYSZEL, M.; GLOWACKI, E.

Contribution: Inventor of the idea, device fabrication and characterization, data evaluation, and manuscript writing.

Motivation

The growing demand pushes development in bioelectronics for materials that can enhance the performance and reliability of bioelectronic devices. TiN is a promising material due to its excellent electrical conductivity, chemical stability, and biocompatibility. Additionally, the price of TiN is much lower than the cost of popular materials such as iridium oxide (IrO_x) or Pt. High-conductivity materials are critical to ensure efficient signal transmission and durability in biological environments. Bioelectronic devices often struggle with material degradation and poor electrical properties, limiting their functionality and lifespan. This study aimed to investigate the properties of stoichiometric TiN, focusing on its potential to improve the performance of bioelectronic devices. TiN is one of the leading materials in developing next-generation bioelectronic interfaces, sensors, and implants. Encapsulation is another important

aspect and is often problematic in guaranteeing device reliability for chronic experiments. Therefore, we also investigated the combination of AlN and parylene.

Conclusion

We fabricated high-performance microelectrode arrays (MEAs) utilizing microstructured surfaces with TiN as electrode material showcasing low-impedance optimal for signal recording. We showed that stoichiometric TiN exhibits high conductivity and excellent stability, making it suitable for bioelectronic applications. Experimental results showed that TiN maintains its electrical properties and structural integrity in stimulated biological conditions and accelerated aging tests. We confirmed its potential for long-term use in bioelectronic devices. The high conductivity of TiN enhances signal transmission, which is crucial for the efficient functioning of sensors and implants, especially where the electrode diameter is usually in tens of μm . Furthermore, combining AlN and parylene-C as an encapsulation layer proved its durability compared to commercial MEAs, which are encapsulated with Si_3N_4 . This study underscores the significance of material selection in bioelectronics and highlights TiN and AlN with parylene-C capabilities in improving device performance and reliability.

2.5.2 Development of sub-micrometer PEDOT transistors for signal recording

(Manuscript 12)

Manuscript title: Downsizing the Channel Length of Vertical Organic Electrochemical Transistors. [346]

Authors: BRODSKÝ, J.; GABLECH, I.; MIGLIACCIO, L.; HAVLÍČEK, M.; DONAHUE, M.; GLOWACKI, E.

Contribution: Co-inventor of idea, device fabrication and characterization, and manuscript writing.

The motivation

The advancement of organic electrochemical transistors (OECTs) is vital for improving their performance and sensing weak signals. Downsizing the channel length is one possibility for improving the electrical properties of OECTs, such as speed and sensitivity, which is important in the constantly evolving field of biomedicine. OECTs face limitations due to relatively long channel lengths, which can decrease their response times and sensitivity. This study addressed these challenges by employing advanced fabrication technologies to develop vertical OECTs (vOECTs) with reduced channel lengths lower than one micrometer. By employing precise microfabrication techniques, this research focuses on developing high-performance vOECTs with significantly improved electrical characteristics compared to their planar alternatives.

Conclusion

We developed a new technique for fabricating sub-micrometer channel length of ≈ 350 nm vOECTs using advanced microfabrication techniques. We also compared spin-coated PEDOT:PSS and electropolymerized PEDOT:PF₆, both showing excellent performance.

Experimental results showed a marked improvement in the performance in the OECTs field. Reduced channel lengths lead to faster response times and enhanced sensitivity. Our vOECTs with sub-micrometer channels exhibited excellent electrical characteristics with an ON/OFF ratio of $\approx 8.6 \times 10^4$, making them suitable for applications in bioelectronics, including biosensors and neural interfaces. This research demonstrates the critical role of advanced microfabrication techniques in enhancing the performance of organic electronic devices.

2.6 Micro- and nanostructured surfaces

Microstructured and nanostructured surfaces have become essential in scientific and industrial research due to their unique properties related to specific geometries. These surfaces are often created from thin films prepared by PVD and CVD techniques and offer enhanced functionalities that can be modified for specific applications ranging from optical devices to biomedical implants. Fabricating microstructured surfaces usually relies on advanced microfabrication techniques described above, including dry and wet etching or anodization processes. [347-350]

These surfaces' electrical and mechanical properties are significantly influenced by the material composition and shape, size, and aspect ratio, which affect their interaction with light, fluids, and biological entities. Microstructured surfaces can exhibit optical properties such as anti-reflective behavior, light trapping, and diffraction effects. These properties are suitable for applications like solar cells to enhance light absorption and efficiency. Similarly, microstructured surfaces improve performance in optical sensors and display technologies by controlling light propagation and reducing glare. [351-356]

The interaction of fluids with microstructured surfaces differs from that with flat surfaces. Microstructures can induce superhydrophobicity or superhydrophilicity, affecting fluid flow, droplet formation, and evaporation rates. These properties can be used in the development of microfluidic devices. Mechanical properties, such as hardness and elasticity, can be tuned by adjusting the geometry and selection of material or its composition. In biomedical applications, the topography created by microstructures influences cell behavior, including adhesion, proliferation, and differentiation. Microstructured and nanostructured surfaces can also be used in implants and tissue engineering scaffolds to promote desirable cellular interactions and improve biocompatibility. [260,351,354,357,358]

2.6.1 Micropillars for cellular traction force evaluation (Manuscript 13)

Manuscript title: SiO₂-Decorated Parylene C Micropillars Designed to Probe Cellular Force. [350]

Authors: FOHLEROVÁ, Z.; GABLECH, I.; OTÁHAL, A.; FECKO, P.

Contribution: Inventor of structures fabrication technology, micropillars fabrication and characterization, and manuscript writing.

Motivation

This study aimed to develop an advanced tool for probing cellular traction forces with high precision and sensitivity. Cellular force measurement is essential for understanding various biological processes, such as cell migration and differentiation. Traditional methods for measuring cellular forces often lack the required sensitivity or resolution. The integration of SiO₂-decorated parylene-C micropillars offers a novel approach to enhance the sensitivity and specificity of these measurements. Parylene-C was chosen for its excellent biocompatibility and mechanical properties, while the SiO₂ decoration improves the surface characteristics and interaction with cells since it allows covalent binding with proteins. Therefore, we designed and fabricated chips for probing cellular forces to observe cellular mechanics.

Conclusion

The experimental results demonstrated that our SiO₂-decorated parylene-C micropillars achieved high sensitivity and accuracy in determining cellular traction forces. The top-down fabrication approach, including photolithography, RIE, and IBE, proved straightforward and adaptable for developing these and other similar structures. The experiments confirmed the patterning of micropillars via the selective chemistry of the SiO₂ interface and the surface chemistry of the parylene-C sidewalls. The main benefit of this technological advancement is eliminating the need for micro-contact printing of proteins on the micropillar array tops. Furthermore, the cytocompatibility of the micropillars was validated through the morphology of 3T3-fibroblasts adhered to the micropillar arrays, and we evaluated cell spread area, cell proliferation, qualitative evaluations of the cytoskeleton, and the development of focal contacts. In summary, micropillars exhibited excellent mechanical stability and consistent performance. Our findings highlight the potential of this technology in tissue engineering and fundamental cell biology research. We introduced an innovative method for flexible micropillar substrate fabrication, enabling cell traction forces to be quantified.

2.6.2 Development of hydrophilic and superhydrophobic surfaces (Manuscript 14)

Manuscript title: Nature-inspired parylene/SiO₂ core-shell micro-nano pillars: Effect of topography and surface chemistry. [351]

Authors: LIU, X.; FOHLEROVÁ, Z.; GABLECH, I.; PUMERA, M.; NEUŽIL, P.

Contribution: Structures fabrication, data evaluation, and manuscript writing.

Motivation:

An attractive scientific area is the imitation of various natural phenomena, which can be carried out using advanced micro- and nanostructured surfaces that mimic the sophisticated functionalities observed in nature. Natural systems often exhibit hierarchical structures that enhance mechanical, optical, and chemical properties, making them highly efficient and adaptable to various environments. Therefore, researchers aim to create materials with superior properties observed in nature suitable for a wide range of applications. Parylene/SiO₂ core-shell micropillars represent a significant advancement in this area because they combine the advantages of both materials to achieve desired properties. Integrating these materials into core-shell structures enables the creation of surfaces that mimic natural topographies and exhibit

enhanced functionality due to their flexibility. Therefore, this study aimed to explore the effects of topography and surface chemistry on wettability. Furthermore, the specific topography can lead to increased sensitivity and selectivity of sensors. In summary, this study aimed to contribute to developing next-generation materials that enhance natural design principles to achieve superior performance and functionality in terms of surface wettability.

Conclusion

We investigated topography and surface chemistry modifications via silanes of nature-inspired Parylene/SiO₂ core-shell micropillars and their influence on surface properties, leading to different levels of wettability and adhesion force. Experimental results based on force-distance measurement probed by AFM and water droplet contact angle measurements revealed that these micro pillars offer unique properties comparable to one of the gecko setae commonly observed in nature. We could generally create surfaces with varying properties, from hydrophilic to superhydrophobic. Overall, the Parylene/SiO₂ core-shell structures show great potential for a wide range of modifications, resulting in surfaces with specific properties suitable for functional materials and surface engineering.

3 CONCLUSION

This habilitation thesis investigates the critical role of thin films, characterization methods, and microfabrication techniques in advanced materials science and modern electronics. The unique properties of thin films and the precision offered by microfabrication methods were demonstrated to be vital in numerous applications. Thin films are necessary for materials and device development thanks to their unique and specific physical and chemical properties, such as electrical conductivity, optical transparency, mechanical strength, and chemical stability. These properties can be controlled by choosing the optimal technique and its deposition process parameters.

Microfabrication techniques, including photolithography, etching, and doping, are fundamental in fabricating complex electronic devices, MEMS, microfluidic systems, and microstructures. Well-optimized thin films and photolithography evolution are essential for developing advanced devices with improved performance and reduced size. This is essential to developing high-performance transistors, diodes, and integrated circuits, which are fundamental entities of modern electronic devices. Furthermore, the integration of thin films into sensor technology has also led to significant improvements in performance and reliability. Thin films enhance the sensitivity and selectivity of sensors, making them suitable for environmental monitoring, industrial safety, and healthcare diagnostics by recognizing many physical and chemical changes. Additionally, thin films such as nitrides, oxides, and carbides can offer excellent resistance to wear, corrosion, and high temperatures, positively influencing the lifespan and performance of devices in harsh environments. Several thin films also enhance the biocompatibility and functionality of medical devices, which is crucial for many *in-vivo* devices. Microstructured surfaces, fabricated from thin films, exhibit unique properties due to

their complex geometries and material properties. These surfaces offer enhanced functionalities optimized for specific applications, such as optical or biomedical devices.

In summary, the content of this thesis shows the impact of thin films and microfabrication techniques on modern technology and science. The evolution of all techniques pushes the development of devices forward and is an indispensable and fast-growing part of the current technology-based world. This progress is necessary for high-performance and reliable devices critical for future technologies.

4 REFERENCES

- [1] SATHISH, M., N. RADHIKA AND B. SALEH Current Status, Challenges, and Future Prospects of Thin Film Coating Techniques and Coating Structures. *Journal of Bio- and Tribo-Corrosion*, 2023/04/06 2023, 9(2), 35.
- [2] ICHOU, H., N. ARROUSSE, E. BERDIMURODOV AND N. ALIEV Exploring the Advancements in Physical Vapor Deposition Coating: A Review. *Journal of Bio- and Tribo-Corrosion*, 2023/11/15 2023, 10(1), 3.
- [3] ARSHAVSKY-GRAHAM, S. AND E. SEGAL. Lab-on-a-Chip Devices for Point-of-Care Medical Diagnostics. In J. BAHNEMANN AND A. GRÜNBERGER eds. *Microfluidics in Biotechnology*. Cham: Springer International Publishing, 2022, p. 247-265.
- [4] URADE, A. R., I. LAHIRI AND K. S. SURESH Graphene Properties, Synthesis and Applications: A Review. *JOM*, 2023/03/01 2023, 75(3), 614-630.
- [5] TWI-YEBOAH, N., D. OSEI, W. H. DONTOH AND M. K. DANQUAH. Two-Dimensional (2D) Hybrid Nanocomposites for Environmental Sensing Applications. In N. TALREJA, D. CHAUHAN AND M. ASHFAQ eds. *Two-dimensional Hybrid Composites: Synthesis, Properties and Applications*. Singapore: Springer Nature Singapore, 2024, p. 169-187.
- [6] GABLECH, I., J. SOMER, Z. FOHLEROVÁ, V. SVATOŠ, et al. Fabrication of buried microfluidic channels with observation windows using femtosecond laser photoablation and parylene-C coating. *Microfluidics and Nanofluidics*, 2018/09/03 2018, 22(9), 105.
- [7] KUMAR, N., M. KUMARI AND R. K. ARUN. Development and Implementation of Portable Biosensors in Microfluidic Point-of-Care Devices for Pathogen Detection. In P. CHANDRA AND K. MAHATO eds. *Miniaturized Biosensing Devices: Fabrication and Applications*. Singapore: Springer Nature Singapore, 2022, p. 99-122.
- [8] KIM, H., C. M. GILMORE, A. PIQUÉ, J. S. HORWITZ, et al. Electrical, optical, and structural properties of indium-tin-oxide thin films for organic light-emitting devices. *Journal of Applied Physics*, 1999, 86(11), 6451-6461.
- [9] MUSLIH, E. Y. AND K. H. KIM Preparation of Zinc Oxide (ZnO) Thin Film as Transparent Conductive Oxide (TCO) from Zinc Complex Compound on Thin Film Solar Cells: A Study of O₂ Effect on Annealing Process. *IOP Conference Series: Materials Science and Engineering*, 2017/07/01 2017, 214(1), 012001.
- [10] GIRTAN, M. Comparison of ITO/metal/ITO and ZnO/metal/ZnO characteristics as transparent electrodes for third generation solar cells. *Solar Energy Materials and Solar Cells*, 2012/05/01/ 2012, 100, 153-161.
- [11] CHAYEUSKI, V., V. ZHYLINSKI, V. KAZACHENKO, A. TARASEVICH, et al. Structural and Mechanical Properties of DLC/TiN Coatings on Carbide for Wood-Cutting Applications. *Coatings*, 2023, 13(7), 1192.
- [12] ZHANG, M., L. XIN, X. DING, S. ZHU, et al. Effects Ti/TiAlN composite multilayer coatings on corrosion resistance of titanium alloy in solid NaCl-H₂O-O₂ at 600 °C. *Journal of Alloys and Compounds*, 2018/02/15/ 2018, 734, 307-317.
- [13] THANKA RAJAN, S., B. SUBRAMANIAN AND A. AROCKIARAJAN A comprehensive review on biocompatible thin films for biomedical application. *Ceramics International*, 2022/02/15/ 2022, 48(4), 4377-4400.
- [14] ZHAO, Y. Growth and Synthesis of Nanostructured Thin Films. In A. ZRIBI AND J. FORTIN eds. *Functional Thin Films and Nanostructures for Sensors: Synthesis, Physics and Applications*. Boston, MA: Springer US, 2009, p. 31-64.
- [15] ATYAOUI, M., B. WIEM, E. INES, C. LASSAAD, et al. Structural, Carrier Life Time and Optical Properties of Vanadium Doped Tin Oxide Films Developed on Silicon Nanowires for Photo-Catalytic Degradation of Organic Dyes. *Chemistry Africa*, 2024/05/16 2024.
- [16] ZHANG, L., W. ZHANG, Y. LIU AND L. LIU Three-Layered Thin Films for Simultaneous Infrared Camouflage and Radiative Cooling. *Materials*, 2023, 16(11), 4188.
- [17] YANG, S., K. CHO AND S. KIM Enhanced Thermoelectric Characteristics of Ag₂Se Nanoparticle Thin Films by Embedding Silicon Nanowires. *Energies*, 2020, 13(12), 3072.
- [18] ABU-THABIT, N. Y. AND A. S. H. MAKHLOUF. Chapter 1 - Fundamental of smart coatings and thin films: synthesis, deposition methods, and industrial applications. In A.S.H. MAKHLOUF AND N.Y. ABU-THABIT eds. *Advances in Smart Coatings and Thin Films for Future Industrial and Biomedical Engineering Applications*. Elsevier, 2020, p. 3-35.
- [19] SUN, L., G. YUAN, L. GAO, J. YANG, et al. Chemical vapour deposition. *Nature Reviews Methods Primers*, 2021/01/14 2021, 1(1), 5.
- [20] SHAFFNER, T. J. A REVIEW OF MODERN CHARACTERIZATION METHODS FOR SEMICONDUCTOR-MATERIALS (AN OVERVIEW OF ELECTRON, ION, X-RAY AND OPTICAL PROBE CHARACTERIZATION TECHNIQUES AVAILABLE FOR PROCESS DIAGNOSTICS IN THE SEMICONDUCTOR INDUSTRY). *Scanning Electron Microscopy*, 1986, 1986, 11-24.
- [21] FENG, P. X. L., D. J. YOUNG AND C. A. ZORMAN. MEMS/NEMS Devices and Applications. In B. BHUSHAN ed. *Springer Handbook of Nanotechnology*. Berlin, Heidelberg: Springer Berlin Heidelberg, 2017, p. 395-429.
- [22] FAYOMI, O. S. I., I. G. AKANDE, O. P. ABIOYE AND O. B. FAKEHINDE New Trend in Thin Film Composite Coating Deposition: A Mini Review. *Procedia Manufacturing*, 2019/01/01/ 2019, 35, 1007-1012.
- [23] MENSHIKOVA, S. I., E. I. ROGACHEVA, A. Y. SIPATOV AND A. G. FEDOROV Dependence of electrical conductivity on Bi₂Se₃ thin film thickness. *Functional Materials*, 2017, 24(4), 555-558.
- [24] SUZUKI, T., I. KOSACKI AND H. U. ANDERSON Microstructure-electrical conductivity relationships in nanocrystalline ceria thin films. *Solid State Ionics*, Nov 2002, 151(1-4), 111-121.
- [25] CHORNOUS, A. M., L. V. DEKHTYARUK, T. P. GOVORUN AND A. O. STEPANENKO Influence of diffusing impurities on the electrical conductivity of single-crystal and polycrystalline metal films. *Metallofizika I Noveishie Tekhnologii*, Feb 2007, 29(2), 249-266.

- [26] PATEL, N. P. AND K. V. CHAUHAN Structural, optical and electrical study of ZnO:Al thin films: A review. *Materials Today: Proceedings*, 2022/01/01/ 2022, 62, 3386-3396.
- [27] LIM, S. C., S. H. KIM, H. Y. CHU, J. H. LEE, et al. New method of driving an OLED with an OTFT. *Synthetic Metals*, Aug 2005, 151(3), 197-201.
- [28] CHO, J. M., J. KIM, H. KIM, M. KIM, et al. ITO/AZO Double-Layered Transparent Conducting Oxide Films for Organic Photovoltaic Cells. *Molecular Crystals and Liquid Crystals*, Jul 2014, 597(1), 1-7.
- [29] KIM, S. M., Y. S. RIM, M. J. KEUM AND K. H. KIM Study on the electrical and optical properties of ITO and AZO thin film by oxygen gas flow rate. *Journal of Electroceramics*, Oct 2009, 23(2-4), 341-345.
- [30] SAMADZAMINI, K., J. FROUNCHI AND H. VELADI A High Optical Transmittance and Low Cost Touch Screen without Patterning. *Advances in Electrical and Computer Engineering*, 2017, 17(1), 109-114.
- [31] KUO, Y. Thin Film Transistor Technology—Past, Present, and Future. *The Electrochemical Society Interface*, 2013/01/01 2013, 22(1), 55.
- [32] ZHANG, L. R., H. M. YU, W. P. XIAO, C. LIU, et al. Strategies for Applications of Oxide-Based Thin Film Transistors. *Electronics*, Mar 2022, 11(6).
- [33] HAN, S. W., H. W. LEE, H. J. LEE, J. Y. KIM, et al. Mechanical properties of Au thin film for application in MEMS/NEMS using microtensile test. *Current Applied Physics*, 2006/08/01/ 2006, 6, e81-e85.
- [34] HODGE, T. C., S. A. BIDSTRUPALLEN AND P. A. KOHL Stresses in thin film metallization. *Ieee Transactions on Components Packaging and Manufacturing Technology Part A*, Jun 1997, 20(2), 241-250.
- [35] EASTMAN, C. D. AND T. H. ETSSELL Performance of a platinum thin film working electrode in a chemical sensor. *Thin Solid Films*, Dec 2006, 515(4), 2669-2672.
- [36] ABBURI, A., N. ABRAMS AND W. J. YEH Synthesis of nanoporous platinum thin films and application as hydrogen sensor. *Journal of Porous Materials*, Oct 2012, 19(5), 543-549.
- [37] MATSUMIYA, M., W. SHIN, N. IZU AND N. MURAYAMA Nano-structured thin-film Pt catalyst for thermoelectric hydrogen gas sensor. *Sensors and Actuators B-Chemical*, Aug 2003, 93(1-3), 309-315.
- [38] LACY, F. AND IAENG. Investigating thin films for use as temperature sensors. In *World Congress on Engineering and Computer Science (WCECS 2007)*. San Francisco, CA, 2007, p. 441-444.
- [39] GABLECH, I., V. SVATOŠ, O. CAHA, M. HRABOVSKÝ, et al. Preparation of (001) preferentially oriented titanium thin films by ion-beam sputtering deposition on thermal silicon dioxide. *Journal of Materials Science*, 2016/04/01 2016, 51(7), 3329-3336.
- [40] TEPPER-FARAN, T., H. NEIBERG, N. YITZHAK AND D. ELATA The Strong Effect of NiCr Adhesion Layers in Surface Micromachined MEMS Sensors. *Ieee Sensors Letters*, Oct 2023, 7(10).
- [41] ALEKSEEVA, A. K., P. M. RAJANNA, A. S. ANISIMOV, O. SERGEEV, et al. Synergistic Effect of Single-Walled Carbon Nanotubes and PEDOT:PSS in Thin Film Amorphous Silicon Hybrid Solar Cell. *Physica Status Solidi B-Basic Solid State Physics*, Jan 2018, 255(1).
- [42] LI, M., Y. C. XIONG, H. X. WEI, F. J. YAO, et al. Flexible Te/PEDOT:PSS thin films with high thermoelectric power factor and their application as flexible temperature sensors. *Nanoscale*, Jul 2023, 15(26), 11237-11246.
- [43] ARTESHI, Y., A. AGHANEJAD, S. DAVARAN AND Y. OMIDI Biocompatible and electroconductive polyaniline-based biomaterials for electrical stimulation. *European Polymer Journal*, 2018/11/01/ 2018, 108, 150-170.
- [44] PULSKAMP, J. S., R. G. POLCAWICH, R. Q. RUDY, S. S. BEDAIR, et al. Piezoelectric PZT MEMS technologies for small-scale robotics and RF applications. *MRS Bulletin*, 2012/11/01 2012, 37(11), 1062-1070.
- [45] TONISCH, K., V. CIMALLA, C. FOERSTER, H. ROMANUS, et al. Piezoelectric properties of polycrystalline AlN thin films for MEMS application. *Sensors and Actuators A: Physical*, 2006/11/20/ 2006, 132(2), 658-663.
- [46] GABLECH, I., J. KLEMPA, J. PEKÁREK, P. VYROUBAL, et al. Simple and Efficient AlN-Based Piezoelectric Energy Harvesters. *Micromachines (Basel)*, Jan 28 2020, 11(2).
- [47] GABLECH, I., V. SVATOŠ, O. CAHA, A. DUBROKA, et al. Preparation of high-quality stress-free (001) aluminum nitride thin film using a dual Kaufman ion-beam source setup. *Thin Solid Films*, 2019/01/31/ 2019, 670, 105-112.
- [48] MUTYALA, M. S. K., J. Z. ZHAO, T. C. LIN AND X. C. LI Study on materials and fabrication of functional thin film AlN force sensors. *Journal of Manufacturing Processes*, Aug 2015, 19, 233-238.
- [49] HSU, Y. C., I. Y. SHEN AND G. Z. CAO. Feasibility study of PZT thin-film sensors and actuators for smart microstructures and MEMS devices. In *Smart Structures and Materials 2002 Conference*. San Diego, Ca, 2002, vol. 4701, p. 20-28.
- [50] CHANG, C. C. AND K. H. CHEN Fabrication and characterization of PZT thin film ultrasonic devices. *Journal of the Chinese Institute of Engineers*, Mar 2000, 23(2), 179-184.
- [51] MAAS, R., M. KOCH, N. R. HARRIS, N. M. WHITE, et al. Thick-film printing of PZT onto silicon. *Materials Letters*, May 1997, 31(1-2), 109-112.
- [52] ICHINO, Y., Y. YOSHIDA, M. MAEDA, Y. TAKAI, et al. Improvement of thermoelectric properties by introducing nanostructures into Bi₂Te₃ thin films. In *26th International Conference on Thermoelectrics (ICT'07)*. Jeju Isl, SOUTH KOREA, 2007, p. 34-37.
- [53] TAJIMA, K., F. B. QIU, W. SHIN, N. SAWAGUCHI, et al. Thermoelectric hydrogen sensor based on SiGe thin film. In M. MIYAYAMA, T. TAKENAKA, M. TAKATA AND K. SHINOZAKI eds. *Electroceramics in Japan VII*. 2004, vol. 269, p. 117-120.
- [54] NISHIBORI, M., W. SHIN, N. IZU, T. ITOH, et al. Thermoelectric hydrogen sensors using Si and SiGe thin films with a catalytic combustor. *Journal of the Ceramic Society of Japan*, Mar 2010, 118(1375), 188-192.

- [55] CHUANG, C. T., C. K. CHAO, R. C. CHANG AND K. Y. CHU Effects of internal stresses on the mechanical properties of deposition thin films. *Journal of Materials Processing Technology*, May 2008, 201(1-3), 770-774.
- [56] SIMUNKOVÁ, S., O. BLÁHOVÁ AND I. STEPÁNEK Mechanical properties of thin film-substrate systems. *Journal of Materials Processing Technology*, Feb 2003, 133(1-2), 189-194.
- [57] KANG, D. Y., A. STANDLEY, J. H. C. CHANG, Y. LIU, et al. EFFECTS OF DEPOSITION TEMPERATURE ON PARYLENE-C PROPERTIES. In *26th IEEE International Conference on Micro Electro Mechanical Systems (MEMS)*. Taipei, TAIWAN, 2013, p. 389-392.
- [58] SUTANI, Y., T. FUKUSHIMA, A. MORI, Y. KOSHIBA, et al. Improvement of thermal stability of an organic pyroelectric infrared sensor with Parylene C coating. *Japanese Journal of Applied Physics*, Apr 2020, 59.
- [59] JUNG, B. J., H. JANG, G. Y. LEE, J. KIM, et al. Surface Functionalization and Bonding of Chemically Inert Parylene Microfluidics Using Parylene-A Adhesive Layer. *Biochip Journal*, Jun 2022, 16(2), 168-174.
- [60] ZHANG, F., C. TUCK, R. HAGUE, Y. F. HE, et al. Inkjet printing of polyimide insulators for the 3D printing of dielectric materials for microelectronic applications. *Journal of Applied Polymer Science*, May 2016, 133(18).
- [61] KANG, Y. S. AND P. S. HO Thickness dependent mechanical behavior of submicron aluminum films. *Journal of Electronic Materials*, Jul 1997, 26(7), 805-813.
- [62] DURBIN, B. M., C. M. SHAH, S. SRIRAM AND M. BHASKARAN. Strain-resistance relationship in gold conductors for elastomeric-based flexible devices. In *Conference on Smart Nano-Micro Materials and Devices/SPIE Smart Nano + Micro Materials and Devices Forum*. Melbourne, AUSTRALIA, 2011, vol. 8204.
- [63] YAZICI, S., M. A. OLGAR, F. G. AKCA, A. CANTAS, et al. Growth of $\text{Cu}_2\text{ZnSnS}_4$ absorber layer on flexible metallic substrates for thin film solar cell applications. *Thin Solid Films*, Aug 2015, 589, 563-573.
- [64] LATTEMANN, M., S. ULRICH, H. HOLLECK, M. STÜBER, et al. Characterisation of silicon carbide and silicon nitride thin films and $\text{Si}_3\text{N}_4/\text{SiC}$ multilayers. *Diamond and Related Materials*, Mar-Jun 2002, 11(3-6), 1248-1253.
- [65] JITHIN, M. A., K. L. GANAPATHI, G. VIKRAM, N. K. UDAYASHANKAR, et al. Pulsed DC magnetron sputtered titanium nitride thin films for localized heating applications in MEMS devices. *Sensors and Actuators a-Physical*, Apr 2018, 272, 199-205.
- [66] SAIT, R. A. AND R. B. M. CROSS Synthesis and characterization of sputtered titanium nitride as a nucleation layer for novel neural electrode coatings. *Applied Surface Science*, Dec 2017, 424, 290-298.
- [67] ZHUANG, Q. H., G. J. LIU, X. H. FU, Q. H. ZHUANG, et al. Optical properties research of a - Si thin film by electron beam evaporation. In *International Conference on Optoelectronics and Microelectronics (ICOM)*. Changchun, PEOPLES R CHINA, 2015, p. 470-473.
- [68] NYKYRUY, L. I., R. S. YAVORSKYI, Z. R. ZAPUKHLYAK, G. WISZ, et al. Evaluation of CdS/CdTe thin film solar cells: SCAPS thickness simulation and analysis of optical properties. *Optical Materials*, Jun 2019, 92, 319-329.
- [69] LU, Y. Q., M. M. LI, Y. FENG, Y. X. XU, et al. Tuning the optical properties of transparent ZIF-8 thin films by adjusting the crystal morphology. *Optical Materials*, Aug 2024, 154.
- [70] BOSCARINO, S., I. CRUPI, S. MIRABELLA, F. SIMONE, et al. TCO/Ag/TCO transparent electrodes for solar cells application. *Applied Physics a-Materials Science & Processing*, Sep 2014, 116(3), 1287-1291.
- [71] DU, W. H., J. J. YANG, C. XIONG, Y. ZHAO, et al. Preferential orientation growth of ITO thin film on quartz substrate with ZnO buffer layer by magnetron sputtering technique. *International Journal of Modern Physics B*, Jul 2017, 31(16-19).
- [72] ZHANG, Z. Q., X. YU, W. J. ZHAO, K. LU, et al. Preparation of Low-Resistance and Residue-free ITO Films for Large-scale 3D Displays. *Acs Applied Materials & Interfaces*, Dec 2019, 11(49), 45903-45913.
- [73] LYUBCHYK, A., A. VICENTE, P. U. ALVES, B. CATELA, et al. Influence of post-deposition annealing on electrical and optical properties of ZnO-based TCOs deposited at room temperature. *Physica Status Solidi a-Applications and Materials Science*, Sep 2016, 213(9), 2317-2328.
- [74] ÖZHAN, A. E. S., T. HACALOGLU AND B. KAFTANOGLU Development of hard, anti-reflective coating for mid wave infrared region. *Infrared Physics & Technology*, Dec 2021, 119.
- [75] BAI, X. Y., Y. SHUAI, L. LV, S. T. HUANG, et al. Mo/Ti multilayer Bragg reflector for LiNbO_3 film bulk acoustic wave resonators. *Journal of Applied Physics*, Sep 2020, 128(9).
- [76] YUN, S., F. NAMIN, D. H. WERNER, T. S. MAYER, et al. Demonstration of a nearly ideal wavelength-selective optical mirror using a metamaterial-enabled dielectric coating. *Applied Physics Letters*, 2013, 102(17).
- [77] AHMED, M., A. BAKRY, E. R. SHAABAN AND H. DALIR Structural, electrical, and optical properties of ITO thin films and their influence on performance of CdS/CdTe thin-film solar cells. *Journal of Materials Science: Materials in Electronics*, 2021/04/01 2021, 32(8), 11107-11118.
- [78] ZHAO, Y., J. D. WU AND N. XU Structures, optical absorption and electrical properties of pulsed-laser-deposited $\text{CuIn}_{0.8}\text{Ga}_{0.2}\text{Se}_2$ thin films and their use in CIGS/PCBM photovoltaic structures. *Materials Research Express*, Oct 2016, 3(10).
- [79] FARAONE, G., R. MODI, S. MAROM, A. PODESTÀ, et al. Increasing the optical absorption in a-Si thin films by embedding gold nanoparticles. *Optical Materials*, Jan 2018, 75, 204-210.
- [80] BORTCHAGOVSKY, E., T. MISHAKOVA AND V. STYOPKIN Plasmonic Properties of Thin Annealed Gold Films. *Plasmonics*, Dec 2020, 15(6), 2011-2017.
- [81] MORAWIEC, S., M. J. MENDES, F. PRIOLO AND I. CRUPI Plasmonic nanostructures for light trapping in thin-film solar cells. *Materials Science in Semiconductor Processing*, Mar 2019, 92, 10-18.

- [82] SU, Y. Y., X. W. CHENG, J. B. LI, Y. K. DOU, et al. Evolution of microstructure in vanadium oxide bolometer film during annealing process. *Applied Surface Science*, Dec 2015, 357, 887-891.
- [83] JUNG, H., T. H. KIM, G. KIM, C. M. YANG, et al. Design and characteristics of a-Si-based micro-bolometers with shared-anchor structure in vacuum packaged systems. *Microsystem Technologies-Micro-and Nanosystems-Information Storage and Processing Systems*, Apr 2014, 20(4-5), 899-905.
- [84] LIU, X. M., H. J. FANG AND L. T. LIU Study on new structure uncooled a-Si microbolometer for infrared detection. *Microelectronics Journal*, Jun-Jul 2007, 38(6-7), 735-739.
- [85] SHIH, K. K. AND D. B. DOVE DEPOSITION OF ALUMINUM-OXIDE FILMS WITH HIGH REFRACTIVE-INDEX. *Journal of Vacuum Science & Technology a-Vacuum Surfaces and Films*, Mar-Apr 1994, 12(2), 321-322.
- [86] CABALLERO-ESPITIA, D. L., E. G. LIZARRAGA-MEDINA, H. A. BORBON-NUÑEZ, O. E. CONTRERAS-LOPEZ, et al. Study of Al₂O₃ thin films by ALD using H₂O and O₃ as oxygen source for waveguide applications. *Optical Materials*, Nov 2020, 109.
- [87] ANWAR, N., N. HUSSAIN, S. AO, S. AMJAD, et al. Tailoring TiO₂/Al₂O₃ heterolayers as optical filters for the visible region. *Nanoscale Advances*, Mar 2022, 4(6), 1608-1616.
- [88] AHLUWALIA, B. S., O. G. HELLESO, A. Z. SUBRAMANIAN, N. M. B. PERNEY, et al. Fabrication and optimization of Tantalum Pentoxide waveguides for optical micro-propulsion. In *Conference on Integrated Optics - Devices, Materials, and Technologies XIV*. San Francisco, CA, 2010, vol. 7604.
- [89] SAHA, M., S. DEB, B. MEDHI AND M. D. BARMA. Utilization of Thin-film to Control Total Phase Shift during Total-internal-reflection. In *2020 IEEE International Women in Engineering (WIE) Conference on Electrical and Computer Engineering (WIECON-ECE)*. 2020, p. 113-116.
- [90] FENG, Z. D., J. J. LIU, J. SU, H. J. TIAN, et al. Efficiency enhancement of a Sb₂Se₃ solar cell after adding a Si₃N₄ interface layer. *Materials Letters*, May 2022, 314.
- [91] MOON, H. C., H. K. KANG, J. Y. HWANG, Y. P. PARK, et al. Vertical alignment of nematic liquid crystal by rubbing-free method on the SiC thin film layer. *Japanese Journal of Applied Physics Part 1-Regular Papers Brief Communications & Review Papers*, Sep 2006, 45(9A), 7017-7019.
- [92] WANG, Y. Z., Z. M. TUOFU, Z. M. YUE, H. SUN, et al. Research on adhesion strength and optical properties of SiC films obtained via RF magnetron sputtering. *Chinese Journal of Physics*, Apr 2020, 64, 79-86.
- [93] PARK, J. Y., H. H. KIM, D. RANA, D. JAMWAL, et al. Surface-area-controlled synthesis of porous TiO₂ thin films for gas-sensing applications. *Nanotechnology*, Mar 2017, 28(9).
- [94] NANTO, H., T. MORITA, H. HABARA, K. KONDO, et al. Doping effect of SnO₂ on gas sensing characteristics of sputtered ZnO thin film chemical sensor. *Sensors and Actuators B-Chemical*, Oct 1996, 36(1-3), 384-387.
- [95] ABEGUNDE, O. O., E. T. AKINLABI, O. P. OLADIJO, S. AKINLABI, et al. Overview of thin film deposition techniques. *Aims Materials Science*, 2019, 6(2), 174-199.
- [96] ARITA, M. AND I. NISHIDA TUNGSTEN FILMS WITH THE A15 STRUCTURE. *Japanese Journal of Applied Physics Part 1-Regular Papers Short Notes & Review Papers*, Apr 1993, 32(4), 1759-1764.
- [97] LEE, E., W. GWON AND S. RYU Nucleation and Growth-Controlled Morphology Evolution of Cu Nanostructures During High-Pressure Thermal Evaporation. *Korean Journal of Metals and Materials*, Feb 2021, 59(2), 135-141.
- [98] LODHA, G. S., K. YAMASHITA, H. KUNIEDA, T. YAMAZAKI, et al. Platinum carbon multilayer grating: Preparation and characterization. *Journal of Electron Spectroscopy and Related Phenomena*, May 1996, 80, 497-500.
- [99] MATTOX, D. M. *Handbook of physical vapor deposition (PVD) processing*. Edition ed. Amsterdam: Amsterdam : Elsevier, 2010.
- [100] AZOULAY, J. Low-temperature crystallization of high T_c Y-Ba-Cu-O thin films by resistive evaporation. *Appl. Supercond.*, 1993/03/01/ 1993, 1(3), 859-865.
- [101] YAMAMOTO, H. AND N. SAIGA Temperature-corrected quartz-crystal microbalance for real-time film thickness monitoring in vacuum evaporation. *Japanese Journal of Applied Physics Part 1-Regular Papers Short Notes & Review Papers*, Sep 1996, 35(9A), 4833-4838.
- [102] NIISAKA, S., T. SAITO, J. SAITO, A. TANAKA, et al. Development of optical coatings for 157-nm lithography. I. Coating materials. *Applied Optics*, Jun 2002, 41(16), 3242-3247.
- [103] SAFARIAN, J. AND T. A. ENGH Vacuum Evaporation of Pure Metals. *Metallurgical and Materials Transactions a-Physical Metallurgy and Materials Science*, Feb 2013, 44A(2), 747-753.
- [104] MIYAUCHI, D. AND S. ARAKI MAGNETORESISTANCE PROPERTIES OF CU/CO/CU/NIFE MULTILAYERS WITH A FEW STACKING NUMBERS. *Japanese Journal of Applied Physics Part 2-Letters*, Jan 1995, 34(1A), L31-L34.
- [105] KOPF, R. F., R. MELENDES, D. C. JACOBSON, A. TATE, et al. Thin-film resistor fabrication for InP technology applications. *Journal of Vacuum Science & Technology B*, May-Jun 2002, 20(3), 871-875.
- [106] JANKOWSKI, A. AND J. HAYES The evaporative deposition of aluminum coatings and shapes with grain size control. *Thin Solid Films*, Jan 2004, 447, 568-574.
- [107] KLEVENZ, M., S. WETZEL, M. MÖLLER AND A. PUCCI Evaporation and Condensation of SiO and SiO₂ Studied by Infrared Spectroscopy. *Applied Spectroscopy*, Mar 2010, 64(3), 298-303.
- [108] TAYLOR, D. M. Vacuum-thermal-evaporation: the route for roll-to-roll production of large-area organic electronic circuits. *Semiconductor Science and Technology*, May 2015, 30(5).
- [109] ENNOS, A. E. HIGHLY-CONDUCTING GOLD FILMS PREPARED BY VACUUM EVAPORATION. *British Journal of Applied Physics*, 1957, 8(3), 113-117.

- [110] DUMAS, L., E. QUESNEL, J. Y. ROBIC AND Y. PAULEAU Characterization of magnesium fluoride thin films deposited by direct electron beam evaporation. *Journal of Vacuum Science & Technology a-Vacuum Surfaces and Films*, Mar-Apr 2000, 18(2), 465-469.
- [111] MATKIVSKYI, V., Y. LEE, H. S. SEO, D. K. LEE, et al. Electronic-beam evaporation processed titanium oxide as an electron selective contact for silicon solar cells. *Current Applied Physics*, Dec 2021, 32, 98-105.
- [112] MUNZERT, P., C. PRAEFKE, U. SCHULZ AND N. KAISER Adhesion of Vacuum Deposited Optical Coatings on PMMA and Polycarbonate. *Journal of Adhesion Science and Technology*, 2012, 26(18-19), 2269-2276.
- [113] LODHA, G. S., R. V. NANDEDKAR AND A. VARMA Electron beam deposition system for X-ray multilayer mirrors. *Bulletin of Materials Science*, Dec 1996, 19(6), 1109-1116.
- [114] GARBACZ, H., P. WIECINSKI, B. ADAMCZYK-CIESLAK, J. MIZERA, et al. Studies of aluminium coatings deposited by vacuum evaporation and magnetron sputtering. *Journal of Microscopy-Oxford*, Mar 2010, 237(3), 475-480.
- [115] FADAAM, S. A., M. H. MUSTAFA, A. H. ABD ALRAZAK AND A. A. SHIHAB. Enhanced efficiency of CdTe Photovoltaic by thermal evaporation Vacuum. In *International Conference on Technologies and Materials for Renewable Energy, Environment and Sustainability (TMREES)*. Athens, GREECE, 2018, vol. 157, p. 635-643.
- [116] LI, A. M., J. QIN, W. M. SHI AND G. P. WEI. Fabrication and properties study of Cu(In_xGa_{1-x})Se₂ films by vacuum evaporation. In *6th International Conference on Thin Film Physics and Applications*. Shanghai, PEOPLES R CHINA, 2007, vol. 6984, p. C9841-C9841.
- [117] WANG, Y. C., H. JEONG, M. CHOWDHURY, C. B. ARNOLD, et al. Exploiting physical vapor deposition for morphological control in semi-crystalline polymer films. *Polymer Crystallization*, Dec 2018, 1(4).
- [118] SIAOSU, D., M. I. HRECHANIUK, P. P. KUCHERENKO, A. G. MELNIK, et al. INDUSTRIAL ELECTRON-BEAM EQUIPMENT FOR DEPOSITION OF PROTECTIVE COATINGS: OVERVIEW. *Powder Metallurgy and Metal Ceramics*, Jun 2019, 58(1-2), 113-124.
- [119] BAPTISTA, A., F. J. G. SILVA, J. PORTEIRO, J. L. MÍGUEZ, et al. On the Physical Vapour Deposition (PVD): Evolution of Magnetron Sputtering Processes for Industrial Applications. In *28th International Conference on Flexible Automation and Intelligent Manufacturing (FAIM) - Global Integration of Intelligent Manufacturing and Smart Industry for Good of Humanity*. Columbus, OH, 2018, vol. 17, p. 746-757.
- [120] KIM, T., P. J. GRESS AND S. VARLAMOV Metallisation and Interconnection of e-Beam Evaporated Polycrystalline Silicon Thin-Film Solar Cells on Glass. *International Journal of Photoenergy*, 2012, 2012.
- [121] SINGH, B. P. AND R. KUMAR. Vacuum Deposition of Sulfide Semiconductors Films in Sulfurizing Environment by Modified Evaporation Technique. In *8th National Conference on Thermophysical Properties (NCTP)*. Jaipur, INDIA, 2015, vol. 22, p. 3867-3871.
- [122] LU, X. W., Z. W. LI, C. K. YANG, W. J. MOU, et al. Synthesis of uniform two-dimensional MoS₂ films via thermal evaporation. *Nano Research*, Apr 2024, 17(4), 3217-3223.
- [123] BRÄUER, G., B. SZYSZKA, M. VERGÖHL AND R. BANDORF Magnetron sputtering - Milestones of 30 years. *Vacuum*, Jun 2010, 84(12), 1354-1359.
- [124] DESIDERI, D., M. BAGATIN, M. SPOLAORE, V. ANTONI, et al. Characterization of a DC magnetron sputtering device. *Compel-the International Journal for Computation and Mathematics in Electrical and Electronic Engineering*, 2005, 24(1), 261-270.
- [125] COOKE, K. E., J. HAMPSHIRE, W. SOUTHALL AND D. G. TEER Industrial Application of Pulsed Dc Bias Power Supplies in Closed Field Unbalanced Magnetron Sputter Ion Plating. *Surface Engineering*, 2004, 20(3), 189-195.
- [126] KELLY, P. J. AND R. D. ARNELL Magnetron sputtering: a review of recent developments and applications. *Vacuum*, 2000/03/01/ 2000, 56(3), 159-172.
- [127] DARMA, T. H., A. A. OGWU AND F. PLACIDO Effects of sputtering pressure on properties of copper oxide thin films prepared by rf magnetron sputtering. *Materials Technology*, Feb 2011, 26(1), 28-31.
- [128] KIM, C., S. KIM AND C. LEE Effects of RF power and substrate temperature during RF magnetron sputtering on crystal quality of ZnO thin films. *Japanese Journal of Applied Physics Part 1-Regular Papers Brief Communications & Review Papers*, Dec 2005, 44(12), 8501-8503.
- [129] MWEMA, F. M., E. T. AKINLABI AND O. P. OLADIJO A systematic review of magnetron sputtering of AlN thin films for extreme condition sensing. *Materials Today: Proceedings*, 2020/01/01/ 2020, 26, 1546-1550.
- [130] DUQUENNE, C., B. POPESCU, P. Y. TESSIER, M. P. BESLAND, et al. Magnetron Sputtering of Aluminium Nitride Thin Films for Thermal Management. *Plasma Processes and Polymers*, Apr 2007, 4, S1-S5.
- [131] MERIE, V. V., A. MOLEA, V. N. BURNETE, B. V. NEAMTU, et al. Structural and optical characterization of titanium nitride thin films deposited by magnetron sputtering. In *5th International Conference on Powder Metallurgy and Advanced Materials (RoPM and AM)*. Cluj Napoca, ROMANIA, 2017, vol. 8, p. 134-142.
- [132] XU, Z., X. Z. YU AND Z. G. SHEN Coating metals on micropowders by magnetron sputtering. *China Particuology*, Oct 2007, 5(5), 345-350.
- [133] GIBSON, D. R., I. BRINKLEY, E. M. WADDELL AND J. M. WALLS. Closed field magnetron sputtering: new generation sputtering process for optical coatings. In *Conference on Advances in Optical Thin Films III*. Glasgow, SCOTLAND, 2008, vol. 7101.
- [134] DE, R., S. M. HAQUE, S. TRIPATHI, C. PRATHAP, et al. Effect of Sputtering Power on MgF₂ Thin Films Deposited by Sputtering Technique under Fluorine Trapping. In *DAE Solid State Physics Symposium*. Amity Univ, Noida, INDIA, 2015, vol. 1731.

- [135] SHEU, W. H. AND S. T. WU Epitaxial growth of TiN(100) on Si(100) by reactive magnetron sputtering at low temperature. *Japanese Journal of Applied Physics Part 1-Regular Papers Brief Communications & Review Papers*, Jun 1998, 37(6A), 3446-3449.
- [136] LIU, L., T. WANG, J. L. HUANG, Z. B. HE, et al. Diamond-like carbon thin films with high density and low internal stress deposited by coupling DC/RF magnetron sputtering. *Diamond and Related Materials*, Nov 2016, 70, 151-158.
- [137] BEWILOGUA, K., R. WITTORF, H. THOMSEN AND M. WEBER DLC based coatings prepared by reactive d.c. magnetron sputtering. *Thin Solid Films*, Jan 2004, 447, 142-147.
- [138] BHUVANESWARI, H. B., I. N. PRIYA, R. CHANDRAMANI, V. R. REDDY, et al. Studies on zirconium nitride films deposited by reactive magnetron sputtering. *Crystal Research and Technology*, 2003, 38(12), 1047-1051.
- [139] WESTLINDER, J., J. MALMSTRÖM, G. SJÖBLOM AND J. OLSSON Low-resistivity ZrN_x metal gate in MOS devices. *Solid-State Electronics*, 2005/08/01/ 2005, 49(8), 1410-1413.
- [140] POTJAN, R., M. WISLICENUS, O. OSTIEN, R. HOFFMANN, et al. 300 mm CMOS-compatible superconducting HfN and ZrN thin films for quantum applications. *Applied Physics Letters*, 2023, 123(17).
- [141] DOBROWOLSKI, J. A., J. R. PEKELSKY, R. PELLETIER, M. RANGER, et al. PRACTICAL MAGNETRON SPUTTERING SYSTEM FOR THE DEPOSITION OF OPTICAL MULTILAYER COATINGS. *Applied Optics*, Jul 1992, 31(19), 3784-3789.
- [142] COMPAAN, A. D., A. GUPTA, S. Y. LEE, S. L. WANG, et al. High efficiency, magnetron sputtered CdS/CdTe solar cells. *Solar Energy*, 2004, 77(6), 815-822.
- [143] ZHANG, H. X. AND R. J. HONG CIGS absorbing layers prepared by RF magnetron sputtering from a single quaternary target. *Ceramics International*, Oct 2016, 42(13), 14543-14547.
- [144] GULTOM, N. S., M. Z. SILITONGA AND D. H. KUO Bimetallic Cobalt-Nickel Electrode Made by a Sputtering Technique for Electrocatalytic Hydrogen Evolution Reaction: Effect of Nickel Ratios. *Acs Applied Energy Materials*, 2022 Jul 2022.
- [145] DEPLA, D. AND R. DE GRUYSE Target poisoning during reactive magnetron sputtering: Part I: the influence of ion implantation. *Surface & Coatings Technology*, May 2004, 183(2-3), 184-189.
- [146] DEPLA, D. AND R. DE GRUYSE Target poisoning during reactive magnetron sputtering: Part II: the influence of chemisorption and gettering. *Surface & Coatings Technology*, May 2004, 183(2-3), 190-195.
- [147] DEPLA, D. AND R. DE GRUYSE Target poisoning during reactive magnetron sputtering: Part III: the prediction of the critical reactive gas mole fraction. *Surface & Coatings Technology*, May 2004, 183(2-3), 196-203.
- [148] BUNDESMANN, C. AND H. NEUMANN Tutorial: The systematics of ion beam sputtering for deposition of thin films with tailored properties. *Journal of Applied Physics*, Dec 2018, 124(23).
- [149] WANG, X., A. KOLITSCH, F. PROKERT AND W. MOLLER Ion beam assisted deposition of AlN monolithic films and Al/AlN multilayers: a comparative study. *Surface & Coatings Technology*, May 1998, 104, 334-339.
- [150] HUANG, J. H., C. H. LIN AND H. D. CHEN Ion beam assisted deposition of TiN thin film on Si (100). *Materials Chemistry and Physics*, Apr 1999, 59(1), 49-56.
- [151] DANIEL, M. V. AND M. DEMMLER. Multilayer Coating of Optical Substrates by Ion Beam Sputtering. In *Optifab Conference*. Rochester, NY, 2017, vol. 10448.
- [152] LEE, C. C., K. H. LEE, C. J. TANG, C. C. JAING, et al. Reduction of residual stress in optical silicon nitride thin films prepared by radio-frequency ion beam sputtering deposition. *Optical Engineering*, Jun 2010, 49(6).
- [153] LV, Q. P., M. L. HUANG, S. Q. ZHANG, S. W. DENG, et al. Effects of Annealing on Residual Stress in Ta₂O₅ Films Deposited by Dual Ion Beam Sputtering. *Coatings*, Apr 2018, 8(4).
- [154] HAIDER, A. J., T. ALAWSI, M. J. HAIDER, B. A. TAHA, et al. A comprehensive review on pulsed laser deposition technique to effective nanostructure production: trends and challenges. *Optical and Quantum Electronics*, Aug 2022, 54(8).
- [155] ZHANG, S. T., B. YANG, X. J. ZHANG, Y. F. CHEN, et al. Pulsed laser deposition of ferroelectric Sr₄Bi₄Ti₇O₂₄ thin films. *Materials Letters*, Oct 2002, 56(3), 221-225.
- [156] CALTUN, O. F. Pulsed laser deposition of Ni-Zn ferrite thin films. *Journal of Optoelectronics and Advanced Materials*, Apr 2005, 7(2), 739-744.
- [157] VISPUTE, R. D., S. CHOOPUN, R. ENCK, A. PATEL, et al. Pulsed laser deposition and processing of wide band gap semiconductors and related materials. *Journal of Electronic Materials*, Mar 1999, 28(3), 275-286.
- [158] RIJNDERS, G., G. KOSTER, D. H. A. BLANK AND H. ROGALLA In-situ growth monitoring during PLD of oxides using RHEED at high oxygen pressure. *Materials Science and Engineering B-Solid State Materials for Advanced Technology*, Nov 1998, 56(2-3), 223-227.
- [159] BOWMAN, R. M., G. CATALAN, M. H. CORBETT, D. O'NEILL, et al. PLD of metal-insulator and relaxor electro-ceramic thin films. In *11th International School on Quantum Electronics*. Varna, Bulgaria, 2000, vol. 4397, p. 273-284.
- [160] STURM, K., S. FÄHLER AND H. U. KREBS Pulsed laser deposition of metals in low pressure inert gas. *Applied Surface Science*, Feb 2000, 154, 462-466.
- [161] SZÖRÉNYI, T., R. STUCK, F. ANTONI AND E. FOGARASSY Number density and size distribution of droplets in KrF excimer laser deposited boron carbide films. *Applied Surface Science*, Jul 2005, 247(1-4), 45-50.
- [162] VERARDI, P., M. DINESCU AND F. CRACIUN Pulsed laser deposition and characterization of PZT thin films. *Applied Surface Science*, Feb 2000, 154, 514-518.
- [163] MA, B., M. LI, R. E. KORITALA, B. L. FISHER, et al. Direct deposition of YBCO on polished Ag substrates by pulsed laser deposition. *Physica C-Superconductivity and Its Applications*, Sep 2002, 377(4), 501-506.

- [164] STANOI, D., G. SOCOL, C. RISTOSCU, I. N. MIHAILESCU, et al. Pulsed laser deposition of chromium oxides for applications in spintronics. In *12th International School on Quantum Electronics*. Varna, Bulgaria, 2002, vol. 5226, p. 352-356.
- [165] MILLON, E., J. PERRIÈRE, S. TRICOT AND C. BOULMER-LEBORGNE. Pulsed-laser deposition of ZnO and related compound thin films for optoelectronics. In *Conference on High-Power Laser Ablation VII*. Taos, NM, 2008, vol. 7005.
- [166] NAGAI, T., T. INOUE AND H. SHIMURA Pulsed laser driven deposition of spattered molten particles and its application to the manufacturing of wear-resistant coatings. *Journal of Laser Applications*, Aug 2002, 14(3), 191-197.
- [167] DOLL, G. L., B. A. MENSAH, H. MOHSENI AND T. W. SCHARF Chemical Vapor Deposition and Atomic Layer Deposition of Coatings for Mechanical Applications. *Journal of Thermal Spray Technology*, Jan 2010, 19(1-2), 510-516.
- [168] KASHIMA, N., T. NIWA, M. MORI, S. NAGAYA, et al. YBCO coated conductor by multiple-stage CVD. *Physica C: Superconductivity and its Applications*, 2005/10/01/ 2005, 426-431, 887-892.
- [169] BREVAL, E. AND S. VUORINEN Structure and hardness of titanium carbide coatings on hard metals. *Materials Science and Engineering*, 1980/01/01/ 1980, 42, 361-366.
- [170] VASUDEV, M. C., K. D. ANDERSON, T. J. BUNNING, V. V. TSUKRUK, et al. Exploration of Plasma-Enhanced Chemical Vapor Deposition as a Method for Thin-Film Fabrication with Biological Applications. *ACS Applied Materials & Interfaces*, May 2013, 5(10), 3983-3994.
- [171] KABONGO, G. L., B. M. MOTHUDI AND M. S. DHLAMINI Advanced Development of Sustainable PECVD Semitransparent Photovoltaics: A Review. *Frontiers in Materials*, Nov 2021, 8.
- [172] YOTA, J., M. JANANI, L. E. CAMILLETI, A. KAR-ROY, et al. Comparison between HDP CVD and PECVD silicon nitride for advanced interconnect applications. In *3rd Annual International Interconnect Technology Conference*. San Francisco, Ca, 2000, p. 76-78.
- [173] CHOI, J.-K., J. LEE, J.-B. YOO, J.-S. MAENG, et al. Residual stress analysis of SiO₂ films deposited by plasma-enhanced chemical vapor deposition. *Surface and Coatings Technology*, 2000/09/01/ 2000, 131(1), 153-157.
- [174] BURSÍKOVÁ, V., V. NAVRÁTIL, L. ZAJÍCKOVÁ AND J. JANCA Temperature dependence of mechanical properties of DLC/Si protective coatings prepared by PECVD. *Materials Science and Engineering a-Structural Materials Properties Microstructure and Processing*, Feb 2002, 324(1-2), 251-254.
- [175] ZOU, X. D. AND J. W. ZHANG Study on PECVD SiO₂/Si₃N₄ double-layer electrets with different thicknesses. *Science China-Technological Sciences*, Aug 2011, 54(8), 2123-2129.
- [176] PANDRAUD, G., P. J. FRENCH AND P. M. SARRO Fabrication and characteristics of a PECVD SiC evanescent wave optical sensor. *Sensors and Actuators a-Physical*, Mar 2008, 142(1), 61-66.
- [177] CHO, S. J. AND J. H. BOO Characteristics of multilayered plasma-polymer thin films using toluene and TEOS by PECVD. *Microelectronic Engineering*, Jan 2012, 89, 19-22.
- [178] SANTANA, G. AND A. MORALES-ACEVEDO Optimization of PECVD SiN:H films for silicon solar cells. *Solar Energy Materials and Solar Cells*, Jan 2000, 60(2), 135-142.
- [179] HÖSSLER, D. AND M. ERNST Optimization of a TiSi₂ formation based on PECVD Ti using DoE methodology. *Solid-State Electronics*, Aug 2019, 158, 51-58.
- [180] MAEDA, K. AND I. UMEZU. Defect formation mechanism during PECVD of a-Si:H. In *Symposium on Amorphous and Microcrystalline Silicon Technology*. San Francisco, Ca, 1997, vol. 467, p. 573-578.
- [181] OH, U. C., K. N. KIM, S. C. KIM, H. D. KIM, et al. Segregation of aluminum in Si and SiO₂ films deposited by plasma-enhanced chemical vapor deposition in fabrication of low-temperature poly Si thin-film transistor. *Journal of Materials Research*, Apr 2003, 18(4), 973-978.
- [182] LI, S. Z., N. YANG, X. YUAN, X. J. YE, et al. Plasma-induced damage and annealing repairing in ALD-Al₂O₃/PECVD-SiN_x stacks. *Materials Science in Semiconductor Processing*, Sep 2019, 100, 214-219.
- [183] KERN, W. AND G. L. SCHNABLE LOW-PRESSURE CHEMICAL VAPOR-DEPOSITION FOR VERY LARGE-SCALE INTEGRATION PROCESSING - REVIEW. *Ieee Transactions on Electron Devices*, 1979, 26(4), 647-657.
- [184] AHN, J., W. TING AND D. L. KWONG HIGH-QUALITY MOSFETS WITH ULTRATHIN LPCVD GATE SiO₂. *Ieee Electron Device Letters*, Apr 1992, 13(4), 186-188.
- [185] BESHKOV, G., V. LAZAROVA AND D. B. DIMITROV MORPHOLOGY OF LPCVD Si₃N₄ FILMS AFTER HIGH-TEMPERATURE TREATMENT AND HF ETCHING. *Journal of Non-Crystalline Solids*, Jul 1995, 187, 301-307.
- [186] SHEN, H. H., L. Y. CHUNG AND D. J. YAO Improving the dielectric properties of an electrowetting-on-dielectric microfluidic device with a low-pressure chemical vapor deposited Si₃N₄ dielectric layer. *Biomicrofluidics*, Mar 2015, 9(2).
- [187] BIELLEDASPET, D., E. SCHEID, C. AZZARO, B. DEMAUDUIT, et al. MATERIAL AND ELECTRONIC-PROPERTIES OF BORON-DOPED SILICON FILMS DEPOSITED FROM SiH₄-BCL₃-N₂ MIXTURES IN AN INDUSTRIAL LOW-PRESSURE CHEMICAL VAPOR-DEPOSITION FURNACE. *Thin Solid Films*, Sep 1991, 204(1), 33-48.
- [188] LEE, Y. H. AND S. PARK Gate bias-dependent junction characteristics of silicon nanowires suspended between polysilicon electrodes. *Science and Technology of Advanced Materials*, Dec 2011, 12(6).
- [189] GUO, H., P. F. SHAO, C. K. ZENG, H. E. BAI, et al. Improved LPCVD-SiN_x/AlGaIn/GaN MIS-HEMTs by using *in-situ* MOCVD-SiN_x as an interface sacrificial layer. *Applied Surface Science*, Jul 2022, 590.

- [190] KIM, D., I. YUN AND H. KIM Fabrication of rough Al doped ZnO films deposited by low pressure chemical vapor deposition for high efficiency thin film solar cells. *Current Applied Physics*, May 2010, 10(3), S459-S462.
- [191] BAUER, J., O. FURSENKO, S. VIRKO, B. KUCK, et al. Optimization of anti-reflective coatings for lithography applications. In *21st European Mask and Lithography Conference (EMLC 2005)*. Dresden, GERMANY, 2005, vol. 5835, p. 263-272.
- [192] KIM, K. K., A. HSU, X. T. JIA, S. M. KIM, et al. Synthesis of Monolayer Hexagonal Boron Nitride on Cu Foil Using Chemical Vapor Deposition. *Nano Letters*, Jan 2012, 12(1), 161-166.
- [193] JIANG, W. L., D. H. XU, B. XIONG AND Y. L. WANG Effects of rapid thermal annealing on LPCVD silicon nitride. *Ceramics International*, Jan 2016, 42(1), 1217-1224.
- [194] LESKELÄ, M. AND M. RITALA Atomic layer deposition (ALD):: from precursors to thin film structures. *Thin Solid Films*, Apr 2002, 409(1), 138-146.
- [195] GEORGE, S. M. Atomic Layer Deposition: An Overview. *Chemical Reviews*, Jan 2010, 110(1), 111-131.
- [196] WEBER, M., A. JULBE, S. S. KIM AND M. BECHELANY Atomic layer deposition (ALD) on inorganic or polymeric membranes. *Journal of Applied Physics*, Jul 2019, 126(4).
- [197] GRANIEL, O., M. WEBER, S. BALME, P. MIELE, et al. Atomic layer deposition for biosensing applications. *Biosensors & Bioelectronics*, Dec 2018, 122, 147-159.
- [198] CHOI, M. J., H. H. PARK, D. S. JEONG, J. H. KIM, et al. Atomic layer deposition of HfO_2 thin films using H_2O as oxidant. *Applied Surface Science*, May 2014, 301, 451-455.
- [199] LI, X. Z., M. VEHKAMÄKI, M. CHUNDAK, K. MIZOHATA, et al. Atomic Layer Deposition of Boron-Doped Al_2O_3 Dielectric Films. *Advanced Materials Interfaces*, Jun 2023, 10(18).
- [200] YUN, H. J., H. KIM AND B. J. CHOI Nucleation and growth behavior of aluminum nitride film using thermal atomic layer deposition. *Ceramics International*, Jun 2020, 46(9), 13372-13376.
- [201] KIM, H. Characteristics and applications of plasma enhanced-atomic layer deposition. *Thin Solid Films*, Aug 2011, 519(20), 6639-6644.
- [202] TEN EYCK, G. A., S. PIMANPANG, J. S. JUNEJA, H. BAKHRU, et al. Plasma-enhanced atomic layer deposition of palladium on a polymer substrate. *Chemical Vapor Deposition*, Jul 2007, 13(6-7), 307-311.
- [203] LEE, J. Y., D. W. KIM, W. S. KANG, J. O. LEE, et al. Growth mechanism of Al_2O_3 film on an organic layer in plasma-enhanced atomic layer deposition. *Journal of Physics D-Applied Physics*, Jan 2018, 51(1).
- [204] BOSUND, M., T. SAJAVAARA, M. LAITINEN, T. HUHTIO, et al. Properties of AlN grown by plasma enhanced atomic layer deposition. *Applied Surface Science*, Jun 2011, 257(17), 7827-7830.
- [205] KIM, D., H. KANG, J. M. KIM AND H. KIM The properties of plasma-enhanced atomic layer deposition (ALD) ZnO thin films and comparison with thermal ALD. *Applied Surface Science*, Feb 2011, 257(8), 3776-3779.
- [206] LESKELÄ, M. AND M. RITALA Rare-earth oxide thin films as gate oxides in MOSFET transistors. *Journal of Solid State Chemistry*, Feb 2003, 171(1-2), 170-174.
- [207] YUM, J. H., G. BERSUKER, T. AKYOL, D. A. FERRER, et al. Epitaxial ALD BeO : Efficient Oxygen Diffusion Barrier for EOT Scaling and Reliability Improvement. *Ieee Transactions on Electron Devices*, Dec 2011, 58(12), 4384-4392.
- [208] KLOOTWIJK, J., A. KEMMEREN, R. WOLTERS, F. ROOZEBOOM, et al. Extremely high-density capacitors with ALD high-k dielectric layers. In *NATO Advanced Research Workshop on Defects in Advanced High -K Dielectric Nano-Electronic Semiconductor Devices*. St Petersburg, RUSSIA, 2005, vol. 220, p. 17-+.
- [209] AZADMANJIRI, J., C. C. BERNDT, J. WANG, A. KAPOOR, et al. A review on hybrid nanolaminate materials synthesized by deposition techniques for energy storage applications. *Journal of Materials Chemistry A*, 2014, 2(11), 3695-3708.
- [210] THOMPSON, A. G. MOCVD technology for semiconductors. *Materials Letters*, Mar 1997, 30(4), 255-263.
- [211] WEI, W. C. J. AND M. H. LO Processing and properties of (Mo,Cr) oxycarbides from MOCVD. *Applied Organometallic Chemistry*, Mar 1998, 12(3), 201-220.
- [212] KARAKOVSKAYA, K. I., S. I. DOROVSKIKH, E. S. VIKULOVA, I. Y. ILYIN, et al. Volatile Iridium and Platinum MOCVD Precursors: Chemistry, Thermal Properties, Materials and Prospects for Their Application in Medicine. *Coatings*, 2021, 11(1), 78.
- [213] IQBAL, M. Z., A. MAJID, S. H. KHAN, A. ALI, et al. Rhodium-related deep levels in n-type MOCVD GaAs. *Physica B-Condensed Matter*, Dec 2001, 308, 816-819.
- [214] CHU, H. J., T. W. YEH, L. STEWART AND P. D. DAPKUS. Wurtzite InP nanowire arrays grown by selective area MOCVD. In *36th International Symposium on Compound Semiconductors (ISCS)*. Santa Barbara, CA, 2009, vol. 7.
- [215] DAI, J. N., H. C. LIU, W. Q. FANG, L. WANG, et al. Atmospheric pressure MOCVD growth of high-quality ZnO films on $\text{GaN}/\text{Al}_2\text{O}_3$ templates. *Journal of Crystal Growth*, Sep 2005, 283(1-2), 93-99.
- [216] ITO, A., R. TU AND T. GOTO Amorphous-like nanocrystalline $\gamma\text{-Al}_2\text{O}_3$ films prepared by MOCVD. *Surface & Coatings Technology*, Apr 2010, 204(14), 2170-2174.
- [217] LIU, W., M. F. LI, Z. C. FENG, S. J. CHUA, et al. Material properties of GaN grown by MOCVD. *Surface and Interface Analysis*, Aug 1999, 28(1), 150-154.
- [218] TUNA, Ö., H. BEHMENBURG, C. GIESEN, H. KALISCH, et al. Dependence of InN properties on MOCVD growth parameters. In *International Workshop on Nitride Semiconductors (IWN)/Fall Meeting of the European-Materials-Research-Society (E-MRS)/Symposium N/Symposium H*. Tampa, FL, 2010, vol. 8.

- [219] YAO, H. H., C. F. LIN, H. C. KUO AND S. C. WANG MOCVD growth of AlN/GaN DBR structures under various ambient conditions. *Journal of Crystal Growth*, Feb 2004, 262(1-4), 151-156.
- [220] IZYUMSKAYA, N., Y. ALIVOV, S. J. CHO, H. MORKOC, et al. Processing, structure, properties, and applications of PZT thin films. *Critical Reviews in Solid State and Materials Sciences*, 2007, 32(3-4), 111-202.
- [221] YIN, H. B., X. L. WANG, J. X. RAN, G. X. HU, et al. High quality GaN-based LED epitaxial layers grown in a homemade MOCVD system. *Journal of Semiconductors*, Mar 2011, 32(3).
- [222] TODA, A., T. MARGALITH, D. IMANISHI, K. YANASHIMA, et al. MOCVD-GROWN BLUE-GREEN LASER-DIODE. *Electronics Letters*, Oct 1995, 31(22), 1921-1922.
- [223] WANG, X. L., C. M. WANG, G. X. HU, H. L. MAO, et al. MOCVD-grown high-mobility Al_{0.3}Ga_{0.7}N/AlN/GaN HEMT structure on sapphire substrate. *Journal of Crystal Growth*, Jan 2007, 298, 791-793.
- [224] CHANG, Y. C., T. WANG, F. YIN, J. W. WANG, et al. InAs/GaSb superlattices grown by LP-MOCVD for ~10 μm wavelength infrared range. *Infrared Physics & Technology*, Nov 2011, 54(6), 478-481.
- [225] PLAUSINAITIENE, V., A. ABRUTIS, B. VENGALIS, R. BUTKUTE, et al. Spin-polarized quasiparticle injection effect in MOCVD-grown YBa₂Cu₃O₇/SrTiO₃/La_{1-x}Sr_xMnO₃ heterostructures. *Physica C*, Mar 2001, 351(1), 13-16.
- [226] MORGAN, D. V. AND K. BOARD *An Introduction to Semiconductor Microtechnology*. Edition ed.: Wiley, 1983. ISBN 9780471901488.
- [227] VICKRIDGE, I., J. GANEM, Y. HOSHINO AND I. TRIMAILLE Growth of SiO₂ on SiC by dry thermal oxidation:: mechanisms. *Journal of Physics D-Applied Physics*, Oct 2007, 40(20), 6254-6263.
- [228] CHEN, H. J., X. Y. HOU, G. B. LI, F. L. ZHANG, et al. Role of oxygen in surface kinetics of SiO₂ growth on single crystal SiC at elevated temperatures. *Ceramics International*, Jan 2021, 47(2), 1855-1864.
- [229] KIM, S. W., P. ZHENG, K. KATO, L. RUBIN, et al. Tilted ion implantation as a cost-efficient sublithographic patterning technique. *Journal of Vacuum Science & Technology B*, Jul 2016, 34(4).
- [230] PANEK, P., K. DRABCZYK, A. FOCSA AND A. SLAOUI A comparative study of SiO₂ deposited by PECVD and thermal method as passivation for multicrystalline silicon solar cells. *Materials Science and Engineering B-Advanced Functional Solid-State Materials*, Nov 2009, 165(1-2), 64-66.
- [231] ZHANG, Y. J., S. X. LIANG, Y. ZHANG, R. L. LI, et al. Role of oxygen in surface kinetics of SiO₂ growth on single crystal SiC at elevated temperatures. *Ceramics International*, Jan 2021, 47(2), 1855-1864.
- [232] WU, Z. G., J. H. BIAN, Z. G. WANG, Z. Y. WU, et al. Current-voltage characterization of epitaxial grown barium titanate thin films on Si substrate. *Journal of Materials Science-Materials in Electronics*, Nov 2015, 26(11), 8315-8318.
- [233] QI, M., J. R. XIAO AND C. Y. GONG Thermal annealing effects on the electrophysical characteristics of sputtered MoS₂ thin films by Hall effect measurements. *Semiconductor Science and Technology*, Apr 2019, 34(4).
- [234] KJAER, D., O. HANSEN, F. W. OSTERBERG, H. H. HENRICHSEN, et al. Characterization of positional errors and their influence on micro four-point probe measurements on a 100 nm Ru film. *MEASUREMENT SCIENCE and TECHNOLOGY*, Sep 2015, 26(9).
- [235] BIERWAGEN, O., T. IVE, C. G. VAN DE WALLE AND J. S. SPECK Causes of incorrect carrier-type identification in van der Pauw-Hall measurements. *Applied Physics Letters*, Dec 2008, 93(24).
- [236] LIN, Y., H. B. YANG, M. LIU AND G. ZHANG Impedance spectroscopy analysis of Bi_{0.85}Pr_{0.15}Fe_{0.9}Co_{0.1}O₃ thin films. *Materials Research Bulletin*, Mar 2014, 51, 44-48.
- [237] GOGOI, P., P. SRINIVAS, P. SHARMA AND D. PAMU Optical, Dielectric Characterization and Impedance Spectroscopy of Ni-Substituted MgTiO₃ Thin Films. *Journal of Electronic Materials*, Feb 2016, 45(2), 899-909.
- [238] KIDNER, N. J., A. MEIER, Z. J. HOMRIGHAUS, B. W. WESSELS, et al. Complex electrical (impedance/dielectric) properties of electroceramic thin films by impedance spectroscopy with interdigital electrodes. *Thin Solid Films*, Apr 2007, 515(11), 4588-4595.
- [239] YAMADA, H., K. YOSHII, M. ASAHI, M. CHIKU, et al. Cyclic Voltammetry Part 1: Fundamentals. *Electrochemistry*, 2022, 90(10).
- [240] WANG, H. W., C. BRINGANS, A. J. R. HICKEY, J. A. WINDSOR, et al. Cyclic Voltammetry in Biological Samples: A Systematic Review of Methods and Techniques Applicable to Clinical Settings. *Signals*, Mar 2021, 2(1), 138-158.
- [241] HUANG, X., Z. L. WANG, R. KNIBBE, B. LUO, et al. Cyclic Voltammetry in Lithium-Sulfur Batteries-Challenges and Opportunities. *Energy Technology*, Aug 2019, 7(8).
- [242] GIANNAKOU, P., R. C. T. SLADE AND M. SHKUNOV Cyclic Voltammetry Studies of Inkjet-printed NiO supercapacitors: Effect of Substrates, Printing and Materials. *Electrochimica Acta*, Sep 2020, 353.
- [243] CHEN, J. S., J. P. DIARD, R. DURAND AND C. MONTELLA Hydrogen insertion reaction with restricted diffusion .1. Potential step-EIS theory and review for the direct insertion mechanism. *Journal of Electroanalytical Chemistry*, Apr 1996, 406(1-2), 1-13.
- [244] CHOU, J. C., P. H. SHIH, J. E. HU, Y. H. LIAO, et al. Electrochemical Analysis of Photoelectrochromic Device Combined Dye-Sensitized Solar Cell. *Ieee Transactions on Nanotechnology*, Sep 2014, 13(5), 954-962.
- [245] MWEMA, F. M., O. P. OLADIJO, T. S. SATHIARAJ AND E. T. AKINLABI Atomic force microscopy analysis of surface topography of pure thin aluminum films. *Materials Research Express*, Apr 2018, 5(4).

- [246] NGWA, W., W. LUO, A. KAMANYI, K. W. FOMBA, et al. Characterization of polymer thin films by phase-sensitive acoustic microscopy and atomic force microscopy: a comparative review. *Journal of Microscopy-Oxford*, Jun 2005, 218, 208-218.
- [247] KINOSHITA, H. AND N. MATSUMOTO Novel Method for Direct Observation of Friction Interfaces between SUJ2 Ball and Si₃N₄ Thin Film Using Scanning Electron Microscopy. *Tribology Online*, 2019, 14(5), 382-387.
- [248] BHUSHAN, B. Nanotribology, nanomechanics and nanomaterials characterization. *Philosophical Transactions of the Royal Society a-Mathematical Physical and Engineering Sciences*, Apr 2008, 366(1869), 1351-1381.
- [249] OSBORNE, J., S. Q. HU, H. M. WANG, Y. HU, et al. High-speed atomic force microscopy for patterned defect review. In *27th Conference on Metrology, Inspection, and Process Control for Microlithography*. San Jose, CA, 2013, vol. 8681.
- [250] CRACIUNOIU, F., M. MIU, R. GAVRILA, A. DINESCU, et al. Investigation of the piezoelectric properties of the thin films by AFM. In *International Semiconductor Conference*. Sinaia, ROMANIA, 2007, p. 99-+.
- [251] JEFFERY, S., A. ORAL AND J. B. PETHICA Quantitative electrostatic force measurement in AFM. *Applied Surface Science*, Apr 2000, 157(4), 280-284.
- [252] PHILLIPS, R. W. ATOMIC-FORCE MICROSCOPY FOR THIN-FILM ANALYSIS. *Surface & Coatings Technology*, Dec 1994, 68, 770-775.
- [253] LAI, Y. W., M. KRAUSE, A. SAVAN, S. THIENHAUS, et al. High-throughput characterization of film thickness in thin film materials libraries by digital holographic microscopy. *Science and Technology of Advanced Materials*, Oct 2011, 12(5).
- [254] TORRES, E. A. AND A. J. RAMÍREZ *In situ* scanning electron microscopy. *Science and Technology of Welding and Joining*, Jan 2011, 16(1), 68-78.
- [255] MATSUHATA, H., N. SUGIYAMA, B. CHEN, T. YAMASHITA, et al. Surface defects generated by extrinsic origins on 4H-SiC epitaxial-wafers observed by scanning electron microscopy. *Microscopy*, Apr 2017, 66(2), 103-109.
- [256] KUMAR, A., M. BHASIN AND M. CHITKARA Morphological analysis and grain size distribution of SnO₂ nanoparticles via digital image processing across diverse calcination temperatures. *Journal of Microscopy*, Dec 2023, 292(3), 123-134.
- [257] WANG, C. X., X. ZHOU AND M. WANG Influence of sintering temperatures on hardness and Young's modulus of tricalcium phosphate bioceramic by nanoindentation technique. *Materials Characterization*, Jul 2004, 52(4-5), 301-307.
- [258] PALACIO, M. L. B. AND B. BHUSHAN Depth-sensing indentation of nanomaterials and nanostructures. *Materials Characterization*, Apr 2013, 78, 1-20.
- [259] MAITI, P., A. EQBAL, M. BHATTACHARYA, P. S. DAS, et al. Micro pop-in issues in nanoindentation behaviour of 10 ZTA ceramics. *Ceramics International*, May 2019, 45(7), 8204-8215.
- [260] SCHWEITZ, J.-Å. AND F. ERICSON Evaluation of mechanical materials properties by means of surface micromachined structures. *Sensors and Actuators A: Physical*, 1999/04/20/ 1999, 74(1), 126-133.
- [261] HUFF, M. Review Paper: Residual Stresses in Deposited Thin-Film Material Layers for Micro- and Nano-Systems Manufacturing. *Micromachines (Basel)*, 11/26 2022, 13, 2084.
- [262] HARRINGTON, G. F. AND J. SANTISO Back-to-Basics tutorial: X-ray diffraction of thin films. *Journal of Electroceramics*, Dec 2021, 47(4), 141-163.
- [263] WISNIEWSKI, W., C. GENEVOIS, E. VERON AND M. ALLIX Experimental evidence concerning the significant information depth of X-ray diffraction (XRD) in the Bragg-Brentano configuration. *Powder Diffraction*, Jun 2023, 38(2), 139-144.
- [264] CAO, W. J., S. BATES, G. E. PECK, P. L. D. WILDFONG, et al. Quantitative determination of polymorphic composition in intact compacts by parallel-beam X-ray powder diffractometry. *Journal of Pharmaceutical and Biomedical Analysis*, Nov 2002, 30(4), 1111-1119.
- [265] GHOBEIRA, R., P. S. E. TABAEI, R. MORENT AND N. DE GEYTER Chemical characterization of plasma-activated polymeric surfaces via XPS analyses: A review. *Surfaces and Interfaces*, Jul 2022, 31.
- [266] KRISHNA, D. N. G. AND J. PHILIP Review on surface-characterization applications of X-ray photoelectron spectroscopy (XPS): Recent developments and challenges. *Applied Surface Science Advances*, Dec 2022, 12.
- [267] MCARTHUR, S. L. Applications of XPS in bioengineering. *Surface and Interface Analysis*, Nov 2006, 38(11), 1380-1385.
- [268] OSWALD, S., W. HÄSSLER, R. REICHE, J. LINDNER, et al. XPS depth profile analysis of a thin non-conducting titanate superlattice. *Mikrochimica Acta*, 2000, 133(1-4), 303-306.
- [269] BAKER, M. A., S. R. BACON, S. J. SWEENEY, S. J. HINDER, et al. Femtosecond laser ablation (fs-LA) XPS - A novel XPS depth profiling technique for thin films, coatings and multi-layered structures. *Applied Surface Science*, May 2024, 654.
- [270] SCIMECA, M., S. BISCHETTI, H. K. LAMSIRA, R. BONFIGLIO, et al. Energy Dispersive X-ray (EDX) microanalysis: A powerful tool in biomedical research and diagnosis. *European Journal of Histochemistry*, 2018, 62(1), 88-97.
- [271] RUPP, A., J. GÖSER, Z. J. LI, P. ALTPETER, et al. Energy-Dispersive X-Ray Spectroscopy of Atomically Thin Semiconductors and Heterostructures. *Physical Review Applied*, Dec 2022, 18(6).
- [272] VISSER, M. M., S. WEICHEL, P. STORÅS, R. DE REUS, et al. Sodium distribution in thin-film anodic bonding. *Sensors and Actuators a-Physical*, Aug 2001, 92(1-3), 223-228.

- [273] TRIGO, J. F., J. HERRERO, L. SORIANO AND M. T. GUTIÉRREZ. Optical characterization procedure for large thin films. In *Conference on Modeling Aspects in Optical Metrology*. Munich, GERMANY, 2007, vol. 6617, p. 61712-61712.
- [274] JORIO, A. AND R. SAITO Raman spectroscopy for carbon nanotube applications. *Journal of Applied Physics*, Jan 2021, 129(2).
- [275] OGIEGLO, W., H. WORMEESTER, K. J. EICHHORN, M. WESSLING, et al. In situ ellipsometry studies on swelling of thin polymer films: A review. *Progress in Polymer Science*, Mar 2015, 42, 42-78.
- [276] SOUISSI, A., A. BOUKHACHEM, Y. BEN TAHER, A. AYADI, et al. Structural and vibrational studies of Mo and In-doped ZnO sprayed thin films. *Optik*, 2014, 125(13), 3344-3349.
- [277] TENNE, D. A. AND X. X. XI Raman spectroscopy of ferroelectric thin films and superlattices. *Journal of the American Ceramic Society*, Jun 2008, 91(6), 1820-1834.
- [278] SAITO, R., M. HOFMANN, G. DRESSELHAUS, A. JORIO, et al. Raman spectroscopy of graphene and carbon nanotubes. *Advances in Physics*, 2011, 60(3), 413-550.
- [279] LI, Z. L., L. B. DENG, I. A. KINLOCH AND R. J. YOUNG Raman spectroscopy of carbon materials and their composites: Graphene, nanotubes and fibres. *Progress in Materials Science*, Jun 2023, 135.
- [280] BERTHOMIEU, C. AND R. HIENERWADEL Fourier transform infrared (FTIR) spectroscopy. *Photosynthesis Research*, Sep 2009, 101(2-3), 157-170.
- [281] SCHRIVER-MAZZUOLI, L., A. SCHRIVER AND A. HALLOU IR reflection-absorption spectra of thin water ice films between 10 and 160 K at low pressure. *Journal of Molecular Structure*, Nov 2000, 554(2-3), 289-300.
- [282] TAMADA, M., H. KOSHIKAWA, F. HOSOI AND T. SUWA FTIR reflection absorption spectroscopy for organic thin film on ITO substrate. *Thin Solid Films*, Mar 1998, 315(1-2), 40-43.
- [283] DE LOS ARCOS, T., H. MÜLLER, F. Z. WANG, V. R. DAMERLA, et al. Review of infrared spectroscopy techniques for the determination of internal structure in thin SiO₂ films. *Vibrational Spectroscopy*, May 2021, 114.
- [284] RESENDE, J., D. FUARD, D. LE CUNFF, J. H. TORTAI, et al. Hybridization of ellipsometry and energy loss spectra from XPS for bandgap and optical constants determination in SiON thin films. *Materials Chemistry and Physics*, Feb 2021, 259.
- [285] JUDY, J. W. Microelectromechanical systems (MEMS): fabrication, design and applications. *Smart materials and Structures*, 2001, 10(6), 1115.
- [286] PIMPIN, A. AND W. SRITURAVANICH Review on Micro- and Nanolithography Techniques and their Applications. *Engineering Journal-Thailand*, 2012, 16(1), 37-55.
- [287] TILLI, M., M. PAULASTO-KRÖCKEL, M. PETZOLD, H. THEUSS, et al. *Handbook of silicon based MEMS materials and technologies*. Edition ed.: Elsevier, 2020. ISBN 012817787X.
- [288] SEISYAN, R. P. Nanolithography in microelectronics: A review. *Technical Physics*, 2011/08/01 2011, 56(8), 1061-1073.
- [289] MADOU, M. J. *Fundamentals of microfabrication: the science of miniaturization*. Edition ed.: CRC press, 2018. ISBN 1482274000.
- [290] FAY, B. Advanced optical lithography development, from UV to EUV. *Microelectronic Engineering*, Jul 2002, 61-2, 11-24.
- [291] TOTZECK, M., W. ULRICH, A. GÖHNERMEIER AND W. KAISER Pushing deep ultraviolet lithography to its limits. *Nature Photonics*, 2007/11/01 2007, 1(11), 629-631.
- [292] RONSE, K., A. M. GOETHALS, G. VANDENBERGHE AND M. MAENHOUDT. Recent trends and progress in deep-UV lithography. In *Conference on Lithography for Semiconductor Manufacturing*. Edinburgh, Scotland, 1999, vol. 3741, p. 34-39.
- [293] WU, B. AND A. KUMAR Extreme ultraviolet lithography: A review. *Journal of Vacuum Science & Technology B: Microelectronics and Nanometer Structures Processing, Measurement, and Phenomena*, 2007, 25(6), 1743-1761.
- [294] OBER, C. K., H. XU, V. KOSMA, K. SAKAI, et al. EUV photolithography: resist progress and challenges. *Extreme Ultraviolet (EUV) Lithography IX*, 2018, 10583, 15-27.
- [295] LIDDLE, J. A., G. P. WATSON, S. D. BERGER AND P. D. MILLER Proximity effect correction in projection electron beam lithography (Scattering with angular limitation projection electron-beam lithography). *Japanese Journal of Applied Physics*, 1995, 34(12S), 6672.
- [296] HOHN, F. J. H. F. J. Electron beam lithography-tools and applications. *Japanese Journal of Applied Physics*, 1991, 30(11S), 3088.
- [297] CHEN, Y. Nanofabrication by electron beam lithography and its applications: A review. *Microelectronic Engineering*, 2015/03/05/ 2015, 135, 57-72.
- [298] HAMZAH, A. A., B. Y. MAJLIS AND I. AHMAD HF etching of sacrificial spin-on glass in straight and junctioned microchannels for MEMS microstructure release. *Journal of the Electrochemical Society*, 2007, 154(8), D376.
- [299] BAHREYNI, B. AND C. SHAFAI Investigation and simulation of XeF₂ isotropic etching of silicon. *Journal of Vacuum Science & Technology A*, 2002, 20(6), 1850-1854.
- [300] PANDHUMSOPORN, T., L. WANG, M. FELDBAUM, P. GADGIL, et al. *High-etch-rate deep anisotropic plasma etching of silicon for MEMS fabrication*. Edition ed.: SPIE, 1998.
- [301] AIROLA, K., S. MERTIN, J. LIKONEN, E. HARTIKAINEN, et al. High-fidelity patterning of AlN and ScAlN thin films with wet chemical etching. *Materialia*, 2022/05/01/ 2022, 22, 101403.

- [302] GOSÁLVEZ, M. A., I. ZUBEL AND E. VIINIKKA. Chapter 17 - Wet etching of silicon. In M. TILLI, M. PAULASTO-KROCKEL, M. PETZOLD, H. THEUSS, T. MOTOOKA AND V. LINDROOS eds. *Handbook of Silicon Based MEMS Materials and Technologies (Third Edition)*. Elsevier, 2010, p. 447-480.
- [303] FRÜHAUF, J. AND B. HANNEMANN Wet etching of undercut sidewalls in {001}-silicon. *Sensors and Actuators A: Physical*, 2000/01/25/ 2000, 79(1), 55-63.
- [304] KELLY, J. J. AND H. G. G. PHILIPSEN Anisotropy in the wet-etching of semiconductors. *Current Opinion in Solid State and Materials Science*, 2005/02/01/ 2005, 9(1), 84-90.
- [305] GABLECH, I., J. BRODSKÝ, J. PEKÁREK AND P. NEUŽIL Infinite Selectivity of Wet SiO₂ Etching in Respect to Al. *Micromachines (Basel)*, 2020, 11(4), 365.
- [306] HUFF, M. Recent Advances in Reactive Ion Etching and Applications of High-Aspect-Ratio Microfabrication. *Micromachines (Basel)*, 2021, 12(8), 991.
- [307] DUBREUIL, P. AND D. BELHARET Plasma impedance monitoring for real time endpoint detection of bulk materials etched in ICP tool. *Microelectronic Engineering*, 2010/11/01/ 2010, 87(11), 2275-2281.
- [308] KIM, T. AND J. LEE Optimization of deep reactive ion etching for microscale silicon hole arrays with high aspect ratio. *Micro and Nano Systems Letters*, 2022/09/09 2022, 10(1), 12.
- [309] LAERMER, F., S. FRANSSILA, L. SAINIEMI AND K. KOLARI. Chapter 16 - Deep reactive ion etching. In M. TILLI, M. PAULASTO-KROCKEL, M. PETZOLD, H. THEUSS, T. MOTOOKA AND V. LINDROOS eds. *Handbook of Silicon Based MEMS Materials and Technologies (Third Edition)*. Elsevier, 2020, p. 417-446.
- [310] TIDDIA, M., I. MIHARA, M. P. SEAH, G. F. TRINDADE, et al. Chemical Imaging of Buried Interfaces in Organic-Inorganic Devices Using Focused Ion Beam-Time-of-Flight-Secondary-Ion Mass Spectrometry. *Acs Applied Materials & Interfaces*, 2019/01/30 2019, 11(4), 4500-4506.
- [311] REYNTJENS, S. AND R. PUERS A review of focused ion beam applications in microsystem technology. *Journal of micromechanics and microengineering*, 2001, 11(4), 287.
- [312] PÉCZ, B. AND A. BARNA Reactive ion milling—thinning of compound semiconductors. *Vacuum*, 1994/01/01/ 1994, 45(1), 1-3.
- [313] CALVO, J., M. DRESCHER, K. KÜHNEL, B. SAUER, et al. LPCVD in-situ doped silicon for thermoelectric applications. *Materials Today: Proceedings*, 2018/01/01/ 2018, 5(4, Part 1), 10249-10256.
- [314] FOXON, C. T. Three decades of molecular beam epitaxy. *Journal of Crystal Growth*, 2003/04/01/ 2003, 251(1), 1-8.
- [315] NIKKOLA, J., J. SIEVÄNEN, M. RAULIO, J. WEI, et al. Surface modification of thin film composite polyamide membrane using atomic layer deposition method. *Journal of Membrane Science*, 2014/01/15/ 2014, 450, 174-180.
- [316] MOSTAFAVI, A. H., A. K. MISHRA, F. GALLUCCI, J. H. KIM, et al. Advances in surface modification and functionalization for tailoring the characteristics of thin films and membranes via chemical vapor deposition techniques. *Journal of Applied Polymer Science*, 2023, 140(15), e53720.
- [317] EOM, C.-B. AND S. TROLIER-MCKINSTRY Thin-film piezoelectric MEMS. *MRS Bulletin*, 2012, 37(11), 1007-1017.
- [318] MABECK, J. T. AND G. G. MALLIARAS Chemical and biological sensors based on organic thin-film transistors. *Analytical and Bioanalytical Chemistry*, 2006/01/01 2006, 384(2), 343-353.
- [319] SBERVEGLIERI, G. Recent developments in semiconducting thin-film gas sensors. *Sensors and Actuators B: Chemical*, 1995/02/01/ 1995, 23(2), 103-109.
- [320] HIERLEMANN, A., O. BRAND, C. HAGLEITNER AND H. BALTES Microfabrication techniques for chemical/biosensors. *Proceedings of the IEEE*, 2003, 91(6), 839-863.
- [321] VOSSSEN, J. L. AND W. KERN. Preface. In J.L. VOSSSEN AND W. KERN eds. *Thin Film Processes*. San Diego: Academic Press, 1991, p. xiii.
- [322] WISE, K. D. AND K. NAJAFI MICROFABRICATION TECHNIQUES FOR INTEGRATED SENSORS AND MICROSYSTEMS. *Science*, Nov 1991, 254(5036), 1335-1342.
- [323] GABLECH, I., O. CAHA, V. SVATOŠ, J. PEKÁREK, et al. Stress-free deposition of [001] preferentially oriented titanium thin film by Kaufman ion-beam source. *Thin Solid Films*, 2017/09/30/ 2017, 638, 57-62.
- [324] ZHU, H., E. GABLECH, I. GABLECH AND P. NEUŽIL The collective photothermal effect of silver nanoparticles probed by a microbolometer. *Communications Materials*, 2024/05/01 2024, 5(1), 66.
- [325] GABLECH, I., J. BRODSKÝ, P. VYROUBAL, J. PIASTEK, et al. Mechanical strain and electric-field modulation of graphene transistors integrated on MEMS cantilevers. *Journal of Materials Science*, 2022/01/01 2022, 57(3), 1923-1935.
- [326] CHMELA, O., I. GABLECH, J. SADÍLEK, J. BRODSKÝ, et al. ChemFET gas nanosensor arrays with alignment windows for assembly of single nanowires. *Nano Research*, 2023/07/01 2023, 16(7), 10234-10244.
- [327] MANZ, A., P. NEUŽIL, J. S. O'CONNOR AND G. SIMONE *Microfluidics and Lab-on-a-Chip*. Edition ed.: The Royal Society of Chemistry, 2020. ISBN 978-1-78262-833-0.
- [328] CHAKRABORTY, S. *Microfluidics and microfabrication* 2010.
- [329] LI, M., W. LI, J. ZHANG, G. ALICI, et al. A review of microfabrication techniques and dielectrophoretic microdevices for particle manipulation and separation. *Journal of Physics D: Applied Physics*, 2014, 47(6), 063001.
- [330] NGE, P. N., C. I. ROGERS AND A. T. WOOLLEY Advances in Microfluidic Materials, Functions, Integration, and Applications. *Chemical Reviews*, 2013/04/10 2013, 113(4), 2550-2583.
- [331] LIM, Y. C., A. Z. KOUZANI AND W. DUAN Lab-on-a-chip: a component view. *Microsystem Technologies*, 2010/12/01 2010, 16(12), 1995-2015.

- [332] AKCEOGLU, G. A., Y. SAYLAN AND F. INCI A Snapshot of Microfluidics in Point-of-Care Diagnostics: Multifaceted Integrity with Materials and Sensors. *Advanced Materials Technologies*, 2021, 6(7), 2100049.
- [333] ANDERSSON, M., J. EK, L. HEDMAN, F. JOHANSSON, et al. Thin film metal sensors in fusion bonded glass chips for high-pressure microfluidics. *Journal of micromechanics and microengineering*, 2016, 27(1), 015018.
- [334] RESNIK, D., D. VRTAČNIK, M. MOŽEK, B. PEČAR, et al. Experimental study of heat-treated thin film Ti/Pt heater and temperature sensor properties on a Si microfluidic platform. *Journal of micromechanics and microengineering*, 2011, 21(2), 025025.
- [335] LIN, W.-Y., Y. WANG, S. WANG AND H.-R. TSENG Integrated microfluidic reactors. *Nano Today*, 2009/12/01/ 2009, 4(6), 470-481.
- [336] ZHANG, H., J. PEKÁREK, J. FENG, X. LIU, et al. nanolithography toolbox—Simplifying the design complexity of microfluidic chips. *Journal of Vacuum Science & Technology B*, 2020, 38(6).
- [337] ZHU, H., H. LI, H. ZHANG, Z. FOHLEROVA, et al. Heat transfer time determination based on DNA melting curve analysis. *Microfluidics and Nanofluidics*, 2019/12/12 2019, 24(1), 7.
- [338] MIDLIK, Š., I. GABLECH, M. GOLEŇA, J. BRODSKÝ, et al. Parylene-bonded micro-fluidic channels for cryogenic experiments at superfluid He-4 temperatures. *Review of Scientific Instruments*, 2024, 95(3).
- [339] FOTOVVATI, B., N. NAMDARI AND A. DEHGHANGHADIKOLAEI On Coating Techniques for Surface Protection: A Review. *Journal of Manufacturing and Materials Processing*, 2019, 3(1), 28.
- [340] KOMIYA, S., N. UMEZU AND C. HAYASHI Titanium nitride film as a protective coating for a vacuum deposition chamber. *Thin Solid Films*, 1979/11/01/ 1979, 63(2), 341-346.
- [341] DENG, J. AND M. BRAUN DLC multilayer coatings for wear protection. *Diamond and Related Materials*, 1995/05/15/ 1995, 4(7), 936-943.
- [342] KOLA, P. V., S. DANIELS, D. C. CAMERON AND M. S. J. HASHMI Magnetron sputtering of tin protective coatings for medical applications. *Journal of Materials Processing Technology*, 1996/01/01/ 1996, 56(1), 422-430.
- [343] HASSLER, C., R. P. VON METZEN, P. RUTHER AND T. STIEGLITZ Characterization of parylene C as an encapsulation material for implanted neural prostheses. *Journal of Biomedical Materials Research Part B: Applied Biomaterials*, 2010, 93B(1), 266-274.
- [344] EL-CHAMI, M. F., J. MAYOTTE, M. BONNER, R. HOLBROOK, et al. Reduced bacterial adhesion with parylene coating: Potential implications for Micra transcatheter pacemakers. *Journal of Cardiovascular Electrophysiology*, Mar 2020, 31(3), 712-717.
- [345] CONSTANTIN, C. P., M. AFLORI, R. F. DAMIAN AND R. D. RUSU Biocompatibility of Polyimides: A Mini-Review. *Materials*, 2019, 12(19), 3166.
- [346] BRODSKÝ, J., I. GABLECH, L. MIGLIACCIO, M. HAVLÍČEK, et al. Downsizing the Channel Length of Vertical Organic Electrochemical Transistors. *Acs Applied Materials & Interfaces*, 2023/06/07 2023, 15(22), 27002-27009.
- [347] BUTT, M. A., C. TYSZKIEWICZ, P. KARASIŃSKI, M. ZIĘBA, et al. Optical Thin Films Fabrication Techniques—Towards a Low-Cost Solution for the Integrated Photonic Platform: A Review of the Current Status. *Materials*, 2022, 15(13), 4591.
- [348] PETROV, I., P. B. BARNA, L. HULTMAN AND J. E. GREENE Microstructural evolution during film growth. *Journal of Vacuum Science & Technology A*, Sep-Oct 2003, 21(5), S117-S128.
- [349] MOSTAFAVI, A. H., A. K. MISHRA, F. GALLUCCI, J. H. KIM, et al. Advances in surface modification and functionalization for tailoring the characteristics of thin films and membranes via chemical vapor deposition techniques. *Journal of Applied Polymer Science*, Apr 2023, 140(15).
- [350] FOHLEROVA, Z., I. GABLECH, A. OTAHAL AND P. FECKO SiO₂-Decorated Parylene C Micropillars Designed to Probe Cellular Force. *Advanced Materials Interfaces*, 2021, 8(6), 2001897.
- [351] LIU, X., Z. FOHLEROVÁ, I. GABLECH, M. PUMERA, et al. Nature-inspired parylene/SiO₂ core-shell micro-nano pillars: Effect of topography and surface chemistry. *Applied Materials Today*, 2024/04/01/ 2024, 37, 102117.
- [352] GABLECH, I., L. MIGLIACCIO, J. BRODSKÝ, M. HAVLÍČEK, et al. High-Conductivity Stoichiometric Titanium Nitride for Bioelectronics. *Advanced Electronic Materials*, 2023, 9(4), 2200980.
- [353] OKUYAMA, S., S. I. MATSUSHITA AND A. FUJISHIMA Preparation of periodic microstructured diamond surfaces. *Chemistry Letters*, May 2000, (5), 534-535.
- [354] AIZAWA, T., T. INOHARA AND K. WASA Femtosecond Laser Micro-/nano-texturing of Stainless Steels for Surface Property Control. *Micromachines (Basel)*, 2019, 10(8), 512.
- [355] ROTICH, S. K., J. G. SMITH, A. G. R. EVANS AND A. BRUNNSCHWEILER Micromachined thin solar cells with a novel light trapping scheme. *Journal of micromechanics and microengineering*, Jun 1998, 8(2), 134-137.
- [356] BARONI, P. Y., B. PÄIVÄNRANTA, T. SCHARF, W. NAKAGAWA, et al. Nanostructured surface fabricated by laser interference lithography to attenuate the reflectivity of microlens arrays. *Journal of the European Optical Society-Rapid Publications*, 2010, 5.
- [357] HOWELL, C., A. GRINTHAL, S. SUNNY, M. AIZENBERG, et al. Designing Liquid-Infused Surfaces for Medical Applications: A Review. *Advanced Materials*, Dec 2018, 30(50).
- [358] CHU, S.-F., M.-T. HUANG, K.-L. OU, E. SUGIATNO, et al. Enhanced biocompatible and hemocompatible nano/micro porous surface as a biological scaffold for functionalizational and biointegrated implants. *Journal of Alloys and Compounds*, 2016/11/05/ 2016, 684, 726-732.



Contents lists available at ScienceDirect

Thin Solid Films

journal homepage: www.elsevier.com/locate/tsf

Stress-free deposition of [001] preferentially oriented titanium thin film by Kaufman ion-beam source



Imrich Gablech^{a,b,*}, Ondřej Caha^{c,d}, Vojtěch Svatoš^{a,b}, Jan Pekárek^{a,b}, Pavel Neužil^{a,b,e}, Tomáš Šíkola^{a,f}

^a Central European Institute of Technology, Brno University of Technology, Purkyňova 123, CZ-61200 Brno, Czech Republic

^b Brno University of Technology, Faculty of Electrical Engineering and Communication, Department of Microelectronics, Technická 3058/10, CZ-61600 Brno, Czech Republic

^c Central European Institute of Technology, Masaryk University, Kamenice 753/5, CZ-62500 Brno, Czech Republic

^d Masaryk University, Faculty of Science, Department of Condensed Matter Physics, Kotlářská 2, CZ-60200 Brno, Czech Republic

^e Northwestern Polytechnical University, 127 West Youyi Road, Xi'an, Shaanxi, PR China

^f Brno University of Technology, Institute of Physical Engineering, Technická 2896/2, CZ-61669 Brno, Czech Republic

ARTICLE INFO

Article history:

Received 2 March 2017

Received in revised form 10 July 2017

Accepted 14 July 2017

Available online 15 July 2017

Keywords:

Ion-beam sputtering deposition

Kaufman ion-beam source

Titanium thin film

[001] preferential orientation

Residual stress

Rocking curve

ABSTRACT

We proposed a method to control and minimize residual stress in [001] preferentially oriented Ti thin films deposited by a Kaufman ion-beam source using a substrate temperature during deposition (T) as the parameter. We determined the residual stress, corresponding lattice parameters, and thickness of deposited films using X-ray diffraction and X-ray reflectivity measurements. We showed that the Ti film deposited at $T \approx 273$ °C was stress-free with corresponding lattice parameters a_0 and c_0 of (2.954 ± 0.003) Å and (4.695 ± 0.001) Å, respectively. The stress-free sample has the superior crystallographic quality and pure [001] orientation. The Ti thin films were oriented with the c -axis parallel to the surface normal. We also investigated root mean square of surface roughness of deposited films by atomic force microscopy and it was in the range from ≈ 0.58 nm to ≈ 0.71 nm. Such smooth and stress-free layers are suitable for microelectromechanical systems.

© 2017 Elsevier B.V. All rights reserved.

1. Introduction

Ti is a commonly used material in planar technologies either for the fabrication of integrated circuits, microelectromechanical systems (MEMS) or microfluidic systems. Ti has a reasonably good electrical conductivity, an excellent thermal stability, high hardness, high melting point, high elasticity and a very low concentration of crystallographic imperfections [1]. Ti belongs to a group of biocompatible materials and is also compatible with the complementary-metal-oxide-semiconductor (CMOS) process; thus, it is capable of being used in fabrication lines dedicated to CMOS production and research [2]. Ti thin films are used in MEMS applications such as cochlear implants [3], infrared bolometers [4–6], flexible and wearable heartbeat sensors [7], piezoelectric energy harvesters [8], microfluidic devices [9], and piezoelectric resonators [10]. Layers used in MEMS technologies are typically required to have minimal residual stress as this significantly affects the mechanical [11] and electrical [12] properties of a final device. Once the stress level exceeds a certain limit it can even cause damage to the structural integrity of the device [13].

Ti thin films are usually deposited by processes such as physical vapor deposition, including thermal and electron beam evaporation, pulsed laser deposition, or sputtering, either magnetron or ion-beam based. Each technique results in the formation of layers with different properties, such as crystallographic parameters, roughness, residual stress, electrical sheet resistance, and thermal coefficient of resistance [14]. Control of the Ti crystallographic orientation is of crucial significance as it directly affects its properties and, together with surface roughness, it is important for properties of layers subsequently deposited on top of the Ti layer, such as AlN piezoelectric material [10,15,16]. The magnetron sputtering technique allows residual stress control by modulating Ar gas pressure, magnetron power, or substrate deposition temperature (T) [17]. Unfortunately, these parameters cannot be set independently from each other. The other extended technique employing the assisted ion-beam source for concurrent substrate ion-beam bombardment during the layer growth allows only limited control of residual stress [18].

Here, we report on the preparation of stress-free highly [001] oriented Ti thin films deposited using a 3-grid radio frequency-inductively coupled plasma (RFICP) Kaufman ion-beam source. The major advantage of this ion-beam source type is a well-defined process control that allows us, contrary to conventional deposition techniques, to set parameters like ion-beam energy and atomic sputtering direction independently, and also in one order magnitude lower operational pressure compared with magnetron sputtering [1]. On the other hand, its disadvantage is a

* Corresponding author at: Central European Institute of Technology, Brno University of Technology, Purkyňova 123, CZ-61200 Brno, Czech Republic.

E-mail address: imrich.gablech@ceitec.vutbr.cz (I. Gablech).

rather more complex control of residual stress. In our work, we concentrated on the investigation of the control of residual stress by T and its influence on crystallography and surface roughness of a Ti layer deposited on a plasma enhanced chemical vapor deposited (PECVD) SiO_2 layer.

2. Experimental details

2.1. Titanium deposition process

For all experiments, we used p-type Si wafers with diameter of ≈ 100 mm, crystallographic orientation of [100], thickness of ≈ 375 μm , and specific resistivity in the range from ≈ 6 Ω cm to ≈ 12 Ω cm covered with PECVD SiO_2 with a thickness of ≈ 200 nm. These wafers were diced into individual substrates with dimensions of ≈ 20 mm \times ≈ 20 mm.

The Ti layers were deposited by an ion-beam sputtering system inside a vacuum chamber with the RFICP Kaufman ion-beam source (Kaufman & Robinson—KRI®) with a ≈ 4 cm diameter Mo 3-grid dished focused ion optics with an $\approx 45^\circ$ ellipse pattern. We used an Ar ion-beam with purity of 99.99999% to provide the bombardment of an ≈ 100 mm \times ≈ 100 mm Ti target with the purity of 99.995% under an incidence angle of $\approx 45^\circ$. Reduction of the ion-beam space charge was provided by a KRI LFN 2000 charge neutralizer (KRI®). The vacuum chamber was evacuated to the pressure of $\approx 5 \cdot 10^{-7}$ Pa before each deposition process. The final Ti thickness (t_f) of (80 ± 1) nm was monitored in-situ by quartz crystal microbalance method and subsequently verified by X-ray reflectivity (XRR) measurement.

The deposition parameters were selected under conditions determined in our previously reported work [1]. We set the ion-beam energy to ≈ 200 eV, acceleration voltage to ≈ -220 V to control the extraction and optical parameters of the ion-beam, ion-beam current to ≈ 5 mA at the target, radio frequency power to ≈ 70 W supplied to the plasma discharge, Ar flow to ≈ 2.2 sccm, and T was used as the parameter. We performed a contact temperature measurement using a type K thermocouple during the sputter deposition process to investigate the T caused by the combination of deposited material energy and the built-in substrate heater. The lowest value of T was ≈ 105 $^\circ\text{C}$ which is generated only by the deposited material flux with no additional heating. We controlled the T in the range from ≈ 105 $^\circ\text{C}$ to ≈ 295 $^\circ\text{C}$ with an accuracy of ± 3 $^\circ\text{C}$. The pressure during the all depositions was constant with the value of $\approx 9 \cdot 10^{-3}$ Pa.

2.2. X-ray scattering methods

We characterized the Ti layers by several X-ray diffraction (XRD) methods (Fig. 1). We used a Rigaku SmartLab system with a Cu X-ray tube.

We used the standard Bragg–Brentano setup (Fig. 1A) to determine the lattice parameter (c) of the planes parallel to the surface. The lattice

parameter (a) in the perpendicular direction was measured in a grazing-incidence setup (Fig. 1B) using a parabolic multilayer mirror as a monochromator and parallel plate collimator with a divergence of $\approx 0.15^\circ$ and $\approx 0.11^\circ$ in the incident and the scattered beam, respectively. We performed this measurement at an angle of incidence (α_i) of 0.3° , which is close to the critical angle of total external reflection of 0.298° . The diffracted signal was integrated over the exit angle (α_f) from 0° up to 2° . We extracted values of lattice parameters by curve fitting using Rigaku PDXL2 software.

We measured the t_f in the XRR configuration using a two bounce Ge (220) channel cut monochromator.

We determined the preferential orientation of the Ti lattice via the pole figures measurement. We performed the measurement with the parallel beam and the parallel plate collimator as in the grazing incidence setup (Fig. 1B). The diffractometer with an in-plane arm allowed to map the full half space above the sample's surface. The background of pole figure was measured 2° off the peak position.

We measured the curvature (Fig. 1C) of the Si substrate before (R_0) and after (R) Ti deposition to determine the elastic stress of Ti layers. The curvature radius was determined from the dependence of Bragg angle (θ) on the substrate position. Its slope is inversely proportional to the curvature radius of crystallographic planes. The stress of a Ti layer (σ_f) can be calculated by the Stoney formula (Eq. (1)) for [001] oriented Si [19]:

$$\sigma_f t_f = \frac{h^2}{6} \cdot \frac{1}{s_{11} + s_{12}} \cdot \left(\frac{1}{R} - \frac{1}{R_0} \right) \quad (1)$$

where h is the substrate thickness and s_{11} and s_{12} are the components of the Si elastic compliance tensor. We used a four bounce Ge (220) Bartels-type monochromator and measured the position of Si 004 diffraction peak dependence on the sample position.

2.3. Surface roughness measurement method

We determined the root mean square of surface roughness (R_{RMS}) from surface scanning by atomic force microscope (AFM) Dimension Icon by Bruker in the ScanAsyst®-Air mode. We used the ScanAsyst-Air probe with a cantilever spring constant of ≈ 0.4 N \cdot m $^{-1}$ and tip radius of ≈ 2 nm.

3. Results and discussion

3.1. Crystallography and stress characterization

We performed phase analysis measurement using XRD in the Bragg–Brentano setup with the 2θ angle in the range from 30° to 85° for all layers with T as the parameter. The interval from 60° to 78° was excluded

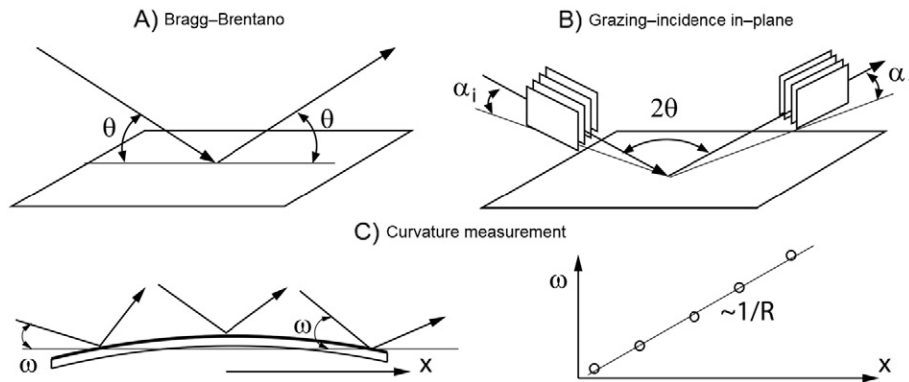


Fig. 1. Setup of the XRD experimental methods: A) Bragg–Brentano setup to measure the out-of-plane c lattice parameter; B) In-plane diffraction for a lattice parameter determination was measured with the parallel plate collimator and analyzer shown in the figure; C) Curvature measurement determines average σ_f in the layer. The angle of incidence with respect to the mean surface is noted as ω .

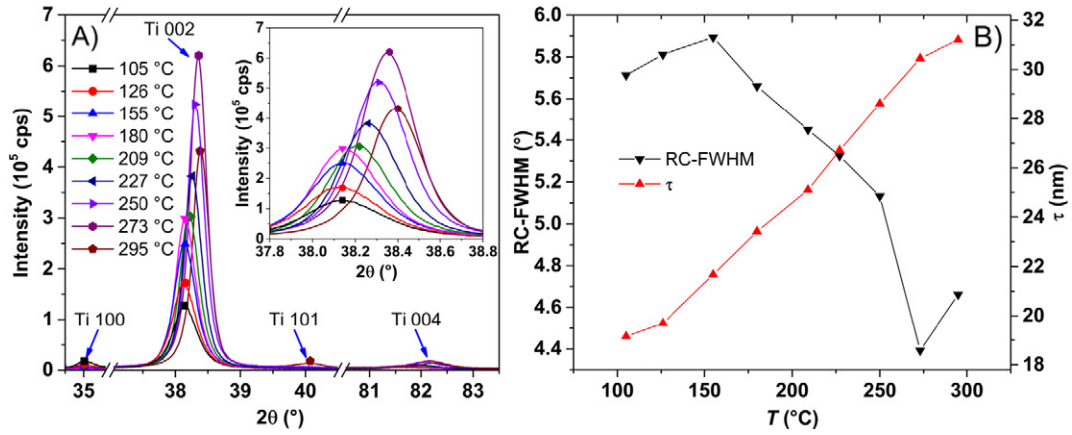


Fig. 2. A) X-ray diffractograms of deposited thin films obtained at different T . The range from 60° to 78° was excluded due to Si 400 diffraction with intensity of several orders of magnitude higher than of the Ti peaks; B) RC-FWHM and τ dependence on T .

to avoid the high intensity of Si 400 diffraction in this range. We detected the diffraction peaks that belongs to the (100), (001) and (101) crystallographic planes. We detected the 2nd order 002 and the 4th order 004 diffraction peaks since the 1st order diffraction is forbidden (Fig. 2A) for the (001) crystallographic plane (Fig. 2A). We used XRD in the parallel beam setup to determine the rocking curve (RC) width (Fig. 2B). We calculated the minimal average crystallite size (τ) using the Scherrer equation [20] (Eq. (2)) from the full width at half maximum (FWHM) of the 002 diffraction peak in the Bragg-Brentano setup (Fig. 2B):

$$\tau = \frac{K \cdot \lambda}{\beta \cdot \cos(\theta)} \quad (2)$$

where K is the Scherrer constant, λ is the X-ray wavelength, and β is the line broadening at half the maximum intensity. The 004 diffraction peak was not resolved at all samples, thus the inhomogeneous strain induced peak widening could not be determined.

The Bragg-Brentano analysis results proved that the crystallites in all deposited layers had the [001] preferential orientation. We also observed a small contribution of the (100) plane belonging to the samples deposited with T from $\approx 105^\circ\text{C}$ to $\approx 155^\circ\text{C}$. Only one (001) crystallographic plane was presented for samples deposited in the range from $\approx 180^\circ\text{C}$ to $\approx 273^\circ\text{C}$. The small contribution of the (101) plane was presented for the highest $T \approx 295^\circ\text{C}$.

T increased from $\approx 155^\circ\text{C}$ to $\approx 273^\circ\text{C}$, resulting in increased diffraction peak intensity and decreased RC width. We observed the highest diffraction intensity with the lowest FWHM value of $\approx 0.27^\circ$ and the lowest RC width with FWHM $\approx 4.4^\circ$ at $T \approx 273^\circ\text{C}$. Increasing T from $\approx 105^\circ\text{C}$ to $\approx 295^\circ\text{C}$ also resulted in the increase of τ from $\approx 19\text{ nm}$ to $\approx 31\text{ nm}$.

The dependence of the lattice parameters on T is shown in Fig. 3B. The strain ε_{ij} was calculated (Eq. (3)) using experimental and tabulated values of the lattice parameters:

$$\varepsilon_{xx} = \frac{a_{\text{exp}} - a_0}{a_0}, \quad \varepsilon_{zz} = \frac{c_{\text{exp}} - c_0}{c_0} \quad (3)$$

where x and z , respectively, are the in-plane and out-of-plane coordinates, a_{exp} , c_{exp} the experimental lattice parameters and a_0 , c_0 the tabulated values of the unstrained lattice. Then assuming in-plane isotropy, the in-plane and out-of-plane stress components can be calculated as (Eq. (4)):

$$\sigma_{xx} = (C_{11} + C_{12}) \cdot \varepsilon_{xx} + C_{13} \cdot \varepsilon_{zz}, \quad \sigma_{zz} = 2C_{13} \cdot \varepsilon_{xx} + C_{33} \cdot \varepsilon_{zz} = 0 \quad (4)$$

where C_{ij} are the components of the Ti elastic stiffness tensor [21], the in-plane σ_{xx} , and the out-of-plane σ_{zz} stress components equal zero since the surface is stress-free. However, the tabulated values of the lattice parameters vary in a relatively broad range and, therefore the uncertainty of the calculated stress would be in the order of GPa and, therefore, not acceptable for MEMS applications. Thus, we measured the σ_f via the curvature of the substrate; the measured σ_f dependence on T is plotted in Fig. 3A. The σ_f has the same qualitative dependence as the a and opposite one as the c in agreement with the previous equations (Eq. (4)).

The Ti thin film deposited at $T \approx 273^\circ\text{C}$ exhibits the zero residual σ_f value within the experimental precision of 0.1 GPa. Corresponding a_0 and c_0 of this unstrained Ti film are $(2.954 \pm 0.003)\text{ \AA}$ and $(4.695 \pm 0.001)\text{ \AA}$, respectively and their ratio c/a is (1.5891 ± 0.0015) . Using these values of Ti lattice parameters, we calculated the average amplitudes of σ_{xx} and σ_{zz} using formulas (Eq. (3)) and (Eq. (4)). We obtained values which were in good agreement with the ones determined by the

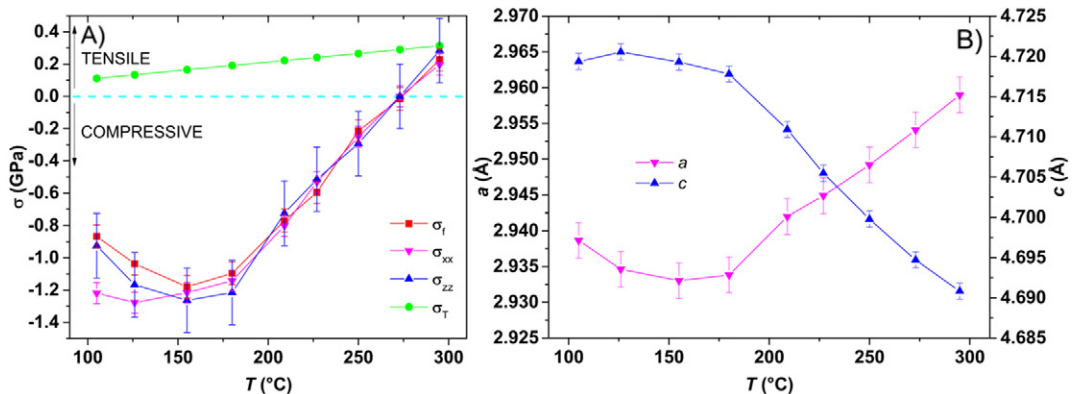


Fig. 3. A) Stress σ dependence of measured σ_f and calculated σ_{xx} , σ_{zz} , and σ_f values (Eq. (4)) on T ; B) Dependence of measured a and c of deposited Ti thin films on T .

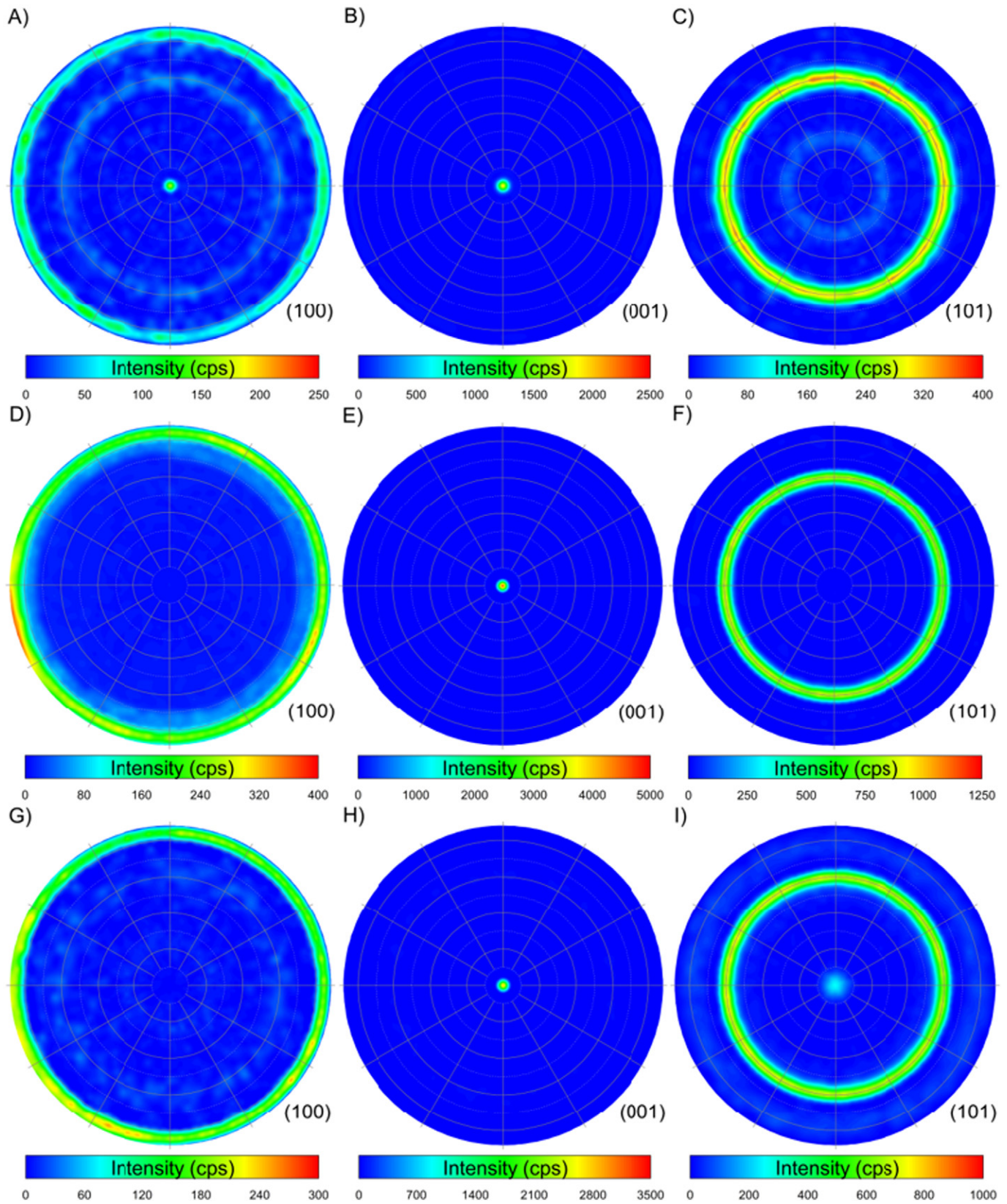


Fig. 4. Pole figures of three diffractions 100, 002 [second order diffraction on the (001) crystallographic planes], and 101 are plotted in the left, center, and right column, respectively: A, B, C) The sample grown at $T \approx 105$ °C with the compressive stress; D, E, F) The sample grown at $T \approx 273$ °C with no residual stress; G, H, I) The sample grown at $T \approx 295$ °C with tensile stress.

independent curvature measurements (Fig. 3A). The tensile stress for the layers deposited at high T can be explained by the different thermal expansion of Si and Ti material. The Ti thermal expansion coefficient is

larger than for the Si by $\approx 6 \cdot 10^{-6} \text{ K}^{-1}$. This corresponds to a thermally induced stress (σ_T) of ≈ 0.3 GPa for the $T \approx 295$ °C, which is in good agreement with the experimental value (Fig. 3A). The layers deposited

at lower T were compressively stressed, with the highest stress value reached at $T \approx 155$ °C. Higher T resulted in stress relaxation. The layer deposited at $T \approx 295$ °C was grown as stress-free and the tensile stress was induced during cooling down to the ambient temperature.

3.2. Pole figure analysis

The Bragg–Brentano setup showed the crystallographic planes parallel to the surface. We performed pole figure analyses to obtain full information of the preferential orientation of the layer. The pole figures were measured on three selected samples with different symmetric diffraction patterns and stress (Fig. 4). The first one was grown at $T \approx 105$ °C exhibits the (100) and (001) crystallographic planes oriented preferentially in crystallites parallel to a surface and the stress was compressive. The second, grown at $T \approx 273$ °C, was purely [001] oriented and stress-free. The third one has the (001) and (101) planes parallel to a surface and the layer possess tensile stress.

The sample grown at optimal $T \approx 273$ °C (Fig. 4D, E, F) shows that the (001) crystallographic planes are oriented in crystallites exclusively parallel to the sample surface, noted as a peak in the center of the circular stereographic projection. The (100) planes are randomly oriented perpendicular to the surface, shown as a ring at the outer circle boundary, the (101) planes are oriented with a theoretical angle of $\approx 61^\circ$ with respect to the surface. The other samples show the major contribution of the [001] orientation giving rise to the result equivalent to the optimal T . The samples grown at low and high T show an additional minor contribution of another orientation. The sample grown at a lower $T \approx 105$ °C shows the (100) planes in two preferential orientations: parallel to the surface [[100] oriented crystallites] and perpendicular to the surface [[001] oriented crystallites]; the ring at angle of $\approx 60^\circ$ with respect to the surface corresponds also to the [100] orientation since 60° is an angle between various equivalent [17] crystallographic planes (Fig. 4A, B). The (101) planes also show two orientations (Fig. 4C): the more intensive ring at angle of $\approx 61^\circ$ corresponds to the crystallites with the [001] orientation and the weaker one at $\approx 29^\circ$ corresponds to the [100] oriented crystallites. The sample deposited at $T \approx 295$ °C has the major [001] orientation of crystallites and minor contribution of the [101] orientation (Fig. 4G, H, I). The 100 pole figure shows except of the most intensive ring perpendicular to the surface two weak rings at angles of $\approx 29^\circ$ and $\approx 64^\circ$ corresponding to the angles of the (100) planes with respect to the (101) equivalent planes.

The pole figures analysis confirmed that the deposition at $T \approx 105$ °C with a compressive stress has mixed [001] and [100] orientation. The stress-free Ti thin film exhibits only [001] orientation at optimum growth $T \approx 273$ °C. The highest $T \approx 295$ °C results in a tensile stress and preferential orientations [001] and [101].

All XRD analyses showed the sample grown at the optimal T has [001] preferential orientation, with the narrowest rocking curve RC with RC-FWHM of $\approx 4.4^\circ$ and big crystallites with size of ≈ 30 nm. Thus, we concluded this sample had the superior microstructure quality from all samples.

3.3. Surface roughness characterization

We performed AFM topography scans by using the ScanAsyst®–Air mode to study the surface roughness of Ti thin films deposited at different T . The obtained amplitude of R_{RMS} with T as the parameter indicates a certain correlation with the curve that describes the dependence of RC-FWHM on T as shown in Fig. 2B.

Nevertheless, all samples had a rather smooth surface with R_{RMS} in the range from ≈ 0.58 nm to ≈ 0.71 nm (Fig. 5A). The surface topography of the stress-free sample deposited at $T \approx 273$ °C and having the lowest R_{RMS} value is shown in Fig. 5B.

4. Conclusions

We presented a method to modulate the residual stress in [001] preferentially oriented Ti thin films deposited using the Kaufman ion-beam source by changing T . The experiments showed that T has an essential influence on the residual stress and lattice parameters of deposited Ti thin films. At low T , compressive residual stress was obtained, which decreased with increasing T from ≈ 155 °C up to ≈ 273 °C, when zero residual stress was achieved. The corresponding lattice parameters for this stress-free film were $a_0 = (2.954 \pm 0.003)$ Å and $c_0 = (4.695 \pm 0.001)$ Å. At $T \approx 295$ °C, the tensile residual stress was measured due to differences in thermal expansion coefficients of the Ti and Si substrate. The layers have a very well defined preferential orientation, with the c-axis oriented perpendicular to the surface with a negligible contribution of other orientation at T between ≈ 155 °C and ≈ 273 °C. At T lower than ≈ 155 °C, [100] oriented crystallites are present, whereas at T higher than ≈ 273 °C [101] oriented crystallites were detected. The sample grown at $T \approx 273$ °C showed not only zero residual stress, but also a superior crystallographic quality and the lowest R_{RMS} value of ≈ 0.58 nm among the whole sample series.

Acknowledgment

We acknowledge the support of CEITEC Nano Research Infrastructure (ID LM2015041, MEYS CR, 2016–2019), CEITEC Brno University of Technology and Grant Agency of the Czech Republic under the contracts GA13-19947S, GA16-11140S and GACR 17-20716S. Authors I. Gablech and J. Pekárek also acknowledge the Brno University of Technology support FEKT/STI-J-17-4136.

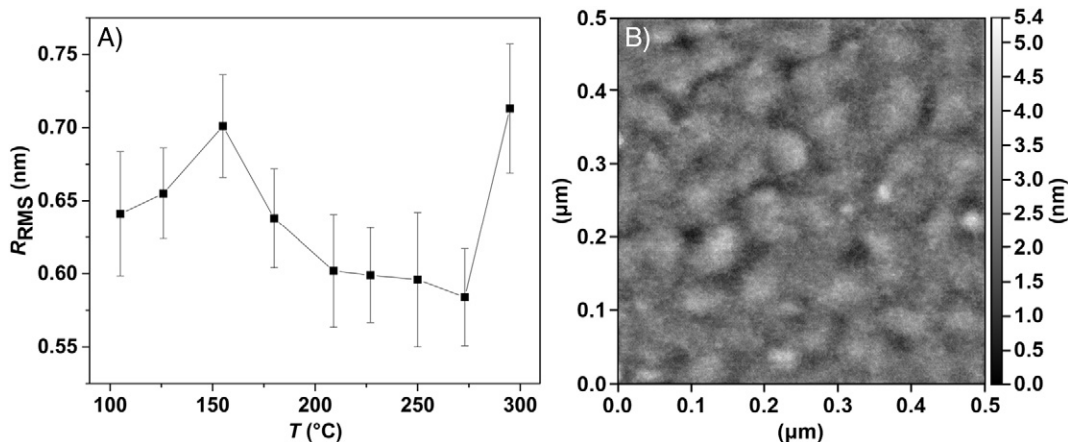


Fig. 5. A) Dependence of measured R_{RMS} values of Ti thin films on T ; B) Smooth Ti surface achieved at $T \approx 273$ °C and with the [001] preferential crystal orientation.

References

- [1] I. Gablech, V. Svatoš, O. Caha, M. Hrabovský, J. Prášek, J. Hubálek, T. Šíkola, Preparation of (001) preferentially oriented titanium thin films by ion-beam sputtering deposition on thermal silicon dioxide, *J. Mater. Sci.* 51 (2016) 3329–3336.
- [2] N. Jackson, L. Keeney, A. Mathewson, Flexible-CMOS and biocompatible piezoelectric AlN material for MEMS applications, *Smart Mater. Struct.* 22 (2013) 9.
- [3] K. Knisely, C. Zhao, K. Grosh, A MEMS AlN transducer array with flexible interconnections for use as a cochlear implant, *AIP Conf. Proc.* 1703 (2015) 100004.
- [4] P. Neuzil, T. Mei, A method of suppressing self-heating signal of bolometers, *IEEE Sensors J.* 4 (2004) 207–210.
- [5] P. Neuzil, Y. Liu, H.H. Feng, W.J. Zeng, Micromachined bolometer with single-crystal silicon diode as temperature sensor, *IEEE Electr. Device L* 26 (2005) 320–322.
- [6] P. Neuzil, T. Mei, Evaluation of thermal parameters of bolometer devices, *Appl. Phys. Lett.* 80 (2002) 1838–1840.
- [7] Y. Khan, A.E. Ostfeld, C.M. Lochner, A. Pierre, A.C. Arias, Monitoring of vital signs with flexible and wearable medical devices, *Adv. Mater.* 28 (2016) 4373–4395.
- [8] G. Urban, J. Wöllenstein, J. Kieninger, A. Sharma, O.Z. Olszewski, J. Torres, A. Mathewson, R. Houlihan, Eurosensors 2015 Fabrication, simulation and characterisation of MEMS piezoelectric vibration energy harvester for low frequency, *Procedia Eng.* 120 (2015) 645–650.
- [9] M.W. Ashraf, S. Tayyaba, N. Afzulpurkar, Micro Electromechanical Systems (MEMS) based microfluidic devices for biomedical applications, *Int. J. Mol. Sci.* 12 (2011) 3648–3704.
- [10] J.C. Doll, B.C. Petzold, B. Ninan, R. Mullapudi, B.L. Pruitt, Aluminum nitride on titanium for CMOS compatible piezoelectric transducers, *J. Micromech. Microeng.* 20 (2010) 8.
- [11] R.C. Chang, F.Y. Chen, C.T. Chuang, Y.C. Tung, Residual stresses of sputtering titanium thin films at various substrate temperatures, *J. Nanosci. Nanotechnol.* 10 (2010) 4562–4567.
- [12] M. Khan, M. Islam, A. Akram, Z.M. Qi, L.B. Li, Residual strain and electrical resistivity dependence of molybdenum films on DC plasma magnetron sputtering conditions, *Mater. Sci. Semicond. Process.* 27 (2014) 343–351.
- [13] H.-C. Seo, I. Petrov, H. Jeong, P. Chapman, K. Kim, Elastic buckling of AlN ribbons on elastomeric substrate, *Appl. Phys. Lett.* 94 (2009), 092104.
- [14] W. Kern, K.K. Schuegraf, K. Seshan, *Handbook of Thin Film Deposition Processes and Techniques*, William Andrew Publishing, New York, 2001.
- [15] A.T. Tran, G. Pandraud, F.D. Tichelaar, M.D. Nguyen, H. Schellevis, P.M. Sarro, The extraordinary role of the AlN interlayer in growth of AlN sputtered on Ti electrodes, *Appl. Phys. Lett.* 103 (2013) 221909.
- [16] M. Patru, L. Isac, L. Cunha, P. Martins, S. Lanceros-Mendez, G. Oncioiu, D. Cristea, D. Munteanu, Structural, mechanical and piezoelectric properties of polycrystalline AlN films sputtered on titanium bottom electrodes, *Appl. Surf. Sci.* 354 (2015) 267–278.
- [17] V. Chawla, R. Jayaganthan, A.K. Chawla, R. Chandra, Microstructural characterizations of magnetron sputtered Ti films on glass substrate, *J. Mater. Process. Technol.* 209 (2009) 3444–3451.
- [18] Y. Watanabe, N. Kitazawa, Y. Nakamura, C. Li, T. Sekino, K. Niihara, Mechanical properties and residual stress in AlN films prepared by ion beam assisted deposition, *J. Vac. Sci. Technol. A* 18 (2000) 1567–1570.
- [19] G.C.A.M. Janssen, M.M. Abdalla, F. van Keulen, B.R. Pujada, B. van Venrooy, Celebrating the 100th anniversary of the Stoney equation for film stress: developments from polycrystalline steel strips to single crystal silicon wafers, *Thin Solid Films* 517 (2009) 1858–1867.
- [20] A. Guinier, *X-ray Diffraction in Crystals, Imperfect Crystals, and Amorphous Bodies*, Dover Publications, 1994.
- [21] A. Goldmann, 2.11.3 Ti (Titanium) (Z = 22): Datasheet from Landolt-Börnstein—Group III Condensed Matter Volume 23C1: “Noble Metals, Noble Metal Halides and Nonmagnetic Transition Metals” in SpringerMaterials, in: A. Goldmann (Ed.), Springer-Verlag Berlin Heidelberg, (doi:http://dx.doi.org/10.1007/10714318_18).



ELSEVIER

Contents lists available at ScienceDirect

Thin Solid Films

journal homepage: www.elsevier.com/locate/tsf

Preparation of high-quality stress-free (001) aluminum nitride thin film using a dual Kaufman ion-beam source setup



Imrich Gablech^{a,b,*}, Vojtěch Svatoš^{a,b}, Ondřej Caha^{c,d}, Adam Dubroka^{c,d}, Jan Pekárek^{a,b}, Jaroslav Klempla^{a,b}, Pavel Neužil^{a,b,e}, Michael Schneider^f, Tomáš Šikola^{a,g}

^a Central European Institute of Technology, Brno University of Technology, Technická 3058/10, 61600 Brno, Czech Republic

^b Brno University of Technology, Faculty of Electrical Engineering and Communication, SIX Centre, Department of Microelectronics, Technická 3058/10, 61600 Brno, Czech Republic

^c Central European Institute of Technology, Masaryk University, Kamenice 753/5, 62500 Brno, Czech Republic

^d Masaryk University, Faculty of Science, Department of Condensed Matter Physics, Kotlářská 2, 60200 Brno, Czech Republic

^e Northwestern Polytechnical University, 127 West Youyi Road, Xi'an, Shaanxi, PR China

^f Department of Microsystems Technology, Vienna University of Technology, Floragasse 7, 1040 Vienna, Austria

^g Brno University of Technology, Institute of Physical Engineering, Technická 2896/2, 61669 Brno, Czech Republic

ARTICLE INFO

Keywords:

Ion-beam sputtering deposition
Kaufman ion-beam source
Aluminum nitride thin film
(001) preferential orientation
X-ray diffraction
Optical properties
Ellipsometry
 d_{33} piezoelectric coefficient

ABSTRACT

We proposed and demonstrated a preparation method of (001) preferentially oriented stress-free AlN piezoelectric thin films. The AlN thin films were deposited by a reactive sputtering technique at substrate temperatures up to 330 °C using a dual Kaufman ion-beam source setup. We deposited the AlN on Si (100), Si (111), amorphous SiO₂, and a (001) preferentially oriented Ti thin film and compared their crystallographic, optical, and piezoelectric properties. The AlN thin films deposited on the (001) preferentially oriented Ti thin films have the highest crystallographic quality. The stress-free AlN reached a high value of the piezoelectric coefficient $d_{33} = (7.33 \pm 0.08) \text{ pC}\cdot\text{N}^{-1}$. The properties of the AlN thin film prepared at such low temperatures are suitable for numerous microelectromechanical systems, piezoelectric sensors, and actuators monolithically integrated with complementary metal-oxide-semiconductor signal-processing circuits.

1. Introduction

Piezoelectric materials have huge potential in many common applications. Lead zirconate titanate (PZT), quartz, lithium niobate, lithium tantalate, aluminum nitride (AlN), or zinc oxide (ZnO) is generally used [1–4]. They often have to be integrated with complementary metal-oxide-semiconductor (CMOS) devices. The crucial requirement for this technology is to deposit thin films at substrate temperatures below 450 °C using such techniques as physical vapor deposition. AlN is a CMOS-compatible material, thus eliminating the contamination risk of the fabrication line compared with PZT and ZnO [5,6]. AlN is also popular due to its bio-compatibility [7].

The AlN thin films have been already employed in various technical fields as an insulator and a passivation layer for thin film applications [8,9], as energy harvesters [10,11], mass sensors [12–15], acoustic sensors [16,17], wave guides [18], optoelectronic devices [19,20], tunable resonators [21], and many others. Excluding the piezoelectricity, there are some extraordinary properties of AlN thin films

such as high thermal conductivity ($320 \text{ W}\cdot\text{mK}^{-1}$ at a temperature of 300 K), low thermal expansion coefficient at high temperatures, wide bandgap (6.2 eV), and high electric resistance ($10^{13} \Omega\cdot\text{cm}$), which results in a relatively high dielectric constant, mechanical stiffness, and high elasticity [22–24]. The AlN thin film is typically a wurtzite structured material and shows the major piezoelectric response along (001) direction, usually with the piezoelectric coefficient up to $6 \text{ pC}\cdot\text{N}^{-1}$ [24,25]. The piezoelectric coefficients of AlN are highly dependent on the crystal orientation and its misorientation. For instance, deposition conditions of magnetron sputtering such as pressure, power, bias, and deposition temperature directly influence crystallography. The most important condition is to achieve a low value of misorientation which increases piezoelectric coefficients [5,26]. Such properties can be modified at temperatures above 1000 °C [27,28], which is not compatible with standard CMOS technology, after the deposition process is complete.

Numerous techniques of AlN deposition have been previously employed. They can be sorted into two major groups. The first uses a high

* Corresponding author.

E-mail address: imrich.gablech@ceitec.vutbr.cz (I. Gablech).

<https://doi.org/10.1016/j.tsf.2018.12.035>

Received 22 June 2018; Received in revised form 16 November 2018; Accepted 18 December 2018

Available online 19 December 2018

0040-6090/ © 2018 Elsevier B.V. All rights reserved.

deposition substrate temperature up to 1000 °C and the second uses a lower substrate temperature. The first group contains deposition methods such as metalorganic chemical vapor deposition (MOCVD) [29–31], molecular beam epitaxy [32], and hydride vapor phase epitaxy [33]. The second one consists of such methods as reactive sputtering and evaporation, often assisted with ion-beam [34], pulsed laser deposition [35,36], and plasma enhanced atomic layer deposition [37]. The piezoelectric properties and internal stress are sensitive to deposition process parameters [28].

In the present study, we investigated AlN thin films with (001) preferential crystallographic orientation deposited on Si (100), Si (111), amorphous SiO₂, and a (001) preferentially oriented Ti thin film, comparing their properties for various deposition conditions. Our aim was to grow AlN thin films for potential microelectromechanical systems (MEMS) application. The requirements were to achieve (i) high piezoelectric coefficient, (ii) zero residual stress at room temperature, (iii) grow at conductive substrate serving as a bottom electrode, and (iiii) deposition process at low temperature. Titanium (001) preferentially oriented substrate was studied the most since it can serve both as a bottom electrode and as a seed layer for AlN growth improving preferential orientation of AlN (001). Highly preferentially orientated layers also benefit from high piezoelectric coefficients. Other substrates can also be used for MEMS applications where the bottom electrode is not metal or is not required. We used these substrates as a reference. All thin films presented in this report were deposited by a Kaufman ion-beam source (IBS) utilizing radio frequency inductively coupled plasma (RFICP) and, optionally, a secondary RFICP Kaufman IBS. We controlled the deposition substrate temperature in the range from 100 °C to 340 °C. We also varied the ion-beam current and its energy, which affected the kinetic energy of atoms of the sputtered material and deposition rate. We determined the material properties such as crystallographic parameters, residual stress, optical properties, and piezoelectric coefficient.

2. Experimental details

2.1. Aluminum nitride deposition process

We deposited 200 nm AlN thin films on square-shaped substrates with a size of 20 mm × 20 mm diced from silicon wafers with a diameter of 100 mm and thickness of 525 μm. The deposition was performed on four different Si wafers: two bare wafers Si (111) and Si (100), Si (100) wafer covered with an amorphous layer of SiO₂ with a thickness of 100 nm, and the same one covered with a layer of (001) preferentially oriented Ti [38,39] with a thickness of 80 nm. All the substrates were pre-cleaned prior to the actual deposition by Ar ion bombardment from the secondary RFICP Kaufman IBS with a 2-grid μ-dished collimated ion optics with a diameter of 40 mm. The pre-cleaning parameters were set as follows: ion-beam energy (BE) - 30 eV, ion-beam current (BC) - 15 mA, and sputter time - 180 s.

All thin films were deposited either by using the primary RFICP Kaufman IBS (KRI®) with a 3-grid dished focused ion optics (4 cm in diameter and with 45° ellipse pattern) only, or concurrent using the primary and secondary IBS (KRI®) for the ion-beam assisted deposition described above (Fig. 1).

We used an aluminum square-shaped target with a size of 100 mm × 100 mm and 99.9999% purity for AlN deposition by Ar sputtering assisted with N₂ or Ar gas or their mixtures, both gases with 99.999999% purity. The deposition parameters are listed in Table 1. Reduction of the ion-beam space charge was achieved by a KRI LFN 2000 charge neutralizer (KRI®). The sputtering chamber was evacuated to a base pressure of 5·10⁻⁷ Pa by a turbomolecular pump with a pumping speed of 1200 l s⁻¹ backed by a dry scroll vacuum pump. The process pressure was in the range from 8.5·10⁻³ Pa to 1.5·10⁻² Pa. We monitored the AlN deposition rate and film thickness *in situ* using a quartz crystal sensor. Finally, the thickness was verified *ex situ* by

ellipsometry and the average thickness was (195.9 ± 8.2) nm. We employed atomic force microscopy (AFM) using a Dimension Icon, Bruker, for surface roughness measurement. The surface roughness of all deposited AlN films was investigated in the ScanAsyst® – air measuring mode of AFM. The average surface roughness of all samples was (1.2 ± 0.3) nm with no evident dependence on the deposition parameters.

2.2. X-ray diffraction methods

We characterized the deposited AlN thin films using four X-ray diffraction (XRD) methods [38]. The first three methods were carried out by a Rigaku SmartLab system with a Cu X-ray tube containing a linear D/teX Ultra detector. The fourth method was conducted by a home-assembled diffractometer with a Cu X-ray tube, Bartels-type Ge 4 × (220) monochromator, and scintillation detector.

The first method was based on the Bragg–Brentano (BB) geometry used to determine the lattice parameter of the planes parallel to the sample surface. The scanning speed was 5°·min⁻¹. The width of the diffraction peak is inversely proportional to the coherently diffracting domain size (roughly grain size) and includes other contributions, namely resolution, wavelength spread, and inhomogeneous strain distribution. Since we were able to measure only a single diffraction peak, full analysis is not possible, and we report only full width at half maximum (FWHM) of the diffraction peaks as a measure of layer quality.

The second one, the grazing-incidence (GIXRD) method, was then used to measure the lattice parameter in the perpendicular direction to the sample surface with scanning speed of 1°·min⁻¹. This in-plane measurement employed a parabolic multilayer mirror as a monochromator and parallel plate collimators with a divergence of 0.15° and 0.11° in the incident and scattered beam, respectively.

The third method was the rocking curve (RC) measurement with scanning speed of 3°·min⁻¹ in a standard parallel-beam (PB) setup using a 0.114° parallel slit analyzer. We fitted the measured data by the Rigaku PDXL2 software. The width of the rocking curve is a measure of the preferential orientation; rocking curve width is roughly equal to the mean misorientation of the individual grains with respect to the surface normal.

The fourth method was used to extract the elastic stress σ_f of deposited AlN thin films. The stress was determined from the curvature difference of the Si (100) substrate before and after AlN deposition. The scanning speed was 0.6°·min⁻¹. The curvature radius of the sample was extracted from the Bragg angle dependence on the sample position. Its slope is inversely proportional to the curvature radius of crystallographic planes. The value of σ_f was calculated from the Stoney formula (Eq. 1) for Si (001) [40]:

$$\sigma_f t_f = \frac{h^2}{6} \cdot \frac{1}{s_{11} + s_{12}} \cdot \left(\frac{1}{R} - \frac{1}{R_0} \right) \quad (1)$$

where t_f is the layer thickness, h the substrate thickness, R_0 and R the initial and final substrate curvature radii, and s_{11} and s_{12} are the components of the silicon elastic compliance tensor. This method was conducted to determine the Si 004 diffraction peak position as a function of sample coordinates.

2.3. Ellipsometry

The optical properties were probed in the range from near infrared (0.6 eV) to ultraviolet (6.5 eV) energy by variable angle spectroscopy ellipsometry using a J.A. Woollam VASE ellipsometer equipped with a photomultiplier. The resolution of the spectrometer was set to 0.7 nm. We have collected the ellipsometric angles ψ and Δ and depolarization at angles of incidence 50°, 60°, 70°, and 80°. The results were then analyzed by the WVASE software.

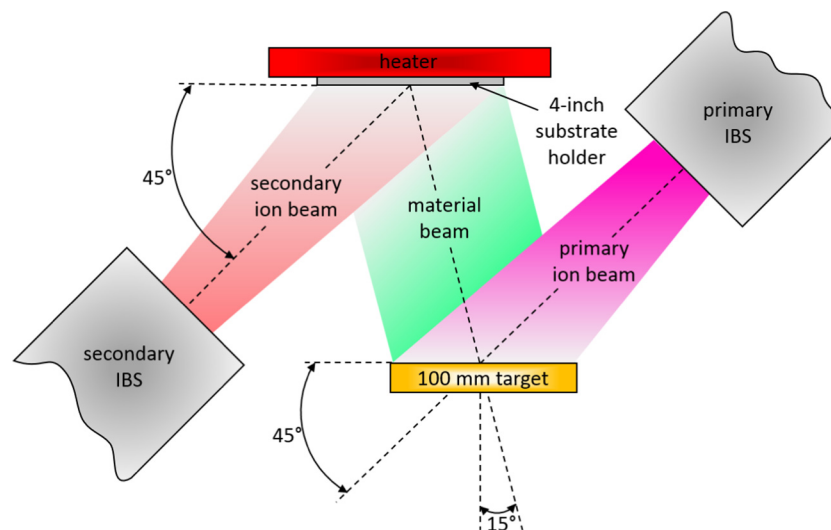


Fig. 1. Schematic of sputtering apparatus geometry with Kaufman ion-beam sources.

2.4. Quasi-static measurement

We determined the piezoelectric coefficient (d_{33}) using a system for quasi-static measurement while applying a force in the c -axis and measuring the generated charge between electrodes in the same direction. We used the PiezoMeter PM300 from Piezotest. The measurement was realized in a very low range mode for expected values in the range from $0 \text{ pC}\cdot\text{N}^{-1}$ to $10 \text{ pC}\cdot\text{N}^{-1}$ with an accuracy of $\pm 2\%$. The set parameters of force amplitude and test frequency amplitude were 0.25 N and 110 Hz , respectively.

3. Results and discussion

3.1. Crystallography

First, we investigated the influence of the primary IBS energy and substrate temperature on the crystallographic quality of AlN layers deposited on various substrates. Here, we used only nitrogen ions and the secondary IBS was off. We used XRD in the BB setup with the 2θ angle ranging from 30° to 60° to perform the phase analysis of all thin films deposited at various deposition temperatures, BEs, and substrates.

All thin films exhibited only a second-order 002 diffraction peak corresponding to the (001) crystallographic AlN plane. In the sample

deposited on the Ti underlayer, the Ti (001) crystallographic plane was also detected. The AlN thin films different from those deposited on Si (100), Si (111), and SiO_2 at the BE above 1 keV and substrate temperatures below 150°C exhibited only the c -axis orientation. The thin films deposited on Si (100), Si (111), and SiO_2 at the BE above 1 keV and substrate temperature below 150°C did not have any preferential orientation. We also performed the RC measurement in the PB setup to determine average misorientation of individual crystallites.

Fig. 2A shows the highest diffraction intensity of the AlN (001) appears for the AlN thin film deposited on the (001) preferentially oriented Ti thin film, and it is also $\approx 1.8\times$ and $2.5\times$ higher than that one related to this film deposited on the SiO_2 and bare silicon surfaces, respectively. The highest peak intensity from the film deposited on the (001) preferentially oriented Ti thin film is caused by the similarity of unstrained Ti crystal lattice parameters [38] to those of AlN [41].

Fig. 3A shows that the smallest BB-FWHM and RC-FWHM of the AlN (001) were achieved for the AlN thin film deposited on the (001) preferentially oriented Ti thin film, hence all further experiments discussed in this part are the thin films deposited on this film. Fig. 2B,C show the positive effect of lower BEs and higher substrate temperatures on the peak intensity and its shift toward a tabulated value of 36.06° [42,43]. This phenomenon is described in the following section. Higher temperatures and BEs below 1000 eV have a positive influence on the BB-

Table 1

Description of realized experiments. Experiments were optimized according to peak shift toward to tabulated values. 1st series was conducted to the optimization of BE and T. The 2nd series was aimed at the optimization of secondary IBS parameters which partly eliminated stress. The 3rd series was focused on getting stress-free thin films using different Ar: N_2 gas ratios.

Experiment series	Primary IBS				Secondary IBS				T ($^\circ\text{C}$)
	BE (eV)	BC (mA)	Ar flow (sccm)	N_2 flow (sccm)	BE (eV)	BC (mA)	Ar flow (sccm)	N_2 flow (sccm)	
1	1200	65	0	8.0	IBS OFF				100
	1000	50		6.5					150
	800	36		6.0					200
	600	23		5.5					250
	500	18		5.2					300
	400	13		5.0					
2	400	13	0	5.0	20	6	10	0	330
							0	10	
					30	7	10	0	340
3	400	13	0	5.0	20	6	0	10	330
			1.5	3.5					
			2.5	2.5					
			3.5	1.5					
			5.0	0					

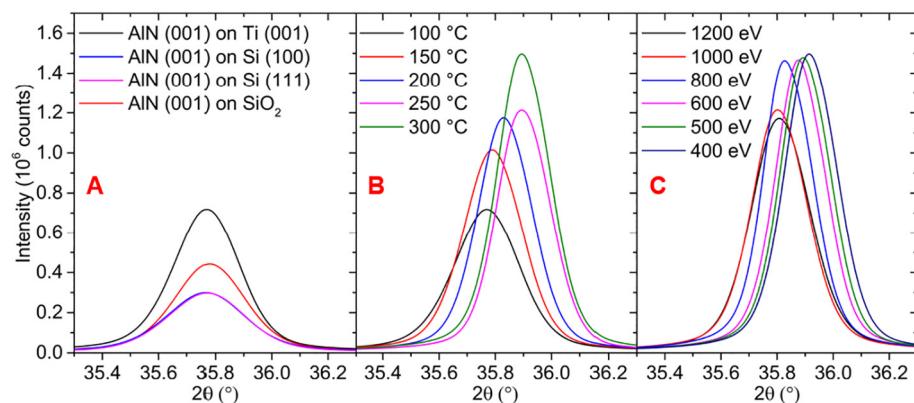


Fig. 2. X-ray diffractograms showing influence of various deposition parameters on AlN (with a thickness of 200 nm) 002 diffraction peak belonging to (001) plane: A) deposition on various surfaces with the constant BE 400 eV and substrate temperature 100 °C; B) depositions at various substrate temperatures on the (001) preferentially oriented Ti thin film at the constant BE = 400 eV; C) depositions at various BEs and at substrate temperature of 300 °C for thin films grown on the (001) preferentially oriented Ti thin film.

FWHM and RC-FWHM of the AlN (001) (Fig. 3B,C).

We analyzed the previous results, and then we set the deposition parameters as BE = 400 eV and temperature 300 °C. We also employed the secondary IBS and investigated the effect of related BE and type of the working gas (see Fig. 4).

The ion-beam bombardment of the substrate from the secondary IBS had a positive influence on decreasing the BB-FWHM and the RC-FWHM of the AlN (001) (Fig. 4). Two effects occurred during this AlN deposition. First, this bombardment at the BE below 100 eV reduced the tensile stress and caused compressive stress [44]. Second, the low energy (< 100 eV) ion-beam bombardment provided continuous cleaning of physisorbed impurities, eliminating the compressive stress. We show that the bombardment at BE = 30 eV in comparison to the one at 20 eV shifts the AlN diffraction peak to the smaller values of the diffraction angle (Fig. 4A). The thin films deposited under assisting ion beams of BE = 30 eV resulted in the diffraction peaks of slightly higher intensities than of those related to the films deposited at BE = 20 eV. The deposition without the secondary IBS resulted in a diffraction peak shift to lower values of the diffraction angle.

Because the peak position differs from the optimal one by 0.04° to 0.06°, we decided to optimize the deposition parameters. The secondary IBS parameters such as BE and gas types were fixed to a value of 20 eV and pure N₂, respectively. We then investigated the influence of the N₂:Ar ratio in the primary IBS (Table 1) leading to the optimal diffraction peak angle (Fig. 5).

The N₂:Ar ratio causes a minimal change in the BB-FWHM of the AlN (001) in the order of 1/1000, and the RC-FWHM of the AlN (001) is marginally decreased for higher Ar concentration (Fig. 5B) while the diffraction peak shift is more pronounced (Fig. 5A). Higher Ar concentration during the deposition resulted in the change of stress values from compressive to tensile. Such phenomenon is also generally known from magnetron sputtering technique [28]. We observed that the thin film deposited at the same N₂ and Ar flow rates, both of 2.5 sccm,

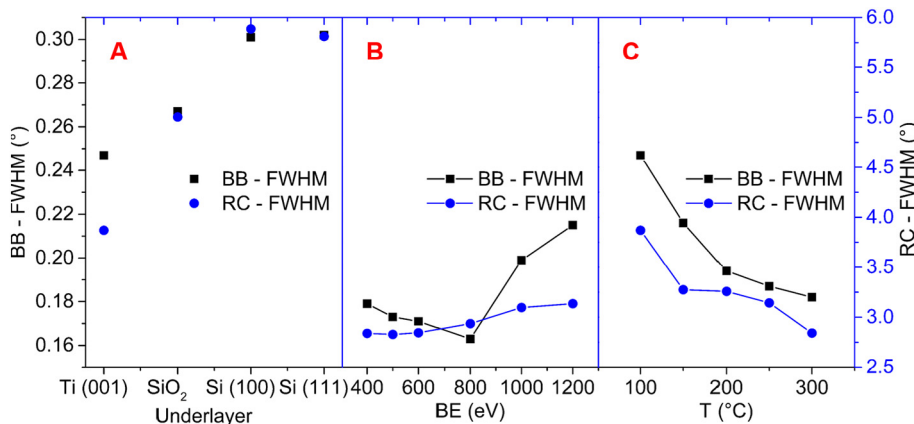


Fig. 3. Extracted data of BB – FWHM and RC – FWHM of the AlN (001) for previously mentioned samples: A) influence of the substrate surface for films deposited at the constant BE = 400 eV and substrate temperature 100 °C; B) influence of BE for a constant substrate temperature of 300 °C grown on the (001) preferentially oriented Ti thin film; C) influence of different substrate temperatures in the range from 100 °C to 300 °C at the constant BE = 400 eV grown on the (001) preferentially oriented Ti thin film.

resulted in a diffraction peak position of 36.06°, which is in good agreement with the tabulated value.

We also deposited 400 nm, 600 nm, 800 nm, and 1000 nm thick AlN layers with a preferential orientation of (001) to prove there is no peak shift related to layer thickness (Fig. 6A). We observed both decreasing BB-FWHM and RC-FWHM of the AlN (001) with the increasing thickness of the thin films (Fig. 6B).

3.2. Stress characterization

Stress in thin films for MEMS applications is one of the most important parameters. The investigated AlN thin film was deposited on a Si (100) substrate and characterized by an XRD curvature measurement. We chose several samples from the previous experiments possessing different 2θ (BB) peak positions to demonstrate the dependence of the peak position on the residual stress (Fig. 7).

Fig. 7A shows the linear dependence of the 2θ (BB) position of the 002 diffraction peak corresponding to the *c* lattice parameter and 2θ (in-plane) position of the 110 diffraction peak for corresponding to the *a* lattice parameter on the residual stress. The residual stress can then be determined from the diffraction peak position. We found the 002 and 110 diffraction angles for the zero-stress thin film to be (36.059 ± 0.005)° and (59.327 ± 0.006)°, respectively. We used those values to calculate the lattice parameters using Bragg's law. We obtained *c* = (4.978 ± 0.001) Å and *a* = (3.113 ± 0.001) Å, where uncertainties in the brackets are given by fitting errors, which is in good agreement with the tabulated values *a* = 3.111 Å and *c* = 4.979 Å [42,43]. We also found that the residual stress is independent of thin film thickness (Fig. 7B).

Consequently, we fabricated a stress-testing diamond ring structure [45] to prove there is no buckling of the deposited layer. The deposition parameters were set to achieve an AlN stress-free thin film with a thickness of ≈ 1000 nm on the Si (100) substrate. Fig. 8 shows the

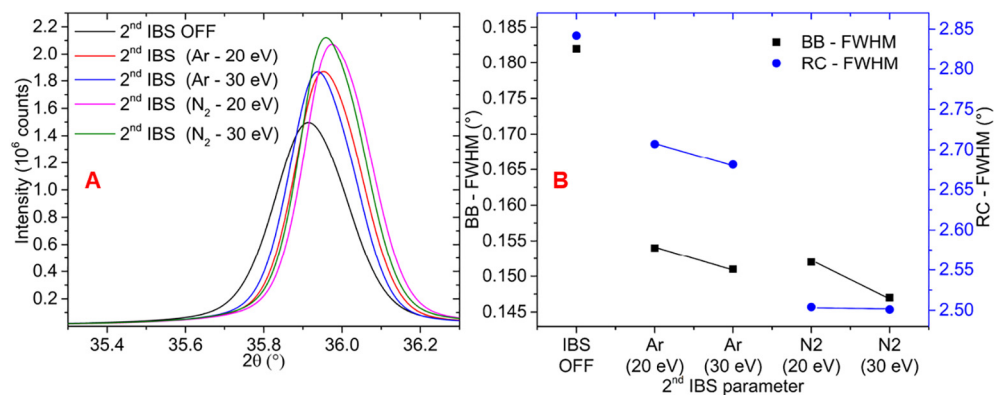


Fig. 4. A) X-ray diffractograms of AlN (001) showing the dependence on the secondary IBS parameters as BE = 20 eV or 30 eV and working gas either Ar or N₂ with a flow rate of 10 sccm; B) extracted data of BB - FWHM and RC - FWHM of the AlN (001) from the X-ray diffractogram and RC measurement showing the influence of the secondary IBS parameters.

scanning electron microscopy (SEM) images of the fabricated structure with no evident buckling of the layer.

3.3. The optical response

The optical response of AlN thin films was investigated by ellipsometry for the wavelengths from 0.6 eV to 6.5 eV. Fig. 9A,B show an example of the spectra of the ellipsometric angles Ψ and Δ , respectively, obtained for the AlN layer deposited on Si (111) at various angles of incidence. The sharp structures in the spectra are fringes caused by interference in the AlN thin film that disappears above 6 eV where the interband absorption sets in. We analyzed the data with a model of coherent interferences in the AlN thin film on a substrate. The anisotropic properties of the AlN layer were taken into account with a uniaxial model with the ordinary and extraordinary axis oriented in- and out-of-plane, respectively. The dielectric functions in both axes were modeled with a set of Kramers–Kronig consistent oscillators. The spectra exhibit a weak intraband absorption that was modeled with a Gaussian oscillator centered at 6.5 eV. A small thickness inhomogeneity of 1% was taken into consideration. The surface and interface roughness were modeled with the effective medium approximation (Bruggeman model) [46]. The model spectra are displayed as solid lines in Fig. 9. The measured and modeled data are in good agreement for all angles of incidence.

Fig. 10A shows the real part of the dielectric function along the ordinary (black solid line) and the extraordinary (red solid line) axis, respectively, obtained for AlN grown on Si (111). The spectra display the well-known anisotropy [47]. The obtained values are in good agreement with the results reported earlier [48] being displayed as dotted lines.

Fig. 10B displays the imaginary part of the ordinary dielectric function of AlN thin films deposited on all four substrates (solid lines). The extraordinary spectrum for the AlN (001) thin film deposited on Si

(111) (dashed line) is shown for comparison as well. The strong absorption above 6 eV is due to the direct interband absorption that sets in 6.1 eV in the ordinary direction and at 5.8 eV in the extraordinary direction. These values are slightly lower compared with the values obtained on MOCVD grown samples [47]. Below the bandgap, the absorption does not drop to zero but down to 3.5 eV exhibits values significantly high above the sensitivity limits of the measurements (about 0.01). This intragap absorption is well known [49] and was attributed to Al interstitials [43]. Interestingly, this absorption is approx. 3× smaller in the thin film deposited on the substrate with the (001) preferentially oriented Ti thin film (black solid line) than in the thin films deposited on the other substrates. These results correlate well with the higher structural quality as seen in the X-ray data and can be interpreted as a result of smaller concentration of Al interstitials in AlN grown on the (001) preferentially oriented Ti thin film. Note that this intragap absorption is essentially absent in thin films grown by MOCVD [47].

3.4. Determination of d₃₃ piezoelectric coefficient

We measured the d₃₃ piezoelectric coefficient of seven chosen samples using the quasi-static method. All measured AlN thin films were deposited on the (001) preferentially oriented Ti thin films that also serve as a bottom electrode. The samples were chosen according to their different RC-FWHM and σ_f . The measured d₃₃ values of thin films and a description of their deposition parameters are listed in Table 2.

All the samples have the (001) preferential orientation while the difference between these samples is their value of RC-FWHM in the PB setup and residual stress. The first sample has the highest RC-FWHM of the AlN (001) in PB and has the lowest value of d₃₃ in comparison with sample numbers 5, 6, and 7 with the lowest RC. The RC-FWHM of the last three samples is almost the same while the change of RC-FWHM between samples 5 and 7 is approx. 0.15°. The only difference between

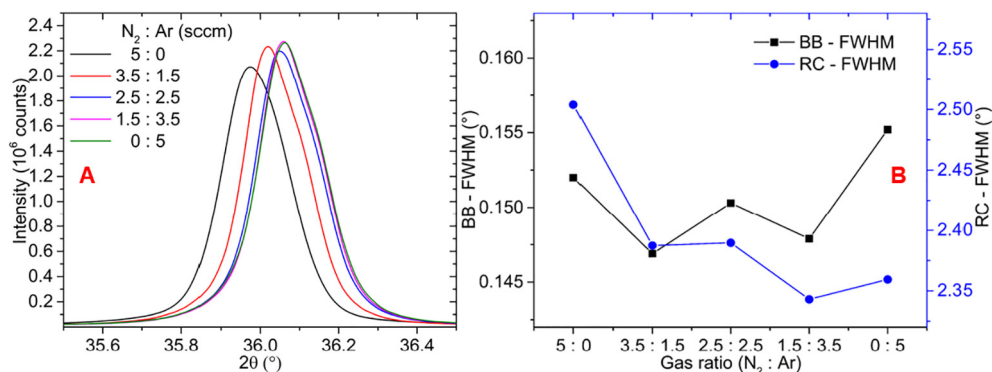


Fig. 5. Influence of the N₂:Ar ratio in the primary IBS: A) X-ray diffractogram of AlN (001); B) extracted data of BB - FWHM and RC - FWHM of the AlN (001) from the X-ray diffractogram and RC measurement.

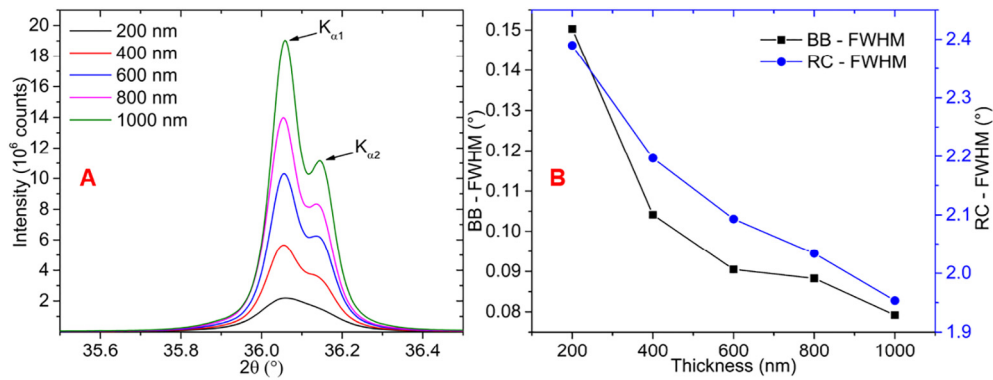


Fig. 6. A) X-ray diffractogram of AlN (001) showing the influence of the AlN thin film thickness on the peak position and its profile; B) extracted data of BB – FWHM and RC – FWHM of the AlN (001) from the X-ray diffractograms and RC measurement showing the influence of AlN thin film thickness.

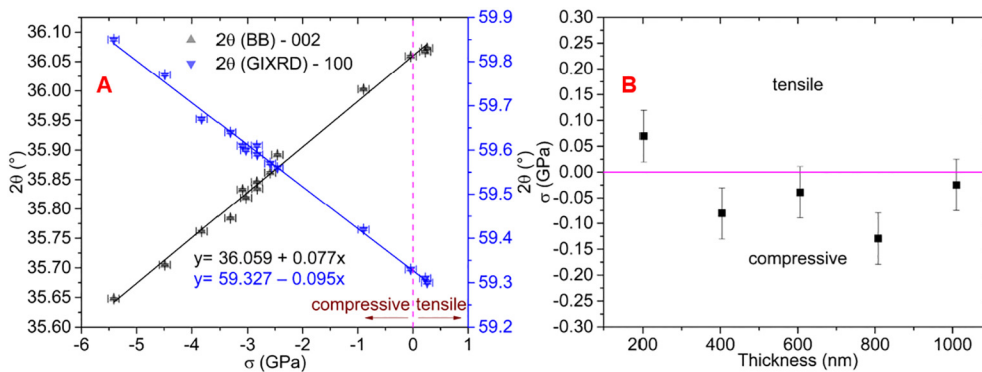


Fig. 7. A) 2θ (BB) position of the 002 diffraction peak corresponding to the c lattice parameter and 2θ (GIXRD) position of the 110 diffraction peak corresponding to the a lattice parameter as a function of the residual stress derived from the XRD curvature measurement; B) influence of the thin film thickness on the residual stress.

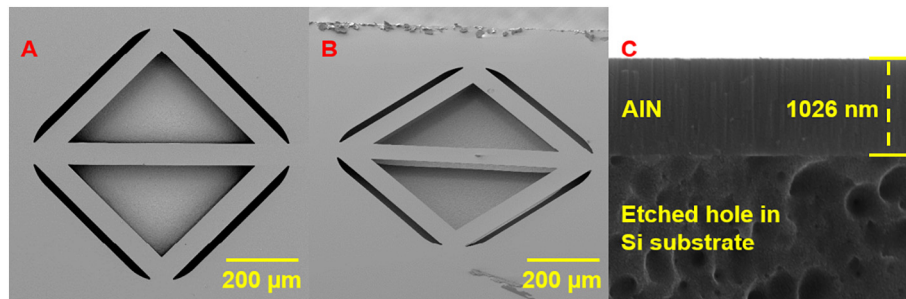


Fig. 8. SEM images AlN diamond ring structure with no buckling: A) top view; B) tilted view at 45°; C) cross-section image of suspended structure showing a measured thickness of 1026 nm.

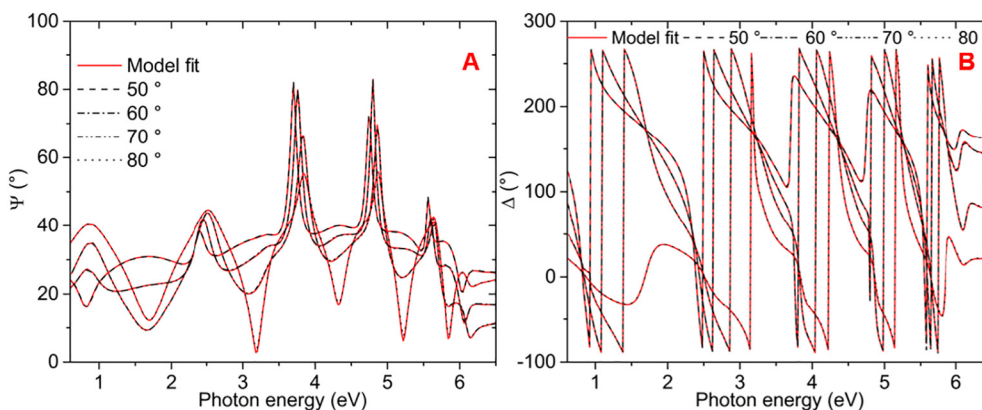


Fig. 9. Spectra of the ellipsometric angles A) ψ and B) Δ for the AlN (001) thin film deposited on Si (111) measured at angles of incidence 50°, 60°, 70°, and 80° (dashed lines represent the measured data and solid lines correspond to the model specified in the text).

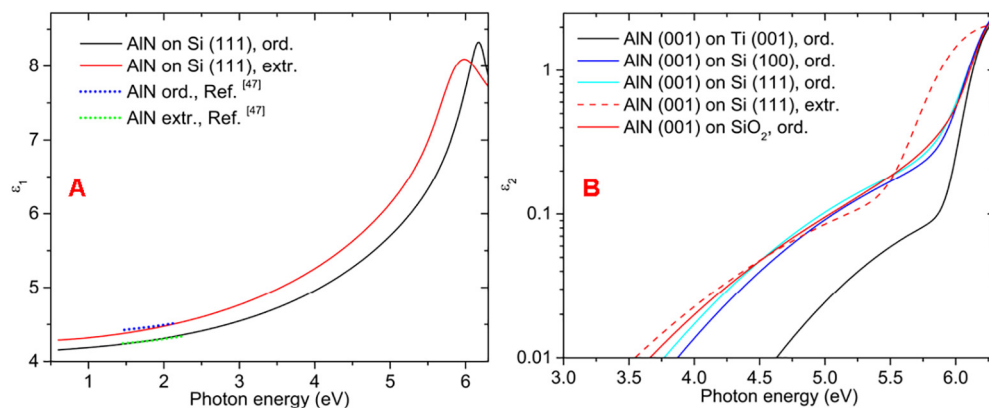


Fig. 10. A) Real and B) imaginary parts of the dielectric function obtained from the analysis of ellipsometry data: A) spectra along the ordinary (solid black line) and extraordinary (solid red line) direction of AlN deposited on Si (111) compared with data from Ref. [48] (dotted lines). B) imaginary part of the ordinary dielectric function of AlN deposited on different substrates (solid lines) together with the extraordinary spectrum of AlN deposited on Si (111) (red dashed line). (For interpretation of the references to colour in this figure legend, the reader is referred to the web version of this article.)

Table 2

Measured d_{33} values of selected samples and their fabrication parameters. Samples for quasi-static measurement were selected to show the influence of different deposition conditions on d_{33} . The experiment number corresponds to the experiment series in Table 1.

Sample/experiment	d_{33} (pC·N ⁻¹)	Primary IBS			Secondary IBS			T (°C)	BB-FWHM (°)	RC-FWHM (°)	σ_f (GPa)
		BE (eV)	Ar flow (sccm)	N ₂ flow (sccm)	BE (eV)	Ar flow (sccm)	N ₂ flow (sccm)				
1/1	6.53 ± 0.13	1200	0	8.0	IBS OFF			100	0.68	8.2	7.0
2/1	6.78 ± 0.12	800	0	6.0	IBS OFF			250	0.21	3.2	5.4
3/1	6.95 ± 0.14	500	0	5.2	IBS OFF			200	0.19	3.2	3.8
4/1	7.11 ± 0.12	400	0	5.0	IBS OFF			250	0.19	3.1	2.6
5/2	7.32 ± 0.10	400	0	5.0	20	0	10	330	0.15	2.5	0.9
6/3	7.33 ± 0.08	400	2.5	2.5	20	0	10	330	0.15	2.4	0
7/3	7.33 ± 0.09	400	5.0	0	20	0	10	330	0.16	2.4	-0.2

the samples is their residual stress. Although the difference in residual stress between samples 5 and 7 is 1.1 GPa, there is no evident influence of residual stress on the d_{33} values. We can see that the d_{33} values of all samples are high although their thin films were prepared under non-optimal deposition parameters. The best optimized layer with no residual stress (sample 6) has the highest obtained value of $d_{33} = (7.33 \pm 0.08)$ pC·N⁻¹, which is essential for the fabrication of MEMS.

4. Conclusions

We have presented a method suitable for the deposition of high-quality (001) preferentially oriented AlN thin films with a high value of the d_{33} piezoelectric coefficient for MEMS applications using primary and assisted Kaufman ion-beam sources. During the experiment, we controlled the operational parameters of these ion-beam sources and also substrate temperature *via* a built-in substrate heater.

The first part of the experiments showed that lower BE of the primary IBS and higher T have a positive influence on all important parameters as BB-FWHM, RC-FWHM, and residual stress, which leads to a higher value of d_{33} . In the second part of the experiments, the secondary IBS was used for ion-beam bombardment of growing thin films by Ar or N₂ ions with BE of 20 eV and 30 eV, respectively. We found that the bombardment by N₂ ions at a lower BE value of 20 eV has a positive influence on reducing the compressive stress. In the last experiments, we changed only the gas ratio between Ar and N₂ in the primary IBS, which led to a change of compressive stress to tensile residual stress while the other parameters as BB-FWHM and RC-FWHM remained almost unchanged. These experiments provided complex information about the method for preparation of high-quality (001) preferentially oriented AlN thin films suitable for MEMS applications.

During these experiments, we obtained the linear dependence of c and a lattice parameters on the residual stress among a series of 14 samples. The dependence of the diffraction peak shift on the residual

stress can be described by functions $y = 36.059 + 0.77 \times$ and $y = 59.327 - 0.95 \times$ for the 002 and 110 diffractions, respectively. These expressions give us the values of the unstrained lattice parameters c_0 and a_0 for $x = 0$. These values perfectly fit the measured lattice parameters of the sample without residual stress which also has the best parameters from the whole set of experiments. This sample belongs to one of three samples with the highest d_{33} , such as (7.33 ± 0.08) pC·N⁻¹, and the best crystallographic parameters as the lowest values of BB-FWHM 0.15° and RC-FWHM 2.4° for a thin film thickness of 200 nm. We also investigated the optical properties of AlN thin films using ellipsometry. The obtained spectra exhibit a direct bandgap at 6.1 eV in the ordinary direction and at 5.8 eV in the extraordinary direction, which are values close to those previously published [47]. In addition, the spectra exhibit an intragap absorption due to Al interstitials. This absorption is the lowest in the AlN thin films deposited on the (001) preferentially oriented Ti thin films that correlate with the highest structural quality as seen from the XRD analysis. This is probably caused by the fact that both Ti and AlN thin films possess a hexagonal structure with similar lattice parameters.

Acknowledgements

We acknowledge the support of Grant Agency of the Czech Republic under contract GJ18-06498Y and CEITEC Nano Research Infrastructure (ID LM2015041, MEYS CR, 2016–2019), CEITEC Brno University of Technology. Authors I. Gablech and J. Pekárek also acknowledge the foundation support of FEKT/STI-J-17-4136. The infrastructure of the SIX Center of BUT and facilities of the Department of Microsystems Technology at TUW were utilized to conduct the experiments.

References

- [1] D.M. Kim, C.B. Eom, V. Nagarajan, J. Ouyang, R. Ramesh, V. Vaithyanathan, D.G. Schlom, Thickness dependence of structural and piezoelectric properties of epitaxial Pb(Zr_{0.52}Ti_{0.48})O₃ films on Si and SrTiO₃ substrates, *Appl. Phys. Lett.*

- 88 (2006), <https://doi.org/10.1063/1.2185614>.
- [2] M.H. Zhao, Z.L. Wang, S.X. Mao, Piezoelectric characterization of individual zinc oxide nanobelt probed by piezoresponse force microscope, *Nano Lett.* 4 (2004) 587–590, <https://doi.org/10.1021/nl035198a>.
- [3] Y. Saigusa, 5 - Quartz-based piezoelectric materials, in: K. Uchino (Ed.), *Advanced Piezoelectric Materials*, Woodhead Publishing, 2010, pp. 171–203.
- [4] V.Y. Shur, 6 - Lithium niobate and lithium tantalate-based piezoelectric materials, in: K. Uchino (Ed.), *Advanced Piezoelectric Materials*, Woodhead Publishing, 2010, pp. 204–238.
- [5] J.C. Doll, B.C. Petzold, B. Ninan, R. Mullapudi, B.L. Pruitt, Aluminum nitride on titanium for CMOS compatible piezoelectric transducers, *J. Micromech. Microeng.* 20 (2010), <https://doi.org/10.1088/0960-1317/20/2/025008>.
- [6] M. Al Ahmad, R. Plana, Vertical displacement detection of an aluminum nitride piezoelectric thin film using capacitance measurements, *Int. J. Microw. Wirel. Technol.* 1 (2009) 5–9, <https://doi.org/10.1017/s1759078709000026>.
- [7] N. Jackson, L. Keeney, A. Mathewson, Flexible-CMOS and biocompatible piezoelectric AlN material for MEMS applications, *Smart Mater. Struct.* 22 (2013), <https://doi.org/10.1088/0964-1726/22/11/115033>.
- [8] M.M. De Souza, S. Jejurikar, K.P. Adhi, Impact of aluminum nitride as an insulator on the performance of zinc oxide thin film transistors, *Appl. Phys. Lett.* 92 (2008), <https://doi.org/10.1063/1.2890034>.
- [9] D. Kueck, P. Leber, A. Schmidt, G. Speranza, E. Kohn, AlN as passivation for surface channel FETs on H-terminated diamond, *Diam. Relat. Mat.* 19 (2010) 932–935, <https://doi.org/10.1016/j.diamond.2010.02.026>.
- [10] R. Elfrink, T.M. Kamel, M. Goedbloed, S. Matova, D. Hohlfeld, Y. van Andel, R. van Schaijk, Vibration energy harvesting with aluminum nitride-based piezoelectric devices, *J. Micromech. Microeng.* 19 (2009), <https://doi.org/10.1088/0960-1317/19/9/094005>.
- [11] A.B.A. Dow, A. Bittner, U. Schmid, N.P. Kherani, Design, fabrication and testing of a piezoelectric energy microgenerator, *Microsyst. Technol.* 20 (2014) 1035–1040, <https://doi.org/10.1007/s00542-014-2116-9>.
- [12] P. Ivaldi, J. Abergel, M.H. Matheny, L.G. Villanueva, R.B. Karabalin, M.L. Roukes, P. Andreucci, S. Hentz, E. Defay, 50 nm thick AlN film-based piezoelectric cantilevers for gravimetric detection, *J. Micromech. Microeng.* 21 (2011), <https://doi.org/10.1088/0960-1317/21/8/085023>.
- [13] A. Heidari, Y.J. Yoon, M.I. Lee, L. Khine, M.K. Park, J.M.L. Tsai, A novel checker-patterned AlN MEMS resonator as gravimetric sensor, *Sens. Actuator A Phys.* 189 (2013) 298–306, <https://doi.org/10.1016/j.sna.2012.09.027>.
- [14] J. Xiong, X.L. Sun, P. Guo, D. Zheng, H.S. Gu, Analysis of resonance characteristics of solidly mounted resonator for mass sensing applications, *Appl. Phys. A Mater. Sci. Process.* 116 (2014) 1573–1577, <https://doi.org/10.1007/s00339-014-8399-y>.
- [15] J. Toledo, V. Ruiz-Diez, G. Pfusterschmied, U. Schmid, J.L. Sanchez-Rojas, Flow-through sensor based on piezoelectric MEMS resonator for the in-line monitoring of wine fermentation, *Sens. Actuator B-Chem* 254 (2018) 291–298, <https://doi.org/10.1016/j.snb.2017.07.096>.
- [16] J. Jang, J. Lee, S. Woo, D.J. Sly, L.J. Campbell, J.H. Cho, S.J. O'Leary, M.H. Park, S. Han, J.W. Choi, J.H. Jang, H. Choi, A microelectromechanical system artificial basilar membrane based on a piezoelectric cantilever array and its characterization using an animal model, *Sci. Rep.* 5 (2015), <https://doi.org/10.1038/srep12447>.
- [17] B.Z. Chen, F.T. Chu, X.Z. Liu, Y.R. Li, J. Rong, H.B. Jiang, AlN-based piezoelectric micromachined ultrasonic transducer for photoacoustic imaging, *Appl. Phys. Lett.* 103 (2013), <https://doi.org/10.1063/1.4816085>.
- [18] Y.J. Chen, V. Krishnamurthy, Y.C. Lai, Y. Luo, Z.B. Hao, L. Wang, S.T. Ho, Fabrication of sub-200 nm AlN-GaN-AlN waveguide with cleaved end facet, *J. Vac. Sci. Technol. B* 32 (2014), <https://doi.org/10.1116/1.4890487>.
- [19] S. Zhao, A.T. Connie, M.H.T. Dastjerdi, X.H. Kong, Q. Wang, M. Djavid, S. Sadaf, X.D. Liu, I. Shih, H. Guo, Z. Mi, Aluminum nitride nanowire light emitting diodes: breaking the fundamental bottleneck of deep ultraviolet light sources, *Sci. Rep.* 5 (2015), <https://doi.org/10.1038/srep08332>.
- [20] W. Zheng, F. Huang, R.S. Zheng, H.L. Wu, Low-dimensional structure vacuum-ultraviolet-sensitive ($\lambda < 200$ nm) photodetector with fast-response speed based on high-quality AlN micro/nanowire, *Adv. Mater.* 27 (2015) 3921–3927, <https://doi.org/10.1002/adma.201500268>.
- [21] R.B. Karabalin, M.H. Matheny, X.L. Feng, E. Defay, G. Le Rhun, C. Marcoux, S. Hentz, P. Andreucci, M.L. Roukes, Piezoelectric nanoelectromechanical resonators based on aluminum nitride thin films, *Appl. Phys. Lett.* 95 (2009), <https://doi.org/10.1063/1.3216586>.
- [22] S.C. Jain, M. Willander, J. Narayan, R.V. Overstraeten, III–nitrides: growth, characterization, and properties, *J. Appl. Phys.* 87 (2000) 965–1006, <https://doi.org/10.1063/1.371971>.
- [23] S.N. Ivanov, P.A. Popov, G.V. Egorov, A.A. Sidorov, B.I. Kornev, L.M. Zhukova, V.P. Ryabov, Thermophysical properties of aluminum nitride ceramic, *Phys. Solid State* 39 (1997) 81–83, <https://doi.org/10.1134/1.1129837>.
- [24] S. Trolier-McKinstry, P. Muralt, Thin film piezoelectrics for MEMS, *J. Electroceram.* 12 (2004) 7–17, <https://doi.org/10.1023/b:ejcr.0000033998.72845.51>.
- [25] E. Wistrela, M. Schneider, A. Bittner, U. Schmid, Impact of the substrate dependent polarity distribution in c-axis oriented AlN thin films on the etching behaviour and the piezoelectric properties, *Microsyst. Technol.* 22 (2016) 1691–1700, <https://doi.org/10.1007/s00542-015-2799-6>.
- [26] K. Tonisch, V. Cimalla, C. Foerster, D. Dontsov, O. Ambacher, Piezoelectric properties of thin AlN layers for MEMS application determined by piezoresponse force microscopy, *Phys. Status Solidi C* 3 (2006) 2274–2277, <https://doi.org/10.1002/pssc.200565123>.
- [27] K.S. Ramadan, D. Sameoto, S. Evoy, A review of piezoelectric polymers as functional materials for electromechanical transducers, *Smart Mater. Struct.* 23 (2014), <https://doi.org/10.1088/0964-1726/23/3/033001>.
- [28] M.A. Dubois, P. Muralt, Stress and piezoelectric properties of aluminum nitride thin films deposited onto metal electrodes by pulsed direct current reactive sputtering, *J. Appl. Phys.* 89 (2001) 6389–6395, <https://doi.org/10.1063/1.1359162>.
- [29] A. Kakanakova-Georgieva, D. Nilsson, E. Janzen, High-quality AlN layers grown by hot-wall MOCVD at reduced temperatures, *J. Cryst. Growth* 338 (2012) 52–56, <https://doi.org/10.1016/j.jcrysgro.2011.10.052>.
- [30] A.C. Jones, J. Auld, S.A. Rushworth, E.W. Williams, P.W. Haycock, C.C. Tang, G.W. Critchlow, The deposition of aluminum nitride thin films by metal-organic CVD—an alternative precursor system, *Adv. Mater.* 6 (1994) 229–231, <https://doi.org/10.1002/adma.19940060310>.
- [31] Z. Chen, S. Newman, D. Brown, R. Chung, S. Keller, U.K. Mishra, S.P. Denbaars, S. Nakamura, High quality AlN grown on SiC by metal organic chemical vapor deposition, *Appl. Phys. Lett.* 93 (2008), <https://doi.org/10.1063/1.2988323>.
- [32] M.A. Sanchez-Garcia, E. Calleja, E. Monroy, F.J. Sanchez, F. Calle, E. Munoz, R. Beresford, The effect of the III/V ratio and substrate temperature on the morphology and properties of GaN- and AlN-layers grown by molecular beam epitaxy on Si(111), *J. Cryst. Growth* 183 (1998) 23–30, [https://doi.org/10.1016/s0022-0248\(97\)00386-2](https://doi.org/10.1016/s0022-0248(97)00386-2).
- [33] A. Volkova, V. Ivantsov, L. Leung, Hydride vapor phase epitaxy of high structural perfection thick AlN layers on off-axis 6H-SiC, *J. Cryst. Growth* 314 (2011) 113–118, <https://doi.org/10.1016/j.jcrysgro.2010.11.109>.
- [34] G.E. Stan, M. Botea, G.A. Boni, I. Pintilie, L. Pintilie, Electric and pyroelectric properties of AlN thin films deposited by reactive magnetron sputtering on Si substrate, *Appl. Surf. Sci.* 353 (2015) 1195–1202, <https://doi.org/10.1016/j.apsusc.2015.07.059>.
- [35] W.L. Wang, W.J. Yang, Z.L. Liu, H.Y. Wang, L. Wen, G.Q. Li, Interfacial reaction control and its mechanism of AlN epitaxial films grown on Si(111) substrates by pulsed laser deposition, *Sci. Rep.* 5 (2015), <https://doi.org/10.1038/srep11480>.
- [36] Z.P. Wang, A. Morimoto, T. Kawae, H. Ito, K. Masugata, Growth of preferentially-oriented AlN films on amorphous substrate by pulsed laser deposition, *Phys. Lett. A* 375 (2011) 3007–3011, <https://doi.org/10.1016/j.physleta.2011.06.043>.
- [37] C. Ozgüt, I. Donmez, M. Alevli, N. Biyikli, Self-limiting low-temperature growth of crystalline AlN thin films by plasma-enhanced atomic layer deposition, *Thin Solid Films* 520 (2012) 2750–2755, <https://doi.org/10.1016/j.tsf.2011.11.081>.
- [38] I. Gablech, O. Caha, V. Svatoš, J. Pekárek, P. Neuzil, T. Šikola, Stress-free deposition of [001] preferentially oriented titanium thin film by Kaufman ion-beam source, *Thin Solid Films* 638 (2017) 57–62, <https://doi.org/10.1016/j.tsf.2017.07.039>.
- [39] I. Gablech, V. Svatoš, O. Caha, M. Hrabovsky, J. Prasek, J. Hubalek, T. Šikola, Preparation of (001) preferentially oriented titanium thin films by ion-beam sputtering deposition on thermal silicon dioxide, *J. Mater. Sci.* 51 (2016) 3329–3336, <https://doi.org/10.1007/s10853-015-9648-y>.
- [40] G.C.A.M. Janssen, M.M. Abdalla, F. van Keulen, B.R. Pujada, B. van Venrooy, Celebrating the 100th anniversary of the Stoney equation for film stress: Developments from polycrystalline steel strips to single crystal silicon wafers, *Thin Solid Films* 517 (2009) 1858–1867, <https://doi.org/10.1016/j.tsf.2008.07.014>.
- [41] PDF-2 database entry 00-025-1133, ICDD-JCPDS.
- [42] O. Madelung, *Semiconductors: Data Handbook*, Springer, Berlin Heidelberg, 2012.
- [43] T.L. Tansley, R.J. Egan, Point-defect energies in the nitrides of aluminum, gallium, and indium, *Phys. Rev. B* 45 (1992) 10942–10950, <https://doi.org/10.1103/PhysRevB.45.10942>.
- [44] H.R. Kaufman, J.M.E. Harper, Ion-assist applications of broad-beam ion sources, *Proc. Soc. Photo Opt. Ins.* 5527 (2004) 50–68, <https://doi.org/10.1117/12.559785>.
- [45] K.C. Balram, D.A. Westly, M. Davanco, K.E. Grutter, Q. Li, T. Michels, C.H. Ray, L.Y. Yu, R.J. Kasica, C.B. Wallin, L.J. Gilbert, B.A. Bryce, G. Simelgor, J. Topolancik, N. Lobontiu, Y.X. Liu, P. Neuzil, V. Svatoš, K.A. Dill, N.A. Bertrand, M.G. Metzler, G. Lopez, D.A. Czaplowski, L. Ocola, K.A. Srinivasan, S.M. Stavits, V.A. Aksyuk, J.A. Little, S. Krylov, B.R. Ilic, The nanolithography toolbox, *J. Res. Natl. Inst. Stan.* 121 (2016) 464–475, <https://doi.org/10.6028/jres.121.024>.
- [46] H. Fujiwara, *Data Analysis Examples, Spectroscopic Ellipsometry*, John Wiley & Sons, Ltd, 2007, pp. 249–310.
- [47] G. Rossbach, M. Roppischer, P. Schley, G. Gobsch, C. Werner, C. Cobet, N. Esser, A. Dadgar, M. Wieneke, A. Krost, R. Goldhahn, Valence-band splitting and optical anisotropy of AlN, *Phys. Status Solidi B* 247 (2010) 1679–1682, <https://doi.org/10.1002/pssb.200983677>.
- [48] A.R. Goni, F. Kaess, J.S. Reparaz, M.I. Alonso, M. Garriga, G. Callens, M.R. Wagner, A. Hoffmann, Z. Sitar, Dependence on pressure of the refractive indices of wurtzite ZnO, GaN, and AlN, *Phys. Rev. B* 90 (2014), <https://doi.org/10.1103/PhysRevB.90.045208>.
- [49] H. Demiryont, L.R. Thompson, G.J. Collins, Optical properties of aluminum oxy-nitrides deposited by laser-assisted CVD, *Appl. Opt.* 25 (1986) 1311–1318, <https://doi.org/10.1364/AO.25.001311>.

<https://doi.org/10.1038/s43246-024-00509-0>

The collective photothermal effect of silver nanoparticles probed by a microbolometer

Check for updates

Hanliang Zhu^{1,3}, Evelína Gablech^{2,3}, Imrich Gablech²✉ & Pavel Neuzil¹✉

Nanoparticles have become a significant area of research, offering properties that bridge the gap between bulk materials and atomic structures. Silver nanoparticles (AgNPs), specifically, have shown promise due to their plasmonic properties. Despite extensive studies, capturing the photon-to-heat conversion efficiency of individual nanoparticles has been challenging. Here, we present an approach to determine these properties using an ultra-sensitive bolometer with a power resolution of ≈ 26 pW. Our investigations reveal that a single AgNP can dissipate power with a magnitude between ≈ 101.3 fW and ≈ 205.3 fW, an observation that underscores the potential of these particles for efficient energy conversion. This finding enhances the understanding of AgNPs' behavior and pushes the field of nanoparticle plasmon physics forward. Therefore, the refined use of such nanoparticles could bring advancements across a range of applications, from high-resolution imaging and advanced spectroscopy to environmental surveillance and innovative medical treatments.

Plasmonic nanoparticles, with their distinctive optical properties, have garnered significant attention in many scientific domains^{1,2}, from biomedicine to environmental science^{3,4}. Among all nanoparticles, silver nanoparticles (AgNPs) attract attention due to their pronounced localized surface plasmon resonance (LSPR) capabilities^{5,6}. This LSPR phenomenon, a collective oscillation of conduction electrons stimulated by incoming light, grants AgNPs the remarkable capability to amplify and confine electromagnetic fields at the nanoscale⁷, rendering them applicable to diverse sectors⁸. Furthermore, these nanoparticles can transform absorbed light energy into heat through the photothermal effect (PTE)^{9,10}. This feature has been instrumental in various domains, including cancer treatment, where light-induced heating targets and eradicates cancer cells^{11,12}.

Bolometers, known for their ultra-sensitive heat detection capable of sensing heat from a human even from considerable distances¹³⁻¹⁵, operate by converting thermal variations into changes in electrical resistance. Their versatile applications span infrared astronomy¹³, thermal imaging¹⁶, materials characterization¹⁷, preventive maintenance¹⁸, and, in recent years, thermal imaging of newly constructed homes¹⁹.

Introducing AgNPs to bolometer membrane surfaces seems promising, given bolometers' power sensitivity and resolution. Unfortunately,

bolometers cannot measure individually local events on their membrane, only a global membrane dynamic and static temperature response. The deposition process of AgNPs is influenced by electrostatic adsorption between the bolometer membrane and the AgNPs. This adsorption is subject to the surface charges of both entities, which can be modulated by the environmental pH value. As pH levels shift, the activity of hydroxonium ions (H_3O^+) changes, potentially impacting the surface charge through protonation or deprotonation events²⁰. Harnessing the heat-conversion capability of AgNPs could further optimize bolometer power efficiency.

In this study, we provide a comprehensive examination of the power dissipated at the bolometer surface after illumination due to the presence of attached AgNPs. Investigation into resulting changes in the bolometers' thermal and spectral behaviors enabled us to estimate the power dissipated by a single AgNP. Furthermore, we explored the influence of pH values on the deposition process of AgNPs on bolometer surfaces. Evaluations considering the distribution and size effects of AgNPs on bolometer response are also shared. Our findings elucidate the potential of AgNPs to probe plasmonic properties and enhance bolometer efficiency. We anticipate that our insights will inspire further exploration in this innovative field of nanotechnology.

¹Northwestern Polytechnical University, Ministry of Education Key Laboratory of Micro/Nano Systems for Aerospace, Department of Microsystem Engineering, School of Mechanical Engineering, 127 West Youyi Road, 710072 Xi'an, Shaanxi, P. R. China. ²Department of Microelectronics, Faculty of Electrical Engineering and Communication, Brno University of Technology, Technická 3058/10, 616 00, Brno, Czech Republic. ³These authors contributed equally: Hanliang Zhu, Evelína Gablech. ✉e-mail: imrich.gablech@vutbr.cz; pavel.neuzil@nwpu.edu.cn

Results and discussion

Design and characterization of the high-sensitive bolometer

The bolometer employed in this study builds on previous designs^{21,22}, refined using the Nanolithography Toolbox^{23,24} for layout generation. Our bolometer membrane, with a designed sensitive area of $(25 \times 25) \mu\text{m}^2$, was anchored by two SiO_2 legs to improve the thermal insulation. The sensing element of the bolometer was in a resistance temperature detector (RTD) made from Ti in the suspended area. The bolometer membrane was ultra-sensitive to radiation power; here, it functioned as a temperature sensor to study the PTE of AgNPs (Fig. 1a). We fabricated the bolometers through micromachining technology and modified AgNPs on their surface using the electrostatic deposition method (Fig. 1b). Each chip featured 48 individual bolometers at the center, and each bolometer had its extension leads and pads for further wire bonding (Fig. 1c and d). Our final bolometer legs each had measured dimensions of $\approx 1.2 \mu\text{m}$ for width, $\approx 0.424 \mu\text{m}$ for thickness, and $\approx 62 \mu\text{m}$ for length for excellent thermal isolation.

The device, comprising two Si chips, each housing 48 bolometers, having one device with and the other without the AgNPs paired together, was positioned in a vacuum chamber. Each bolometer had an independent electrical connection. Two bolometers, one with and one without AgNPs and both with a resistance (R) of $\approx 10.86 \text{ k}\Omega$ ²⁵, were incorporated into an AC-powered Wheatstone bridge under a voltage bias (V_B) in differential mode. The differential voltage ($\Delta V = V_1 - V_2$) derived from the bridge outputs was further processed by a lock-in amplifier, with the result (ΔV_L) being recorded by an oscilloscope (Fig. 2a)²⁶. The bolometers were exposed to light from an Xe lamp via a grating monochromator and liquid core optical fiber. The vacuum chamber was thermally shielded and maintained an internal pressure of $\approx 12 \text{ mPa}$, reducing the bolometer membrane's temperature fluctuations.

The PTE of AgNPs was evaluated by monitoring the dissipated power by bolometer when shining light on the AgNPs deposited membrane. We used an Xe lamp providing light with a spectrum wavelength from 260 to 1000 nm. This light source was connected via liquid core optical fiber to a grating monochromator to select the desired wavelength to illuminate the bolometer in the vacuum chamber (Fig. 2b). During the PTE measurement,

the scanning step duration for each photon wavelength (λ) was set to 10 s, with an additional $\approx 1 \text{ s}$ needed for changing values and stabilization of the monochromator. A MATLAB script was used to compute the average value for each wavelength, with data processing undertaken using the *Origin* software (Fig. 2c).

The temperature coefficient of resistance TCR (α) of the bolometer was characterized using the method mentioned in the previous section, and the results of R as a function of temperature (T) were plotted. We adopted a linear curve fitting as the resistance (R) varied with temperature (ΔT) can be approximated this way:

$$R = R_0(1 + \alpha \cdot \Delta T), \quad (1)$$

where R_0 is the sensor's resistance at 0°C , and α represents the TCR. The calculated values, R_0 and α , of the tested bolometer were $(9.98 \pm 1.14 \times 10^{-3}) \text{ k}\Omega$ and $(0.27 \pm 7.63 \times 10^{-4}) \% \text{ K}^{-1}$, respectively, both with (mean value \pm fitting error) (Fig. S1 in Supplementary section 1). We then formed the Wheatstone bridge consisting of a single bolometer and three fixed resistors and powered it with V_B set to 50 mV, resulting in a P_j of $\approx 58.6 \text{ nW}$, per Eq. (2) in the "Methods" section, and a bolometer temperature rise of $\approx 1.47^\circ\text{C}$, per Eq. (3) in the "Methods" section. The self-heating method facilitated the measurement of the bolometer's thermal parameters using short V_B pulses with variable V_{DC} bias²⁷ (Fig. S2a, b in Supplementary Section 2). Measurements from three bolometer sets revealed the following both thermal capacitance (H) and conductance (G), as well as the time constant (τ) as $\approx 0.84 \text{ nJ K}^{-1}$, $\approx 45.95 \text{ nW K}^{-1}$, and $\tau \approx 18.32 \text{ ms}$, respectively (Fig. S2c in Supplementary Section 2). All measured thermal parameters of the different bolometers are listed in Table 1.

The resolution of the bolometer was influenced by two key aspects: thermal isolation evaluated by the G magnitude and the temperature noise of the system. The bolometer used was well isolated by the "L" shaped legs, obtaining a G value of $\approx 45.95 \text{ nW K}^{-1}$ in a vacuum test chamber. Thus, the resolution of our bolometer depended on the temperature noise, including electrical noise in the test circuit and heat fluctuation in the test

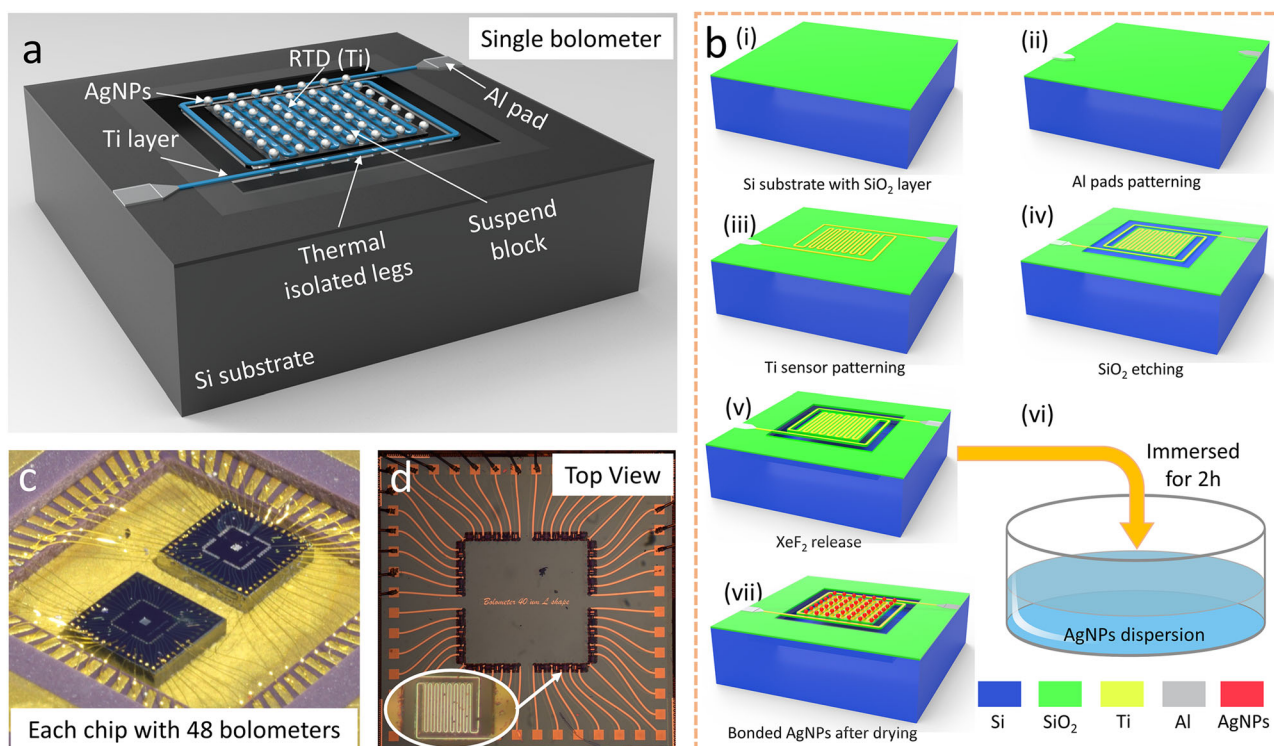


Fig. 1 | Schematic of the bolometer design and its fabrication. **a** Schematic of the single bolometer structure with silver nanoparticles (AgNPs). **b** Fabrication process flow of the bolometer device and AgNPs deposition. **c** Photograph of two Si chips, each with 48 individual bolometers and **d** its top view.

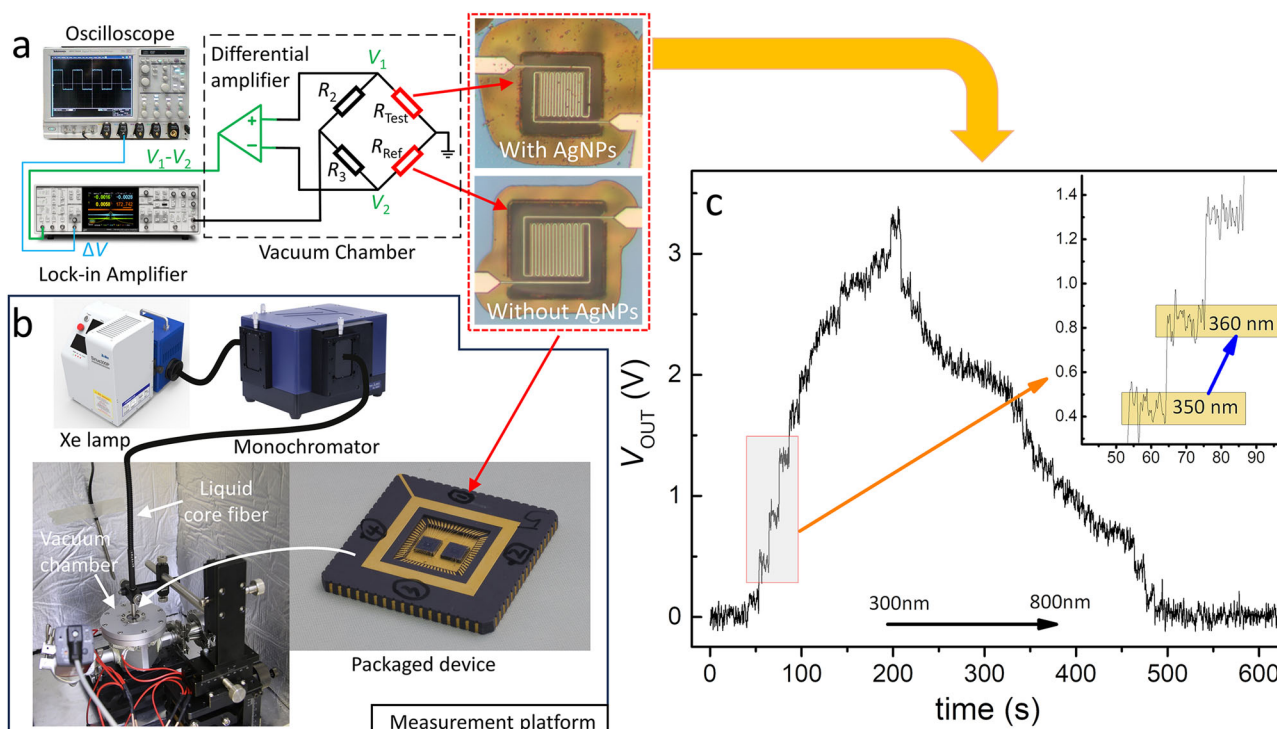


Fig. 2 | Measurement setup using a bolometer for heat detection. **a** Reference and testing bolometer was connected to a Wheatstone bridge with its outputs processed by a differential amplifier ($V_1 - V_2$) and subsequently by a lock-in amplifier with its output (ΔV_L) recorded by an oscilloscope. **b** Two Si chips with bolometers, one with and one without silver nanoparticles (AgNPs), were placed into a vacuum chamber,

and the whole chamber was located in a temperature-controlled thermally shielded box. Light projected onto the bolometers originated from an Xe lamp, with a particular wavelength selected by a monochromator and delivered via a liquid core fiber. **c** Measurement output demonstrated an observed response to monochromatic light across various wavelengths.

environment. The temperature stability of the thermal isolation box was characterized using a thermometer with a resolution of ≈ 1 mK, which showed a fluctuation of ≈ 0.3 K at ≈ 296.15 K (≈ 23 °C) throughout ≈ 2.8 h. This fluctuation of the environment was further decreased by the employment of the vacuum chamber, thus lowering the temperature noise. We measured the temperature noise with settings adjusted to V_B , lock-in amplifier gain factor (S), and differential amplifier gain factor (B) values of 50, 1 mV, and 10,000, respectively, and the T_T valve acquired as ≈ 3.41 kV K $^{-1}$, per Eq. (5) in the “Methods” section. The system noise was captured and calculated at 1.381 V, obtaining the temperature noise and resolution of ≈ 404.7 μ K and ≈ 26 pW, respectively (Fig. S2d in Supplementary Section 2). Maintaining a consistent temperature is essential for accurate measurements, especially when assessing minute changes that can significantly impact readings.

The power sensitivity of the bolometer was evaluated using light radiation on the membrane. We utilized bolometer “d” with a resistance (R_r) of ≈ 12.06 k Ω and a G value of ≈ 39.96 nW K $^{-1}$ for this measurement. It was determined to be ≈ 12.74 μ V K $^{-1}$, using Eq. (5). A light source was used for calibrating the bolometer’s response. We employed a blue light-emitting

diode (LED) with a wavelength of 490 nm as the radiation source. The LED power was quantified using an optical power meter at a distance between the light probe and the fiber of ≈ 12 mm. The lighting power density (D_L) was then calculated by dividing the power meter detector area (0.79 cm 2). After positioning the fiber above the vacuum chamber, we illuminated the bolometer surface. The power induced in the bolometer (P_{IN}) by radiation was calculated based on its area and the lighting power density (Fig. S3a and Table S1 in Supplementary Section 3). The lock-in amplifiers’ time constant was set to 1 ms, enabling the recording of thermal response and extraction of the τ value using exponential curve fitting. Subsequently, V_B , S , and B were set to 50, 500 mV, and 2000, respectively, resulting in a T_T of ≈ 1.365 V K $^{-1}$ and a power transformation coefficient (T_P) of ≈ 34.16 mV nW $^{-1}$ (Fig. S3b in Supplementary Section 3).

Evaluation of the AgNPs distribution on the bolometer membrane

The electrostatic adsorption of silver nanoparticles (AgNPs) onto bolometer membranes is influenced by the interplay of surface potentials initiated by the addition of diluted HCl. This process is significantly affected by the surface charge of Ti and Si materials, which are vital for interaction with citrate-stabilized AgNPs. These interactions are dependent on the isoelectric points of the natively oxidized surfaces (like TiO $_2$ and SiO $_2$) and the pH level of the AgNP dispersion. Effective surface interaction is expected in conditions where citrate remains deprotonated ($pK_a > 3.1$), and the surface gains a positive charge through protonation. We used a scanning electron microscopy (SEM) type MIRA II SEM instrument (Tescan a.s.), setting its parameters, such as working distance and magnifications, to ≈ 4.3 mm and $\times 7220$, respectively, resulting in a field of view of 30 μ m. The SEM images were used to confirm the immobilization of AgNPs onto the microbolometer membranes at various pH levels by counting the number of particles using *Image J* software²⁸. The number of AgNPs was calculated based on the total area occupied by them. Per the datasheet, the size of the AgNP was ≈ 100 nm. Thus the area of each particle was ≈ 7850 nm 2 , serving

Table 1 | Thermal parameters and number of AgNPs on the membrane of each microbolometer used in the experiment

Number	R_r (k Ω)	G (nW K $^{-1}$)	τ (ms)	Number of AgNPs	Total P (nW)	P of AgNP (fW)
a	11.07	73.01	14.80	7049	1.2	170.2
b	11.37	55.63	15.78	8196	0.83	101.3
c	11.52	45.06	22.23	6576	1.23	187.0
d	12.06	39.96	22.99	7063	1.45	205.3
r1	10.15	41.02	20.34	0	\	\
r2	10.17	40.78	20.80	0	\	\

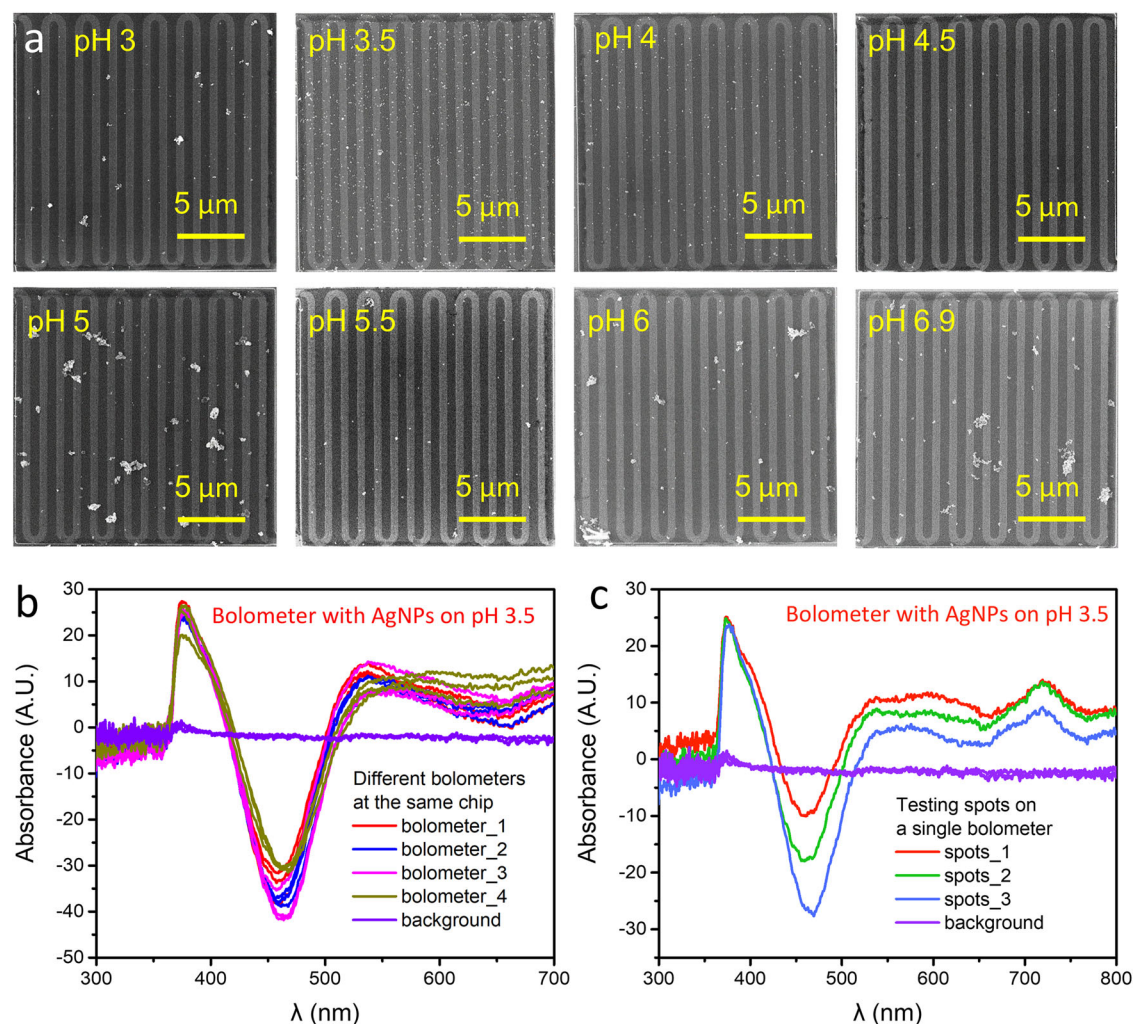


Fig. 3 | Characterization of the deposited AgNPs on the bolometer membrane. a SEM images of the bolometer membrane with adsorbed AgNPs at different pH values from 3.0 to 6.9 showing an optimized results at a pH of 3.5. b Measured relative light absorbance by scanning near-field optical microscopy (SNOM) at three

different spots at four bolometers having the AgNPs adsorbed at the membrane at pH of ≈ 3.5 as well as SNOM measurement at the membrane without AgNPs as background reference. c The SNOM measurement from a single device at three spots is marked in the SEM image of AgNPs in pH 3.5.

as the reference for the subsequent counting processes. Each SEM image was analyzed three times, and the average value of the number of AgNPs was obtained (Table 1).

The SEM images revealed that the AgNPs tend to aggregate below a pH of 3.5, a phenomenon likely due to the complete protonation of citrate molecules surrounding the nanoparticles. The concentration of H_3O^+ ions in the surrounding environment crucially impacts the chemical equilibrium, causing changes in surface charge due to protonation or deprotonation. This change enhances the electrostatic interaction between the SiO_2 on the bolometer surface and the AgNPs. We demonstrated the influence of the pH with AgNPs suspension to achieve the optimized spread of AgNPs across the membrane. Our focus was getting large area coverage without the formation of clusters. The best results were obtained using suspension with a pH of 3.5, as is shown in Fig. 3a.

The quantity of AgNPs adsorbed on the bolometer membrane increased as the pH of the colloidal suspension decreased, with aggregation observed below pH 3.5 and above 4.5. For light scanning measurements, we evaluated bolometer membranes with both high and low AgNP densities, prepared at pH 3.5 and 4.5, respectively. This approach allowed us to assess the signal from varying particle densities. Bolometers with aggregated AgNPs, especially those outside the ideal pH range, were excluded from further testing due to their adverse impact on the localized surface plasmon resonance (LSPR) effect. Our findings highlight the delicate balance

required in pH manipulation to optimize the adsorption of AgNPs onto bolometer membranes, underscoring the nuanced interplay between nanoparticle chemistry and surface physics. This understanding is crucial for advancing applications in high-precision sensors and nanoscale thermal imaging.

Optical absorbance measurements were performed using the Multi-View 4000 scanning near-field optical microscope (Nanonics Imaging Ltd.) in dark field observation mode. These measurements were conducted on three distinct spots, as shown in Fig. 3a, of a single bolometer, evaluated both with and without silver nanoparticles (AgNPs), to assess the uniformity of the measurements using an objective with 100 \times magnification.

The absorbance spectrum revealed the immobilization of 100 nm AgNPs on the bolometer membrane at a pH of ≈ 3.5 measured at four different bolometers showed a peak absorbance at ≈ 380 nm (Fig. 3b). Moreover, a noticeable dip in absorbance was observed, reaching its lowest point at ≈ 460 nm. In contrast, the bolometer without AgNPs displayed a flat absorption curve, missing significant peaks, thus conclusively confirming the presence of AgNPs on the membrane. Details measured at the device with adsorption performed at a pH of 3.5 having an SEM image in (Fig. 3a) are shown in (Fig. 3c) and all measurements at 23 bolometers in Fig. S4 of Supplementary Section 4.

The variation in amplitude ≈ 460 nm could be attributed to impurities associated with the immobilization of AgNPs and the scattering effect,

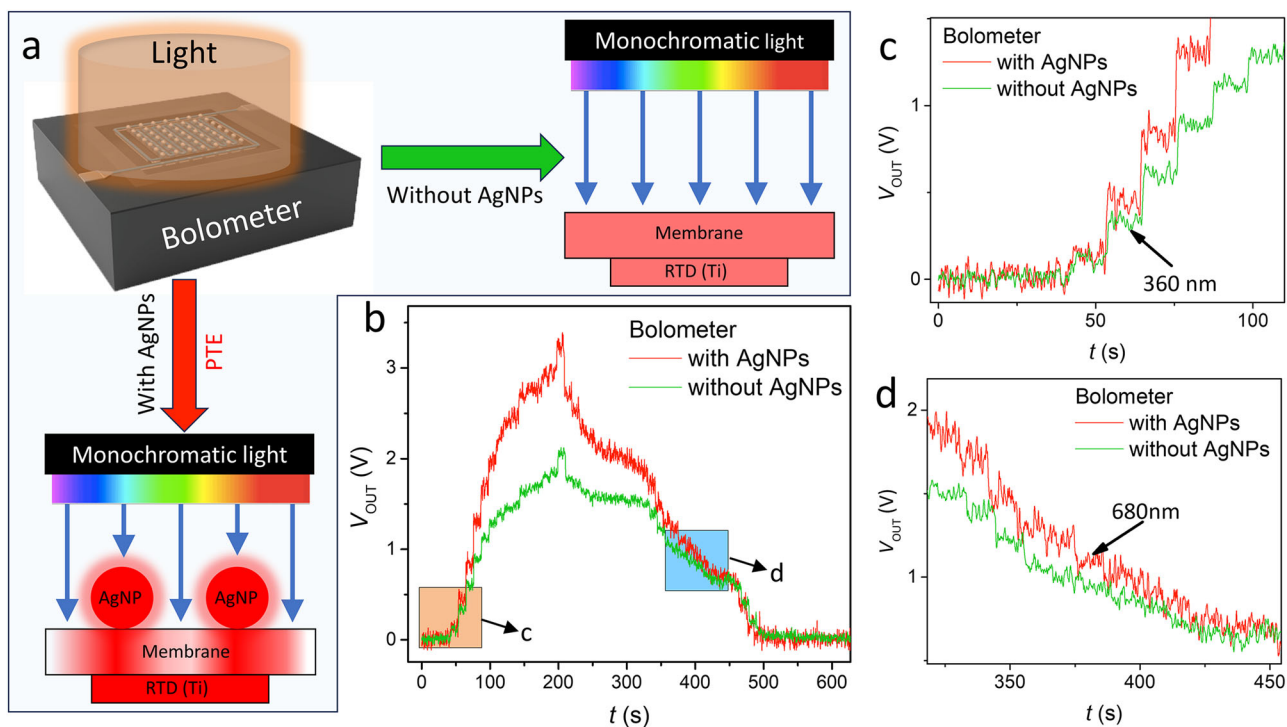


Fig. 4 | Photothermal effect measurement of silver nanoparticles (AgNPs) using bolometer. **a** Principal diagram of heat generation and transfer on bolometer membrane with and without AgNPs. **b** Response of the bolometer during light scanning in different λ . **c** The bolometers have identical responses when λ below

340 nm, and the difference increases with the changing of λ . **d** The response of monochromatic light back to the same level with λ of 680 nm for bolometer with and without AgNPs.

which may contribute to reflectance. This variation could also be due to changes in the roughness of the Si surface beneath the membrane following XeF₂ etching²⁹. It should be noted that the negative part of the spectra, although overlapping with the absorption maximum of AgNPs, does not hold significant meaning, as the device's construction did not allow for detailed analysis such as transmission spectra. The issue of the rough surface on the Si substrate beneath the membrane might be mitigated by prolonging the etching duration of Si, thereby distancing the substrate surface from the membrane. However, this method poses a substantial risk of under-etching the bolometer leads, potentially resulting in membrane collapse. A preferable strategy might involve adopting a different fabrication technology, which includes exposing the substrate from the backside to reduce scattered light and utilizing a silicon-on-insulator wafer as the substrate for bolometer fabrication. The actual SPR absorption maximum is not at ≈ 380 nm but rather higher, as later confirmed by power dissipation measurements. Manufacturer data indicates the maximum absorption range to be between 490 and 515 nm. Hence, the apparent discrepancy can likely be attributed to the aforementioned optical effects and the rough Si substrate beneath the bolometer membrane.

Calorimetry for localized surface plasmon resonance effect of AgNPs

The AgNPs utilized in our experiment exhibited a strong plasmonic resonance at a specific wavelength (SPR absorbance maxima) within the visible range. When illuminated with light that matched this SPR absorbance maximum, efficient photon-to-heat conversion occurred due to LSPR. This increased the temperature within the AgNPs, which was then immediately transferred to the bolometer membrane and measured by the temperature sensor (Fig. 4a). For reference, we also utilized a bolometer without AgNPs to respond directly to light. We investigated the bolometer's response to varying light wavelengths, particle counts, and sizes. The power detection limit of the employed bolometer was calculated to be ≈ 26 pW. We used a broadband light source from an Xe lamp with a nominal power of 100 W for

illumination and light detection. The light source was connected via a monochromator and spectrum analyzer, respectively (Fig. S5 in Supplementary Section 5).

The liquid core fiber was directly in contact with the optical window on the vacuum chamber, ensuring a constant distance between the fiber and the device. This maintained identical light conditions for different measurements. The λ of the light illuminating the bolometer membrane was varied from 300 to 800 nm in increments of 10 nm. Each wavelength was held for 10 s, allowing the bolometer to reach a stabilized state with a τ of ≈ 18 ms. The filters inside the monochromator were adjusted based on the desired λ and duration. The response of the bolometer heating varied depending on the interrogating wavelength, so we used a bolometer without AgNPs as a benchmark to detect the effect of AgNPs' presence. We compared the measurements of the bolometer with and without AgNPs to observe the differences caused by the presence of nanoparticles (Fig. 4b). The response of the light scanning for λ below 350 nm was identical in both cases, with a similar increase observed for λ of 340 nm. However, the heat generation on the bolometer with AgNPs exhibited different behavior to the bolometer without AgNPs, from 350 to 680 nm (Fig. 4c and d). The additional heat generation was caused by enhanced light absorption when the AgNPs were presented at the surface.

Photothermal power output from a single AgNP

We performed measurements on various bolometers with different parameters and AgNPs, as listed in Table 1, to assess the response of the PTE. Four bolometers with varying distributions of AgNPs, along with two without AgNPs, were measured under identical conditions and settings. Each measurement was repeated four times (Fig. 5a). The bolometers without AgNPs exhibited good repeatability for λ ranging from ≈ 300 to ≈ 780 nm, with negligible differences observed for λ values exceeding ≈ 500 nm. The increase in response observed on the bolometer without AgNPs during λ scanning can be attributed to nonuniformity in monochromatic light intensity. Consequently, the average value obtained from

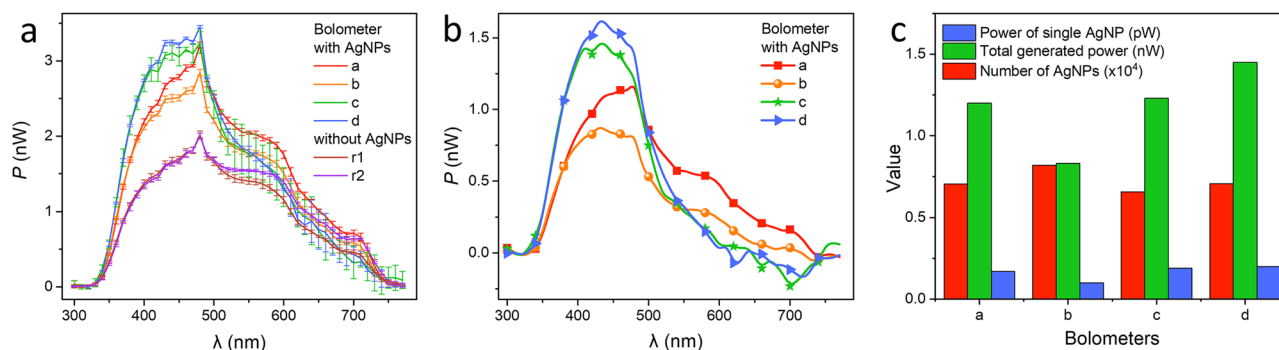


Fig. 5 | Measurement results of heat generation from a single silver nanoparticle (AgNP). **a** Response to the heat change of AgNPs on a bolometer using monochromatic light for wavelength scanning. **b** Subtracted power generation on different bolometers using the bolometer without AgNP as the baseline, showing AgNPs a

wide wavelength range sensitive to light. **c** Total power generated on the bolometer (green) and counted AgNPs on their surface (red), resulting in an average power generated from a single AgNP of (101.3–205.3) fW (data from four devices).

the measurements on bolometers without AgNPs was considered as a baseline for extracting heat generation by the PTE (Fig. 5b). Our results reveal that the absorption maxima of the AgNPs are between 400 and 500 nm. Results from all four bolometers are shown in Fig. 5c. We selected bolometer “d” for a detail description of the measurements. This device had a total 7063 AgNPs at its membrane and reached a maximum heat generation of ≈ 1.45 nW, corresponding to the heat generation by a single AgNP of ≈ 205.3 fW (Fig. 5c). The average AgNPs has a nominal diameter of 100 nm, corresponding to the area of 7854 nm², which is 7.85×10^{-15} m². Then, we can recalculate the heat generation at the unit of area of the AgNPs as ≈ 22.9 W m⁻².

Our study revealed the interactions between the bolometer membrane and AgNPs. A central finding of our research is the precise determination of the power dissipated in a single AgNP, which was found to be between ≈ 101.3 and ≈ 205.3 fW. The enhanced PTE of AgNPs on the surface of a bolometer is based on the unique surface plasmon resonance properties of AgNPs. In addition to being influenced by the light source, it also significantly relates to the uniformity, density, and inter-particle spacing of the particles on the bolometer surface. Our process achieves the distribution of AgNPs on the bolometer surface by adjusting the pH value of AgNP colloidal dispersion. The adhesion behavior of AgNPs depends on both the bolometer membrane’s surface potential and the pH of the suspension containing the AgNPs. Effective adsorption of AgNPs was observed within the pH range of ≈ 3.5 to ≈ 4.5 . Outside this window, the nanoparticles tended to cluster. In terms of plasmonic properties, integrating AgNPs with micromachined bolometer membranes led to a marked increase in power dissipation when exposed to light near their resonance frequency. Our studies identified the peak of power dissipation to be ≈ 460 nm, even though the SNOM measurement showed that the resonance frequency is at a wavelength of ≈ 480 nm. However, even within the same batch of chips, there are differences in the distribution of AgNPs during self-assembly, leading to variations in photothermal power with the same light source. Therefore, representing the photothermal power of individual nanoparticles in terms of a range is more scientific than using a standard deviation. This significant achievement paves the way for a variety of practical applications and provides a clearer understanding of nanoparticle behavior at a single level.

The ability to measure and harness power from individual nanoparticles might revolutionize several fields³⁰. Enhanced absorption and dissipation properties of AgNPs could significantly improve medical imaging tools, leading to clearer magnetic resonance imaging outputs. Moreover, the photon-to-heat conversion capability of AgNPs might play a crucial role in cancer treatments, offering a method to eliminate cancer cells while sparing healthy ones^{31,32}. This phenomenon has paved the way for innovative developments, such as a new generation of polymerase chain reaction systems known as photonic PCR^{9,33}. Outside the realm of

healthcare, AgNPs promise to transform environmental sensing with ultra-sensitive pollutant detectors and to advance spectroscopy across various sectors. Our study has brought to light the extraordinary attributes of AgNPs, especially when examined with an ultra-sensitive bolometer that possesses a power resolution of ≈ 26 pW. A pivotal discovery of our research is that a single AgNP can dissipate power with an amplitude between ≈ 101.3 and ≈ 205.3 fW, demonstrating the efficiency of its energy conversion from photon to heat. Conversely, the device enables the measurement of total dissipated power, facilitating the estimation of the number of AgNPs present on the bolometer surface. These insights provide a strong basis for further exploration into the physics of nanoparticle plasmons. The unique qualities of nanoparticles hold great promise for sparking innovations across a wide spectrum of fields, including imaging, spectroscopy, environmental monitoring, and medical treatments.

Methods

Bolometer fabrication

We initiated the lithography process by priming the substrate surface with hexamethyldisilazane (HMDS) vapor. We used a vacuum oven setting the temperature to 150 °C and performed the recommended sequence of pumping the oven to vacuum, purging with N₂, and pumping again several times. Then we applied vapor of HMDS for 30 s, purged several times again and then vented.

We always used an i-line photoresist (PR) for lithography through the spin-coating process using ≈ 4000 RPM, achieving its recommended thickness of ≈ 0.9 μ m after pre-baking at ≈ 110 °C for ≈ 60 s. The PR was exposed by a 5:1 stepper and then post-baked using identical conditions as we used for pre-baking. The lithography process concluded with PR development using a tetramethylammonium hydroxide-based developer solution and the subsequent removal of any residual undeveloped PR using O₂ plasma for ≈ 30 s.

First, we formed the fiducial alignment marks in bare Si substrate by etching it after the lithography into a depth of ≈ 0.1 μ m using SF₆/O₂-based plasma. Then, we removed the PR and cleaned the wafers.

The first device fabrication step was the deposition of a ≈ 0.25 μ m layer of SiO₂ through a plasma-enhanced chemical vapor deposition process (PECVD) (Fig. 1b [i]) followed by sputter-deposition of a ≈ 0.9 μ m Al layer subsequently patterned to create bond pads and lead-outs (Fig. 1b [ii]). We sputter-deposited a ≈ 0 nm-thick Ti layer, which, after undergoing reactive ion etching, served as the temperature sensor on the bolometer membrane (Fig. 1b [iii]). A protective ≈ 0.25 μ m-thick SiO₂ layer covered the Ti sensor layer by PECVD. After patterning this layer to expose the bonding pads, we created Si substrate access holes for subsequent Si etching (Fig. 1b [iv]). XeF₂ vapor etching of the bolometer substrate isolated the bolometer membrane, minimizing heat losses to the Si substrate (Fig. 1b [v]). The process used here was the same as the one used before^{21,22,26}.

AgNPs deposition

Chemicals employed in the electrostatic deposition of AgNPs on the chips with bolometers encompassed an AgNP dispersion with a concentration of $\approx 20 \mu\text{g ml}^{-1}$ and a nominal diameter of $\approx 100 \text{ nm}$, sourced from Sigma-Aldrich. This dispersion, stabilized using sodium citrate, presented a pH value near 6.9 and had a maximum extinction wavelength of $\approx 480 \text{ nm}$, as indicated by the material data sheet. Additional chemicals included HCl with a concentration of $\approx 37\%$, propane-2-ol (commonly known as isopropanol or IPA) with a purity of 99.98%, acetone with 99.5% purity, and deionized water (DI H_2O). For pH adjustment purposes, the HCl was diluted with DI H_2O in a 1:100 ratio. The AgNP working solutions were prepared by mixing $\approx 1.5 \text{ mL}$ of AgNP colloidal dispersion with the calculated quantity of diluted HCl. This ensured the adjustment of its pH to the specific values of 3, 3.5, 4, 4.5, 5, 5.5, 6, and 6.9.

The process of depositing AgNPs on the bolometer's surface involved an electrostatic adsorption technique using AgNP colloidal dispersion with different pH values. First, we cleaned the chips with bolometers using acetone to effectively remove organic residues and then cleaned them with IPA to eliminate any acetone traces. After being cleaned, the chips underwent a drying process using compressed N_2 . Each cleaned chip with bolometers was then submerged into one of these AgNPs colloidal suspensions for a duration of $\approx 2 \text{ h}$ (Fig. 1b [vi]). Post-immersion, the bolometer chips were cleaned with DI H_2O and then dried using compressed N_2 (Fig. 1b [vii]). This methodological approach to fabrication was important in realizing a device of high performance, providing important insights into the photothermal dynamics related to AgNPs.

Characterization of the bolometer

The RTD, made from Ti thin film, was utilized as the temperature sensing element²⁷. We first evaluated its TCR. The bolometer chip was placed on a hotplate and its resistance was measured as a function of temperature using the four-point probe method. This resistance (R) varied with temperature (ΔT) can be approximated by Eq. (1). Bolometer heat balance consists of dissipated Joule heat (P_j), convection loss (P_{CV}), radiation (P_R), and conduction (P_{CD}), achieved with Eq. (2):

$$P_j = \frac{V_B^2}{4R_T} = P_R + P_{CV} + P_{CD} \simeq P_{CD}. \quad (2)$$

In the vacuum testing environment, P_{CV} and P_R were negligible due to the calculated low G value of the bolometer device and the absence of a gaseous environment, respectively. The thermal conductance (G), capacitance (H), and temperature difference (ΔT) between the microbolometer membrane and the substrate chip define P_{CD} , as per Eq. (3):

$$P_{CD} = H \frac{d\Delta T}{dt} + G \cdot \Delta T. \quad (3)$$

The Wheatstone bridge output (ΔV) is achieved with Eq. (4):

$$\Delta V_L = \frac{10 \cdot B \cdot P \cdot \alpha \cdot V_B}{4 \cdot S \cdot G} = \frac{10 \cdot B \cdot \alpha \cdot V_B}{4 \cdot S} \Delta T = T_T \cdot \Delta T, \quad (4)$$

where B represents the amplifier gain, S is the lock-in amplifier sensitivity, and T_T is the transformation coefficient of temperature. T_T is then achieved with Eq. (5)²²:

$$T_T = \frac{10 \cdot B \cdot \alpha \cdot V_B}{4 \cdot S}, \quad (5)$$

allowing for converting measured ΔV_L into T .

Data availability

Data are available upon request.

Received: 17 October 2023; Accepted: 22 April 2024;

Published online: 01 May 2024

References

- Olson, J. et al. Optical characterization of single plasmonic nanoparticles. *Chem. Soc. Rev.* **44**, 40–57 (2015).
- Lim, W. Q. & Gao, Z. Plasmonic nanoparticles in biomedicine. *Nano Today* **11**, 168–188 (2016).
- Saha, K., Agasti, S. S., Kim, C., Li, X. & Rotello, V. M. Gold nanoparticles in chemical and biological sensing. *Chem. Rev.* **112**, 2739–2779 (2012).
- Dreaden, E. C., Alkilany, A. M., Huang, X., Murphy, C. J. & El-Sayed, M. A. The golden age: gold nanoparticles for biomedicine. *Chem. Soc. Rev.* **41**, 2740–2779 (2012).
- Huang, X. & El-Sayed, M. A. Plasmonic photo-thermal therapy (PPTT). *Alex. J. Med.* **47**, 1–9 (2011).
- Willets, K. A. & Van Duyne, R. P. Localized surface plasmon resonance spectroscopy and sensing. *Annu. Rev. Phys. Chem.* **58**, 267–297 (2007).
- Jain, P. K., Huang, X., El-Sayed, I. H. & El-Sayed, M. A. Review of some interesting surface plasmon resonance-enhanced properties of noble metal nanoparticles and their applications to biosystems. *Plasmonics* **2**, 107–118 (2007).
- Homola, J., Yee, S. S. & Gauglitz, G. Surface plasmon resonance sensors. *Sens. Actuators B: Chem.* **54**, 3–15 (1999).
- Kim, M., Lee, J. H. & Nam, J. M. Plasmonic photothermal nanoparticles for biomedical applications. *Adv. Sci.* **6**, 1900471 (2019).
- de Aberasturi, D. J., Serrano-Montes, A. B. & Liz-Marzán, L. M. Modern applications of plasmonic nanoparticles: from energy to health. *Adv. Opt. Mater.* **3**, 602–617 (2015).
- Zhou, C. et al. Activatable NIR-II plasmonic nanotheranostics for efficient photoacoustic imaging and photothermal cancer therapy. *Adv. Mater.* **33**, 2006532 (2021).
- Vines, J. B., Yoon, J.-H., Ryu, N.-E., Lim, D.-J. & Park, H. Gold nanoparticles for photothermal cancer therapy. *Front. Chem.* **7**, 167 (2019).
- Richards, P. L. Bolometers for infrared and millimeter waves. *J. Appl. Phys.* **76**, 1–24 (1994).
- Niesler, F. B. P., Gansel, J. K., Fischbach, S. & Wegener, M. Metamaterial metal-based bolometers. *Appl. Phys. Lett.* **100**, 203508 (2012).
- El Fatimy, A. et al. Epitaxial graphene quantum dots for high-performance terahertz bolometers. *Nat. Nanotechnol.* **11**, 335–338 (2016).
- Niklaus, F., Vieider, C. & Jakobsen, H. MEMS-based uncooled infrared bolometer arrays: a review. *Proceedings of SPIE, MEMS/MOEMS Technologies and Applications III*. 68360D-2 (2007).
- Huang, J., Wang, T., Zhu, P. & Xiao, J. Preparation, characterization, and thermal properties of the microencapsulation of a hydrated salt as phase change energy storage materials. *Thermochim. Acta* **557**, 1–6 (2013).
- Sarawade, A. A. & Charniya, N. N. Infrared Thermography and its Applications: A Review. *Proceedings of the International Conference on Communication and Electronics Systems (ICCES 2018)* 280–285 (IEEE).
- Husein, H. A. Thermal imaging for improving energy conservation behaviors: an infrared thermography survey for residential buildings. *ITJEMAST* **13**, 1–17 (2022).
- Kolibal, M. et al. Guided assembly of gold colloidal nanoparticles on silicon substrates prepatterned by charged particle beams. *ACS Nano* **6**, 10098–10106 (2012).
- Pekárek, J. et al. Self-compensating method for bolometer-based IR focal plane arrays. *Sens. Actuators A: Phys.* **265**, 40–46 (2017).
- Svatoš, V., Gablech, I., Ilic, B. R., Pekárek, J. & Neužil, P. In situ observation of carbon nanotube layer growth on microbolometers

- with substrates at ambient temperature. *J. Appl. Phys.* **123**, 114503 (2018).
23. Balram, K. C. et al. The nanolithography toolbox. *J. Res. Natl Inst. Stand. Technol.* **121**, 464 (2016).
 24. Zhang, H. et al. Nanolithography toolbox—simplifying the design complexity of microfluidic chips. *J. Vacuum Sci. Technol. B* **38**, 063002 (2020).
 25. Neuzil, P. & Mei, T. A method of suppressing self-heating signal of bolometers. *IEEE Sens. J.* **4**, 207–210 (2004).
 26. Svatoš, V., Gablech, I., Pekárek, J., Klempa, J. & Neuzil, P. Precise determination of thermal parameters of a microbolometer. *Infrared Phys. Technol.* **93**, 286–290 (2018).
 27. Neuzil, P. & Mei, T. Evaluation of thermal parameters of bolometer devices. *Appl. Phys. Lett.* **80**, 1838–1840 (2002).
 28. Schneider, C. A., Rasband, W. S. & Eliceiri, K. W. NIH Image to ImageJ: 25 years of image analysis. *Nat. Methods* **9**, 671–675 (2012).
 29. Liu, X., Zhu, H., Sabó, J., Lánský, Z. & Neuzil, P. Improvement of the signal to noise ratio for fluorescent imaging in microfluidic chips. *Sci. Rep.* **12**, 18911 (2022).
 30. Jiang, K., Smith, D. A. & Pinchuk, A. Size-dependent photothermal conversion efficiencies of plasmonically heated gold nanoparticles. *J. Phys. Chem. C* **117**, 27073–27080 (2013).
 31. Zhang, Y. et al. Tumor-targeting gene-photothermal synergistic therapies based on multifunctional polydopamine nanoparticles. *J. Chem. Eng.* **457**, 141315 (2023).
 32. Park, J. H. et al. Cooperative nanoparticles for tumor detection and photothermally triggered drug delivery. *Adv. Mater.* **22**, 880–885 (2010).
 33. You, M. et al. Ultrafast photonic PCR based on photothermal nanomaterials. *Trends Biotechnol.* **38**, 637–649 (2020).

Author contributions

H.Z. prepared the optical setup (including a vacuum chamber), conducted optical measurements of the devices using modulated wavelength and processed data, and contributed to manuscript writing. E.G. prepared solutions with AgNPs and immobilized them on membranes, established optical spectra acquisition and data evaluation, and contributed to manuscript writing. I.G. is a co-inventor of the idea and was responsible for chips mounting into the socket and final etching using XeF₂. He also contributed to the data evaluation, manuscript writing, and SEM image

capturing. P.N. devised the measurement and system properties evaluation and also contributed to measurement setup, data evaluation, and manuscript writing.

Competing interests

The authors declare no competing interests.

Additional information

Supplementary information The online version contains supplementary material available at <https://doi.org/10.1038/s43246-024-00509-0>.

Correspondence and requests for materials should be addressed to Imrich Gablech or Pavel Neuzil.

Peer review information *Communications Materials* thanks the anonymous reviewers for their contribution to the peer review of this work. Primary Handling Editor: Aldo Isidori. A peer review file is available.

Reprints and permissions information is available at <http://www.nature.com/reprints>

Publisher's note Springer Nature remains neutral with regard to jurisdictional claims in published maps and institutional affiliations.


Open Access This article is licensed under a Creative Commons Attribution 4.0 International License, which permits use, sharing, adaptation, distribution and reproduction in any medium or format, as long as you give appropriate credit to the original author(s) and the source, provide a link to the Creative Commons licence, and indicate if changes were made. The images or other third party material in this article are included in the article's Creative Commons licence, unless indicated otherwise in a credit line to the material. If material is not included in the article's Creative Commons licence and your intended use is not permitted by statutory regulation or exceeds the permitted use, you will need to obtain permission directly from the copyright holder. To view a copy of this licence, visit <http://creativecommons.org/licenses/by/4.0/>.

© The Author(s) 2024

Electronic materials



Mechanical strain and electric-field modulation of graphene transistors integrated on MEMS cantilevers

Imrich Gablech^{1,3,*} , Jan Brodský^{1,2}, Petr Vyroubal², Jakub Piastek^{1,4}, Miroslav Bartošík^{1,4,5}, and Jan Pekárek^{1,*}

¹Central European Institute of Technology, Brno University of Technology, Purkyňova 123, 612 00 Brno, Czech Republic

²Department of Electrical and Electronic Technology, Faculty of Electrical Engineering and Communication, Brno University of Technology, Technická 3058/10, 616 00 Brno, Czech Republic

³Department of Microelectronics, Faculty of Electrical Engineering and Communication, Brno University of Technology, Technická 3058/10, 616 00 Brno, Czech Republic

⁴Institute of Physical Engineering, Faculty of Mechanical Engineering, Brno University of Technology, Technická 2896/2, 616 69 Brno, Czech Republic

⁵Department of Physics and Materials Engineering, Faculty of Technology, Tomas Bata University in Zlín, Vavrečkova 275, 760 01 Zlín, Czech Republic

Received: 6 August 2021

Accepted: 21 December 2021

Published online:

6 January 2022

© The Author(s), under exclusive licence to Springer Science+Business Media, LLC, part of Springer Nature 2022

ABSTRACT

This work proposes a structure which allows characterization of graphene monolayers under combined electric field and mechanical strain modulation. Our approach is based on a cantilever integrated into a two-dimensional graphene-based Field effect transistor (FET). This allows us to change graphene properties either separately or together via two methods. The first way involves electric field induced by the gate. The second is induction of mechanical strain caused by external force pushing the cantilever up or down. We fabricated devices using silicon-on-insulator wafer with practically zero value of residual stress and a high-quality dielectric layer which allowed us to precisely characterize structures using both mentioned stimuli. We used the electric field/strain interplay to control resistivity and position of the charge neutrality point often described as the Dirac point of graphene. Furthermore, values of mechanical stress can be obtained during the preparation of thin films, which enables the cantilever to bend after the structure is released. Our device demonstrates a novel method of tuning the physical properties of graphene in silicon and/or complementary metal-oxide-semiconductor technology and is thus promising for tunable physical or chemical sensors.

Handling Editor: Till Froemling.

Address correspondence to E-mail: imrich.gablech@ceitec.vutbr.cz; pekarek@vutbr.cz

<https://doi.org/10.1007/s10853-021-06846-6>

Introduction

Graphene as a unique material is used for physical and chemical sensing. Several types of gas and vapor nanosensors employing graphene were reported [1, 2]. To this end, graphene is most often deployed in resistive sensors [3], Field effect transistors (FET) [4], Surface acoustic wave (SAW) sensors [5], Quartz crystal microbalance (QCM) sensors [6], Microelectromechanical systems (MEMS) or Nanoelectromechanical systems (NEMS), gravimetric sensors [7], MEMS or NEMS Infrared (IR) detectors [8], and semiconductor modified hybrid sensors [9].

A single layer of carbon atoms in the sp^2 hybridization arranged in a hexagonal (honeycomb) lattice called graphene was first calculated using the tight-binding method by Wallace as a model for graphite in 1946 [10] and prepared by Geim and Novoselov in 2004 [11]. It has been an extensively studied material with numerous interesting thermal, mechanical, electrical, and optical properties [12–14]. As a monatomic layer, it exhibits a high mechanical flexibility and ambipolar electrical charge transport [14].

Furthermore, its electronic properties, such as electrical charge mobility, can be greatly influenced by induced strain. Stretching graphene results in changes of the bond length between neighboring atoms in its lattice. This has a strong effect on the electronic transport properties of graphene. This influence is not yet completely understood, and it is an avenue of many possibilities worth exploring [15]. Measurement of graphene properties as a function of the controlled induced strain can be used for determination of the strain's influence on the graphene's electrical properties. Charge carrier mobility is an essential part of any electronic device, and altering it means that we can tailor the device parameters. The electrical conductivity and mechanical strength of graphene in the in-plane direction are much higher than those in the out-plane direction. Thus, the anisotropy in the physical properties of graphene can be obtained by its orientation [16].

Uniaxial and biaxial strain on graphene has been studied using a variety of methods, schematized in Fig. 1. Uniaxial strain was induced by bending graphene on a deformable substrate (Fig. 1A) and subsequently characterized using Raman spectroscopy to probe its phonon modes [17, 18]. The uniaxial strain

moves the relative positions of the Dirac points and has a significant influence on the intervalley double-resonance processes (D and 2D peaks).

Biaxial strain is more suited to studying the strain effects on the double-resonance processes since it mimics the realistic experimental conditions where the graphene is supported by a planar substrate. Biaxial strain in graphene can be intentionally induced and controlled by three commonly used methods:

1. The graphene is placed on a material with a different thermal coefficient of expansion and is subjected to temperature changes, causing the graphene to stretch (Fig. 1B) [19].
2. The graphene is clamped across a hole in a substrate, and it is mechanically stretched by pushing the graphene into the hole using an atomic force microscopy tip (Fig. 1C) [20] or electrostatically [21].
3. The graphene can be transferred onto a piezoelectric substrate, which is controllably shrunk or elongated by applying a bias voltage. It results in the graphene having a uniform biaxial strain (Fig. 1D) [22].

Graphene is known as an excellent material capable of sustaining reversible elastic tensile strain as large as 25% [23]. This feature can be used to control graphene's electrical properties either statically or dynamically by integrating them with cantilevers leading to the novel applications of graphene [23]. These cantilevers based on MEMS or NEMS can be made of various materials. They can significantly impact the final structural properties, such as residual stress, stiffness, strain, resonance frequency, and quality factor. The structure should be fabricated by planar technology as it is a MEMS/NEMS process. Planar process compatibility offers monolithic integration of a sensing part with readout electronic circuits [24]. Biocompatibility further increases its attractiveness as it can be used in healthcare [25] to measure and detect cells, enzymes, amino acids, deoxyribonucleic acid, ribonucleic acid, etc. [26]. MEMS-based cantilever sensors have been demonstrated as feasible alternative solutions to the conventional assaying tools due to advantages such as compactness, lower detection limits, better sensitivity, cost-effectiveness, and real-time operation [27].

In this work, we studied the graphene monolayer through the simple Complementary metal-oxide

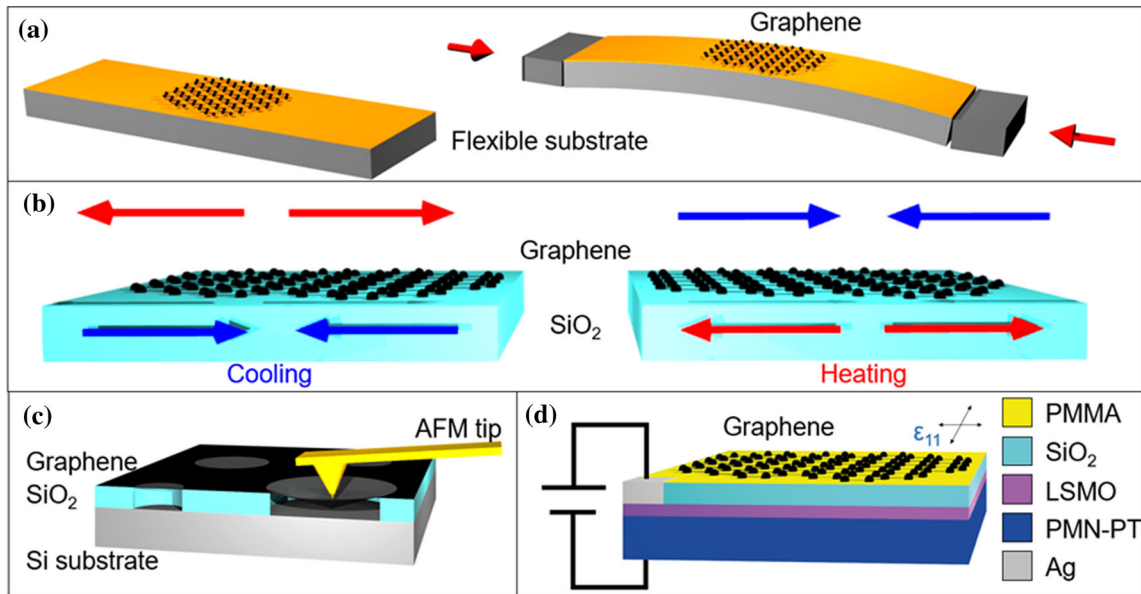


Figure 1 Schematic of engineering strain on graphene: **A** uniaxial straining on a flexible substrate, **B** thermal expansion and contraction of graphene on thermally heated or cooled SiO₂

substrate, **C** suspended graphene membrane nanoindentation, **D** the electromechanical device for inducing in-plane biaxial strain to the graphene.

semiconductor (CMOS)-compatible MEMS cantilever with planar 2D-FET structure. We electrically characterized graphene on the cantilever under different conditions such as an applied electric field and uniaxial strain. These characterizations are supported by ANSYS® Workbench mechanical analysis. We confirmed the quality of the prepared graphene by measuring its Raman spectroscopy and showing the significant peaks. Here, we demonstrate the technological processing and the utilization of the proposed structure for 2D-material strain engineering.

Experimental details

This chapter focuses on experimental details describing the most important aspects for device functionality and its fabrication to achieve graphene properties modulation in Si-based technology. Figure 2 represents the idea of device used for graphene behavior modification via electrical and mechanical stimuli.

Device design

Our goal was to fabricate a single-clamped beam (cantilever) with 2D-FET structure for the electrical measurement of graphene subjected to mechanical strain in static mode. Here, we discuss a few

important layout parameters related to the cantilever. We designed a device with $(6 \times 6) \text{ mm}^2$ dimensions containing the array of 64 cantilevers (Fig. 3). The width and length of the cantilevers were $60 \text{ }\mu\text{m}$ and $100 \text{ }\mu\text{m}$, respectively. The dimensions of the cantilever were chosen and based on our fabrication experience to make this structure easily fabricated with no critical dimensions. The length was set according to maximum achievable displacement of the micromanipulator used for cantilever bending. These dimensions do not affect the bending profile of the cantilever as much as the $(3.0 \pm 0.5) \text{ }\mu\text{m}$ thickness of Si, causing the high value of stiffness with the largest strain values on the fixed-end of cantilever. The cantilevers contain two electrodes for graphene connection placed at the clamped end of the cantilever. The gap between the electrodes determined the length of the graphene FET was set to $25 \text{ }\mu\text{m}$. Finally, the graphene width was set to $10 \text{ }\mu\text{m}$. The relatively large size of the cantilever allowed us to precisely place a micromanipulator tip for bending on the free end of the cantilever. The gate electrode is electrically contacted from the top side through the $(100 \times 100) \text{ }\mu\text{m}^2$ window in the top gate SiO₂ layer. We also employed van der Pauw structures allowing us to measure and evaluate sheet resistance of the metal layer. The dimension of all pads for probe contacts was $(100 \times 100) \text{ }\mu\text{m}^2$.

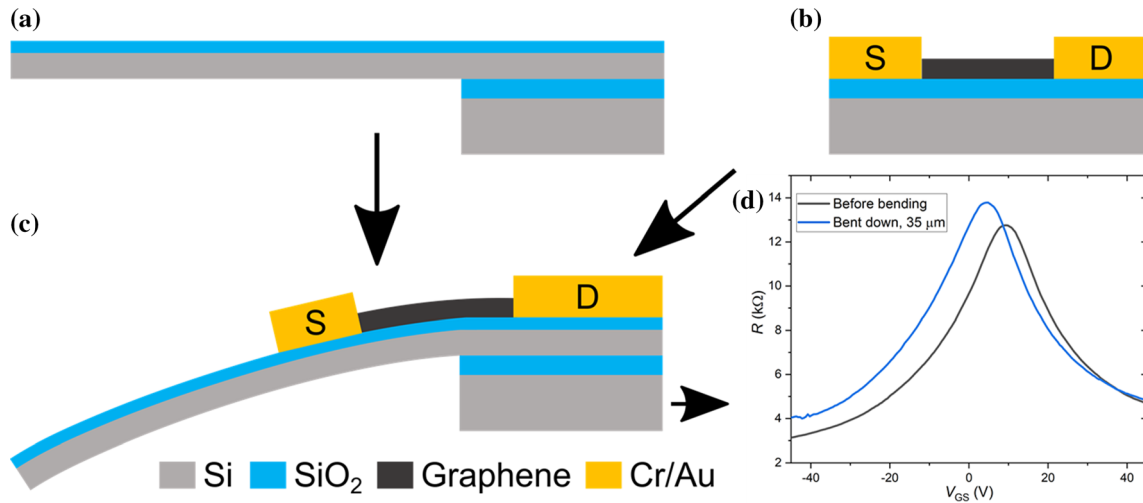
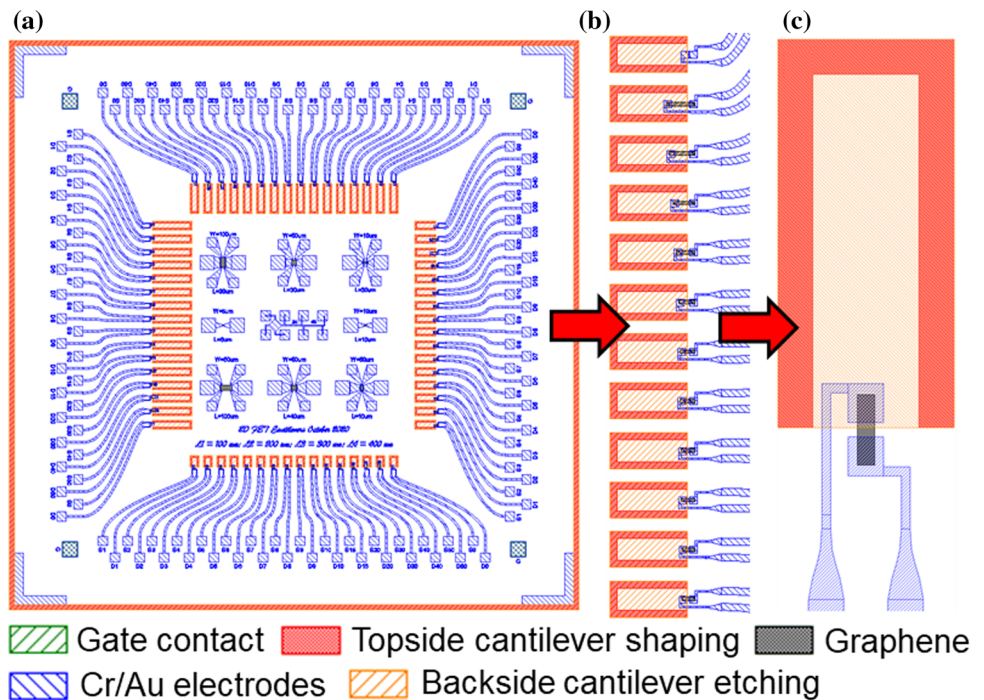


Figure 2 **A** Simple one-clamped cantilever; **B** simplified graphene FET; **C** schematic of proposed device, a combination of cantilever with graphene FET; **D** transfer characteristics shift as a result of induced strain in graphene.

Figure 3 Layout of 2D-FET device with structures for graphene strain modulation: **A** whole device with dimensions of (6 × 6) mm²; **B** cantilever array; **C** electrodes connected to shaped graphene.



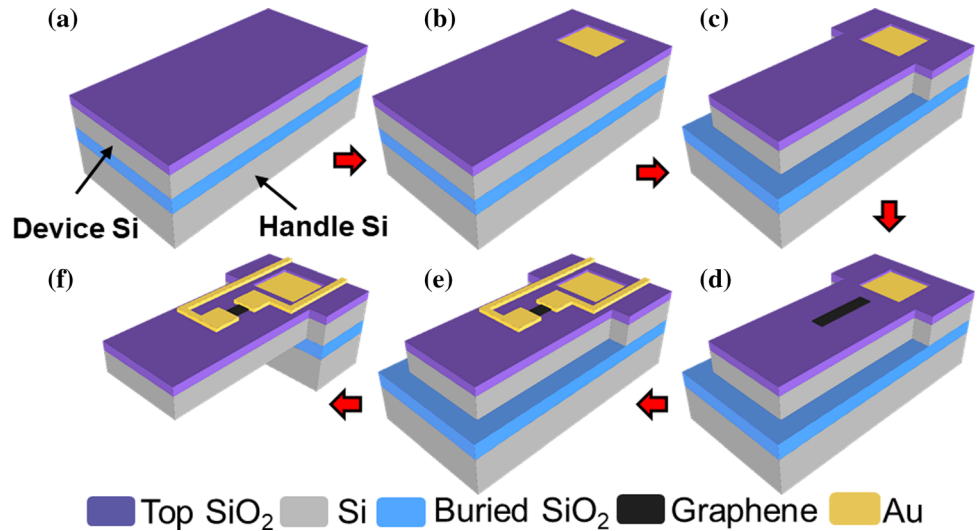
Fabrication

The fabrication of the device was done using five lithography steps (Fig. 4), including graphene patterning. The chosen substrate was Silicon on Insulator (SOI) wafer with structural (handle) Si thickness of (500 ± 10) μm and diameter of (100.0 ± 0.5) mm, while the insulation (buried SiO₂) layer was (0.50 ± 0.25) μm thick. N-doped device Si (100) layer with thickness of (3.0 ± 0.5) μm was highly

conductive with resistivity < 0.005 Ω•cm. As the first step, we grew ≈ 100 nm of SiO₂ on both sides of the substrate using the thermal oxidation process.

Next, we coated bottom resist AR-BR 5480 and positive photoresist (PR) AZ 5214 E enabling etching of SiO₂ window and lift-off process employing one lithography step to fabricate contacts to the gate electrode. The gate electrode was formed by the device Si layer of SOI wafer. SiO₂ was etched by CHF₃/Ar/O₂ plasma in a Reactive ion etching (RIE)

Figure 4 Fabrication flow of cantilever with 2D-FET structure for graphene strain engineering: **A** substrate with deposited SiO₂ layer; **B** gate contact after SiO₂ etching and Ti/Au lift-off; **C** shaping of the cantilever from topside; **D** graphene shaping; **E** Cr/Au electrode lift-off; **F** releasing the cantilever from the bottom side.

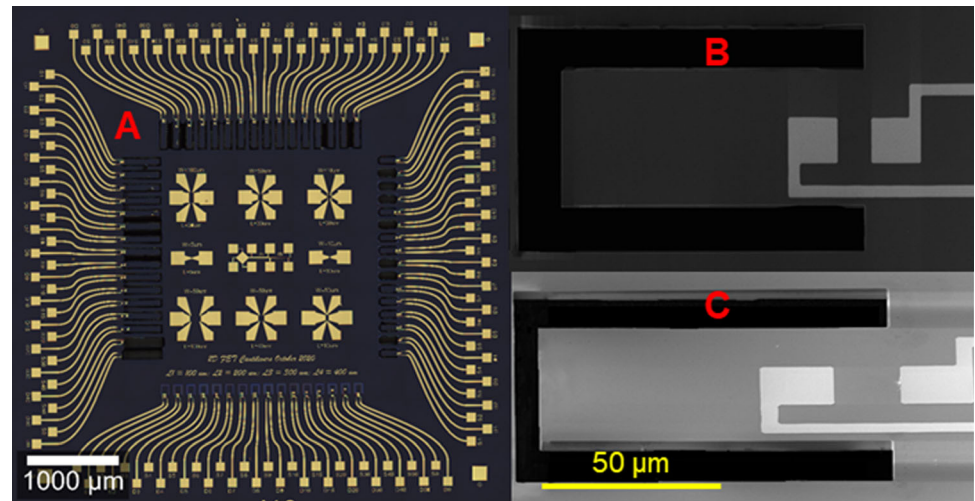


system. Subsequently, we deposited ≈ 3 nm of Ti and ≈ 50 nm of Au and lift-off process was performed in 1-Methyl-2-pyrrolidone (NMP) solution at ≈ 80 °C rinsed in propan-2-ol (IPA) and finished with O₂ plasma cleaning (Fig. 4B). In the second step, we coated the substrate with the same positive PR as before. Then, we used Deep reactive ion etching (DRIE) of the device Si layer to shape the cantilevers from top side (Fig. 4C). This process was followed by the same cleaning procedure as before.

In the next step, we transferred graphene via the wet-transfer method. The CVD-grown single-layer graphene on ≈ 100 mm of Cu foil (fabricated by Graphenea S.A., Spain) was coated with a double-layer of polymethyl methacrylate (PMMA), and the non-coated side of the Cu foil was cleansed with O₂ plasma. We dissolved the Cu layer through wet etching in an FeNO₃ solution. The floated PMMA/graphene stack layer was scooped out and displaced into a beaker filled with deionized (DI) water purified by the Millipore system to wash the solution residues out. Finally, the PMMA/graphene layer was transferred onto fabricated device and dried under a low flux of N₂. The transfer process was completed with the removal of the PMMA layer in an acetone bath overnight at ≈ 53 °C, followed by washing with IPA and DI water and drying with N₂. The CVD method is the most suitable for tasks in this framework due to the sufficient quality of graphene and the ability to cover a large area.

The graphene was subsequently patterned (Fig. 4D) using lithography with the PMMA AR-P 639.04 and AZ 5214 E PR. After the development, we used RIE, employing O₂ plasma to etch the PMMA and graphene, which took 300 s with power of ≈ 50 W at constant pressure of ≈ 0.25 Pa. Subsequently, we cleaned the wafer in acetone at ≈ 35 °C and dried it with N₂. The patterning was followed by the same lift-off process as before to create contact electrodes (Fig. 4E) for graphene. In this step, we evaporated ≈ 3 nm of Cr and ≈ 100 nm of Au, followed by the same cleaning procedure as before excluding the O₂ cleaning step. The last lithography step was aimed at shaping the cantilever (Fig. 4F) from the backside of the wafer using etching of SiO₂/handle Si/SiO₂ via DRIE. The wafer was split into single devices during the last etching step, meaning no dice cutting was necessary. The fabricated device is shown in Fig. 5. The PR was removed in NMP solution and rinsed by IPA after these steps. After these steps, we mounted devices into a leadless carrier chip with 68 pads (LCC68) using epoxy paste EPOTEK H31-D and dried the whole device at ≈ 95 °C for 4 h in the vacuum furnace at pressure of $\approx 5 \times 10^{-4}$ Pa to ensure stable mechanical connection, which is sufficient for using the device in temperatures up to ≈ 200 °C. The last step of fabrication was wire-bonding using Au wire with a diameter of ≈ 25 μ m, and the package with the device was placed

Figure 5 **A** Optical image of fabricated device; **B** SEM image of cantilever from topside; **C** SEM image of cantilever tilted by 55°.



into a socket on printed circuit board with SMA terminals.

Finite element analysis

We performed static structural analysis using ANSYS® Workbench to determine the value of stress and strain induced to the fixed end of the cantilever. A Finite element method (FEM) was used for analysis of the single-clamped cantilever. The corresponding material properties were set for each part of the model.

We chose the following types of elements for mesh generation. We used quadratic element type SOLID186, which is higher order 3D 20-node solid element that exhibits quadratic displacement behavior. Additionally, the contacts between parts were bonded to each layer, which is due to the chip construction, so the layers could not slip separately onto each other. Thus, we used the CONTA174 element, representing behavior of the contact and the slide between 3D target surfaces and a deformable surface, and TARGE170, which represents the 3D target surfaces for the associated contact elements. We also used SHELL281, which is suitable for analyzing thin to moderately thick shell structures. This element has eight nodes with six degrees of freedom at each node. This element was used for thin graphene geometry because of structure thickness of ≈ 340 pm, with lower order thickness than the rest of the model, so it must be modeled as a thin-walled entity.

We set the steady-state numerical model with 15 sub-steps, defining the displacement in ranges from -70 μm to 70 μm with two boundary

conditions (Fig. 6). The left side of the cantilever, with the graphene, was set as fixed support, and the right side of the cantilever was attributed to displacement sweeping.

Raman spectra of graphene

We measured the Raman spectra of graphene once the device was fabricated. We used the Confocal Raman imaging system Alpha 300R by WITEC, which employs a green laser with a wavelength of ≈ 532 nm and an optical microscope with objective magnification of $100\times$ (numerical aperture of 0.9 and working distance of 0.31 mm). Grating with 600 grooves $\cdot\text{mm}^{-1}$ was used. Integration time was set to 2 s with number of accumulations set to 20 to suppress the distortion in obtained spectra.

Electrical measurement

We measured the current between the source and drain electrodes (I_{DS}) by changing drain-source

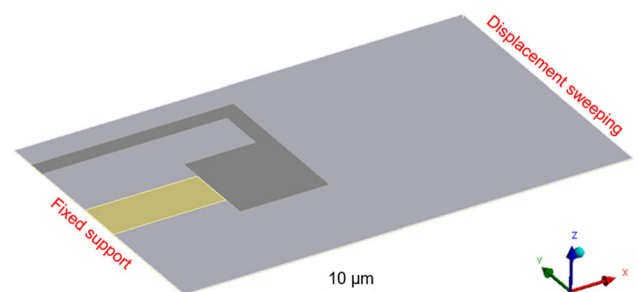


Figure 6 3D model of structure for ANSYS® Workbench computation showing the boundary conditions.

voltage (V_{DS}) at different gate-source voltages (V_{GS}). We also monitored the gate current (I_G) to inspect eventual current leak through the dielectric SiO_2 layer. The measurements were done in a N_2 atmosphere to avoid I_{DS} fluctuations due to unstable air humidity and for preventing other sorption phenomena on local graphene defects. We used a probe station MPS 150 (Cascade Microtech, USA) connected with the parameter analyzer 4200A SCS (Keithley instruments, USA). In case of the dependency of I_{DS} on mechanical strain induced by cantilever and V_{GS} , we used the micromanipulator with tip which was aimed perpendicularly to the end of the cantilever.

Results and discussion

Quality of transferred graphene

Since the devices with graphene were prepared, we wanted to check the number of graphene layers and their quality. Thus, we employed Raman spectroscopy to obtain significant graphene peaks in the Raman spectrum. We set the laser power to 5 mW, since it has been experimentally proven that higher power damages the graphene. Recorded Raman spectrum and maps are depicted in Fig. 7.

The peak position of the G and 2D peaks was at $\approx 1592 \text{ cm}^{-1}$ and $\approx 2677 \text{ cm}^{-1}$, respectively. Obtained Raman spectra show the high quality of the transferred graphene. The ratio of the G and 2D

peaks ($\approx 1:2$) proves that the transferred graphene is single-layered [28]. The low intensity of the D peak shows very low presence of defects [29]. However, as seen in Fig. 7B, the intensity of D peak is higher in specific locations, suggesting local abnormalities in graphene disorder, which is also visible in the optical image (Fig. 7E). That being said, the quality of the patterned graphene area is still more than sufficient, since most of the area has very low D-peak intensity and the defects accumulate only in local spots. Such quality is enough for intended application focused on stretching of the graphene and evaluation of the change in electrical properties.

Simulation of strain and stress

We applied mechanical force emulating the tip of the micromanipulator, causing strain through the bending of the free end of the cantilever. We did the simulation (Fig. 8) for the cantilever with a length of $100 \mu\text{m}$ with an etched hole underneath of $\approx 70 \mu\text{m}$, which was experimentally determined by a contact profilometer. Thus, we simulated the influence of displacement on the free end of the cantilever along the z axis (d_z) with a range from $-70 \mu\text{m}$ to $+70 \mu\text{m}$ on the induced strain and stress (Fig. 8).

Normal elastic strain (ε) and stress (σ) were evaluated on the model. The values of ε_{max} dependency on d_z are plotted in Fig. 9A. From the σ/ε curve (Fig. 9B), the highest value of ε_{max} and σ_{max} on the model was at maximal d_z of $-70 \mu\text{m}$ and $+70 \mu\text{m}$ at

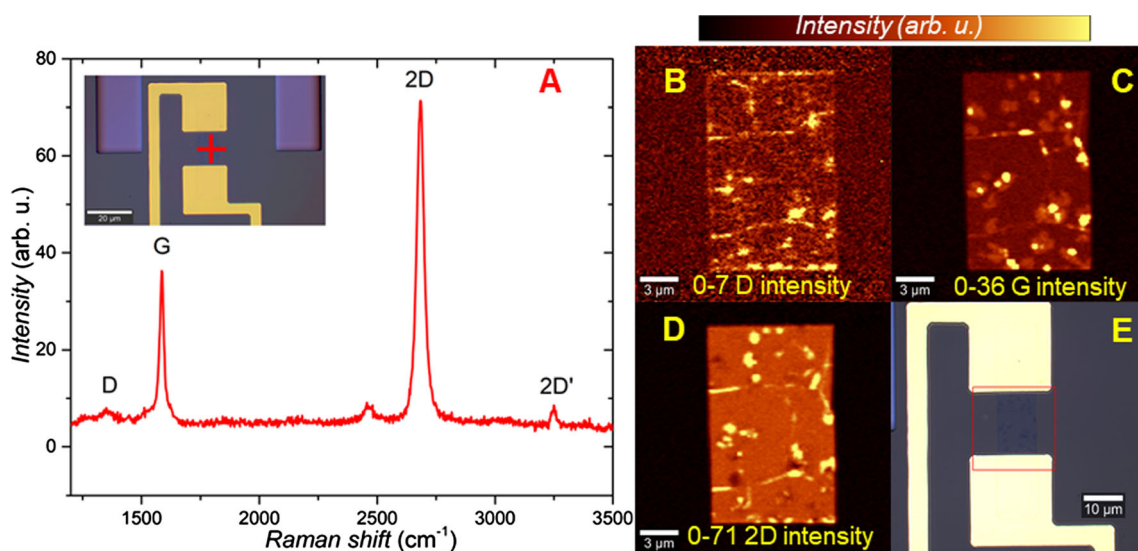


Figure 7 Raman spectra of graphene on structure after patterning: A single spectra after patterning; Raman map of B D peak, C G peak; D 2D peak; E optical image of electrode with graphene.

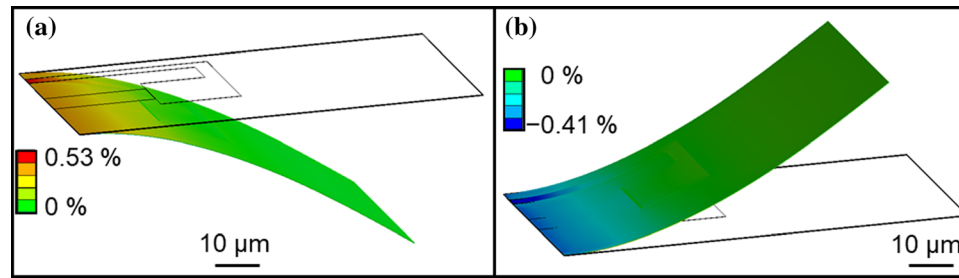


Figure 8 Obtained ϵ_{\max} values from ANSYS® Workbench for the cantilever: **A** bent down to $-70 \mu\text{m}$ causing tensile strain to graphene; **B** bent up to $+70 \mu\text{m}$ along z-axis causing compressive strain to graphene.

the fixed end of the cantilever. These values of ϵ_{\max} and σ_{\max} for the downward bent cantilever were $\approx 0.53\%$ and $\approx 2.59 \text{ GPa}$, respectively. The maximal values for the bend in the opposite direction were $\approx -0.41\%$ and $\approx -2.58 \text{ GPa}$, respectively. Such a value of σ_{\max} can be achieved and further controlled by deposition parameters, which will allow the fabrication of device containing structures with prestressed layers and will cause the bending of structure upon releasing.

Electrical characterization of the 2D-FET structure

We measured I_{DS} dependence on V_{DS} for different V_{GS} of 2D-FET graphene-based structures after the device was fabricated. Prior to electrical measurements, the sample was soaked in acetone for 24 h and also annealed in vacuum furnace at $\approx 150 \text{ }^\circ\text{C}$ for 36 h with low temperature ramp of $\approx 3 \text{ }^\circ\text{C}\cdot\text{min}^{-1}$.

Dirac point voltage (V_{Dirac}) of pristine graphene should be at value of $V_{\text{GS}} \approx 0 \text{ V}$. However, when exposed to air, the graphene becomes p-doped [30, 31] and the Dirac point moves towards higher values of V_{GS} . This is related to the adsorption of water from air humidity. The cleaning of graphene samples in acetone and annealing partly restores the original position of Dirac point which is described in the next chapter.

We wanted to prove the behavior of graphene employed as 2D-FET structure. We also measured the I_{DS} dependence on V_{GS} (transfer characteristics). The output characteristics were measured for V_{DS} in a range from -1 V to $+1 \text{ V}$. Because of the excellent quality of the SiO_2 serving as the gate dielectric, we were able to sweep the V_{GS} in a range from -50 V to $+50 \text{ V}$ with 10 V step, without any significant leakage current (I_{G}), which was monitored during all experiments and was in the order of pA units. Throughout these measurements, we verified the

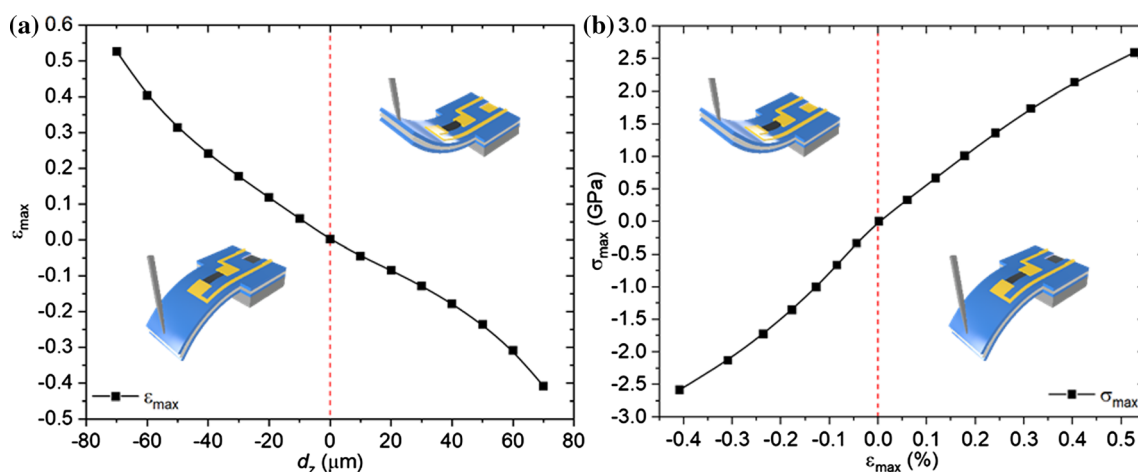


Figure 9 Obtained ϵ_{\max} values from ANSYS® Workbench for the cantilever: **A** bent down to $-70 \mu\text{m}$; **B** bent up to $+70 \mu\text{m}$ along z-axis.

functionality of 2D-FET structure with corresponding output characteristics that are shown in Fig. 10. We observed normal behavior of gated p-doped graphene [30, 31], showing a decrease in conductivity with positive V_{GS} near Dirac point of graphene. The p-doping can be attributed to the residual water molecules [30] as a consequence of sample manipulation and measurement at atmospheric conditions. The conductivity is in range from $\approx 219 \mu\text{S}\cdot\text{m}^{-1}$ to $\approx 688 \mu\text{S}\cdot\text{m}^{-1}$ and the lowest value is for $V_{GS} = 0 \text{ V}$ and 10 V (Fig. 10) which are close to Dirac point as expected. This is discussed in the next chapter and shown in Fig. 11.

Influence of the cantilever bending on IDS

As the last step, we measured I_{DS} during the cantilever bending along the z-axis at constant $V_{DS} = 1 \text{ V}$. We also changed the V_{GS} within the same range of previous measurements. The free end of the cantilever was firmly bent by the microtip fixed on sliding table with possible movement in the range from $-70 \mu\text{m}$ to $+70 \mu\text{m}$ along the z-axis. We observed a significant change of I_{DS} (Fig. 12), which was dependent on the bending. For the first set of measurements, we used a bent probe with adhesive on the tip to bend the cantilever first in downwards direction and then in the upwards direction, hence, such measurement is not so accurate, but important prediction for next experiment.

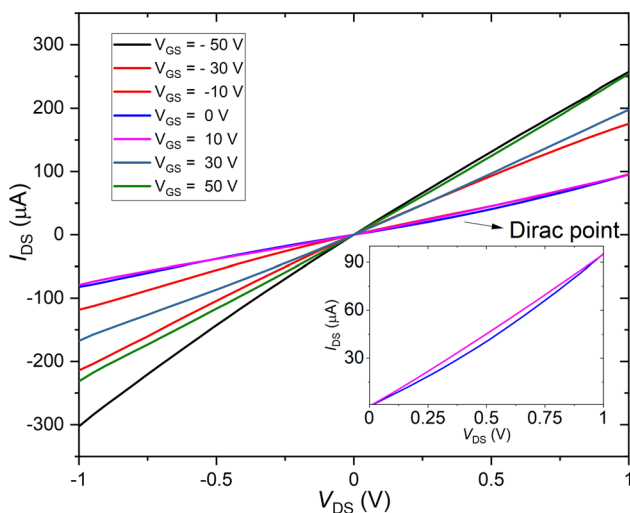


Figure 10 Output characteristics of graphene-based FET structure in range of V_{DS} from -1 V to 1 V for different V_{GS} . The detail of I_{DS} in dependence on V_{DS} for V_{DS} in the range from 0 to 1 V is depicted in the inset.

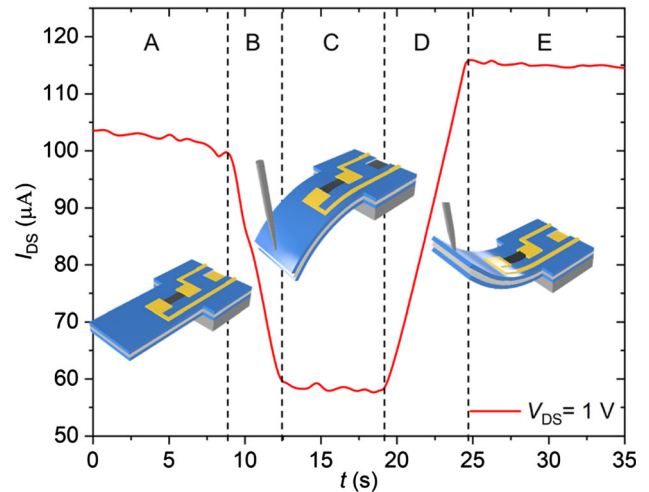


Figure 11 Time dependence of strain induction into graphene at constant $V_{DS} = 1 \text{ V}$ and $V_{GS} = -3 \text{ V}$: region **A** from $\approx 0 \text{ s}$ to $\approx 8 \text{ s}$: cantilever in straight position with $d_z = 0 \mu\text{m}$; region **B** from $\approx 8 \text{ s}$ to $\approx 12 \text{ s}$: cantilever is bending down to $d_z = -70 \mu\text{m}$; region **C** from $\approx 12 \text{ s}$ to $\approx 19 \text{ s}$: cantilever bent at the position $d_z = -70 \mu\text{m}$; region **D** from $\approx 19 \text{ s}$ to $\approx 25 \text{ s}$: cantilever is bending up to $+70 \mu\text{m}$; region **E** from $\approx 25 \text{ s}$ to $\approx 35 \text{ s}$: cantilever bent at the position $d_z = +70 \mu\text{m}$.

For the second set of measurements, more precise control over the bend depth was introduced. We used probes which were placed on top at the free end of the cantilever in the perpendicular direction to its surface. These probes were controlled by a micro-manipulator with $\approx 0.5 \mu\text{m}$ precision. We determined the distance per rotation of the microslider in the z-axis, enabling us to control the bending in the range of μm (Fig. 13).

To show the repeatability of the process, we bent the cantilever $5 \times$ during one continuous experiment with d_z of $\approx -30 \mu\text{m}$. The result can be seen in Fig. 13.

Position of the Dirac point voltage was determined in N_2 atmosphere, which ensured that no more undesired doping from air humidity took place. On one sample, the effect of Dirac point voltage shift was observed after exposing the sample to air atmosphere, as shown in (Fig. 11A).

During the first measurement (Fig. 11B) before bending of the cantilever, the V_{Dirac} of graphene was found at $V_{GS} \approx 9.3 \text{ V}$ (p-doping $2 \cdot 10^{12} \text{ cm}^{-2}$). After bending of the cantilever in downwards direction, the shift of V_{Dirac} by $\approx 4.9 \text{ V}$ was observed towards $V_{GS} \approx 4.4 \text{ V}$ (p-doping $1 \cdot 10^{12} \text{ cm}^{-2}$), as captured in second sweep of the transfer characteristic. For the

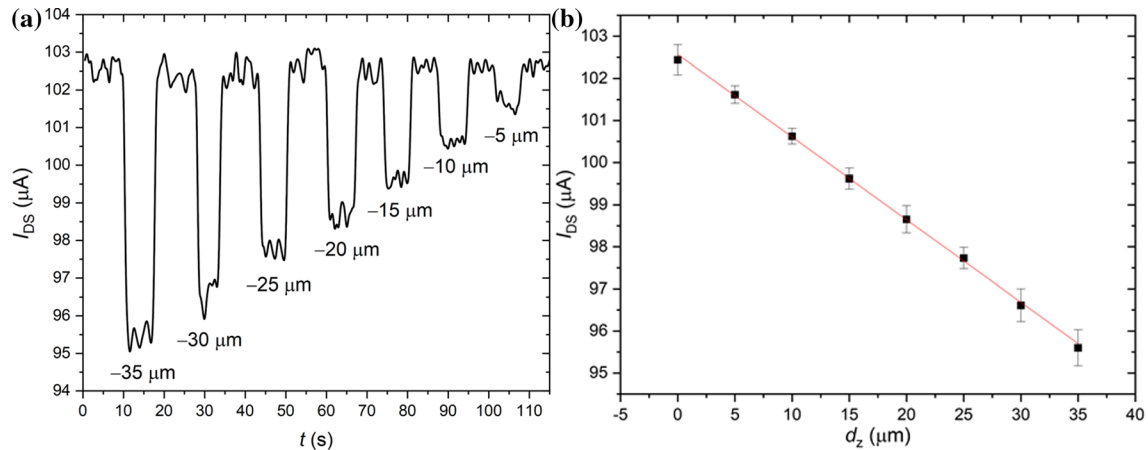


Figure 12 **A** The decrease of I_{DS} for various bending depths; **B** I_{DS} dependency on the bending, $V_{GS} = 0$ V, $V_{DS} = 1$ V..

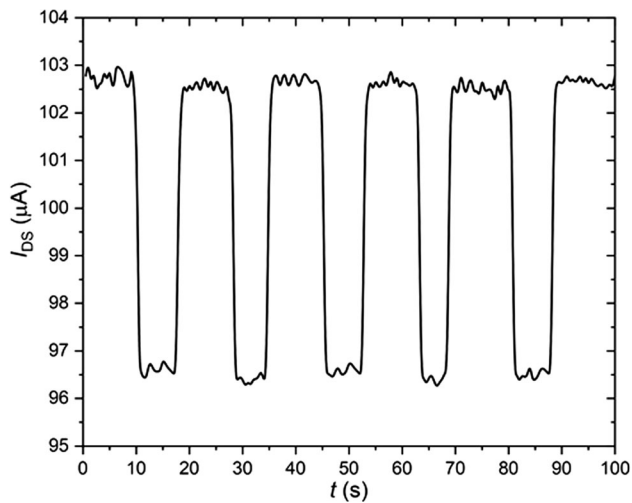


Figure 13 Repeatable decrease of I_{DS} at bending depth of ≈ -30 μm .

last sweep, the cantilever was returned to its original position. The V_{Dirac} was almost fully recovered to the same position as in the first measurement. The observed shift is a direct result of bending of the graphene sheet. The shift towards lesser values of V_{GS} means that the concentration of doped charge carriers (holes) is decreasing. Bending of the cantilever downwards induces tensile strain into the graphene, elongating the channel. This changes the distances between the atoms in crystal lattice and polarization occurs. The polarization creates electrical

field in the channel. In order to compensate for the induced field, accumulation of electrons has to take place. These electrons recombine with holes; therefore, the concentration of holes decreases. This leads to the shift of V_{Dirac} . When the cantilever is bent upwards, the vector of polarization has the opposite direction. To compensate for the induced field, charge carriers of opposite polarity have to accumulate [32].

We observed that maximum tensile ϵ_{max} of $\approx 0.53\%$ with corresponding σ_{max} of ≈ 2.59 GPa induced into graphene, caused a decrease of the I_{DS} by $\approx 10.9\%$. On the other side, the maximum ϵ_{max} of $\approx -0.41\%$ with corresponding compressive σ_{max} of ≈ -2.58 GPa increased the I_{DS} by $\approx 4.1\%$. Our obtained results correspond well to results in other publications where the graphene was strained in uniaxial directions on other non-silicon substrates [33]. These obtained results of I_{DS} in combination with σ_{max} values predict the possibility of device fabrication with built-in stress. It is generally known that the values of residual stress, in order of GPa, are possible to fabricate. Additionally, there have been many papers describing the control of residual stress, well-suited for the fabrication of structures with built-in stress that bend after cantilever release. Such phenomena will cause induced strain in the graphene, and there will be no need to bend the cantilever manually by tip or any other method. The induced strain in graphene can be adjusted for the sensitivity and/or selectivity of sensor-based

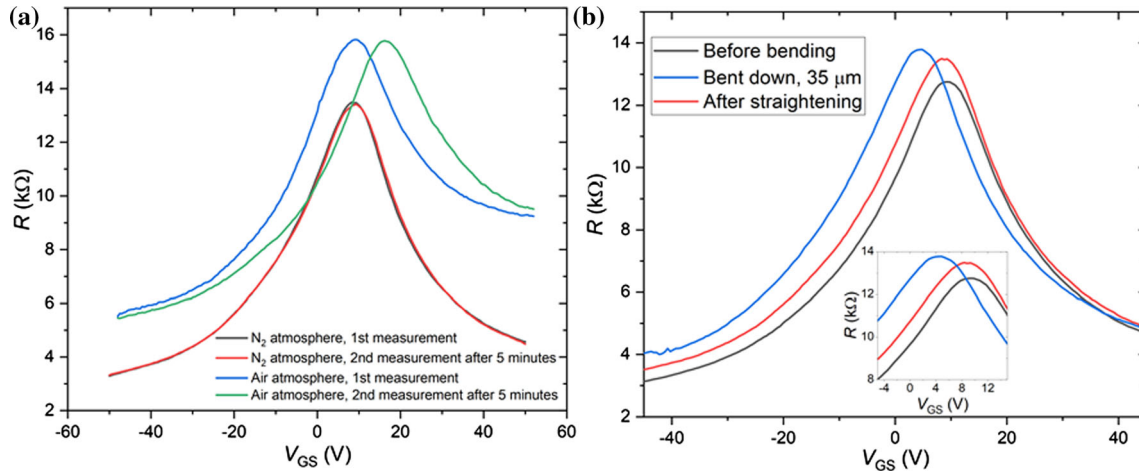


Figure 14 Transfer characteristics of graphene. **A** Effect of atmosphere on Dirac point voltage; **B** Shifting of the V_{Dirac} due to induced mechanical strain by bending.

platforms [34]. The induced strain should modify the adsorption behavior on the surface of graphene. It was shown that the selectivity towards certain gases may be improved because of the strain [35]. Control over the doping level, with the shift of Dirac point, could be important for wearable mechanical sensors and flexible electric devices [32]. Moreover, the work shows the magnitude of conductivity changes is in order of percent, which is comparable to a standard response of graphene FET-based gas and biosensors. Therefore, the induced strain artificially prepared, or as a result of a production process, must be considered.

Conclusions

We proposed and proved a new method for stretching of graphene 2DFET structure on a simple MEMS cantilever in Si technology. The bending of the cantilever with graphene was done using a micromanipulator with a micro-hook, which allowed us to bend the cantilever up and down along the z-axis but with moderate precision; nevertheless, it proved the functionality of structure. We achieved ϵ_{max} and σ_{max} values of $\approx 0.53\%$ and ≈ 2.59 GPa, respectively, while the cantilever was bent down to $-70 \mu\text{m}$. When we bent the cantilever to the opposite side, up to $+70 \mu\text{m}$, we achieved an ϵ_{max} of $\approx -0.41\%$ and an σ_{max} of ≈ -2.58 GPa, respectively. Next, we evaluated downward cantilever bending using a

micromanipulator with a very thin and sharp tip with precision of $\pm 0.125 \mu\text{m}$, which was placed on the cantilever end in the perpendicular direction. We were able to control the bending with d_z in the range from $\approx 0 \mu\text{m}$ to the $\approx -35 \mu\text{m}$. Such stimuli had direct influence on resistivity and position of Dirac point. We observed significant changes in I_{DS} while the cantilever was bending; V_{GS} did not influence the perceptual change of I_{DS} because it only caused the shift along x-axis meaning the shift of Dirac point which is accompanied with change of physical properties mainly due to changes of atomic spacing causing the induction of local electric field. This results in the change of charge carrier concentration.

Our experiment proves the possibility of MEMS fabrication with controlled built-in residual stress, which will modulate the graphene’s mechanical properties after the cantilever is released. Such a structure can be bent up or down according to the value of built-in stress, which can be comfortably controlled in order of GPa with utilization of standard physical vapor deposition methods, such as evaporation or sputtering. This work opens the door for sensitivity and selectivity selection by tuning the physical properties in graphene-based sensors, or alternatively, the same structures can be adapted to other 2DFET materials in silicon or eventually CMOS-based technology.

Acknowledgements

We acknowledge the support of the Grant Agency of the Czech Republic under contract GJ18-06498Y and CEITEC Nano Research Infrastructure (ID LM2015041, MEYS CR, 2016–2019), CEITEC Brno University of Technology. The infrastructure of the SIX Center of BUT was utilized to conduct the experiments. This work was also supported by the specific graduate research of the Brno University of Technology No. FEKT-S-20-6206.

References

- [1] Yang L, Xiao W, Wang J, Li X, Wang L (2021) Formaldehyde gas sensing properties of transition metal-doped graphene: A first-principles study. *J Mater Sci* 56(21):12256–12269. <https://doi.org/10.1007/s10853-021-05951-w>
- [2] You X, Yang J, Dong S (2021) Structural and functional applications of 3d-printed graphene-based architectures. *J Mater Sci* 56(15):9007–9046. <https://doi.org/10.1007/s10853-021-05899-x>
- [3] Schedin F, Geim AK, Morozov SV, Hill EW, Blake P, Katsnelson MI, Novoselov KS (2007) Detection of individual gas molecules adsorbed on graphene. *Nat Mater* 6(9):652–655. <https://doi.org/10.1038/nmat1967>
- [4] Ohno Y, Maehashi K, Matsumoto K (2010) Chemical and biological sensing applications based on graphene field-effect transistors. *Biosens Bioelectron* 26(4):1727–1730. <https://doi.org/10.1016/j.bios.2010.08.001>
- [5] Arash B, Wang Q, Duan WH (2011) Detection of gas atoms via vibration of graphenes. *Phys Lett A* 375(24):2411–2415. <https://doi.org/10.1016/j.physleta.2011.05.009>
- [6] Yao Y, Chen XD, Guo HH, Wu ZQ (2011) Graphene oxide thin film coated quartz crystal microbalance for humidity detection. *Appl Surf Sci* 257(17):7778–7782. <https://doi.org/10.1016/j.apsusc.2011.04.028>
- [7] Basu S, Bhattacharyya P (2012) Recent developments on graphene and graphene oxide based solid state gas sensors. *Sens Actuators B-Chem* 173:1–21. <https://doi.org/10.1016/j.snb.2012.07.092>
- [8] Qian Z, Hui Y, Liu F, Kang S, Kar S, Rinaldi M (2016) Graphene–aluminum nitride nems resonant infrared detector. *Microsyst Nanoeng* 2:16026
- [9] Yi J, Lee JM, Il PW (2011) Vertically aligned zno nanorods and graphene hybrid architectures for high-sensitive flexible gas sensors. *Sens Actuators B-Chem* 155(1):264–269. <https://doi.org/10.1016/j.snb.2010.12.033>
- [10] Wallace PR (1947) The band theory of graphite. *Phys Rev* 71(9):622–634
- [11] Novoselov KS, Geim AK, Morozov SV, Jiang D, Zhang Y, Dubonos SV, Grigorieva IV, Firsov AA (2004) Electric field effect in atomically thin carbon films. *Science* 306(5696):666–669. <https://doi.org/10.1126/science.1102896>
- [12] Allen MJ, Tung VC, Kaner RB (2010) Honeycomb carbon: A review of graphene. *Chem Rev* 110(1):132–145. <https://doi.org/10.1021/cr900070d>
- [13] Fiori G, Bonaccorso F, Iannaccone G, Palacios T, Neumaier D, Seabaugh A, Banerjee SK, Colombo L (2014) Electronics based on two-dimensional materials. *Nat Nano* 9(10):768–779. <https://doi.org/10.1038/nnano.2014.207>
- [14] Novoselov KS, Falko VI, Colombo L, Gellert PR, Schwab MG, Kim K (2012) A roadmap for graphene. *Nature* 490(7419):192–200
- [15] Zhang ZH, Liu XF, Yu J, Hang Y, Li Y, Guo YF, Xu Y, Sun X, Zhou JX, Guo WL (2016) Tunable electronic and magnetic properties of two-dimensional materials and their one-dimensional derivatives. *Comput Mol Sci* 6(4):324–350. <https://doi.org/10.1002/wcms.1251>
- [16] Zhang XY, Xu ZW, Hui L, Xin J, Ding F (2012) How the orientation of graphene is determined during chemical vapor deposition growth. *J Phys Chem Lett* 3(19):2822–2827. <https://doi.org/10.1021/jz301029g>
- [17] Biro LP, Nemes-Incze P, Lambin P (2012) Graphene: Nanoscale processing and recent applications. *Nanoscale* 4(6):1824–1839. <https://doi.org/10.1039/c1nr11067e>
- [18] Roldan R, Castellanos-Gomez A, Cappelluti E, Guinea F (2015) Strain engineering in semiconducting two-dimensional crystals. *J Phys Condens Matter*. <https://doi.org/10.1088/0953-8984/27/31/313201>
- [19] Yoon D, Son YW, Cheong H (2011) Negative thermal expansion coefficient of graphene measured by raman spectroscopy. *Nano Lett* 11(8):3227–3231. <https://doi.org/10.1021/nl201488g>
- [20] Lee C, Wei X, Kysar JW, Hone J (2008) Measurement of the elastic properties and intrinsic strength of monolayer graphene. *Science* 321(5887):385
- [21] Lindahl N, Midtvedt D, Svensson J, Nerushev OA, Lindvall N, Isacson A, Campbell EEB (2012) Determination of the bending rigidity of graphene via electrostatic actuation of buckled membranes. *Nano Lett* 12(7):3526–3531. <https://doi.org/10.1021/nl301080v>
- [22] Ding F, Ji HX, Chen YH, Herklotz A, Dorr K, Mei YF, Rastelli A, Schmidt OG (2010) Stretchable graphene: A close look at fundamental parameters through biaxial straining. *Nano Lett* 10(9):3453–3458. <https://doi.org/10.1021/nl101533x>

- [23] Si C, Sun ZM, Liu F (2016) Strain engineering of graphene: A review. *Nanoscale* 8(6):3207–3217. <https://doi.org/10.1039/c5nr07755a>
- [24] Fischer AC, Forsberg F, Lapisa M, Bleiker SJ, Stemme G, Roxhed N, Niklaus F (2015) Integrating mems and ics. *Microsyst Nanoeng* 1(1):15005. <https://doi.org/10.1038/micronano.2015.5>
- [25] Hasan MM, Hossain MM (2021) Nanomaterials-patterned flexible electrodes for wearable health monitoring: A review. *J Mater Sci* 56(27):14900–14942. <https://doi.org/10.1007/s10853-021-06248-8>
- [26] Grayson ACR, Shawgo RS, Johnson AM, Flynn NT, Li YW, Cima MJ, Langer R (2004) A biomems review: Mem technology for physiologically integrated devices. *Proc IEEE* 92:6–21. <https://doi.org/10.1109/jproc.2003.820534>
- [27] Mathew R, Ravi SA (2018) A review on surface stress-based miniaturized piezoresistive su-8 polymeric cantilever sensors. *Nano-Micro Letters* 10(2):35. <https://doi.org/10.1007/s40820-018-0189-1>
- [28] Gayathri S, Jayabal P, Kottaisamy M, Ramakrishnan V (2014) Synthesis of few layer graphene by direct exfoliation of graphite and a raman spectroscopic study. *AIP Adv* 4(2):027116. <https://doi.org/10.1063/1.4866595>
- [29] Wu J-B, Lin M-L, Cong X, Liu H-N, Tan P-H (2018) Raman spectroscopy of graphene-based materials and its applications in related devices. *Chem Soc Rev* 47(5):1822–1873. <https://doi.org/10.1039/C6CS00915H>
- [30] Melios C, Giusca CE, Panchal V, Kazakova O (2018) Water on graphene: Review of recent progress. *2D Materials* 5:022001. <https://doi.org/10.1088/2053-1583/aa9ea9>
- [31] Bartošik M, Mach J, Piastek J, Nezval D, Konečný M, Švarc V, Ensslin K, Šikola T (2020) Mechanism and suppression of physisorbed-water-caused hysteresis in graphene fet sensors. *ACS Sensors* 5(9):2940–2949. <https://doi.org/10.1021/acssensors.0c01441>
- [32] Hu G, Wu J, Ma C, Liang Z, Liu W, Liu M, Wu JZ, Jia C-L (2019) Controlling the dirac point voltage of graphene by mechanically bending the ferroelectric gate of a graphene field effect transistor. *Mater Horiz* 6(2):302–310. <https://doi.org/10.1039/C8MH01499J>
- [33] Topsakal M, Bagci K, Ciraci S (2010) Current-voltage (*i-v*) characteristics of armchair graphene nanoribbons under uniaxial strain. *Phys Rev B*. <https://doi.org/10.1103/PhysRevB.81.205437>
- [34] Cao ZX, Yao BC, Qin CY, Yang R, Guo YH, Zhang YF, Wu Y, Bi L, Chen YF, Xie ZD, Peng GD, Huang SW, Wong CW, Rao YJ (2019) Biochemical sensing in graphene-enhanced microfiber resonators with individual molecule sensitivity and selectivity. *Light-Sci Appl*. <https://doi.org/10.1038/s41377-019-0213-3>
- [35] Qiao X, Zhang Q, Suzuki K (2020) Development of a strain-controlled graphene-based highly sensitive gas sensor In ASME 2020. Int Mech Eng Congress Exposition. <https://doi.org/10.1115/imece2020-23581>

Publisher's Note Springer Nature remains neutral with regard to jurisdictional claims in published maps and institutional affiliations.



Article

Simple and Efficient AlN-Based Piezoelectric Energy Harvesters

Imrich Gablech ^{1,2,*} , Jaroslav Klempa ^{1,2} , Jan Pekárek ^{1,2} , Petr Vyroubal ³ , Jan Hrabina ⁴ ,
Miroslava Holá ⁴ , Jan Kunz ⁵ , Jan Brodský ¹ and Pavel Neužil ⁶

¹ Central European Institute of Technology, Brno University of Technology, CZ-61600 Brno, Czech Republic; ja.klempa@gmail.com (J.K.); pekarek@vutbr.cz (J.P.); jan.brodsky@ceitec.vutbr.cz (J.B)

² Department of Microelectronics, Faculty of Electrical Engineering and Communication, Brno University of Technology, CZ-61600 Brno, Czech Republic

³ Department of Electrical and Electronic Technology, Faculty of Electrical Engineering and Communication, Brno University of Technology, CZ-61600 Brno, Czech Republic; vyroubal@feec.vutbr.cz

⁴ Institute of Scientific Instruments, Czech Academy of Sciences, CZ-61264 Brno, Czech Republic; hrabina@isibrno.cz (J.H.); hola@isibrno.cz (M.H.)

⁵ Department of Control and Instrumentations, Faculty of Electrical Engineering and Communication, Brno University of Technology, CZ-61600 Brno, Czech Republic; kunzj@feec.vutbr.cz

⁶ Department of Microsystem Engineering, School of Mechanical Engineering, Northwestern Polytechnical University, Xi'an 710072, China; pavel.neuzil@gmail.com

* Correspondence: imrich.gablech@ceitec.vutbr.cz; Tel.: +420-54114-9221

Received: 3 January 2020; Accepted: 27 January 2020; Published: 28 January 2020



Abstract: In this work, we demonstrate the simple fabrication process of AlN-based piezoelectric energy harvesters (PEH), which are made of cantilevers consisting of a multilayer ion beam-assisted deposition. The preferentially (001) orientated AlN thin films possess exceptionally high piezoelectric coefficients d_{33} of (7.33 ± 0.08) pC·N⁻¹. The fabrication of PEH was completed using just three lithography steps, conventional silicon substrate with full control of the cantilever thickness, in addition to the thickness of the proof mass. As the AlN deposition was conducted at a temperature of ≈ 330 °C, the process can be implemented into standard complementary metal oxide semiconductor (CMOS) technology, as well as the CMOS wafer post-processing. The PEH cantilever deflection and efficiency were characterized using both laser interferometry, and a vibration shaker, respectively. This technology could become a core feature for future CMOS-based energy harvesters.

Keywords: AlN; micro-electro-mechanical systems (MEMS) cantilever; complementary metal oxide semiconductor (CMOS) compatible; energy harvesting; high performance

1. Introduction

Energy harvesting has recently attracted significant attention as a key power source where changing batteries in applications is not practical, or in low-power autonomous sensors and micro-devices, as a replacement of electrochemical batteries.

Several methods of harvesting ambient energies have been investigated, including solar energy, wind, flowing water, waste heat, electromagnetic waves, or vibrations [1,2]. However, most of them require the outside environment. The utilization of mechanical vibrations represent a suitable alternative for any environment, including indoors, as well as low-power autonomous sensors and microdevices [3].

Electrostatic and electromagnetic induction, and piezoelectricity can all typically be exploited as transducing mechanisms to convert mechanical energy into electrical [4]. However, from these, piezoelectric energy harvesters (PEHs) exhibit high-energy density and are, therefore, more suitable for practical applications [5]. Moreover, piezoelectric materials have an inherent capability to directly

convert mechanical stress/strain energy into electrical energy, therefore, such devices are compact and possess simpler designs, compared to their electromagnetic and electrostatic counterparts. Furthermore, such devices can be fabricated by micromachining techniques and directly integrated into monolithic, micro-electro-mechanical systems (MEMS) [6].

Numerous piezoelectric materials were investigated for energy harvesting in MEMS applications, but the most commonly used are ZnO [7], lead zirconate titanate (PZT) [8,9], polyvinylidene fluoride (PVDF) [10], and AlN [11]. In particular, AlN, prepared by sputtering, can be implemented in standard complementary metal oxide semiconductor (CMOS) technology, as well as the CMOS wafer post-processing [12], thereby, enabling the integration of PEH with active devices. Other piezoelectric materials such as PZT, ZnO, and PVDF possess contamination risks for CMOS processing lines [13], while AlN, deposited by the metal-organic chemical vapor deposition (MOCVD) technique, requires high temperature, which prohibits its integration with CMOS devices.

Sputtered AlN is a promising material for PEH applications, due to low-temperature preparation, unique physical properties (such as a high thermal stability, with a melting point of ≈ 2100 °C and piezoelectric effect up to temperatures of ≈ 1150 °C; high longitudinal velocity of $\approx 11,000$ m·s⁻¹; and wide band gap of ≈ 6.2 eV), high level of mechanical stiffness, and good piezoelectric and dielectric properties [11].

The single side clamped cantilever structure, due to its simple design and fabrication, is a convenient device to characterize properties of PEHs: It can produce large mechanical strain within the piezoelectric layer with its vibrations [14]. The amplitude of generated piezoelectric voltage and power depends on the device's working frequency, as well as the value of induced strain. The first resonance frequency (f_r) of a cantilever is the lowest vibrational mode, exhibiting the highest achievable strain and displacement. The goal of the harvester design is to operate at the f_r to achieve maximum power output.

Normalized power density (NPD), together with output power (P) and frequency range, also known as bandwidth (BW), are the most widely used metrics to evaluate the performance of PEH [15]. They enable the comparison of different PEHs and provide necessary information for figure of merit (FoM) calculations [16],

$$FoM = NPD \times BW \quad (1)$$

where the NPD is defined as P divided by the effective volume (V) and the square of the input acceleration (A),

$$NPD = \frac{P}{V \cdot A^2} \quad (2)$$

and where BW is defined as,

$$BW = f_2 - f_1 \quad (3)$$

where $f_{1,2}$ are half-power, cut-off frequencies, also known as full width at half maximum (FWHM). Bandwidth comparison is often complicated, as its definition is not standardized: Sometimes it is defined by frequencies at FWHM of the spectrum, by 1 dB or 3 dB bandwidth, or the data is not available.

Fabrication of PEHs is notoriously complex, requiring five or more lithography steps, in addition to expensive silicon-on-insulator (SOI) substrates. Here we show a simple method to prepare PEH with a high value of piezoelectric coefficients of (7.33 ± 0.08) pC·N⁻¹, using low temperature ion-assisted deposition, making it fully CMOS-compatible, including the CMOS wafer post-processing.

2. Materials and Methods

2.1. Chip Design and Fabrication

Technology flow and layout were designed to allow all thin films to be deposited sequential inside the sputtering system. This is a key feature, as it enables the deposition of all layers without breaking the vacuum, thereby, resulting in high-quality layers and good adhesion between them, while eliminating contamination and achieving a high performance in the piezoelectric layer.

The beam and proof mass had dimensions of $2000\ \mu\text{m} \times 4000\ \mu\text{m}$ and $2000\ \mu\text{m} \times 2000\ \mu\text{m}$, respectively. A piezoelectric layer between two electrodes, with dimensions of $1500\ \mu\text{m} \times 2000\ \mu\text{m}$, is placed on one end close to the fixed edge (Figure 1).

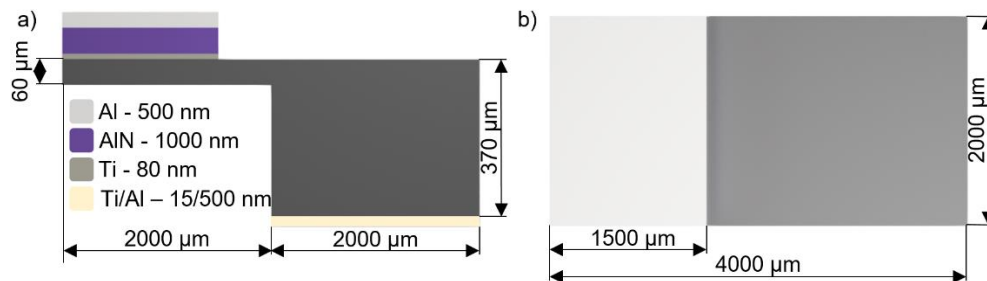


Figure 1. Layer composition and their dimensions of piezoelectric energy harvesters (PEH) (not to scale): (a) side view; (b) top view.

We had to remove a relatively large area of Si substrate, as its direct etching would result in a high loading factor and etching process instability. We designed $40\ \mu\text{m}$ wide trenches around the PEH beams, on the both sides of the substrate. Once the deep reactive ion etching (DRIE) from both sides was completed, the area surrounded by the trenches fell away from the substrate without the necessity to etch it, as demonstrated in the design in supplementary materials of previously published work [17]. A large-area substrate removal around the PEH beams led to their unobstructed movement.

The fabrication was conducted using double-side polished Si (100) N-doped wafers with a diameter of $\approx 100\ \text{mm}$, thickness of $\approx 370\ \mu\text{m}$, and resistivity of $< 0.005\ \Omega\cdot\text{cm}$. We deposited all sequential thin films, layer by layer (Figure 2a), using an ion-beam assisted deposition (IBAD) instrument, without breaking the vacuum between depositions. The wafers were loaded into the IBAD instrument and the system was evacuated to a base pressure of $\approx 9 \times 10^{-7}\ \text{Pa}$. Wafers were then pre-cleaned using a secondary ion-beam source with Ar plasma with $30\ \text{V}$ beam voltage (BV), for a duration of $300\ \text{s}$. We then deposited $\approx 80\ \text{nm}$ of Ti, serving as a seed layer for consequent AlN (001) deposition, as well as an electrical connection between the AlN and Si substrate. We activated the primary Kaufman ion-beam source, using a BV of $200\ \text{V}$, resulting in a (001) oriented layer of Ti [18,19]. This was followed with a change in the BV to $400\ \text{V}$ and the addition of N_2 to the primary ion-beam source, with a ratio of 1:1 to Ar. In addition, we employed the secondary ion-beam source for substrate bombardment, using N_2 plasma at a $BV = 30\ \text{V}$ and performed reactive sputtering of highly (001) oriented AlN from the Al target, to achieve the desired thickness of $\approx 1000\ \text{nm}$ [20].

Finally, we halted the secondary ion-beam source and N_2 from the primary source and deposited the Al layer using a BV of $900\ \text{V}$, achieving an Al thickness of $\approx 500\ \text{nm}$, suitable for subsequent wire-bonding.

The wafers were then subjected to just three lithography steps. The first lithography step was completed using positive photoresist (PR), with a desired thickness of $\approx 1.4\ \mu\text{m}$, to define the shape of the top electrode, piezoelectric layer, and underneath Ti in a single stage. It was followed by reactive ion etching (RIE) with combined Cl_2 and BCl_3 gases, using an optical spectrometer to monitor the etching process (Figure 2b). After etching and PR removal, we performed the second lithography, using PR with a thickness of $\approx 10\ \mu\text{m}$ to define the PEH shape and the DRIE process to etch $\approx 40\ \mu\text{m}$ wide and $\approx 150\ \mu\text{m}$ deep trenches around them (Figure 2c). Following this, we removed the thick PR and spin-coated, front side of the Si substrate with a standard PR to protect it; this subsequently deposited Ti and Al with a thickness of $\approx 15\ \text{nm}$, and $\approx 500\ \text{nm}$, respectively, on the back side of the Si wafer, forming backside electrode contact. We conducted backside lithography, with front-to-back alignment, using thick PR and etched both metals using Cl_2/BCl_3 -based reaction ion etching (RIE). We continued with DRIE, through the Si substrate, until the inner parts and chips were separated from each other (Figure 2d). The thickness of PEH in areas without the proof mass was $\approx 50\ \mu\text{m}$. The chips were mounted individually on a supporting base of Si substrate, using a drop of Fomblin[®] oil, and

etched using the DRIE method, until we reached the desired thickness (Figure 2e) of a few tens of μm . The proof mass thickness was $\approx 370 \mu\text{m}$, allowing us to fabricate the PEH with a high mass-to-volume ratio. The residual PR and Fomblin[®] were then removed with O_2 plasma.

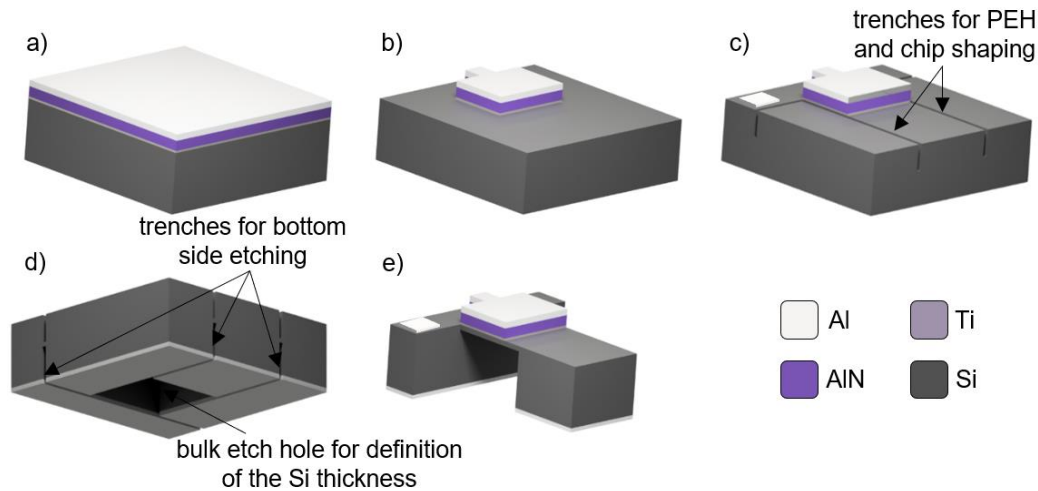


Figure 2. Fabrication process flow (not to scale): (a) Deposited layers on top side of Si substrate; (b) patterning of Ti/AlN/Ti/Al structure; (c) top-side trench etching using deep reactive ion etching (DRIE) method; (d) metallization followed by back-side etching causing separation of chips; (e) back-side etching, using DRIE method to form final structure.

Finally, we cut a $4.5 \times 4.5 \text{ mm}^2$ hole, using an yttrium aluminum garnet (also known as YAG) laser into the center of the leadless chip carrier with 68 pads (LCC68). The individual chips were then mounted using silver conductive paste into the LCC68 (Figure 3a). The mounted chips had free vertical movement within the mass of the package (Figure 3b).

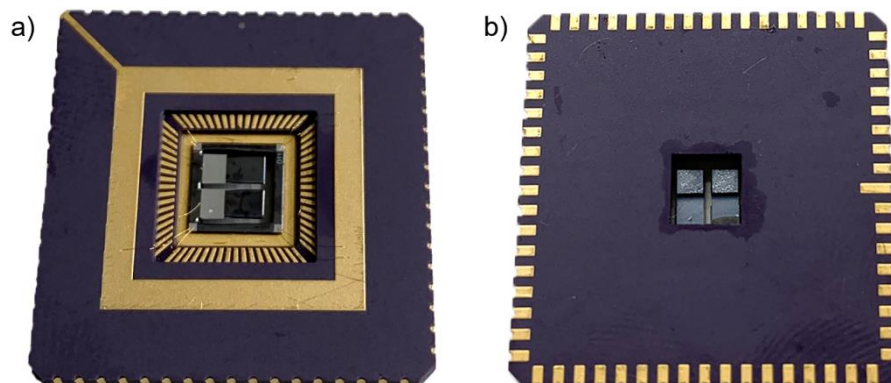


Figure 3. Fabricated PEH mounted in LCC68: (a) top view; (b) bottom view showing hole and PEH mass.

2.2. X-Ray Characterization

Deposited Ti and AlN layers were residual stress-free, which was determined from wafer curvature measurement. We also conducted the X-ray measurement using Bragg-Brentano setup to determine corresponding peak positions (Figure 4) for $2\theta \approx 38.35^\circ$ for Ti (001) and $2\theta \approx 36.06^\circ$ for AlN (001). These peaks positions also perfectly fit residual stress-free values determined from lattice parameters we published earlier [18,20]. Such prepared (001) oriented AlN exhibits a high value of piezoelectric coefficient d_{33} of $(7.33 \pm 0.08) \text{ pC}\cdot\text{N}^{-1}$ along c-axis.

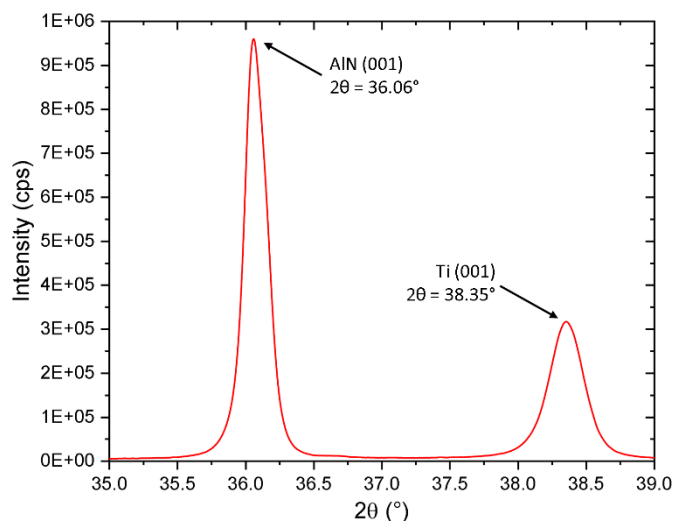


Figure 4. X-ray diffractogram determined using Bragg-Brentano setup showing 2θ peak positions of Ti (001) $\approx 38.35^\circ$ and AlN (001) $\approx 36.06^\circ$.

2.3. Finite Element Simulation

We performed finite element method (FEM) analyses of single clamped PEH using the ANSYS® Workbench with the Piezo and MEMS module. The model geometry was formed with a SOLID186 and SOLID226 3D element with a 20-node coupled-field, solid supporting piezoelectric analysis [21]. We performed coupled solution using an electrostatic and structural solver (Figure 5) via the piezoelectric matrix where $\{T\}$ is the stress matrix, $\{c\}$ is the elastic stiffness matrix, $\{S\}$ is the elastic strain vector, $\{e\}$ is the piezoelectric matrix, $\{E\}$ is the electric field intensity vector, $\{D\}$ is the electric flux density vector, and $\{\epsilon_d\}$ is the dielectric permittivity matrix.

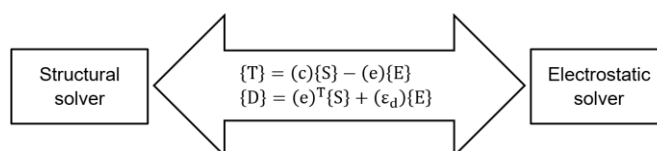


Figure 5. Scheme of coupled solution for electrostatic and structural solver, employing piezoelectric matrix.

Once we built the model, we performed modal analysis to determine resonance frequencies of the entire system. It was followed by a harmonic analysis used to determine PEH behavior under an external force, using the results from the modal analysis as boundary conditions. Then we applied the excitation voltage on electrodes to determine the displacement of PEH and compare it with experimental results.

Following this, we added a load resistor (R_L) into the model, applying CIRCU94 circuit 2-node beam elements using ANSYS® parametric design language (also known as APDL) commands, and examined the dependence of generated power (P_S) on the amplitude of acceleration and the value of parallel connected R_L (Figure 6).

This task was realized as a combined analysis, involving the mechanics of a rigid body with a link to a piezoelectric effect (or the inverse piezoelectric effect) and the provision of a bond to an electrical circuit simulating R_L .

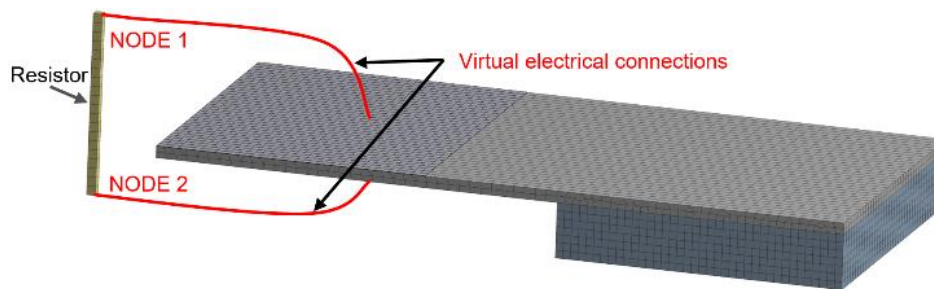


Figure 6. Scheme of PEH model with electrically connected R_L .

3. Results and Discussion

We characterized PEHs using two methods to validate their parameters and compare them to the FEM simulations from the ANSYS® Workbench.

3.1. Laser Interferometer Characterization

We chose the laser interferometer measurement as the first method for resonance frequency and displacement determination (Figure 7a). We used a diode-pumped solid-state laser with single longitudinal-mode operation and output wavelength (λ) of ≈ 532 nm. The interferometric setup employs a classic Michelson arrangement. Illuminating light enters the polarizing beam-splitter, where it is split into two beams: The measuring beam passes to the sample, where it is reflected with phase shift into the beam splitter and on to the detector; the second (reference) beam is reflected from a fixed-reference mirror. Both beams interfere at the detector, which converts the optical signal of the incident beams into an electrical signal that is displayed on an oscilloscope (Figure 7b). The voltage power supply, with an alternate current (V_{AC}) and sinusoidal signal, was applied on PEH electrodes. Displacement of the PEH on z-axis (D_Z) is proportional to the number of interferometric fringes between minimum and maximum amplitudes of the exciting signal, multiplied by $\lambda/2$.

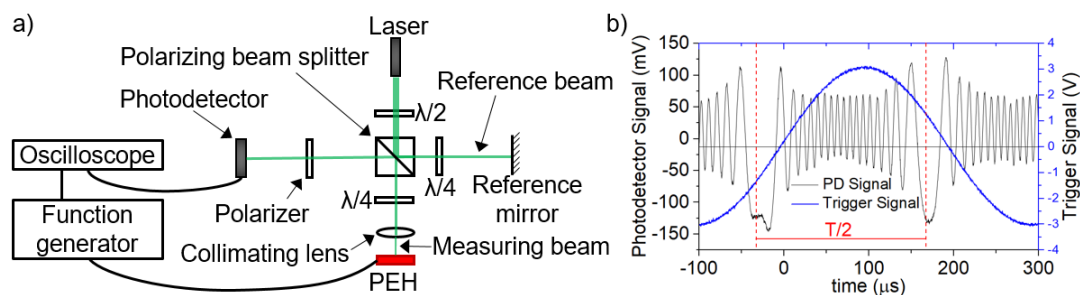


Figure 7. Interferometric measurement: (a) setup; (b) oscilloscope electrical signal.

The V_{AC} with a sinusoidal signal was applied on PEH electrodes. We adjusted V_{AC} within a range of 0.05 V to 0.2 V. We observed the first f_r at ≈ 2520 Hz, which agrees with results obtained by simulations with the corresponding value of ≈ 2500 Hz. The D_Z obtained from the measurement at f_r varied within a range of ≈ 4.5 μm to ≈ 18.2 μm for different V_{AC} , this corresponded with measurement data for a range of ≈ 4.1 μm to ≈ 17.1 μm for the same V_{AC} values. The dependence of measured D_Z on frequency is shown in Figure 8a. The measured values of D_Z correlate with values determined in FEM analyses in Figure 8b.

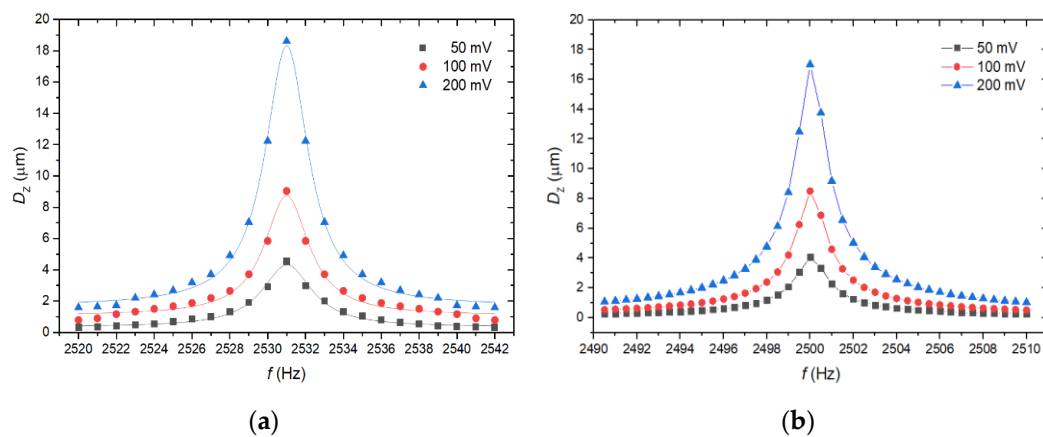


Figure 8. (a) Measured D_Z at $f_r = 2520$ Hz with various V_{AC} . (b) The results of FEM simulations for the same V_{AC} bias.

3.2. Vibrational Characterization

Next, we characterized generated power (P_M) using an automatized measurement system (Figure 9) [22].

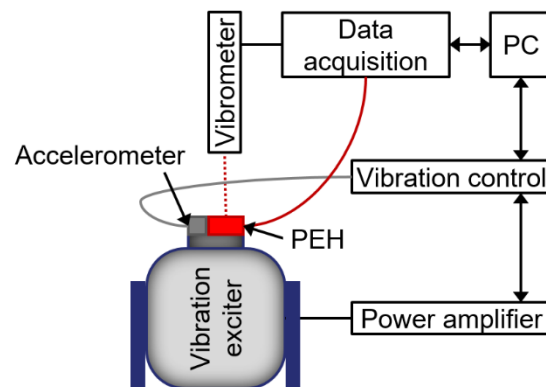


Figure 9. Measurement setup, based on vibration excitation of PEH for determination of P_M .

We placed the PEH on a table with controlled sinusoidal vibrations of specific amplitude and frequency, near to the first f_r , as extracted from the previous interferometric measurement. The test system was able to determine the f_r value, thus, we performed the measurement in proximity to this value. The measurement started by connecting an R_L to the PEH, while the stage was vibrating. Once the amplitude of the vibrations was stabilized, we recorded voltage across R_L (V_{RL}) amplitude, together with the free end of PEH displacement. The power output of the harvester was calculated from the known R_L and V_{RL} [23]. This procedure was then performed repeatedly for all pre-set combinations of R_L , frequencies, and amplitudes.

We observed a slight shift in f_r in comparison to the f_r determined during interferometric measurement. We changed the R_L in the range from 100Ω to $1 \text{ M}\Omega$, with a logarithmic stepping for frequencies in a range of 2476 Hz to 2484 Hz with constant $A \approx 0.5$ g. The optimized R_L value of $\approx 67.56 \text{ k}\Omega$ was found for maximal generated P_M of $\approx 0.91 \mu\text{W}$ at f_r with $A \approx 0.5$ g (Figure 10a).

We also determined the dependence of P_M on A for maximized R_L . The obtained values showed a remarkable correlation between predicted parameters from FEM analyses and the one of the fabricated device (deviation lower than 1%). We observed values of P_M in the range of $\approx 0.25 \mu\text{W}$ to $\approx 10.33 \mu\text{W}$ for the A in the range of ≈ 0.25 g to ≈ 2 g at f_r (Figure 10b).

Additionally, we identified a difference of $\approx 1.6\%$ between the f_r determined from interferometric and vibrometer measurements.

We subsequently calculated NPD and BW values from the results obtained in the last experiment. The NPD was determined (according to the Equation (2) with an assumption that the effective volume was $\approx 1.72 \times 10^{-3} \text{ cm}^3$) having a value in a range of $\approx 2.3 \text{ mW} \cdot \text{cm}^{-3} \cdot \text{g}^{-2}$ to $\approx 1.5 \text{ mW} \cdot \text{cm}^{-3} \cdot \text{g}^{-2}$ for A in range of 0.25 g to 2 g (Figure 10b).

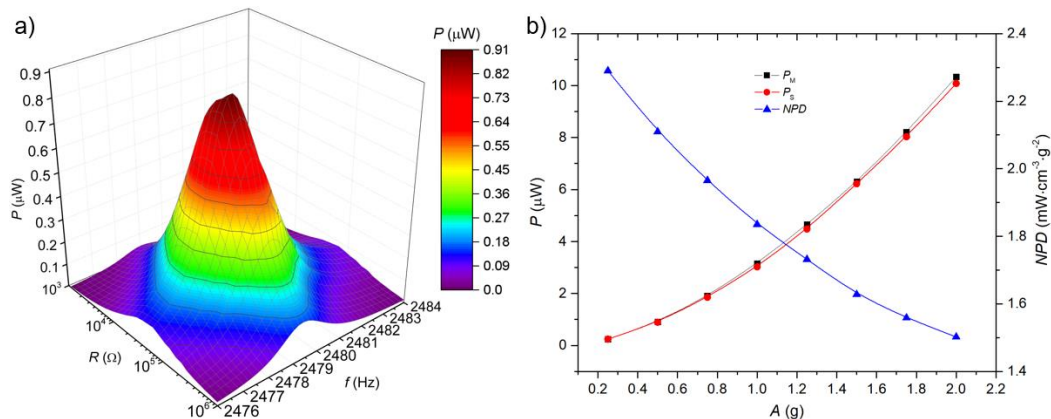


Figure 10. (a) Power spectra of measured PEH near $f_r = 2480$ Hz with constant $A \approx 0.5$ g, (b) dependence of maximum generated P_S and P_M and calculated value of NPD on A .

Such values of NPD are ≈ 2 – 10 times higher in comparison to previously published NPD [24–28]. The BW value was also determined for frequencies at FWHM of the spectrum, at a constant of $A \approx 0.5$ g and reached a value of ≈ 2.8 Hz.

4. Conclusions

This work presents a simplified method of PEH fabrication at a low temperature, using just three lithographical steps, and without the necessity of using costly SOI wafers, which dramatically reduces the manufacturing timeframes and costs. This method also allows the control of the thickness of the PEH layer from tens to hundreds of micrometers. We characterized the PEH properties using interferometric measurements, and automated power measurement using a vibration exciter. First, we applied V_{AC} on PEH electrodes to determine f_r and D_Z , comparing them with FEM analyses to verify the model. Next, we characterized P_M at f_r and determined the optimized R_L value to maximize P_M at $\approx 67.56 \text{ k}\Omega$. The PEH generated P_M in a range of $\approx 0.25 \text{ }\mu\text{W}$ to $\approx 10.33 \text{ }\mu\text{W}$ for A in a range of $\approx 0.25 \text{ g}$ to $\approx 2 \text{ g}$, respectively. The determined NPD and BW values performed better than those of previously published studies, making the proposed technology highly promising for the future development of CMOS-compatible piezoelectric harvesters.

Author Contributions: I.G., J.K. (Jaroslav Klempa), J.B. and J.P. conceived of the idea of this work, designed and fabricated chips and performed the experiments. P.V. performed finite element simulations, J.H. and M.H. performed laser interferometer characterization, J.K. (Jan Kunz) and P.N. performed the vibrational characterization. All co-authors offered helpful discussions and analyses of the results and wrote the manuscript. All authors have read and agreed to the published version of the manuscript.

Funding: The work was supported by the Grant Agency of the Czech Republic under contract GJ18-06498Y and CEITEC Nano Research Infrastructure (ID LM2015041, MEYS CR, 2016–2019), CEITEC Brno University of Technology (BUT). The infrastructure of the SIX Center of BUT was utilized to conduct the experiments. This work was also supported by the BUT specific research program (project No. FEKT-S-17-4595).

Conflicts of Interest: The authors declare no conflict of interests.

References

1. Liu, H.C.; Zhong, J.W.; Lee, C.; Lee, S.W.; Lin, L.W. A comprehensive review on piezoelectric energy harvesting technology: Materials, mechanisms, and applications. *Appl. Phys. Rev.* **2018**, *5*, 041306. [[CrossRef](#)]
2. Du, Y.; Xu, J.; Paul, B.; Eklund, P. Flexible thermoelectric materials and devices. *Appl. Mater. Today* **2018**, *12*, 366–388. [[CrossRef](#)]
3. Toshiyoshi, H.; Ju, S.; Honma, H.; Ji, C.H.; Fujita, H. MEMS vibrational energy harvesters. *Sci. Technol. Adv. Mater.* **2019**, *20*, 124–143. [[CrossRef](#)] [[PubMed](#)]
4. Meninger, S.; Mur-Miranda, J.O.; Amirtharajah, R.; Chandrakasan, A.; Lang, J.H. Vibration-to-electric energy conversion. *IEEE Trans. Very Large Scale Integr. (VLSI) Syst.* **2001**, *9*, 64–76. [[CrossRef](#)]
5. Tian, W.C.; Ling, Z.Y.; Yu, W.B.; Shi, J. A Review of MEMS Scale Piezoelectric Energy Harvester. *Appl. Sci.* **2018**, *8*, 645. [[CrossRef](#)]
6. Todaro, M.T.; Guido, F.; Mastronardi, V.; Desmaele, D.; Epifani, G.; Algieri, L.; De Vittorio, M. Piezoelectric MEMS vibrational energy harvesters: Advances and outlook. *Microelectron. Eng.* **2017**, *183*, 23–36. [[CrossRef](#)]
7. Wang, P.H.; Du, H.J. ZnO thin film piezoelectric MEMS vibration energy harvesters with two piezoelectric elements for higher output performance. *Rev. Sci. Instrum.* **2015**, *86*, 075002. [[CrossRef](#)]
8. Tian, Y.W.; Li, G.M.; Yi, Z.R.; Liu, J.Q.; Yang, B. A low-frequency MEMS piezoelectric energy harvester with a rectangular hole based on bulk PZT film. *J. Phys. Chem. Solids* **2018**, *117*, 21–27. [[CrossRef](#)]
9. Yeo, H.G.; Ma, X.K.; Rahn, C.; Trolier-McKinstry, S. Efficient Piezoelectric Energy Harvesters Utilizing (001) Textured Bimorph PZT Films on Flexible Metal Foils. *Adv. Funct. Mater.* **2016**, *26*, 5940–5946. [[CrossRef](#)]
10. Toprak, A.; Tigli, O. MEMS Scale PVDF-TrFE-Based Piezoelectric Energy Harvesters. *J. Microelectromech. Syst.* **2015**, *24*, 1989–1997. [[CrossRef](#)]
11. Fei, C.; Liu, X.; Zhu, B.; Li, D.; Yang, X.; Yang, Y.; Zhou, Q. AlN piezoelectric thin films for energy harvesting and acoustic devices. *Nano Energy* **2018**, *51*, 146–161. [[CrossRef](#)]
12. Conrad, H.; Schmidt, J.U.; Pufe, W.; Zimmer, F.; Sandner, T.; Schenk, H.; Lakner, H. Aluminum Nitride—A promising and Full CMOS Compatible Piezoelectric Material for MOEMS Applications. *Proc. SPIE* **2009**, *7362*, 73620J.
13. Doll, J.C.; Petzold, B.C.; Ninan, B.; Mullanpudi, R.; Pruitt, B.L. Aluminum nitride on titanium for CMOS compatible piezoelectric transducers. *J. Micromech. Microeng.* **2009**, *20*, 025008. [[CrossRef](#)] [[PubMed](#)]
14. Zhao, X.Q.; Shang, Z.G.; Luo, G.X.; Deng, L.C. A vibration energy harvester using AlN piezoelectric cantilever array. *Microelectron. Eng.* **2015**, *142*, 47–51. [[CrossRef](#)]
15. Yang, Z.; Zhou, S.; Zu, J.; Inman, D. High-Performance Piezoelectric Energy Harvesters and Their Applications. *Joule* **2018**, *2*, 642–697. [[CrossRef](#)]
16. Hadas, Z.; Smilek, J. Efficiency of vibration energy harvesting systems: Technology, Components and System Design. In *Energy Harvesting for Wireless Sensor Networks*; Kanoun, O., Ed.; De Gruyter: Berlin, Germany, 2018; pp. 45–64.
17. Ahrberg, C.D.; Ilic, B.R.; Manz, A.; Neuzil, P. Handheld real-time PCR device. *Lab Chip* **2016**, *16*, 586–592. [[CrossRef](#)]
18. Gablech, I.; Caha, O.; Svatos, V.; Pekarek, J.; Neuzil, P.; Sikola, T. Stress-free deposition of [001] preferentially oriented titanium thin film by Kaufman ion-beam source. *Thin Solid Films* **2017**, *638*, 57–62. [[CrossRef](#)]
19. Gablech, I.; Svatos, V.; Caha, O.; Hrabovsky, M.; Prasek, J.; Hubalek, J.; Sikola, T. Preparation of (001) preferentially oriented titanium thin films by ion-beam sputtering deposition on thermal silicon dioxide. *J. Mater. Sci.* **2016**, *51*, 3329–3336. [[CrossRef](#)]
20. Gablech, I.; Svatoš, V.; Caha, O.; Dubroka, A.; Pekárek, J.; Klempa, J.; Neuzil, P.; Schneider, M.; Šikola, T. Preparation of high-quality stress-free (001) aluminum nitride thin film using a dual Kaufman ion-beam source setup. *Thin Solid Films* **2019**, *670*, 105–112. [[CrossRef](#)]
21. Mallik, P.K.S.; Rao, D.S. Vibration control on composite beams with multiple piezoelectric patches using finite element analysis. *Int. Res. J. Eng. Technol.* **2017**, *4*, 6.
22. Kunz, J.; Fialka, J.; Benes, P.; Havranek, Z. An Automated measurement system for measuring an overall power efficiency and a characterisation of piezo harvesters. *J. Phys. Conf. Ser.* **2018**, *1065*, 202008. [[CrossRef](#)]
23. Erturk, A.; Inman, D.J. *Piezoelectric Energy Harvesting*; Wiley: Hoboken, NJ, USA, 2011; ISBN 978-0470682548.

24. Minh, L.V.; Kuwano, H. Highly Efficient Piezoelectric Micro-Energy Harvesters with AlN Thin Films Grown Directly on Flexible Ti Foils. In Proceedings of the 2017 IEEE 30th International Conference on Micro Electro Mechanical Systems (MEMS), Las Vegas, NV, USA, 22–26 January 2017; pp. 833–836.
25. Nabavi, S.; Zhang, L.H. Nonlinear Multi-Mode Wideband Piezoelectric MEMS Vibration Energy Harvester. *IEEE Sens. J.* **2019**, *19*, 4837–4848. [[CrossRef](#)]
26. Iannacci, J.; Sordo, G.; Schneider, M.; Schmid, U.; Camarda, A.; Romani, A. A Novel Toggle-Type MEMS Vibration Energy Harvester for Internet of Things Applications. In Proceedings of the 2016 IEEE SENSORS, Orlando, FL, USA, 30 October–3 November 2016.
27. He, X.M.; Wen, Q.; Lu, Z.; Shang, Z.G.; Wen, Z.Y. A micro-electromechanical systems based vibration energy harvester with aluminum nitride piezoelectric thin film deposited by pulsed direct-current magnetron sputtering. *Appl. Energy* **2018**, *228*, 881–890. [[CrossRef](#)]
28. Jia, Y.; Seshia, A.A. Power Optimization by Mass Tuning for MEMS Piezoelectric Cantilever Vibration Energy Harvesting. *J. Microelectromech. Syst.* **2016**, *25*, 108–117. [[CrossRef](#)]



© 2020 by the authors. Licensee MDPI, Basel, Switzerland. This article is an open access article distributed under the terms and conditions of the Creative Commons Attribution (CC BY) license (<http://creativecommons.org/licenses/by/4.0/>).



Article

Infinite Selectivity of Wet SiO₂ Etching in Respect to Al

Imrich Gablech ^{1,2} , Jan Brodský ¹, Jan Pekárek ¹ and Pavel Neuzil ^{1,3,*}

¹ Central European Institute of Technology, Brno University of Technology, 612 00 Brno, Czech Republic; imrich.gablech@ceitec.vutbr.cz (I.G.); jan.brodsky@ceitec.vutbr.cz (J.B.); pekarek@vutbr.cz (J.P.)

² Department of Microelectronics, Faculty of Electrical Engineering and Communication, Brno University of Technology, 616 00 Brno, Czech Republic

³ Department of Microsystem Engineering, School of Mechanical Engineering, Northwestern Polytechnical University, Xi'an 710072, China

* Correspondence: pavel.neuzil@nwpu.edu.cn; Tel.: +86-150-9133-1869

Received: 29 February 2020; Accepted: 31 March 2020; Published: 31 March 2020



Abstract: We propose and demonstrate an unconventional method suitable for releasing microelectromechanical systems devices containing an Al layer by wet etching using SiO₂ as a sacrificial layer. We used 48% HF solution in combination with 20% oleum to keep the HF solution water-free and thus to prevent attack of the Al layer, achieving an outstanding etch rate of thermally grown SiO₂ of $\approx 1 \mu\text{m}\cdot\text{min}^{-1}$. We also verified that this etching solution only minimally affected the Al layer, as the chip immersion for ≈ 9 min increased the Al layer sheet resistance by only $\approx 7.6\%$. The proposed etching method was performed in an ordinary fume hood in a polytetrafluorethylene beaker at elevated temperature of ≈ 70 °C using water bath on a hotplate. It allowed removal of the SiO₂ sacrificial layer in the presence of Al without the necessity of handling highly toxic HF gas.

Keywords: SiO₂ etching; microelectromechanical systems (MEMS); sacrificial layer; selectivity

1. Introduction

Over the last 50 years, there has been a development in the semiconductor industry, primarily based on Si substrate for fabricating integrated circuits such as complementary metal oxide semiconductor (CMOS) devices [1]. Subsequently, due to its favorable published Young's modulus value of 130 GPa for (100)-oriented Si [2], low thermal coefficient of expansion of $2.56 \times 10^{-6} \text{ K}^{-1}$, and high thermal conductivity of $157 \text{ W}\cdot\text{m}^{-1}\cdot\text{K}^{-1}$, Si has also been used to fabricate a large variety of microelectromechanical systems (MEMS) [3,4].

Many methods of Si micromachining, using Si as mechanical, thermal and electrical material, were developed during the evolution of MEMS technology, including wet anisotropic etching using either potassium hydroxide (KOH), tetramethyl ammonium hydroxide (TMAH) or ethylene diamine pyrocatechol solutions [5,6], and wet isotropic etching using a mixture of HF, HNO₃ and CH₃COOH, known as HNA solution [6]. Next, dry etching of Si was introduced, either anisotropic reactive ion etching (RIE) [7] and deep RIE (DRIE) [8], or semi-anisotropic etching using the plasma process [9], and finally isotropic etching using XeF₂ vapor [10,11]. At the beginning, bulk micromachining prevailed [12,13] followed by more complex devices-based surface micromachining [14]. SiO₂, typically in its low-stress form prepared by the plasma-enhanced chemical vapor deposition (PECVD) method, is another mechanical material commonly used in micromachining [15]. This material has full compatibility with Si processing and can also be used for high temperature deposition processes.

With the development of digital mirror device technology beginning in the 1980s [16], Al became another structural material used in MEMS fabrication. It can be used for numerous applications

due to its compatibility with CMOS fabrication, such as making waveguides [17]. Al is also used as an electrical leadout for MEMS devices.

The etching of SiO₂ by employing HF/NH₄F solution (buffered oxide etch, BOE) can also be used, but unfortunately, it does etch Al; therefore, all structures made of Al have to be protected. Pinhole-free materials deposited by conventional technology such as PECVD do not exist; there are always some pinholes [18] allowing etch solution to penetrate through and to damage the Al layer underneath. The only option is protection by polymers as photoresist, but they cannot be applied for a long SiO₂ release etch.

What about sacrificial etching of SiO₂ in the presence of Al, though? Because, as is known, HF is only dissociated by H₂O into H₃O⁺ and F⁻ etches Al, the presence of water is therefore required. There have been several attempts to remove SiO₂ using anhydrous gas HF [19] adding alcohol vapors using rather complex and expensive equipment achieving a slow etch rate of ≈15 nm·min⁻¹ of thermally grown SiO₂ [20].

SiO₂ in presence of Al has also been wet etched in liquid form using difficult-to-obtain 73% HF [21], achieving a high etch rate of 1.6 μm·min⁻¹ without attacking the Al layer, but this solution is classified as a weapon, as it can probably also be used for uranium enrichment, and thus the supply of this chemical is controlled.

A mixture of readily available 48% (28.9 M) HF/96% (18 M) H₂SO₄ solution, as well as only 48% HF solution, was also employed to conduct this SiO₂ etching in the presence of Al [22], but there is a problem, as this etching produces water



at the device surface, causing dissociation of HF there and etching the Al layer.

There are numerous MEMS devices, such as inertial sensors, made of single-crystal silicon using silicon on insulator (SOI) substrates [23], inertial sensors integrated with CMOS based on α-Si [24], and bolometers made of α-Si [25] or α-SiGe [26], typically using SiO₂ as sacrificial material employing anhydrous gas HF to remove the SiO₂ layer [19]. This process works very well, but the capital investment is high, as HF is highly corrosive, as well as toxic, and the machine using HF gas has to be built to follow safety standards.

A similar problem arises with nitration of organic compounds to produce explosives with 99% HNO₃. One of the reaction products is also H₂O, which dilutes HNO₃ and gradually stops the nitration process. The reaction is therefore conducted in the presence of highly hygroscopic H₂SO₄·SO₃ (oleum), binding H₂O to itself, and keeping HNO₃ concentrated, and thus active, for the nitration process [27].

In this contribution, we used a similar principle to etch SiO₂ by 48% HF solution in the presence of oleum, concurrently binding H₂O as an SiO₂ etching product, keeping HF in non-dissociated form and thereby keeping the Al layer intact:



Our method requires only minimal technical equipment, such as a fume hood and a hotplate and personal protective equipment such as glasses, face shield, chemically resistive gloves, and an apron resistive to strong acids.

2. Materials and Methods

2.1. Test Layout Design

We designed a test pattern containing torus shapes with identical outer radius and variable inner radius forming a set of features with linewidth in a range from 2 μm to 20 μm with step of 0.5 μm using Nanolithography toolbox [28]. The stepping of 0.5 μm gave us an etch rate resolution of 0.25 μm as the torus shapes were etched from both sides, which was sufficient for the purposes of this work

(Figure 1a). Then, we fabricated a photolithography mask for contact printing using soda lime glass substrate with size of ($\approx 127 \times \approx 127$) mm².

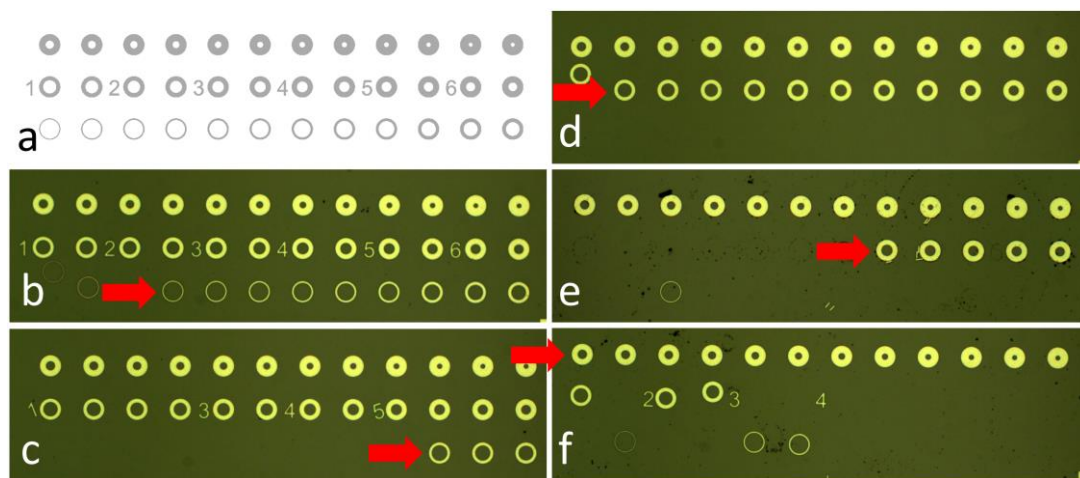


Figure 1. Test structure to determine the SiO₂ etch via lateral under etching. (a) Structure layout containing structures with identical outer diameter and different width starting from 2 μ m and ending with 20 μ m with step of 0.5 μ m. Photographs of structures after SiO₂ etching for: (b) ≈ 1.5 min, (c) ≈ 3.0 min, (d) ≈ 4.5 min, (e) ≈ 6.0 min and (f) ≈ 7.5 min. The red arrow points at the torus shape with the smallest linewidth not fully undercut.

2.2. Sample Preparation

We used p-type Si (100) wafers with a diameter of ≈ 100 mm to fabricate the test structures. The wafers were oxidized to grow (398 ± 3) -nm-thick (mean \pm standard deviation from three measurements using ellipsometry) SiO₂. Then we deposited an Al layer using an e-beam evaporation technique with a thickness of ≈ 1.5 μ m as measured by an in situ quartz crystal microbalance system. Subsequently, we coated the Al layer with a positive photoresist (PR) with a target thickness of ≈ 1.4 μ m, and performed pre-exposure baking at ≈ 110 $^{\circ}$ C for ≈ 50 s on a hot plate in N₂ atmosphere. We exposed the PR using an ultraviolet light source with a dose of ≈ 90 mJ \cdot cm⁻² using a contact printer through a soda lime glass mask with a design as described above. Then we developed the PR using a TMAH-based developer for ≈ 60 s, washed it with deionized water and dried with an N₂ flow.

Once we performed descumming process using O₂ plasma for set duration, power and pressure of 60 s, 300 W and 7 Pa, respectively. The Al layer was subsequently etched by RIE using a mixture of Cl₂ and BCl₃ gas in the set ratio of 3:1. Then we removed the PR using 1-methyl-2-pyrrolidone, rinsed the wafer with propanol-2-ol (IPA), and dried it with a flow of N₂. Finally, we cut the wafers into smaller pieces using the diamond scribing method into sizes of $\approx (10 \times 10)$ mm², each containing a set of six test structures for etching evaluation.

2.3. Etch Solution Preparation

We mixed ≈ 50 mL of 48% HF (Sigma-Aldrich, Hampton, NH, USA) with ≈ 50 mL of 20% oleum (Fluke, St. Gallen, Switzerland) in a beaker made of polytetrafluorethylene (PTFE). The dilution heat warmed up the solution to elevated temperature up to its boiling point with white fumes coming out of the beaker; thus, a working in fume hood or a laminar box was essential as those fumes should consist of toxic HF and SO₃ as well as non-toxic H₂O. In the next step, we placed PTFE baker into bigger borosilicate glass beaker filled with water with its temperature set to ≈ 70 $^{\circ}$ C.

3. Experimental

We immersed six samples of devices as described above Al/SiO₂ sandwich in the SiO₂ etch solution for time in range from ≈ 1.5 min to ≈ 9 min with interval of ≈ 1.5 min to determine the etch rate. We also immersed two more samples into etch solution for ≈ 7.5 min, one with patterned Al and the other without. The first sample was used to determine the SiO₂ etch rate via the undercutting of Al rings with different sizes. We also measured the Al thickness using a stylus type profilometer. The second sample was used to measure Al sheet resistance before and after its immersion. Each sample after etching was washed three times, twice with IPA followed by deionized H₂O, then we dried it with a flow of N₂.

4. Results and Discussion

First, we determined the etch rate of SiO₂. We observed the etched structures using optical microscope and evaluated torus shapes washed away from the surface, i.e., completely undercut (Figure 1b–f). The last structures not fully undercut with their linewidths (Table 1) were 3.5 μm , 7.5 μm , 9.5 μm , 12.5 μm , and 15.0 μm for etching durations of ≈ 1.5 min, ≈ 3.0 min, ≈ 4.5 min, ≈ 6.0 min, and ≈ 7.5 min, respectively. The half of a linewidth of last surviving torus was plotted as a function of time (Figure 2), with its slope defining the SiO₂ etch rate as $(0.93 \pm 0.05) \mu\text{m}\cdot\text{min}^{-1}$ (mean \pm fitting error), which is $\approx 14\times$ faster than BOE with 6:1 ratio of 48% HF and 40% NH₄F [29].

Table 1. Line width of the layout shown in Figure 1a having three rows and 12 columns. Please note that there was a mistake on the layout, and thus the linewidths with size of 6.5 μm and 7.0 μm are missing.

Column/Row	1	2	3	4	5	6	7	8	9	10	11	12
1	15.0	15.5	16.0	16.5	17.0	17.5	18.0	18.5	19.0	19.5	20.0	20.0
2	9.0	9.5	10.0	10.5	11.0	11.5	12.0	12.5	13.0	13.5	14.0	14.5
3	2.0	2.5	3.0	3.5	4.0	4.5	5.0	5.5	6.0	7.5	8.0	8.5

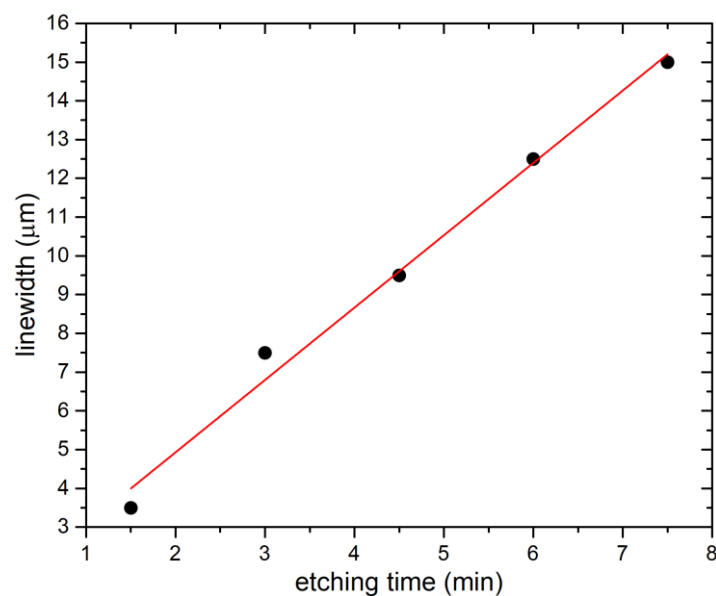


Figure 2. SiO₂ etching as function of time. The curve was obtained as linear approximation for six etched samples for different time in range from ≈ 1.5 min to ≈ 7.5 min with an interval of ≈ 1.5 min.

Next, we etched samples in XeF₂ vapor and set pressure and time to 0.33 Pa and 225 s, respectively, divided into 5 cycles to increase contrast between SiO₂ and Al, and then checked them using scanning electron microscopy (SEM). SEM images show that the both Al and SiO₂ layers were not mechanically damaged (Figure 3).

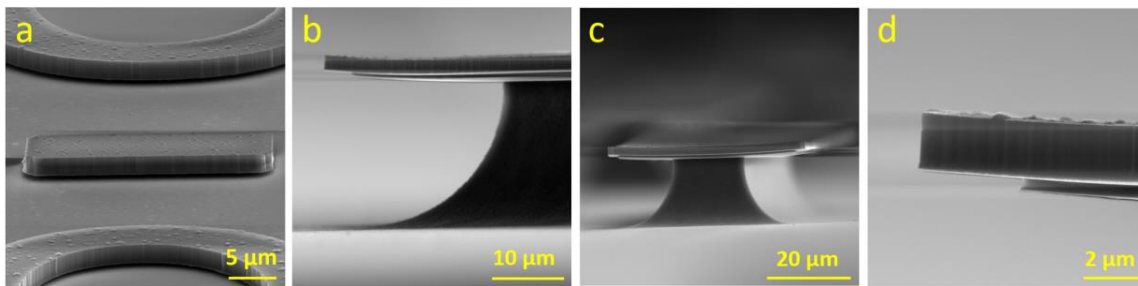


Figure 3. SiO₂ etched with HF/oleum, showing the undercutting with Al layer intact: (a) Structures undercut by SiO₂ etch solution leaving intact Al. (b) The same etching of SiO₂ followed by partial Si removal by XeF₂ vapor to enhance visibility of SiO₂ etch boundary. (c) Different angle and magnification show whole structure (d) and corner detail.

We measured the Al thickness by stylus profiler at the structures used for SiO₂ etch rate testing and found that it was (1887 ± 46) nm (mean \pm standard deviation from 3 measurements) of whole Al/SiO₂ sandwich. These results show that the etching time had no influence on the sandwich thickness.

We measured Al sheet resistance (R_{\square}), before and after dipping it into SiO₂ etch solution for ≈ 9 min. We used a custom-made four-point probe system, set the electric current (I) on the outer probes to the range from 10 mA to 60 mA, while monitoring the voltage (V) measured between the inner probes (Figure 4). Then we performed linear curve fitting determining the slope $V \cdot I^{-1}$ and calculated the R_{\square} value using the following equation:

$$R_{\square} = \frac{\pi}{\ln 2} \cdot \frac{V}{I} \quad (3)$$

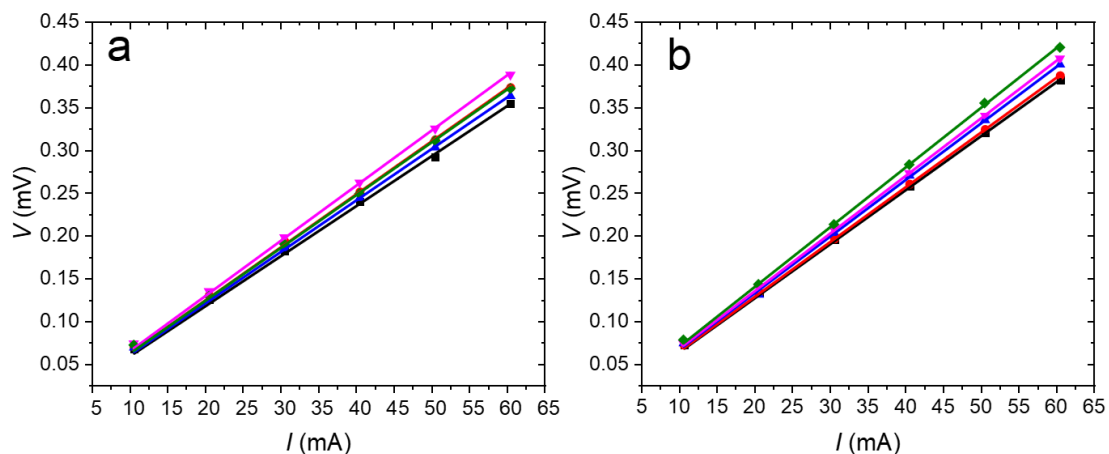


Figure 4. Graphs showing the value of V as a function of interrogating I from the four-point probe system at Al layer before (a) and after (b) dipping in SiO₂ etch solution. The fitted slope $V \cdot I^{-1}$ with an assumption of intercept of 0 V changed by $\approx 7.5\%$.

We calculated the R_{\square} value of the Al layer from the geometry factor constant and the slope (Figure 4) [30], before and after SiO₂ etching for ≈ 9 min, as (27.8 ± 1.0) m $\Omega \cdot \square^{-1}$ and (29.9 ± 1.2) m $\Omega \cdot \square^{-1}$, respectively (both mean \pm fitting errors from five measurements). The small increase in R_{\square} values before and after SiO₂ etching was probably caused by measuring on different area of substrate which can be influenced by Al thickness inhomogeneity and impurities on surface as the results from stylus profiler shown that the etch time had no influence on the Al thickness.

Here we summarize advantages and disadvantages of both, dry and wet etching systems. Dry etching is a convenient, user friendly and safe technique using a load lock system practically

eliminating an option of an operator to get into contact with the HF gas. Also, there is no need for critical dry release of the structure, as there is no liquid involved in the process. The disadvantage is often prohibited cost of the system as well as its slow etch rate of $\approx 15 \text{ nm}\cdot\text{min}^{-1}$.

The wet etch proposed in this contribution has a high etch rate of $(0.93 \pm 0.05) \mu\text{m}\cdot\text{min}^{-1}$ (mean \pm fitting error), as well as requiring practically no special equipment besides a fume hood, PTFE beaker and personal protective equipment. The disadvantage is requirement of critical dry release or similar method to prevent the MEMS structures to collapse. Also, this etching technique should only be performed by skilled personnel, as they will be dealing with hazardous chemicals. Disposing the etch solution should be done in an appropriate manner using conventional HF types of waste.

5. Conclusions

We proposed and verified the wet SiO_2 etching method with excellent selectivity towards Al, practically leaving the Al layer intact. HF solution in the absence of H_2O does not etch Al; thus, we used 48% HF in combination with oleum to etch SiO_2 by HF, with concurrent removal of H_2O , product of SiO_2 etching by hygroscopic oleum. We tested this idea by etching thermally grown SiO_2 , achieving a very high etch rate of $(0.93 \pm 0.05) \mu\text{m}\cdot\text{min}^{-1}$ (mean \pm fitting error from three measurements), $\approx 14\times$ faster in comparison with a typical 6:1 BOE etch rate $\approx 70 \text{ nm}\cdot\text{min}^{-1}$. During this process, the SiO_2 and the Al layer present at the tested chip remained intact, as the sheet resistance before and after exposure to the solution stayed almost the same. The presented method is a simple alternative to anhydrous gas HF etching of SiO_2 , sacrificial etching, with the Al layer presented on the substrate conducted by complex gas systems.

Author Contributions: P.N. conceived of the idea of this work, designed and performed the experiments. I.G., J.B., J.P., and P.N. performed the experiments. All authors have read and agreed to the published version of the manuscript.

Funding: We acknowledge the support of Grant Agency of the Czech Republic under the contract GJ18-06498Y and support of the Ministry of Education, Youth and Sports of the Czech Republic under the project OP VVV CEITEC Nano+ (CZ.02.1.01/0.0/0.0/16_013/0001728). CzechNanoLab project LM2018110 funded by MEYS CR is gratefully acknowledged for the financial support of the measurements/sample fabrication at CEITEC Nano Research Infrastructure. The SIX Center of BUT was used to conduct the experiments.

Conflicts of Interest: The authors declare no conflict of interests.

References

1. Radamson, H.H.; He, X.; Zhang, Q.; Liu, J.; Cui, H.; Xiang, J.; Kong, Z.; Xiong, W.; Li, J.; Gao, J.; et al. Miniaturization of Cmos. *Micromachines* **2019**, *10*, 293. [[CrossRef](#)] [[PubMed](#)]
2. Janssen, G.C.; Abdalla, M.M.; Van Keulen, F.; Pujada, B.R.; Van Venrooy, B. Celebrating the 100th Anniversary of the Stoney Equation for Film Stress: Developments from Polycrystalline Steel Strips to Single Crystal Silicon Wafers. *Thin Solid Film.* **2009**, *517*, 1858–1867. [[CrossRef](#)]
3. Gablech, I.; Klempa, J.; Pekárek, J.; Vyroubal, P.; Hrabina, J.; Holá, M.; Kunz, J.; Brodský, J.; Neuzil, P. Simple and Efficient Aln-Based Piezoelectric Energy Harvesters. *Micromachines* **2020**, *11*, 143. [[CrossRef](#)] [[PubMed](#)]
4. Petersen, K.E. Silicon as a Mechanical Material. *Proc. IEEE* **1982**, *70*, 420–457. [[CrossRef](#)]
5. Dutta, S.; Imran, M.; Kumar, P.; Pal, R.; Datta, P.; Chatterjee, R. Comparison of Etch Characteristics of Koh, Tmah and Edp for Bulk Micromachining of Silicon (110). *Microsyst. Technol.* **2011**, *17*, 1621. [[CrossRef](#)]
6. Hamzah, A.A.; Aziz, N.A.; Majlis, B.Y.; Yunas, J.; Dee, C.F.; Bais, B. Optimization of Hna Etching Parameters to Produce High Aspect Ratio Solid Silicon Microneedles. *J. Micromech. Microeng.* **2012**, *22*, 095017. [[CrossRef](#)]
7. Rangelow, I.W.; Löschner, H. Reactive Ion Etching for Microelectrical Mechanical System Fabrication. *J. Vac. Sci. Technol. B Microelectron. Nanometer Struct. Process. Meas. Phenom.* **1995**, *13*, 2394–2399. [[CrossRef](#)]
8. Laerme, F.; Schilp, A.; Funk, K.; Offenber, M. Bosch Deep Silicon Etching: Improving Uniformity and Etch Rate for Advanced Mems Applications. In Proceedings of the Paper presented at the Technical Digest. IEEE International MEMS 99 Conference. Twelfth IEEE International Conference on Micro Electro Mechanical Systems (Cat. No. 99CH36291), Orlando, FL, USA, 21–21 January 1999.

9. Eisele, K.M. *Sf 6*, a Preferable Etchant for Plasma Etching Silicon. *J. Electrochem. Soc.* **1981**, *128*, 123–126. [[CrossRef](#)]
10. Winters, H.F.; Coburn, J.W. The Etching of Silicon with Xef₂ Vapor. *Appl. Phys. Lett.* **1979**, *34*, 70–73. [[CrossRef](#)]
11. Svatoš, V.; Gablech, I.; Ilic, B.R.; Pekárek, J.; Neuzil, P. In Situ Observation of Carbon Nanotube Layer Growth on Microbolometers with Substrates at Ambient Temperature. *J. Appl. Phys.* **2018**, *123*, 114503. [[CrossRef](#)]
12. Kovacs, G.T.A.; Maluf, N.I.; Petersen, K.E. Bulk Micromachining of Silicon. *Proc. IEEE* **1998**, *86*, 1536–1551. [[CrossRef](#)]
13. Guan, D.; Bruccoleri, A.R.; Heilmann, R.K.; Schattenburg, M.L. Stress Control of Plasma Enhanced Chemical Vapor Deposited Silicon Oxide Film from Tetraethoxysilane. *J. Micromech. Microeng.* **2013**, *24*, 027001. [[CrossRef](#)]
14. Judy, J. Microelectromechanical Systems (Mems): Fabrication, Design and Applications. *Smart Mater. Struct.* **2001**, *10*, 1115–1134. [[CrossRef](#)]
15. Tarraf, A.; Daleiden, J.; Irmer, S.; Prasai, D.; Hillmer, H. Stress Investigation of Pecvd Dielectric Layers for Advanced Optical Mems. *J. Micromech. Microeng* **2003**, *14*, 317–323. [[CrossRef](#)]
16. Hornbeck, L.J. Current Status of the Digital Micromirror Device (Dmd) for Projection Television Applications. In Proceedings of the Paper presented at the IEEE International Electron Devices Meeting, Washington, DC, USA, 5–8 December 1993.
17. Tea, N.H.; Milanovic, V.; Zincke, C.A.; Suehle, J.S.; Gaitan, M.; Zaghoul, M.E.; Geist, J. Hybrid Postprocessing Etching for Cmos-Compatible Mems. *J. Microelectromech. Syst.* **1997**, *6*, 363–372. [[CrossRef](#)]
18. Domanský, K.; Petelenz, D.; Janata, J. Effect of Thermal Treatment of Passivation Integrity of Chemical Vapor Deposition Silicon Nitride. *Appl. Phys. Lett.* **1992**, *60*, 2074–2076. [[CrossRef](#)]
19. Jang, W.I.; Choi, C.A.; Lee, M.L.; Jun, C.H.; Kim, Y.T. Fabrication of Mems Devices by Using Anhydrous Hf Gas-Phase Etching with Alcoholic Vapor. *J. Micromech. Microeng* **2002**, *12*, 297. [[CrossRef](#)]
20. Witvrouw, A.; Bois, B.D.; de Moor, P.; Verbist, A.; van Hoof, C.A.; Bender, H.; Baert, C. Comparison between Wet Hf Etching and Vapor Hf Etching for Sacrificial Oxide Removal. In Proceedings of the Paper presented at the Micromachining and Microfabrication Process Technology VI, Santa Clara, CA, USA, 25 August 2000.
21. Gennissen, P.T.J.; French, P.J. Sacrificial Oxide Etching Compatible with Aluminum Metallization. In Proceedings of the International Solid State Sensors and Actuators Conference (Transducers '97), Chicago, IL, USA, 19–19 June 1997; Volume 1, pp. 225–228.
22. Clews, P.J.; Mani, S.S. Selective Etchant for Oxide Sacrificial Material in Semiconductor Device Fabrication. U.S. Patent 6,893,578, 17 May 2005.
23. Amini, B.V.; Abdolvand, R.; Ayazi, F. A 4.5-Mw Closed-Loop $\Delta\sigma$ Micro-Gravity Cmos Soi Accelerometer. *IEEE J. Solid State Circuits* **2006**, *41*, 2983–2991. [[CrossRef](#)]
24. Kuehnel, W.; Sherman, S. A Surface Micromachined Silicon Accelerometer with on-Chip Detection Circuitry. *Sens. Actuators A Phys.* **1994**, *45*, 7–16. [[CrossRef](#)]
25. Syllaios, A.J.; Schimert, T.R.; Gooch, R.W.; McCardel, W.L.; Ritchey, B.A.; Tregilgas, J.H. Amorphous Silicon Microbolometer Technology. *MRS Online Proc. Libr. Arch.* **2000**, *609*, A14.4. [[CrossRef](#)]
26. Sedky, S.; Fiorini, P.; Baert, K.; Hermans, L.; Mertens, R. Characterization and Optimization of Infrared Poly Sige Bolometers. *IEEE Trans. Electron Devices* **1999**, *46*, 675–682. [[CrossRef](#)]
27. Akhavan, J. *The Chemistry of Explosives*; Royal Society of Chemistry: London, UK, 2011.
28. Balram, K.C.; Westly, D.A.; Davanco, M.; Grutter, K.E.; Li, Q.; Michels, T.; Ray, C.H.; Yu, L.Y.; Kasica, R.J.; Wallin, C.B.; et al. The Nanolithography Toolbox. *J. Res. Natl. Inst. Stand. Technol.* **2016**, *121*, 464–475. [[CrossRef](#)]
29. Walker, P.; Tarn, W.H. *Crc Handbook of Metal Etchants*; CRC press: Boca raton, FL, USA, 1990.
30. Miccoli, I.; Edler, F.; Pfnür, H.; Tegenkamp, C. The 100th Anniversary of the Four-Point Probe Technique: The Role of Probe Geometries in Isotropic and Anisotropic Systems. *J. Phys. Condens. Matter* **2015**, *27*, 223201. [[CrossRef](#)] [[PubMed](#)]



ChemFET gas nanosensor arrays with alignment windows for assembly of single nanowires

Ondřej Chmela^{1,2} (✉), Imrich Gablech^{1,2}, Jakub Sadílek^{1,2}, Jan Brodský¹, and Stella Vallejos^{1,2,3} (✉)

¹ Central European Institute of Technology, Brno University of Technology, Purkyňova 123, 61200 Brno, Czech Republic

² Faculty of Electrical Engineering and Communication, Brno University of Technology, Department of Microelectronics, Technická 3058/10, 61200 Brno, Czech Republic

³ Instituto de Microelectrónica de Barcelona (IMB-CNM, CSIC), Campus UAB, Carrer dels Til·lers, Cerdanyola del Vallès, 08193 Barcelona, Spain

© The Author(s) 2023

Received: 13 January 2023 / Revised: 24 February 2023 / Accepted: 5 March 2023

ABSTRACT

This work focuses on the fabrication and characterization of Chemical Field-Effect Transistor (ChemFET) gas nanosensor arrays based on single nanowire (SNW). The fabrication processes include micro and nanofabrication techniques enabled by a combination of ultraviolet (UV) and e-beam lithography to build the ChemFET structure. Results show the integration and connection of SNWs across the multiple pairs of nanoelectrodes in the ChemFET by dielectrophoresis process (DEP) thanks to the incorporation of alignment windows (200–300 nm) adapted to the diameter of the NWs. Measurements of the SNW ChemFET array's output and transfer characteristics prove the influence of gate bias on the drain current regulation. Tests upon hydrogen (H₂) and nitrogen dioxide (NO₂) as analyte models of reducing and oxidizing gases show the ChemFET sensing functionality. Moreover, results demonstrate better response characteristics to H₂ when the ChemFET operates in the subthreshold regime. The design concepts and methods proposed for fabricating the SNW-based ChemFET arrays are versatile, reproducible, and most likely adaptable to other systems where SNW arrays are required.

KEYWORDS

Chemical Field-Effect Transistor (ChemFET) nanosensors, nanowires, nanoelectrodes, gas sensors

1 Introduction

In the past years, gas-sensitive nanowires, nanobelts, and nanorods, belonging to the group of one-dimensional (1D) semiconducting metal-oxide (MOX) nanostructures, have attracted considerable attention in the field of chemical (gas) sensors due to their capability to improve sensor's functionality by enhancing the surface response as opposed to alternative structures with boundary connection effect [1–3]. These structures also adapt better to the sensor's miniaturization, providing further advantages of size and cost production compared to other chemical sensors (e.g., operating with electrochemical principles [4, 5]).

Usually, the gas sensors based on 1D MOX nanostructures are assembled as chemoresistive (two-electrode) or Chemical Field-Effect Transistor (ChemFET) (three-electrode) devices. In chemoresistive and ChemFET sensors, the electrical transport through the 1D MOX nanostructure(s) is modulated by the gas-solid interactions at the MOX surface. However, in ChemFET, the conductive channel can also be modulated by applying a voltage potential to the third electrode, regularly integrated as a bottom (back) gate electrode, bringing the possibility of tuning further the gas sensor response and dynamics [6–9]. Hence, the fabrication of ChemFET structures requires more elements with respect to a chemoresistor adding complexity to the fabrication process of these sensor devices.

Our previous studies on nanowire-based gas sensors have

generally focused on chemoresistive structures with multiple or single nanowires, demonstrating the advantage of such systems over traditional nanoparticle-based sensors [10, 11]. Further works in the literature have also shown that a single or few nanowire structures connected in parallel are the ideal architectures to detect the external stimuli coming from the adsorption of gaseous molecules at the nanowire surface more efficiently [1, 12–15]. However, current methods for assembling aligned and isolated single nanowire (SNW) structures in chemoresistive or ChemFET configuration still represent a technological challenge. Sometimes, this challenge is overcome by connecting a unique 1D nanostructure (chosen from various random 1D nanostructures dispersed over a substrate) via focus ion beam (FIB), although this method restricts the scalability of the process and increases the cost and time of fabrication [16, 17].

Alternative routes for the alignment of 1D nanostructures (amongst them, the Langmuir-Blodgett and the electric/magnetic fields assisted techniques) have been shown to be appropriate for aligning various 1D nanostructures [18]. However, face to the on-chip integration, techniques assisted by electric field via dielectrophoresis process (DEP) may represent a technological advantage. The DEP allows aligning and connecting NWs suspended in a droplet solution by applying a nonuniform electric field that creates a dipole moment on the NWs, causing the droplet to be electrostatically pulled toward the biased electrodes. As such, this process may facilitate precise placement and lining up of several 1D nanostructures in parallel [19, 20]. However, the

Address correspondence to Ondřej Chmela, ondrej.chmela@ceitec.vutbr.cz; Stella Vallejos, stella.vallejos@imb-cnm.csic.es

integration of isolated single 1D nanostructures may depend further on the characteristics of the electrodes and the electrical environment.

Our previous studies on chemoresistive nanosensors, for instance, demonstrated that the use of several pairs of electrodes with nanoscale features facilitates to some extent the integration of isolated SNWs [10]. Recently, we have also noticed that the incorporation of dielectric shielding windows further favors the electrical environment for the integration of isolated SNWs, avoiding the aggregation of multiple NWs within a pair of nanoelectrodes. In this context, herein, we further improve the SNW arrays reported earlier [10] by developing new structures that operate with the ChemFET principles to tune the sensor response thanks to the buried gate electrode and locally drain-source (faced) electrodes nano-shaped by electron beam lithography (EBL) technique. As a novelty, the present work also explores the incorporation of alignment windows over the top of the ChemFET structure to confine the SNWs integrated across the drain-source nanoelectrodes. The gas sensing functionality of these structures is validated in the ChemFET regime using nitrogen dioxide and hydrogen gases as oxidizing and reducing model analytes.

2 Experimental

2.1 Design and layout of ChemFET nanosensors platform

We designed a layout containing several chips on a 4-inch wafer. Each chip has a size of 5 mm × 5 mm and incorporates four independent nanoelectrode array structures (Fig. 1(a)). Such structures consist of drain and source electrodes with a buried local gate to use as ChemFET. The design includes two modifications with different electrode pairs separated by a constant spacing of 50 μm between them (Fig. 1(b)). The first modification consists of five pairs drain-source electrodes and the second contains nine pairs. The in-plane gap between drain and source electrodes was set to 3.5 μm, as this dimension proved ideal for the NWs alignment in our previous study [10]. The gate electrode with a width of 1.5 μm is locally placed between this gap formed by a SiO₂ trench (Fig. 1(c)). Each array is surrounded by circular gold stripes that serve as hydrophobic rings. These rings ensure the confinement of the droplet with suspended NWs on the electrode area during DEP (Fig. 1(d)) technique.

To fabricate these structures, EBL was first used to perform nanoelectrode arrays with a “clothespin” pattern. The red color in

Fig. 1(c) represents the EBL pattern, and the yellow color is the remaining nanoelectrode ends created by the dry etching procedure. The nanoelectrode arrays contain electrode fingers with two different widths. Thus, the electrode fingers on the two left arrays have a width of 200 nm, whereas those on the right have a width of 300 nm (Fig. 1(a)). The entire electrode finger is 48 μm long and is divided into three parts. The first part corresponds to the triangularly shaped incoming microelectrodes connected to the middle electrode with a width of 1.5 μm. The last is finally connected to the nanoelectrode, which ends at the gate channel boundary (Fig. 1(c)).

Generally, the integration of the NWs and the number of aligned NWs across the faced nanoelectrodes in the array can be influenced by several factors, including the geometry and width of electrodes (which should be comparable to the NW diameter), DEP parameters, NWs concentration, and volume of droplets during DEP [21, 22]. In this work, we paid special attention to the reproducible integration of aligned SNW across the ChemFET nanoelectrodes, further improving our previous design of nanoelectrodes for chemoresistive operation [10]. Therefore, to achieve the alignment of SNW across the electrodes, we designed two dielectric shielding window structures based on a SiO₂ layer fabricated with atomic layer deposition (ALD): the wide one of 10 μm × 20 μm, and the narrow one of 200–300 nm × 10 μm. Figure 2 shows a schematic view of the dielectric shielding (alignment window) to favor the SNW interconnection.

2.2 Fabrication of ChemFET nanosensors platform

We fabricated the ChemFET arrays using standard surface microfabrication techniques such as thermal oxidation, ALD, reactive ion etching (RIE), and both EBL and ultraviolet (UV) lithography for dimensions lower or larger than 1 μm, respectively.

The fabrication process starts on a Si wafer with a diameter of ~100 mm thermally oxidized to form ~300 nm thick SiO₂ layer (Fig. 3(a)). The SiO₂ trenches are fabricated in the first step. To this end, we coated the wafer with a positive photoresist (PR) and then exposed it using UV lithography through a soda-lime mask employing mask aligner MA8 (Süss MicroTec, Switzerland). Then, we used a standard tetramethylammonium hydroxide (TMAH) based developer and performed descum using O₂ plasma. The SiO₂ was etched by RIE with Ar/CHF₃ gas mixture. Subsequently, we removed the PR in 1-methyl-2-pyrrolidinone (NMP) solution, rinsed the wafer with distilled water, and dried it with nitrogen steam.

The second step aimed to fabricate the gate electrode by lift-off

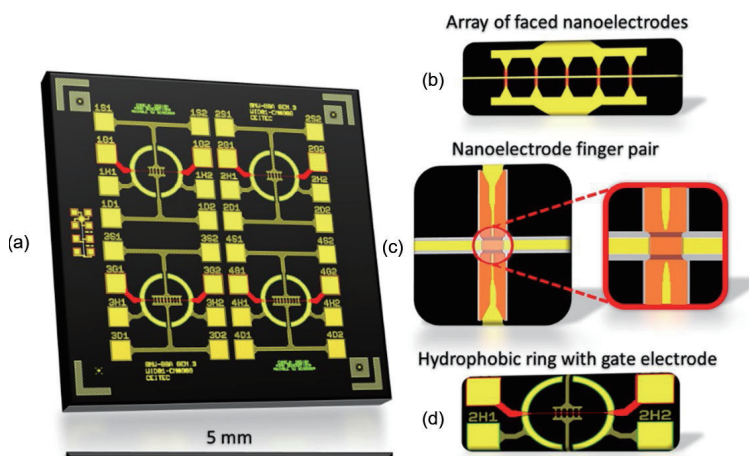


Figure 1 Chip design and layout of the functional blocks (yellow: microelectrodes and faced nanoelectrodes system (Au layer); orange: EBL pattern; black: thermal SiO₂ layer; red: the gate electrode; grey: channel for the gate electrode). (a) Detailed view of the full-size chip. (b) Array with five faced nanoelectrodes. (c) Detailed view of the nanoelectrode “clothespin” pattern at the crossings with the gate electrode. (d) Gold ring surrounding the array of nanoelectrodes and the gate electrode.

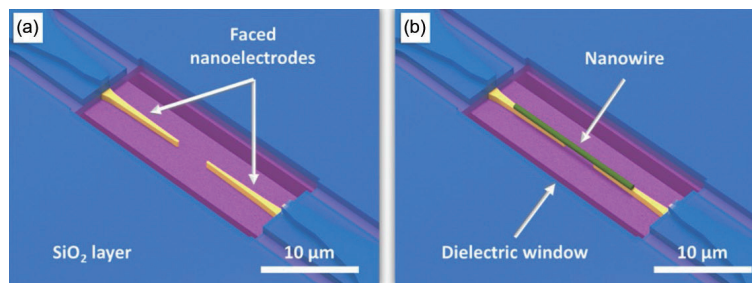


Figure 2 Illustration of the alignment dielectric (shielding) windows (a) before and (b) after integrating SNW by DEP.

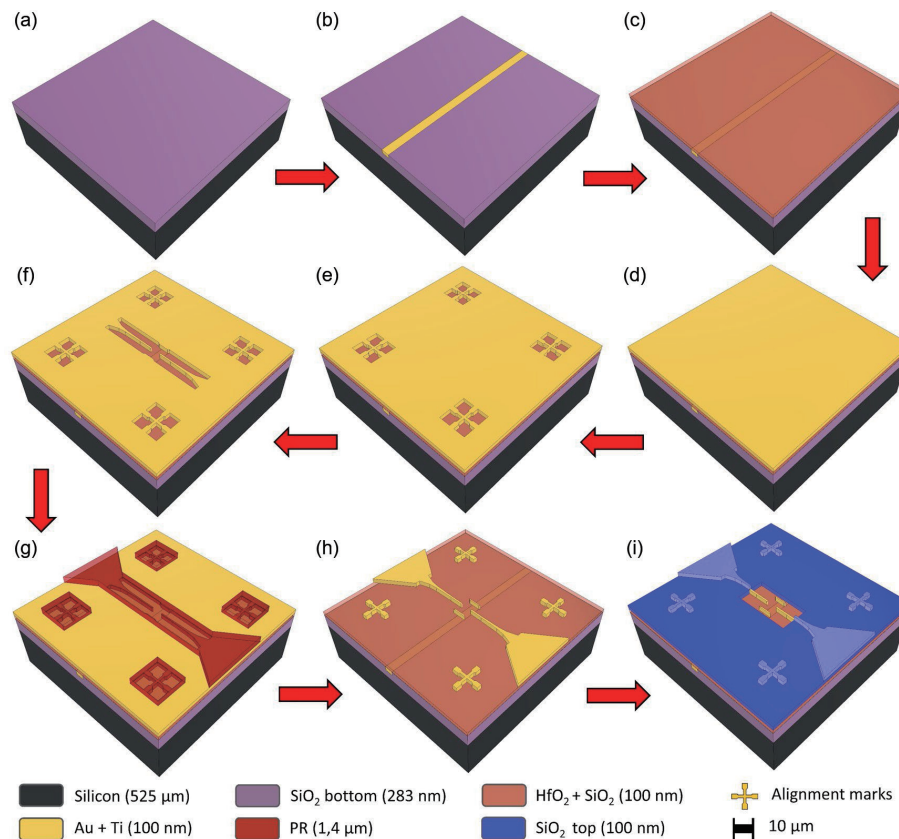


Figure 3 Schematic view of the chip fabrication process. (a) Si substrate with SiO₂ layer (thermal oxidation). (b) Buried gate electrode Ti/Au layer (e-beam evaporation). (c) Dielectric stack HfO₂ + SiO₂ layer (ALD deposition). (d) Ti/Au layer (e-beam evaporation). (e) EBL automatic calibration marks. (f) Faced nanoelectrodes (ion-milling). (g) Remaining electrode pattern fabrication (UV lithography). (h) Remaining electrode system linked to the faced nanoelectrodes after Au/Ti etching (ion-milling). (i) Wide window pattern created in SiO₂ layer (RIE).

process using a combination of bottom resist with standard positive PR. This process was performed as described above. Then, we deposited ~ 3 nm thick Ti as an adhesion layer and ~ 97 nm of Au using e-beam evaporator P397 (Bestec, Germany). Following, we removed the PR in NMP solution by placing the wafer upside-down to avoid the contamination caused by metal particles from the deposited layer on PR (Fig. 3(b)).

For the next step, we used ALD Fiji 200 system (Ultratech/Cambridge NanoTech, USA) to deposit the ~ 10 nm of HfO₂ and ~ 90 nm of SiO₂ that serve as gate dielectric stack (Fig. 3(c)). We also deposited a new Ti/Au stack over the dielectric stack with the same thickness as previously and spun the positive EBL resist, which was then exposed in e-beam writer Raith150 Two (Raith, Germany) (Figs. 3(d)–3(f)).

We used sophisticated tools to achieve high-resolution structures without distortion. A high-resolution EBL is severely impacted by process effects such as beam scattering effects (proximity) and tool implied artifact forming effects. Hence, we employed the GenISys Tracer[®] and Beamer[®] software that allow calibrating the exposition parameters by simulation for a specific resist type or thickness, taking into account the underlayer

materials. These effects cause the nonideal pattern transfer by various error sources. We extracted dose distribution data (Fig. 4) from Beamer software, which calculates according to GenISys Tracer[®] monte-carlo simulations to obtain high-resolution shapes. The resulting proximity effect simulation for the faced nanoelectrodes is shown in Fig. 4.

Thus, we exposed only the small areas to create the sharp ends of electrodes with ~ 200 and ~ 300 nm widths. Following, we used amyl acetate-based developer to create a pattern for the subsequent ion-milling. We used ion-milling system (SCIA, Germany) equipped with Kaufman ion-beam source to remove the Au and Ti and stop on underneath SiO₂ layer. An ion-mass spectrometer controlled this process. Then, we removed EBL resist in NMP solution.

Additionally, we created the pattern which connects the conductive paths to previously shaped “clothespin” (Figs. 5(a) and 5(b)). This pattern made of Ti/Au stack layer was defined by UV lithography using a negative PR followed by exposure on MA8. We used the PGMA (2-methoxy-1-methylethyl acetate)-based developer recommended by the supplier for this PR. We then used ion-milling instrument as described before to remove the rest

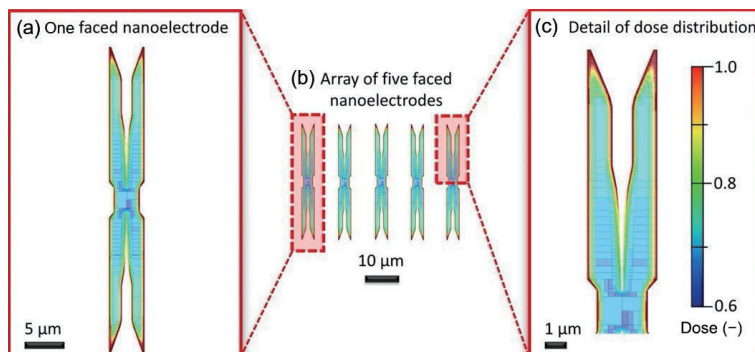


Figure 4 Illustration of EBL proximity effect simulation. (a) One faced nanoelectrode (“clothespin”), (b) array of five faced nanoelectrodes, and (c) detail of dose distribution with a dose scale bar.

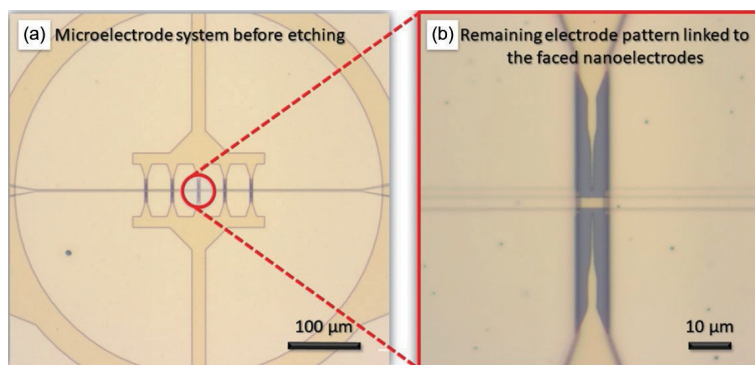


Figure 5 Connecting the remaining microelectrode system to the nanoelectrode array. (a) Microelectrode with a hydrophobic ring structure before etching. (b) Remaining electrode pattern linked to the faced nanoelectrodes.

of the Ti/Au layers. The PR was removed in NMP solution, and the wafer was rinsed by IPA and dried by nitrogen (Figs. 3(g) and 3(h)).

Finally, we performed the last deposition of ~ 100 nm thick SiO_2 layer using ALD. Such a layer forms the alignment windows that allow connecting the NWs between the faced nanoelectrodes during DEP, avoiding the connection with surrounding conductive paths (Fig. 3(i)). This step also allowed for opening the windows to the connection pads for wire bonding. As mentioned above, the design includes two types of windows. The wide window was formed using UV lithography employing the same positive PR as the first step. The narrow window was additionally shaped by EBL to achieve a small alignment window. We etched the SiO_2 layer in RIE instrument with Ar/CHF_3 plasma.

To finalize the whole process, the wafer was covered by positive PR as a protective layer and then diced using a saw into single chips with a size of ~ 5 mm \times 5 mm.

2.3 Nanowire synthesis and characteristics

Tungsten oxide NWs were synthesized at ~ 390 °C on small Si wafer tiles (~ 2 mm \times 2 mm) to facilitate the subsequent steps, including the dispersion of nanowires and DEP. The NWs were synthesized without catalyst seeds using Aerosol-Assisted Chemical Vapor Deposition (AACVD) method. The precursor solution consisted of a mixture of 5 mL of methanol (Penta, ≥ 99.8 %) and 20 mg of $\text{W}(\text{CO})_6$ (Sigma-Aldrich, ≥ 97 %). This solution was atomized using a piezoelectric ultrasonic atomizer (Johson Matthey Liquifog) and delivered to the reaction zone using N_2 flow as carrier gas. Further details of the process and equipment are described elsewhere [23, 24]. The structures synthesized by this method display NW-like morphology with diameters and lengths of ~ 100 nm and ~ 10 μm , respectively, as shown in the scanning electron microscope (SEM) image in Fig. 6(a). The NWs are crystalline, showing highly ordered lattices by high-resolution transmission electron microscopy (HRTEM) (Fig. 6(b)) with a

spacing distance (d) of ~ 3.5 Å. X-ray diffraction analysis of these films using Bragg-Brentano setup generally displayed intense diffraction peaks at 23.5° and 48.2° , corresponding to the 020 and second-order 040 diffractions of a monoclinic P21/n space group tungsten oxide (ICCD card no. 72-0677) as resolved previously [25]. This indicates a preferred orientation of the NWs in the (010) direction over the substrate, which is consistent with the planar spacing in the growth direction found by HRTEM. The inset in Fig. 6(b) shows the typical diffraction pattern recorded for the NWs. XPS of the nanowire displayed typical $\text{W } 4f_{7/2}$, $\text{W } 4f_{5/2}$, and $\text{W } 5p_{3/2}$ XPS core level peaks (Fig. 7, the adventitious C 1s peak located at 284.3 eV was used to calibrate the spectra), in agreement with previous reports on tungsten oxide nanowires synthesized via AACVD [26]. Two doublets were needed to fit the $\text{W } 4f$ core level spectrum. The main doublet peak at 35.4 eV is associated to the tungsten atoms with oxidation state of +6 from WO_3 , whereas the second doublet peak at 34.3 eV relates to the presence of tungsten atoms with oxidation state lower than +6, suggesting the presence of sub-stoichiometric tungsten oxide (WO_{3-x}). The spectrum also displays a small component centered at 41.2 eV assigned to the $\text{W } 5p_{3/2}$ core level spectrum.

2.4 Sensor assembling and NWs integration by DEP process

We used a TO-8 package of a soldered custom-made Al_2O_3 ceramic substrate with an isolated Pt heater fabricated using thick-film technology as a chip holder. Then we used thermal conductive paste Epotek H31D (Epoxy technology, USA) to stick the chip on the alumina (Al_2O_3) substrate. We made electrical connections between the chip and TO-8 package using wire-bonding method. The assembly structure was then placed into a printed circuit board connected to a waveform generator for the DEP procedure.

We detached the NWs from the Si tiles by immersing and sonicating them using SONOREX-Digital 10P (Bandelin,

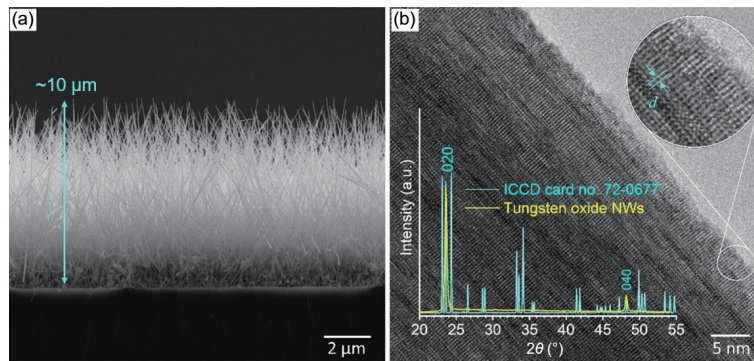


Figure 6 (a) Cross-section SEM image of the as-deposited NWs on Si substrate, and (b) HRTEM of a SNW showing in the insets of the interplanar spacings and the X-ray diffraction pattern of the NWs.

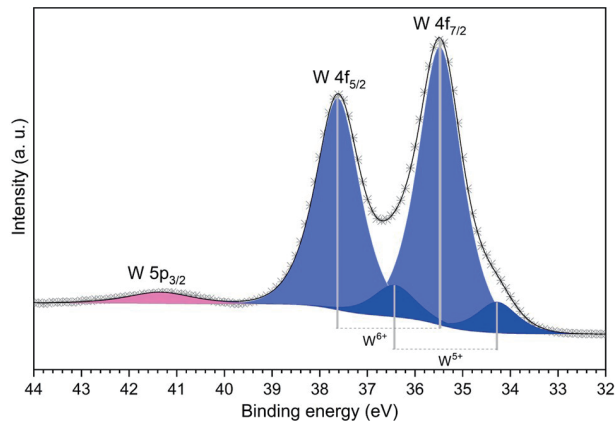


Figure 7 XPS core levels of the AACVD deposited nanowires showing the W 4f levels for stoichiometric WO_3 (light blue colour) and sub-stoichiometric WO_{3-x} (blue colour).

Germany) for ~ 10 s in a beaker with ~ 1 mL of deionized (DI) H_2O . DI H_2O is a polar medium with high permittivity and low evaporation coefficient that has proved better suitability for DEP process in comparison to volatile liquids such as isopropyl alcohol, methanol, ethanol, or acetone [22]. The DI H_2O solution containing the dispersed NWs was placed into a ~ 3 mL syringe connected to a contact angle measurement station Phoenix 300 (SEO, South Korea) equipped with charge coupled device (CCD) cameras (Fig. 8(a)). Then, a droplet with a volume of ~ 5 μL of the solution was deposited over the chip while connected to a waveform generator 33220A (Agilent, USA). This instrument generated an AC sine wave signal with peak-to-peak voltage of ~ 2.5 V with no DC offset at a frequency of ~ 9.5 MHz for ~ 120 s to align the SNW between the electrode pairs by dielectrophoretic forces. After a few seconds of the DEP process running, the droplet was dried by N_2 flow. Figure 8(b) shows an example of a pair of nanoelectrodes after integrating the nanowires.

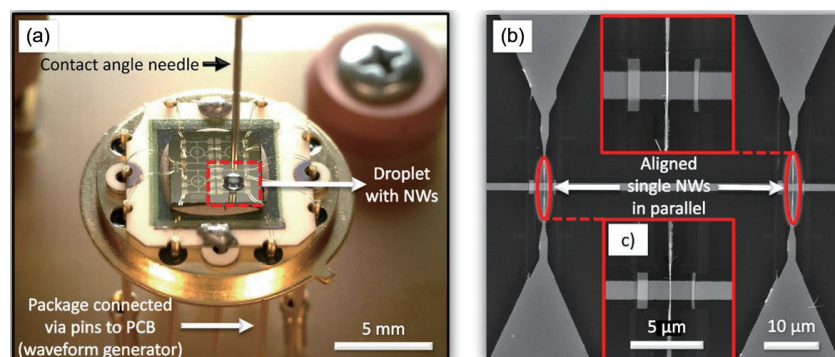


Figure 8 (a) Photograph of the chip and the drop containing the suspended nanowires ready for the DEP step. (b) View of the aligned SNWs integrated across the faced nanoelectrodes after DEP process. (c) Detailed view on a SNW between an electrode pair.

2.5 Electrical and gas sensing characterization

The behavior of the ChemFET's nanowire channel under the influence of sweeping gate voltage potential was measured in air at room temperature (RT) using a probe station MPS150 (Cascade Microtech, USA) connected to the parameter analyzer 4200-SCS (Keithley, USA). We used four-wire Kelvin arrangement to ensure the correct readout of drain-source voltage (V_{DS}) and drain current (I_{DS}), neutralizing the effect of probes and conductors. The ChemFET's output characteristics were obtained using common tests for MOSFET devices from the project library of the parameter analyzer's software Clarius (Tektronix, USA), which offers many pre-programmed characterization tests for various device measurements. Specifically, output characteristics were performed by sweeping the drain-source voltage ($V_{\text{DS}} = \pm 20$ V), keeping constant gate voltage (V_{G}) while measuring drain current (I_{DS}) flowing through the NW channel, whereas the transfer characteristics were recorded by keeping the V_{DS} constant when sweeping the ($V_{\text{G}} = \pm 10$ V) and measuring the channel current (I_{DS}) conductivity changes. The measured drain current (I_{DS}) flowing through the NW channel was limited to 120 nA ($I_{\text{DSmax}} = 120$ nA) to prevent damaging the NWs for both characterization tests.

The tests were performed in a custom-made gas station system equipped with three mass-flow controllers (MFCs) for precise gas flow adjustment in a range from ~ 1 $\text{mL}\cdot\text{min}^{-1}$ to ~ 2000 $\text{mL}\cdot\text{min}^{-1}$. The whole system is controlled by LabVIEW software, which allows the setting of automatically controlled measurement procedures and controls the MFCs, solenoid valves, stepper motor, and electronics for measurement. We used a source meter unit SMU 2450 (Keithley, USA) for the resistance measurement, and SMU 2401 (Keithley, USA) for gate voltage setting (V_{G}). For the heater, we employed a voltage source 3633A (Agilent, USA) controlled by a feedback loop and a calibrated temperature sensor Au 220 monitored by a multimeter 33410A (Agilent, USA). We

also used a power supply U3606A (Agilent, USA) to control the chamber heating system.

The assembled ChemFET was validated by testing the structures at various temperatures (T) ranging from RT \sim 22 to \sim 200 °C and towards H_2 and NO_2 due to tungsten oxide sensitivity to this gaseous analyte [25]. The sensor response (S_R) was defined as $[(R_{air}/R_{gas}) \times 100]$ for H_2 (reducing gas) and $[(R_{gas}/R_{air}) \times 100]$ for NO_2 (oxidizing gas), where R_{air} is the sensor resistance in air at the stationary state and R_{gas} is the sensor resistance after thirty minutes of analyte exposure. The response time (t_{resp}) was defined as the time required to reach 90% of the sensor response. Also, we explored the influence of the gate voltage (V_G) changes on the sensitivity to H_2 gas while monitoring the electrical resistance of the tungsten oxide SNWs between the drain and source electrodes and applying different I_{DS} . The isothermal measurements were performed using a constant I_{DS} and several cycles with different V_G . Each cycle included a stabilization period, response and recovery time equally long. The measurement cycle started with the V_G of 0 V and continued with different V_G in the following order of -5 and 5 V.

3 Results and discussion

The test and results of the assembled structures focussed on three aspects related to (1) the influence of the dielectric window size on the integration of SNWs by DEP process, (2) the influence of the gate voltage bias on the electrical properties of the SNW ChemFET channel and (3) the validation of the SNW ChemFET structure as a gas sensor.

3.1 Influence of dielectric window size

Figure 9 shows the surface topography mapping of the two types of fabricated dielectric windows recorded by atomic force microscopy (AFM) in ScanAsyst mode. These images evidence the difference between the wide (Fig. 9(a)) and narrow modifications (Fig. 9(b)). The green-colored surface shows the SiO_2 shielding layer, whereas the surface in yellow or orange displays the areas in which the gold layer was patterned. The opened windows, both wide and narrow, are displayed in dark

blue color.

Both window structures were tested for the integration of NWs by DEP process. Results in Fig. 10 show the SEM images of the structures after DEP and the significant difference between the number of captured NWs in both windows. One can notice from these results that the wide window holds bunches of multiple randomly connected NWs (MNWs) (Fig. 10(a)). In contrast, the narrow window facilitates the integration of SNW, allowing a good alignment of the NW between electrodes (Fig. 10(b)). These results indicate that despite the more complex fabrication process required to structure the narrow windows, such structures are well-suitable to limit the number of connected NWs to only SNW between the faced nanoelectrodes (Fig. 10(c)). While the electrode geometry is a key factor for the precise integration of one-dimensional structures, as demonstrated in previous reports [10, 27, 28], our results also indicate that the incorporation of shielding windows with similar dimensions to those of the NWs are more convenient for the NW integration process. Previously, we experimentally determined the most convenient nanoelectrode geometry for the AACVD tungsten nanowires. These structures allowed for integrating single nanowires in an array of nanoelectrodes with a success rate of approximately 33% [10]. The present system incorporating the shielding nanowindows showed a similar success rate. However, it added advantages compared to the previous system, including a better alignment of the NWs, and avoiding their aggregation along and across the faced nanoelectrodes, as shown in Fig. 10(a).

Therefore, we used the narrow dielectric window structures to study further the SNW-based ChemFET gas sensors. Further analysis of these structures by AFM also demonstrates the integration of the wire, and its contact with the nanoelectrodes suggests that the NWs are flexible and attempt to reproduce the surface topography in the window (Fig. 11).

3.2 Electrical properties of ChemFET structure

The output characteristics of the ChemFET using a constant gate voltage V_G (from -6 to 6 V with steps of 1 V) and varying the drain to source voltage V_{DS} (from 0 to 3 V) are shown in Fig. 12(a).

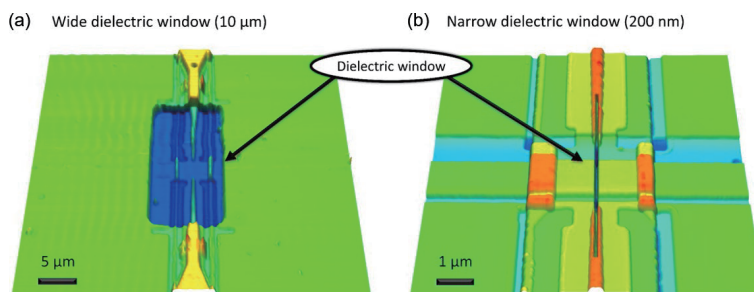


Figure 9 AFM topography images of the alignment windows. (a) Wide alignment window ($10 \mu\text{m}$), and (b) narrow alignment window (200 nm).

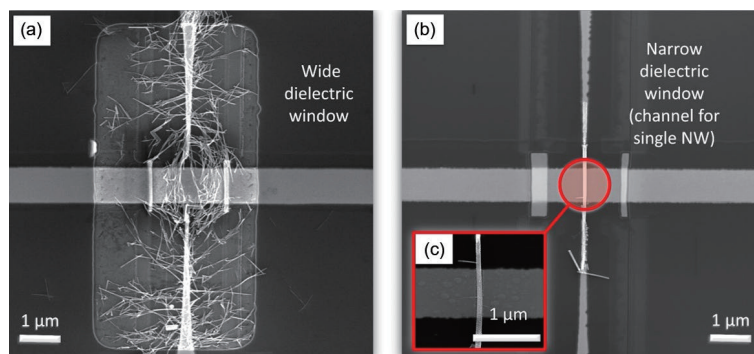


Figure 10 SEM inspection of two dielectric windows modification after DEP process. (a) Wide dielectric window with multiple interconnected NWs. (b) Narrow dielectric window with SNW interconnection. (c) Detail of SNW aligned within the window channel.

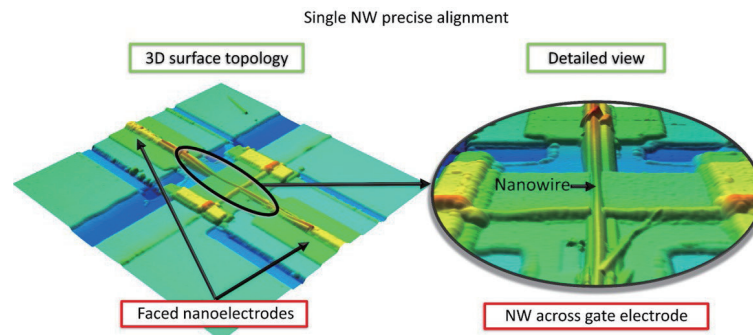


Figure 11 Detailed 3D surface topography obtained by AFM ($15\ \mu\text{m} \times 15\ \mu\text{m}$) showing an aligned SNW inside the narrow dielectric window and across the gate electrode.

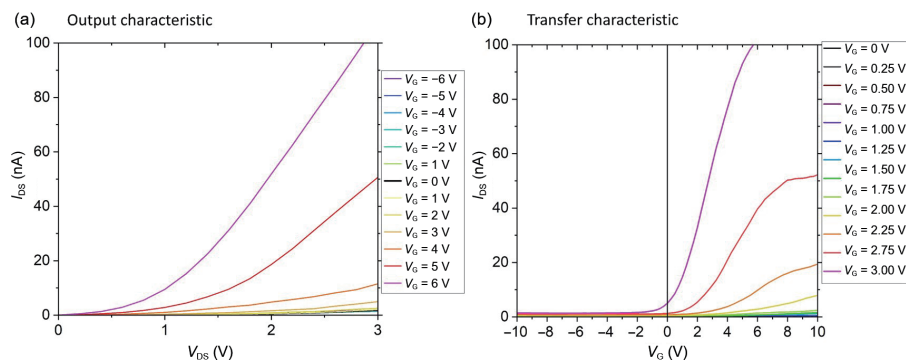


Figure 12 (a) Output, and (b) transfer characteristic of the nanowire channel of the ChemFET structure.

Significant enhancement of the current density through the channel is particularly noticeable at gate bias voltage above $V_G = 3\ \text{V}$. For example, when we applied a drain to source voltage V_{DS} of $3\ \text{V}$ and gate voltage V_G of $6\ \text{V}$ (see the output characteristic curve), the drain current I_{DS} is two times higher ($I_{DS} > 100\ \text{nA}$) than the drain current I_{DS} recorded for a gate voltage V_G of $5\ \text{V}$ ($I_{DS} \sim 50\ \text{nA}$) applied at the same drain to source voltage ($V_{DS} = 3\ \text{V}$). Results in Fig. 12a demonstrate that the drain current (I_{DS}) flowing through the nanowire channel has a direct proportional increase to the positive increments of the gate voltage (V_G) and the drain to source bias V_{DS} is in agreement with previous literature [29]. In contrast, the negative gate bias tends to close the channel, and drop the drain current I_{DS} . The influence of the gate bias on the switching properties (ON and OFF) of the drain current I_{DS} is better interpreted by evaluating the transfer characteristic displayed in Fig. 12(b). The transfer characteristic was measured at a constant drain to source voltage V_{DS} (from 0 to $3.5\ \text{V}$) with steps of $0.25\ \text{V}$ and varying the gate voltage V_G from -10 to $10\ \text{V}$. The influence of the gate voltage V_G on the channel's drain current I_{DS} can be observed in Fig. 12(b). Results show that positive gate biases lead to higher NW channel conductivity, especially when applying a drain to source voltage V_{DS} of $3\ \text{V}$. In contrast, negative gate biases generally deplete of charge carriers in the NW channel diminishing the conductivity through it. However, this behavior depends partly on the drain to source voltage V_{DS} . Thus, we observed that when the drain to source voltage V_{DS} reaches a certain level, for example: for $V_{DS} = 3\ \text{V}$, the negative gate bias is unable to keep the channel closed, showing a small drain current I_{DS} as the gate voltage V_G changes from 0 to $-2\ \text{V}$ approximately. Despite this, the transfer characteristic clearly shows the switching behavior of the SNW-based ChemFET channel and exhibits the control of the gate bias V_G on drain current I_{DS} by opening or closing the conduction channel as the gate bias V_G passes from positive to negative bias.

The observed output and transfer characteristics prove the presence of a n-type channel material integrated across the faced nanoelectrodes, similar to other reports on NW FET structures in

the literatures [30, 31]. The following section describes the gas sensing properties and mechanism of detection in this type of structures with more details.

3.3 Gas sensing characterization

To evaluate the gas sensing properties of the ChemFETs, we tested the influence of various parameters, including the operating temperature, gate voltage, and drain current. The baseline resistances remained at stable values during the whole measurement. The assembled ChemFET structures were validated to reducing (H_2) and oxidizing (NO_2) gases at $200\ ^\circ\text{C}$, as this temperature was found to deliver the maximum responses to these analytes, in agreement with our previous evaluations for tungsten oxide SNWs [10]. The measurement of the baseline resistance in air (R_{air}) towards different drain-source currents (I_{DS}) displayed an inverse dependence of the R_{air} to I_{DS} , showing a R_{air} saturation point for drain-source currents above $20\ \text{nA}$. Results in Fig. 13 also show the dependency of R_{air} on V_G , showing a noticeable increase of the SNW's resistance as the V_G changes from $0\ \text{V}$ to negative bias. This is consistent with the literature and attributed to the withdrawal of electrons from the n-type tungsten oxide NW, which narrows the conduction channel (D_{cond}) and increases the wire's electrical resistance [32].

In contrast, when V_G changes from $0\ \text{V}$ to positive bias, the NW's resistance decreases, suggesting a nonlinear behavior for the conductivity. This is also in agreement with other ChemFET gas sensors in the literatures [32–34], and it is believed to occur due to the saturation of the electron density in the NW channel [32]. The inset in Fig. 13 illustrates this phenomenon by showing the widening and narrowing of the NW conduction channel as V_G changes from positive to negative bias, respectively.

Measurements of the NW response (S_R) to H_2 and NO_2 revealed a different tendency concerning the V_G for each gas (Fig. 14). For instance, results for H_2 showed an improvement of the response by applying negative V_G instead of positive, whereas results for NO_2 indicated a soft diminution of the response as a function of the positive and negative V_G . Overall, results show a

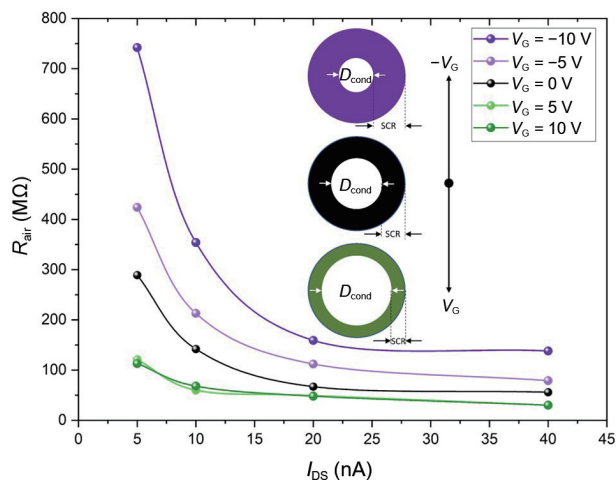


Figure 13 Dependency of the baseline resistance (in air) on V_G and I_{DS} . The inset illustrates the effect of V_G on the NW conduction channel (D_{cond}).

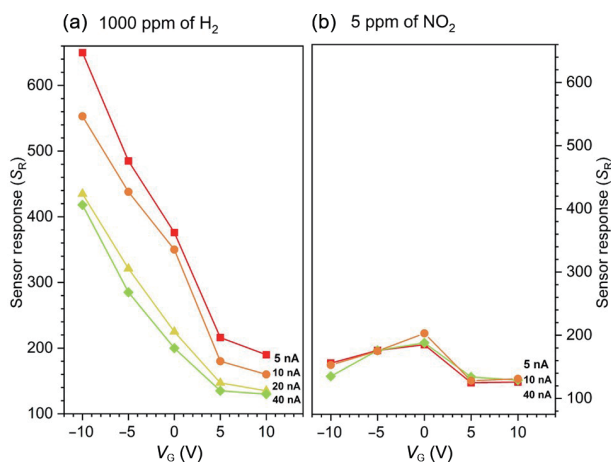


Figure 14 Dependency of the sensor response on the gate bias (V_G) and drain current (I_{DS}) in the presence of (a) 1000 ppm of H_2 , and (b) 5 ppm of NO_2 .

similar tendency, regardless of the I_{DS} applied, displaying greater response magnitudes for an I_{DS} of 5 nA than that of 10, 20, or 40 nA in the case of H_2 . The sensor response became noisy and unstable for some of the measurements as V_G reached -10 V, suggesting these conditions are close to the operation limit of the ChemFET structure when working at a high temperature (200 °C). **Figure 15(a)** displays the influence of the response time (t_{resp}) towards V_G , showing an improvement of the response dynamics to H_2 for negative V_G . Better response dynamics were also noticed for NO_2 by operating the sensor in ChemFET with both positive and negative V_G . Moreover, the tests to different concentrations of H_2 showed proportional changes with the concentrations, suggesting a linear behavior (**Fig. 15(b)**).

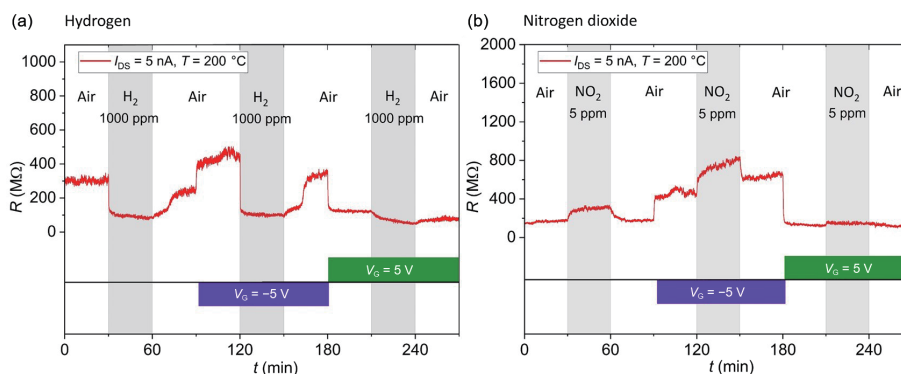


Figure 16 Effect of the V_G sweeping on the response of the SNW-based WO_{3-x} gas sensor in the presence of (a) 1000 ppm of H_2 , and (b) 5 ppm of NO_2 measured both at the same temperature of 200 °C and constant current $I_{DS} = 5$ nA.

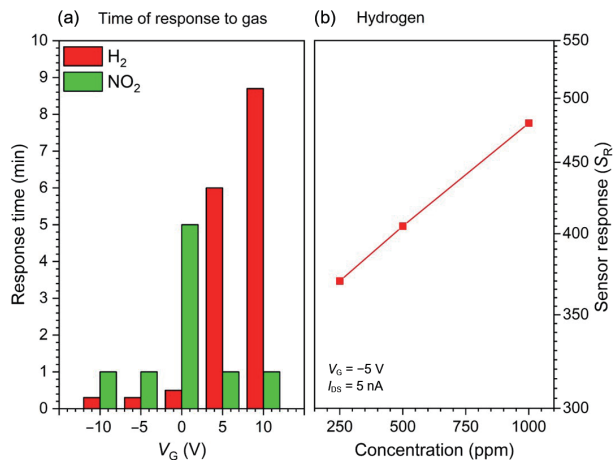


Figure 15 (a) Response time of ChemFET to H_2 (1000 ppm) and NO_2 (5 ppm). (b) Dependency of the response on different H_2 concentrations.

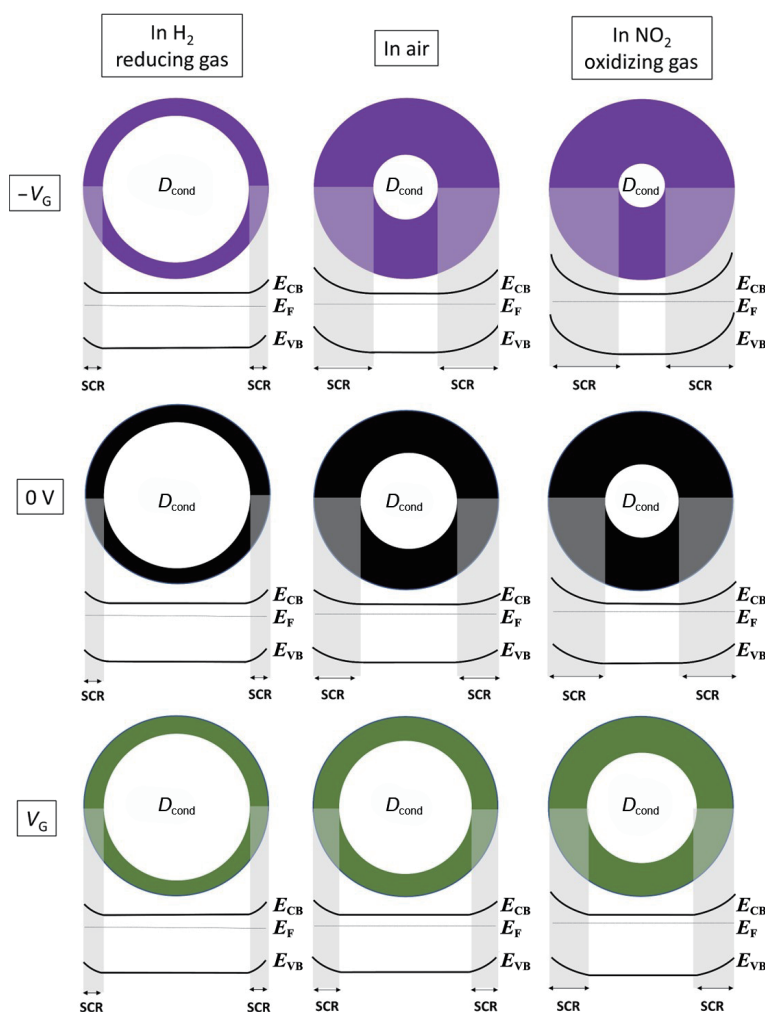
Figure 16 compares the typical responses to hydrogen and nitrogen dioxide recorded on the ChemFET sensors for V_G of 0 and ± 5 V. The responses corroborate the n-type semiconductor behavior of the tungsten oxide NWs, showing a decrease of the electrical resistance towards hydrogen (reducing gas), and reversely an increase of the electrical resistance towards nitrogen dioxide (oxidizing gas).

The response magnitudes of the ChemFET are also comparable or better than other nanowire-based gas sensors in the literatures (**Table 1**), including those based on multiple nanowires (M-NWs). The single nanowire arrays (S-NWA) evaluated here also show better response time (e.g., to H_2 , 20 s) compared to previous chemoresistive sensors based on multiple nanowires (290 s) [25]. Overall, results suggest that the ChemFET structures are good at improving the sensor response and the time of response (particularly to H_2) with respect to resistive sensors based on single or multiple nanowires. It is worth noticing, though, that these comparisons represent only an approximation of the quality of the sensors as their performance generally depends on a variety of other parameters, including the sensing material, sensor architecture, and test parameters.

Figure 17 illustrates the effect of the reducing and oxidizing gases on the conduction channel of the semiconducting wires after the air pre-adsorption cycle. The illustration depicts how the initial change of the baseline resistance (observed both in **Figs. 16** and **17**) has a strong influence on the magnitude of response as a function of applied V_G . This is noticed particularly for the reducing analyte, which shows a response dominated by the V_G dependant conductivity changes in the pre-adsorption stage rather than hydrogen exposure (the resistance in hydrogen shows a non-dependant behavior concerning applied V_G , **Fig. 16(a)**). This is also observed for the oxidizing gas, although at lower proportion,

Table 1 Comparative table displaying the response and recovery times recorded in this work and the literatures towards H₂ and NO₂

Structures	Material	Operation principle	Gas	S _R (%)	t _{resp} (s)	T(°C)	Concentration ppm	Reference
S-NWA	WO _{3-x}	FET (V _G = -10V)	H ₂	650	20	200	1000	This work
S-NW	SnO ₂	Resistive	H ₂	342	20	200	500	[35]
M-NWs	WO _{3-x}	Resistive	H ₂	450	290	250	500	[25]
M-NWs	SnO ₂	Resistive	H ₂	140	35	210	400	[36]
S-NWA	WO _{3-x}	FET (V _G = -10V)	NO ₂	156	60	200	5	This work
S-NWA	WO _{3-x}	Resistive	NO ₂	248	360	250	5	[10]
S-NW	ITO	Resistive	NO ₂	108	60	200	5	[37]
M-NWA	ZnO	Resistive	NO ₂	250	140	~ 160	5	[38]

**Figure 17** Illustration of the gas sensing mechanism, and the influence of the gate voltage (V_G) and gas type on the conduction channel of the gas-sensitive NW (cross-sectional view). D_{cond} is the diameter of the non-depleted region available for charge conduction through the NW, E_{CB} is the conduction band minimum, E_F is the Fermi level, E_{VB} is the valence band maximum, and SCR represents the space charge region at the NW surface (not to scale).

as both air and NO₂ have similar effects on the wire surface. This is because (regardless of the conductivity type of the sensing material) the oxidizing gases withdraw electrons from the conductive channel and the material becomes depleted of electrons. In contrast, reducing gases donate electrons to the sensing material [10]. This is the reason why the response of the n-type ChemFET does not show significant improvement to NO₂ compared to the resistive mode ($V_G = 0$ V). To favor the response to oxidizing gases, p-type sensing materials are suggested [31].

Figure 14 corroborates and summarizes this statement by showing that the main contribution to the ChemFET response upon H₂ occurs in the subthreshold regime, particularly under conditions when the negative gate bias is applied and the NW

channel is almost closed, in agreement with other reports in the literatures dealing with NW ChemFET sensors [39, 40].

Overall, results indicate that the sensor response to reducing gases is especially influenced by the changes of the baseline resistance in the preabsorbed state (in air) induced by the gate voltage (Fig. 17). Also, the tests show that the responses to H₂ increase by setting a low drain current through the NW channel, i.e., by operating the ChemFET in the subthreshold regime.

The results above validate the functionality of the ChemFET sensor array, showing consistent behavior with previous single ChemFET sensors based on n-type semiconductors towards reducing and oxidizing gases. Such a sensing device, which includes other complementary nanoelectrode arrays in the same

chip, could favor the selectivity of gas sensors by introducing sensing structures (i.e., conduction channels) with different characteristics. Using one type of semiconductor is not beneficial in distinguishing the types of gases as long as no metal-oxide material is exclusively selective for a given analyte. In this context, the design and fabrication methods showed in this work may be an attractive route for developing the next generation of e-nose based on ChemFET gas sensors operating with single gas-sensitive nanowires.

4 Conclusions

This work described and discussed the design, fabrication, and functionality of ChemFET nanosensor arrays based on SNWs. The fabrication of these new structures exploited the use of micro and nanofabrication techniques combining both UV and e-beam lithography and adding unique processing steps for building ChemFET array structures (taking further the processes we previously developed for chemoresistive sensors [10]). The new structures improved the selective integration of SNWs due to each element of the ChemFET array containing shielding nanoscale windows (200–300 nm) adapted to the diameter of the SNW (100 nm). The SNW-based ChemFET array's output and transfer characteristics demonstrated the gate bias role in regulating the drain current. These properties allowed the structures to operate as stable ChemFET gas detectors registering low deviations of the baseline resistance during the tests. Overall, results proved the possibility of tuning the response of the SNWs by modulating the applied voltage gate and drain current, demonstrated improved characteristics to H₂ when the ChemFET operates in the subthreshold regime. The new structure and methods proposed for fabricating SNW-based ChemFET arrays proved to be versatile, reproducible, and most likely capable of adapting to other systems where SNW arrays are required.

Acknowledgements

This work was supported by the Czech Science Foundation (GAČR, No. 22-14886S), and the MCIN/AEI/10.13039/501100011033 (No. PID2019-107697RB-C42 (ERDF A way of making Europe)).

Conflict of Interest

The authors declare no conflict of interest.

Author Contributions

O. C. conceived of the presented idea, run experiments, and wrote the manuscript with support from I. G. and J. B. J. S. contributed to the chip design and fabrication. S. V. wrote and revised the manuscript, and got the funding for realizing this work. All authors provided critical feedback and discussed the results to the final manuscript.

Funding note: Open access publishing supported by the National Technical Library in Prague.

Open Access This article is licensed under a Creative Commons Attribution 4.0 International License, which permits use, sharing, adaptation, distribution and reproduction in any medium or format, as long as you give appropriate credit to the original author(s) and the source, provide a link to the Creative Commons licence, and indicate if changes were made.

The images or other third party material in this article are included in the article's Creative Commons licence, unless

indicated otherwise in a credit line to the material. If material is not included in the article's Creative Commons licence and your intended use is not permitted by statutory regulation or exceeds the permitted use, you will need to obtain permission directly from the copyright holder.

To view a copy of this licence, visit <http://creativecommons.org/licenses/by/4.0/>.

References

- Miller, D. R.; Akbar, S. A.; Morris, P. A. Nanoscale metal oxide-based heterojunctions for gas sensing: A review. *Sens. Actuat. B Chem.* **2014**, *204*, 250–272.
- Liu, L.; Wang, Y. Y.; Liu, Y. H.; Wang, S. Q.; Li, T.; Feng, S. M.; Qin, S. J.; Zhang, T. Heteronanostructural metal oxide-based gas microsensors. *Microsyst. Nanoeng.* **2022**, *8*, 85.
- Gurlo, A. Nanosensors: Towards morphological control of gas sensing activity. *SnO₂, In₂O₃, ZnO and WO₃ case studies. Nanoscale* **2011**, *3*, 154–165.
- Gao, W. Y.; Zdrachek, E.; Xie, X. J.; Bakker, E. A solid-state reference electrode based on a self-referencing pulstrode. *Angew. Chem., Int. Ed.* **2020**, *132*, 2314–2318.
- Zhai, J. Y.; Yuan, D. J.; Xie, X. J. Ionophore-based ion-selective electrodes: Signal transduction and amplification from potentiometry. *Sens. Diagn.* **2022**, *1*, 213–221.
- Kaisti, M. Detection principles of biological and chemical FET sensors. *Biosens. Bioelectron.* **2017**, *98*, 437–448.
- Chartuprayoon, N.; Zhang, M. L.; Bosze, W.; Choa, Y. H.; Myung, N. V. One-dimensional nanostructures based bio-detection. *Biosens. Bioelectron.* **2015**, *63*, 432–443.
- Lu, Z. C.; Zhou, H.; Wang, Y.; Liu, Y. X.; Li, T. A controllable fabrication improved silicon nanowire array sensor on (111) SOI for accurate bio-analysis application. *Nano Res.* **2022**, *15*, 7468–7475.
- Zou, X. M.; Wang, J. L.; Liu, X. Q.; Wang, C. L.; Jiang, Y.; Wang, Y.; Xiao, X. H.; Ho, J. C.; Li, J. C.; Jiang, C. Z. et al. Rational design of sub-parts per million specific gas sensors array based on metal nanoparticles decorated nanowire enhancement-mode transistors. *Nano Lett.* **2013**, *13*, 3287–3292.
- Chmela, O.; Sadilek, J.; Domènech-Gil, G.; Samà, J.; Somer, J.; Mohan, R.; Romano-Rodríguez, A.; Hubálek, J.; Vallejos, S. Selectively arranged single-wire based nanosensor array systems for gas monitoring. *Nanoscale* **2018**, *10*, 9087–9096.
- Vallejos, S.; Gràcia, I.; Chmela, O.; Figueras, E.; Hubálek, J.; Cané, C. Chemoresistive micromachined gas sensors based on functionalized metal oxide nanowires: Performance and reliability. *Sens. Actuat. B Chem.* **2016**, *235*, 525–534.
- Brunet, E.; Maier, T.; Mutinati, G. C.; Steinhauer, S.; Köck, A.; Gspan, C.; Grogger, W. Comparison of the gas sensing performance of SnO₂ thin film and SnO₂ nanowire sensors. *Sens. Actuat. B Chem.* **2012**, *165*, 110–118.
- Chen, X. P.; Wong, C. K. Y.; Yuan, C. A.; Zhang, G. Q. Nanowire-based gas sensors. *Sens. Actuat. B Chem.* **2013**, *177*, 178–195.
- Penner, R. M. Chemical sensing with nanowires. *Annu. Rev. Anal. Chem.* **2012**, *5*, 461–485.
- Ramgir, N. S.; Yang, Y.; Zacharias, M. Nanowire-based sensors. *Small* **2010**, *6*, 1705–1722.
- Hernández-Ramírez, F.; Tarancón, A.; Casals, O.; Rodríguez, J.; Romano-Rodríguez, A.; Morante, J. R.; Barth, S.; Mathur, S.; Choi, T. Y.; Poulidakos, D. et al. Fabrication and electrical characterization of circuits based on individual tin oxide nanowires. *Nanotechnology* **2006**, *17*, 5577–5583.
- Domènech-Gil, G.; Barth, S.; Samà, J.; Pellegrino, P.; Gràcia, I.; Cané, C.; Romano-Rodríguez, A. Gas sensors based on individual indium oxide nanowire. *Sens. Actuat. B Chem.* **2017**, *238*, 447–454.
- Wang, M. C. P.; Gates, B. D. Directed assembly of nanowires. *Mater. Today* **2009**, *12*, 34–43.
- Burg, B. R.; Poulidakos, D. Large-scale integration of single-walled carbon nanotubes and graphene into sensors and devices using dielectrophoresis: A review. *J. Mater. Res.* **2011**, *26*, 2123.
- Smith, B. D.; Mayer, T. S.; Keating, C. D. Deterministic assembly of

- functional nanostructures using nonuniform electric fields. *Annu. Rev. Phys. Chem.* **2012**, *63*, 241–263.
- [21] Raychaudhuri, S.; Dayeh, S. A.; Wang, D. L.; Yu, E. T. Precise semiconductor nanowire placement through dielectrophoresis. *Nano Lett.* **2009**, *9*, 2260–2266.
- [22] Maijenburg, A. W.; Maas, M. G.; Rodijk, E. J. B.; Ahmed, W.; Kooij, E. S.; Carlen, E. T.; Blank, D. H. A.; Ten Elshof, J. E. Dielectrophoretic alignment of metal and metal oxide nanowires and nanotubes: A universal set of parameters for bridging prepatterned microelectrodes. *J. Colloid Interface Sci.* **2011**, *355*, 486–493.
- [23] Vallejos, S.; Gràcia, I.; Figueras, E.; Cané, C. Catalyst-free vapor-phase method for direct integration of gas sensing nanostructures with polymeric transducing platforms. *J. Nanomater.* **2014**, *2014*, 932129.
- [24] Vallejos, S.; Pizúrová, N.; Čechal, J.; Gràcia, I.; Cané, C. Aerosol-assisted chemical vapor deposition of metal oxide structures: Zinc oxide rods. *J. Vis. Exp.* **2017**, *127*, 56127.
- [25] Vallejos, S.; Umek, P.; Stoycheva, T.; Annanouch, F.; Llobet, E.; Correig, X.; De Marco, P.; Bittencourt, C.; Blackman, C. Single-step deposition of au- and pt-nanoparticle-functionalized tungsten oxide nanoneedles synthesized via aerosol-assisted CVD, and used for fabrication of selective gas microsensor arrays. *Adv. Funct. Mater.* **2013**, *23*, 1313–1322.
- [26] Navío, C.; Vallejos, S.; Stoycheva, T.; Llobet, E.; Correig, X.; Snyders, R.; Blackman, C.; Umek, P.; Ke, X. X.; Van Tendeloo, G. et al. Gold clusters on WO₃ nanoneedles grown via AACVD: XPS and TEM studies. *Mater. Chem. Phys.* **2012**, *134*, 809–813.
- [27] Xu, D. D.; Subramanian, A.; Dong, L. X.; Nelson, B. J. Shaping nanoelectrodes for high-precision dielectrophoretic assembly of carbon nanotubes. *IEEE Trans. Nanotechnol.* **2009**, *8*, 449–456.
- [28] Montemurro, D.; Stornaiuolo, D.; Massarotti, D.; Ercolani, D.; Sorba, L.; Beltram, F.; Tafuri, F.; Roddaro, S. Suspended InAs nanowire Josephson junctions assembled via dielectrophoresis. *Nanotechnology* **2015**, *26*, 385302.
- [29] Huo, J. P.; Zou, G. S.; Lin, L. C.; Wang, K. H.; Xing, S. L.; Zhao, G. L.; Liu, L.; Zhou, Y. N. Highly focused femtosecond laser directed selective boron doping in single SiC nanowire device for n-p conversion. *Appl. Phys. Lett.* **2019**, *115*, 133104.
- [30] Jakhar, A.; Dhyani, V.; Das, S. Room temperature terahertz detector based on single silicon nanowire junctionless transistor with high detectivity. *Semicond. Sci. Technol.* **2020**, *35*, 125020.
- [31] Han, J. W.; Rim, T.; Baek, C. K.; Meyyappan, M. Chemical gated field effect transistor by hybrid integration of one-dimensional silicon nanowire and two-dimensional tin oxide thin film for low power gas sensor. *ACS Appl. Mater. Interfaces* **2015**, *7*, 21263–21269.
- [32] Zhang, Y.; Kolmakov, A.; Chretien, S.; Metiu, H.; Moskovits, M. Control of catalytic reactions at the surface of a metal oxide nanowire by manipulating electron density inside it. *Nano Lett.* **2004**, *4*, 403–407.
- [33] Feng, P.; Shao, F.; Shi, Y.; Wan, Q. Gas sensors based on semiconducting nanowire field-effect transistors. *Sensors (Basel)* **2014**, *14*, 17406–17429.
- [34] Zhou, X. Y.; Wang, Y.; Wang, J. X.; Xie, Z.; Wu, X. F.; Han, N.; Chen, Y. F. Amplifying the signal of metal oxide gas sensors for low concentration gas detection. *IEEE Sens. J.* **2017**, *17*, 2841–2847.
- [35] Tonezzer, M. Selective gas sensor based on one single SnO₂ nanowire. *Sens. Actuat. B Chem.* **2019**, *288*, 53–59.
- [36] Thai, N. X.; Van Duy, N.; Hung, C. M.; Nguyen, H.; Tonezzer, M.; Van Hieu, N.; Hoa, N. D. Prototype edge-grown nanowire sensor array for the real-time monitoring and classification of multiple gases. *J. Sci. Adv. Mater. Dev.* **2020**, *5*, 409–416.
- [37] Afshar, M.; Preiß, E. M.; Sauerwald, T.; Rodner, M.; Feili, D.; Straub, M.; König, K.; Schütze, A.; Seidel, H. Indium-tin-oxide single-nanowire gas sensor fabricated via laser writing and subsequent etching. *Sens. Actuat. B Chem.* **2015**, *215*, 525–535.
- [38] Chen, X. X.; Shen, Y. B.; Zhang, W.; Zhang, J.; Wei, D. Z.; Lu, R.; Zhu, L. J.; Li, H. S.; Shen, Y. S. In-situ growth of ZnO nanowire arrays on the sensing electrode via a facile hydrothermal route for high-performance NO₂ sensor. *Appl. Surf. Sci.* **2018**, *435*, 1096–1104.
- [39] Ahn, J. H.; Yun, J.; Choi, Y. K.; Park, I. Palladium nanoparticle decorated silicon nanowire field-effect transistor with side-gates for hydrogen gas detection. *Appl. Phys. Lett.* **2014**, *104*, 013508.
- [40] Kim, D.; Park, C.; Choi, W.; Shin, S. H.; Jin, B.; Baek, R. H.; Lee, J. S. Improved long-term responses of Au-decorated Si nanowire FET sensor for NH₃ detection. *IEEE Sens. J.* **2020**, *20*, 2270–2277.







NANOLITHOGRAPHY TOOLBOX—Simplifying the design complexity of microfluidic chips

Cite as: J. Vac. Sci. Technol. B 38, 063002 (2020); doi: 10.1116/6.0000562

Submitted: 17 August 2020 · Accepted: 9 October 2020 ·

Published Online: 10 November 2020



Haoqing Zhang,¹  Jan Pekárek,^{1,2,3}  Jianguo Feng,¹  Xiaocheng Liu,¹ Huanan Li,¹ Hanliang Zhu,¹  Vojtěch Svatoš,³ Imrich Gablech,³  Pavel Podešva,¹  Sheng Ni,⁴  Levent Yobas,⁴  and Pavel Neuzil^{1,2,3,a)} 

AFFILIATIONS

¹Ministry of Education Key Laboratory of Micro/Nano Systems for Aerospace, Department of Microsystem Engineering, School of Mechanical Engineering, Northwestern Polytechnical University, 127 West Youyi Road, Xi'an, Shaanxi 710072, People's Republic of China

²Central European Institute of Technology, Brno University of Technology, Purkyňova 123, 612 00 Brno, Czech Republic

³Department of Microelectronics, Faculty of Electrical Engineering and Communication, Brno University of Technology, Technická 3058/10, 616 00 Brno, Czech Republic

⁴Department of Electronic and Computer Engineering, Hong Kong University of Science and Technology, Kowloon, Hong Kong, SAR, People's Republic of China

^{a)}Electronic mail: pavel.neuzil@nwpu.edu.cn

ABSTRACT

Microfluidic devices typically require complex shapes such as funnels, spirals, splitters, channels with different widths, or customized objects of arbitrary complexity with a smooth transition between these elements. Device layouts are generally designed by software developed for the design of integrated circuits or by general computer-aided design drawing tools. Both methods have their limitations, making these tasks time consuming. Here, a script-based, time-effective method to generate the layout of various microfluidic chips with complex geometries is presented. The present work uses the NANOLITHOGRAPHY TOOLBOX (NT), a platform-independent software package, which employs parameterized fundamental blocks (cells) to create microscale and nanoscale structures. In order to demonstrate the functionality and efficiency of the NT, a few classical microfluidic devices were designed using the NT and then fabricated in glass/silicon using standard microfabrication techniques and in poly(dimethylsiloxane) using soft lithography as well as more complex techniques used for flow-through calorimetry. In addition, the functionality of a few of the fabricated devices was tested. The powerful method proposed allows the creation of microfluidic devices with complex layouts in an easy way, simplifying the design process and improving design efficiency. Thus, it holds great potential for broad applications in microfluidic device design.

Published under license by AVS. <https://doi.org/10.1116/6.0000562>

I. INTRODUCTION

The first modern microfluidic device¹ introduced in 1979 brought about an awareness of the new application of planar technology, but it failed to trigger an actual interest in it. About ten years later, the recent expansion in microfluidics was instigated by the introduction of a new concept of miniaturized microfluidic chips,^{2–4} for example, performing traditional analytical chemistry, capillary electrophoresis (CE),⁵ and a flow-through polymerase chain reaction (PCR).⁶ The device layout was typically designed using either software developed for the design of integrated circuits (ICs) or general drawing tools such as computer-aided design

(CAD). Interfacing with mask-making tools, such as a direct-write laser or electron-beam machines, is commonly done via a semiconductor standard binary format graphic data system II (GDSII). Alternatively, text-based Caltech intermediate form (CIF) is used but less frequently. Another option is to use a nontraditional data exchange (interchange) format (DXF) to form an interface with general purpose CAD software.

The typical IC layout editor uses a layout editing-friendly form with hierarchical architecture and limited nonorthogonal features, such as circles, arcs, and donut shapes. Often, the software has the option to form parameterized blocks called cells, making

09 May 2024 07:37:01

the layout editing work fast and efficient. Nevertheless, the cells typically have to be made on demand to create the parameterized cells set by users. A spiral with their vertex locations generated was created using a mathematical formula in a spreadsheet application. Then, the polygon was converted into a CIF format and uploaded into a cell of the IC layout editor software. This procedure was tedious, and the subsequent layout editing required the repetition of this procedure a number of times.

Popular CAD software can also be used to create complex layouts. However, a typical problem with this software is a lack of hierarchy, which makes layout editing a time-consuming task. In addition, CAD software only exports DXF files instead of files in the standard GDSII or CIF file formats. Often, the generated layouts have open polygons and the feature dimensions are incompatible.

Microfluidic devices typically necessitate much more complex shapes, such as funnels, spirals, splitters, and channels with sections of different widths, and require an especially smooth transition between objects and sections to eliminate singularities and dead volumes. A novel layout designer is necessary for a microfluidic layout to be generated in an effective way and also to fulfill the proposed requirements.

Here, a new, platform-independent method of generating microfluidic chip layouts is introduced. The method leverages script-based parameterized structures offered with the microfluidic library of the NANOLITHOGRAPHY TOOLBOX (NT).⁷ The library was developed in collaboration with the researchers who are also the creators of the NT at the National Institute of Standards and Technology's (NIST's) Center for Nanoscale Science and Technology (CNST) in Gaithersburg, MD. It is freely accessible from the site: <https://www.nist.gov/services-resources/software/cnst-nanolithography-toolbox>.

Users can create a layout by choosing existing parameterized objects/shapes from the library. Each basic building block is called a cell and is represented by a single line of text with corresponding parameters. The text file containing the entire design can be hierarchical following conventional layout logic making the entire file short and easily editable. Users can also create customized objects of arbitrary complexity. The designs presented here are based on an extensive set of parameterized blocks and features described in a text file. They were subsequently converted into the GDSII data format and then used to fabricate lithography reticles. Finally, the functionality of some of the fabricated devices was tested. This powerful method, by rendering the generation of complex microfluidic layouts a simple task, considerably shortens the design turnaround time and also makes optimal designs more accessible for increased functionality and performance.

II. EXPERIMENT

A. Layout design

The NT is a JAVA-based platform software consisting of more than 400 parameterized fundamental blocks, which were primarily designed at the NIST's CNST for lithography. Users simply choose the most suitable parameterized building blocks, identify their parameters and locations, form cells, and place them into the hierarchy of their design as it can be used in any conventional layout editing software.

The basic primitive blocks (Fig. 1) that are of interest for microfluidics contain spirals for the following applications: mixing and cell separations, injectors for forming segmented flow, Bezier curves for smooth connections between individual blocks, funnels for smooth transition elements (from narrow to wide channels and vice versa), Y-bends and fractals for fluid distribution into chambers, rectangular, hexagonal and polar arrays, with the latter being used for centrifugal force-based devices, rounded paths for complex microfluidic channels, and function plot-based shapes for mixers. Once the blocks' locations and other parameters are identified and the layout hierarchy has been completed, the generated text file is loaded into the NT software and converted into a GDSII file format. The GDSII file can be checked in a GDSII viewer, and if anything is inconsistent with the designer's original idea, then the parameters in the script file can be corrected and a new GDSII file can be generated. The most important features are simplicity, platform independence, and the fact that no programming skills are required.

Each design that is created using the NT starts with the definition resolution of the layout, after which there is a GDSII file, and then, the actual layout description starts. A few examples of the typical microfluidic devices that were selected with the aim of making functional chips are shown in the supplementary material.²³

This simple chamber for biological applications [Fig. 2(a)] consists of a basic block *funnelJunctionV2* with the entire design script comprising seven lines. Users can select the funnel shape, such as the inlet channel width, its length, and the chamber length and width. There is the option for an inlet channel to have a different width from the outlet. A cell containing the chamber and two inlet/outlet circles was formed, and an 8×2 array was created. Then, the chamber identification, the alignment marks, and the logo in the center were added to complete the layout.

One of the first commercialized microfluidic devices was a chip used for CE that had a T-junction injector capable of dosing the precise analyte volume. This device was originally introduced by Caliper and later transferred to Agilent⁸ [Fig. 2(b)]. Here, the channels were designed using a primitive block called *roundPath*, which is defined by corner coordinates, a radius at each corner, its precision (number of vertexes per round segment), and channel width. The entire layout of this rather complex chip is then simplified into defining coordinates for six channels consisting of six lines of the script.

A device [Fig. 2(c)] employing the inertial (Dean) forces for cell separation and sorting was designed⁹ using the key primitive block of the Archimedes spiral (*spiralArchST*), which contains straight connections with parameterized lengths. The spiral is terminated with two inputs connected to the spiral via channels made by Bezier curves. There are eight outputs on the other side. They are connected via channels with smooth shapes defined by the Bezier function *bezierCurve* and subsequently organized into a single block made of a funnel *sBendFunnel* to match the final channel width with one of the spirals.

Several research groups have used centrifugal force in a compact disc read-only memory (known as CD-ROM) format to move fluids in microfluidic chips and process biological samples,¹⁰ such as conducting real-time PCR (Ref. 11) or generating droplets with microfluidic emulsion generator array (MEGA) devices.¹²

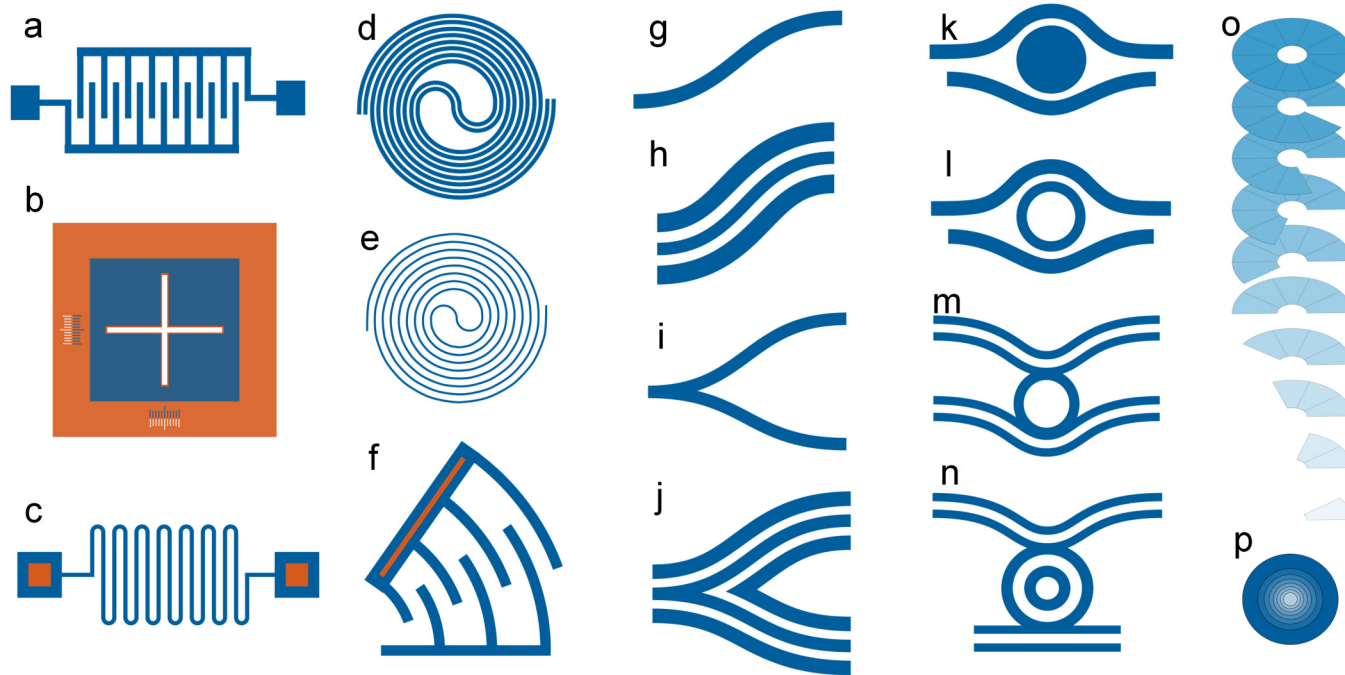


FIG. 1. Examples of fundamental blocks in the NT database. (a) Interdigitated electrodes. (b) Two-level alignment mark including Vernier's structure for precise alignment. (c) Folded springs with two anchored pads. (d) Archimedes double and (e) single spiral. (f) Radial comb drive with an anchor. (g) Bezier curve and its derivative structures such as (h) S-bend inverse slot, (i) Y-bend, and (j) Y-bend inverse slot. (k) Disc and (l) ring pulley structure with an additional coupling pulley. (m) Disc symmetric inverse positive structure with a coupling pulley. (n) Ring symmetric inverse positive structure with an additional coupling waveguide. (o) Grayscale spiral staircase with overlapping arc segments. (p) Concentric circles with different diameters using grayscale segments.

Making these layouts using a conventional layout editor is rather difficult as IC layout-dedicated software often does not allow for instance cells with arbitrary rotation angles. In example six, a MEGA device [Fig. 2(d)] with a diameter of 32.5 mm was designed. Here, a basic *roundPath* primitive block was used and the cell was stepped using the *arrayPolar* feature to step the basic block 12 times with a 30° rotation step.

The combined microfluidic device consists of a double spiral-based mixer using a double Archimedes spiral (*spiralDelayLineArchV2*), a symmetrical droplet generator (*funnelJunctionV1R*), and a fractal-based uniform fluid distributor in a chamber [Fig. 2(e)]. Uniform fluid distribution in a microfluidic chamber can be done with the help of conventional layout editing software, but it is a tedious and time-consuming process.¹³ Here, it is shown how this block is formed by using *curvedTree*'s four-level fractal function to evenly distribute the fluid within the chamber. The block only has five parameters, with two of them being the X and Y locations of the block, one being the number of fractal levels, and two identifying the location of the curve tree size, which makes the generation of this complex layout extremely simple. Another polar array-based structure was created, forming a combined microfluidic layout with center symmetry to use a centrifugal force. A few previously described features were used to accomplish this, namely, *roundPath*, *spiralDelayLineArchV2*, *funnelJunctionV2*, and *arrayPolar*.

A microfluidic chip with a double T-junction injector [Fig. 2(f)] can be applied to perform CE.¹⁴ Alternatively, it could be used for heat transfer time determination by heating up different sides of the chip.¹⁵ The primitive block's parameter *crossJunctionV3* is part of the NT library, thus reducing the CE's basic design to filling parameters in a single line of text. The parameter for the distance between two T-junctions can also be set as 0 μm, thus converting the double T-junction injector into a cross-junction.¹⁶

The gradient generator/mixer was originally designed using a simple zigzag-shaped design.¹⁷ The original layout was modified to make the structure more compact by introducing channels in the shape of a sine function [Fig. 2(g)]. The NT has a primitive block called *Function Plot* that allows the formation of channels using different mathematical functions. Here, the basic channel block was a sine-shaped function $150 * \text{Math.sin}(x/80)$, where the parameters define the amplitude and frequency, i.e., size in X and Y directions. Interconnections were made using a rounded path to eliminate the dead volume and shape singularities.

Also shown here is a device consisting of a virtual reaction chamber (VRC) consisting of a sample covered in a layer of oil located on a glass substrate with a heater and a temperature sensor¹⁸ [Fig. 2(h)]. This is a simple system that is used to study chemical and biochemical reactions by using a resistive temperature detector to monitor the temperature inside the chamber. Its

09 May 2024 07:37:01

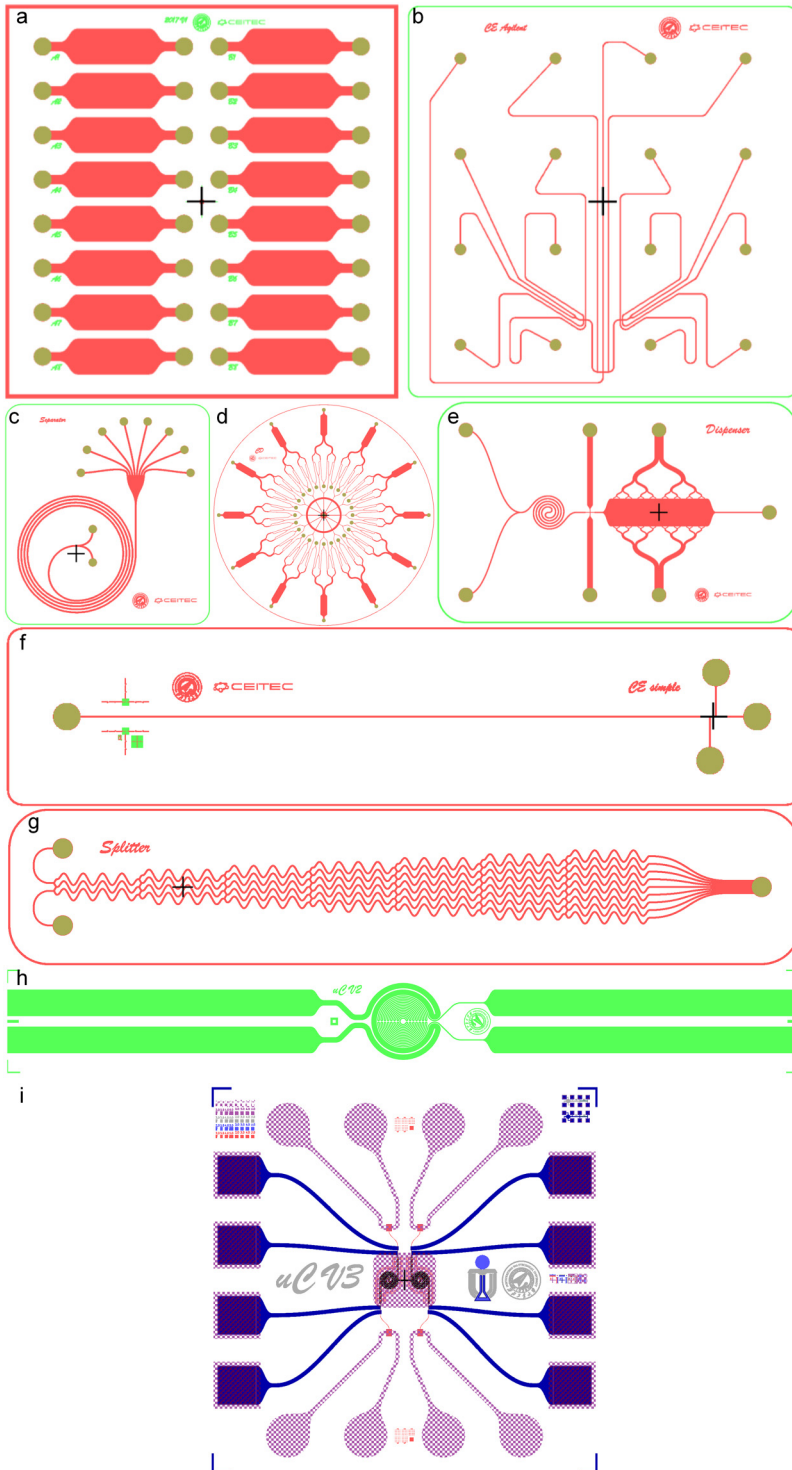


FIG. 2. Microfluidic devices' layouts: (a) a simple array of microfluidic chambers on a chip with dimensions of $(22 \times 22) \text{ mm}^2$ using *funnelJunctionV2*, (b) layout of a chip for a CE sized $(18 \times 18) \text{ mm}^2$ using *roundPath*, (c) inertial force-based cell sorter based on a spiral and Bezier curves using the *bezierCurve* function, (d) CD-ROM-based system used to generate segmented flow for further processing, (e) a combination of two fluid mixers with a symmetrical droplet generator based on *funnelJunctionV1R* and *curvedTree*, (f) a simple device for CE or heat transfer determination that has double T-cross junctions, (g) a splitter/gradient generator based on a $150^\circ \text{Math.sin}(x/80)$ sine shape, and (h) VRC-based and (i) flow-through calorimeter.

09 May 2024 07:37:01

fabrication required only an Au deposition with an adhesion layer, a single lithography round, followed by Au patterning, and wafer dicing into individual chips.

The micromachined flow-through calorimeter was designed by using a double Archimedes spiral *spiralDelayLineArchV2* for the key part of the calorimeter [Fig. 2(i)]. The suspended capillary tube was integrated with a thin film metal heater and a sensor, and it was meant to operate in a vacuum environment. Each chip consisted of two calorimeters to enable the performance of differential scanning calorimetry.^{19,20}

B. Chips fabrication

Si wafers were used for most of the work with a double deep reactive ion etching (DRIE) process being employed, followed by alignment-free anodic bonding between Si and the glass cover [Figs. 3(a)–3(f)]. Alternatively, the poly-(dimethylsiloxane) (PDMS) double molding technique²¹ was employed for the gradient generator/mixer device [Fig. 3(g)] with single metal etching used for the VRC-based calorimeter¹⁸ or a complex process used for the flow-through calorimeter.^{19,20}

For the double DRIE process, Si wafers with a diameter of ≈ 100 mm and a thickness of ≈ 500 μm were thermally oxidized to grow a SiO_2 layer with a target thickness of 200 nm. Then, the first lithography was conducted and SiO_2 was etched using reactive ion etching by means of CHF_3 -based chemistry. The photoresist (PR) was then removed, and a second lithography was performed using a PR with a thickness of ≈ 14 μm . Inlet and outlet ports were created using the wafer by etching the Si substrate with DRIE. The PR was removed and the Si was subsequently etched to a depth of ≈ 50 μm to form channels and chambers using the SiO_2 layer patterned during the first lithography round as a mask. The wafers were then cleaned, the SiO_2 was removed with an $\text{HF}/\text{NH}_4\text{F}$ -buffered oxide etch solution, and the Si substrate was oxidized in dry oxygen to form a new layer of SiO_2 with a target thickness of 5 nm. The purpose of this SiO_2 layer was to create a clean, well-defined surface for the microfluidics. It is an important step for the subsequent surface modification using the chemical vapor deposition technique routinely performed by the authors. As the second-to-last step, the Si substrate wafer was anodically bonded to a glass wafer of the same size, and finally, a diamond blade dicing saw was used to dice the stack of bonded wafers into individual chips.

We used a Si substrate with a diameter of ≈ 100 mm to form the first mold for the soft lithography-based double molding technique. The Si was patterned and then etched to the target depth of 50 μm . After the removal of the PR, the etched silicon layer was passivated by the C_4F_8 -based plasma process. Then, the PDMS precursor was poured into the Si mold and cured at ≈ 60 $^\circ\text{C}$ for ≈ 4 h. Then, the PDMS layer was peeled off, placed into a desiccator, and exposed to hexamethyldisilazane (HMDS) vapor in a vacuum created by means of a membrane pump. The HMDS layer formed an antisticking coating that prevented the subsequent PDMS layer from bonding to the first one. The precursor for the second PDMS layer was then poured on the first one and cured again in the same way as the first layer. Subsequently, the second PDMS was peeled off and all of the fluid access holes were

punched through the PDMS layer. Then, it was brought together using a glass substrate exposed to O_2 plasma for ≈ 30 s at a power of ≈ 80 W. Both substrates were brought into contact, and they bonded to each other. The glass device was mounted on a microscope stage, three holes were punched through the PDMS layer and three hollow stainless-steel needles with an outer diameter of ≈ 0.6 mm were placed in the holes. Two needles were connected to syringe pumps, and one needle was connected to waste reservoirs via polytetrafluorethylene tubes with an inner diameter of ≈ 0.5 mm [Fig. 3(g)].

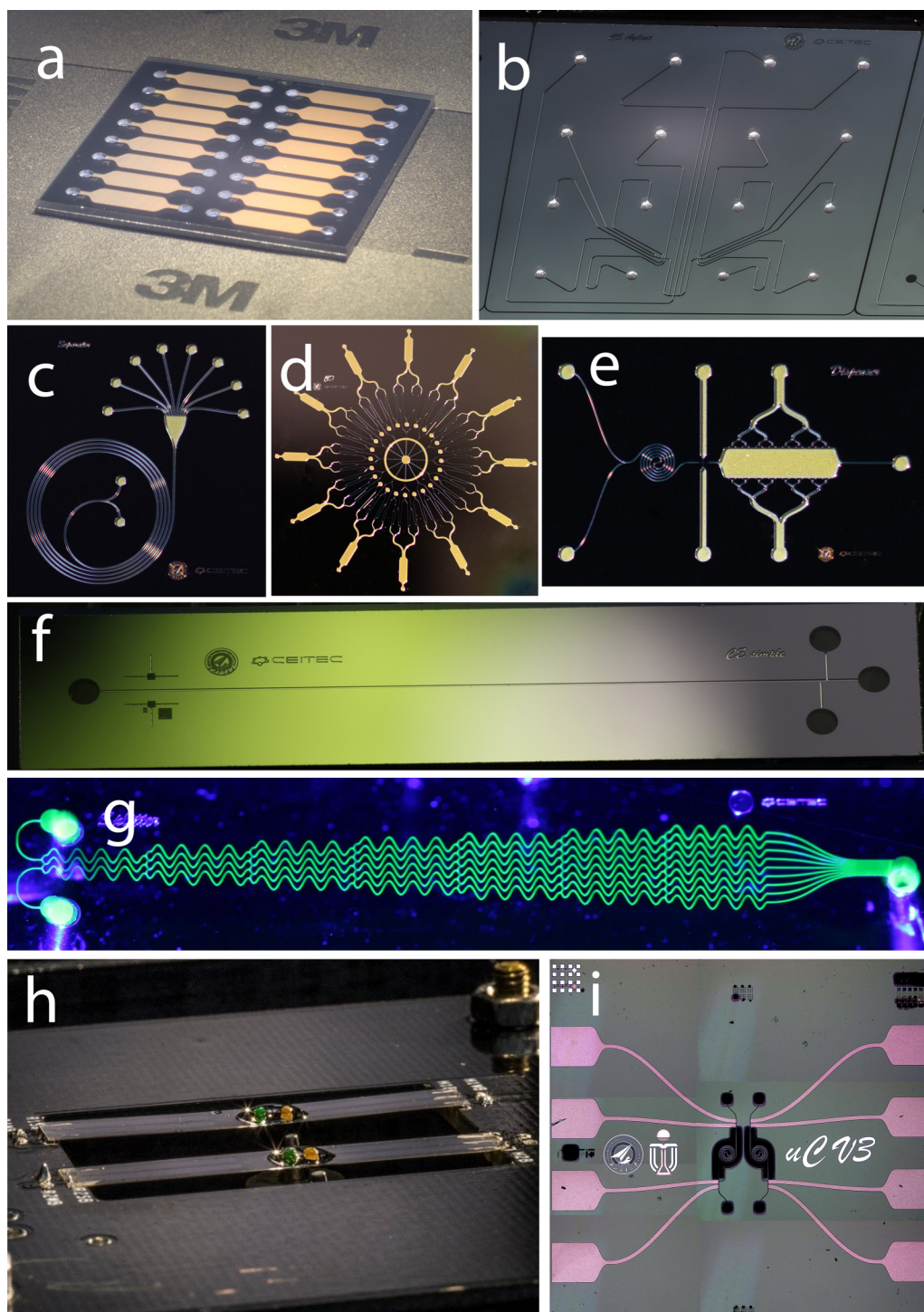
The VRC-based calorimeter was made up of a glass substrate with a diameter and a thickness of ≈ 100 mm and ≈ 100 μm , respectively. The wafer was sputter coated with Cr and Au with target thicknesses of 20 nm and 100 nm, respectively; then, the lithography was performed and a metal sandwich pattern was etched using a wet etching process. Once the PR was removed, the wafer was diced using a diamond dicing saw. The chips were soldered to a printed circuit board and placed into a chamber for testing [Fig. 3(h)].

The major process steps in the fabrication of a flow-through calorimeter^{19,20} [Fig. 3(i)] are schematically described in Fig. 4. We used silicon substrates with a diameter and thickness of ≈ 100 mm and ≈ 500 μm , respectively. The wafers initially received a deposition of a low-stress nitride (LSN) or low-temperature oxide (LTO) layer with a target thickness of 1 μm in a low-pressure chemical vapor deposition (LPCVD) furnace. The layer was then lithographically patterned with a slit opening of 800 nm followed by etching silicon under SF_6 plasma to form a microchannel [Fig. 4(a)]. The channel was subsequently sealed by a further layer of LSN placed in an LPCVD furnace [Fig. 4(b)]. For metallization, an ≈ 1 μm Al layer and a ≈ 200 nm Ti layer were deposited and patterned to form a heater and resistance temperature detector sensor [Fig. 4(c)]. Finally, the microchannel was fully released by XeF_2 etching [Fig. 4(d)].

III. RESULTS AND DISCUSSION

First, a simple CE chip was placed on two heaters at different temperatures, ≈ 60 $^\circ\text{C}$ and ≈ 90 $^\circ\text{C}$, respectively. The heaters were mounted on an inverted microscope at a distance of ≈ 16 mm from each other, forming a thermal gradient of 1.875 K mm^{-1} across the chips. Next, a solution containing double-stranded deoxyribonucleic acid (dsDNA) in the presence of Eva Green dye was pumped into the chip to perform a melting curve analysis (MCA)²² with a known DNA melting temperature of ≈ 84 $^\circ\text{C}$. The chip was exposed to a light-emitting diode light with a principal wavelength of ≈ 470 nm, and its fluorescence image was captured using a photographic camera and a bandpass filter with a center wavelength of ≈ 525 nm and a bandpass width of ≈ 50 nm [Fig. 5(a)]. The captured image was processed by means of a script in MATLAB to show the functionality and performance of this microfluidic device [Figs. 5(b) and 5(c)]. Additionally, this setup was also used to determine the thermal properties of the chip by performing a spatial MCA on the dsDNA and Eva Green intercalating dye. As a result, a temperature resolution of ≈ 1.2 mK pixel^{-1} was achieved to distinguish the different dsDNA molecules.¹⁵

The second device that was tested was the generator/mixers in order to show the formation of a concentration gradient. Two water-based solutions containing fluorescein at $\approx 2 \times 10^{-4}$ kg m^{-3}



09 May 2024 07:37:01

FIG. 3. Photographs of the designed microfluidic chips: (a) simple chamber arrays, (b) a commercial CE chip now used by Agilent, (c) a chip for cell separation and sorting, (d) a CD-ROM-based system, (e) a combination of two fluid mixers with a symmetrical droplet generator, (f) a device for CE, (g) a gradient generator filled with fluorescein, and (h) a VRC-based calorimeter. Reproduced with permission from Feng *et al.*, *Sens. Actuators B* **312**, 127967 (2020). Copyright 2020, Elsevier. (i) A flow-through calorimeter such as the one used before and described in [Refs. 19 and 20](#).

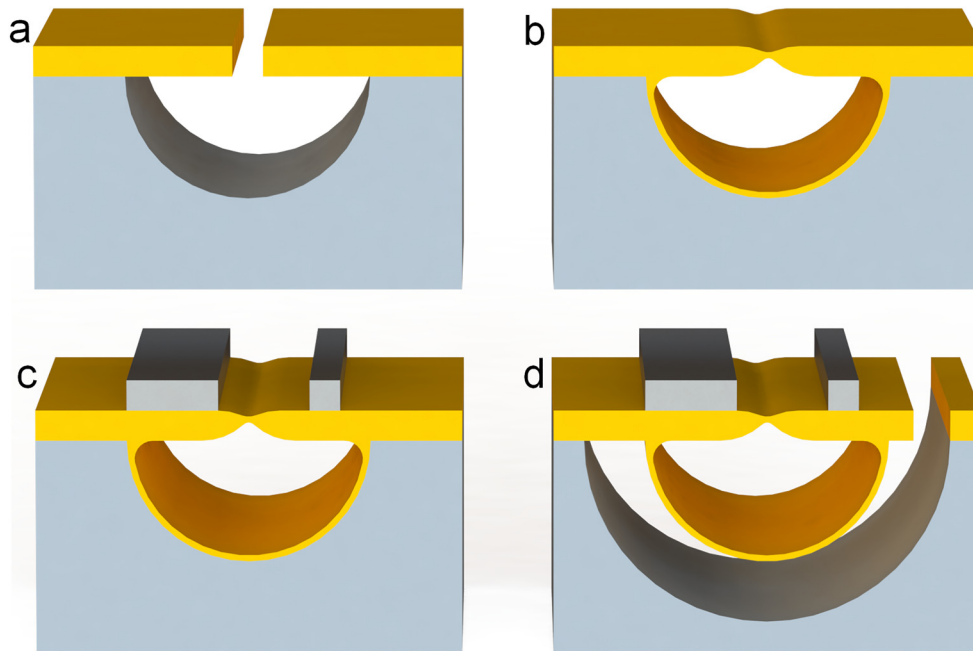
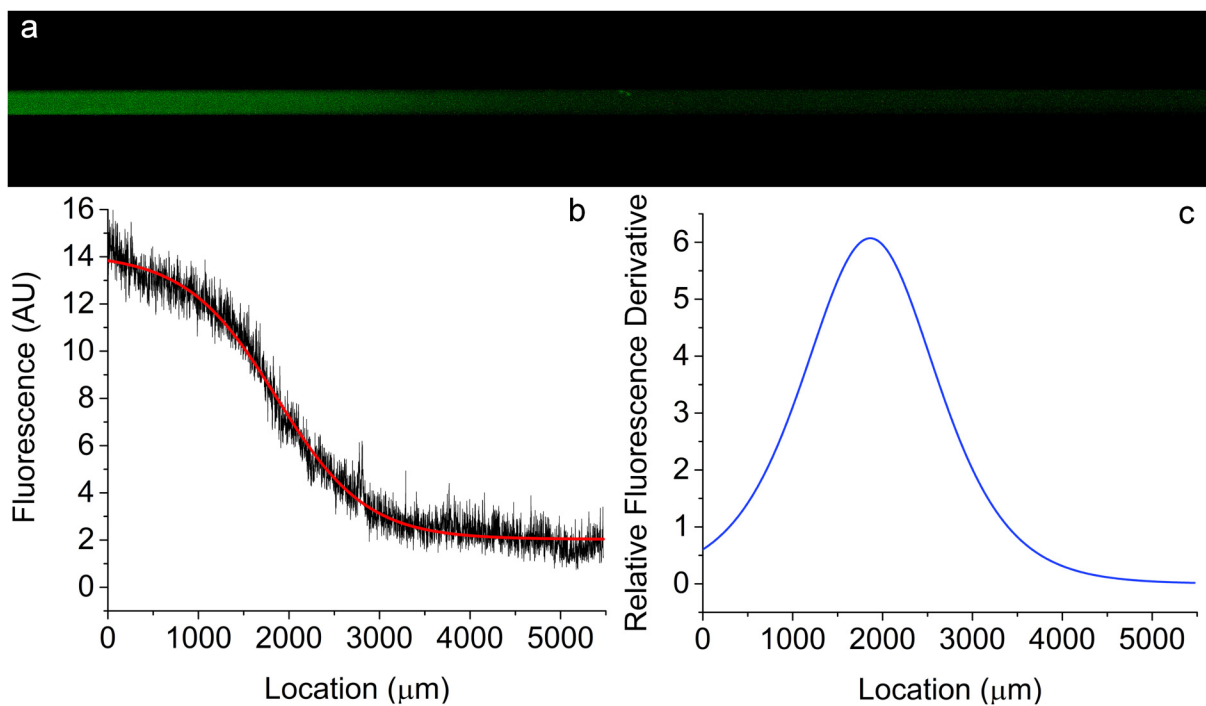


FIG. 4. Major process steps in the fabrication process of a flow-through calorimeter (see the text).



09 May 2024 07:37:01

FIG. 5. (a) Fluorescence image of a chip with a temperature gradient filled with dsDNA with Eva Green intercalating dye to perform an MCA. (b) Extracted amplitude of the fluorescence in black as a function of location and a fitting curve (solid line) with the Boltzmann function showed the location of the melting DNA, and (c) negative derivation of the extracted melting curve showed the location of the melting point.

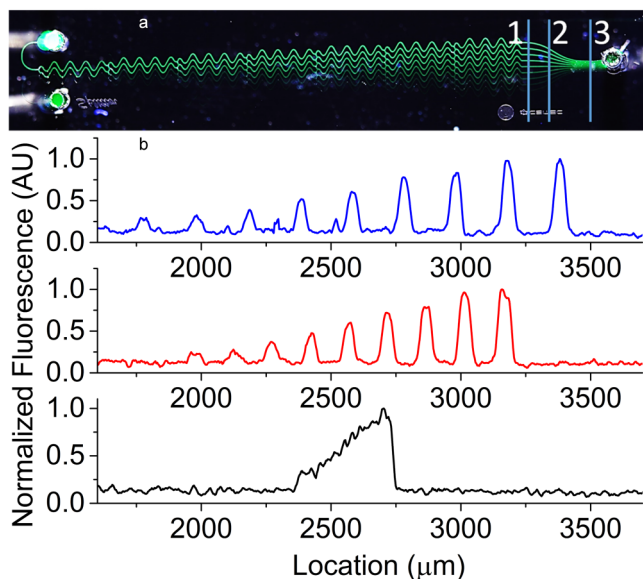


FIG. 6. (a) Fluorescence image of a chip fabricated by means of the double molding technique based on PDMS filled with two solutions with two different concentrations of fluorescein and (b) the profile of fluorescence intensity as a function of the locations of points one, two, and three in the top, middle, and the bottom part of the chart, respectively.

and $\approx 2 \times 10^{-5} \text{ kg m}^{-3}$, respectively, were both pumped into the chip at a pumping speed of $\approx 2 \mu\text{l min}^{-1}$. A fluorescence setup similar to the one in the above paragraph was used for the MCA described in the previous paragraph.²² The image that was captured was then processed using a script in the MATLAB environment (Fig. 6).

IV. SUMMARY AND CONCLUSIONS

In conclusion, a new script-based method for the generation of complex layouts of microfluidic devices using NT Beta version 2018.11.01 software has been demonstrated. It contains features specifically added for microfluidic device layouts such as funnels, chambers, and T-junctions with tangential termination having minimized dead volume, cross-junction, devices for CE and temperature gradient experiments,¹⁵ and rounded path. These cells are too complicated to be designed by conventional layout editing software. Here, the design is based on an extensive set of parameterized cells and features that greatly simplify the design process, thus improving the efficiency of the microfluidic layout design. The NT software saves the scientists' time on layout preparation that they can dedicate to scientific work.

Once the design was finished, it had a form of a simple text file, that was subsequently converted into a GDSII format for lithography masks fabrication. The utilization of NT software for the creation of structures, such as CE chips, MEGA chips using centrifugal forces, chambers, splitters, and mixers, has been shown. The generated layout was used to fabricate microfluidic devices,

and the performance of two of these devices was then demonstrated. This NT software is a powerful yet easy-to-use tool for the generation of the layout of microfluidic devices.

ACKNOWLEDGEMENTS

The authors are grateful to Dr. B. Ilic from CNST NIST for implementing the requested cells necessary for microfluidic design. The authors acknowledge the financial support of Grant No. 20GH020178 from People's Republic of China and the GACR Project No. GA19-04270Y from Czech Republic. We also acknowledge CzechNanoLab Research Infrastructure supported by MEYS CR (No. LM2018110) and support from CEITEC Nano+ Project CZ.02.1.01/0.0/0.0/16_013/0001728, Czech Republic, and Grant No. 16209316 provided by the Research Grant Council of Hong Kong.

REFERENCES

- ¹S. C. Terry, J. H. Jerman, and J. B. Angell, *IEEE Trans. Electron Devices* **26**, 1880 (1979).
- ²A. Manz, N. Graber, and H. M. Widmer, *Sens. Actuators B Chem.* **1**, 244 (1990).
- ³A. Manz, J. C. Fetting, E. Verpoorte, H. Ludi, H. M. Widmer, and D. J. Harrison, *Trends Anal. Chem.* **10**, 144 (1991).
- ⁴A. Manz, D. J. Harrison, E. M. J. Verpoorte, J. C. Fetting, H. Ludi, and H. M. Widmer, *Chimia* **45**, 103 (1991).
- ⁵D. J. Harrison, K. Fluri, K. Seiler, Z. H. Fan, C. S. Effenhauser, and A. Manz, *Science* **261**, 895 (1993).
- ⁶M. U. Kopp, A. J. de Mello, and A. Manz, *Science* **280**, 1046 (1998).
- ⁷K. C. Balram *et al.*, *J. Res. Nat. Inst. Stand. Technol.* **121**, 464 (2016).
- ⁸A. R. Kopf-Sill, A. van den Berg, W. Olthuis, and P. Bergveld, *μTAS 2000* (Enschede, Netherlands, Springer, Dordrecht, 2000), pp. 233–238, available at <https://www.ingentaconnect.com/content/scs/chimia/1991/00000045/00000004/art00003#expand/collapse>.
- ⁹S. S. Kuntaegowdanahalli, A. A. S. Bhagat, G. Kumar, and I. Papautsky, *Lab Chip* **9**, 2973 (2009).
- ¹⁰J. Ducree, S. Haerberle, S. Lutz, S. Pausch, F. von Stetten, and R. Zengerle, *J. Micromech. Microeng.* **17**, S103 (2007).
- ¹¹M. Keller *et al.*, *RSC Adv.* **5**, 89603 (2015).
- ¹²Y. Zeng, R. Novak, J. Shuga, M. T. Smith, and R. A. Mathies, *Anal. Chem.* **82**, 3183 (2010).
- ¹³J. K. Park, C. D. M. Campos, P. Neuzil, L. Abelmann, R. M. Guijt, and A. Manz, *Lab Chip* **15**, 3495 (2015).
- ¹⁴U. Backofen, F. M. Matsysik, and C. E. Lunte, *Anal. Chem.* **74**, 4054 (2002).
- ¹⁵H. Zhu *et al.*, *Microfluid. Nanofluid.* **24**, 7 (2019).
- ¹⁶D. J. Harrison, A. Manz, Z. H. Fan, H. Ludi, and H. M. Widmer, *Anal. Chem.* **64**, 1926 (1992).
- ¹⁷S. K. W. Dertinger, D. T. Chiu, N. L. Jeon, and G. M. Whitesides, *Anal. Chem.* **73**, 1240 (2001).
- ¹⁸J. Feng *et al.*, *Sens. Actuators B* **312**, 127967 (2020).
- ¹⁹S. Ni, H. Zhu, P. Neuzil, and L. Yobas, *J. Microelectromech. Syst.* **29**, 1 (2020).
- ²⁰S. Ni, H. Zhu, P. Neuzil, and L. Yobas, *2020 IEEE 33rd International Conference on Micro Electro Mechanical Systems (MEMS)*, Vancouver, Canada (IEEE, 2020), pp. 1006–1009.
- ²¹D. C. Duffy, J. C. McDonald, O. J. A. Schueller, and G. M. Whitesides, *Anal. Chem.* **70**, 4974 (1998).
- ²²K. M. Ririe, R. P. Rasmussen, and C. T. Wittwer, *Anal. Biochem.* **245**, 154 (1997).
- ²³See the supplementary material's Secs. A–H at <https://doi.org/10.1116/6.0000562> for all scripts of all the structures.

09 May 2024 07:37:01



Heat transfer time determination based on DNA melting curve analysis

Hanliang Zhu¹ · Huanan Li¹ · Haoqing Zhang¹ · Zdenka Fohlerova^{2,3} · Sheng Ni⁴ · Jaroslav Klempa³ · Imrich Gablech³ · Jaromir Hubalek^{2,3} · Honglong Chang¹ · Levent Yobas⁴ · Pavel Neuzil^{1,2,3}

Received: 19 July 2019 / Accepted: 20 November 2019 / Published online: 12 December 2019
© Springer-Verlag GmbH Germany, part of Springer Nature 2019

Abstract

The determination of the physical properties of fluids—such as the thermal characteristics, which include heat transfer time (Δt)—is becoming more challenging as system sizes shrink to micro- and nanometer scales. Hence, knowledge of these properties is crucial for the operation of devices requiring precise temperature (T) control, such as polymerase chain reactions, melting curve analysis (MCA), and differential scanning fluorimetry. In this paper, we introduced a flow-through microfluidic system to analyze thermal properties such as Δt among samples and the sidewall of a silicon chip using microscopic image analysis. We performed a spatial MCA with double-stranded deoxyribonucleic acid (dsDNA) and EvaGreen intercalator, using a flow-through microfluidic chip, and achieved a T gradient of $\approx 2.23 \text{ K mm}^{-1}$. We calculated the mean value of Δt as $\approx 33.9 \text{ ms}$ from a melting temperature (T_M) location shift along the microchannel for a variable flow rate. Our system had a T resolution of $\approx 1.2 \text{ mK pixel}^{-1}$ to distinguish different dsDNA molecules—based on the T_M location within the chip—providing an option to use it as a high-throughput device for rapid DNA or protein analysis.

Keywords dsDNA · Melting curve analysis · Heat transfer · Microfluidics

1 Introduction

Much of the development in biomolecular research involves a detailed understanding of the many variables associated with identifying biomolecule functioning, stability, and

ligand interaction (Tetala and Vijayalakshmi 2016). The advancement of microfabrication technologies such as microelectromechanical systems (MEMS) and other microfluidic devices enables the development of microscale functional platforms for a broad range of biological and biochemical applications (Samiei and Tabrizian 2016; Yu et al. 2017; Feng et al. 2018). Microfluidic technology (Nge et al. 2013) has many advantages that allow for precise fluidic manipulation from μL to pL , as well as rapid mixing and heat/mass transfer. The minute size of microfluidic devices also makes them ideal platforms for point-of-care diagnostics and high-throughput experiments (Streets and Huang 2013; Feng et al. 2018). Several techniques and analyses, including polymerase chain reaction (PCR) (Thomas et al. 2017), melting curve analysis (MCA) (Farrar and Wittwer 2017), and differential scanning fluorimetry (Menzen and Friess 2013; Seabrook and Newman 2013), require precise control of working temperature (T), as well as knowledge of system thermal parameters such as thermal heat transfer (Erickson et al. 2003; Launay et al. 2006; Yang et al. 2005; Zhao et al. 2013), which can be complicated to determine at the micro-/nanoscale level.

Electronic supplementary material The online version of this article (<https://doi.org/10.1007/s10404-019-2308-9>) contains supplementary material, which is available to authorized users.

✉ Pavel Neuzil
pavel.neuzil@nwpu.edu.cn

¹ Ministry of Education Key Laboratory of Micro and Nano Systems for Aerospace, School of Mechanical Engineering, Northwestern Polytechnical University, 127 West Youyi Road, Xi'an 710072, Shaanxi, People's Republic of China

² Central European Institute of Technology, Brno University of Technology, Purkyňova 123, 612 00 Brno, Czech Republic

³ Department of Microelectronics, Faculty of Electrical Engineering and Communication, Brno University of Technology, Technická 3058/10, 61600 Brno, Czech Republic

⁴ Department of Electronic and Computer Engineering, Hong Kong University of Science and Technology, Clear Water Bay, Hong Kong, People's Republic of China

The thermal stability measurement of biomolecules such as proteins and double-stranded deoxyribonucleic acids (dsDNAs) is important in experiments and is typically performed through the use of differential scanning calorimetry and MCA, respectively. The dsDNA will be melted to single-stranded DNA (ssDNA) above a threshold T known as melting temperature (T_M). As an integral part of quantitative PCR (Pryor and Wittwer 2006), the MCA method is performed based on the T ramping of dsDNA with an intercalating dye such as EvaGreen (Wang et al. 2006), while simultaneously monitoring fluorescence intensity (F). The F value of the dsDNA-EvaGreen mixture significantly decreases in quantum yield upon melting, resulting in defined T_M as the value of T when 50% of dsDNA melts into ssDNA (Wright et al. 2017; Lo et al. 2004; Johnson et al. 2014; Ericsson et al. 2006).

A glass chip performing continuous flow PCR (Kopp et al. 1998), sometimes referred to as the *space domain* (Neuzil et al. 2014), was one of the first microfluidic devices, later also developing MCA capability (Pješčić et al. 2010), and observing T_M location shift as a function of flow rate (ν). Another space-domain microfluidic device was introduced to perform thermal gradient PCR, followed by a spatial MCA for single- and multi-gene analysis (Crews et al. 2009). The distribution of T at the device surface, with ν as a parameter, was determined by non-contact infrared (IR) thermometry (Crews et al. 2008), where precision was affected by the emission coefficient of the device's properties. A droplet-based microfluidic device was also proposed to perform a DNA methylation assay based on MCA, while the distribution of T was again determined through IR thermometry, providing values of T at the surface but not in the tested solution, which led to an error during the experiments (Liu et al. 2018).

In this paper, we introduce a simple flow-through setup consisting of a silicon/glass chip with a constant thermal gradient to analyze the influence of flow inside the microchannel on T distribution. We utilize the spatial MCA method to determine heat transfer time (Δt) from the chip sidewalls to the center of the microfluidic channel, using MATLAB processing in terms of the fluorescence imaging of the microchannel. The system proof of principle was verified through performing MCA of the dsDNA-EvaGreen mixture with known T_M . The Δt was calculated from T_M shift with ν as a parameter. The microfluidic setup proposed and characterized in this work has significant potential in the fields of biotechnology and medical diagnostics, where the determination of the thermal stability of nucleic acids and proteins is an important parameter.

2 Materials and methods

2.1 Fabrication of the microfluidic device

The layout of the microfluidic chip consists of a cross-shaped microfluidic device using a standard cell, which is called *crossJunctionV3*. It has four inputs/outputs and is part of the cell library from the script-based Nanolithography Toolbox (Balram et al. 2016). We used this cell for the sake of convenience, as the generation of the microfluidic device layout only requires parameter selection. We used the single port as the fluid inlet and the other three ports as fluid outlets. The actual layout is shown in Fig. 1a.

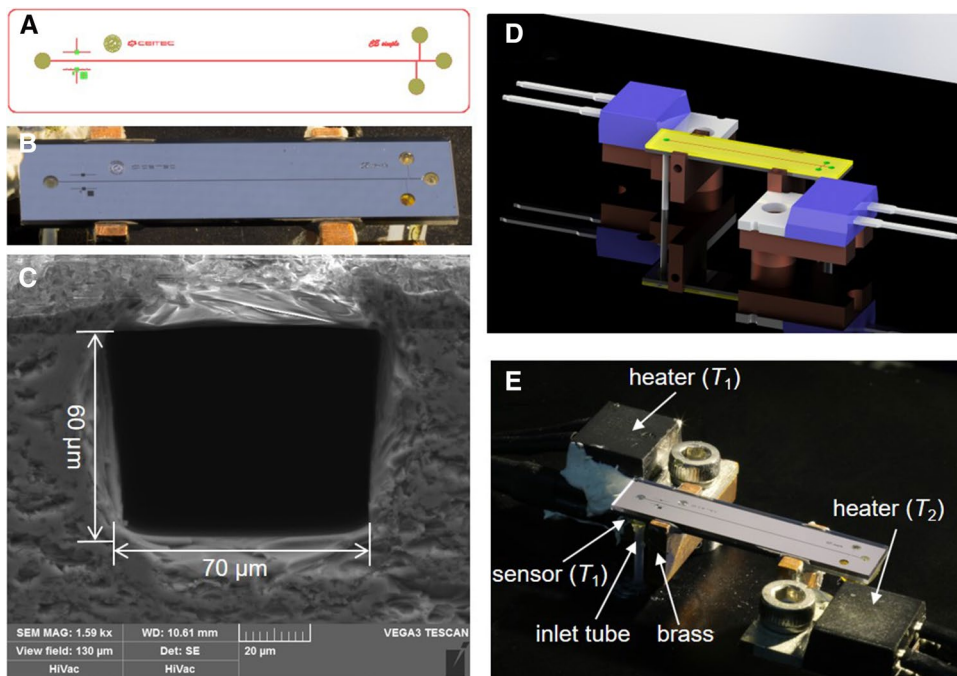
The devices were fabricated using a $\approx 500\text{-}\mu\text{m}$ -thick silicon wafer as a substrate by a process described previously (Feng et al. 2018). The wafer was first oxidized at $\approx 1000\text{ }^\circ\text{C}$ to grow a $\approx 200\text{-nm}$ -thick SiO_2 layer. We then performed contact lithography and etched the SiO_2 with $\text{HF}/\text{NH}_4\text{F}$ -based solution (BOE) to define microfluidic channels. The second lithographic process was performed with $\approx 12\text{-}\mu\text{m}$ -thick photoresist (PR) to define inlet/outlet holes with diameters of $\approx 900\text{ }\mu\text{m}$. The holes were etched through the entire silicon wafer using deep reactive ion etching (DRIE). Next, the PR was removed and the second DRIE step was conducted to etch the Si to a depth of $\approx 50\text{ }\mu\text{m}$, using a previously patterned SiO_2 layer as a mask, thus forming microchannels.

The SiO_2 layer was removed in the BOE, and the wafers were oxidized at $\approx 950\text{ }^\circ\text{C}$ to form a $\approx 5\text{-nm}$ -thick SiO_2 layer, primarily to achieve well-defined surface properties inside the microchannel. Subsequently, the silicon wafers were anodically bonded to a borosilicate glass wafer to form closed channels. As the final fabrication step, the two bonded wafers were diced into individual chips using a diamond-blade dicing saw and were then washed in deionized water (Fig. 1b). We used a scanning electron microscope (SEM) to measure (estimate) the size of the cross section of the microchannel and found a width of $\approx 60\text{ }\mu\text{m}$, and a height of $\approx 70\text{ }\mu\text{m}$ (Fig. 1c).

2.2 Setup of the system

The microfluidic chip was placed on a pair of brass blocks fabricated by a computer numerical control (CNC) machine, each mounted to an aluminum plate that served as the heat sink at a distance of $\approx 12\text{ mm}$. We equipped each brass block with a resistor that had a nominal value of $20\text{ }\Omega$ in the TO-220 socket to serve as a heater and a resistive temperature detector (type Pt100) for a closed-loop T control system. Each heater with a corresponding sensor was connected to a proportional integrative derivative

Fig. 1 **a** The designed microfluidic chip had a size of $\approx 6 \text{ mm} \times 27 \text{ mm}$. The layout consisted of two levels; the red and brown colors represent the channels and the through-holes, respectively. **b** Photograph of a fabricated chip made of silicon (bottom) capped with borosilicate glass. **c** SEM image of the channel cross section with a total area of $\approx 4200 \mu\text{m}^2$. **d** Computer-aided design (CAD) of the setup for the MCA measurement. **e** Photograph of the system setup showing the silicon/glass chip placed on two brass blocks, each heated by a heater, in a TO-220 socket equipped with an RTD type of Pt100 (color figure online)



controller, with a set T of $T_1 \approx 60 \text{ }^\circ\text{C}$ and $T_2 \approx 110 \text{ }^\circ\text{C}$ (Fig. 1d, e). The chip inlet was connected to a syringe pump and outlets to waste reservoir via four glued polytetrafluoroethylene tubes with an outer and inner diameter of $\approx 0.9 \text{ mm}$ and $\approx 0.5 \text{ mm}$, respectively. Then, the chip was placed under a fluorescence microscope to monitor the F amplitude inside the channel. A complementary metal-oxide semiconductor (CMOS) camera with a 20.2 effective megapixels imager was connected to the c-mount of the microscope to capture images of selected microchannel segments via a $5\times$ objective lens.

2.3 Sample preparation

We prepared $\approx 200 \mu\text{L}$ of a sample by performing a PCR with an intercalating dye (EvaGreen) having selected sequences of dsDNA of glyceraldehyde-3-phosphate dehydrogenase (GAPDH) and human immune deficiency virus (HIV) with a different T_M of $(80.0 \pm 0.4) \text{ }^\circ\text{C}$ and $(82.9 \pm 0.6) \text{ }^\circ\text{C}$ (mean \pm standard deviation), respectively.

2.4 On-chip melting curve analysis

The captured images were processed using a MATLAB code. Each fluorescent image was first converted to a grayscale image, and only the channel area was extracted for analysis. Following this, we extracted the mean value of the amplitude of F across the channel, with x being the pixel count.

The melting curve was described through a sigmoid equation expressing F as a function of T :

$$F(T) = A_2 + \frac{(A_1 - A_2)}{\left(1 + e^{\frac{T-T_M}{dT}}\right)} \cdot (A_0 + B_0 \cdot T), \tag{1}$$

or alternatively, through a more complex double-sigmoid function because of the two different dsDNAs:

$$F(T) = A_2 + \frac{(A_1 - A_2)}{\left(1 + e^{\frac{T-T_{M1}}{dT}}\right)} \cdot (A_0 + B_0 \cdot T) + A_4 + \frac{(A_3 - A_4)}{\left(1 + e^{\frac{T-T_{M2}}{dT}}\right)} \cdot (C_0 + D_0 \cdot T), \tag{2}$$

where $A_0, B_0, C_0,$ and D_0 are fitting parameters, $A_1, A_2, A_3,$ and A_4 are normalization parameters of the sigmoid functions, and dT_1 and dT_2 are values corresponding to the slopes at the inflection points. Since the location (L) along the chip relates to the specific value of T , we thus translated the L values into the corresponding T values. The T_M location with an apparent change of T_M (ΔT_M) as a function of v was determined using the value of Δt (Neuzil et al. 2010).

3 Results and discussion

In a vacuum at low temperature with no sample flow, the temperature gradient between both heaters will be constant. Here, however, the chip operates in an ambient environment surrounded by air causing heat transfer through convection. The constant gradient also must be affected by heat flux due

to the aqueous-based sample flowing through the microchannel. Finally, the device operates at an elevated temperature, meaning heat emission may also play a role (Svatos et al. 2018; Svatoš et al. 2018). We first dealt with an analytical consideration before we performed numerical modeling and finally verified the results through infrared imaging.

3.1 Analytical consideration

The chip was comprised of a silicon/glass sandwich, with both materials having identical thicknesses (t) and widths (w) and a pair of heaters separated by a distance (D) (Fig. 1e). The heat flux (P_1) between the heaters through the microfluidic chip can be defined as:

$$P_1 = \frac{(\lambda_{\text{Si}} + \lambda_{\text{SiO}_2})t \cdot w}{L} \cdot \Delta T_1, \quad (3)$$

where λ_{Si} and λ_{SiO_2} is the thermal conductance of Si and SiO₂, respectively, (L) is chip length, and ΔT_1 is the T difference between the heaters.

The magnitude of convection in air (P_2) is determined through its coefficient (h) (Varona et al. 2007), the surface area (A), and the temperature difference between the T of the sample and T of ambient (ΔT_2):

$$P_2 = A \cdot h \cdot \Delta T_2, \quad (4)$$

giving an amplitude of P_2 as ≈ 77.4 mW. This value is 5.5% of the P_1 value, showing that there is a small influence of the heat convection, with this effect resulting in minor non-uniformity of the ∇T along the microchannel.

The influence of the water-based sample flow can be determined from the energy being transferred due to this flow. The maximum value of ν was set at $5 \mu\text{L min}^{-1}$ (corresponding to $\approx 8.3 \cdot 10^{-11} \text{ m}^3 \text{ s}^{-1}$) transferring of P_3 power:

$$P_3 = \nu \cdot \rho \cdot c \cdot \Delta T_1, \quad (5)$$

where ρ is the specific mass of the sample and c is the sample heat capacitance resulting in a P_3 value of ≈ 17 mW. This is ≈ 4.4 times smaller than the P_2 value, showing that this low flow rate has very little influence on the ∇T and can thus be ignored.

Finally, there is also a radiation effect that may influence the ∇T following the Stefan–Boltzmann law:

$$P_4 = A \cdot \varepsilon \cdot \sigma \cdot (T^4 - T_1^4), \quad (6)$$

where P_4 is radiated power, ε is surface emissivity, σ is the Stefan–Boltzmann constant, and T_1 is the thermodynamic temperature of the ambient environment. The amplitude of P_4 is then ≈ 80 mW assuming a surface emissivity of 0.4 and an entire chip T of ≈ 110 °C. The details of all the

calculations, including governing equations, are presented in supplementary section A.

3.2 FEM simulation

The model of microfluidic chip and two heaters was created in CAD software and consisted of four parts: two brass heated blocks, a chip made of Si covered with glass and had a microchannel filled with water, which was placed on the two heaters (Fig. 1d, e). We then performed the finite element method (FEM) analysis using COMSOL Multiphysics software, including the Heat Transfer in Solids and Fluids and Creeping Flow modules. The meshed model had a total number of 2,610,926 elements, with the constraint of using elements with a maximum size of $1.1 \mu\text{m}$ inside the microchannel to obtain a T profile. The influence of heat convection and radiation on the temperature profile along the microchannel was studied through simulation (Fig. 2c) with the heat convection coefficient set to $5 \text{ W m}^{-2} \text{ K}^{-1}$ and surrounding temperature of 23 °C. The maximum value of the T deviation (ΔT) was 0.64 K, corresponding to a location shift of 0.17 mm (inset in Fig. 2c).

We also modeled the influence of ν from stagnant $0 \mu\text{L min}^{-1}$ value up to the extreme value of $1000 \mu\text{L min}^{-1}$ (Fig. 2d). The influence of ν on the T distribution was found to be negligible for flow rates of up to $\approx 10 \mu\text{L min}^{-1}$ (inset in Fig. 2d), with a flow rate of that amplitude causing an error of $(0.0157 \pm 4 \cdot 10^{-4}) \text{ mm per } \mu\text{L min}^{-1}$ (mean \pm fitting error). However, high ν values that approach or exceed $\approx 1 \text{ mL min}^{-1}$ will significantly change the T profile and thus the ∇T value.

3.3 IR imaging

Once the FEM was completed, we performed an IR imaging of the chip using a mid-IR camera producing images with a size of 640×480 pixels and a focal plane array with a nominal noise equivalent temperature difference of 9 mK. Prior to the imaging, the chip surface was cleaned and coated with carbon tape to assure that the entire surface had as uniform emissivity as possible. This was verified through chip surface imaging under identical T values (both heaters were switched off), and we found that the emission from the entire chip was uniform. Following this, we switched the heaters to set T value of 60 °C and 110 °C, respectively, and captured images with ν of $(0$ and $5) \mu\text{L min}^{-1}$. No significant difference was found; thus, we assumed that the small value of the ν had not influenced the ∇T value. We extracted the surface T from the image with and without a flow rate set to 5 mL min^{-1} and correlated it with chip location. We found that the ∇T value

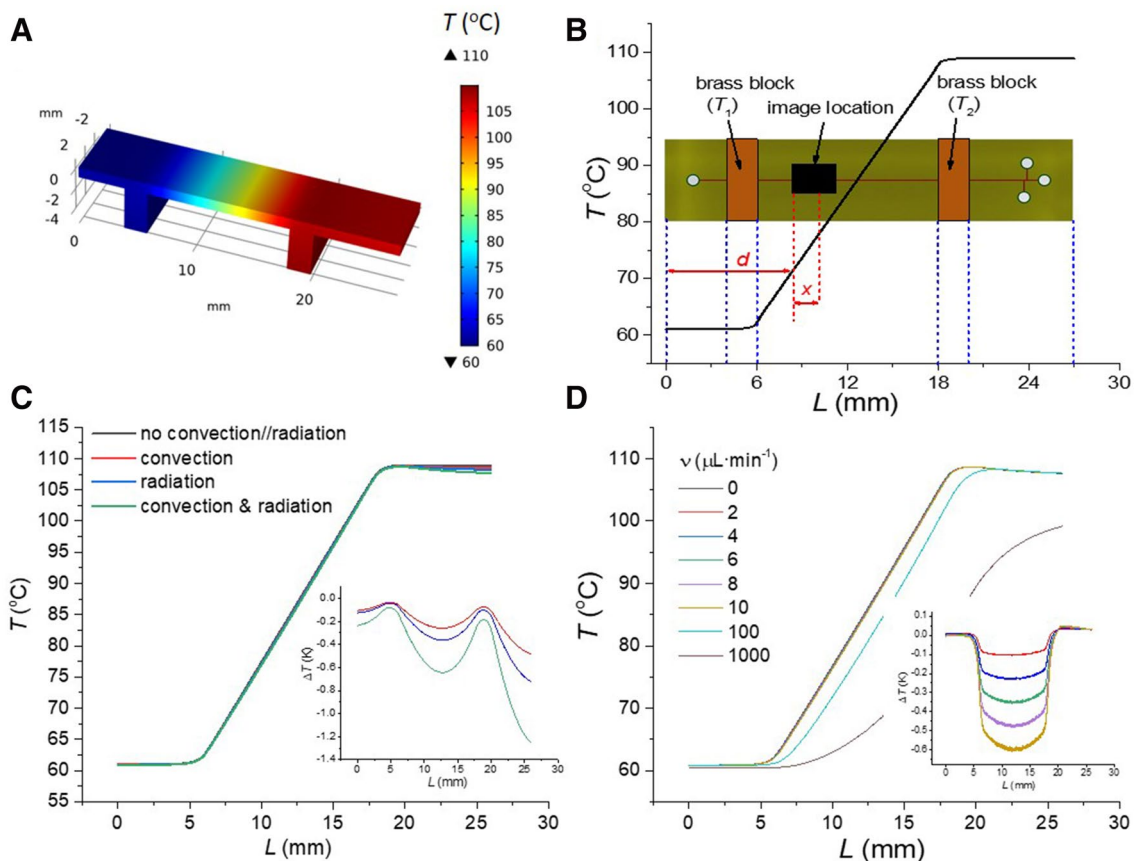


Fig. 2 FEM of the microfluidic chip. **a** Temperature distribution simulated by COMSOL with the heaters' T values set to 60 °C and 110 °C, respectively. **b** The graphs of T as function of (L) along the chip microchannel extracted from the simulation result (black line in **a**), exhibiting a constant temperature gradient (∇T) between the contacts to two brass blocks. For better visualization, we placed a simplified drawing of the chip behind the graph, including the area of the

chip used to capture the fluorescent image (black rectangle) through a CMOS camera. **c** Temperature distribution along the microchannel, considering the influence of convection or/and radiation. The inset is the temperature difference of each corresponding case. **d** Temperature distribution along the microchannel with ν as parameter (inset), showing its negligible influence with values up to 10 $\mu\text{L min}^{-1}$ (color figure online)

between the heaters had a constant value and that the flow rate had no influence on the IR imaging in terms of precision (see supplementary section B).

3.4 Temperature calibration

The distribution of T inside the channel was a key parameter of this MCA experiment; thus, we calibrated the device T distribution through precise T measurement inside the chip, using a time-domain method developed earlier (Neuzil et al. 2010). This method eliminates the influence of convection and radiation as long as the T values of both heaters do not change, and no forced convection is involved. During the measurement, only the ν variable could play a role (Fig. 2d), while for levels up to 10 $\mu\text{L min}^{-1}$, this influence can be ignored.

The dsDNA of GAPDH and HIV with known T_M was used to calibrate the MCA system. Subsequently, we took a fluorescent image from a selected area of the chip at

5472 × 3648 pixels, with a sensitivity and exposure time set to 2000 ISO and 20 s, respectively. We determined that the channel length within the camera's field of view was (3.03 ± 0.02) mm (mean ± standard deviation from five measurements). We then registered the image in MATLAB, extracted the amplitude of F as described above, and performed curve fitting using Eq. (1). The inflection point at the sigmoid curve represented the location where 50% of dsDNA melting occurred, which is denoted by T_M . The inflection point of L in the chip (location with T_M) can be calculated using the following formula:

$$L = d + 3.03 \times (x/5472), \tag{7}$$

where d is the distance from the left side of the image to the left side of the chip, and x is the pixel location along the microchannel in the image (Fig. 2b). The extracted x values for the GAPDH and HIV genes were ≈ 1764 (pixels)

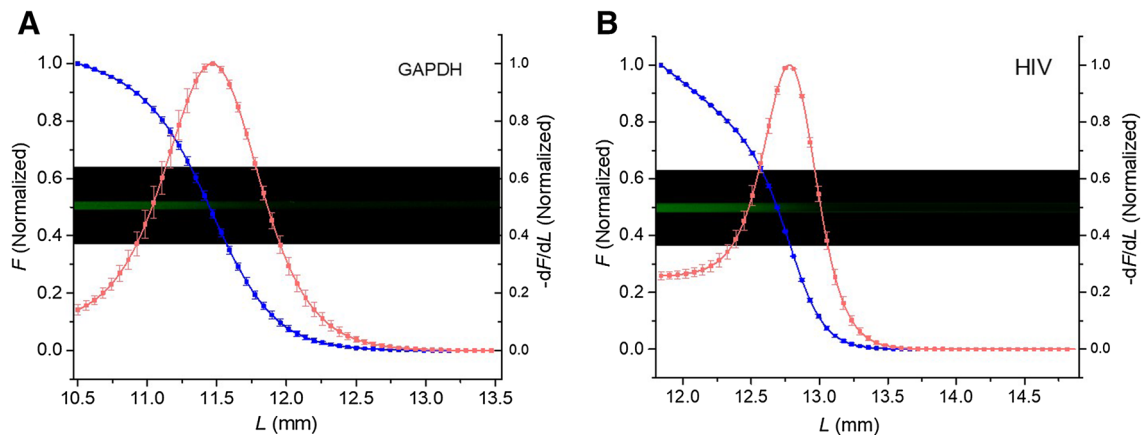


Fig. 3 Temperature calibration of the channel. **a** First, we filled the channel with a dsDNA solution of a cDNA from the GAPDH gene. Then, we captured a fluorescence image (inset), and from this, we extracted the amplitude of F as a function of its location in the MATLAB environment. We plotted its normalized value (blue) and its normalized derivative $-dF/dL$ (red) as a function of L with peak

of the $-dF/dL$ at location of ≈ 11.48 mm corresponding to T_{M1} with value of (80.0 ± 0.4) °C. **b** The same procedure was applied to the results from the channel filled with the dsDNA solution from the cDNA of HIV gene obtaining the location of T_{M2} with a value of (82.9 ± 0.6) °C (mean \pm fitting error) (color figure online)

and ≈ 1693 (pixels) with a d of ≈ 10.50 mm and ≈ 11.84 mm, respectively (Fig. 3a, b). Thus, we obtained the inflection location of the GAPDH and HIV genes as ≈ 11.48 mm and ≈ 12.78 mm using Eq. (7), respectively, which corresponds to the actual T of (80.0 ± 0.4) °C and (82.9 ± 0.6) °C. We performed linear fitting that resulted in a ∇T value of ≈ 2.23 K mm^{-1} and a theoretical amplitude of T_0 (for a value of $L=0$ mm) of ≈ 54.4 °C with the assumption of linear distribution of T , which is correct for v with an amplitude below ≈ 10 $\mu\text{L min}^{-1}$.

The captured image with a width of 5472 pixels had a physical size (field of view) of ≈ 3.03 mm, resulting in a channel resolution of ≈ 0.55 $\mu\text{m pixel}^{-1}$. For the ∇T of ≈ 2.23 K mm^{-1} , we found the T resolution along the microchannel to be ≈ 1.2 mK pixel^{-1} .

Based on these results, we converted the L values into T based on calibration:

$$T(L) = T_0 + \nabla T \cdot L. \quad (8)$$

Here, the value of L ranged from 6 to 18 mm, varying with the heat source position of our setup.

3.5 Flow-induced T_M shift

Once the T calibration was completed, we switched on the syringe pump, sweep the value of v of dsDNA taken from GAPDH from 0 to 5 $\mu\text{L min}^{-1}$ with a step size of 1 $\mu\text{L min}^{-1}$, every time we waited for a few minutes to make the flow to stabilize. For each value of v , we took average of four images to suppress random noise. The same procedure was then repeated for the dsDNA from the HIV gene.

We extracted the MCAs from all the captured images the same way as had been employed for the temperature calibration, then performed the averaging of the MCAs and then converted the L values into T , before plotting the curves with v as a parameter (Fig. 4a) for the dsDNA taken from the GAPDH gene. Following this, we calculated $-dF/dT$ and plotted the obtained values as a function of T , again with v as a parameter (Fig. 4b). The results for the dsDNA from the HIV sample were processed in the same manner (Fig. 4c, d). Here, it should be noted that the calculation of $-dF/dT$ was mainly for visualization purpose, as the extraction of the T_M values was affected directly by the parameters of the sigmoid curve used for $F(x)=f(x)$ fitting, and through x to T conversion.

Finally, we plotted the extracted T_M values as a function of v for both dsDNAs and performed linear regression, calculating the slope (S) corresponding to heat transfer time (Δt) (Fig. 4e) to be (0.34 ± 0.02) K $\text{min } \mu\text{L}^{-1}$ and (0.26 ± 0.01) K $\text{min } \mu\text{L}^{-1}$, respectively (both mean \pm fitting error). The value of Δt was the time required for heat to reach the center of the microchannel from the channel sidewalls.

The channel cross section had an area of ≈ 4200 μm^2 ; thus, we converted v into fluid velocity, determining that 1 $\mu\text{L min}^{-1}$ corresponded to ≈ 3.97 mm s^{-1} . We then used thermal gradient $dT/dL \approx 2.23$ K mm^{-1} to convert the fluid velocity into corresponding T per time (t). The value of S was then converted into t corresponding to $\Delta t = S/\nabla T$, resulting in $\Delta t \approx 38.4$ ms and ≈ 29.4 ms for cDNA of GAPDH and HIV, respectively. The differences in the two values were likely caused by the image processing and by averaging the

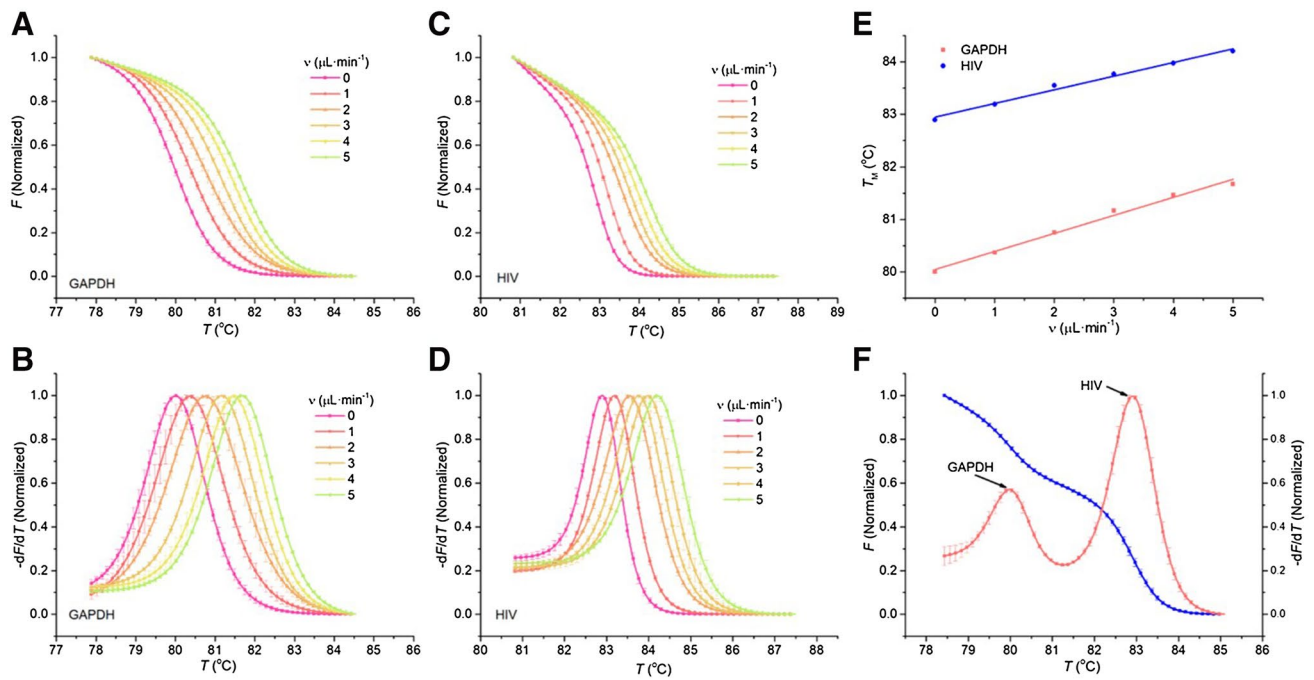


Fig. 4 Comparison of dsDNA melting on the spatial melting device with variable v . **a** Normalized fluorescence intensity of GAPDH data extracted from the image using a MATLAB script fitted with Eq. (1), with amplitude of v as a parameter to show the inflection point shift. Extracted data were used to calculate the value of Δt . **b** Normalized negative derivative of fluorescence of GAPDH with respect to T with v as parameter shows the peak had shifted, with increased amplitude

of v . **c** and **d** The same process was conducted using the HIV sample. **e** T_M extracted from **b** and **d** plotted as a function of v shows its linear dependency on the amplitude of v . **f** Results of a stationary ($v = 0 \mu\text{L min}^{-1}$) MCA using a solution with two different DNAs, both F (blue) as well as $-dF/dT$ (red) are a function of T (color figure online)

F values perpendicular to the channel. Subsequently, the mean value of Δt was ≈ 33.9 ms.

We also performed multiplex MCA using a mixture of dsDNA from the GAPDH and HIV genes. We captured fluorescent images using the same method as described above. We then analyzed the values of F as a function of x and performed curve fitting using Eq. (2), converted L into T and plotted both F as well as $-dF/dT$ as functions of T (Fig. 4f). The extracted T_M values of the cDNA from GAPDH and HIV were $(79.98 \pm 0.08)^\circ\text{C}$ and $(82.91 \pm 0.05)^\circ\text{C}$, respectively, (both mean \pm standard deviation from three measurements), practically identical to the values extracted from the individual cDNA measurements.

4 Conclusion

The flow-induced temperature shifts in the temperature gradient microfluidic device had a significant influence on fluid temperature. The temperature difference between the sample and the channel primarily depended on the thermal conductivities of the chip sidewalls and the fluid, as well as flow rate. In conclusion, we demonstrated a method for the precise calibration of the temperature distribution and its

gradient of $\approx 2.23 \text{ K mm}^{-1}$ in a microfluidic system, based on an MCA of a dsDNA at micrometer and nanometer levels. We then introduced a fluid at a constant flow rate as a parameter and determined the time delay (thermal heat transfer time) Δt between the channel sidewalls and the fluid center, using a microfluidic chip with a gradient mean value of Δt as ≈ 33.9 ms. In this work, we used two cDNAs reverse-transcribed from GAPDH and HIV genes with a ΔT_M of $\approx 2.9 \text{ K}$ for temperature calibration. We found that the system allows measurement with a T resolution of $\approx 1.2 \text{ mK pixel}^{-1}$. The proposed system is simple and fast and has significant potential for being used as a high-throughput device for rapid DNA or protein analysis as well as drug screening.

Acknowledgements The authors wish to acknowledge the financial support of the W099109 grant from P.R. China, the GACR Project Number GA16-11140S from the Czech Republic and the technical support provided by Nano⁺ and by Centrum SIX of Brno University of Technology, Czech Republic. LY and SN acknowledge the funding from the Research Grant Council of Hong Kong, received under Grant Number 16209316.

References

- Balram KC et al (2016) The nanolithography toolbox. *J Res Natl Inst Stand* 121:464–475
- Crews N, Ameen T, Wittwer C, Gale B (2008) Flow-induced thermal effects on spatial DNA melting. *Lab Chip* 8:1922–1929
- Crews N, Wittwer C, Montgomery J, Pryor R, Gale B (2009) Spatial DNA melting analysis for genotyping and variant scanning. *Anal Chem* 81:2053–2058
- Erickson D, Sinton D, Li D (2003) Joule heating and heat transfer in poly (dimethylsiloxane) microfluidic systems. *Lab Chip* 3:141–149
- Ericsson UB, Hallberg BM, DeTitta GT, Dekker N, Nordlund P (2006) Thermofluor-based high-throughput stability optimization of proteins for structural studies. *Anal Biochem* 357:289–298
- Farrar JS, Wittwer CT (2017) High-resolution melting curve analysis for molecular diagnostics. In: *Molecular diagnostics*. Elsevier, pp 79–102. <https://www.sciencedirect.com/science/article/pii/B9780128029718000067>
- Feng J, Svatoš V, Liu X, Chang H, Neuzil P (2018a) High-performance microcalorimeters: design, applications and future development. *TrAC Trend Anal Chem* 109:43–49
- Feng J, Fohlerová Z, Liu X, Chang H, Neuzil P (2018b) Microfluidic device based on deep reactive ion etching process and its lag effect for single cell capture and extraction. *Sens Actuator B Chem* 269:288–292
- Johnson RJ, Savas CJ, Kartje Z, Hoops GC (2014) Rapid and adaptable measurement of protein thermal stability by differential scanning fluorimetry: updating a common biochemical laboratory experiment. *J Chem Educ* 91:1077–1080
- Kopp MU, Mello AJD, Manz A (1998) Chemical amplification: continuous-flow PCR on a chip. *Science* 280:1046–1048
- Launay S, Fedorov AG, Joshi Y, Cao A, Ajayan PM (2006) Hybrid micro-nano structured thermal interfaces for pool boiling heat transfer enhancement. *Microelectron J* 37:1158–1164
- Liu F-W, Liao HF, Lin SP, Lu Y-W (2018) DNA methylation assay using droplet-based DNA melting curve analysis. *Lab Chip* 18:514–521
- Lo MC, Aulabaugh A, Jin GX, Cowling R, Bard J, Malamas M, Ellstad G (2004) Evaluation of fluorescence-based thermal shift assays for hit identification in drug discovery. *Anal Biochem* 332:153–159
- Menzen T, Friess W (2013) High-throughput melting-temperature analysis of a monoclonal antibody by differential scanning fluorimetry in the presence of surfactants. *J Pharm Sci* 102:415–428
- Neuzil P, Cheng F, Soon JBW, Qian LL, Reboud J (2010) Non-contact fluorescent bleaching-independent method for temperature measurement in microfluidic systems based on DNA melting curves. *Lab Chip* 10:2818–2821
- Neuzil P, Campos CDM, Wong CC, Soon JBW, Reboud J, Manz A (2014) From chip-in-a-lab to lab-on-a-chip: towards a single hand-held electronic system for multiple application-specific lab-on-a-chip (ASLOC). *Lab Chip* 14:2168–2176
- Nge PN, Rogers CI, Woolley AT (2013) Advances in microfluidic materials, functions, integration, and applications. *Chem Rev* 113:2550–2583
- Pješčić I, Tranter C, Hindmarsh PL, Crews N (2010) Glass-composite prototyping for flow PCR with in situ DNA analysis. *Biomed Microdev* 12:333–343
- Pryor RJ, Wittwer CT (2006) Real-Time polymerase chain reaction and melting curve analysis. In: Lo YMD, Chiu RWK, Chan KCA (eds) *Clinical applications of PCR*. Humana Press, Totowa, pp 19–32. <https://doi.org/10.1385/1-59745-074-X:19>
- Samiei E, Tabrizian M (2016) Hoorfar M A review of digital microfluidics as portable platforms for lab-on-a-chip applications. *Lab Chip* 16:2376–2396
- Seabrook SA, Newman J (2013) High-throughput thermal scanning for protein stability: making a good technique more robust. *ACS Comb Sci* 15:387–392
- Streets AM, Huang Y (2013) Chip in a lab: microfluidics for next generation life science research. *Biomicrofluidics* 7:011302
- Svatoš V, Gablech I, Ilic BR, Pekarek J, Neuzil P (2018) In situ observation of carbon nanotube layer growth on microbolometers with substrates at ambient temperature. *J Appl Phys* 123:7
- Svatoš V, Gablech I, Pekárek J, Klempa J, Neuzil P (2018) Precise determination of thermal parameters of a microbolometer. *Infrared Phys Techn* 93:286–290
- Tetala KKR, Vijayalakshmi MA (2016) A review on recent developments for biomolecule separation at analytical scale using microfluidic devices. *Anal Chem Acta* 906:7–21
- Thomas S, Orozco RL, Ameen T (2017) Microscale thermal gradient continuous-flow PCR: a guide to operation. *Sens Actuator B Chem* 247:889–895
- Varona J, Tecpoyotl-Torres M, Hamoui AA (2007) Modeling of MEMS thermal actuation with external heat source. *Electron Robot Automot Mech Conf (CERMA 2007)*. <https://doi.org/10.1109/cerma.2007.4367751>
- Wang W, Chen K, Xu C (2006) DNA quantification using EvaGreen and a real-time PCR instrument. *Anal Biochem* 356:303–305
- Wright TA, Stewart JM, Page RC, Konkolewicz D (2017) Extraction of thermodynamic parameters of protein unfolding using parallelized differential scanning fluorimetry. *J Phys Chem Lett* 8:553–558
- Yang Y, Zhang ZG, Grulke EA, Anderson WB, Wu G (2005) Heat transfer properties of nanoparticle-in-fluid dispersions (nanofluids) in laminar flow. *Int J Heat Mass Transf* 48:1107–1116
- Yu S, Wang S, Lu M, Zuo L (2017) Review of MEMS differential scanning calorimetry for biomolecular study. *Front Mech Eng* 12:526–538
- Zhao Y, Zhao C, He J, Zhou Y, Yang C (2013) Collective effects on thermophoresis of colloids: a microfluidic study within the framework of DLVO theory. *Soft Matter* 9:7726–7734

Publisher's Note Springer Nature remains neutral with regard to jurisdictional claims in published maps and institutional affiliations.

Parylene-bonded micro-fluidic channels for cryogenic experiments at superfluid He-4 temperatures

Cite as: Rev. Sci. Instrum. 95, 033901 (2024); doi: 10.1063/5.0162532

Submitted: 15 June 2023 • Accepted: 6 February 2024 •

Published Online: 1 March 2024



View Online



Export Citation



CrossMark

Š. Midlik,^{1,a)} I. Gablech,² M. Goleňa,¹ J. Brodský,² and D. Schmoranzer¹

AFFILIATIONS

¹ Faculty of Mathematics and Physics, Charles University, Prague, Czech Republic

² Department of Microelectronics, Faculty of Electrical Engineering and Communication, Brno University of Technology, Brno, Czech Republic

^{a)} Author to whom correspondence should be addressed: midliks@o365.cuni.cz

ABSTRACT

We present the manufacturing process of a $(24.5 \times 100) \mu\text{m}^2$ -sized on-chip flow channel intended for flow experiments with normal and superfluid phases of ^4He and showcase such a proof-of-concept experiment. This work proves the suitability of chip-to-chip bonding using a thin layer of Parylene-C for cryogenic temperatures as a simpler alternative to other techniques, such as anodic bonding. A monocrystalline silicon chip embeds the etched meander-shaped micro-fluidic channel and a deposited platinum heater and is bonded to a Pyrex glass top. We test the leak tightness of the proposed bonding method for superfluid ^4He , reaching temperatures of ≈ 1.6 K and evaluate its possible effects on flow experiments. We demonstrate that powering an on-chip platinum heater affects the superfluid flow rate by local overheating of a section of the micro-fluidic channel.

Published under an exclusive license by AIP Publishing. <https://doi.org/10.1063/5.0162532>

I. INTRODUCTION

Today, micro-fluidic devices have found use in numerous appliances ranging from common inkjet printers to precise chemical or pharmaceutical dosage systems, in highly specialized research equipment, or generally in any subject where miniaturization intersects with fluid dynamics. A review is presented in Ref. 1. Naturally, precise control over fluid properties and flow rates is also beneficial in studies of quantum fluid dynamics when working with superfluids, such as liquid helium. The superfluid phase of ^4He , called He II, or rather its intriguing properties, were experimentally discovered in the 1930s by measuring the viscosity of helium at cryogenic temperatures.^{2,3} This superfluid phase exists below the so-called Lambda transition occurring at $T = 2.17$ K. Besides direct analogies of classical fluid dynamical experiments on shear flow in narrow channels, micro-fluidic or nanofluidic devices have found their use in investigations of 2D superfluid turbulence,⁴ controlled nucleation of quantized vortices,^{5,6} studies of vortex (de-) pinning dynamics on MEMS devices,⁷ or superfluid quantum interference devices (SHeQUIDS)^{8,9} that allow measuring the absolute state of

rotation with unmatched precision, resolving safely, e.g., the rotation of the planet Earth. Confinement at micron and sub-micron scales opens the door toward research in 2D superfluidity¹⁰ or the Kosterlitz–Thouless transition in confined ^4He ,^{11–13} as well as toward the exploration of confined ^3He .¹⁴

It is perhaps fair to note that the development of cryogenic applications of micro-/nano-fluidic devices trails in the wake of their room temperature counterparts and, with a few notable exceptions, the required technology is not widely used or accessible. The prime reasons can often be tracked down to rather stringent requirements on leak tightness of some of the devices using superfluids, in conjunction with significant differential thermal contraction between typical Si or SiO_2 wafers, glue materials, and interfacing metal or plastic capillaries. The typical techniques used in the manufacture of devices include either direct bonding of cleaned glass surfaces,^{15–17} monocrystalline quartz,¹⁷ silicon,¹⁸ or anodic bonding.^{19–22} These techniques are demanding and often prevent the use of surface metallic electrodes that would be needed for the operation of sensors and actuators. In fact, in most devices, electrical measurements are performed directly in a volume of superfluid only by feeding

the input and output wires directly through the etched fluidic channels.¹⁵ In this work, we present an alternative approach, where two wafers containing both micro-fluidic channels and electrical circuitry are bonded by a microscopically thin Parylene-C layer. We test the resulting device for leak tightness directly in the superfluid ⁴He and report a preliminary measurement of the flow rate vs the applied pressure drop.

II. EXPERIMENTAL SETUP

In this chapter, we will describe the fabrication process of our silicon-to-Pyrex-glass Parylene-bonded micro-fluidic chips and the low-temperature experimental setup used for the flow experiments employing superfluid ⁴He. The chip prototype consists of an etched (24.5×100) μm^2 -sized micro-channel in the shape of a ~ 15 cm long meander with a 1 cm long straight part in the middle of the chip. Next to the straight part of the channel, a Pt on-chip heater was placed to allow overheating of this section. Therefore, the heat transfer between the heater and liquid helium was mediated through the Si chip. The channel was closed from the top with a Pyrex glass slide using Parylene-C bonding. Details of the chip arrangement are shown in Fig. 1.

A. Chip fabrication

The micro-channel and the platinum heater were fabricated on a float zone intrinsic Si (100) wafer with a resistivity greater than 10 k Ω cm, diameter of ~ 100 mm, and thickness of ~ 525 μm . The detailed step-by-step description of the chip fabrication process is schematically shown in Fig. 2.

In the first step, we deposited a 2 nm adhesion Ti layer and a Pt with the thickness of ~ 120 nm and performed standard optical lithography using a positive photoresist (PR) AZ 1518 with the thickness of ~ 1.8 μm . After the PR was spun on the wafer, it was soft-baked at 100 $^\circ\text{C}$ for 90 s. Contact lithography was then performed with ultraviolet light exposure of 140 mJ cm^{-2} . The exposed PR was developed using a TMAH-based developer AZ 726 for ~ 45 s. Then,

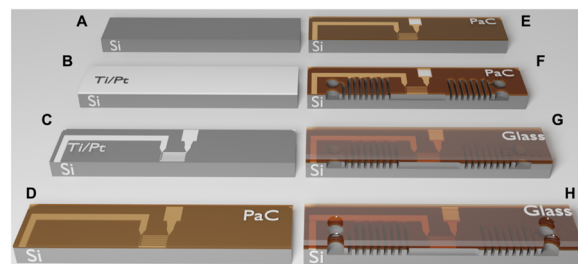


FIG. 2. Step-by-step scheme of the fabrication process. (a) Starting with the float zone intrinsic Si (100) wafer. (b) Deposition of a 2 nm adhesion Ti layer and ~ 120 nm of Pt on the whole wafer. (c) Etching of the heaters using ion-milling by the three-grid micro-wave source. (d) Deposition of a ~ 5 μm parylene-c layer on the wafer and the Pyrex glass pieces. (e) Parylene-C etching by RIE using oxygen gas in order to clean the Pt connection pads. (f) Parylene-C etching by RIE and a subsequent 20 μm etch of Si by DRIE using SF_6 plasma, creating ~ 25 μm deep flow channels (the parylene-c layer adds ~ 5 μm to the channel height). (g) Dicing of the wafer into individual chips and bonding with Pyrex glass slides. (h) Cutting holes in the glass cover with the Yb:KGW femtosecond laser to open the inlets for micro-fluidics interconnect ports.

we performed ion-milling of the exposed Pt/Ti using a three-grid micro-wave ion-beam source. After this step, we removed the PR using an AZ MLO-07 stripper for ~ 300 s at 80 $^\circ\text{C}$, rinsed it by DI water and dried by nitrogen flow.

This was followed by O_2 plasma treatment and deposition of a ~ 5 μm thick parylene-c layer on the Si wafer and glass slides with dimensions of (12.5×39.0) mm^2 , which were prepared using a dicing saw from a Pyrex wafer. For better adhesion, we used Silane A-174. When the parylene-c deposition was done, we performed the second lithography step using AZ 12XT PR with the thickness of ~ 10 μm at a soft-bake temperature of 110 $^\circ\text{C}$ for 180 s, the exposure dose of ~ 300 mJ cm^{-2} , at a post-exposure bake temperature of 90 $^\circ\text{C}$ for 60 s, and development time of 120 s, which created openings for Parylene etching, in order to clean the Pt connection pads. Parylene-C etching was then performed in a capacitively coupled

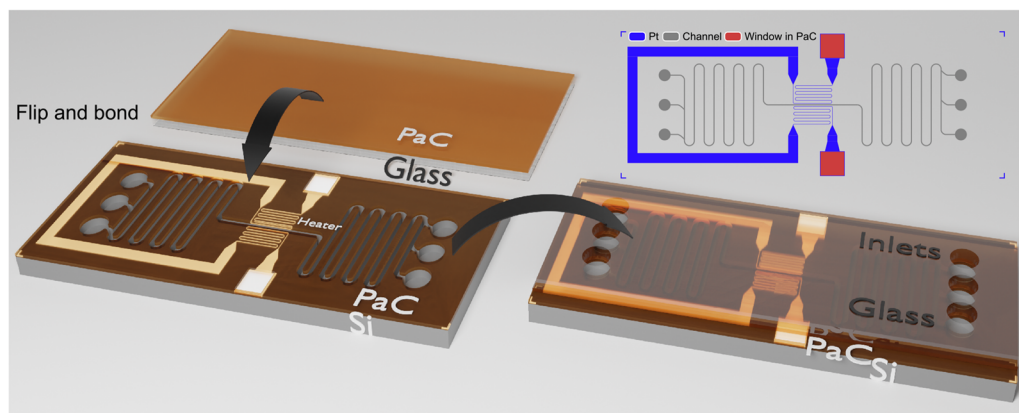


FIG. 1. 3D view illustrating the bonding process. The covering Pyrex piece is narrower than the chip to leave heater connection pads accessible. Top right: the layout of the meandered micro-fluidic channel with capillary terminals (gray), a platinum resistive heater near the channel center (blue), and its connection pads (red), where the Parylene-C (PaC) layer was stripped for access. The thick (lower resistance) Pt loop is connecting two parts of the heater placed on the opposite sides of the channel.

plasma reactive ion etching (RIE) instrument using oxygen gas with the power of 200 W for 20 min at ≈ 13 Pa with the corresponding bias of ≈ 480 V.

Subsequently, we removed the PR using the same MLO-07 solution as before and performed the last lithography step, which was focused on the fabrication of microchannels using the Bosch process. We used the same PR as in the previous step, etched Parylene-C, and then, moved the wafer to a DRIE instrument for the etching of ≈ 20 μm of Si. The etching was done using SF_6 plasma with pressure of ≈ 4 Pa and plasma power of 1800 W. The passivation step was performed with C_4F_8 gas at ≈ 3.3 Pa and corresponding plasma power of 1500 W. We used 35 loops to etch the substrate. Such an etched wafer was again stripped and coated with a protection PR using the same procedure as before. We then diced it using a saw into individual chips with dimensions of (15×39) mm^2 and finally, stripped the remaining PR.

The resulting dimensions of the fabricated channel, width $w = 100$ μm and height $h = 24.5$ μm (being the sum of the Si etch depth and PaC layer thickness), were measured using a mechanical profile meter. Based on the roughness of the scan and the size of the tip, we estimate the uncertainty to be of order 5 % in the horizontal direction and of order 1 % in the vertical direction. The fabricated chips were intended for proof-of-principle experiments only, and more precise measurements are accessible if knowledge of the exact dimensions or surface structure is crucial for the application.

Fabricated Si chips and Pyrex slides with Parylene-C were then prepared for the final bonding step. We used an inductively coupled plasma source for oxygen treatment with a power of 400 W at ≈ 6.5 Pa for 120 s. Then, we placed the samples on a hot plate for 60 s at the temperature of 240 $^\circ\text{C}$. The samples were then stuck together with a manual force applied through a polytetrafluorethylene roller for a few seconds, until light refraction/interference disappeared, suggesting that the layers are bonded together.

The last fabrication step was to cut holes with a diameter of ≈ 0.6 mm in the glass cover to open the interconnect ports for the micro-fluidic channel using a Yb:KGW femtosecond micro-machining laser with a principal wavelength of ≈ 515 nm, pulse duration of ≈ 270 fs, and pulse energy of ≈ 20 μJ . Cutting the holes in the glass cover before the bonding resulted in the occurrence of cracks. Therefore, our laser cutting technique had to be optimized to prevent channel contamination with glass particles, which might become problematic especially for nano-scale channels. Each side of the channel has three alternative connection holes, allowing for redoing of the capillary gluing if necessary.

B. Cryogenic setup

All low-temperature experiments were performed in a glass, vacuum-isolated, helium bath cryostat with an outer liquid-nitrogen vessel. The chip interconnection ports (one on each side of the channel) were glued to brass capillaries with an inner diameter of ≈ 0.55 mm and length of ≈ 5 cm, using conductive EPO-TEK H20E silver epoxy, as shown in Fig. 3. The same epoxy was used to connect the Pt heater and to blank all the unused chip openings.

On the high pressure (inlet) side of the chip, a brass capillary was soldered to a heat exchanger and then to about 1 m long stainless steel capillary, with an inner diameter of ≈ 0.8 mm, exiting the cryostat via a soldered feedthrough. The heat exchanger, providing

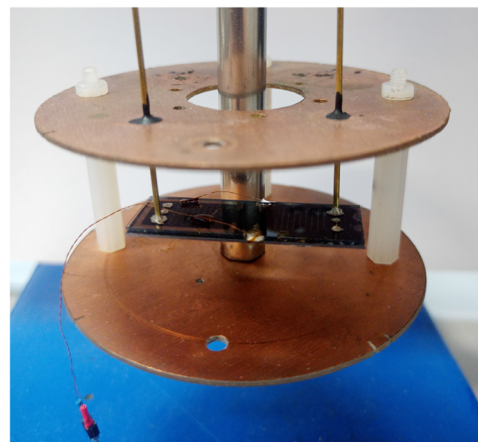


FIG. 3. Photo of the chip installed on the experimental insert. The interconnection ports are glued to the brass capillaries using EPO-TEK H20E silver epoxy. The same epoxy is used for on-chip heater connection and to blank all the unused ports.

an efficient liquefaction of incoming gas and good thermalization to the bath, was constructed from a ≈ 30 cm long copper capillary spiral with an inner diameter of ≈ 0.4 mm. The low pressure (outlet) side brass capillary was connected directly to a stainless steel capillary. As a result, the inner helium circulation was entirely separated from the bath, which provided only temperature stabilization. The bath temperature was regulated by setting the saturated vapor pressure using rotary and Roots pumps.

The full setup for the flow experiments, including the room-temperature part of the apparatus, is shown in Fig. 4. Evaporation from a transport Dewar was providing the source of the clean helium gas. Any impurities admixed into the flowing gas were further adsorbed into a cold liquid nitrogen trap. The inlet pressure could be set using a fine-regulating valve. After this valve, a helium

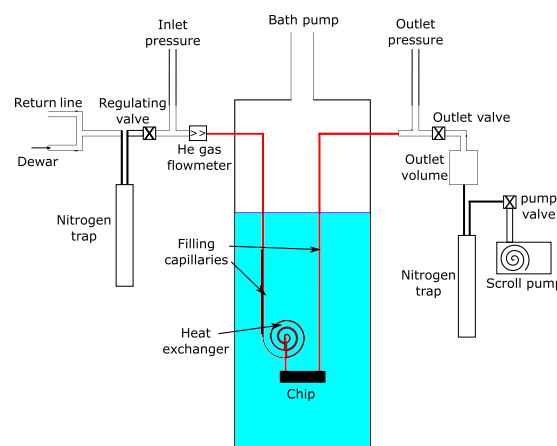


FIG. 4. Detailed schematic of the cryogenic experimental setup. The inner helium circulation lines, connected through the chip, are fully separated from the bath, which is used for temperature control only.

gas flow meter McMillan model 50K-7 was installed to measure the flow rate in the circuit. Then, the entering gas was liquefied in the heat exchanger and fed through the micro-fluidic channel. The flowing liquid was consequently evaporated in the outlet capillary and led to a valve-sealed outlet volume, back at room temperature. This volume was connected through another liquid nitrogen trap to a scroll pump, allowing pressure regulation on the outlet side.

In order to monitor the pressure drop across the micro-fluidic channel, a differential pressure transducer, the MKS Baratron Model 120AD01000RBU, was connected between the front of the gas flow meter (inlet pressure) and the end of the stainless capillary feedthrough (outlet pressure). In addition, two Honeywell MIP series with 50 psi pressure gauges were installed at the same places for absolute pressure readings. All capillary connections were soft-soldered, and the whole inner helium circuit was carefully leak-tested at room temperature. Prior to all cryogenic experiments, we carefully evacuated the whole inner helium circuit using a turbo-molecular pump (at least for 24 h), to remove most of the gas impurities present.

III. RESULTS AND DISCUSSION

A. Leak test

First, a leak-test was performed in order to test the tightness level of the Parylene-bonded chip during the initial cooldown, immersion into the liquid helium bath, and the transition to the superfluid phase. Here, we have used a simplified apparatus, having the Pfeiffer HLT 270 leak detector employing a ^4He mass spectrometer, connected directly to both chip filling lines, after the inlet “regulating” valve and the outlet valve. The setup also allowed to pressurize the inlet volume and to measure the outlet volume filling through the chip. This was done in order to verify chip continuity after the leak test, ruling out possible blockages. Bath temperature was evaluated based on the saturated vapor pressure measurement. Temperature evolution, during the initial pre-cooling with the nitrogen bath and cold helium gas, was evaluated based on a Pt100 platinum thermometer (measuring in the range from $\approx 110\ \Omega$ at room-temperature to $\approx 1\ \Omega$ when submerged in liquid helium).

The entire tested volume, including the chip and its filling lines, was first carefully evacuated by a turbo-molecular pump operated 24 h before the test. The cryostat was simultaneously pumped by using rotary and Roots pumps. The turbo-molecular pump was then exchanged for the leak detector to allow leak rate evolution measurement on the circulation volume during the cooldown procedure, reaching bath temperatures down to 1.6 K. Fig. 5 shows the leak rate level, Pt100 thermometer resistance, and bath pressure, highlighting all significant events.

The base level of the leak rate measured on the closed valve of the detector was of an order of 2×10^{-9} mbar \times l/s. The leak detector was then opened to the volume under test, and the leak rate level was left to decrease below 9×10^{-9} mbar \times l/s, before any manipulation with the cryostat. The first introduction of He gas (at full atmospheric pressure) into the cryostat volume, typically used to flush the cryostat and used here as a room-temperature leak test, showed a gradual increase in the leak rate to a value of $\approx 9 \times 10^{-9}$ mbar \times l/s. This behavior, as shown in Fig. 5 between (a) and (b) lines, reveals the presence of a small diffusive He gas

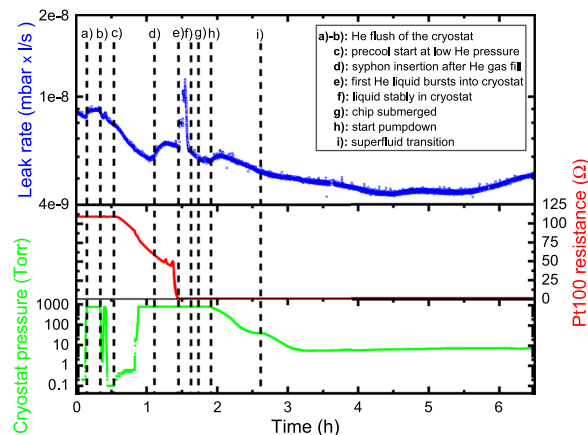


FIG. 5. Evolution of the helium leak rate (top panel), the Pt100 platinum thermometer resistance (middle panel), and the cryostat pressure (bottom panel) measured during the cryostat flush with helium gas, pre-cool by cold helium vapors, liquid helium transfer, and following cooldown to the superfluid phase. The leak rate signal was additionally filtered to remove periodically occurring noise peaks, being an inherent property (also appearing when the leak tester is run with a blanked input) of the mass spectrometer used. All significant events are visualized by vertical dashed lines (a)–(i). The leak test was conducted in a simplified setup with a leak detector connected directly (right after the feedthroughs exiting the cryostat) to both sides of the filling lines (inlet and outlet stainless steel capillaries).

leak. The origin of this leak is either from the epoxy-glued joints or the Parylene-C layer itself. However, our previous tests which used Stycast 2850FT epoxy, instead of H20E, showed that this leak depends on the gluing technique and points toward a leak origin likely in epoxy joints. After this test, the cryostat was evacuated again.

Later, the outer cryostat vessel was filled with liquid nitrogen to initiate cooling (and provide thermal shielding), which started to be effective after the introduction of a small amount of He exchange gas into the cryostat [line (c) shown in Fig. 5]. After some time, full He pressure was set to prepare for the transfer syphon insertion [line (d)], following cooling with the use of cold He vapors. As the cryostat was cooling down, we observed a gradual decrease in the leak rate (initially due to a lower He content, but it continued after reaching full pressure in the cryostat). The leak rate starts to rise again, already before syphon insertion, as the temperature falls below ≈ 150 K (deduced from Pt100 resistance). Finally, two step-like increments in the leak rate occurred with the first bursts of the liquid He entering the cryostat [line (e)]. After stabilization of the liquid He presence [line (f)] in the cryostat, the leak rate level started to decrease, with no significant changes upon chip submersion [line (g)], start of the bath pump-down [line (h)], and most importantly, upon superfluid transition [line (i)]. Eventually, a base level of $\approx 5 \times 10^{-9}$ mbar \times l/s was reached. After the leak test (with the chip still submerged), the flow channel continuity was checked by pressurizing the inlet volume and letting the outlet volume be filled through the chip to rule out possible cold plugs in the filling capillaries.

The described behavior during the cool-down supports the presence of a small diffusive leak, which is gradually closing as

temperature decreases. However, at temperatures below ≈ 150 K, most likely the differential thermal contraction of the individual components starts to play a role, opening a new temporal leak, as different materials are cooled down at their respective rates. This is most profound during the first liquid He bursts, causing rapid equalization of the temperature throughout the whole cryostat. After stabilization of the temperature, with a continuous presence of the liquid, the temporal leak disappears.

An additional effect that must be considered, causing the measured leak rate to decrease at liquid He temperatures, is the cryosorption of He atoms to the inner channel walls. This would result in masking of the leak until all surfaces are saturated with a few layers of adsorbed helium. According to the DRK model of helium adsorption on stainless steel presented in Eq. (9) in Ref. 23, a detectable pressure of 1 Pa would correspond to a coverage of approximately one layer of helium on the walls. However, this approach may disregard the possibility of the formation of a solid layer; therefore, we consider three atomic layers of helium atoms as a more reliable sensitivity threshold. With the duration of our experiment at the low temperature of 1.6 K close to 4 h and considering the surface area of the micro-fluidic channel and parts of the filling capillaries submerged in the bath, we obtain the maximum masked leak rate as 4.2×10^{-9} mbar \times l/s. The minimum measured leak rate $\approx 3 \times 10^{-9}$ mbar \times l/s (after subtracting the background) corresponds quite well with this value. This shows that while the chip is immersed in superfluid helium, the maximum leak rate is below the diffusive leak of $\approx 10^{-8}$ mbar \times l/s observed during the cooldown and, importantly, will not interfere with any flow experiments conducted in the channel.

As a result, this experiment proves the usability of the Si-to-Pyrex Parylene-bonded chips for the proposed applications. We were able to identify a diffusive He gas leak, present mainly at higher temperatures, which is not greater than 1×10^{-8} mbar \times l/s. Nevertheless, it gives a limitation of the bonding technique for certain specific applications, where the chip would need to be kept under a good vacuum. The leak most likely originated from epoxy-glued joints, as discussed above, opening room for further improvement and not ruling out the full leak tightness of the parylene bond. Most importantly, no significant changes in the leak rate were observed, neither upon the chip being submerged in liquid nor at the superfluid transition. Both of these events would have greatly affected the real leak rate in case of a liquid/superfluid leak, leading to an order-of-magnitude increase in the signal. Additionally, the maximum leak rate at helium temperatures falls within acceptable values $< 10^{-8}$ mbar \times l/s. This shows a sufficient bond tightness to inviscid superfluid helium flows, and as for most intended experiments, where the channel is eventually filled with liquid/superfluid helium, the present small-scale diffusive leak is immaterial and will not significantly affect the mass or heat transport through the channel.

B. Flow experiment

Finally, we have performed the initial proof-of-concept measurements of the flow rate of superfluid ^4He through the micro-fluidic channel, while at the same time investigating the effects of local overheating of the straight section of the micro-channel by the Pt heater. Here, we have employed the full apparatus, as described in Sec. II B. At first, a steady state with an equal inlet and outlet

pressure (given by Dewar pressure) and zero mass flow was prepared, while the volume past the outlet valve was pre-pumped and then disconnected from the pump. This was done to prevent a direct long-lasting connection between the atmosphere and the cryogenic parts of the setup, which would inevitably lead to the development of a blockage due to cryo-pumping of oxygen, nitrogen, or water vapor. The helium flow was initiated by an instant outlet valve opening, causing a quick pressure drop to occur across the channel. The time evolution of mass flow rate and pressure difference was then recorded as the outlet volume was being filled through the micro-fluidic channel. Fig. 6 shows the evolution of liquid flow velocity as a function of differential pressure, driving the flow. Such measurements were performed at two different bath temperatures, 2.13 and 2.02 K, and in two distinct states of the on-chip heater, 0 mW or ≈ 100 mW power.

The velocity of the liquid helium v_l in the channel was obtained via

$$v_l = \frac{\xi U \rho_g}{wh\rho_l} \quad (1)$$

from the measured voltage U on a McMillan 50K-7 flow meter, with the range of 1000 ml/min at 5 V. The conversion ratio for the volumetric helium gas flow rate is $\xi = 3.33 \times 10^{-6}$ m 3 s $^{-1}$ V $^{-1}$. Additionally, assuming the conservation of mass, in a steady state, the liquid flow rate is calculated from the ratio of room temperature gas density $\rho_g = 0.179$ kg m $^{-3}$ and cryogenic liquid density

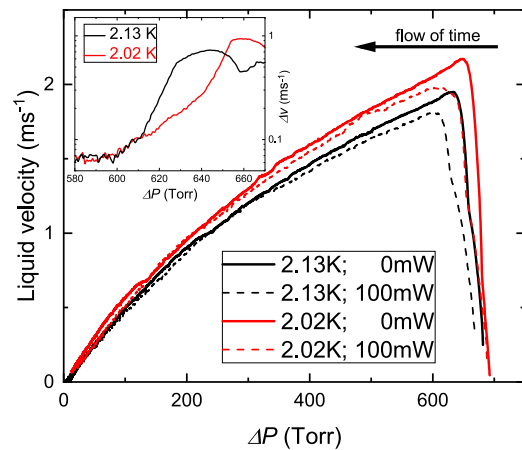


FIG. 6. Measured flow velocity of superfluid helium through the chip as a function of differential pressure across the micro-fluidic channel at two temperatures. The filling of the low pressure side volume, corresponding to the pressure vs velocity trace shown took over 1000 s. The absolute velocity scales correctly with the temperature, having a higher relative content of inviscid superfluid component at a lower temperature. The full/dashed lines represent the experiment realization with the on-chip Pt heater switched off/on at 100 mW. The velocity evolution is clearly affected by the heater, mainly, shortly after the start of the flow experiment (the outlet valve opening). In the inset, we show the difference in the flow velocity between the states with the heater off/on as a function of differential pressure. Velocity difference is calculated for the points at the same differential pressure and it drops to the base level (no significant difference in flow velocity) in about 20 s, at a pressure below ≈ 600 Torr.

$\rho_1 = 145 \text{ kg m}^{-3}$. The dimensions of the channel cross section, channel width $w = 100 \text{ }\mu\text{m}$ and channel height $h = 24.5 \text{ }\mu\text{m}$, are described in Sec. II A.

The absolute flow rates show complex features related to the interaction of rapid gas flow in the capillaries with the liquefaction/evaporation processes and with the flow of the superfluid through the micro-fluidic channel, which will be discussed in a separate publication. In each case, it was observed that in the initial phase, the flow was significantly faster with the heater off, as shown in Fig. 6. The superfluid ^4He flow is clearly affected by the heater, but the initial velocity difference eventually decreases and disappears on the time scale of $\approx 20 \text{ s}$. Qualitatively, the same behavior was observed at both the measured temperatures. This might be explained considering the relatively high absolute flow velocity of the order of 1 ms^{-1} . Initially, the overheated stationary fluid offers more drag (due to the higher relative density of the normal component), but it is being gradually replaced with a new cold liquid entering from the capillary at the bath temperature. The heater power is then insufficient to preheat the fluid entering the channel at such high velocities, as Kapitza resistance between the silicon chip and the flowing helium presents a limiting factor, reducing the efficiency of the heat transfer to the flowing liquid.

Nonetheless, this experiment shows the potential of the tunability of the flow through the micro-fluidic channels using an on-chip heater in a further optimized geometry. The range of absolute flow velocities might also be tuned by employing different flow generation mechanisms, e.g., submerged bellows, a superfluid fountain, a room temperature circulation pump, or, simply, hydrostatic pressure, as in the case of the pioneering experiments of Allen and Misener.³

IV. CONCLUSIONS

We have tested a simple bonding technique using parylene-c in the preparation of micro-fluidic devices for use in cryogenic experiments with superfluid helium. This technique allows for the rapid production of micro-fluidic devices of a higher complexity than previously fabricated, as it is compatible with metallic electrodes on bonded surfaces. Despite a transient diffusive leak not greater than $1 \times 10^{-8} \text{ mbar} \times \text{l/s}$ and a possible persistent cryogenic leak of the order of $10^{-9} \text{ mbar} \times \text{l/s}$, the device proves to be sufficiently tight for superfluid helium to allow performing fluid dynamical experiments. As a demonstration, an on-chip heater has been used to manipulate the temperature in a section of the channel, affecting the total flow rate. The future work will involve exploring the limitations of the applied bonding technique with respect to the reduction of the channel dimensions as well as the fabrication of other on-chip devices for use with superfluids, such as micropumps, cold valves, or controllable impedances.

ACKNOWLEDGMENTS

The authors acknowledge the CzechNanoLab project LM2023051 funded by MEYS CR for the financial support of the measurements/sample fabrication at CEITEC Nano Research Infrastructure. We greatly thank Jakub Somer from NETWORK GROUP, s.r.o. in Brno, for helping with the final chip fabrication

step using femtosecond laser cutting of channel connection orifices in the glass. We acknowledge the support from the Czech Science Foundation under projects 20-13001Y (design, cryogenic experiments) and 20-30129Y (fabrication). J.B. acknowledges the support through the Brno Ph.D. Talent Scholarship funded by the Brno City Municipality.

AUTHOR DECLARATIONS

Conflict of Interest

The authors have no conflicts to disclose.

Author Contributions

Š. Midlik: Data curation (lead); Formal analysis (lead); Writing – original draft (equal); Writing – review & editing (equal). **I. Gablech:** Funding acquisition (equal); Resources (lead); Writing – original draft (equal); Writing – review & editing (equal). **M. Goleňa:** Data curation (equal); Formal analysis (supporting). **J. Brodský:** Resources (lead); Writing – original draft (equal). **D. Schmoranzer:** Conceptualization (lead); Data curation (supporting); Formal analysis (supporting); Funding acquisition (equal); Writing – original draft (equal); Writing – review & editing (equal).

DATA AVAILABILITY

The data that support the findings of this study are available upon reasonable request from the corresponding author.

REFERENCES

- 1 A.-G. Niculescu, C. Chircov, A. C. Birca, and A. M. Grumezescu, "Fabrication and applications of microfluidic devices: A review," *Int. J. Mol. Sci.* **22**, 2011 (2021).
- 2 P. Kapitza, "Viscosity of liquid helium below the λ -point," *Nature* **141**, 74 (1938).
- 3 J. F. Allen and A. D. Misener, "Flow of liquid helium II," *Nature* **141**, 75 (1938).
- 4 E. Varga, V. Vadakkumbatt, A. J. Shook, P. H. Kim, and J. P. Davis, "Observation of bistable turbulence in quasi-two-dimensional superflow," *Phys. Rev. Lett.* **125**, 025301 (2020).
- 5 R. Goto, S. Fujiyama, H. Yano, Y. Nago, N. Hashimoto, K. Obara, O. Ishikawa, M. Tsubota, and T. Hata, "Turbulence in boundary flow of superfluid ^4He triggered by free vortex rings," *Phys. Rev. Lett.* **100**, 045301 (2008).
- 6 N. Hashimoto, R. Goto, H. Yano, K. Obara, O. Ishikawa, and T. Hata, "Control of turbulence in boundary layers of superfluid ^4He by filtering out remanent vortices," *Phys. Rev. B* **76**, 020504 (2007).
- 7 C. S. Barquist, W. G. Jiang, K. Gunther, N. Eng, Y. Lee, and H. B. Chan, "Damping of a microelectromechanical oscillator in turbulent superfluid ^4He : A probe of quantized vorticity in the ultralow temperature regime," *Phys. Rev. B* **101**, 174513 (2020).
- 8 K. Schwab, N. Bruckner, and R. Packard, "Detection of the Earth's rotation using superfluid phase coherence," *Nature* **386**, 585–587 (1997).
- 9 Y. Sato and R. Packard, "Superfluid helium quantum interference devices: Physics and applications," *Rep. Prog. Phys.* **75**, 016401 (2012).
- 10 D. J. Bishop and J. D. Reppy, "Study of the superfluid transition in two-dimensional ^4He films," *Phys. Rev. Lett.* **40**, 1727–1730 (1978).
- 11 G. Agnolet, D. F. McQueeney, and J. D. Reppy, "Kosterlitz–Thouless transition in helium films," *Phys. Rev. B* **39**, 8934–8958 (1989).
- 12 J. M. Kosterlitz, "Superfluidity in thin films of ^4He ," *J. Low Temp. Phys.* **201**, 541–584 (2020).

- ¹³F. M. Gasparini, M. O. Kimball, K. P. Mooney, and M. Diaz-Avila, "Finite-size scaling of ^4He at the superfluid transition," *Rev. Mod. Phys.* **80**, 1009–1059 (2008).
- ¹⁴L. V. Levitin, R. G. Bennett, A. Casey, B. Cowan, J. Saunders, D. Drung, T. Schurig, and J. M. Parpia, "Phase diagram of the topological superfluid ^3He confined in a nanoscale slab geometry," *Science* **340**, 841–844 (2013).
- ¹⁵X. Rojas and J. P. Davis, "Superfluid nanomechanical resonator for quantum nanofluidics," *Phys. Rev. B* **91**, 024503 (2015).
- ¹⁶E. Varga, C. Undershute, and J. P. Davis, "Surface-dominated finite-size effects in nanoconfined superfluid helium," *Phys. Rev. Lett.* **129**, 145301 (2022).
- ¹⁷F. Souris, X. Rojas, P. H. Kim, and J. P. Davis, "Ultralow-dissipation superfluid micromechanical resonator," *Phys. Rev. Appl.* **7**, 044008 (2017).
- ¹⁸P. J. Heikkinen, A. Casey, L. V. Levitin, X. Rojas, A. Vorontsov, P. Sharma, N. Zhelev, J. M. Parpia, and J. Saunders, "Fragility of surface states in topological superfluid ^3He ," *Nat. Commun.* **12**, 1574 (2021).
- ¹⁹S. Dimov, R. G. Bennett, A. Córcoles, L. V. Levitin, B. Ilic, S. S. Verbridge, J. Saunders, A. Casey, and J. M. Parpia, "Anodically bonded submicron microfluidic chambers," *Rev. Sci. Instrum.* **81**, 013907 (2010).
- ²⁰N. Zhelev, T. Abhilash, R. Bennett, E. Smith, B. Ilic, J. Parpia, L. Levitin, X. Rojas, A. Casey, and J. Saunders, "Fabrication of microfluidic cavities using Si-to-glass anodic bonding," *Rev. Sci. Instrum.* **89**, 073902 (2018).
- ²¹D. Lotnyk, A. Eyal, N. Zhelev, T. S. Abhilash, E. N. Smith, M. Terilli, J. Wilson, E. Mueller, D. Einzel, J. Saunders, and J. M. Parpia, "Thermal transport of helium-3 in a strongly confining channel," *Nat. Commun.* **11**, 4843 (2020).
- ²²N. Zhelev, T. S. Abhilash, E. N. Smith, R. G. Bennett, X. Rojas, L. Levitin, J. Saunders, and J. M. Parpia, "The A–B transition in superfluid helium-3 under confinement in a thin slab geometry," *Nat. Commun.* **8**, 15963 (2017).
- ²³V. Baglin, "Cryopumping and vacuum systems," [arXiv:2006.01574](https://arxiv.org/abs/2006.01574) [physics.ins-det] (2020).

High-Conductivity Stoichiometric Titanium Nitride for Bioelectronics

Imrich Gablech, Ludovico Migliaccio, Jan Brodský, Marek Havlíček, Pavel Podešva, Radim Hrdý, Jiří Ehlich, Maciej Gryszel, and Eric Daniel Głowacki**

Bioelectronic devices such as neural stimulation and recording devices require stable low-impedance electrode interfaces. Various forms of nitridated titanium are used in biointerface applications due to robustness and biological inertness. In this work, stoichiometric TiN thin films are fabricated using a dual Kaufman ion-beam source setup, without the necessity of substrate heating. These layers are remarkable compared to established forms of TiN due to high degree of crystallinity and excellent electrical conductivity. How this fabrication method can be extended to produce structured AlN, to yield robust AlN/TiN bilayer micropylamids, is described. These electrodes compare favorably to commercial TiN microelectrodes in the performance metrics important for bioelectronics interfaces: higher conductivity (by an order of magnitude), lower electrochemical impedance, and higher capacitive charge injection with lower faradaicity. These results demonstrate that the Kaufman ion-beam sputtering method can produce competitive nitride ceramics for bioelectronics applications at low deposition temperatures.

1. Introduction

Implantable neural interface devices are vital to fundamental neuroscience research as well as the rapidly growing clinical field of bioelectronic medicine.^[1] Bioelectronic implants are used to stimulate peripheral nerves to treat conditions ranging from epilepsy to Crohn's disease. Implantable brain probes enable deep-brain stimulation for Parkinson's patients, and retinal stimulators restore visual perception to patients with degenerative blindness.^[2] The list of applications of bioelectronic medicine grows, and in parallel advanced neural interfaces are required to push the forefront of understanding in neuroscience. Encapsulation layers and conducting pathways must survive the chemical and electrical stresses of a physiological environment. Chronically implanted devices must additionally withstand degradation and mechanical stresses of implantation for periods up to decades.^[3] These requirements of bioelectronics are extremely demanding and often challenge aspects of nano- and microfabrication, which the electronics industry normally does not need to solve. The conductor layers in neural interface devices must be made with high reproducibility and should have the lowest possible ohmic losses on all electrical leads. The most critical component is the actual electrode interfacing with the physiological environment.^[4] Various figures of merit are important for biointerface electrodes: electrochemical impedance, charge injection capacity, and finally the electrochemical passivity window, particularly the overpotential values for possibly harmful irreversible reactions.^[5] Moreover, this electrode must fulfill the strictest requirements for stability. At present, the conductor used in nearly all research-scale devices, including flexible devices, is gold. This is to minimize ohmic losses. While suitable for passivated leads, gold is not a good biointerface electrode. This is due to relatively high impedance values and its ability to catalyze harmful faradaic reactions, including oxygen reduction to hydrogen peroxide. Materials suitable for biointerface electrodes, which are used with more success are platinum or its alloys, iridium oxide, and conducting polymers like polythiophenes.^[6] All these materials have low electrochemical impedance and relatively high charge-injection capacity, and reasonable stability in biological environment. They are all, however, relatively faradaic electrodes, and the possibility


of

I. Gablech, L. Migliaccio, J. Brodský, M. Havlíček, P. Podešva, R. Hrdý, J. Ehlich, E. D. Głowacki
 Central European Institute of Technology
 Brno University of Technology
 Brno 612 00, Czech Republic
 E-mail: imrich.gablech@ceitec.vutbr.cz;
 eric.daniel.glowacki@ceitec.vutbr.cz

I. Gablech
 Department of Electrical and Electronic Technology
 Faculty of Electrical Engineering and Communication
 Brno University of Technology
 Brno 616 00, Czech Republic

M. Havlíček
 Czech Metrology Institute
 Brno 638 00, Czech Republic

M. Gryszel
 Laboratory of Organic Electronics
 Linköping University
 Norrköping 602 21, Sweden

 The ORCID identification number(s) for the author(s) of this article can be found under <https://doi.org/10.1002/aelm.202200980>.

© 2023 The Authors. Advanced Electronic Materials published by Wiley-VCH GmbH. This is an open access article under the terms of the Creative Commons Attribution License, which permits use, distribution and reproduction in any medium, provided the original work is properly cited.

DOI: 10.1002/aelm.202200980

of harmful reactions must always be considered. At present, a state-of-the-art material for fully capacitive current injection with hindered faradaic reactions is TiN. TiN is well established in in vitro electrophysiology protocols, especially in commercial multi-electrode array (MEA) recording devices.^[6,7] TiN electrodes on silicon probes are the state-of-the-art for ultrahigh density recording arrays.^[8]

The TiN layers in these devices are fabricated at relatively high temperatures up to ≈ 400 °C in the case of physical vapor deposition.^[9] In the case of chemical vapor deposition, the deposition process requires various precursors and the temperature is usually higher than ≈ 600 °C,^[10] which makes fabrication process more difficult due to compatibility with underlying materials, which are often necessary. While not always a problem for the rigid substrates used for multielectrode arrays, the necessity of high-temperature growth conditions for quality TiN has impeded its successful adoption in flexible devices for plastic neural interfaces. There are a few examples in the literature of TiN on plastics;^[11] however performance is very modest and it appears clear that there is much room for improvements to bring TiN to a competitive level with Pt, IrO_x, and conducting polymers. The primary reason for poor performance on plastics is the necessity of high temperatures for achieving high-quality TiN, which is incompatible with organic materials used in ultrathin flexible bioelectronics. For that reason, demand exists for low-temperature preparation of high-quality TiN with favorable conductivity.

Electrical and electrochemical properties of TiN are strongly based on the real ratio between Ti, N, and other impurities, such as oxygen. In reality, there is a wide range of variability in the stoichiometry of TiN electrodes that are reported in the literature, and nearly all cases relating to bioelectronics applications, the composition of these electrodes is not characterized. Therefore, it is not possible to easily generalize properties such as electrochemical impedance, charge injection capacity, and electrochemical passivity window. As will be shown in our results, stoichiometric 1:1 TiN can be attractive. Meanwhile, it would appear that much of what is labeled as TiN in the literature may in fact be oxynitride, with a significant oxide character. Furthermore, electrochemical parameters are also dependent on the surface roughness and real surface area. These properties, in turn, vary with the degree of crystallinity and the corresponding crystal orientation(s). In any case, nearly all examples of TiN fabricated for bioelectronics applications are obtained via reactive magnetron sputtering from a titanium target. For instance, F. Rodrigues et al. prepared TiN via direct current (DC) magnetron reactive sputtering in mixed Ar:N₂ atmosphere. Such prepared TiN possessed with wide passive water window in the range from -0.6 to 0.8 V with charge injection capacity of (154 ± 16) $\mu\text{C cm}^{-2}$. Additionally, they measured impedance of ≈ 59 k Ω at 1 kHz on microelectrodes with dimensions of (80×80) μm^2 .^[12] A well-recognized standard in the field of microelectrode arrays was established by U. Egert et al. in 1998. They used DC magnetron for fabrication of TiN microelectrodes for stimulation and recording from brain slices. The diameter of these microelectrodes was 30 μm , a later widely used commercial standard, and the impedance was in the range from ≈ 80 to ≈ 250 k Ω at 1 kHz.^[13] These results are the basis of the commercial Multichannel Systems (MCS) microelectrode

arrays (MEAs) and will be regarded as a “standard” sample in this paper. The most high-performance system reported to-date, is the “*Neuropixel 2.0*” platform by Steinmetz et al. This device is able to control 10 240 recording sites in one implant. The dimension of one electrode, which has amplitude of impedance of (145 ± 8) k Ω at 1 kHz, is only (12×12) μm^2 .^[14] Any details on how this TiN is obtained are completely missing, presumably for commercial reasons. TiN obtained via ion-beam assisted e-beam evaporation of Ti afforded 30 μm electrodes with ≈ 85 k Ω at 1 kHz.^[15] This study employed silicon nitride as the encapsulation, which proved prone to delaminating during measurements in physiological solution. Such behavior can lead to wrong determination of microelectrode parameters. Due to lack of compositional details of the TiN samples, the direct comparison of properties between publications can be misleading. The preparation of stoichiometric TiN and its electrochemical evaluation in the context of bioelectronics is, to the best of our knowledge, lacking in the literature.

Here, we propose low-temperature method of TiN ion-beam sputter deposition, which can be used to obtain a highly stoichiometric material, with high electrical conductivity and large capacitive charge-injection capacity. Thanks to these properties, we were able to obtain low-impedance, stable, and reproducible MEA. (Figure 1a–e) The deposition technique, we have elaborated, relies on a dual Kaufman ion beam source (IBS) setup. This method involves reactive sputtering of Ti with a higher energy argon and nitrogen ion-beam than magnetron sputtering, and is performed at over two orders-of-magnitude lower deposition pressure, making the deposition process cleaner with lower content of undesirable contaminants such as oxygen. IBS was optimized in the semiconductor industry for high-performance optoelectronic devices, and is rarely used outside of industry and, to the best of our knowledge, has not been deployed for bioelectronic nitride materials.^[16] Using IBS, we achieve stoichiometric nitridation by directing a secondary nitrogen ion beam at the substrate, leading to TiN deposition at low temperature. We detail the favorable conductivity and electrochemical properties of planar TiN samples. To raise the capacitance, we grow the TiN on structured substrates. The most favorable modification, we found, is to prepare a layer of anisotropically etched AlN micropylamids using the same IBS method. This yields perfectly conformal AlN/TiN pyramids. MEAs based on these micropylamids are completed with a robust bilayer of AlN and Parylene-C encapsulation (Figure 1f–l). The end result of our efforts is an electrochemical characterization of high-quality TiN deposited using a low-temperature method, with better performance parameters than an established commercial TiN-based MEA.

2. Results and Discussion

2.1. Material Fabrication and Characterization

The experimental track followed in this paper involved optimizing deposition of TiN using the Kaufman IBS system and characterizing the resulting materials, exploring techniques to increase the geometrical and electrochemical surface area, and perform a series of electrical and electrochemical tests to

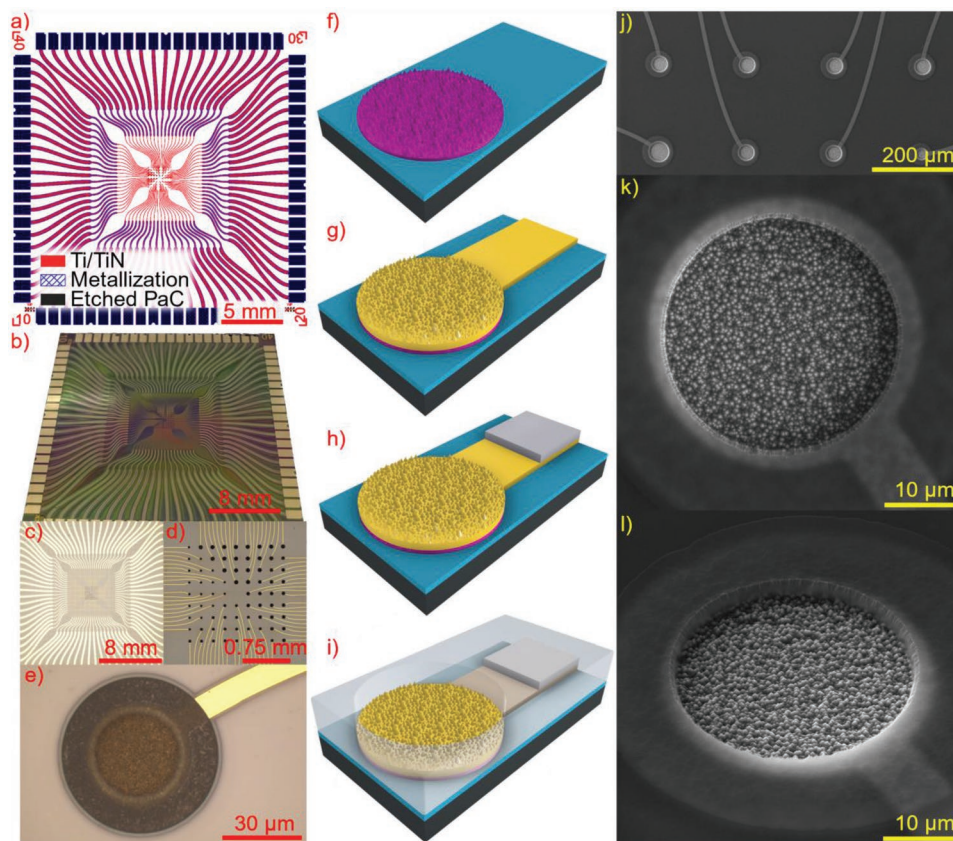


Figure 1. Multi-electrode arrays (MEAs) with AlN/TiN micropylramids. a) Chip layout of multi-electrode arrays, followed by b) macro camera photo of the fabricated chip. c–e) Optical microscopy images of MEAs with increasing magnification. f–i) Schematic of the fabrication process, starting with AlN pyramid formation (f), deposition of Ti/TiN as electrode material (g), metallization covering the paths and pads outside of active area (h), encapsulation with AlN and Parylene-C (i). j–l) Scanning electron microscopy images of several 30 μm electrodes with micropylramids, with zoomed in images from the top (k), and with tilt of 45° (l).

benchmark performance. At all steps of this process, commercial TiN samples from Multichannel Systems GmbH served as a reference standard. We report detailed results for six types of TiN samples. To ensure a controlled comparison, all six samples are prepared on substrates of smooth silicon with thermally-grown $\approx 3 \mu\text{m}$ -thick SiO_2 (root-mean square, R_q , value $< 0.5 \text{ nm}$). The thermal oxide is utilized to minimize any parasitic impedances during measurements. The six samples are chosen to elucidate the effects deposition temperature, and the effect of substrate geometric surface area. Samples where low- or high-temperature type. (no heating = low temperature, LT; versus heating during deposition to 350°, HT). Three surface roughness conditions were tested: flat Si/ SiO_2 , Si/ SiO_2 where the Si was pre-roughened by XeF_2 vapor etching, and finally Si/ SiO_2 with AlN micropylramids. The AlN micropylramids are prepared using tetramethylammonium hydroxide (TMAH) anisotropic etching of a highly oriented (001) AlN thin film. Hence, we describe six types of wafers to compare properties of layers and performance of fabricated devices: The first wafer, second wafer, and third wafer were prepared at low temperature TiN on layers on smooth surface (LT-TiN-smooth), surface roughened by XeF_2 (LT-TiN-rough), and finally structured surface with AlN micropylramids (LT-TiN-pyramids). The next three wafers belonged to the high-temperature group. TiN layers on smooth

(HT-TiN-smooth), XeF_2 roughened (HT-TiN-rough), and AlN micropylramids (HT-TiN-pyramids) surfaces.

In the first stage of our work, we characterized IBS-deposited TiN using X-ray diffraction (XRD), X-ray photoelectron spectroscopy (XPS), atomic force microscopy (AFM), and scanning electron microscopy (SEM) methods to evaluate the materials characteristic properties of LT and HT TiN layers and compare them to MCS TiN. X-ray diffractograms (Figure 2a) show different level of crystallinity between the $\approx 600 \text{ nm}$ -thick MCS TiN and our LT and HT 300 nm-thick TiN samples, even though our samples had half the thickness of the MCS TiN, they possessed a higher degree of crystallinity. We detected 111 and 200 TiN diffractions belonging to (111) and (100) for all samples. Furthermore, for the MCS TiN and HT TiN, also 2nd order 222 diffraction belonging to the (111) plane. The remaining diffraction peaks in the spectra of LT and HT TiN samples originate from the Si (100) substrate and the polycrystalline 300 nm-thick Ti underlayer prepared under the TiN. XPS analysis (Figure 2b) revealed significantly different composition of our layers in comparison to MCS TiN. The MCS TiN contains built-in oxygen between 35 and 40 at%. Our layers possess between 5 and 10 at.% which is in large part caused by ambient XPS instrument chamber oxygen according to the base pressure of $2 \times 10^{-6} \text{ Pa}$. Most significantly, the titanium and nitrogen

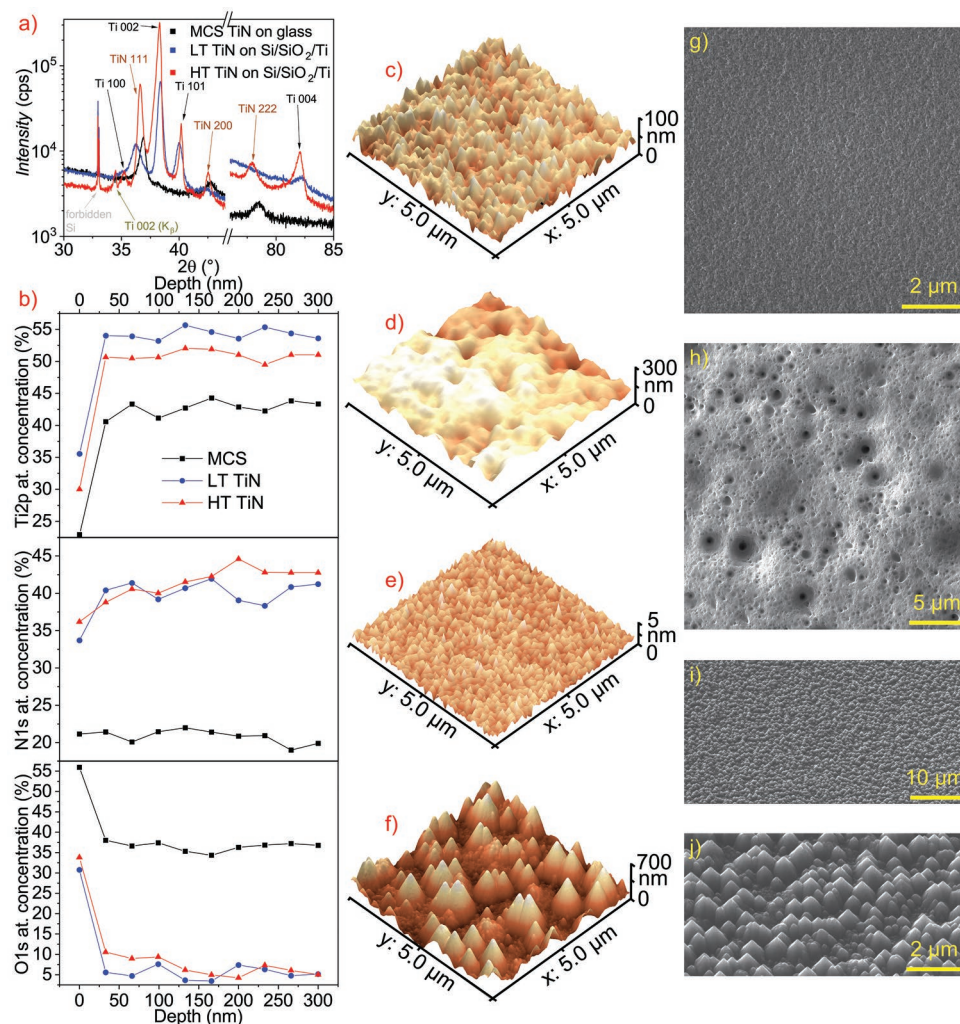


Figure 2. Crystallinity and surface morphology. a) X-ray diffractogram of MCS TiN and LT and HT TiN layers showing the highest order of crystallinity for HT TiN. b) Depth profile obtained from measured X-ray photoelectron spectra show the poor stoichiometry and high content of oxygen in MCS TiN in comparison to highly-stoichiometric LT and HT TiN layers. c,d) AFM measurements show surface roughness of XeF₂ etched Si: c) wafer center and d) edge of the wafer. e,f) The following AFM images show the surface roughness of AlN after deposition (e) and after micro-pyramids fabrication (f) showing the highest roughness of all samples. h,i) The additional SEM images show the surface of rough Si in the center of the wafer (g) and on the edge of the wafer (h). i,j) The tilted SEM images at 45° of micro-pyramids on bulk sample are shown in (i) with detailed caption in (j).

content in our layers is close to stoichiometric TiN, while the commercial sample is in fact oxynitride, with more oxygen content than nitrogen content. This stoichiometry is a remarkable result that apparently reveals a major advantage of the IBS deposition technique.

SEM and AFM were used to characterize sample surface morphology (Figure 2c–j), with the latter technique being used to calculate R_q and surface area, SA . We prepared LT and HT TiN on smooth and rough Si and on micro-pyramids fabricated from AlN. The point of this approach was to increase R_q and SA and test its influence on the electrochemical properties of fabricated microelectrodes in terms of their charge injection capacity and impedance. In the literature, TiN is often described as having high capacitance due to high roughness or porosity but this is rarely quantified and appears to never be measured against a “flat” reference. **Table 1** summarizes the R_q and SA data. Silicon substrate etching with XeF₂ increases roughness

by about two orders of magnitude, but surface area increase is on the order of 1%. It should also be noted that roughness produced by XeF₂ etching has radial inhomogeneity, with the wafer edges being rougher than the center. To contrast with this relatively small increase in R_q and SA , we fabricated AlN micro-pyramids. (Figure 2e–j). Fabrication is based on etching of stoichiometric and highly oriented (001) AlN using a 25% TMAH bath at 10 °C, which is highly anisotropic process and creates pyramids (Figure 2f,j). We also measured the surface of ≈1 μm flat AlN after deposition to show that the layer was perfectly flat before etching in TMAH solution. R_q and SA of AlN-micro-pyramids are significantly higher than flat substrates, with a three orders of magnitude roughness increase and roughly 60% increase in geometric surface area.

The next key parameter to evaluate is electrical conductivity. This has a profound effect on microdevice design, especially with systems with many channels where electrode and

Table 1. Parameters of root-mean square of roughness (R_q) and surface area (SA) from AFM measurements and calculated increase of SA in comparison to flat sample.

Sample type – scanned area (5×5) μm^2	R_q [nm]	SA [μm^2]	SA increase [%]
Flat Si	0.3	25.0	–
Rough Si in the wafer center	13.7	25.1	0.4 %
Rough Si on the wafer edge	52.6	25.6	2.4 %
$\approx 1 \mu\text{m}$ -thick AlN, after deposition	1.1	25.0	–
AlN micropylramids, after etching	152.4	39.7	58.8 %

conductive path geometry should be miniaturized. Using four-probe techniques, we characterized the conductivity of LT and HT TiN fabricated by IBS (Table 2). We measured sheet resistance (R_s) of prepared thin films on 4 inch wafer and calculated the resistivity (ρ) and conductivity (σ). We found that IBS-prepared samples have approximately two orders of magnitude higher conductivity than MCS TiN. Furthermore, we compared ρ and σ to recently published papers and found out that values of our layers are closer to bulk TiN in comparison than to less conductive thin film TiN reported in manuscripts.^[17]

2.2. Electrochemical Characterization

TiN is regarded as a relatively electrochemically passive material and is valued as a capacitive charge-injection electrode for neuromodulation devices. We characterized the electrochemical behavior of our TiN samples using cyclic voltammetry (CV) and electrochemical impedance spectroscopy (EIS), and finally voltage-transient recording during biphasic stimulation pulses. CVs were measured first in a larger range of +0.7 to –0.9 V to characterize the passivity of the electrodes with respect to faradaic reactions (Figure 3a). These scans were performed at three levels of electrolyte oxygenation: 0% O_2 /100% N_2 , 21% O_2 (ambient), and 100% O_2 . This is done in order to determine the magnitude of oxygen reduction currents, since the oxygen reduction reaction is the dominant faradaic process that occurs within the measured voltage range.^[18] CVs of all samples featured an oxygen reduction reaction (ORR) onset around –0.5 V versus Ag/AgCl, however current magnitudes differed significantly based on type of sample. A critical finding was that all TiN samples produced by IBS were clearly less faradaic than the commercial MCS sample, which supported ORR currents roughly an order of magnitude higher than the IBS samples. Next we performed CVs in a smaller passive voltage range

Table 2. Determined electrical parameters of sheet resistance (R_s), resistivity (ρ), and conductivity (σ) of low-temperature (LT) and high temperature (HT) TiN compared to MCS TiN.

Sample	Thickness [nm]	R_s [$\Omega \square^{-1}$]	ρ [Ωm] $\times 10^{-7}$	σ [S m^{-1}] $\times 10^6$
MCS TiN	600	32.35 ± 0.27	194.12	0.05
LT TiN	300	2.38 ± 0.20	7.15	1.40
LT TiN on Ti	(300 + 300)	1.61 ± 0.11	–	–
HT TiN	300	0.78 ± 0.01	2.33	4.28
HT TiN on Ti	(300 + 300)	0.75 ± 0.02	–	–

from –0.2 to +0.3 V in order to calculate double-layer capacitance. Two important conclusions can be drawn from these measurements. The first is that our structured samples of IBS-prepared TiN could exceed the double-layer capacitance values of the porous MCS sample by >50% (Figure 3b). The second conclusion is that results with AlN/TiN were highly reproducible and consistent, while samples prepared using XeF_2 gas treatment (LT-TiN-smooth, LT-TiN-rough, HT-TiN-smooth, and HT-TiN-rough) showed poor reproducibility and homogeneity. A calculated value of areal capacitance should be independent of the sample size. We found that calculating capacitance using different sized sampling area of XeF_2 samples could yield results varying over an order of magnitude. This clearly signals that the surface area is not uniform across the wafer and is consistent with the SEM and AFM findings shown in Figure 2c,d,g,h. From CV measurements, we can confirm that IBS-prepared TiN is relatively passive and is less ORR-active than MCS TiN. The AlN/TiN micropylramid samples emerge as the most competitive in terms of low faradaicity and high double-layer capacitance.

Double-layer capacitance is obtained in a small voltage scanning window where no faradaic reactions take place. Most commonly in the field of neurostimulation electrodes, the value of charge storage capacity (CSC) is used instead. The CSC is loosely defined as being the cathodic charge that can be supplied by the electrode within the voltage window of water electrolysis. Using this definition, we extract CSC from the voltage range –0.9 to +0.7 V. Results are given in Table 3. Since ORR takes place within this voltage window, we report CSC values at three different oxygen levels (0%; 21% (ambient), and 100%) for all the samples.^[6] This allows one to see the cathodic charge injection contribution from ORR.

2.3. Multielectrode Arrays with TiN Microelectrodes

As the main application of TiN in bioelectronics is in the form of MEAs, we next moved on to evaluate the performance of IBS-prepared TiN in MEAs, as shown in Figure 1, with 30 μm diameter electrodes. As a passivation/insulation layer on the MEA, we used a bilayer of AlN/Parylene-C. Parylene-C is a well-established low-dielectric constant insulator with good bioinertness and stability.^[19] However, we found that using Parylene-C alone as a passivation results in a specific problem for TiN electrodes: Parylene-C is lithographically patterned by reactive ion etching in oxygen-containing plasma. This plasma will inevitably also react with the surface of the underlying TiN electrode. We found that this apparent plasma-induced modification of the TiN surface irreversibly lowers capacitance/increases impedance, therefore we introduced a work-around procedure involving a capping layer of AlN below the Parylene-C. The AlN protects the TiN surface from the plasma, and can then be removed by wet etching in TMAH, which in turn does not adversely affect the TiN surface. We found that TiN microelectrode MEAs with this type of passivation performed reliably and reproducibly, and we prepared MEAs with all six types of TiN surfaces to compare their impedance and stability with respect to chemical/thermal stress and biphasic current pulsing. The electrochemical impedance values are summarized

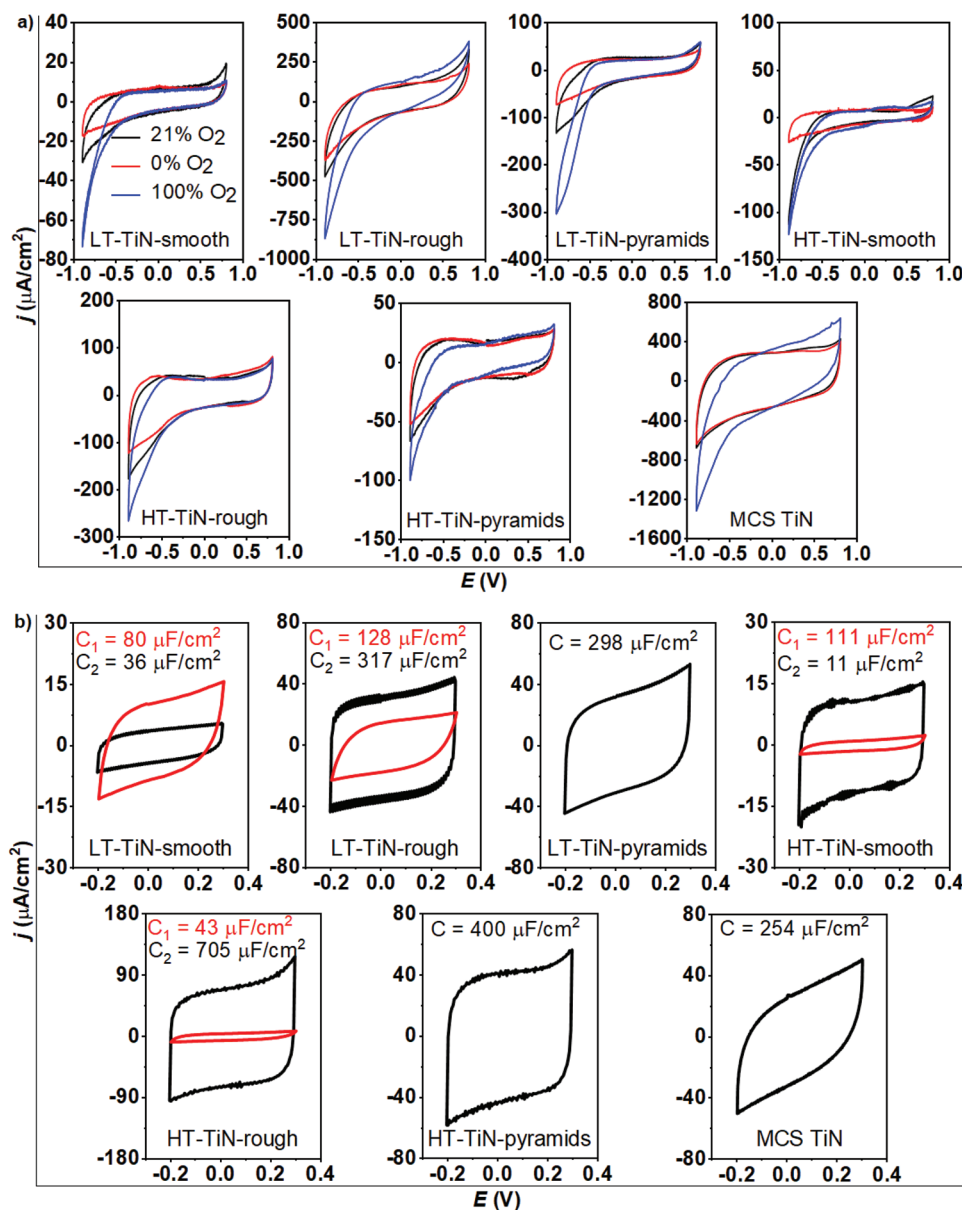


Figure 3. Electrochemical characterization by cyclic voltammetry (CV). a) CVs recorded in 0.1 M KCl solution showing the electrochemical window of bulk TiN samples on different substrates measured in air (21% O₂), in deoxygenated atmosphere (0% O₂), and in oxygenated atmosphere (100% O₂), versus the MSC TiN sample for comparison. The y-axis of each single voltammogram is reported with a different scale due to the different current density delivered by each single sample, due to the apparent different faradaicity. The scan rate used for this analysis is 0.05 V s⁻¹ and the range of potential used goes from -0.9 to +0.7 V. b) Capacitive double layer determination via cyclic voltammetry of bulk TiN samples using as scan rate a value of 0.1 V s⁻¹ and a smaller, passive, voltage range.

in Table 4 and Figure 4c and impedance and phase are plotted separately in Figure 4a,b. All samples featured “control” microelectrodes where the AlN/Parylene-C passivation was not removed. Such electrodes allow measurement of the parasitic impedance and can be used to verify the quality of the passivation layer during ageing/stressing studies. These control pixels in all cases retain at least an order of magnitude higher impedance than exposed microelectrodes. The impedance values of IBS TiN “planar” samples LT-TiN-smooth and HT-TiN-smooth did not compare impressively with the commercial MCS sample, having higher impedance. However, the porosity of

the MCS TiN is well known, and this is not surprising when considering the calculated double-layer capacitance values from Figure 3b that the impedance of the MCS samples will be lower. The AlN micropyramid samples, in turn, has lower impedances than the MCS MEA. The AlN/TiN micropyramid samples, both low and high temperature, emerged as the best performers. It is immediately possible to see in both Figure 4a,c how the use of AlN-based micropyramids not only can drastically decrease the value of $|Z|$ comparing with MCS TiN or the XeF₂ roughened samples, but also leads to more reproducible values. The standard deviation in impedance

Table 3. Charge storage capacity (CSC) calculated in the voltage range from -0.9 to $+0.7$ V, measured for oxygenated, ambient, and fully deoxygenated conditions.

Sample type	0% O ₂ [$\mu\text{C cm}^{-2}$]	21% O ₂ [$\mu\text{C cm}^{-2}$]	100% O ₂ [$\mu\text{C cm}^{-2}$]
LT-TiN-smooth	181	222	156
LT-TiN-rough	2937	3023	3420
LT-TiN-pyramids	757	959	953
HT-TiN-smooth	241	206	289
HT-TiN-rough	1319	1482	1581
HT-TiN-pyramids	565	615	476
MCS TiN	8,825	8889	9858

values is the smallest for the AlN micropyramid samples LT-TiN-pyramids and HT-TiN-pyramids.

MEAs were next characterized with respect to stability. Samples were subjected to two types of tests: accelerated aging test in phosphate buffered saline (PBS) + H₂O₂ 30×10^{-3} M at 60 °C for 5 days; and biphasic cathodic-leading pulse cycling (1 million pulses at a charge density of 200 $\mu\text{C cm}^{-2}$ phase⁻¹). The first aspect to underline based on voltage transient data is that such a charge density is just within the water window, with cathodic voltage excursions not exceeding -0.7 V versus Ag/AgCl. Sample performance was monitored by registered electrochemical impedance before and after stressing, as well as registering voltage transients during biphasic pulsing. For the best performing microelectrode types, namely the low-impedance LT-TiN-pyramids and HT-TiN-pyramids AlN/TiN micropyramid samples, an additional 6 h of accelerated chemical aging were added after as well. We found that all types of MEA samples survive chemical and biphasic pulsing stress without any failures. Indeed, the impedance of the samples decreases after aging. This could indicate a degradation of the passivation/encapsulation layer, leading to a decrease in parasitic impedance and thus a lower overall measured impedance value. However, the values of $|Z|$ for the closed pixels after the stress remained unchanged (4–5 M Ω). This shows that the passivation is not degrading, and that the decrease in impedance is caused by a favorable change in the surface of the TiN electrodes. We hypothesize that this could originate from a partial oxidation of the TiN surface leading to a stable and lower-impedance oxynitride species,

however we have not explored a definitive mechanism except to conclude that the favorable drop in impedance appears irreversible (Figure 5). It is possible to appreciate that the voltage transient trace retains its own starting value and for sake of stability investigation, $|Z|$ values have been recorded for all the electrodes tested showing that in the case of LT-TiN-pyramids and MCS TiN the electrical stress leads to a slight drop in impedance differently than for HT-TiN-pyramids where the impedance value is retained. Further, LT-TiN-pyramids and HT-TiN-pyramids have been additionally stressed after biphasic pulses with an accelerated chemical aging test soaking them in a solution mixture of PBS/H₂O₂ for 6 h in an oven at 60 °C. The result reported in Figure 6 shows an unchanged value of $|Z|$ for LT-TiN-pyramids but a slight decrease in $|Z|$ for HT-TiN-pyramids reaching a saturation-like regime around ≈ 116 k Ω . The values of $|Z|$ for LT-TiN-pyramids and HT-TiN-pyramids are always lower than MCS TiN, before and after all treatment conditions and measurements. To furthermore enhance the concept of stability and reproducibility of LT-TiN-pyramids and HT-TiN-pyramids in terms of reliable materials for MEAs fabrication, we decided to carry out another run of electrical stress test conducting additional 1 million cycles of biphasic pulses to the devices previously stressed and is possible to appreciate that the $|Z|$ value is retained even after the second stress as reported in Table 4.

3. Conclusion

We have presented the utilization of micromachining techniques accompanied with unconventional ion-beam sputtering using two Kaufman ion-beam sources for preparation of TiN with highly favorable properties for bioelectronics applications. We compared low and high-temperature prepared TiN to commercially available TiN by MCS and found that our TiN is highly 1:1 stoichiometric with $\approx 5\times$ lower content of oxygen than the commercial sample, and is also more crystalline than the commercial one. It should be noted that the commercial sample is better described as TiON rather than TiN. While electrodes labeled as “TiN” are frequently used in bioelectronics and electrophysiology applications, the amount of detail about the identity of the actual material is very low in most of the literature. It is probably that the magnetron reactive sputtering used for preparation of most reported TiN samples leads to electrodes

Table 4. Absolute value of impedance ($|Z|$), at 1 kHz reported for microelectrode arrays (MEAs), before and after electrical and electrochemical stress tests conducted to test the stability over time.

Sample type	$ Z $ at 1 kHz after MEAs fabrication [k Ω]	$ Z $ after PBS/H ₂ O ₂ [k Ω]	$ Z $ after 1×10^6 biphasic pulses [k Ω]	$ Z $ subsequent PBS/H ₂ O ₂ after pulses [k Ω]	$ Z $ after 2×10^6 biphasic pulses [k Ω]
Control	4,660 \pm 800	4540 \pm 540	–	4700 \pm 800	4600 \pm 700
LT-TiN-smooth	1,060 \pm 370	–	–	–	–
LT-TiN-rough	490 \pm 20	–	–	–	–
LT-TiN-pyramids	230 \pm 40	140 \pm 10	150 \pm 50	130 \pm 30	120 \pm 20
HT-TiN-smooth	780 \pm 70	–	–	–	–
HT-TiN-rough	1,120 \pm 310	–	–	–	–
HT-TiN-pyramids	190 \pm 10	110 \pm 10	180 \pm 20	120 \pm 20	110 \pm 20
MCS TiN	480 \pm 60	–	300 \pm 30	–	–

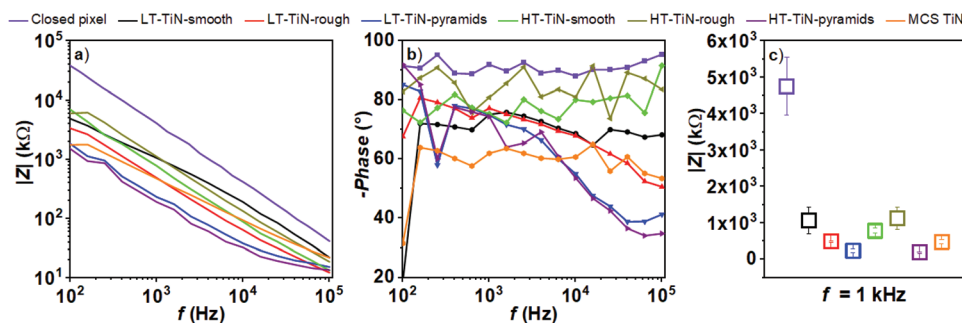


Figure 4. a) Impedance and b) phase measurements of TiN microelectrode arrays with 30 μm diameter electrodes of MEAs fabricated with the six different types of TiN, and the MCS TiN reference. “Control” refers to a measurement of a 30 μm diameter electrode without the AlN/Parylene-C passivation layer removed, thereby giving the value of parasitic parallel impedance. All traces are the average of 16 different microelectrodes. c) The value of the absolute impedance ($|Z|$) at 1 kHz for the MEA samples ($n = 16$, mean value \pm standard deviation).

with inferior properties than what can be achieved with more crystalline and more stoichiometric TiN. The first obvious advantage is that TiN prepared by IBS has significantly higher conductivity, by at least an order of magnitude. This is a major advantage that makes device layout design easier, as the necessity of extra interconnect layers to compensate for low conductivity of “TiN” disappears and one can rely in stoichiometric TiN as a good conductor. Electrochemically, TiN from IBS appears to be more inert than commercial TiN, with lower faradaic currents for the dominant oxygen reduction reaction. However, layers produced by IBS were ultra-smooth, which results in low areal capacitance compared with commercial TiN which is relatively porous. To compensate for this, we sought to prepare the high-quality TiN on an underlying layer with high surface area. Silicon roughened by XeF_2 vapors appeared as an easy solution;

however, while sometimes leading to impressive performance increases, this method was not homogenous and did not lead to high reproducibility. Finally, we found that fabricating micropyrramids from highly oriented (001) AlN led to a profound performance increase as well as excellent reproducibility and low electrode-to-electrode variability. Moreover, the AlN is produced using an analogous IBS process to that which yields TiN. The resulting samples of TiN, regardless of underlayer, proved to be electrochemically and chemically stable. MEAs fabricated with microelectrodes of 30 μm diameter proved to have not only excellent stability and low standard error, but also outcompeted the established commercial MEAs in terms of impedance by a factor of 4. Our results showcase the promise of high-performance thin film nitrides for bioelectronics, and draw attention to the fact that focusing on the intrinsic materials properties

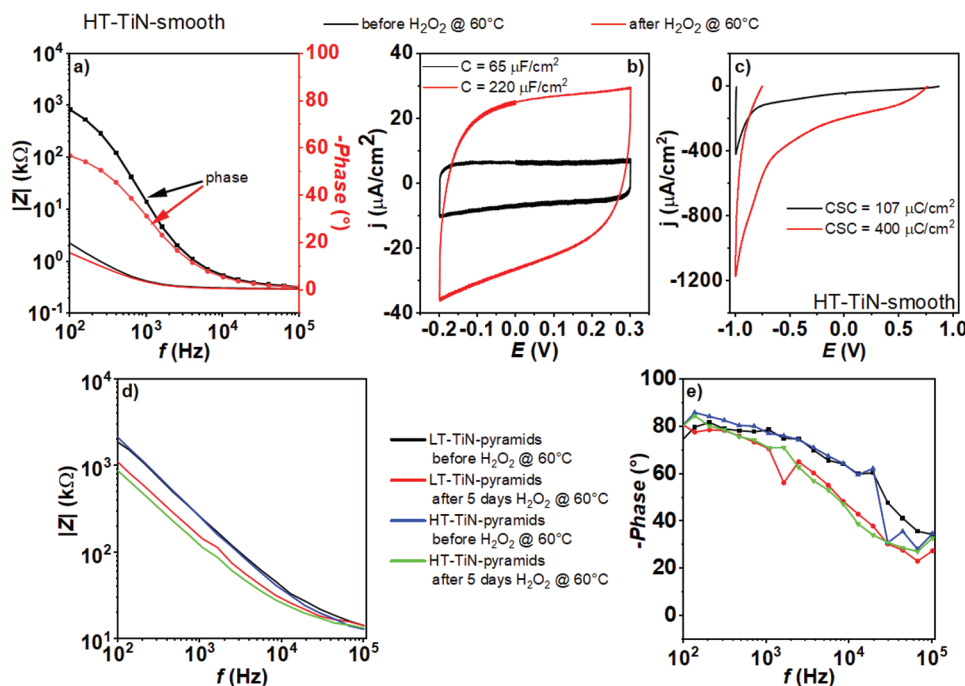


Figure 5. a–c) Illustrative example of the influence of H_2O_2 accelerated chemical treatment over: a) impedance ($|Z|$), b) capacitance (C), and c) charge storage capacity (CSC) for high temperature TiN on smooth surface sample (HT-TiN-smooth). d) Impedance and e) phase monitoring before and after chemically accelerated oxidative aging stress. The stress condition was $30 \times 10^{-3} \text{ M}$ H_2O_2 in PBS solution at 60°C .

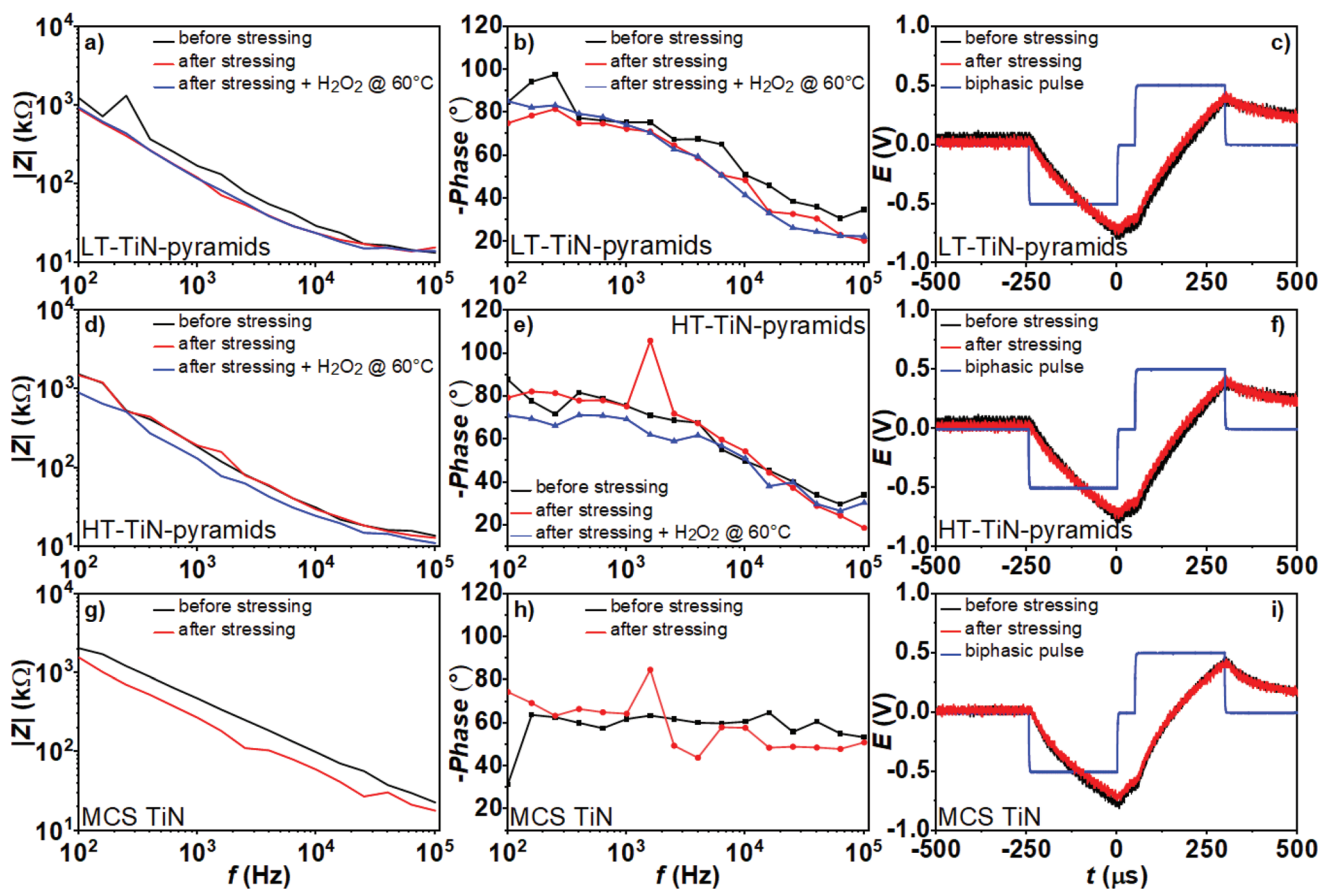


Figure 6. a,d,g) The impedance and b,e,h) phase were recorded before and after the pulsing stress test and for LT-TiN-pyramids and HT-TiN-pyramids a subsequent chemical accelerated aging test was carried out. The stress condition was 30×10^{-3} M H_2O_2 in PBS solution, $T = 60^\circ\text{C}$. c,f,i) Cathodic-leading biphasic pulse stress test on microelectrodes using a charge density of $200 \mu\text{C cm}^{-2} \text{ phase}^{-1}$.

and stoichiometry/crystallinity can lead to better outcome. Our findings recommend the IBS method as an advantageous technique to the bioelectronics community.

4. Experimental Section

Si Substrate Roughening: XeF_2 was used for preparation of roughened substrates, as it is used for isotropic etching of silicon with high specificity versus other materials. This process is well known from the field of microelectromechanical systems fabrication. The etching process was performed in a custom-built instrument according to the following parameters: Chamber and gas cylinder were self-heated due to dissipated heat power from oil pump to steady state temperature of $\approx 34^\circ\text{C}$. Subsequently, 50 etching cycles were performed at XeF_2 pressure of ≈ 666 Pa. Every etching step consisted of chamber pumping below 13 Pa and then filling during 20 s with XeF_2 to the set pressure. When the pressure was reached, the countdown of 60 s was started. Then the whole process was repeated, with etching being controlled by the number of fill-purge cycles.

AlN Micropyramids Fabrication: Anisotropic AlN wet etching was utilized in tetramethylammonium hydroxide, TMAH.^[9] This effect is stronger when the AlN film has a high degree of (001) orientation, and the TMAH is cold. A 25% TMAH bath was used at 10°C for etching of $1 \mu\text{m}$ -thick AlN with excellent (001) orientation on 80 nm of Ti (001) prepared using dual Kaufman ion-beam source setup according to the published procedures.^[20]

Ion-Beam Sputtering (IBS): A deposition tool containing dual Kaufman IBS sources from Kaufman & Robinson (KRI) was used for deposition of all thin films. The base pressure is $< 5 \times 10^{-7}$ Pa and is connected to Ar and N_2 lines with gas purity of 99.99999%, allowing preparation of high-quality layers with extremely low oxygen contamination. Additionally, space charge neutralization was provided by a LFN2000 electron source by KRI with the electron current emission set to equal the total ion current emissions from both sources. At first, a pre-cleaning procedure of the substrate via bombardment was done with Ar^+ ions from the secondary (2nd) radio-frequency inductive coupled plasma (RFICP) Kaufman IBS with 40 mm in diameter 2-grid μ -dished collimated ion optics. Pre-cleaning parameters were set for beam energy (BE) 36 eV as follows: ion-beam voltage (BV) 30 V, acceleration voltage (AV) 6 V, ion-beam current (BC) 10 mA for 300 s. Then the primary (1st) IBS was used for deposition of 300 nm of Ti on pre-cleaned substrates from target with purity of 99.995% at set parameters of BV 600 V and BC 44 mA (Table 5). The primary RFICP Kaufman IBS is equipped with 3-grid dished focused optics with 40 mm diameter and 45° ellipse pattern allowing more precise control of beam optics and energy than a 2-grid version. Finally, reactive sputtering of 300 nm-thick TiN with deposition rate of $\approx 0.018 \text{ nm s}^{-1}$ was performed using both primary and secondary IBSs at deposition pressure of 5×10^{-2} Pa. Parameters were set according to the previous experience with preparation of AlN. In the case of low-temperature TiN (deposition of LT-TiN-smooth, HT-TiN-smooth and LT-TiN-pyramids), the substrate temperature rose to a peak of 110°C due to heating caused by deposited material and N_2 ions bombardment from secondary IBS. This temperature is considered as maximal for continuous deposition without breaks and/or additional heating in this

Table 5. Optimized deposition parameters for both ion-beam sources for TiN reactive sputtering. (IBS = ion-beam source, BV = ion-beam voltage, BC = ion-beam current, AV = acceleration voltage and BE = ion-beam energy).

IBS	BV [V]	BC [mA]	AV [V]	BE [eV]	Ar flow [sccm]	N ₂ flow [sccm]
1st	600	44	600	600	3.5	3.0
2nd	20	10	5	25	0	15.0

instrument. The high-temperature TiN (deposition of HT-TiN-smooth, HT-TiN-rough and HT-TiN-pyramids) was deposited at temperature of ≈ 350 °C, which was caused by the above-mentioned heating effect and additional heat was produced by non-contact radiation heater placed above the substrate-stage.

Thicknesses of all deposited layers were controlled by quartz crystal microbalance connected to deposition control card Inficon SQM-242. Furthermore, thickness was verified using a scanning profilometer (Bruker Dektak) on fabricated structures after etching during MEAs fabrication.

Chip Design and Fabrication of Microelectrode Arrays: MEAs were designed to be able to determine electrochemical properties of microelectrodes, 30 μm diameter. The chip size was (21.2×21.2) mm², which allowed use of a customized 3D-printed polycarbonate (PC) cell with a 1.3 mm diameter. The cell contains an Ag/AgCl reference, and a Pt wire coil as counter electrode, and inlet and outlet for gas purging. This cell was used for electrochemical measurements of microelectrodes as well as bulk samples for the determination of the double layer capacitance of each sample. Poly(dimethylsiloxane) (PDMS) has been used to guarantee the adhesion of the PC cell to the surface of the microelectrode array chips for CV measurements as well as EIS analyses. In the case of bulk samples, an additional tape mask was implemented using 70 μm -thick poly(vinyl chloride) foil (Minitronic elektronik GmbH). The circular opening in the foil had a diameter of 3 mm, defining the electrode under test area (active electrode area 7.07×10^6 μm^2). Furthermore, the pads for electrical connection have dimensions of $(700 \times 1,200)$ μm^2 for comfortable connection with microtips without necessity of any magnifying optics. Additionally, thick Ti/Al/Ti metallization was added on the pathways between pads and microelectrodes to this process flow to minimize serial resistance. In the next step, the combination of AlN and Parylene-C was chosen as the encapsulation layer, which completely covered the whole chips except the microelectrodes and pads for electrical connections. The AlN serves as chemically-resistive and etch-stop layer when the Parylene-C is etched. This is due to this observation that when TiN is bombarded by oxygen plasma ions, double layer capacitance significantly decreases. Photos of the fabricated device are shown in Figure 1b–e.

The substrates were prepared as described at the beginning of this section, creating the AlN pyramids (Figure 1f), or by roughening the Si surface. When the last deposition of TiN for bulk characterization was done the fabrication of MEAs was started. The first step was spin-coating of positive photoresist (PR) AZ 1518 with thickness of 1.8 μm , which was used for patterning of Ti/TiN conductive pathways and microelectrodes. Then this double layer was etched using reactive ion etching instrument (RIE) with Cl-based plasma (Figure 1g). The PR was then removed using dimethylsulfoxide (DMSO) at 80 °C for 5 min. Furthermore, the metallization of conductive pathways was done through a lift-off process via negative PR AZ nLOF 2070 with thickness of 5 μm . The pre-cleaning and deposition processes were done in the sputtering tool. At first, the pre-cleaning procedure was done using 2nd IBS with the same parameters as were used before the first deposition of Ti. This metallization (Figure 1h) consists of three layers: the first was an adhesive 20 nm-thick Ti layer, the second was a more conductive 500 nm-thick Al layer, and the last one was 150 nm-thick Ti layer, which served as protection for Al, since the TMAH was used in one of the following fabrication steps. The PR was then removed using DMSO at 80 °C for few hours until all residues from PR with deposited metals were

removed. These steps were followed by a deposition of 100 nm-thick AlN using both 1st and 2nd IBSs followed by CVD deposition of 2.5 μm -thick Parylene-C layer. This layer was patterned with the same PR as in the first step but with thickness of ≈ 4 μm . Then the RIE with O₂ plasma was used to completely etch the Parylene-C to reach the underlying AlN, which is resistant to O₂ plasma, thus, the process is well controllable, and Parylene-C can be over etched for several minutes to be sure that there are no residues. Then PR in DMSO was removed at ≈ 80 °C for ≈ 5 min and the AlN in TMAH solution was etched for ≈ 1 min at 30 °C (Figure 1). Finally, the wafer was covered with the same PR as in the first step to prevent surface from impurities during cutting at dicing-saw instrument. Before further characterization, SEM images were taken (Figure 1j–l).

Atomic Force Microscopy: Dimension ICON by Bruker was used to determine the surface topography of prepared samples after substrate roughening or micropylamids preparation and also after completed fabrication of devices. The AFM characterization was focused on the investigation of R_q and of total surface area (SA). Thus Tapping mode was chosen with suitable probe RTESPA-525 with 8 nm tip radius and spring constant of ≈ 200 N m⁻¹.

Scanning Electron Microscopy: A Lyra3 XMH instrument by Tescan was employed for surface imaging of layers and microelectrodes after the fabrication. A secondary electron detector was used, with a working distance of 9 mm, while the acceleration voltage was ranging from 10 to 30 kV to obtain good contrast and high-resolution pictures.

X-ray Photoelectron Spectroscopy: XPS was performed using Axis Supra by Kratos to determine the stoichiometry of TiN and estimate the oxygen content. A surface scan was done followed by several scans after sputtering to obtain depth profile. For sputtering, Ar⁺ cluster mode was used with energy of 5 keV.

X-ray Diffraction: Prepared samples were characterized via Bragg–Brentano XRD after the TiN was deposited. 2θ measurements were taken using 3 kW Rigaku SmartLab system equipped with a Cu X-ray tube and linear D/teX Ultra detector. This method was used for determination of presented diffractions belonging to the planes parallel to the sample surface and additionally for the calculation of corresponding lattice parameters. The scanning speed was 3°min⁻¹ and the measurement of 2θ range was set from 20° to 90° while the region between 56° and 68° was omitted due to strong 4th order diffraction of Si (100) to avoid detector damage. The commercial TiN sample on glass substrate was measured in the whole range, but no significant peak was detected in the mentioned interval.

Four-Probe Electrical Characterization: Custom made box equipped with head containing 4 probes arranged in line with 1 mm spacing in combination with parameter analyzer Keithley 4200A-SCS was used. Standard method was employed when outer probes were determined for current bias, while the inner probes measured voltage difference. The optimal measuring current of 30 mA was experimentally determined for all samples according to current sweeping in range from 0 to 100 mA with step of 5 mA. Five measurements were done on each sample on different place to obtain data for calculation of mean value and standard deviation.

Electrochemistry: All measurements were done using a potentiostat (PocketSTAT2, Ivium Technologies) in a three-electrode configuration setup in manual range mode. Capacitance was estimated using a 100 mM KCl electrolyte and E_{step} of 0.001 V using a True Linear scan mode.^[21] CV measurements for establishing the water window and estimating capacitance were done on “bulk” samples with an active area of 7 mm². Furthermore, from wide range cyclic voltammograms, it was possible to extrapolate the value of charge storage capacity obtained from the time integral of the cathodic current within the water electrochemical passive window, for the three different conditions of O₂ content in the electrolyte (0% O₂, 21% O₂ (ambient), and 100% O₂). Electrochemical impedance spectroscopy was measured for microelectrodes in the range from 100 kHz to 10 Hz by applying sinusoidal signal with amplitude of 0.01 V RMS at a bias of 0 V versus Ag/AgCl.

Alternating Current Pulses: The biphasic pulse applied corresponds to a charge density of 200 $\mu\text{C cm}^{-2}$ phase⁻¹ with a cathodic-leading

square waveform 250 μ s cathodic/50 μ s interpulse time/250 μ s anodic; repeated at a frequency of 10 Hz. Pulses were delivered using a Digitimer DS4 biphasic current stimulus isolator and USB oscilloscope PicoScope 3404D with built-in AC waveform generator by Pico Technology. Transient voltage was recorded during current pulsing test using the oscilloscope input channel with input impedance of 1 M Ω , versus a reference electrode Ag/AgCl. All samples were prepared on one-side polished p-type Si (100) wafer substrates of 100 mm diameter and \approx 525 μ m thickness.

Acknowledgements

This work was supported by funding from the European Research Council (ERC) under the European Union's Horizon 2020 research and innovation program (E.D.G. grant agreement no. 949191), and a contribution from the city council of Brno, Czech Republic. The work was also supported by the Grant Agency of the Czech Republic under contract 20-30129Y. Sample fabrication was supported by CzechNanoLab Research Infrastructure financed by MEYS CR (LM2018110). J.B. acknowledges support through the Brno Ph.D. Talent Scholarship funded by the Brno City Municipality.

Conflict of Interest

The authors declare no conflict of interest.

Data Availability Statement

The data that support the findings of this study are available from the corresponding author upon reasonable request.

Keywords

bioelectronics, ion-beam sputtering, multielectrode arrays, titanium nitride

Received: August 26, 2022

Revised: November 22, 2022

Published online: February 2, 2023

- [1] P. Jastrzebska-Perfect, S. Chowdhury, G. D. Spyropoulos, Z. Zhao, C. Cea, J. N. Gelinias, D. Khodagholy, *Adv. Funct. Mater.* **2020**, *30*, 1909165.
 [2] E. S. Krames, A. R. Rezai, P. H. Peckham, in *Neuromodulation*, 2nd ed., (Eds: E. S. Krames, P. H. Peckham, A. R. Rezai), Academic Press, Cambridge, MA, USA **2018**.
 [3] a) S. M. Won, L. Cai, P. Gutruf, J. A. Rogers, *Nat. Biomed. Eng.* **2021**, <https://doi.org/10.1038/s41551-021-00683-3>; b) J. Shi, Y. Fang, *Adv. Mater.* **2019**, *31*, 1804895.

- [4] B. Thielen, E. Meng, *J. Neural Eng.* **2021**, *18*, 041003.
 [5] C. Boehler, S. Carli, L. Fadiga, T. Stieglitz, M. Asplund, *Nat. Protoc.* **2020**, *15*, 3557.
 [6] S. F. Cogan, *Ann. Rev. Biomed. Eng.* **2008**, *10*, 275.
 [7] N. P. Aryan, H. Kaim, A. Rothermel, *Stimulation and Recording Electrodes for Neural Prostheses*, Vol. 1, Springer, Heidelberg, Germany **2015**.
 [8] J. J. Jun, N. A. Steinmetz, J. H. Siegle, D. J. Denman, M. Bauza, B. Barbarits, A. K. Lee, C. A. Anastassiou, A. Andrei, Ç. Aydin, M. Barbic, T. J. Blanche, V. Bonin, J. Couto, B. Dutta, S. L. Gratiy, D. A. Gutnisky, M. Häusser, B. Karsh, P. Ledochowitsch, C. M. Lopez, C. Mitelut, S. Musa, M. Okun, M. Pachitariu, J. Putzeys, P. D. Rich, C. Rossant, W. L. Sun, K. Svoboda, et al., *Nature* **2017**, *551*, 232.
 [9] S. M. Tanner, V. V. Felmetzger, in *2009 IEEE Int. Ultrasonics Symp.*, IEEE, Piscataway, NJ, USA **2009**, pp. 1691–1694.
 [10] J. Su, R. Boichot, E. Blanquet, F. Mercier, M. Pons, *CrystEngComm* **2019**, *21*, 3974.
 [11] M. A. González-González, A. Kanneganti, A. Joshi-Imre, A. G. Hernandez-Reynoso, G. Bendale, R. Modi, M. Ecker, A. Khurram, S. F. Cogan, W. E. Voit, M. I. Romero-Ortega, *Sci. Rep.* **2018**, *8*, 16390.
 [12] F. Rodrigues, J. F. Ribeiro, P. A. Anacleto, A. Fouchard, O. David, P. M. Sarro, P. M. Mendes, *J. Neural Eng.* **2019**, *17*, 016010.
 [13] U. Egert, B. Schlosshauer, S. Fennrich, W. Nisch, M. Fejtl, T. Knott, T. Müller, H. Hämmerle, *Brain Res. Brain Res. Prot.* **1998**, *2*, 229.
 [14] N. A. Steinmetz, C. Aydin, A. Lebedeva, M. Okun, M. Pachitariu, M. Bauza, M. Beau, J. Bhagat, C. Böhm, M. Broux, S. Chen, J. Colonell, R. J. Gardner, B. Karsh, F. Kloosterman, D. Kostadinov, C. Mora-Lopez, J. O'Callaghan, J. Park, J. Putzeys, B. Sauerbrei, R. J. J. v. Daal, A. Z. Vollan, S. Wang, M. Welkenhuysen, Z. Ye, J. T. Dudman, B. Dutta, A. W. Hantman, K. D. Harris, et al., *Science* **2021**, *372*, eabf4588.
 [15] T. Rynänen, M. Toivanen, T. Salminen, L. Ylä-Outinen, S. Narkilahti, J. Leikkala, *Front Neurosci.* **2018**, *13*, 882.
 [16] P. Sharma, Aaryashree, V. G. , S. Mukherjee, *J. Appl. Phys.* **2017**, *121*, 225306.
 [17] a) A. Kavitha, R. Kannan, P. Sreedhara Reddy, S. Rajashabala, *J. Mater. Sci.: Mater. Electron.* **2016**, *27*, 10427; b) M. A. Jithin, K. L. Ganpathi, G. N. V. R. Vikram, N. K. Udayashankar, S. Mohan, *Sens. Actuators, A* **2018**, *272*, 199; c) H. Liang, J. Xu, D. Zhou, X. Sun, S. Chu, Y. Bai, *Ceram. Int.* **2016**, *42*, 2642.
 [18] J. Ehlich, L. Migliaccio, I. Sahalianov, M. Nikic, J. Brodsky, I. Gablech, X. T. Vu, S. Ingebrandt, E. D. Glowacki, *J. Neural Eng.* **2022**, *19*, 036045.
 [19] C. Hassler, T. Boretius, T. Stieglitz, *J. Polym. Sci., Part B: Polym. Phys.* **2011**, *49*, 18.
 [20] a) I. Gablech, V. Svatoš, O. Caha, A. Dubroka, J. Pekárek, J. Klempa, P. Neužil, M. Schneider, T. Šíkola, *Thin Solid Films* **2019**, *670*, 105; b) I. Gablech, O. Caha, V. Svatoš, J. Pekárek, P. Neužil, T. Šíkola, *Thin Solid Films* **2017**, *638*, 57.
 [21] A. Weltin, J. Kieninger, *J. Neural Eng.* **2021**, *18*, 052001.

Downsizing the Channel Length of Vertical Organic Electrochemical Transistors

Jan Brodský, Imrich Gablech, Ludovico Migliaccio, Marek Havlíček, Mary J. Donahue, and Eric D. Glówacki*



Cite This: *ACS Appl. Mater. Interfaces* 2023, 15, 27002–27009



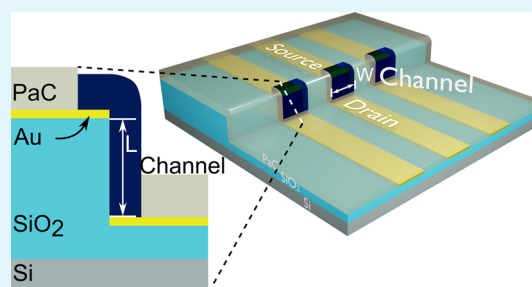
Read Online

ACCESS |

Metrics & More

Article Recommendations

ABSTRACT: Organic electrochemical transistors (OECTs) are promising building blocks for bioelectronic devices such as sensors and neural interfaces. While the majority of OECTs use simple planar geometry, there is interest in exploring how these devices operate with much shorter channels on the submicron scale. Here, we show a practical route toward the minimization of the channel length of the transistor using traditional photolithography, enabling large-scale utilization. We describe the fabrication of such transistors using two types of conducting polymers. First, commercial solution-processed poly(dioxyethylenethiophene):poly(styrene sulfonate), PEDOT:PSS. Next, we also exploit the short channel length to support easy in situ electropolymerization of poly(dioxyethylenethiophene):tetrabutyl ammonium hexafluorophosphate, PEDOT:PF₆. Both variants show different promising features, leading the way in terms of transconductance (g_m), with the measured peak g_m up to 68 mS for relatively thin (280 nm) channel layers on devices with the channel length of 350 nm and with widths of 50, 100, and 200 μm . This result suggests that the use of electropolymerized semiconductors, which can be easily customized, is viable with vertical geometry, as uniform and thin layers can be created. Spin-coated PEDOT:PSS lags behind with the lower values of g_m ; however, it excels in terms of the speed of the device and also has a comparably lower off current (300 nA), leading to unusually high on/off ratio, with values up to 8.6×10^4 . Our approach to vertical gap devices is simple, scalable, and can be extended to other applications where small electrochemical channels are desired.



KEYWORDS: vertical organic electrochemical transistor, microfabrication, PEDOT, electrochemical polymerization

1. INTRODUCTION

Transistors are an essential component of modern electronics and have revolutionized the way in which we interact with technology. Although great advancements have been made in transistor technologies, further improvements in power consumption, device size, and overall performance are continuously sought. This is particularly true for relatively younger organic transistors when compared to their traditional inorganic counterparts. Organic transistors have gained attention as a promising technology for the development of low-cost, flexible, and large-area electronic devices.^{1–3} A subgroup of organic transistors, the organic electrochemical transistor (OECT), has emerged with particularly suitable characteristics for bioelectronic applications such as biosensors and biopotential recordings.^{4–6} OECTs are advantageous in bio-interfacing applications due to the mixed ionic/electronic conduction of their channel materials.^{7–10} This mixed conduction is ideal for ion-to-electron transduction, allowing for highly attainable amplification compared to inorganic or organic field effect transistors, providing quality biopotential recordings and good acquisition of small biosensor signals.^{11–13} Although applications such as these have benefited

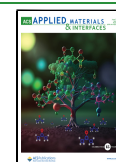
from OECT-related progress, further advances are needed to enable stable devices, high-density arrays, and complementary logic.^{14–16}

When aiming to improve the amplification or speed properties of the OECT, the channel material and geometry are the main factors to consider.^{17–19} The OECT amplification, or transconductance (g_m), is directly proportional to the electronic charge carrier mobility, μ , and the volumetric channel capacitance (C^*)—intrinsic material properties. In contrast, its dependence on the channel width (W), thickness (d), and length (L) (i.e., the channel volume), $g_m \sim Wd/L$, allows for manipulation through engineering approaches. Vertical organic electrochemical transistors (vOECTs) have been introduced as a straightforward method of reducing the physical device footprint and simultaneously significantly

Received: February 13, 2023

Accepted: May 8, 2023

Published: May 22, 2023



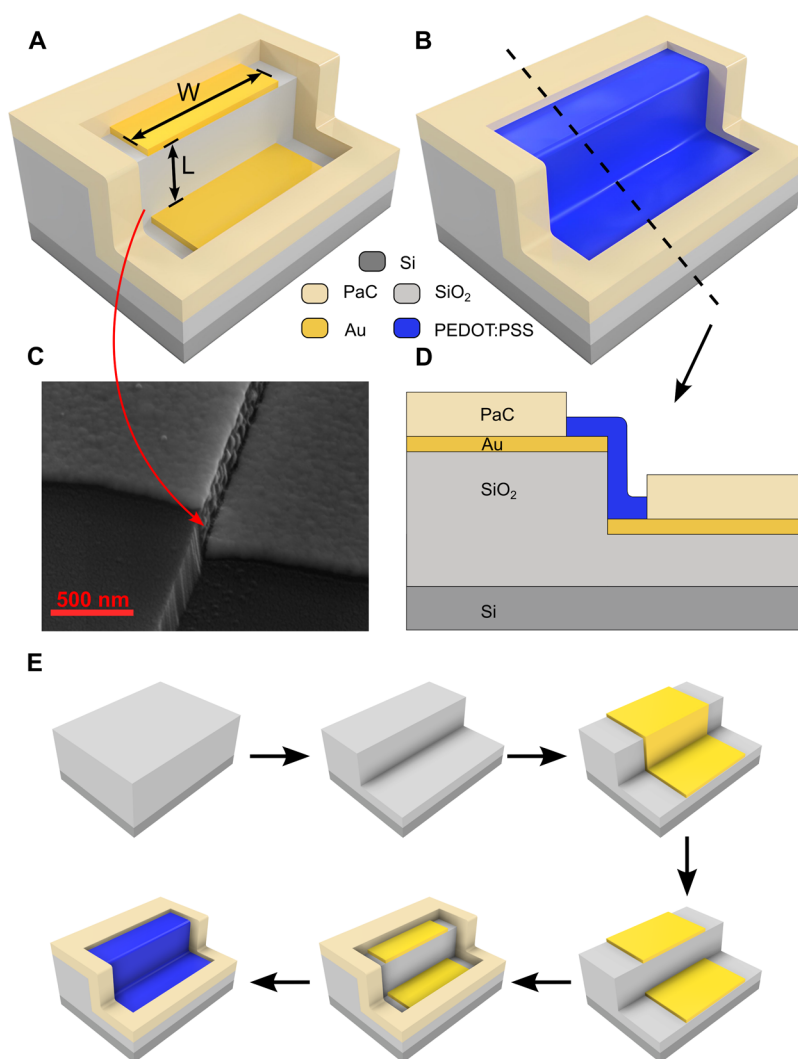


Figure 1. (A) Schematic of the device without the channel material, showing the geometry. (B) Device with spin-coated PEDOT:PSS. (C) SEM with a tilt of 50° of the fabricated channel area with the source and drain electrodes. (D) Cross section of the device. (E) Fabrication process schematic, starting with the Si/SiO₂ substrate, followed by etching of the step in SiO₂, patterning the electrodes and separating S/D, patterning the encapsulation, and creating the PEDOT:PSS channel.

decreasing L , with the aim of enhancing the amplification properties.^{20,21} Although an increase in the overall channel volume generally improves g_{mV} , a trade-off exists when considering the transistor speed.¹² This speed is particularly important for bioelectronic applications such as neural interfacing, where cutoff frequencies of up to at least 1 kHz are essential.²² The vOECT geometry facilitates reduced channel volumes while improving the W/L ratio, thus maintaining a good speed performance. Importantly, vOECTs also offer a useful geometry for electropolymerization, whereas planar devices typically result in poorly controlled, thick polymer film growth.^{23–25} Controlled electropolymerization of vOECT channels opens the door for the exploration of materials that are incompatible with solution-processing techniques and problematic for incorporation into typical OECT fabrication. Advanced geometries thus provide a means of improvement, not only in terms of transistor performance and reduced physical footprint but also in material investigation possibilities.

In this work, we demonstrate a straightforward fabrication technique for vOECTs, achieving highly reproducible channel

geometries with an L value of 350 nm. The use of standard photolithography processes makes our approach widely applicable. High transconductance values of up to 52 and 68 mS are demonstrated for spin-coated PEDOT:PSS and electropolymerized PEDOT:PF₆ channels, respectively. High on/off current ratios ($\approx 8.6 \times 10^4$) as well as useful cutoff frequencies (up to 2.1 kHz) are observed for bioelectronic applications. The vOECT approach developed in this work results in robust device structures, compatible with various channel material deposition methods, thus enabling the exploration of new materials.

2. EXPERIMENTAL METHODS

2.1. Device Fabrication. Si wafers with a thermally grown SiO₂ layer ($525 \pm 25 \mu\text{m}$ and $2.6 \mu\text{m}$, respectively) were used as substrates. All AZ photoresists used in the fabrication were exposed through soda lime masks in a SÜSS MA8 mask aligner with an i-line filter, developed in AZ 726 MIF, and finally the photoresist was stripped in TechniStrip MLO-07 heated to 60°C . In the first lithography step using AZ 701 MIR 29 cPs (4000 rpm, $\approx 1.5 \mu\text{m}$, dose $225 \text{ mJ}\cdot\text{cm}^{-2}$), part of SiO₂ was etched by capacitively coupled plasma reactive ion etching (CCP–RIE, CHF₃/Ar 12/38 sccm, power = 200 W, pressure

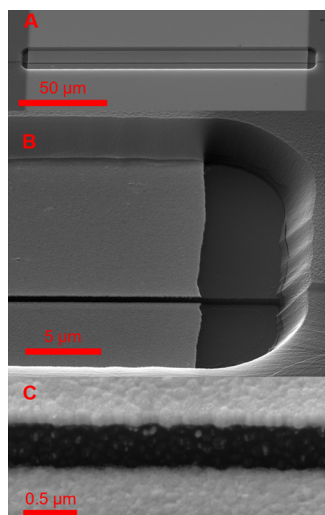


Figure 2. Tilted SEM images of the device with increasing magnification: (A) whole vOECT structure with a tilt of 50°; (B) detail of vOECT structure showing the step between the source and drain electrodes and the encapsulation layer; (C) high-magnification view of the step in between the source and drain electrodes.

= 4 Pa, 580 V DC bias) to create the vertical step of the desired depth for the channel, partially defining the final L (Figure 1A). Ti/Au (3/100 nm) thin films were deposited with an electron beam evaporator (Bestec GmbH) and patterned with wet etching using an AZ 1514H photoresist mask (4000 rpm, $\approx 1.4 \mu\text{m}$, dose $110 \text{ mJ}\cdot\text{cm}^{-2}$) and KI/I₂ and HF:HNO₃:H₂O (1:1:100) etchants for Au and Ti etching, respectively. Even though the sidewall between the electrodes is almost perpendicular, the electrodes were partially shorted due to the ultra-thin deposit of Ti/Au on the sidewall. At this point, the source and drain electrodes were fully separated at the previously created step using an ion-milling instrument (Scia Systems GmbH) equipped with a three-grid ion beam optics and a space charge neutralizer. A collimated Ar⁺ ion beam with an energy of 600 eV (ion beam current

= 200 mA) was used to impact the substrate, at a small angle of 25° with respect to the substrate, to sputter the metals at the vertical sidewall, while the wafer surface etching rate is slower,²⁶ resulting in the device shown in Figure 1C.

Afterward, we used an SCS Labcoater with a Silane A-174 adhesion promoter in the chamber to deposit the 3 μm thick parylene-C encapsulation layer. In the next step, we opened the contact pads and channels using a thick AZ 1518 photoresist and O₂ plasma (200 W, 13.3 Pa, O₂ 50 sccm, 450 V DC bias) in the CCP-RIE system. One substrate was diced using the dicing saw to single (15 × 15) mm² chips, later used for the electrochemical polymerization of PEDOT:PF₆. A device without the polymer channel is shown in Figure 2. On the substrate intended for the spin-coating of the channel material, before depositing a sacrificial parylene-C layer with a thickness of 2 μm , a dilute solution of anti-adhesive soap was spin-coated at 1000 rpm (2% V/V Micro90). With the use of an AZ 12XT-20PL-10 photoresist and RIE, the channel area was opened and prepared for spin-coating of a PEDOT:PSS solution.

2.2. Spin-Coating and Electrodeposition of PEDOT. To create the transistor channel with PEDOT:PSS, a dispersion of PEDOT:PSS (Clevios PH 1000, Heraeus Holding GmbH) with 5 wt % ethylene glycol, 0.1 wt % dodecyl benzene sulfonic acid, and 1 wt % of (3-glycidioxypropyl)-trimethoxysilane (GOPS) was spin-coated on the substrate at 650 rpm to a thickness of 400 nm, determined from a test peel-off using a profilometer and AFM measurements. The substrate was then prebaked at 90 °C for 2 min, and the PEDOT:PSS layer was patterned by peeling off the parylene-C sacrificial layer. A subsequent annealing step at 140 °C for 45 min was performed to cross-link the layer. The substrate was then placed in deionized (DI) water overnight to remove the low-molecular-weight compounds embedded in the organic layer.

To electrochemically polymerize PEDOT:PF₆ on the vOECT channel, 3,4-ethylenedioxythiophene (EDOT), tetrabutylammonium hexafluorophosphate (TBAPF₆), and acetonitrile (CH₃CN) were purchased from Sigma-Aldrich. In order to better control the thickness of the layer, EDOT solutions were prepared with two different concentrations of 1 mM and 5 mM with 100 mM of TBAPF₆ in CH₃CN. Electrochemical polymerization was carried out using a galvanostatic method, varying both the applied current and time, to attain different polymer thicknesses, as shown in Figure 4B. With an

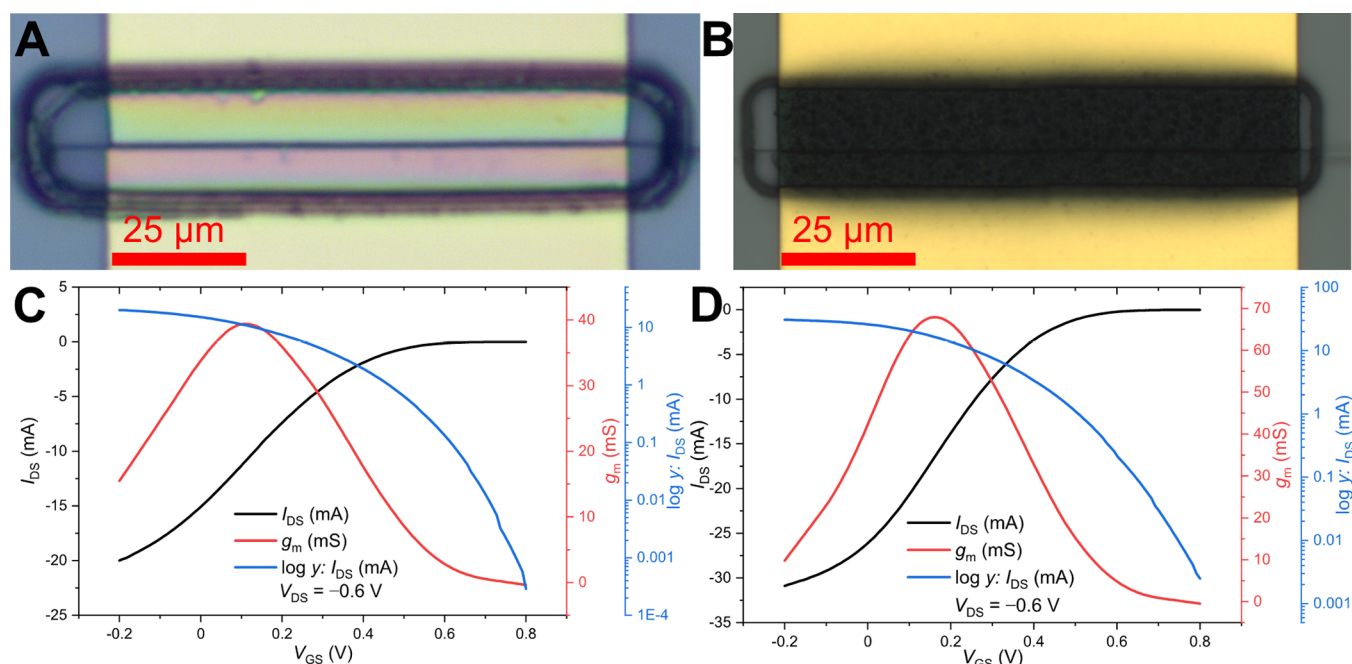


Figure 3. Optical micrographs and the corresponding transfer characteristics of (A,C) spin-coated PEDOT:PSS device with the channel width $W = 100 \mu\text{m}$ and thickness $d = 400 \text{ nm}$. (B,D) Electropolymerized PEDOT:PF₆, with $W = 100 \mu\text{m}$ and $d = 280 \text{ nm}$.

Ivium PocketSTAT2 potentiostat, a two-electrode configuration was used, where the source and drain electrodes were shorted to function as a working electrode, and a commercial Pt wire embedded in a modified syringe containing electrolyte was utilized as the counter electrode. A small drop of the electrolyte was placed on the open channels, while the source and drain electrodes were contacted with micromanipulator probes.

2.3. Characterization. An optical microscope (Zeiss Axio Imager A2) and a scanning electron microscope (Tescan Mira3) were used to observe the devices during and after the fabrication process. To electrically characterize the devices, a probe station with a stereomicroscope was employed. A PDMS well was used to hold a volume of 100 mM KCl, in which an Ag/AgCl gate electrode was immersed. To capture the steady-state characteristics and temporal response, a Keithley 4200A-SCS parameter analyzer was used. The frequency response was obtained by connecting the vOECT as a simple voltage amplifier, with a series drain load resistor $R_L = 1 \text{ k}\Omega$. The drain–source voltage (V_{DS}) was set by a Keysight U2722A source measurement unit, and the output signal was captured by a digital oscilloscope Keysight DSOX2004A with a built-in sine-wave generator, which was used for the gate–source voltage V_{GS} control. We applied a sine wave of $V_{GS} = 20 \text{ mV}$ peak-to-peak, with a DC voltage offset, to work in the regime of maximum g_m . This offset was set individually for each channel and was typically in range from 0 to 200 mV.

The polymer channel thickness was determined by the use of a stylus profilometer DektakXT (Bruker) and verified by an atomic force microscope (Dimensions Icon, Bruker). DektakXT was set to make a $100 \mu\text{m}$ long scan, while the applied force on the tip with a radius of $2.5 \mu\text{m}$ was set to the lowest possible value of $\approx 9.8 \text{ mN}$. At this point, we observed scratches only in the electropolymerized layers after the stylus profilometer measurement; therefore, we decided to verify and solve this issue using AFM, which is gentler to the materials with low hardness. We chose the tapping mode with the RTESPA-525 probe for this purpose.

3. RESULTS AND DISCUSSION

All fabricated devices had the same L of 350 nm . The transistor channel W was varied with values of (50, 100, and 200) μm , with the first two used most often in this work. As mentioned in Experimental Methods, two distinct sample types were fabricated to make a side-by-side comparison of spin-coated and electropolymerized channels. Two devices of similar thickness are shown in Figure 3A,B, with their corresponding transfer characteristics and transconductances. The spin-coated PEDOT is clearly more transparent and uniform. It can be noted that the peak g_m is higher for the electropolymerized (68 mS) than the spin-coated PEDOT (38 mS). This result, however, comes at the cost of higher ($\approx 2 \mu\text{A}$) off current (I_{OFF}) of the electropolymerized device, as is visible in the logarithmic (blue line) scale of I_{DS} in Figure 3C,D. On the contrary, the spin-coated PEDOT:PSS benefits from the short channel L , showing high I_{ON} of $\approx 20 \text{ mA}$ and a low I_{OFF} of only $\approx 290 \text{ nA}$. The peak g_m also shifts noticeably more toward positive V_{GS} for the electropolymerized device.

Another important feature which plays a fundamental role during the polymer electrodeposition is the charge consumed for the growth of the channel, defined as the current applied galvanostatically over a fixed range of time. It is important to optimize and reproduce these values in order to use them as a trustworthy and reliable source of information for the following depositions. The concentration of monomer in the solution used for the electropolymerization also dictates the final thickness of the polymer. This is the major reason for which the concentration of the monomer was reduced five times (from 5 to 1 mM). This provides reasonable thicknesses, useful

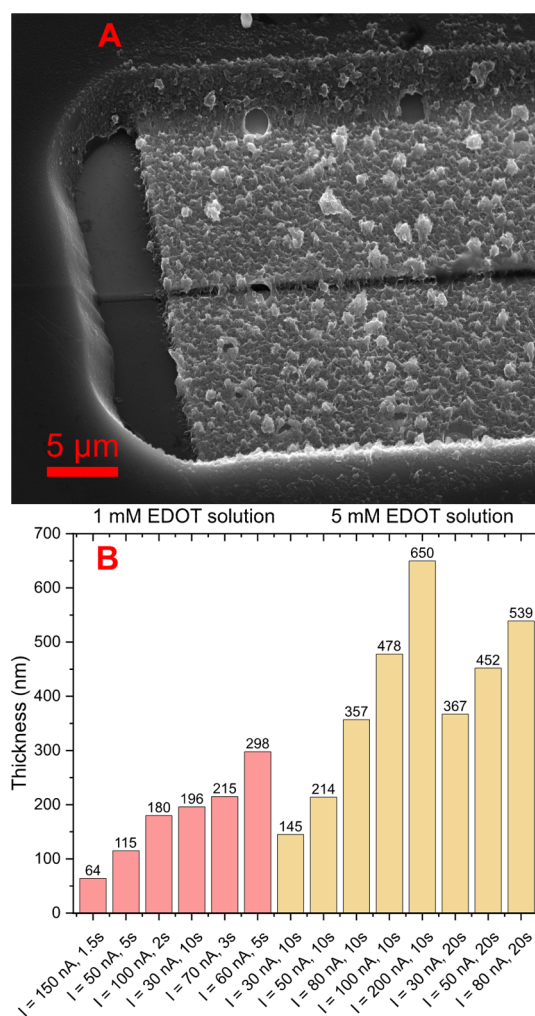


Figure 4. (A) SEM image of the device with $\approx 360 \text{ nm}$ thick electropolymerized PEDOT:PF₆ channel. (B) Thickness of the electropolymerized channel based on the process parameters.

for comparisons and with accessible values of fixed charges during the deposition procedure. Initially, the experiments were carried out using 5 mM solutions of EDOT, resulting in less control over the film growth for thinner ($<150 \text{ nm}$) layers (unreliable results were observed for each experiment despite maintaining the same setup and using fresh solutions for each deposition). Both for the high and low amounts of charge during deposition, the deposited layer thickness was very inconsistent. This issue was not observed for thicker ($>150 \text{ nm}$) layers. On the other hand, when using a fresh solution of 1 mM monomer concentration and optimal parameters, it was possible to coat the surface of the electrodes quite uniformly and obtain thin layers, as shown in the SEM image in Figure 4A. To show the repeatability of the layer thickness with the 1 mM solution, a set of parameters was used twice, and the final thickness was checked by a profilometer.

Transconductance curves of all fabricated devices were acquired. For spin-coated PEDOT:PSS, the number of measured devices (N) for each channel width was 6, with the mean value and standard deviation shown in Figure 5A. An increase in performance is apparent with wider channels, while the deviation between individual devices is quite small. The transconductance curves of electropolymerized layers are displayed in Figure 5B,C. A trend of increasing performance

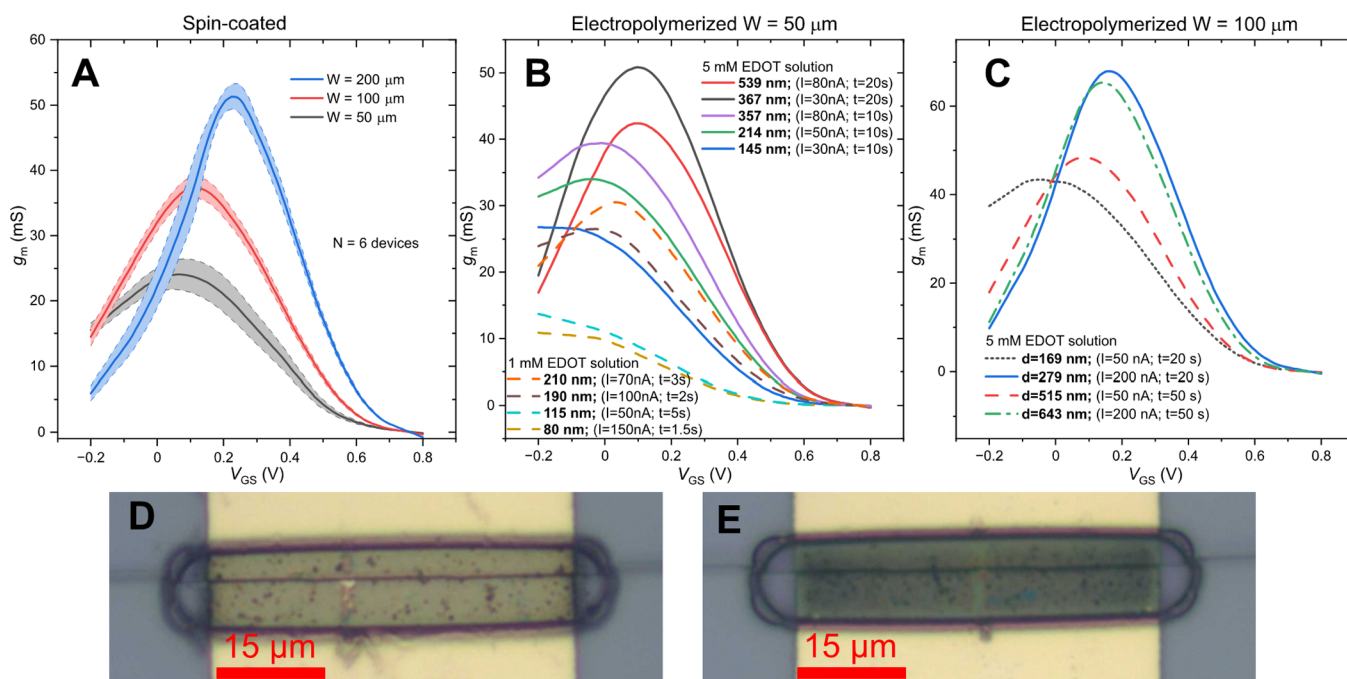


Figure 5. Transconductance (g_m) of (A) spin-coated PEDOT:PSS with thickness $d = 400$ nm and varied channel width W . (B,C) Electropolymerized PEDOT:PF₆ with varied d and W of 50 and 100 μm , respectively. (D,E) Optical microscopy image of the electropolymerized channel with d of 80 and 200 nm.

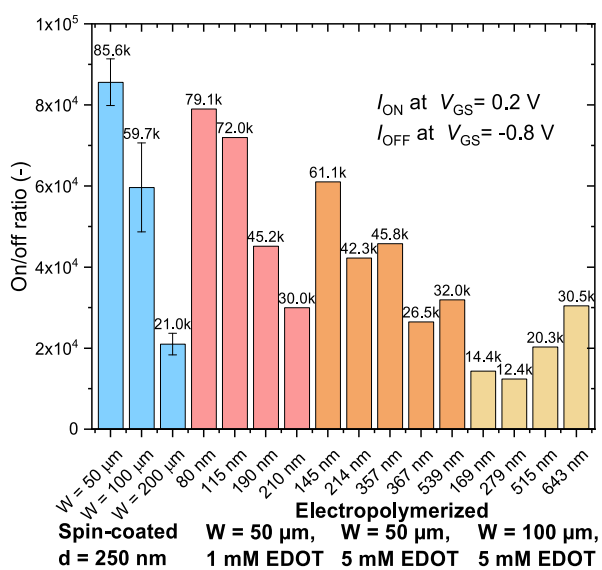


Figure 6. On/off ratio of the fabricated devices, with y-error for the spin-coated devices ($N = 6$).

with the increasing thickness of PEDOT:PF₆ is mostly seen, as it was expected; however it may be noted that there are few outliers. This suggests that not only the thickness but the way the channel was grown also influences the performance of the device. Figure 5D,E shows the electropolymerized layers with d of 80 and 200 nm. It can be seen that at lower thicknesses, the layer is still somewhat transparent, though not as much as spin-coated PEDOT:PSS. Crystal formation from the electropolymerization solution is also visible, despite the fact that active measures were taken to avoid the evaporation of the solution during the deposition process and that the devices were washed thoroughly in clean acetonitrile afterward.

The transistor performance demonstrates the benefits from the short channel geometry, also in terms of the on/off ratio, yielding relatively high values not usually achieved with PEDOT. As shown in Figure 6, spin-coated PEDOT:PSS performs the best with a value of $\approx 8.6 \times 10^4$. The ratio diminishes as W increases, although it remains of the same magnitude. With the electropolymerized devices, the ratio clearly scales down with the thickness of the layer; however, for $W = 100$ μm , this trend is broken, suggesting again that the performance of those layers is dependent on the way they were grown.

From the frequency response at maximum g_m (Figure 7A,B), the cutoff frequency (f_T) of all devices was extracted and is shown in Table 1. It clearly scales down with increasing W or d of the transistor. Due to the short channel L and minimized overlap of PEDOT with Au electrodes, which is in total ≈ 6 μm , competitive values (for the given channel volumes) of f_T were obtained.

The spin-coated device performs better than the electropolymerized ones in terms of the frequency response; therefore, a temporal response of six identical devices was captured as well, yielding averaged time constants of $\tau_{OFF} = (36.4 \pm 1.8)$ μs and $\tau_{ON} = (124.0 \pm 1.9)$ μs for devices with $W = 50$ μm and $d = 400$ nm (Figure 7C). The time constant for turning ON the transistor is significantly slower, showing the same behavior as reported in some other works.^{27–30} Paudel et al.²⁷ showed that for a planar OECT, lateral current in the channel when switching the transistor off is the limiting factor, as the channel length is usually much larger than the thickness of the semiconductor, rendering turning OFF the slower process of the two. Here, we attribute the opposite behavior partly to the fact that the channel length and semiconductor thickness are similar. The second factor could be an increase in the ionic resistance, slowing the switching to the ON state. We extracted the volumetric capacitance (C^*) from EIS according

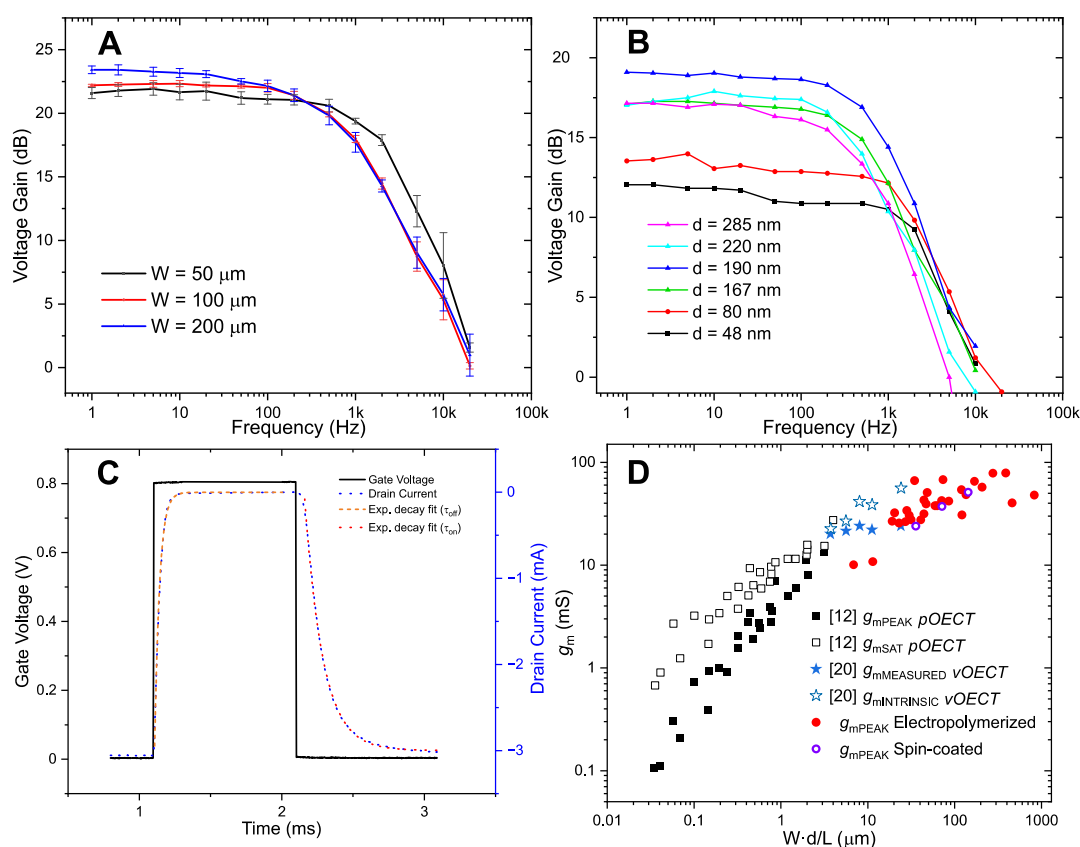


Figure 7. Frequency response of (A) spin-coated PEDOT:PSS with a thickness (d) of 400 nm. (B) Electropolymerized PEDOT:PF₆ with a constant channel width (W) of 50 μm , with d as a varied parameter. (C) Temporal response of the spin-coated device ($W = 50 \mu\text{m}$, $d = 400 \text{ nm}$, and $V_{\text{DS}} = -0.6 \text{ V}$), with extracted time constants of $\tau_{\text{OFF}} \approx 36 \mu\text{s}$ and $\tau_{\text{ON}} \approx 124 \mu\text{s}$. (D) Transconductance figure-of-merit plot comparing the data shown in a previous work with planar¹² and vertical²⁰ OECTs (pOECT, vOECT) to the data obtained in this work (red and violet circles).

Table 1. Values of Cutoff Frequencies of Fabricated Devices

W (μm)	50	100	200	50					
d (nm)	400			48	80	167	190	220	285
f_{T} (Hz)	1230	610	330	1824	2110	510	495	420	375

to a recent review¹⁵ and obtained estimated values of 154 and 282 $\text{F}\cdot\text{cm}^{-3}$ for PEDOT:PSS and PEDOT:PF₆, respectively. We have to note that the volume determination in our electropolymerized channel is not as straightforward as in the case of planar OECT due to significant disproportions between the channel area and overlap on the electrode, as well as rougher morphology; however, it is in any case clear that the electropolymerized PEDOT capacitance is higher, explaining the difference in speed. To make a comparison with a previous work, a transconductance figure-of-merit plot is shown in Figure 7D. Transconductance of planar OECTs¹² (black and white squares) increases linearly with the Wd/L ratio. As the downscaling of L leads to higher values of the ratio, a deviation from the linear trend can be observed, continuing the transconductance growth with a decreased slope of the fit.

4. CONCLUSIONS

In this work, we described a vOECT fabrication method that is scalable, reliable, and uses conventional microfabrication techniques, obtaining a submicrometer channel length without the need for electron beam lithography. The channel length can be precisely tuned to desired values in lower hundreds of nanometers. As the source and drain electrodes do not overlap,

the parasitic properties are reduced, and it is possible to further downscale the channel length to tens of nanometers. Compared to other works, the actual organic layer creating the transistor channel is prepared as the last step, limiting its exposure to undesired contamination or damage from the fabrication process. Finally, the fact that the method is intrinsically compatible with silicon wafer processing means straightforward integration with a silicon circuit. This can be used to make powerful integrated sensors or amplifiers, combining the strengths of mixed ionic–electronic conductor ECTs with silicon CMOS computing. Two different approaches were taken to create the transistor channel, first was the spin-coated PEDOT:PSS, while the second type was electropolymerized PEDOT:PF₆. High peak transconductance was obtained for both types. The spin-coated devices had a maximum transconductance of 52 mS, with the preserved speed parameters of the transistor ($\tau_{\text{OFF}} \approx 36 \mu\text{s}$ and $\tau_{\text{ON}} \approx 124 \mu\text{s}$) and an exceptional on/off current ratio of $\approx 8.6 \times 10^4$. The electropolymerized devices have shown a higher maximum transconductance of 68 mS for layers of similar thickness. However, their speed of operation was considerably slower, with approximately $3 \times$ lower f_{T} . This could be due to the higher density of the electropolymerized PEDOT and/or

due to the lack of PSS-rich phase present in the spin-coated version. Essentially, we have shown a simple platform that could be used for the research of newly synthesized channel materials, regardless of their patterning method. The electro-polymerization process, especially, can be quite easily modified, as its parameter space is very vast. The control of morphology could be advantageous for specific applications. Our platform can also be easily translated to flexible organic bioelectronic substrates (i.e., parylene-C and polyimide) designing predefined trenches mimicking the same step made here in SiO₂. An important conclusion is that our findings add to the growing body of recent research^{15,21} which show that achieving cutoff frequencies in the range above 1 kHz is challenging and that limitations are likely intrinsic to the conducting polymer itself, not the geometric structure.

AUTHOR INFORMATION

Corresponding Author

Eric D. Glowacki – Bioelectronics Materials and Devices Lab, Central European Institute of Technology, Brno University of Technology, 61200 Brno, Czech Republic; orcid.org/0000-0002-0280-8017; Email: eric.daniel.glowacki@ceitec.vutbr.cz

Authors

Jan Brodský – Bioelectronics Materials and Devices Lab, Central European Institute of Technology, Brno University of Technology, 61200 Brno, Czech Republic; Institute of Scientific Instruments of the CAS, 61264 Brno, Czech Republic

Imrich Gablech – Bioelectronics Materials and Devices Lab, Central European Institute of Technology, Brno University of Technology, 61200 Brno, Czech Republic; Department of Electrical and Electronic Technology, Faculty of Electrical Engineering and Communication, Brno University of Technology, 616 00 Brno, Czech Republic

Ludovico Migliaccio – Bioelectronics Materials and Devices Lab, Central European Institute of Technology, Brno University of Technology, 61200 Brno, Czech Republic

Marek Havlíček – Bioelectronics Materials and Devices Lab, Central European Institute of Technology, Brno University of Technology, 61200 Brno, Czech Republic; Czech Metrology Institute, 638 00 Brno, Czech Republic

Mary J. Donahue – Laboratory of Organic Electronics, ITN Campus Norrköping, Linköping University, SE-60174 Norrköping, Sweden

Complete contact information is available at: <https://pubs.acs.org/10.1021/acsami.3c02049>

Author Contributions

The manuscript was written through contributions of all authors. All authors have given approval to the final version of the manuscript. J.B., I.G., M.J.D., and E.D.G. conceived the research idea. J.B., I.G., and L.M. conducted and optimized device fabrication and performed all device measurements. M.H. performed microscopy measurements: AFM and SEM. M.J.D. contributed to the device measurement design. J.B. curated all data and performed data analysis, with input from all coauthors.

Notes

The authors declare no competing financial interest.

ACKNOWLEDGMENTS

This work has been supported by the European Research Council (ERC) under the European Union's Horizon 2020 research and innovation program (E.D.G. grant agreement no. 949191), by the Grant Agency of the Czech Republic under contract 23-07432S, and by funding from the Brno City Municipality. Sample fabrication was supported by CzechNanoLab Research Infrastructure financed by MEYS CR (LM2018110). J.B. acknowledges support through the Brno Ph.D. Talent Scholarship funded by the Brno City Municipality.

REFERENCES

- (1) Kleemann, H.; Krechan, K.; Fischer, A.; Leo, K.; Kleemann, H.; Krechan, K.; Fischer, A.; Leo, K. A Review of Vertical Organic Transistors. *Adv. Funct. Mater.* **2020**, *30*, No. 1907113.
- (2) Liu, K.; Ouyang, B.; Guo, X.; Guo, Y.; Liu, Y. Advances in Flexible Organic Field-Effect Transistors and Their Applications for Flexible Electronics. *npj Flexible Electron.* **2022**, *6*, 1–19.
- (3) Gelinck, G. H.; Huitema, H. E. A.; van Veenendaal, E.; Cantatore, E.; Schrijnemakers, L.; van der Putten, J. B. P. H.; Geuns, T. C. T.; Beenhakkers, M.; Giesbers, J. B.; Huisman, B. H.; Meijer, E. J.; Benito, E. M.; Touwslager, F. J.; Marsman, A. W.; van Rens, B. J. E.; de Leeuw, D. M. Flexible Active-Matrix Displays and Shift Registers Based on Solution-Processed Organic Transistors. *Nat. Mater.* **2004**, *3*, 106–110.
- (4) Rivnay, J.; Inal, S.; Salleo, A.; Owens, R. M.; Berggren, M.; Malliaras, G. G. Organic Electrochemical Transistors. *Nat. Rev. Mater.* **2018**, *3*, 1–14.
- (5) Rivnay, J.; Owens, R. M.; Malliaras, G. G. The Rise of Organic Bioelectronics. *Chem. Mater.* **2014**, *26*, 679–685.
- (6) Liao, C.; Mak, C.; Zhang, M.; Chan, H. L. W.; Yan, F. Flexible Organic Electrochemical Transistors for Highly Selective Enzyme Biosensors and Used for Saliva Testing. *Adv. Mater.* **2015**, *27*, 676–681.
- (7) Rivnay, J.; Inal, S.; Collins, B. A.; Sessolo, M.; Stavrinidou, E.; Strakosas, X.; Tassone, C.; Delongchamp, D. M.; Malliaras, G. G. Structural Control of Mixed Ionic and Electronic Transport in Conducting Polymers. *Nat. Commun.* **2016**, *7*, 1–9.
- (8) Zeglio, E.; Inganäs, O. Active Materials for Organic Electrochemical Transistors. *Adv. Mater.* **2018**, *30*, No. 1800941.
- (9) Proctor, C. M.; Rivnay, J.; Malliaras, G. G. Understanding Volumetric Capacitance in Conducting Polymers. *J. Polym. Sci., Part B: Polym. Phys.* **2016**, *54*, 1433–1436.
- (10) Paulsen, B. D.; Tybrandt, K.; Stavrinidou, E.; Rivnay, J. Organic Mixed Ionic–Electronic Conductors. *Nat. Mater.* **2020**, *19*, 13–26.
- (11) Khodagholy, D.; Rivnay, J.; Sessolo, M.; Gurfinkel, M.; Leleux, P.; Jimison, L. H.; Stavrinidou, E.; Herve, T.; Sanaur, S.; Owens, R. M.; Malliaras, G. G. High Transconductance Organic Electrochemical Transistors. *Nat. Commun.* **2013**, *4*, 2133.
- (12) Rivnay, J.; Leleux, P.; Ferro, M.; Sessolo, M.; Williamson, A.; Koutsouras, D. A.; Khodagholy, D.; Ramuz, M.; Strakosas, X.; Owens, R. M.; Benar, C.; Badier, J. M.; Bernard, C.; Malliaras, G. G. High-Performance Transistors for Bioelectronics through Tuning of Channel Thickness. *Sci. Adv.* **2015**, *1*, No. e1400251.
- (13) Marks, A.; Griggs, S.; Gasparini, N.; Moser, M. Organic Electrochemical Transistors: An Emerging Technology for Biosensing. *Adv. Mater. Interfaces* **2022**, *9*, No. 2102039.
- (14) Sun, H.; Vagin, M.; Wang, S.; Crispin, X.; Forchheimer, R.; Berggren, M.; Fabiano, S. Complementary Logic Circuits Based on High-Performance n-Type Organic Electrochemical Transistors. *Adv. Mater.* **2018**, *30*, No. 1704916.
- (15) Huang, W.; Chen, J.; Yao, Y.; Zheng, D.; Ji, X.; Feng, L. W.; Moore, D.; Glavin, N. R.; Xie, M.; Chen, Y.; Pankow, R. M.; Surendran, A.; Wang, Z.; Xia, Y.; Bai, L.; Rivnay, J.; Ping, J.; Guo, X.; Cheng, Y.; Marks, T. J.; Facchetti, A. Vertical Organic Electrochemical

chemical Transistors for Complementary Circuits. *Nature* **2023**, *613*, 496–502.

(16) Cea, C.; Spyropoulos, G. D.; Jastrzebska-Perfect, P.; Ferrero, J. J.; Gelinas, J. N.; Khodagholy, D. Enhancement-Mode Ion-Based Transistor as a Comprehensive Interface and Real-Time Processing Unit for in Vivo Electrophysiology. *Nat. Mater.* **2020**, *19*, 679–686.

(17) Ohayon, D.; Druet, V.; Inal, S. A Guide for the Characterization of Organic Electrochemical Transistors and Channel Materials. *Chem. Soc. Rev.* **2023**, 1001.

(18) Yu, S.; Kousseff, C. J.; Nielsen, C. B. N-Type Semiconductors for Organic Electrochemical Transistor Applications. *Synth. Met.* **2023**, *293*, No. 117295.

(19) Friedlein, J. T.; McLeod, R. R.; Rivnay, J. Device Physics of Organic Electrochemical Transistors. *Org. Electron.* **2018**, *63*, 398–414.

(20) Donahue, M. J.; Williamson, A.; Strakosas, X.; Friedlein, J. T.; McLeod, R. R.; Gleskova, H.; Malliaras, G. G. High-Performance Vertical Organic Electrochemical Transistors. *Adv. Mater.* **2018**, *30*, No. 1705031.

(21) Rashid, R. B.; Du, W.; Griggs, S.; Maria, I. P.; McCulloch, I.; Rivnay, J. Ambipolar Inverters Based on Cofacial Vertical Organic Electrochemical Transistor Pairs for Biosignal Amplification. *Sci. Adv.* **2021**, *7*, eabh1055.

(22) Jastrzebska-Perfect, P.; Chowdhury, S.; Spyropoulos, G. D.; Zhao, Z.; Cea, C.; Gelinas, J. N.; Khodagholy, D. Translational Neuroelectronics. *Adv. Funct. Mater.* **2020**, *30*, No. 1909165.

(23) Rybakiewicz-Sekita, R.; Gryszel, M.; Pathak, G.; Gańczarczyk, R.; Gańczarczyk, G.; Donahue, M. J.; Głowacki, E. D. Well-Defined Electrochemical Switching of Amphiphilic Glycolated Poly(3,4-Ethylenedioxythiophene). *J. Mater. Chem.* **2022**, *10*, 17208–17215.

(24) Lee, J.; Chhatre, S.; Sitarik, P.; Wu, Y.; Baugh, Q.; Martin, D. C. Electrochemical Fabrication and Characterization of Organic Electrochemical Transistors Using Poly(3,4-Ethylenedioxythiophene) with Various Counterions. *ACS Appl. Mater. Interfaces* **2022**, *14*, 42289–42297.

(25) Wustoni, S.; Hidalgo, T. C.; Hama, A.; Ohayon, D.; Savva, A.; Wei, N.; Wehbe, N.; Inal, S. In Situ Electrochemical Synthesis of a Conducting Polymer Composite for Multimetabolite Sensing. *Adv. Mater. Technol.* **2020**, *5*, No. 1900943.

(26) Harper, J. M. E.; Cuomo, J. J.; Kaufman, H. R. Technology and Applications of Broad-beam Ion Sources Used in Sputtering. Part II. Applications. *J. Vac. Sci. Technol.* **1982**, *21*, 737.

(27) Paudel, P. R.; Skowrons, M.; Dahal, D.; Radha Krishnan, R. K.; Lüssem, B. The Transient Response of Organic Electrochemical Transistors. *Adv. Theory Simul.* **2022**, *5*, No. 2100563.

(28) Ko, J.; Wu, X.; Surendran, A.; Muhammad, B. T.; Leong, W. L. Self-Healable Organic Electrochemical Transistor with High Transconductance, Fast Response, and Long-Term Stability. *ACS Appl. Mater. Interfaces* **2020**, *12*, 33979–33988.

(29) Hütter, P. C.; Rothländer, T.; Haase, A.; Trimmel, G.; Stadlober, B. Influence of Geometry Variations on the Response of Organic Electrochemical Transistors. *Appl. Phys. Lett.* **2013**, *103*, No. 043308.

(30) Rothlander, T.; Hutter, P. C.; Renner, E.; Gold, H.; Haase, A.; Stadlober, B. Nanoimprint Lithography-Structured Organic Electrochemical Transistors and Logic Circuits. *IEEE Trans. Electron Devices* **2014**, *61*, 1515–1519.

SiO₂-Decorated Parylene C Micropillars Designed to Probe Cellular Force

Zdenka Fohlerova,* Imrich Gablech, Alexandr Otahal, and Peter Fecko

Living cells sense and respond to mechanical signals through specific mechanisms generating traction force. The quantification of cell forces using micropillars can be limited by micropillar stiffness, technological aspects of fabrications, and microcontact printing of proteins. This paper develops the new design of SiO₂/Parylene C micropillars with an aspect ratio of 6 and 3.5 and spring constant of 4.7 and 28 μN μm⁻¹, respectively. The upper part of micropillars is coated with a 250 nm layer of SiO₂, and results confirm protein deposition on individual micropillars via SiO₂ interface and non-adhesiveness on the micropillars' sidewalls. Results show an absence of cytotoxicity for micropillar-based substrates and a dependence on its stiffness. Stiffer micropillars enhance cell adhesion and proliferation rate, and a stronger cellular force of ≈25 μN is obtained. The main contribution of SiO₂/parylene C micropillars is the elimination of the step involving the fabrication of polydimethylsiloxane stamp because the array enables covalent binding of proteins via SiO₂ chemistry. These micropillars stand on Si wafer and thus, any warping of underlying polymer membrane does not have to be considered. Additionally, SiO₂/parylene C micropillars can broaden the range of stiffer substrates to be probed by cells.

1. Introduction

The mechanical and adhesion properties of living cells are guided by chemical signals and external physical stimuli; cells have been exposed to different external forces such as the magnetic force,^[1] shear stress,^[2] or the mechanical properties of the substrate.^[3,4] The importance of the interplay between chemical and physical stimuli and the sensitivity of cells' response to

these stimuli through the generation of traction force is fundamental for physiological and pathological pathways.^[5]

The investigation of cellular forces depends on in-vitro platforms that can mimic processes and the stiffness of cellular environments or these platforms serve as sensors detecting the force upon the exposure cells to the, for example, drugs. Recently developed tools to quantify the traction force generated by cells range from microscopy to molecular force sensors.^[6–11] All these techniques possess some advantages and disadvantages^[12] and offer a variety of mechanisms through which cells can move, divide, remodel, differentiate, communicate, and sense their microenvironment.^[13]

One of the approaches to measuring forces transmitted at the focal adhesion is the culturing of cells on patterned micropillars. Microfabrication techniques allow for the production of an array of thousands of elastic pillars of 0.5–5 μm in

diameter, fabricated by photolithography and replica molding with conventional polydimethylsiloxane (PDMS).^[14] The top of the pillar surface is coated with proteins of extracellular matrix via microcontact printing to render them cell-adhesive.^[15] The cylindrical pillars with a defined L/D aspect ratio (length *L*, diameter *D*) and Young's modulus of the material (*E*) allow for the calculation of the cellular force based on the pillar bending and the known spring constant *k*, which is in the range of 1 to 200 nN μm⁻¹ for typical PDMS pillars.^[16] For the small deformation Δ*x*, the lateral force *F* can be calculated using Hooke's law, as described in Equation (1):^[16]

$$F = k \cdot \Delta x = \frac{3\pi E D^4}{64 L^3} \cdot \Delta x \quad (1)$$

Most authors have published the micropillars with lower spring constant and thus the stiffness or high aspect ratio pillars from stiffer polymers for increasing the spatial resolution. The molding technique frequently used for polymers such as PDMS with Young's modulus 1 to 4 MPa^[17] permits the precise fabrication of a low aspect ratio micropillars. The molding high-aspect-ratio micropillars is more challenging because it is difficult to successfully de-mold the structure. Therefore, this technique requires good mold releasability during the de-molding. Additionally, high aspect ratio pillars may have tendency of cracking and clustering.

Prof. Z. Fohlerova, Dr. I. Gablech, P. Fecko
Central European Institute of Technology
Brno University of Technology
Purkynova 123, Brno 61200, Czech Republic
E-mail: zdenka.fohlerova@ceitec.vutbr.cz
Prof. Z. Fohlerova, Dr. I. Gablech, Dr. A. Otahal
Department of Microelectronics
Faculty of Electrical Engineering and Communication
Brno University of Technology
Technicka 3058/10, Brno 61600, Czech Republic
Prof. Z. Fohlerova
Department of Biochemistry
Faculty of Medicine
Masaryk University
Kamenice 753/5, Brno 625 00, Czech Republic

 The ORCID identification number(s) for the author(s) of this article can be found under <https://doi.org/10.1002/admi.202001897>.

DOI: 10.1002/admi.202001897

Nevertheless, molding allowed the production of PDMS micropillars of different stiffness by the modulation of pillar aspect ratio, geometry,^[18] UV-treatment,^[19] and the degree of the polymerization^[20] and this technique was also adopted for the fabrication of PDMS stamp required for microcontact printing of proteins. The variability in PDMS stiffness became an important progress in measurement of cellular forces because a broad range of substrate stiffness can mimic the various stiffness of physiological tissues, which can range from 10^2 to 10^7 Pa, from the softest brain to the stiffest bone, respectively.^[21] Moreover, the rigidity of tissue can be significantly changed due to diseases such as cancers, Alzheimer's disease, or spinal cord injury.^[22]

Besides PDMS, different polymers have been used to fabricate micropillars such as polyacrylamide,^[23] poly(methylmethacrylate),^[24] SU-8,^[25] and polycarbonate (PC).^[26] For instance, a high aspect ratio (≈ 11) of SU-8 micropillars with $E \approx 4$ GPa has been fabricated using lithography technique. Authors well-described the optimization of fabrication process,^[25] particularly when temporal stability and the high spatial resolution of the array should be required. In addition to the SU-8 polymer, a polycarbonate with Young's modulus of 2–3 GPa has been used to fabricate ultrahigh aspect ratio (up to 20) pillars with spring constant ≈ 5 nN μm^{-1} to enhance cell differentiation^[26] and similar aspect ratio has been used to measure cellular forces by other authors.^[4]

In this work, we show “top-down” fabrication of a highly ordered array of SiO₂/parylene C micropillars standing on the Si substrate that can be used as a probe to quantify the force generated from living cells. The array of micropillars with aspect ratio corresponding to 6 and 3.5 was characterized for its chemical and biological properties as a proof-of-principle for the functionality of array to be used as a force sensor. The technological significance of the cellular force transducer here is the elimination of the micro-contact printing of proteins, given that the SiO₂ thin film allows the covalent binding of proteins or peptides, or simply enables a charge or different wettability properties on top of micropillars via SiO₂ chemistry. This could help researchers to skip the fabrication of a PDMS stamp and to prevent the differences in printing quality.^[27,28] The second contribution of this work is to prove that the fabrication of pillars from parylene C as the highly rigid material with a Young's modulus of ≈ 4 GPa can, compared to other polymers used for pillar fabrication, broaden the range of material stiffness to be probed by cells. The third advantage of our micropillars is that our micropillars stand on Si wafer and thus any warping of underlying polymer membrane does not have to be considered as it has been reported for PDMS with lower aspect ratio.

2. Results and Discussion

2.1. Fabrication and Characterization of SiO₂/Parylene Pillars

The array of SiO₂/parylene micropillars was fabricated on a 0.5 mm \times 0.5 mm silicon substrate by “top-down” technology, as described in Figure S1, Supporting Information. The micro-fabrication process of micropillar development provided the array of the hexagonally ordered parylene pillars with a ≈ 1.6 μm

diameter, ≈ 3 μm center-to-center distance, and rod-like morphology, as confirmed by a scanning electron microscopy (Figure 1A). The deposition of a ≈ 250 nm SiO₂ layer on the top of the micropillars to mediate the selective covalent binding of protein was qualitatively analyzed via an scanning electron microscopy (SEM) equipped energy-dispersive X-ray (EDX) spectroscope. High-resolution element mapping enabled this study to discriminate between different elemental compositions, which allowed us to visualize the localization of the SiO₂ on top of the pillars. The EDX image in Figure 1B shows the highly localized EDX oxygen atoms on top of the pillars from the SiO₂ layer (colored red), while parylene C is shown as light blue. The elemental analysis confirmed the selective deposition of SiO₂ on top of the micropillars and therefore the efficacy of the proposed individual fabrication steps.

The stiffness of the micropillars was modulated by varying their height, giving the pillars a height of 9 and 5 μm and an aspect ratio corresponding to 6 and 3.5, respectively. The SiO₂ layer on top of the pillars did not change the bulk properties of parylene C, and the spring constant k of micropillar was approximately calculated according to Equation (1). Based on this Equation (1), the parylene micropillar with a length of 9 and 5 μm has a spring constant of $k = \approx 4.8$ $\mu\text{N} \mu\text{m}^{-1}$ and ≈ 28 $\mu\text{N} \mu\text{m}^{-1}$, respectively. The spring constants of the parylene micropillars are thus significantly higher, compared to the already published spring constant of 1–1500 nN μm^{-1} for widely used PDMS.^[18,19] Moreover, material with a higher Young's modulus of polycarbonate has been already investigated as platforms for the measurement of cellular force.^[4] The authors managed to produce an array of PC pillars with $k = \approx 3$ $\mu\text{N} \mu\text{m}^{-1}$ and $k = \approx 7$ $\mu\text{N} \mu\text{m}^{-1}$ by changing the aspect ratio. To our knowledge, micropillars with such high $k = \approx 28$ $\mu\text{N} \mu\text{m}^{-1}$ have not been used for the measurement of cellular force as we further confirmed that they can be sensed and bent by cells. Additionally, the fabrication process of our micropillars provides technological resolution of ≈ 0.8 μm , ensures good spatial stability of micropillars as well as temporal stability due to the chemical inertness of parylene.

2.2. Micropillars Patterning

Patterning the micropillars to enhance cell adhesion is the first step guaranteed by the use of nanotechnology to selectively deposit a thin layer of SiO₂ on top of pillars. Generally, the protein modification of micropillars in order to measure cellular force requires the selective deposition of a protein such as fibronectin on top of the pillars via microcontact printing^[28] and by the non-adhesive treatment of pillar sidewalls.^[29] Such pillar patterning avoids the undesired attachment of cells to the vertical side of the micropillar and improves cell adhesion. However, the micro-contact printing of proteins requires the additional fabrication of the stamp and is limited in terms of which proteins can be printed as well as the printing quality.^[28] Our design and patterning of SiO₂/parylene micropillars is able to covalently bind any proteins of interest to the upper surface of the micropillars via SiO₂ interface, as shown in Figure S2, Supporting Information. The SiO₂/parylene patterning was first investigated on bulk substrates because the chemistry on such pillars differs from PDMS ones and must be optimized. To ensure the binding of

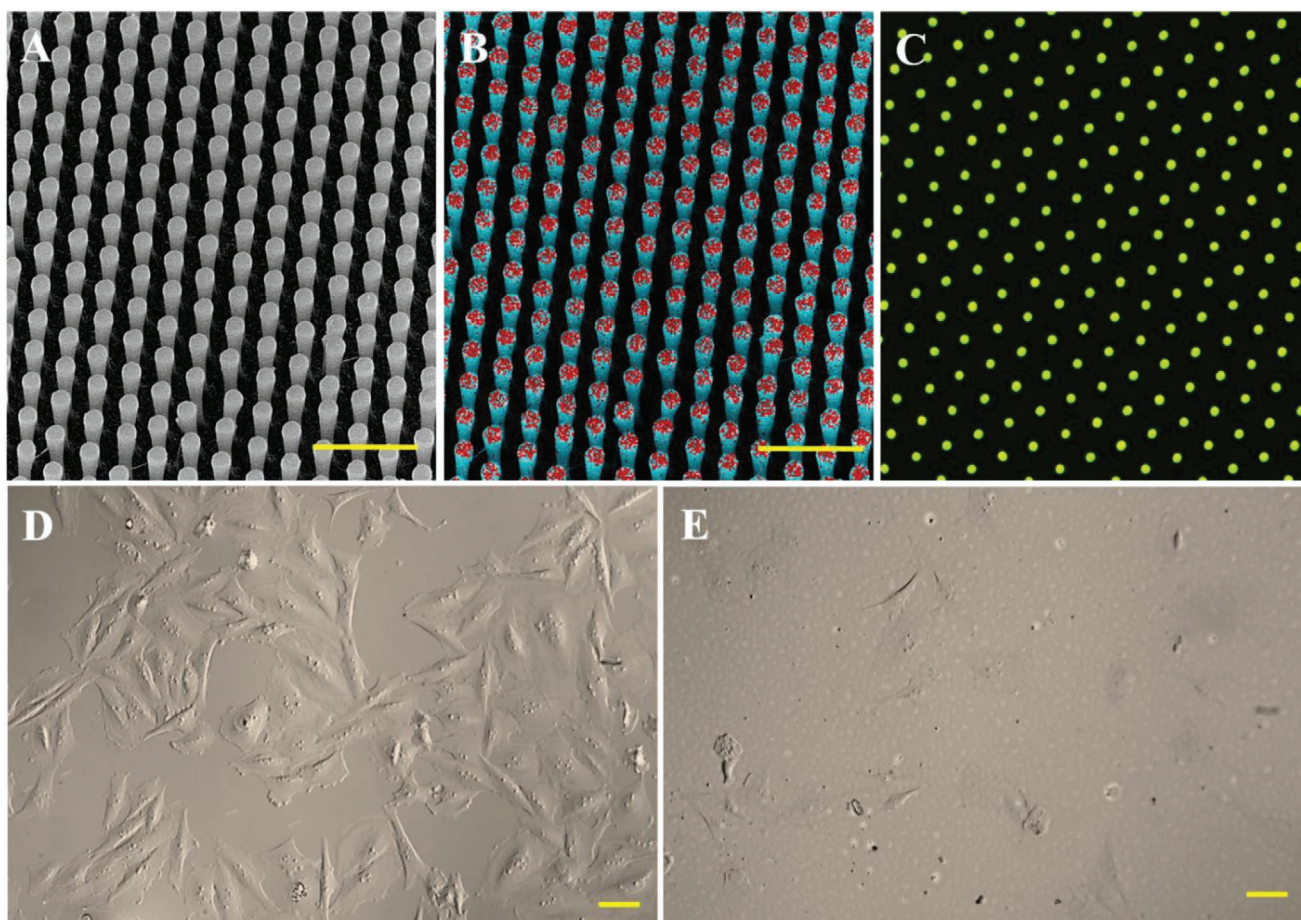


Figure 1. SEM image of an array of well-ordered SiO₂/parylene C micropillars (A). A qualitative EDX analysis of the micropillars. The red spots represent the targeted SiO₂ layer on top of the parylene C micropillars, while the blue represents the parylene C pillars (B). A fluorescent image of the micropillars with covalently bound FITC-collagen protein (C). A DIC image of 3T3-fibroblasts adhered on fibronectin-coated SiO₂ (D). A DIC image of 3T3-fibroblasts adhered on Pluronic F-127-treated parylene C (E). The scale bar of the SEM and DIC image corresponds to 10 μm and 50 μm, respectively.

the protein to the SiO₂ layer, selective SiO₂ oxidation was performed by treating it with a piranha solution at a 5:3 ratio (step 1 in Figure S2, Supporting Information). The procedure exposed hydroxyl groups on the silica surface, while the parylene C sidewalls remained unreacted,^[30] as confirmed by the measurement of contact angle (CA). The piranha-treated SiO₂ decreased the CA value from ≈67° to ≈23°, making the surface more hydrophilic while the parylene C surface remained unchanged ≈109° (Figure 2a,b and a', b'). The silanization of the hydroxyl reached the SiO₂ substrate with the (3-aminopropyl)triethoxysilane (APTES), which fed the amino-terminal groups on the surface that changed the CA from ≈23° to ≈49° and from ≈109° to ≈104° for SiO₂ and parylene C, respectively (Figure 2c,c'). This SiO₂ chemistry has strong support in the literature^[31] and significantly, the result showed that the parylene C remained intact following the piranha oxidation and silanization process.^[30] To ensure non-adhesive pillar sidewalls, the array was further incubated in a non-ionic surfactant Pluronic F-127. The deposition of the Pluronic via its hydrophobic moiety exposed the hydrophilic non-adhesive PEG groups to the parylene C that corresponds to the decreased CA value ≈76° (Figure 2d,d'). A similar CA value for Pluronic to treat polymers has been reported for

PDMS,^[32] suggesting the successful nature of parylene C coating. The amino-functionalized SiO₂ surface remained unmodified because the CA value did not change significantly. The patterned surface of the micropillars was finally modified by the covalent immobilization of the fibronectin on the amino-terminated SiO₂ surface by crosslinking it with glutaraldehyde. The CA value changed for both surfaces because the fibronectin was immobilized on the SiO₂ surface and a small amount of fibronectin was adsorbed on the Pluronic F-127-treated parylene C sidewalls (Figure 2e,e'), which is in strong agreement with the literature.^[33]

Moreover, even if the Pluronic adsorb some portion of the proteins^[34] and the exposition of polyethylene oxide moiety suppresses the cell adhesion,^[32] patterning with Pluronic F-127 is generally accepted for the reduction of protein adsorption and cell adhesion. Based on this phenomenon, fluorescently labeled collagen was covalently immobilized on the top of micropillars and the image was captured to confirm the selective deposition of protein (Figure 1C). Further, the adhesion of 3T3-fibroblasts to fibronectin (Figure 1D) and Pluronic-F127 (Figure 1E) coated surface confirmed the reduced cell viability on Pluronic treated micropillars. The cells adhered to and spread on fibronectin-coated SiO₂ at high

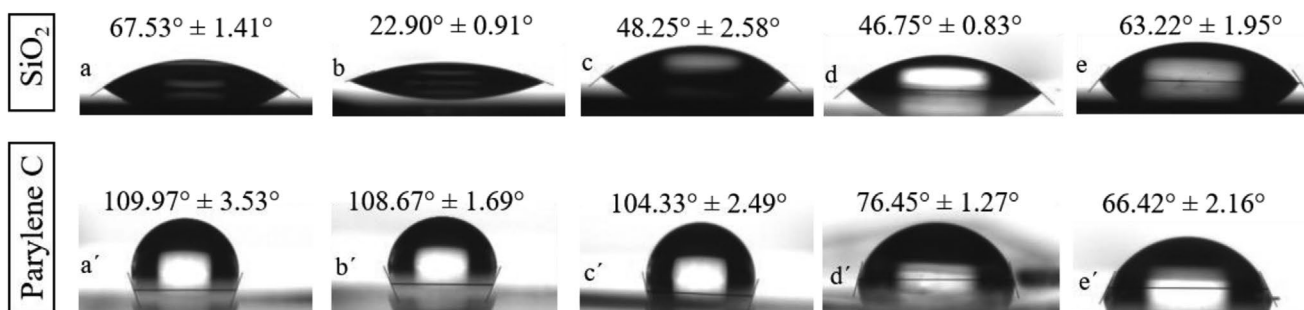


Figure 2. CA of the SiO₂ and parylene C modification. a,a') cleaned SiO₂ and parylene C substrates; b,b') substrates treated in 5:3 piranha solution for 10 min; c,c') substrates silanized with APTES at 120° for 30 min; d,d') surface treated with Pluronic F-127; e,e') covalently bonded fibronectin via glutaraldehyde on APTES-silanized surface.

density and had the characteristic elongated shape, while the cells on Pluronic F-127-treated parylene C adhered in a very small density and showed a smaller cell surface area.

The procedural steps of the surface oxidation and silanization were characterized by an X-ray photoelectron spectroscopy (XPS) analysis, as shown in **Figure 3**. The XPS spectra were analyzed by peak-fitting software (CasaXPS version 2.3.18PR1.0) provided by SPECS GmbH (Berlin, Germany). The raw data were processed by the subtraction of a Shirley background for secondary electrons and element peak fitting was used to estimate the relative elements' molar fraction. The integral of the peak was divided by a relative sensitivity factor that was characteristic of each element. Even if some elemental contaminants were to occur, a significant ≈20% increment of N 1s was observed, which could be attributed to the amino-functionalized SiO₂, while the increase in N 1s on parylene C was just 3.5% as shown in the table of **Figure 3**. A significant increase and unchanged percentage of C 1s was observed for APTES/SiO₂ and APTES/parylene C, respectively, confirming the successful selective silanization of the SiO₂ surface. Additionally, the high-resolution

spectra of nitrogen N 1s and silicon Si 2p for the APTES-treated SiO₂ surface are also shown in **Figure 3**.

2.3. Cell Adhesion and Cell Surface Area

The response of living cells to micro-/nanostructured surfaces is a well-known and widely investigated phenomenon.^[35] Living cells respond to chemical composition, wettability, topography, stiffness, and stress and these cues^[36] have been found to influence cellular adhesion, morphology, metabolic activity, proliferation, migration, and differentiation.^[37–42] The cellular characterization of SiO₂/parylene C micropillars was assessed by the morphology of 3T3-fibroblasts adhered to micropillar arrays to measure the cell spread area and the proliferation of cells on the micropillars, and qualitatively evaluate the organization of cellular cytoskeleton and the presence of focal contacts via fluorescently labeled actin fibers and vinculin. Since our micropillar arrays differed from the pillar height, we compared the cellular behavior of both arrays via the parameter of pillar

SiO ₂ substrate	O 1s %	C 1s %	Si 2p %	N 1s %
untreated	53.6	19.0	26.0	0.1
piranha	59.4	10.6	29.0	0.2
APTES	53.4	17.8	26.6	2.1
Parylene C substrate	O 1s %	C 1s %	Si 2p %	N 1s %
untreated	0.6	89.5	0.3	0.2
piranha	8.4	80.3	4.4	0.3
APTES	6.9	81.1	3.9	0.7

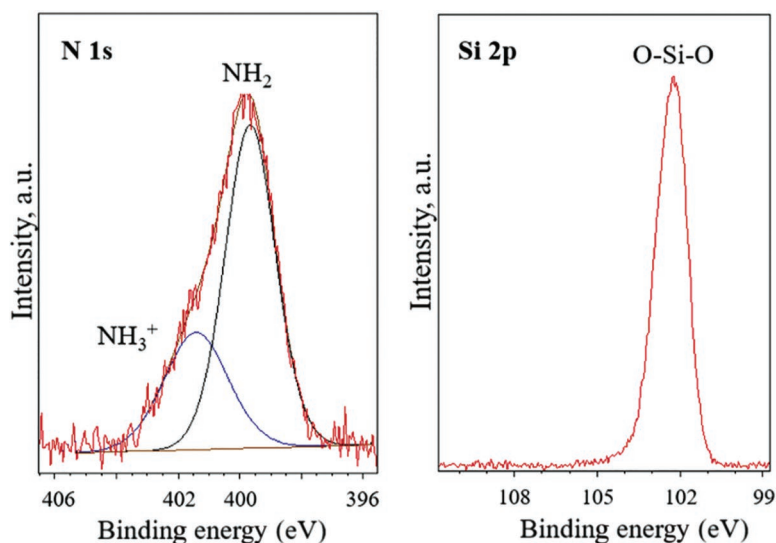


Figure 3. Table shows an elemental analysis of individual steps of SiO₂ and parylene C modification as extracted from the XPS spectrum in percentage; XPS analysis is performed for cleaned untreated SiO₂ and parylene C substrate, SiO₂ and parylene C treated in piranha solution and SiO₂ and parylene C silanized with APTES. The graphs show high-resolution spectra of nitrogen N 1s and silicon Si 2p for the APTES-treated SiO₂ surface.

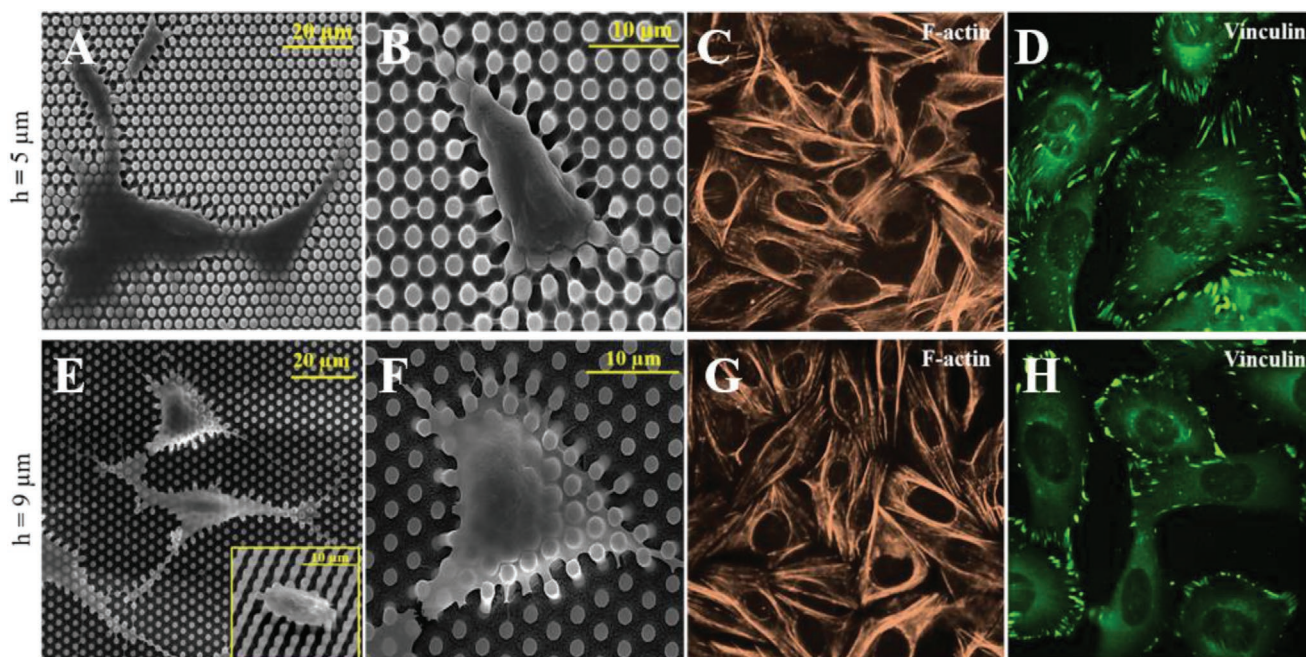


Figure 4. 3T3-fibroblasts on the micropillars with heights of 5 μm (stiffer; upper images) and 9 μm (softer; bottom images), respectively. Scans of the electron microscopy of cells showing the morphology and pillar's deflection (A,B,E,F). Fluorescently labeled actin fibers showing as a red (C, G) and a green staining of vinculin as the protein of the focal contacts (D,H).

stiffness. The morphology of the 3T3-fibroblasts attached to “softer” ($k \approx 4.7 \mu\text{N } \mu\text{m}^{-1}$) and “stiffer” ($k \approx 28 \mu\text{N } \mu\text{m}^{-1}$) pillars did not differ significantly since the shape of the cells ranged from polygonal to elongated (Figure 4A,B,E,F). The shape of 3T3-fibroblasts on both types of micropillars corresponds to the typical morphology in the stationary state of well-spread fibroblastic cells. The cells on both substrates had more extruding protrusions and larger lamellae. The staining of the actin filaments revealed prominent stress fibers that crossed the cell from end to end, and no disruption in the cytoskeletal organization was observed for either softer or stiffer micropillars (Figure 4C,G). A notable finding was observed for the vinculin staining, as shown in Figure 4D,H. The cells on “stiffer” micropillars (Figure 4D) showed a higher number of focal contacts, compared to the “softer” substrate (Figure 4H) and were larger in size and more distributed over the whole cells. The cell surface area was calculated from previously obtained fluorescence

images of cells using ImageJ software. We set the scale to know the number of pixels per area and the individual cells were dragged to measure their surface area. The statistical analysis was performed on hundred cells for each micropillar substrate. The evaluation of the cell spreading area revealed significantly larger areas for cells cultured on “stiffer” micropillars, compared to a “softer” surface (Figure 5A). These findings revealed better adhesion and cell contact with the underlying micropillars on the “stiffer” substrate since the larger surface area and extensive focal contacts were enhanced here, compared to the “softer” substrate.

2.4. Proliferation Assay

Our results from cell adhesion were further supported by the experiment of cell proliferation on both substrates. The

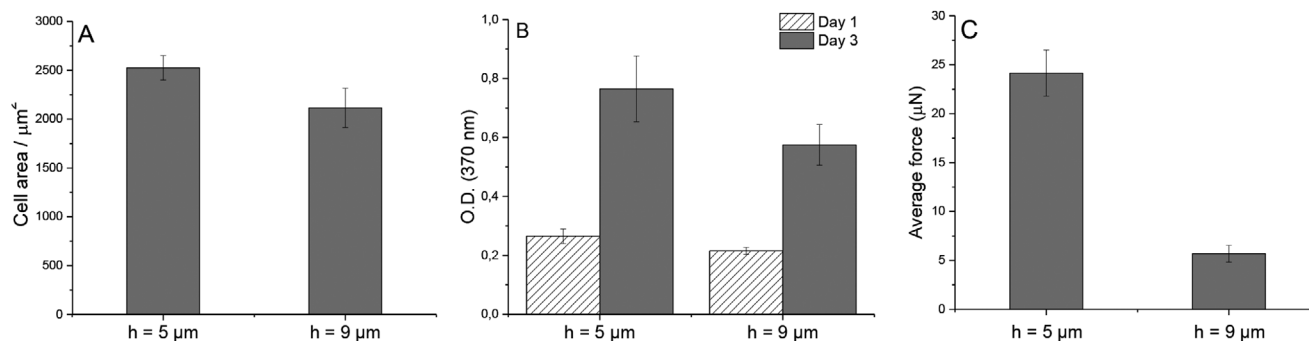


Figure 5. Evaluation of the spreading area of 3T3-fibroblasts per surface area (A). BrdU proliferation assay of fibroblasts on nanopillars (B). The average cellular force calculated from the periphery of stationary cells (C).

measurement of 5-bromo-2'-deoxyuridine (BrdU) was performed on days one and three (Figure 5B). This assay measured the incorporation of BrdU into the newly synthesized DNA and introduced the most reliable information about cell division. On day one, no significant differences in cell proliferation were observed between “stiffer” and “softer” micropillars, while on day three, a significantly higher proliferation rate could be seen for the “stiffer” micropillar array. The higher proliferation of cells could be a consequence of the enhanced cell adhesion on “stiffer” micropillars.

To conclude our preliminary observations of the cytocompatibility of SiO₂/parylene C micropillars, the 3T3-fibroblasts sensed the different stiffness of micropillars due to changes in cell adhesion and proliferation, which is in good agreement with the literature.^[43,44] From a more general perspective, neither micropillar arrays showed any cytotoxic effect in terms of cell viability and adhesive properties.

2.5. Estimation of Cellular Force

A preliminary examination was performed to substantiate the suitability of SiO₂/parylene C micropillars to probe cellular force. The assessment was performed on stationary polygonal-shaped fibroblasts selected from SEM images in order to obtain a symmetric cellular force profile. The deflection of the micropillars were measured from their original, undeflected position using Image J software. The extent of the deflection was then used to quantify the traction forces generated by the 3T3-fibroblasts by applying Equation (1). To compare the force exerted from the cells on the “stiffer” and “softer” micropillars, the average force was calculated from the pillar's deflection that occurred on the cell periphery (Figure 5C). Our finding showed that the cells on the “stiffer” micropillars exert almost five times more traction force than those cultured on the “softer” substrate. For 3T3-fibroblasts, the average traction force calculated at the cell periphery was $\approx 25 \mu\text{N}$ and $\approx 5 \mu\text{N}$ for “stiffer” and “softer” micropillars, respectively. This corresponds well with the findings obtained from our cell adhesion and viability assays. The stronger traction force could be a consequence of the cells' ability to achieve more stable adhesion on an appropriate substrate and to increase the cell surface area to maintain effective cellular homeostasis. Our findings also support the general trend of cellular force to be stronger on a stiffer than a softer substrate;^[45] the force is suggested to be strongest at the lamellipodia and to decrease toward the center of the cell, as has been reported previously.^[4]

The cellular force measured for different aspect ratios of commonly used micropillars made of PDMS as a very soft polymer has been reported around tens to hundreds of nN.^[13] High aspect ratio polycarbonate pillars as the stiffer polymer with Young's modulus, a little bit lower than parylene C, have been fabricated by nanoimprinting method.^[4] Considering the same dimension of parylene C and polycarbonate micropillars, the difference in spring constant is $\approx 2 \mu\text{N} \mu\text{m}^{-1}$ which does not have to be such a significant difference but it can be still successfully recognizable by sensitive cells. Further, we would like to show that cells can sense and bent pillars with very high spring constant of $\approx 28 \mu\text{N} \mu\text{m}^{-1}$ with cellular force calculated $\approx 25 \mu\text{N}$ which has not been published in the literature so far.

3. Conclusion

We introduced “top-down” fabrication of a highly ordered array of SiO₂/parylene C micropillars for use as a probe for the quantification of cellular traction force. Micropillars with different spring constants were fabricated from the parylene C and a thin layer of SiO₂ was introduced to the top of each pillar to enable the covalent binding of proteins via silanization. The experimental results confirmed the patterning of micropillars via the selective chemistry of the SiO₂ interface and the chemistry performed on the parylene C micropillars' sidewalls. Such patterned micropillars constitute a technological advance that eliminates the micro-contact printing of proteins on the top of micropillar array. The cytocompatibility of SiO₂/parylene C micropillars was assessed by the morphology of 3T3-fibroblasts adhered to micropillar arrays, measuring the cell spread area, proliferation of cells, qualitative evaluations of the cytoskeleton, and the development of focal contacts. Our results did not show a cytotoxic effect of the micropillar-based substrates but did indicate a dependence on stiffness. A stiffer micropillar array enhanced the cell adhesion and proliferation rate and consequently led to a stronger cell traction force.

Parylene C is a highly rigid material with a Young's modulus of ≈ 4 GPa; it is more rigid than other polymers used for pillar fabrication and thus broadens the range of material stiffness that can be probed by cells or used as the cellular sensor. We revealed that SiO₂/parylene C micropillars with a high stiffness corresponding to the spring constant $k = \approx 4.8 \mu\text{N} \mu\text{m}^{-1}$ and $\approx 28 \mu\text{N} \mu\text{m}^{-1}$ were sensed by the cells, and that the traction force can be determined even on such stiff micropillars which could give us the information about the magnitude of cellular forces. To conclude, SiO₂/parylene C micropillars demonstrate innovative concept of a flexible micropillar substrate for the quantification of the cell traction force that eliminates the micro-contact printing of proteins, and provides a substrate with higher stiffness.

4. Experimental Section

Fabrication of Micropillars: The array of parylene micropillars with the SiO₂ layer on top of the pillars was fabricated via a “top-down” technological process (Figure S1, Supporting Information). Briefly, a 10 μm thick layer of parylene C (Palmchem) was deposited on the Si wafer using the chemical vapour deposition (CVD) method. A 250 nm thin layer of SiO₂ was deposited via a plasma-enhanced CVD at 100 °C. The deposition of a 500 nm thin Ti layer using the electron beam evaporation technique was followed by standard UV photolithography using the photoresist (PR) AZ 5214E. Photolithography of PR created the pattern of hexagonally arranged features with diameter of 2 μm and center-to-center distance of 4 μm . The titanium and SiO₂ layer was then etched using reactive-ion etching (RIE) in Cl₂ plasma and Ar/CHF₃ plasma by means of chlorine and fluorine-based RIE. Finally, the wafer was placed into the ion beam etching (IBE) instrument employing pure O₂ plasma to etch the parylene C from the areas uncovered by Ti/SiO₂. The PR was completely removed during the IBE process and the Ti residue was additionally removed using chlorine-based RIE.

Micropillar Patterning and Characterization: The micropillar morphology was analyzed via a scanning electron microscopy (SEM, TESCAN MIRA II) and an EDX analysis. The chemical patterning of the micropillars was performed as described in detail in Figure S2,

Supporting Information. The array of the micropillars was treated with piranha solution at a ratio of 5:3 (30% H₂O₂ and 96% H₂SO₄) for 10 min. The SiO₂ layer was silanized with 3-aminopropyl-triethoxysilane (APTES, Sigma) via CVD technique in a vacuum chamber at 120 °C for 30 min. The process of silane deposition spanned 30 min. The micropillars were then incubated with 0.5% (v/v) Pluronic F-127 in phosphate buffer (PBS) (Sigma) to selectively coat the parylene C. The fibronectin (50 µg·mL⁻¹ in PBS, Sigma) was covalently attached via 0.5% (v/v) glutaraldehyde (Sigma) cross-linked to the amino-functionalized SiO₂ layer. The modified micropillar array was characterized by the measurement of the CA (Phoenix 300, SEO) by applying water drop on the surface. The CA was evaluated using Surfaceware 8 software and the statistical analysis was performed on 10 drops from each step of modified surface. The CA measurement was accompanied by X-ray photoelectron spectroscopy analysis (XPS; AXIS SupraTM Kratos Analytical) for the quantification of the elemental composition on the material surface via CasaXPS software. A fluorescence microscopy (Zeiss) of the collagen-FITC conjugate (0.1 mg mL⁻¹ in PBS, Sigma) has been performed to confirm the covalent immobilization of the protein.

Cell Culture and Immunostaining: 3T3 fibroblasts (ATCC) were cultured in a complete DMEM supplemented with 10% (v/v) of fetal bovine serum and antibiotics (streptomycin 100 µg mL⁻¹, penicillin 100 UI mL⁻¹). Fibroblasts were harvested every third day. For immunofluorescence staining, the cells were fixed in 4% (w/v) of paraformaldehyde in PBS for 20 min and permeabilized in 2% (w/v) bovine serum albumin in 0.5% (v/v) Triton X-100 in PBS for 2 h. All chemicals were purchased at Sigma Aldrich. A fluorescence microscope was used to visualize the actin fibers stained with Alexa Fluor 533 RED phalloidin (ready probes from Thermo Fisher Scientific) for 30 min. The vinculin, being the protein of the focal contacts, was detected by the mouse anti-vinculin antibody (10 mg mL⁻¹, 1:100 dilution in PBS, Sigma) for 1 h and an Alexa Fluor 488 goat anti-mouse antibody (2 mg mL⁻¹, 1:100 dilution in PBS, Thermo Fisher Scientific) for 60 min.

Proliferation Assay: The BrdU (5-bromo-2'-deoxyuridine) cell proliferation assay was performed by plating 1 × 10⁴ cells onto the micropillar surface and cultured inside the humidified incubator at 37 °C and 5% CO₂. The proliferation assay was performed on days one and three, following the manufacturer's protocol (Cell proliferation ELISA, BrdU; Roche). Briefly, 10 µl of BrdU solution was added to each sample and re-incubated for an additional 2 h. The labeling medium was then removed and the cells were fixed and denatured with 200 µl of FixDenat solution for 30 min. The FixDenat solution was replaced with 100 µl of a BrdU-peroxidase (POD) antibody solution and incubated at room temperature for 90 min. The samples were rinsed three times with a buffer solution and incubated with 100 µl of the substrate solution for 20 min. The absorbance was measured at 370 nm using the microplate spectrophotometer.

SEM Characterization of Traction Force: SEM imaging was performed after the critical drying of fixed cells on patterned micropillars at an ethanol gradient from 50% to 100% for 5 min for each dilution. The dried cells were evaporated with ≈10 nm layer of gold before imaging to avoid sample charging. The deflection of the micropillars due to the cell traction force was obtained directly from the SEM images. The pillar bending was analyzed with ImageJ software on non-migrating cells at the edge of the extended lamellipodia from the initial position. Scale included in acquired SEM images and straight line selection tool were used for direct distance measurement. Since the fabricated pattern was repetitive, and thus, the distance between each two closest micropillars remains constant, we measured the shift between unbent and bent micropillars as the center-to-center distance. The average cellular traction force (*F*) from 15 imaged cells was calculated with Hooke's law (Equation 1) for higher (*h* = 9 µm) and lower (*h* = 5 µm) micropillars, respectively.

Statistical Analysis: A proliferation assay was conducted in triplicate for each substrate and the average cellular force was calculated for ten cells from each substrate. A student's *t*-test was used to determine significant differences between the groups. *P*-values of <0.05 were considered to be statistically significant.

Supporting Information

Supporting Information is available from the Wiley Online Library or from the author.

Acknowledgements

The authors would like to acknowledge the financial support provided by GACR Project Number GA19-04270Y from the Czech Republic. Thanks also go to Tomas Lednický for the XSP measurements.

Conflict of Interest

The authors declare no conflict of interest.

Data Availability Statement

Research data are not shared.

Keywords

cellular force, mechanobiology, micropillars, parylene C, silanization, silicon dioxide

Received: November 10, 2020

Revised: January 5, 2021

Published online: January 25, 2021

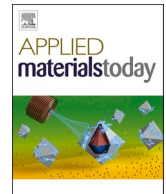
- [1] T. Kojima, A. Husari, M. P. Dieterle, S. Fontaine, O. Prucker, P. Tomakidi, J. R uhe, *Adv. Mater. Interfaces* **2020**, *17*, 1901806.
- [2] R. H. W. Lam, Y. Sun, W. Chen, J. Fu, *Lab Chip* **2012**, *12*, 1865.
- [3] M. Nikkhal, F. Edalat, S. Manoucheri, A. Khademhosseini, *Biomaterials* **2012**, *33*, 5230.
- [4] F. Viel, D. Granados, A. Ayuso-Sacido, I. Rodr guez, *Adv. Funct. Mater.* **2016**, *26*, 5599.
- [5] G. Bao, S. Suresh, *Nat. Mater.* **2003**, *2*, 715.
- [6] T. Lendenmann, T. Schneider, J. Dumas, M. Tarini, C. Giampietro, A. Bajpai, W. Chen, J. Gerber, D. Poulidakos, A. Ferrari, D. Panozzo, *Nano Lett.* **2019**, *19*, 6742.
- [7] C. G. Galbraith, M. P. Sheetz, *Proc. Natl. Acad. Sci.* **1997**, *94*, 9114.
- [8] J. L. Tan, J. Tien, D. M. Pirone, D. S. Gray, K. Bhadriraju, C. S. Chen, *Proc. Natl. Acad. Sci.* **2003**, *100*, 1484.
- [9] B. D. Hoffman, C. Grashoff, M. A. Schwartz, *Nature* **2011**, *475*, 316.
- [10] R. Farhadifar, J.-C. R oper, B. Aigouy, S. Eaton, F. J licher, *Curr. Biol.* **2007**, *17*, 2095.
- [11] R. Serrano, A. Aung, Y.-T. Yeh, S. Varghese, J. C. Lasheras, J. C. del  lamo, *Biophys. J.* **2019**, *117*, 111.
- [12] P. Roca-Cusachs, V. Conte, X. Trepat, *Nat. Cell Biol.* **2017**, *19*, 742.
- [13] W. J. Polacheck, C. S. Chen, *Nat. Methods* **2016**, *13*, 415.
- [14] S. Ghassemi, G. Meacci, S. Liu, A. A. Gondarenko, A. Mathur, P. Roca-Cusachs, M. P. Sheetz, J. Hone, *Proc. Natl. Acad. Sci.* **2012**, *109*, 5328.
- [15] M. Gupta, L. Kocgozlu, B. R. Sarangi, F. Margadant, M. Ashraf, B. Ladoux, *Methods in Cell Biology*, Elsevier, New York **2015**, pp. 289–308.
- [16] I. Schoen, W. Hu, E. Klotzsch, V. Vogel, *Nano Lett.* **2010**, *10*, 1823.
- [17] M. Kim, B.-U. Moon, C. H. Hidrovo, *J. Micromech. Microeng.* **2013**, *23*, 095024.

- [18] J. Fu, Y.-K. Wang, M. T. Yang, R. A. Desai, X. Yu, Z. Liu, C. S. Chen, *Nat. Methods* **2010**, *7*, 733.
- [19] Y. Sun, L.-T. Jiang, R. Okada, J. Fu, *Langmuir* **2012**, *28*, 10789.
- [20] Y.-C. Yeh, E. A. Corbin, S. R. Caliri, L. Ouyang, S. L. Vega, R. Truitt, L. Han, K. B. Margulies, J. A. Burdick, *Biomaterials* **2017**, *145*, 23.
- [21] P. A. Janmey, R. T. Miller, *J. Cell Sci.* **2011**, *124*, 9.
- [22] Z. Li, H. Persson, K. Adolphsson, L. Abariute, M. T. Borgström, D. Hessman, K. Åström, S. Oredsson, C. N. Prinz, *Nanoscale* **2017**, *9*, 19039.
- [23] N. Biais, D. Higashi, M. So, B. Ladoux, *Methods Mol. Biol.* **2012**, *799*, 197.
- [24] E. I. Liang, E. J. Mah, A. F. Yee, M. A. Digman, *Integr. Biol.* **2017**, *9*, 145.
- [25] L. Amato, S. S. Keller, A. Heiskanen, M. Dimaki, J. Emnéus, A. Boisen, M. Tenje, *Microelectron. Eng.* **2012**, *98*, 483.
- [26] C. H. Rasmussen, P. M. Reynolds, D. R. Petersen, M. Hansson, R. M. McMeeking, M. Dufva, N. Gadegaard, *Adv. Funct. Mater.* **2016**, *26*, 815.
- [27] A. Perl, D. N. Reinhoudt, J. Huskens, *Adv. Mater.* **2009**, *21*, 2257.
- [28] A. Bernard, J. P. Renault, B. Michel, H. R. Bosshard, E. Delamar, *Adv. Mater.* **2000**, *12*, 1067.
- [29] M. W. H. Kirkness, C. S. Korosec, N. R. Forde, *Langmuir* **2018**, *34*, 13550.
- [30] B. J. Raos, C. S. Doyle, M. C. Simpson, E. S. Graham, C. P. Unsworth, *Sci. Rep.* **2018**, *8*, 2754.
- [31] P. Saengdee, W. Chairiratanakul, W. Bunjongpru, W. Sripumkhai, A. Srisuwan, W. Jeamsaksiri, C. Hruanun, A. Poyai, C. Promptmas, *Biosens. Bioelectron.* **2015**, *67*, 134.
- [32] J.-C. Wang, W. Liu, Q. Tu, C. Ma, L. Zhao, Y. Wang, J. Ouyang, L. Pang, J. Wang, *Analyst* **2015**, *140*, 827.
- [33] J. Jin, F. Huang, Y. Hu, W. Jiang, X. Ji, H. Liang, J. Yin, *Colloids Surf., B* **2014**, *123*, 892.
- [34] S. Stolnik, B. Daudali, A. Arien, J. Whetstone, C. R. Heald, M. C. Garnett, S. S. Davis, L. Illum, *Biochim. Biophys. Acta* **2001**, *1514*, 261.
- [35] X. Li, L. Lu, J. Li, X. Zhang, H. Gao, *Nat. Rev. Mater.* **2020**, *5*, 706.
- [36] G. Zan, Q. Wu, *Adv. Mater.* **2016**, *28*, 2099.
- [37] Y. Lai, J. Huang, Z. Cui, M. Ge, K.-Q. Zhang, Z. Chen, L. Chi, *Small* **2016**, *12*, 2203.
- [38] B. S. Eftekhari, M. Eskandari, P. A. Janmey, A. Samadikuchaksaraei, M. Gholipourmalekabadi, *Adv. Funct. Mater.* **2020**, *30*, 1907792.
- [39] J. I. Kim, T. I. Hwang, J. C. Lee, C. H. Park, C. S. Kim, *Adv. Funct. Mater.* **2020**, *30*, 1907330.
- [40] Z. Fohlerova, A. Mozalev, *J. Mater. Chem. B* **2019**, *7*, 2300.
- [41] O. Bilek, Z. Fohlerova, J. Hubalek, *PLoS One* **2019**, *14*, e0214066.
- [42] J. Song, J. H. Shawky, Y. Kim, M. Hazar, P. R. LeDuc, M. Sitti, L. A. Davidson, *Biomaterials* **2015**, *58*, 1.
- [43] L. Trichet, J. Le Digabel, R. J. Hawkins, S. R. K. Vedula, M. Gupta, C. Ribault, P. Hersen, R. Voituriez, B. Ladoux, *Proc. Natl. Acad. Sci.* **2012**, *109*, 6933.
- [44] X. Liu, R. Liu, B. Cao, K. Ye, S. Li, Y. Gu, Z. Pan, J. Ding, *Biomaterials* **2016**, *111*, 27.
- [45] M. Sun, G. Chi, P. Li, S. Lv, J. Xu, Z. Xu, Y. Xia, Y. Tan, J. Xu, L. Li, Y. Li, *Int. J. Med. Sci.* **2018**, *15*, 257.



Contents lists available at ScienceDirect

Applied Materials Today

journal homepage: www.elsevier.com/locate/apmt

Nature-inspired parylene/SiO₂ core-shell micro-nano pillars: Effect of topography and surface chemistry

Xiaocheng Liu^a, Zdenka Fohlerová^b, Imrich Gablech^b, Martin Pumera^{c,d,e}, Pavel Neuzil^{a,*}^a Northwestern Polytechnical University, Ministry of Education Key Laboratory of Micro/Nano Systems for Aerospace, Department of Microsystem Engineering, School of Mechanical Engineering, 127 West Youyi Road, Xi'an, Shaanxi 710072, PR China^b Faculty of Electrical Engineering and Communication, Brno University of Technology, Technická 3058/10, 616 00 Brno, Czech Republic^c Department of Medical Research, China Medical University Hospital, China Medical University, No. 91 Hsueh-Shih Road, Taichung 40402, Taiwan^d Faculty of Electrical Engineering and Computer Science, VSB - Technical University of Ostrava, 17. listopadu 2172/15, 70800 Ostrava, Czech Republic^e Department of Chemical and Biomolecular Engineering, Yonsei University, 50 Yonsei-ro, Seodaemun-gu, Seoul 03722, Korea

ARTICLE INFO

Keywords:

Superhydrophobic
Gecko mimicking surface
SiO₂ interface layer
surface covalent bonding
Silanization

ABSTRACT

We investigated the synergy of surface topography and chemistry in micro/nanostructured pillars inspired by nature, specifically mimicking tokay gecko (*Gekko gecko* Linnaeus, 1758) feet and sacred lotus (*Nelumbo nucifera* Gaertn., 1788) leaves. The aim is to understand and replicate their adhesive and self-cleaning properties for diverse applications. Through a detailed fabrication process and chemical modifications, the surfaces exhibit superhydrophobic characteristics. The research precisely examines the fabrication of surfaces with well-defined micropillars using lithography and deep silicon substrate etching. Diverse surface treatments, including silanization and O₂ plasma, are applied to tailor the chemical composition of microstructured surfaces. Utilizing a ≈ 5 nm thin SiO₂ interface layer, the study reveals superhydrophobic properties post-silanization and an eightfold increase in adhesion force (F_A) between the studied surface and reference surfaces. F_A measurements using atomic force microscopy reveal an eightfold increase in adhesion on both flat and microstructured surfaces, emphasizing the transformative effects of microstructures on surface morphology. The findings highlight the potential for multifunctional surface designs, elucidating that superhydrophobic properties correlate with structure topography while F_A amplitude is predominantly determined by surface termination. Inspired by nature, this research unveils novel possibilities in functional materials and surface engineering, with broad implications across various applications.

1. Introduction

Surface interactions, which span the domains of both liquid–solid and solid–solid interfaces, play a vital role in numerous biological and physical phenomena intrinsic to our everyday environment [1]. From the delicate adherence of dew drops to flower petals to the remarkable grip of a gecko on a glass surface, these interactions often surpass the capabilities of human-made technologies. Such phenomena have spurred extensive research aimed at understanding and replicating these natural capabilities in fields such as engineering, medicine, and innovative technology.

The gecko, famous for its ability to climb vertical surfaces and even suspend itself upside down on ceilings, stands as a particular point of interest [2]. Researchers across disciplines have been intrigued by the

extraordinary adhesive properties of the gecko's feet, especially the hair-like setae that densely cover its toes and exhibit tenfold the adhesion force (F_A) expected from theoretical calculations [3,4]. The F_A value of the tokay gecko (*Gekko gecko* Linnaeus, 1758) can surpass an astonishing ≈ 25 N over a small area, despite its modest weight of ≈ 46 g [5]. Many researchers have tried to synthesize materials mimicking the hierarchical architecture and inherent properties of gecko feet [6], focusing on the dynamics of attachment and detachment [7]. Understanding the underlying mechanisms that provide geckos with this remarkable adherence to surfaces, however, remains elusive. The source of this F_A —whether derived mainly from surface chemistry, surface topography, or a combination of both—is a subject that still challenges researchers [8,9]. A strategy to differentiate between the effects of surface chemistry and topography involves the use of controlled

* Corresponding author.

E-mail address: pavel.neuzil@nwpu.edu.cn (P. Neuzil).

<https://doi.org/10.1016/j.apmt.2024.102117>

Received 18 November 2023; Received in revised form 25 January 2024; Accepted 5 February 2024

Available online 22 February 2024

2352-9407/© 2024 Elsevier Ltd. All rights reserved.

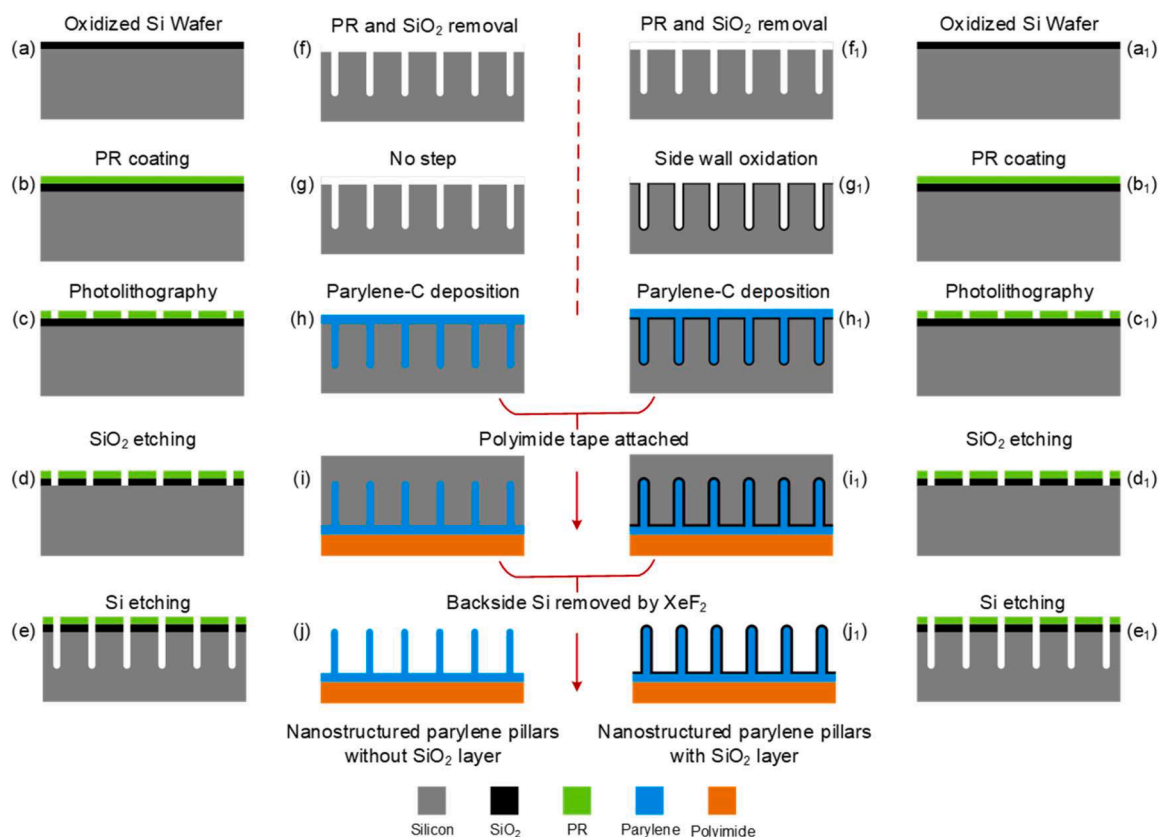


Fig. 1. Biomimetic gecko spatulae were fabricated using flexible nanostructured parylene (left) and parylene/SiO₂ (right) hollow micropillars. (a, a₁) A thermally oxidized Si substrate (b, b₁) was coated with a layer of PR (c, c₁) and patterned through a standard lithography process (d, d₁). The SiO₂ layer was removed by RIE (e, e₁), and the Bosch process etched the underlying Si; PR was removed (f, f₁) and wafers meant to have SiO₂ surface were oxidized (g₁). parylene-C was deposited (h, h₁), polyimide tape attached (i, i₁), and Si substrate removed by XeF₂ (j, j₁).

environments conducting a force-distance measurement (FDM) [10]. Such a technique allows specific measurement of the F_A value of individual gecko hair [11] or spatulae [9]. However, multifaceted interaction forces at the interface, such as van der Waals forces [8], capillary forces (F_C) [9], and other physical phenomena, render these assessments complex.

On the other hand, sacred lotus (*Nelumbo nucifera* Gaertn., 1788) leaves present a fascinating counterpart to gecko feet, showcasing contrasting surface characteristics [12]. Both structures exhibit superhydrophobicity at the macroscale, with a water surface contact angle (θ) of $\approx 150^\circ$ and self-cleaning properties commonly referred to as the *lotus effect* [13], but their surface behaviors are fundamentally different. Lotus leaves possess complex micro- and nanostructures that allow them to repel water and dirt effectively, creating self-cleaning surfaces that have inspired various applications ranging from anti-fouling coatings to water-resistant textiles [14,15]. Unlike the adhesive nature of gecko feet, lotus leaves are notable for their repulsive qualities, phenomena attributed to the unique combination of surface chemistry and topographical arrangement of papillae on the leaf surface [16]. The difference in contact force despite both materials being superhydrophobic, thus self-cleaning [17], presents an exciting opportunity for researchers to explore the underlying mechanisms that govern the behavior of these two naturally occurring nanostructured systems [12].

Silanes are synthetic hybrid C-Si compounds widely used to promote adhesion of other materials to Si-based substrates. Trialkoxysilanes produce hydrophobic surfaces that react chemically with methacrylate-containing resins to form covalent bonds, typically achieved at elevated temperature and lowered pressure. Hexamethyldisilazane (HMDS) is widely used in microelectronics fabrication to promote adhesion of a photoresist (PR) to the substrate via covalent bonding. Some other

silanes modify surfaces, also forming hydrophobic surfaces such as 1H, 1H, 2H, 2H-perfluorodecyltriethoxysilane (FAS-17) [18]. Another silane, (3-aminopropyl)triethoxysilane, is often employed to form a cross-link between a Si-based surface and proteins [19].

In this study, we focus on explaining these interesting aspects, concentrating on the distinct and interconnected roles of surface topography and surface chemistry in defining the F_A value. Through the design and fabrication of artificial surfaces that mirror natural structures such as gecko feet, using an established polymer molding technique, we strive to uncover the synergy between surface topography and chemistry.

We fabricated an array of parylene-C/SiO₂ core-shell microstructured pillars, each subjected to various chemical surface modifications. Parylene, a polymer renowned for its biocompatibility, excellent electrical insulation properties, *chemical resistance*, and *extremely low thermal conductivity*, is typically formed through chemical vapor deposition. This *material* is a popular choice in electronics, medical devices, and aerospace applications. A SiO₂ layer was used as an interface between selected silane and parylene to get the surface contact angle of our choice. Together, microstructures made of these materials were ideal for our exploration of adhesive and repulsive phenomena. Adhesion strength was measured using atomic force microscopy (AFM), and we implemented FDM technique to investigate the influence of topography and chemistry on wettability and F_A value. Our experiments indicated that the self-cleaning properties of these surfaces were predominantly a result of their micro/nanostructuring rather than the materials themselves. This study offers fresh insights into the adhesive behaviors of superhydrophobic surfaces and paves the way for the development of innovative artificial nanostructures crafted from polymer materials. It marks a significant stride toward replicating complex natural systems

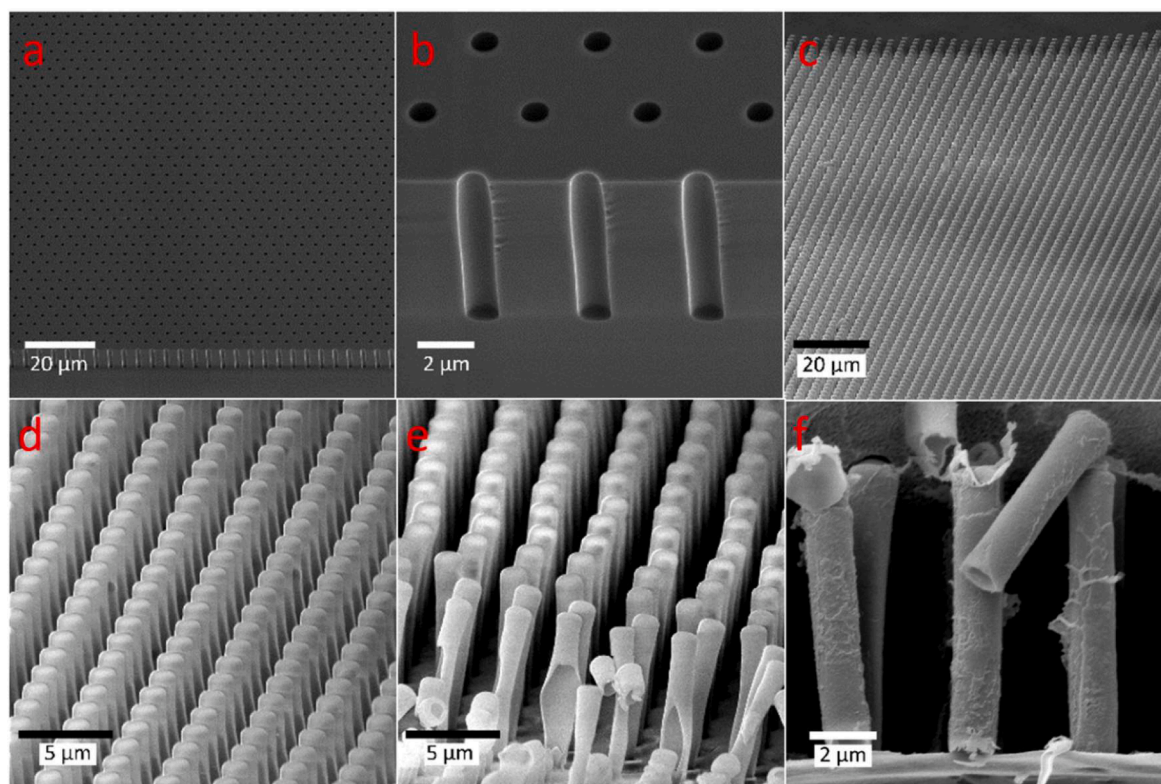


Fig. 2. Scanning electron micrographs of fabrication steps of micropillars covered with an SiO₂ layer. (a) Patterned thermally oxidized Si substrate after SiO₂ and Si are etched by DRIE into the desired depth of $\approx 7.7 \mu\text{m}$; (b) a detail of trench in Si substrate; (c, d) an array of parylene-C pillars after Si removal by the XeF₂ vapor; (e, f) a detailed view of a few pillars showing their hollow nature.

like gecko feet and lotus leaves, thereby advancing our capacity to design optimized and effective materials.

2. Materials and methods

2.1. Micropillars layout design and fabrication

Utilizing the JavaScript-based Nanolithography toolbox [20,21], we designed several arrays of circular holes with an identical diameter of 1 μm and 4 μm X direction pitch. A single chip had a dimension of (5 \times 5) mm², consisting of 1,154,000 pillars.

Si wafers with (100) orientations and dimensions of ≈ 100 mm in diameter and 0.3 mm in thickness were thermally oxidized to obtain a SiO₂ layer of ≈ 350 nm thickness. Next, we spin-coated the wafers with positive PR, patterned circles in a hexagonal configuration onto the wafer surface using a step-and-repeat camera for lithography, and then postbaked the PR at ≈ 110 °C for ≈ 50 s. After development with a tetramethylammonium hydroxide-based solution, the surface was treated with O₂ plasma to remove any remaining PR in the holes' areas.

Once the PR was removed, the SiO₂ layer was etched using reactive ion etching (RIE) that relied on CHF₃/O₂-based chemistry. Then, the exposed Si areas inside the circles were etched to a depth of $\approx 7.7 \mu\text{m}$ using a Bosch process [22] modified to suppress the scalloping effect [23] by an inductively coupled plasma deep RIE (DRIE) system. This modified recipe lowered the pressure to 1.5 Pa and reduced the time for etching by SF₆ and sidewall passivation by C₄F₈ to 3 s and 2 s, respectively. It also lowered the substrate temperature to -10 °C during DRIE and minimized the scalloping effect (Fig. 1A-C).

The PR was stripped off using O₂ plasma for 5 min, set power, and O₂ flow rate of 2000 W and 80 sccm·min⁻¹, respectively. The Si wafers were subsequently cleaned from the potential residues with boiling H₂SO₄/H₂O₂ (piranha) solution for ≈ 5 min. After removing the SiO₂ layer with an NH₄F/HF solution, we performed thermal oxidation to grow a new

SiO₂ layer, targeting a thickness of 10 nm. Oxidation was performed in a furnace at a temperature of ≈ 1050 °C for ≈ 3 min in a dry O₂ environment.

The final step in the fabrication process was the deposition of parylene-C at a low pressure of ≈ 1.6 Pa, targeting a thickness of $\approx 5 \mu\text{m}$. The wafers were then cut into square chips with an area of ≈ 25 mm². After mounting them onto sticky Kapton tape, we etched away the entire silicon substrate with XeF₂ vapor. Finally, the bare parylene-C membrane with parylene/SiO₂ core-shell micropillars was obtained (Fig. 1d-f).

2.2. Surface modification

The surfaces of flat parylene coated with SiO₂ and parylene/SiO₂ core-shell micropillars were modified using O₂ plasma, HMDS, and 1H,1H,2H,2H-perfluorodecyltriethoxysilane (FAS-17). The O₂ plasma treatment involved exposure to plasma with a set power and time exposure of ≈ 120 W and ≈ 30 s, respectively. An HMDS coating formation followed, exposing the surface to HMDS in a vacuum oven heated to ≈ 150 °C. Oxygen plasma cleaned the surface and terminated it with OH groups, making it highly hydrophilic with well-controlled surface properties [24].

A highly hydrophobic coating was created by silanization of the array with FAS-17 at around 170 °C. Silanization was performed inside a vacuum oven, where $\approx 50 \mu\text{L}$ of FAS-17 was added and activated by heating until the chamber temperature reached ≈ 150 °C. Then, the surface was allowed to react with FAS-17 for ≈ 30 min (Fig. 1g-i).

2.3. Contact angle measurement

Measurements of Θ values were conducted using a goniometer. We placed a 0.5 μL droplet of deionized water (DI H₂O) on both flat and microstructured surfaces, and immediately captured images of the

droplet from a horizontal view. The data reflects the mean value \pm standard deviation from ten individual tests.

2.4. Adhesion force measurement

Assessment of the F_A values from both flat and microstructured surfaces was carried out through an FDM method using an AFM, which has been utilized for determining mechanical and surface properties of vertically aligned carbon nanotubes [25]. Also, to measure the F_A values, we used an Si cantilever with tip and tipless variants for flat and microstructured surfaces, respectively, with a spring constant of $0.03 \text{ N}\cdot\text{m}^{-1}$ in both variants and a nominal radius of 6 nm on the tip variant, and subsequently we conducted 200 repetitions for each surface type. The data was processed in MATLAB to extract the F_A values, average them, and determine the standard deviation. All measurements were conducted in relative humidity and temperature of $\approx 42 \%$ and $22 \text{ }^\circ\text{C}$, respectively.

3. Results

3.1. Surface properties and surface forces

Our study began with the fabrication of arrays of pillars as discussed in previous sections (Fig. 2) and the modification of their surfaces with four different types of chemical treatment. Then, we investigated surface properties and the F_A values on different surfaces. Utilizing a

goniometer, we measured the Θ values by placing a droplet of DI H_2O , with a volume set to $0.5 \mu\text{L}$, on different surfaces. These included both flat and microstructures with the following surface chemistries: untreated SiO_2 surfaces, surfaces treated with O_2 plasma, surfaces silanized with HMDS, surfaces of bare parylene-C, and surfaces silanized with FAS-17 (Fig. 3, Table 1).

Table 1

The results of Θ and F_A on flat and microstructured surfaces. The mean value of F_A was calculated using a nonlinear curve fitting of the histogram with a Gaussian function, as well as the curve width (w) and their standard deviations (σ).

Treatment/surface	Flat surface		Microstructured surface	
	Θ ($^\circ \pm \sigma$)	F_A (nN $\pm \sigma$) w (nN $\pm \sigma$)	Θ ($^\circ \pm \sigma$)	F_A (nN $\pm \sigma$) w (nN $\pm \sigma$)
O_2 plasma treatment	32.8 ± 1.4	6.72 ± 0.01 0.27 ± 0.02	118.3 ± 1.2	50.52 ± 0.05 1.96 ± 0.11
HMDS coating	66.1 ± 1.8	3.21 ± 0.01 0.28 ± 0.02	169.1 ± 0.6	28.88 ± 0.05 0.86 ± 0.09
Bare parylene-C	91.9 ± 1.3	2.29 ± 0.06 0.57 ± 0.20	170.3 ± 1.5	19.18 ± 0.15 2.74 ± 1.14
FAS-17 coating	109.3 ± 0.4	1.883 ± 0.001 0.172 ± 0.002	171.0 ± 0.8	13.25 ± 0.03 0.71 ± 0.07

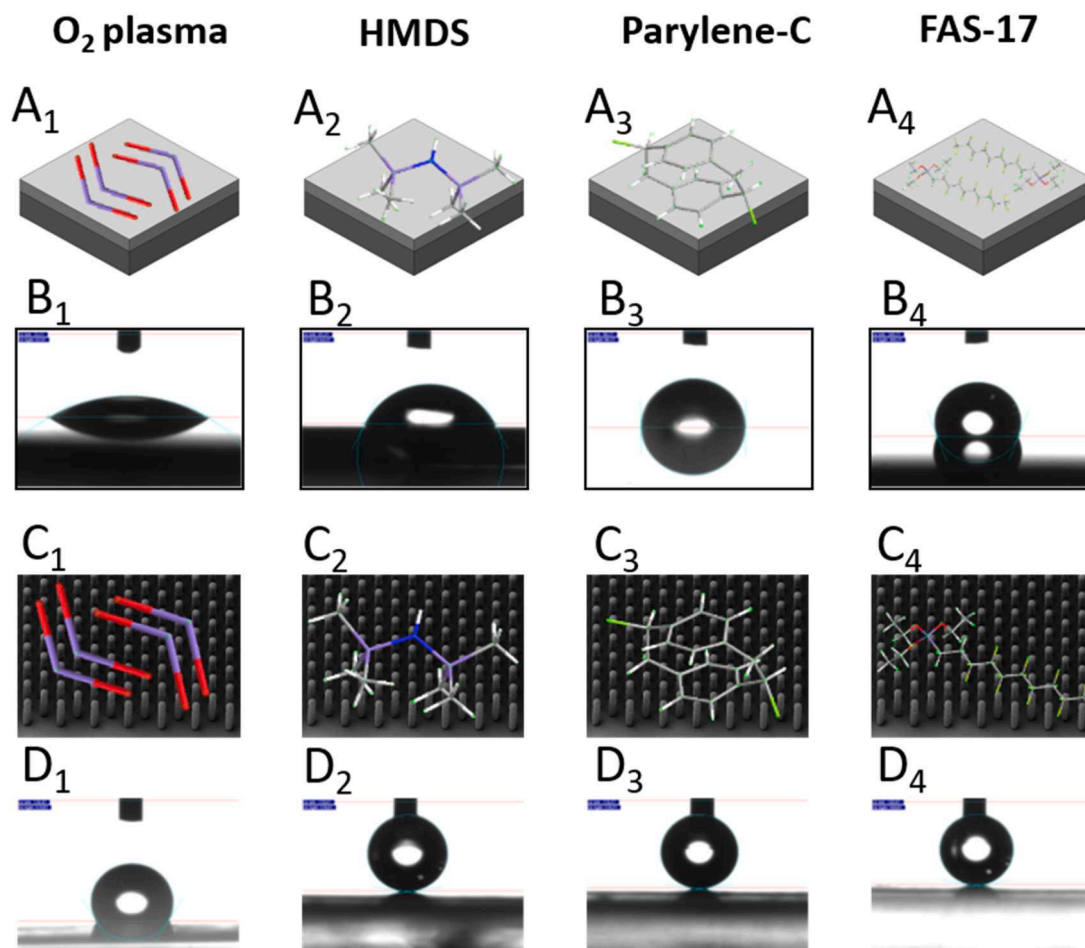


Fig. 3. Contact angle measurement on four different structures. Lower case indexes 1, 2, 3, and 4 are identifying surfaces treated with O_2 plasma, covered with HMDS, left as bare parylene-C, and coated with FAS-17, respectively. (A) Schematic representation of each flat surface with no structures (for reference); (B) photographs showing contact angles on all four surfaces; (C) schematic representation of all four surfaces with microstructured pillars; (D) photographs of water-microstructured surface interaction.

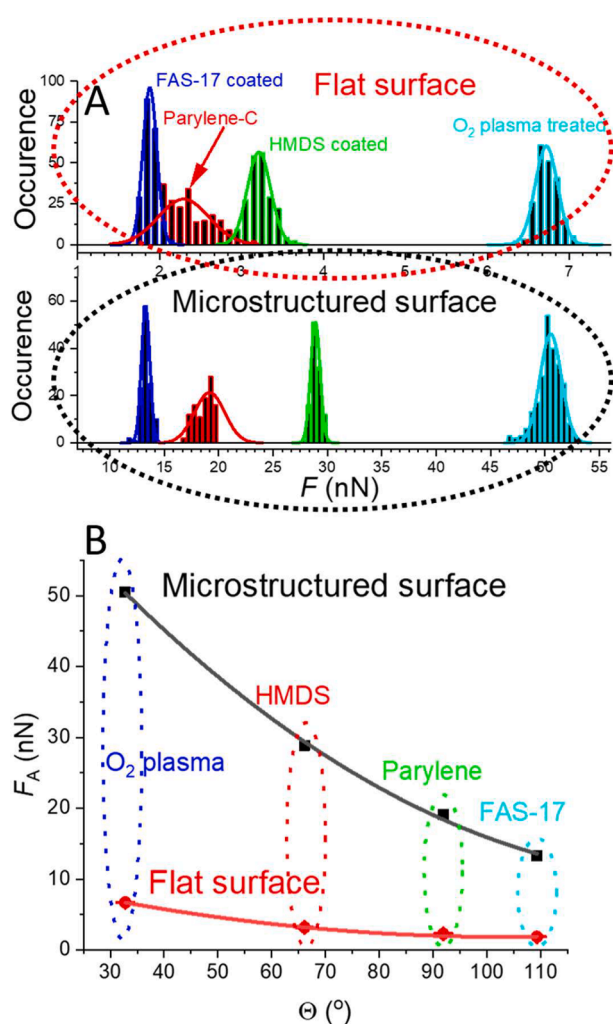


Fig. 4. (A) Contact force measurement on a flat (top) and micro-nano structured (bottom) surface with different treatments. Each measurement was conducted 200×; (B) Extracted F_A values by Gaussian curve fitting, including fitting errors as a function of Θ for flat (red) and micro-nano structured (black) surfaces, both fitted with a polynomial function of the second order showing the same trend.

These diverse surfaces yielded distinct Θ values, emphasizing the significant role of both chemical treatment and physical microstructure in modulating wettability. A similar Θ value of $\approx 170^\circ$, indicating superhydrophobic properties, was obtained for microstructures modified with HMDS and FAS-17, and for those with bare parylene-C. Particularly noteworthy were the reduced Θ values observed for untreated SiO₂ and O₂ plasma-treated surfaces (Table 1). Through an analysis, we attributed this phenomenon to F_C , which induced water infiltration into the interspaces of hydrophobic micropillars.

We also determined the durability of the self-assembly monolayer by measuring the Θ values before and after immersion into a boiling piranha solution for ≈ 5 min. There was no observed change in Θ values after the piranha treatment, demonstrating the layer's excellent durability and the importance of temperature for bond durability.

3.2. Measurement of adhesion force

Our exploration extended into the domain of surface science, where understanding interactions at the micro- and nanoscales is of paramount importance. We conducted an experiment to measure FDM by using an AFM, [26,27] with a cantilever with a tip for flat surfaces or cantilever without a tip for micro-nano structured surfaces. Each experiment was

repeated more than 200 times. Then, we processed data captured by the AFM system using MATLAB script and calculated the F_A values for each surface/cantilever interaction. These results, including histograms, are shown in Fig. 4A. Subsequently, we plotted F_A as a function of Θ for all surfaces (Fig. 4B), showing a quadratic relationship between the F_A value and Θ for both types of surfaces, flat and micro-nano structured.

The total F_A value emerged as a complex function influenced by various factors, including the water meniscus area. This area remained a determinant of F_A , irrespective of whether an AFM tip was interacting with a flat surface or a tipless AFM cantilever was interacting with a microstructured surface. Our results showed that the F_A values changed as follows: O₂ plasma > HMDS > bare parylene > FAS-17, whereas the F_A values were almost seven times lower for the flat surfaces compared to the microstructures (Table 1).

3.3. Self-cleaning experiment

We studied the self-cleaning surface properties by covering the surfaces of interest with silica microspheres ranging in size between 50 μm and 70 μm . These microspheres were distributed on all four types of treated surfaces with micropillars as well as on a lotus leaf. We used a stepper motor equipped with a syringe to dispense 0.5 μL droplets to distinct surfaces. The DI H₂O droplet was pushed against the surface for 5 s and then pulled up (Fig. 5a). First, we tested this method using a lotus leaf (Fig. 5b–c). The circular shape silica microsphere free (Fig. 5d) shows removal of the microspheres due to contact with the water droplet. We performed the same experiment using all four differently treated surfaces (Fig. 5e–h). Subsequent analysis revealed the complete removal of silicon oxide microspheres from the surface areas in contact with the droplets. These interactions simulated real-world events in which water droplets encounter various surfaces, such as rainfall on a lotus leaf or dew formation.

4. Discussion

This research focused on the fabrication of bioinspired micro-structured parylene-C surfaces with micro-nano pillar arrays. We etched an array of holes into Si wafers using SiO₂ layout as a hard mask by utilizing a Bosch process [22] modified to minimize the scalloping effect by getting smooth etched holes into Si. [23] Then, the SiO₂ was removed, Si wafers were oxidized, parylene-C deposited, and Si substrate was removed using XeF₂ vapors, forming an array of pillars. The fabricated parylene-C covered with SiO₂ arrays had an area measuring (5 × 5) mm² and consisting of 1,154,000 pillars.

The micropillars were characterized as having dimensions of approximately 1 μm in diameter and 7.7 μm in length (Fig. 1). We then treated the microstructured surfaces with different chemicals to achieve surfaces with distinct hydrophilic, medium hydrophobic, and highly hydrophobic properties while the structures covered with micropillars had all superhydrophobic properties. These variations were evidenced by the Θ measurements, F_A characterizations, and self-cleaning experiments (Table 1).

We used four different surfaces: O₂ plasma-treated SiO₂, HMDS-coated SiO₂, bare parylene, and FAS-17 coated SiO₂. Both silanes were deposited by a chemical vapor deposition method at a temperature of 150°C. In line with our previous experience, the silanes deposited at this temperature formed stable surface termination, probably due to chemically stable covalent bonds. FAS-17 deposited from vapors at 150°C was immersed into the boiling piranha solution without being affected by it, demonstrating the stability of the FAS-17 coating (unpublished work). The same is valid for HMDS; coating deposited at 150°C forms a stable interface routinely used for priming Si wafers before PR coating is applied. Parylene itself is known as a stable material since it is used to protect keypads and other devices. Finally, SiO₂ is also stable material, as it cannot be oxidized anymore in ambient environment, since Si is already in maximal oxidized form.

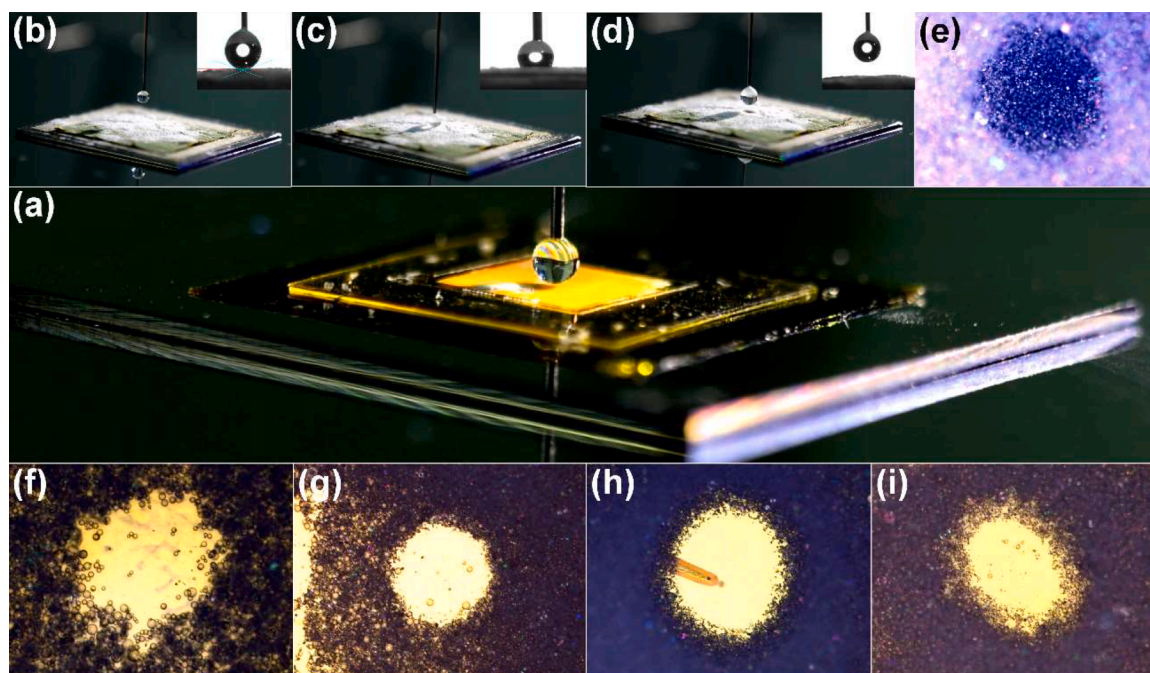


Fig. 5. Self-cleaning experiment. (a) A photograph of a setup of the self-cleaning experiment showing a stainless steel needle with a droplet of DI H₂O above the tested structure made of a nature-mimicking surface; (b) – (d) different stages of self-cleaning testing on a lotus leaf; (e) a spot at the surface of a lotus leaf showing a circular silica-free area with no silica particles; (f) – (i) four different surfaces tested in this work that exhibited nearly identical self-cleaning properties.

Through this detailed investigation, we were able to examine the transformative effects of microstructures on surface morphology and different surface treatments on surface properties. One remarkable result was the induction of superhydrophobic properties on all examined surfaces, regardless of the material's inherent characteristics. Interestingly, based on the Θ value results from various microstructured surfaces (Table 1), it seems that the three surfaces terminated with HMDS, bare parylene, and FAS-17 likely follow the Cassie–Baxter model and their Θ values are independent of the surface termination's value between 169° and 171°. Even surfaces traditionally known for their high hydrophilicity, such as SiO₂ treated with O₂ plasma, exhibited superhydrophobic properties with their Θ values of 118°, suggesting that the transitional superhydrophobic state between the Wenzel and Cassie–Baxter states took place [28]. This revelation not only underscores the impact of surface topography on modifying material properties but also opens up new avenues for creating surfaces with entirely distinct wettability traits.

The relationship between surface type (surface treatment) and F_A value revealed an intriguing eightfold increase in the F_A value on both flat and microstructured surfaces. This substantial increase is fascinating, considering that the intrinsic properties of the surfaces remained unaltered. Our findings suggest that this enhancement is prompted by changes in the water meniscus area, which are, in turn, influenced by the interaction mode—be it between an AFM tip and a flat surface or a tipless cantilever and a microstructured surface.

Additionally, this study provides insights into the role of microstructures in self-cleaning applications. The experimental results demonstrated the feasibility of customizing surfaces to induce unique hydrophilic and hydrophobic attributes. These structures hold significant potential in the development of multifunctional surfaces for enormous applications in areas such as biomedical devices, waterproofing materials, clean energy technologies.

Our research reveals the significant influence of microstructuring and intentional adjustments to surface properties in the realm of surface engineering. We underscore the importance of considering both microstructuring and interaction modes in functional surface design in our current work. We believe that future research will continue to explore

these complexities, driving the development of innovative materials and systems.

The gecko's seta is very complex structure [29], and ideally, we would be able to fabricate it to mimic Mother Nature as closely as possible. Unfortunately, we are not close to being able to fabricate it that well since the diameter of the seta near its anchor measures $\approx 5 \mu\text{m}$. The size of the seta shrinks with its height, and its top is extended into many individual branches measuring $\approx 50 \text{ nm}$, each terminated with a triangular pad. The stiffness of the material is a cube of its diameter, thus the stiffness at the free-end of the spatula is then ≈ 10 [6] lower than the one at the seta bottom. This mechanical structure allows the top to confine along practically any surface while the bottom parts of the setae do not stick to each other due to their stiffness caused by the diameter. This complex structure is indeed a challenge to mimic.

5. Conclusion

Our research has brought to light the tremendous potential of microstructuring in surface engineering through a detailed examination of fabricated micro/nano structured pillars covered with 5 nm thin thermally grown SiO₂ layers that allow surface silanization and thus form covalent bonds at the pillar surface. We have demonstrated the ability to create surfaces with varying properties, from hydrophilic to superhydrophobic. The revelations regarding the self-cleaning mechanism, the substantial increase in F_A , and the tremendous impact of surface topography not only enrich our understanding of surface interactions but also pave the way for innovation across several domains. Future research is anticipated to investigate deeper into these mechanisms, catalyzing the progress of material science and technology, and leading to the creation of innovative multifunctional materials.

Declaration of competing interest

The authors declare no competing conflict of interest.

Acknowledgments

The authors acknowledge the financial support from the National Natural Science Foundation of China under grant No. 52150710541. We extend our appreciation to the Ministry of Education Key Laboratory of Micro/Nano Systems for Aerospace and the Analytical & Testing Center, both of Northwestern Polytechnical University in Xi'an, P.R. China. Special thanks to CEITEC, Brno University of Technology, Brno, Czech Republic for facilitating the experiments conducted there. M.P. also appreciates support by the European Union under the REFRESH -Research Excellence For REgion Sustainability and High-tech Industries project number CZ.10.03.01/00/22_003/0000048 via the Operational Programme Just Transition. We also wish to express our gratitude to Dr. Feng Jianguo, Dr. Zhang Haoqing, Mr. Zhu Hanliang, Dr. Wong Chee Chung, and Dr. Alicia Toh for their invaluable assistance with manuscript preparation.

References

- [1] M. Yu, S. Chen, B. Zhang, D. Qiu, S. Cui, Why a lotus-like superhydrophobic surface is self-cleaning? An explanation from surface force measurements and analysis, *Langmuir*. 30 (45) (2014) 13615–13621.
- [2] M.R. Cutkosky, Climbing with adhesion: from bioinspiration to biounderstanding, *Interface Focus*. 5 (4) (2015) 20150015.
- [3] M. Sitti, R.S. Fearing, Synthetic gecko foot-hair micro/nano-structures as dry adhesives, *J. Adhes. Sci. Technol.* 17 (8) (2003) 1055–1073.
- [4] A. Peressadko, S.N. Gorb, When less is more: experimental evidence for tenacity enhancement by division of contact area, *J. Adhes.* 80 (4) (2004) 247–261.
- [5] N.M. Pugno, E. Lepore, Observation of optimal gecko's adhesion on nanorough surfaces, *Biosystems* 94 (3) (2008) 218–222.
- [6] A.K. Geim, S.V. Dubonos, I.V. Grigorieva, K.S. Novoselov, A.A. Zhukov, S. Y. Shapoval, Microfabricated adhesive mimicking gecko foot-hair, *Nat. Mater.* 2 (7) (2003) 461–463.
- [7] E.R. Naylor, T.E. Higham, Attachment beyond the adhesive system: the contribution of claws to gecko clinging and locomotion, *Integr. Comp. Biol.* 59 (1) (2019) 168–181.
- [8] K. Autumn, M. Sitti, Y.A. Liang, A.M. Peattie, W.R. Hansen, S. Sponberg, T. W. Kenny, R. Fearing, J.N. Israelachvili, R.J. Full, Evidence for van der Waals adhesion in gecko setae, *Proc. Nat. Acad. Sci.* 99 (19) (2002) 12252–12256.
- [9] W. Sun, P. Neuzil, T.S. Kustandi, S. Oh, V.D. Samper, The nature of the Gecko lizard adhesive force, *Biophys. J.* 89 (2) (2005) L14–L17.
- [10] B. Cappella, G. Dietler, Force-distance curves by atomic force microscopy, *Surf. Sci. Rep.* 34 (1-3) (1999) 1–104.
- [11] K. Autumn, Y.A. Liang, S.T. Hsieh, W. Zesch, W.P. Chan, T.W. Kenny, R. Fearing, R. J. Full, Adhesive force of a single gecko foot-hair, *Nature* 405 (6787) (2000) 681–685.
- [12] W. Weng, M. Tenjimbayashi, W.H. Hu, M. Naito, Evolution of and disparity among biomimetic superhydrophobic surfaces with gecko, petal, and Lotus effect, *Small*. 18 (18) (2022) 2200349.
- [13] A. Marmur, The lotus effect: superhydrophobicity and metastability, *Langmuir*. 20 (9) (2004) 3517–3519.
- [14] G.D. Bixler, A. Theiss, B. Bhushan, S.C. Lee, Anti-fouling properties of microstructured surfaces bio-inspired by rice leaves and butterfly wings, *J. Colloid. Interface Sci.* 419 (2014) 114–133.
- [15] X. Du, B. Xin, J. Xu, C. Wang, Biomimetic superhydrophobic membrane with multi-scale porous microstructure for waterproof and breathable application, *Colloids Surf. A: Physicochem. Eng. Aspects* 612 (2021) 125924.
- [16] T. Sun, L. Feng, X. Gao, L. Jiang, Bioinspired surfaces with special wettability, *Acc. Chem. Res.* 38 (8) (2005) 644–652.
- [17] W.R. Hansen, K. Autumn, Evidence for self-cleaning in gecko setae, *Proc. Nat. Acad. Sci.* 102 (2) (2005) 385–389.
- [18] C. Li, P. Dou, R. Zhao, Y. Shi, G. Fu, B. Shen, Preparation and super-hydrophobic mechanism analysis of FAS-17-modified SiO₂/PDMS coatings for high-voltage composite insulators, *Coatings* 13 (3) (2023) 563.
- [19] J.P. Matinlinna, C.Y.K. Lung, J.K.H. Tsoi, Silane adhesion mechanism in dental applications and surface treatments: a review, *Dental Mater.* 34 (1) (2018) 13–28.
- [20] K.C. Balram, D.A. Westly, M. Davanco, K.E. Grutter, Q. Li, T. Michels, C.H. Ray, L. Yu, R.J. Kasica, C.B. Wallin, The nanolithography toolbox, *J. Res. Natl. Inst. Stand. Technol.* (2016) 464–476.
- [21] H. Zhang, J. Pekárek, J. Feng, X. Liu, H. Li, H. Zhu, V. Svatoš, I. Gablech, P. Podešva, S. Ni, nanolithography toolbox—simplifying the design complexity of microfluidic chips, *J. Vacuum Sci. Technol. B, Nanotechnol. Microelectron.: Mater., Process., Measur., Phenomena* 38 (6) (2020) 063002.
- [22] F. Laerme, A. Schilp, K. Funk, M. In Offenber, *Bosch deep silicon etching: improving uniformity and etch rate for advanced MEMS applications*, technical digest, in: IEEE International MEMS 99 Conference. Twelfth IEEE International Conference on Micro Electro Mechanical Systems (Cat. No. 99CH36291), IEEE, 1999, pp. 211–216.
- [23] T.S. Kustandi, V.D. Samper, D.K. Yi, W.S. Ng, P. Neuzil, W. Sun, Self-assembled nanoparticles based fabrication of gecko foot-hair-inspired polymer nanofibers, *Adv. Funct. Mater.* 17 (13) (2007) 2211–2218.
- [24] S. Bhattacharya, A. Datta, J.M. Berg, S. Gangopadhyay, Studies on surface wettability of poly(dimethyl) siloxane (PDMS) and glass under oxygen-plasma treatment and correlation with bond strength, *J. Microelectromech. Syst.* 14 (3) (2005) 590–597.
- [25] V. Svatoš, W. Sun, R. Kalousek, I. Gablech, J. Pekárek, P. Neuzil, Single measurement determination of mechanical, electrical, and surface properties of a single carbon nanotube via force microscopy, *Sens. Actuat. A: Phys.* 271 (2018) 217–222.
- [26] S.C. Chen, J.F. Lin, Detailed modeling of the adhesion force between an AFM tip and a smooth flat surface under different humidity levels, *J. Micromech. Microeng.* 18 (11) (2008) 115006.
- [27] J.N. Israelachvili, *Intermolecular and Surface Forces*, Academic press, 2015.
- [28] S. Ge-Zhang, T. Cai, H. Yang, Y. Ding, M. Song, Biology and nature: bionic superhydrophobic surface and principle, *Front. Bioeng. Biotechnol.* 10 (2022) 1033514.
- [29] C. Guo, J. Sun, Y. Ge, W. Wang, D. Wang, Z. Dai, Biomechanism of adhesion in gecko setae, *Sci. China Life Sci.* 55 (2) (2012) 181–187.